ISTANBUL TECHNICAL UNIVERSITY ★ GRADUATE SCHOOL OF SCIENCE ENGINEERING AND TECHNOLOGY

DYNAMICS OF A LANDING GEAR MECHANISM

Ph.D. THESIS

Elmas ATABAY

Aeronautical and Astronautical Engineering

Aeronautical and Astronautical Engineering

JUNE 2012

ISTANBUL TECHNICAL UNIVERSITY ★ GRADUATE SCHOOL OF SCIENCE ENGINEERING AND TECHNOLOGY

DYNAMICS OF A LANDING GEAR MECHANISM

Ph.D. THESIS

Elmas ATABAY
(511052003)

Department: Aeronautical and Astronautical Engineering

Program: Aeronautical and Astronautical Engineering

Thesis Advisor: Prof. Dr. İbrahim ÖZKOL

JUNE 2012

İSTANBUL TEKNİK ÜNİVERSİTESİ ★ FEN BİLİMLERİ ENSTİTÜSÜ

BİR İNİŞ TAKIMI MEKANİZMASININ DİNAMİĞİ

DOKTORA TEZİ

Elmas ATABAY
(511052003)

Anabilim Dalı: Uçak ve Uzay Mühendisliği

Program: Uçak ve Uzay Mühendisliği

Tez Danışmanı: Prof. Dr. İbrahim ÖZKOL

HAZİRAN 2012

Elmas Atabay, a **Ph.D.** student of ITU **Graduate School of Science, Engineering and Technology** student ID 511052003, successfully defended the **thesis** entitled "Dynamics of a Landing Gear Mechanism", which she prepared after fulfilling the requirements specified in the associated legislations, before the jury whose signatures are below.

Thesis Advisor :	**Prof. Dr. İbrahim ÖZKOL** İstanbul Technical University	…………………..
Jury Members :	**Prof. Dr. Çingiz HACIYEV** İstanbul Technical University	…………………..
	Prof. Dr. Ata MUĞAN İstanbul Technical University	…………………..
	Prof. Dr. Erol UZAL İstanbul University	……….…………
	Asst. Prof. Dr. Hüseyin ALP KTO Karatay University	…………………..

Date of Submission : March 30 2012
Date of Defense : June 14 2012

To my family,

FOREWORD

The author wishes to express her gratitude

to her advisor Prof. Dr. İbrahim ÖZKOL for providing support during the preparation of this thesis,

to her jury members Prof. Dr. Çingiz HACIYEV and Prof. Dr. Ata MUĞAN for providing advice for the progress of this thesis,

to TÜBİTAK for the provision of financial support for four years of her doctoral studies,

to her parents Zernişan ANLI and Sertaç ANLI for the support they have provided in the thirty years of her life,

to her sister Zümrüt ANLI for being a smiling face, no matter what, and

to her husband Dr. Orhan ATABAY for the provision of a tranquil environment, for the long hours of discussion on this thesis and for trying to keep me on the right track and complete this work when I got lost.

Further thanks are due to a number of other names that will not be mentioned here but are not forgotten.

This was a long way, and the author is indebted to anyone who has partaken in this journey of seven years.

June 2012 Elmas ATABAY

TABLE OF CONTENTS

Page

ABBREVIATIONS

ER : Electrorheological
MR : Magnetorheological
MTOW : Maximum take–off weight

LIST OF TABLES

Page

LIST OF FIGURES

Page

DYNAMICS OF A LANDING GEAR MECHANISM

SUMMARY

Shimmy analysis of a torsional nose landing gear model is conducted. Shimmy is the oscillatory motion of the landing gear, caused by the interaction between the dynamics of the tire and the landing gear, and is an important phenomenon as it may lead to damage to the landing gear or the aircraft itself.

Basics and historical overview on landing gear systems and components, related terminology and different wheel arrangements are introduced. Main components of landing gear, namely shock absorbers, tires and brakes, are presented in detail. Shock absorber equations are given. Tire sizes and pressures, tire designs, categorization of tires and the most frequently used tire models are presented.Issues related to landing gear design are discussed. Retraction kinematics is given for both fuselage–mounted and wing–mounted main landing gear assemblies.

Shimmy is defined and causes of shimmy are given. Landing gear models are presented. A thorough literature survey on landing gear and shimmy is presented.Equations governing the torsional nose landing gear model are derived. Equations governing the stretched string tire model are derived. The model is linearized and Routh–Hurwitz criterion is applied to compute stability boundaries in parameter planes. Characteristic equation and eigenvalues are computed. Results show aggreement with literature.Effects of increasing and decreasing the caster length and tire half contact length on stability regions are investigated. Time histories of the linear and nonlinear models are obtained. Limit cycles are obtained and effects of the damping constant and taxiing velocity on limit cycles are observed.

Freeplay is defined and a literature survey on freeplay is given. Freeplay is incorporated into the torsional nose landing gear model. Effect of freeplay on the torsion angle, lateral tire deformation and limit cycles are observed.

Passive, active and semi–active control strategies are defined. Magnetorheological (MR) dampers are introduced. Working principles of MR dampers and various MR damper models are presented. An MR damper modeled using the current–dependent Bouc–Wen model is introduced to the torsional landing gear model with and without freeplay. A landing roll scenario is implemented.

This is a very detailed study in the sense that it includes both linear and nonlinear analysis tools, the concept of freeplay and an MR damper incorporated into the model. There exist a few studies in literature on wheel shimmy analysis or the shimmy analysis of landing gear, however, a detailed analysis of the torsional landing gear model with freeplay has not been performed. Incorporation of an MR damper in the landing gear model with and without freeplay is another originality. Application of the current–dependent Bouc–Wen model, is another brand new concept. Parameter identification of the Bouc–Wen model is accomplished using genetic algorithms.

BİR İNİŞ TAKIMI MEKANİZMASININ DİNAMİĞİ

ÖZET

Burulma serbestlik derecesine sahip bir burun iniş takımı modelinin shimmy (çalkalanma) analizi yapılmıştır. Shimmy, lastik ve iniş takımı dinamiklerinin etkileşiminden ortaya çıkan bir titreşim hareketidir ve iniş takımının veya uçağın kendisinin hasarına yol açabileceğinden önemli bir konudur.

İniş takımı sistemleri ve bileşenleri hakkında temeller ve tarihsel süreç, ilgili terminoloji ve farklı tekerlek yerleşimleri tanıtılmıştır. İniş takımlarının temel bileşenleri olan sönümleyici, lastik ve frenler detaylı biçimde sunulmuştur. Sönümleyici denklemleri verilmiştir. Lastik boyut ve basınçları, lastik tasarımları, lastiklerin sınıflandırılması ve en sık kullanılan lastik modelleri sunulmuştur. İniş takımı tasarımı ile ilgili hususlar tartışılmıştır.Gövdeye ve kanada bağlı ana iniş takımları için kapanma kinematiği denklemleri verilmiştir.

Shimmy tanımlanmıştır ve nedenleri verilmiştir. İniş takımı modelleri sunulmuştur. İniş takımları ve shimmy hakkında detaylı bir literatür araştırması verilmiştir. Burulma serbestlik dereceli bir burun iniş takımının hareket denklemleri verilmiştir. Gerili tel lastik modeli denklemleri çıkarılmıştır. Model lineerleştirilmiştir ve parametre uzayında kararlılık analizi yapılabilmesi için Routh–Hurwitz kriteri uygulanmıştır. Karakteristik denklem ve özdeğerler bulunmuştur. Sonuçlar literatür ile uyum sağlamaktadır. Kaster mesafesi ve lastik yarım temas mesafesinin artırılması ve azaltılmasının kararlılık bölgelerine olan etkisi araştırılmıştır.Lineer ve nonlineer modellerin neticeleri zamana bağlı olarak gösterilmiştir. Limit çevrimler elde edilmiştir ve sönüm katsayısı ile taksi hızının limit çevrimlere etkisi gözlemlenmiştir.

Boşluk tanımlanmıştır ve boşluk hakkında bir literatür araştırması verilmiştir. Burulma serbestlik dereceli burun iniş takımı modeline boşluk eklenmiştir. Boşluğun burulma açısı, yanal lastik deformasyonu ve limit çevrimlere etkisi gözlenmiştir.

Pasif, aktif ve yarı aktif kontrol stratejileri tanımlanmıştır. Manyetoreolojik (MR) sönümleyiciler tanıtılmıştır. MR sönümleyicilerin çalışma prensipleri ve çeşitli MR sönümleyici modelleri sunulmuştur. Akıma bağlı Bouc–Wen modeli ile gösterilen bir MR sönümleyici iniş takımı modeline eklenmiştir.Bir iniş senaryosu uygulanmıştır.

Bu çalışma, hem lineer hem nonlineer analiz araçlarını, boşluk kavramını ve bir MR sönümleyicisi içerdiğinden çok detaylı bir çalışmadır. Literatürde, tekerlek veya iniş takımı shimmy analizi hakkında az sayıda çalışma vardır, ancak boşluğa sahip bir burun iniş takımının detaylı bir analizi yapılmamıştır. Boşluklu ve boşluksuz iniş takımı modellerine bir MR sönümleyicisinin eklenmesi bir yeniliktir. Akıma bağlı Bouc–Wen modelinin uygulanması da bir başka yeniliktir. Bouc–Wen modelinin parametreleri genetik algoritmalar ile bulunmuştur.

1. INTRODUCTION

This thesis covers the shimmy analysis of a torsional nose landing gear model. Shimmy is an oscillatory motion of the landing gear, caused by the interaction between the dynamics of the tire and the landing gear. Shimmy is an important phenomenon as it may lead to damage to the landing gear or the aircraft itself. It is an unstable phenomenon occurring with a certain combination of physical parameters such as mass, damping, geometrical quantities, speed and freeplay. It is difficult to determine shimmy analytically since it is a very complex phenomenon, as factors such as wear and ground conditions are hard to model.

1.1 Contents of Thesis

Section 2 is on landing gear systems and components. Basics and historical overview are given in 2.1. Different wheel arrangements are given in 2.2. Related terminology is given in 2.3. Main components of landing gear, namely shock absorbers, tires and brakes, are presented in detail in 2.4.

2.4.1, 2.4.2, 2.4.3 and 2.4.4 are on shock absorbers, tires, tire models and brakes, respectively. Four different types of shock absorbers are presented in 2.4.1 Rigid axle shock absorbers, solid spring shock absorbers, levered bungee shock absorbers and oleo–pneumatic shock absorbers are defined in sections 2.4.1.1–2.4.1.4, respectively. The section on tires, 2.4.2, includes tire sizes and pressures in 2.4.2.1, tire designs in 2.4.2.2 and categorization of tires in 2.4.2.3. Section 2.4.3 on tire models gives the most frequently used tire models. Point contact model is introduced in 2.4.3.1, stretched string model is introduced in 2.4.3.2, straight tangent model is introduced in 2.4.3.3, rigid ring model is introduced in 2.4.3.4 and the state–of–the–art models are introduced in 2.4.3.5.

Landing gear of the Cessna 172 and Boeing 757 aircraft are given for comparison as numerical examples in 2.5. Issues related to landing gear design are given in 2.8.

Design considerations, concept selection, gear length, wheel, tire and brake selection and shock absorber design are described in 2.8.1–2.8.5.

2.9 is on retraction and stowage. Retraction kinematics is given for both fuselage–mounted and wing–mounted main landing gear assemblies. 2.10 is on landing gear simulation and control. 2.11 gives the definitions of passive, semi–active and active control systems. 2.12 gives the major landing gear manufacturers.

Section 3 is on shimmy. Shimmy is defined in 3.1, causes of shimmy are given in 3.2, an accident related to shimmy is given in 3.3, gear walk, a similar concept, is defined in 3.4, suppression of shimmy is discussed in 3.5, shimmy dampers are introduced in 3.6 and landing gear models are presented in 3.7. A landing gear model with torsional degree of freedom is shown in 3.7.1, the one with torsional and lateral degrees of freedom is shown in 3.7.2 and the one with torsional, lateral and longitudinal degrees of freedom is shown in 3.7.3.

Section 4 is a detailed literature survey on landing gear and shimmy. Literature on landing gear shimmy is summarized in 4.1. Literature on the wheel shimmy problem is summarized in 4.2. Literature on tire models is summarized in 4.3. Literature on solution techniques are summarized in 4.4. Literature on the trend in treating shimmy is summarized in 4.5. Literature on semi–active and active control of shimmy is summarized in 4.6. Literature on software development is summarized in 4.7. Literature on a multibody dynamics approach is summarized in 4.8. Literature on landing gear structural analysis and design is summarized in 4.9. Literature on aeroacoustics and noise prediction is summarized in 4.10. Literature on flight simulators is summarized in 4.11. Selected books on aircraft analysis and design, landing gear design and tire and vehicle dynamics are given in 4.12.1–4.12.3, respectively. Related dissertations found in literature are given in 4.13.

Shimmy analysis of a torsional nose landing gear model is conducted in section 5. Equations governing the torsional nose landing gear model are derived in 5.1. Equations governing the stretched string tire model are derived in 5.2. The model is linearized in 5.3 for stability analysis. Characteristic equation and eigenvalues are computed in 5.4. Routh–Hurwitz criterion is applied in 5.6 to compute stability boundaries in parameter planes. Effects of increasing and decreasing caster length and half contact length are investigated in 5.7. Time histories of the linear model are obtained in 5.8. Limit cycles are obtained and effects of the damping constant and taxiing velocity on shimmy are observed in 5.9.

Section 6 is on freeplay and incorporation of freeplay into the landing gear model. 6.1 is on the definition of freeplay. 6.2 gives a literature survey on freeplay. 6.3 is on the modeling of freeplay. 6.4 is on the incorporation of freeplay into the torsional landing gear model. 6.5 is on the effect of freeplay on the torsion angle, lateral tire deformation and limit cycles.

Section 7 is on semi–active control of shimmy via a magnetorheological (MR) damper. 7.1 is an introduction to suspension systems. Passive, semi–active and active suspension systems are introduced in 7.2. MR dampers are introduced in 7.3. Sections 7.4 and 7.5 are on the physics and working principles of MR dampers. MR damper technology is presented in 7.6. A literature survey on MR dampers is given in 7.7. MR damper models are given in 7.8. Bouc–Wen model, the most frequently used model is presented in detail in 7.9. Simple, modified and current–dependent Bouc–Wen models are presented in 7.9.1–7.9.3. Parameter identification is discussed in 7.10. Application of MR dampers in landing gear shimmy is discussed in 7.1 and an MR damper is applied to the torsional landing gear model in 7.12. An MR damper is introduced into the torsional landing gear model with freeplay in 7.14. A landing roll scenario is implemented in 7.16.

It was decided to work on the geometrical and structural parameters found in literature because the real focus of this study is an analysis of landing gear shimmy, and how various parameters effect shimmy, rather than finding real aircraft data.

1.2 Significance of Thesis

The significance of this thesis can be listed as follows.

- This is a detailed study in the sense that it includes both linear and nonlinear analysis tools, the concept of freeplay and an MR damper incorporated into the model. The nose landing gear model with torsional degree of freedom has been analyzed in depth. First, the model has been linearized to apply linear analysis tools such as eigenvalue analysis and Routh–Hurwitz criterion for determination of stability regions in the parameter space. Effects of increasing and decreasing the caster length and half contact length on stability regions in the parameter plane have been investigated. Next, limit cycles of the nonlinear model have been obtained and effects of the damping constant and taxiing velocity have been investigated. Freeplay has been incorporated into the model and the effect of freeplay on the torsion angle, lateral tire deformation and limit cycles has been investigated. Finally, an MR damper modeled using the current–dependent Bouc–Wen model has been incorporated into the torsional landing gear model.

- There exist a few studies in literature on wheel shimmy analysis or the shimmy analysis of landing gear, however, a detailed analysis of the torsional landing gear model with freeplay has not been performed.
- A unique aspect of this study is that the MR damper has been applied to the landing gear model with freeplay. Incorporation of an MR damper in the landing gear model with and without freeplay is an originality.
- Application of the current–dependent Bouc–Wen model, is another brand new concept. An MR damper modeled using the current–dependent Bouc–Wen model has been applied to a torsional nose landing gear model. Mathematical relations related to the current–dependent Bouc–Wen model have been proposed in literature, however, they have not been applied to any problems in literature to date. The advantage of the model is that parameters do not have to be identified for each current input.
- Parameter identification of the Bouc–Wen model has been accomplished using genetic algorithms.
- The concept of landing gear systems and shimmy has been overlooked by many Ph.D. candidates. This thesis includes a very thorough literature survey on aircraft landing gear systems and shimmy. It also includes a very thorough presentation of the components of landing gear systems, the concept of shimmy, freeplay and MR dampers.

2. AIRCRAFT LANDING GEAR SYSTEMS AND COMPONENTS

Landing is the period of flight starting when an aircraft gains contact with the ground and ending when it is finally stationary. Landing gear is the structure supporting an aircraft on the ground and allowing it to taxi, take off and land. It absorbs the vertical kinetic energy of the landing impact and carries the weight of the aircraft at all ground operations. It is also known as undercarriage, and is a heavy and complex item serving aircraft ground handling. Landing impact marks the first stroke of the aircraft suspension.

Landing gear is a complex multi degree of freedom system and is the most failure prone system of commercial jets. Although the main task of an aircraft is to fly, according to airlines specifications, an aircraft should sustain up to 90000 cycles comprising one take off, cruise and landing, in addition to 500000 km on the ground during its lifetime. More than 50 % of aircraft accidents take place before or right after take off and touchdown and about one third of aircraft accidents are related to landing gear. Apparently, although the ground section of flight takes only a short period of time, landing gear design and maintenance is an issue requiring improvement [1,2].

Typically, wheels equipped with shock absorbers are used for operation on solid ground, but skis or floats can also be used, depending on the terrain that the aircraft is going to land on. Functions of the landing gear components can be listed as [3,4]

- supporting the aircraft when in place or towed
- absorbing landing and taxiing shocks and partially transmitting these loads to the airframe
- providing ability for ground maneuvers such as taxi, take–off run, landing roll and steering
- providing braking capability

- protecting ground surface
- keeping propellers safely apart from the ground

Vertical loads are primarily due to touchdown speeds and taxiing over rough surfaces, longitudinal loads are due to braking loads and rolling friction loads, and lateral loads are due to landing and taxiing in cross wind.

The first wheeled landing gear appeared shortly after the first flight by the Wright brothers in 1903. No 14 bis, manufactured by Santos–Dumont had a wheeled landing gear and performed the first unaided flight by a heavier–than–air aircraft in 1906. Many wheeled aircraft designs were flown in the following years. Configurations had settled down to tail wheel landing gear by the time of the WWI. Landing gear often contained primitive shock absorption on soft surfaces such as grass fields, and this was achieved by wrapping bungee cords around main axles. Apparently, very little absorption was present [5, 6].

In the years between WWI and WWII, landing gear designs developed towards retractable types, employing shock absorbing systems. This was due to the fact that during the war years, aviation progressed as a means to incorporate weaponry. Since aircraft weights and landing speeds were constantly increasing, increased shock absorption became necessary, and so hydraulic cylinders came to use. Some of the desired shock absorption was provided by tires with large sections, though it did not contribute greatly. After WWII, there were improvements in various fields related to landing gear, such as shock absorber design, radial tires and braking systems [5,7].

2.1 Basics and Historical Overview

There are two types of landing gear designs. A conventional landing gear, also referred to as a taildragger or a tail–wheel, has two main wheels towards the front of the aircraft and a single, much smaller, sometimes steerable wheel or skid at the rear, as in figure 2.1. A tricycle landing gear, on the other hand, has two main wheels or wheel assemblies under the wings and a third smaller wheel in the nose, as in figure 2.2.

The conventional landing gear arrangement was common during the early propeller era, because it allows more room for propeller clearance. Conventional landing gear are considered harder to take off and land because the arrangement is unstable. Such a design causes less drag and thereby increases aircraft speed by 2 to 3 %, however the raised nose impairs forward visibility on the ground and the aircraft is prone to the problem of ground looping, which is a rapid rotation of an aircraft in the horizontal plane. It happens particularly when the aircraft still has speed after landing, resulting in instability which can even tip the aircraft over if the overturn angle θ is exceeded [8,9].

Earlier designs had tail–dragging type landing gear, however they have been replaced by nose–wheel tricycle landing gear. The first nose–wheel design appeared in 1908 in a Curtis aircraft. Although there are specialized landing gear manufacturers, like Messier in France and Dowty in the United Kingdom, manufacturers of small aircraft can build their own landing gear, most of which are the fixed type [8].

Most modern aircraft have tricycle landing gear. The tricycle configuration is the most common design since it provides good visibility over the nose during ground operation, is stable against ground loops, has good steering characteristics and is level when on the ground, which is important for passenger aircraft. Tailwheel configuration provides poor visibility over the nose during ground operations, has a strong tendency for ground loops and poor steering characteristics. For these reasons, tailwheel configuration is used primarily in home–built aircraft and aircraft that must operate from rough surfaces because the nose gear tends to become very heavy if it is designed to withstand severe stresses [3].

Figure 2.1 shows the conventional landing gear of a SAN Jodel Mousquetaire, a French monoplane. Figure 2.2 shows the tricycle landing gear of a Mooney M20.

Figure 2.1: Conventional landing gear of a SAN Jodel D.140 Mousquetaire [9].

Figure 2.2: Tricycle landing gear of a Mooney M20 [9].

Landing gear creates a considerable amount of drag in extended position during flight, thus it needs to be retracted to minimize drag. Once the aircraft is airborne, the landing gear is retracted to minimize drag. Landing gear stowage bay should be sized compactly, located either in the wing or the fuselage, though it may sometimes be in the nacelles mounted to the wings, depending on the design. The retraction mechanism of landing gear systems is often hydraulically operated, whereas an electrical motor is sufficient for smaller aircraft. Some are even manually operated. Figure 2.3 shows the schematic of a hydraulically operated landing gear where the wing is stowed into the wing root.

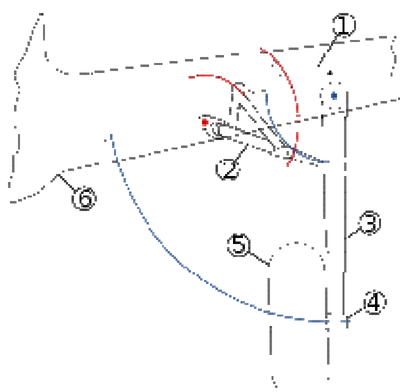

Figure 2.3: A hydraulically retracted landing gear [9].

Most aircraft had fixed landing gear until WWII, but almost all fighters and bombers had retractable landing gear by the time WWII began. A retractable landing gear was first designed in 1876, but it was not until 1917 that a retractable landing gear appeared. The earliest retractable landing gear was used on the Bristol Jupiter racing aircraft. By the end of the 1920's, the aerodynamic advantage of retractable landing gear was favored despite the added complexity, weight and loss of internal space. Lockheed's 8D Altair had a fully retractable landing gear and made its first flight in

1930. In 1934, retractable landing gear were used on commercial aircraft, Douglas DC–2 and Boeing 247–D. Figure 2.4 shows a Boeing 737 with its landing gear retracted in the wheel wells.

Figure 2.4: A Boeing 737 with retracted landing gear [9].

A small tail wheel can be added to aircraft with tricycle landing gear, to prevent tail strikes when taking off. Concorde, for instance, had a retractable tail wheel, as delta winged aircraft need a high angle when taking off. Boeing 727 also has a retractable tail wheel. Some aircraft with retractable conventional landing gear have a fixed tail wheel. Table 2.1 summarizes the advantages and disadvantages of fixed and retractable landing gear [3,9].

Table 2.1: Advantages and disadvantages of fixed and retractable landing gear.

	fixed landing gear	**retractable landing gear**
drag	high	minimal
weight	low	high
complexity and cost	low	high
maintenance cost	low	high

Since WWII, landing gear design has progressed in many areas. Tire design has moved towards radial tires, brake materials such as beryllium and carbon have been developed, skid control systems have been digitized with fiberoptic controls, high–strength steels and stress–corrosion–resistant aluminum alloys have become available and the subject of shock absorption has been better understood. Transport aircraft are heavier than they used to be, so larger landing gear are required and must be stowed in areas that will have the minimum effect on the airframe structure and drag, while not damaging the runway. For example, Boeing 747 is more than twice as heavy as the 707 and 28 times as heavy as the DC–3 [7–9].

Large aircraft employ more wheels to deal with heavy weights. The first giant aircraft that was mass produced was the Zeppelin Staaken R.VI of Germany, a bomber that first flew in 1916, and had a total of 18 wheels for its landing gear, 2 on its nose gear and 16 on its main gear units under engine nacelles. Large aircraft commonly employ bogie configurations. A strut with more than one wheel is called a bogie. Large aircraft have many wheels on a bogie system so that their weight is distributed. Airbus A340–500 has an additional four–wheel bogie on the fuselage centerline. Boeing 747 has a dual nose-wheel assembly and 4 sets of four–wheel bogies. There is one set under each wing and the inner sets are on the fuselage, a little rearward of those under the wings, adding to a total of 18 wheels. Airbus A380 has a four–wheel bogie under each wing and 2 six–wheel bogies under the fuselage, as in figure 2.5. World's largest and heaviest jet Antonov 225 has the largest number of individual wheel–tire assemblies in landing gear design, with 4 wheels on the twin–strut nose gear units and a total of 28 main gear wheel–tire units, adding to a total of 32 wheels and tires. Its main landing gear is a bogie system with 7 struts per side, each with 2 wheels, as in figure 2.6 [1,8,9].

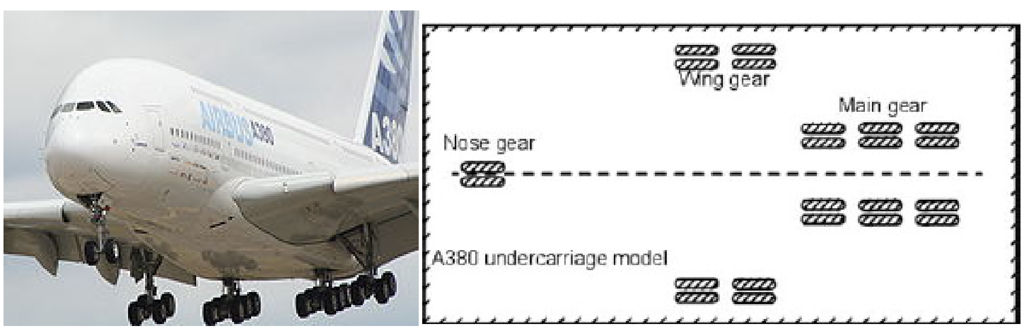

Figure 2.5: a. Airbus A380 landing gear[9].**b.** Airbus A380 wheel arrangement [8].

Figure 2.6: Main landing gear of Antonov 225 [9].

A landing gear is composed basically of a strong support spindle called the strut and a heavy–duty shock absorber that can handle heavy landings due to rapid descent. A strut, also called a landing gear leg, is a support shaft with a shock absorber. It has a steering mechanism with shimmy control. Shimmy is the oscillation of the wheels about the support shaft and strut axis and shimmy control is the control of dynamic instability [3,8].

The role of the shock absorber is to absorb and dissipate energy during landing impact so that the airframe, structural components and passengers are subject to tolerable forces and accelerations. Landing gear shock absorber should be designed for the cases of landing and ground maneuvering. A landing gear should perform satisfactorily in various landing scenarios such as level landings, tail–down landings, one–wheel landings and crabbed landings.

Vertical loads during landing are dissipated by shock absorbers and tires, all of which must absorb the maximum energy at the relevant design vertical velocity. As for the case of ground maneuvers such as braking, taxiing, take–off run, landing roll, steering and towing, an aircraft may experience shock loads due to uneven surfaces, mostly during taxiing and take–off and landing rolls. A shock absorber needs to absorb the energy of landing efficiently, meaning it should compress slowly. During taxiing, axial compression speed of the shock absorber is high when the landing gear rolls over a remarkable roughness on the runway [5,10].

Figures 2.7 and 2.8 show the schematics of a main landing gear and a nosegear, respectively. A main landing gear basically consists of a strut attached to the fuselage, wheels and a damper to absorb the landing impact. The main landing gear should also perform braking and withstand maneuvering or braking loads. In some designs, the nose landing gear also performs braking.

A nose landing gear, or a nosegear, is lighter as it needs to withstand smaller loads. During pushback, nosegear is able to move freely with the aid of a by–pass system allowing the flow of hydraulic fluid from one side to another. This by–pass is shut down when steering is achieved through controls. Depending on the type of aircraft, steering can be achieved through an independent tiller, which is like a steering wheel or a lever, or through the use of rudder pedals. Rudder pedals can only perform minor corrections in steering. Differential braking, or the application of different amounts of braking in the right and left sides, is another method of steering [4].

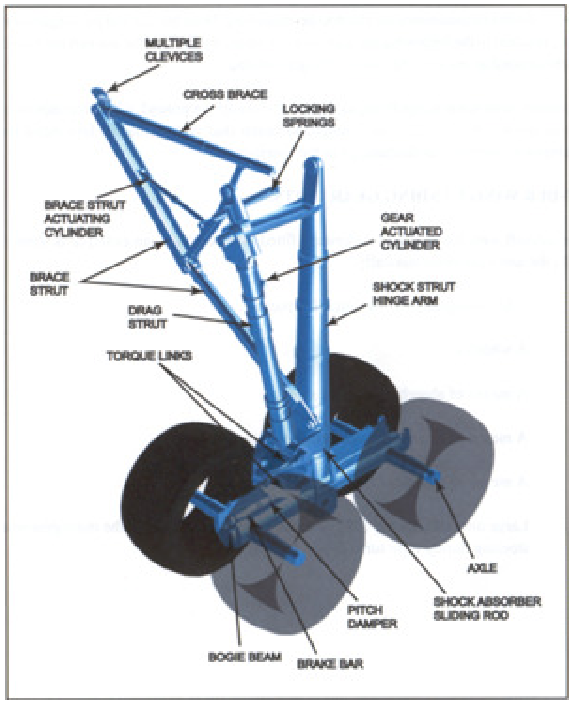

Figure 2.7: Schematic of a main landing gear.

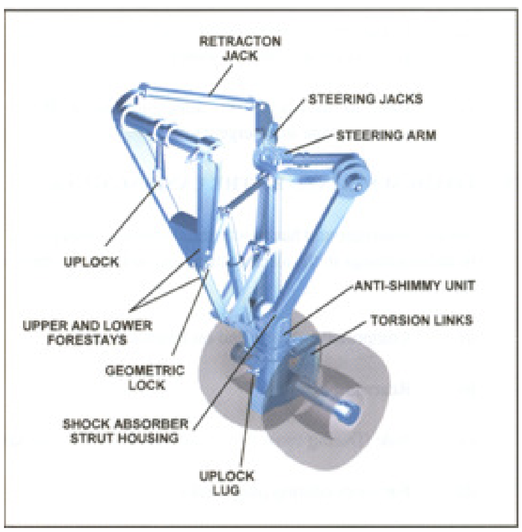

Figure 2.8: Schematic of a nosegear.

Cantilevered, semi–levered and levered landing gear configurations are shown in figure 2.9. Aircraft weighing below 100 tons generally employ nose landing gear with a twin wheeled cantilevered design. A four–wheel bogie is employed for the nose landing gear of aircraft with higher weights. For example, Boeing 747 has four

four–wheel bogies and Airbus A340 has two four–wheel bogies and a twin wheeled center gear mounted on the fuselage. Aircraft with even higher weights employ six–wheel bogies or the tricycle layout can be abandoned and additional landing gear below the fuselage can be introduced, as in the case of Airbus A380, shown in figure 2.5 [1].

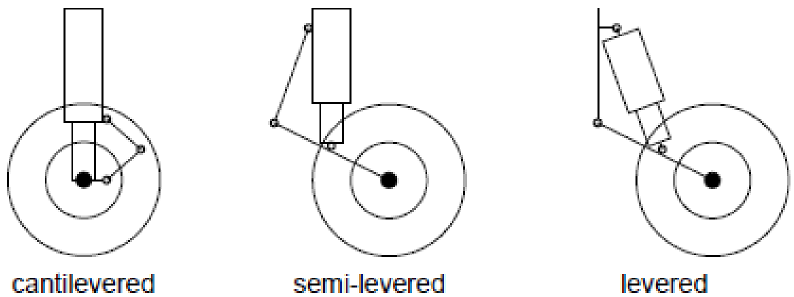

Figure 2.9: Cantilevered, semi–levered and levered landing gear configurations [1].

Figure 2.10 shows the components of a twin–wheeled cantilevered main landing gear [1,11]. Main fitting, the largest part, combines an air spring and a hydraulic damper. Side stay is its lateral support, consisting of two members to allow retraction. Sliding member slides vertically with respect to the main fitting. Torque links transfer moments between the main fitting and the sliding member and prevent rotation of the sliding member with respect to the main fitting. Wheel axle has a mechanical trail with respect to the vertical rotation axis between the sliding member and the main fitting. Shimmy damper is in series with the torque links. It is a hydraulic damper with limited stroke of a few degrees of yaw.

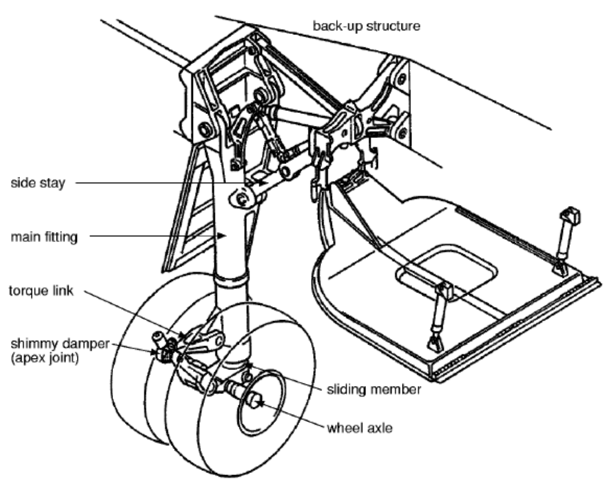

Figure 2.10: Components of a cantilevered main landing gear [1].

A landing gear has an attachment point to the aircraft and can have more than one support point, called a strut. For example, Airbus A380 mentioned above has one nose wheel, two bogies mounted to the wings and two to the fuselage, meaning it has five support points. Various strut designs are seen in figure 2.11.

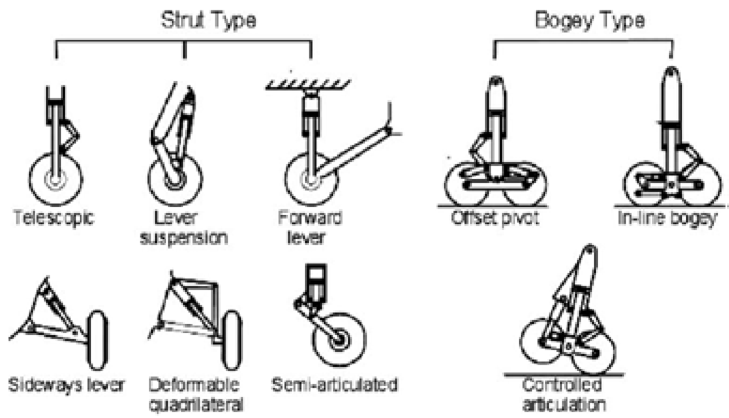

Figure 2.11: Strut types [8].

Mass of the landing gear is typically 4 to 5 % of the maximum take–off mass, $MTOM$. For large aircraft, it can be as much as 7 % of the maximum take–off mass, weighing up to 3 tons and costing up to 5 % of the aircraft total price [8]. Materials considered for aviation purposes are chosen majorly in terms of their strength and weight. Steel is generally considered heavy, but it is chosen for load–bearing structures such as the landing gear, requiring low volume and high strength. New materials may be considered as alternatives where high strength is combined with lighter weight. Aluminum alloys will most likely take the place of steel since their specific strength is greater than that of titanium–based alloys. During the design optimization, each component has to be sized so that the maximum stresses do not result in plastic deformations [5].

Problems may occur when taking off from runways covered with slush, ice or other impurities. In some cases during take–off, the landing gear is covered with water or snow that freezes once the landing gear is retracted such that the landing gear cannot be extended when the aircraft arrives at its destination. In such cases, the pilot should extend the landing gear once more after taking off so as to get rid of the debris on the landing gear.

2.2 Wheel Arrangements

Landing gear are generally categorized by the number and alignment of their wheels. Large aircraft employ more wheels to be able to deal with weights as an aircraft is supported on the ground by the wheels and tires. For heavy aircraft, weight is distributed over several wheels because the load per wheel is restricted. Figure 2.12 shows arrangements for engaging more than one wheel per strut and the accepted terminology. Number of struts, number of wheels per strut, and tire spacing and pressure must be considered when distributing the load. A higher maximum take–off mass requires an increased number of wheels. Conventional wheel arrangements are single, twin, triple and quadruple on a bogie. Next level is to place wheels in a dual row as a single, twin or triple tandem [7,8].

Runways must tolerate the weight of heavy commercial aircraft. For example, if the strength of a field is given as T–50/TT–100, it means the airfield is cleared to accept aircraft weighing 50000 lb with a twin or dual wheel landing gear or 100000 lb with a twin tandem or dual tandem landing gear [7,8].

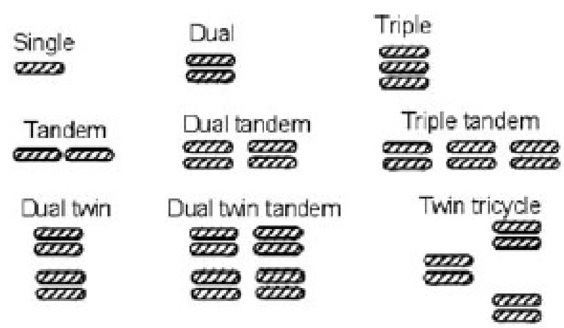

Figure 2.12: Wheel arrangements [8].

2.3 Nomenclature

A landing gear consists of wheels on struts attached to the aircraft. Geometric parameters in placing the wheels relative to the position of the center of gravity of the aircraft are the wheel base and wheel track, and are demonstrated in figure 2.13. Wheel base is the distance between the front and rear wheel axles in the vertical plane of symmetry, and wheel track is the distance between the main wheels in the lateral plane. These parameters determine the aircraft turning radius on the ground.

Ground maneuvering capability of an aircraft is expressed in terms of its minimum turn radius. This minimum radius depends on the location of the landing gear and the steering ability of the nose gear. An aircraft must turn in a specified radius within the runway width. Radius of the turn is the distance between the nose wheel and the center of the turn. Turning is achieved by steering the nose wheel. Combined nose and main assembly steering systems have been developed for newer large aircraft. Tight turns can be achieved by asymmetric braking and thrust [3,8].

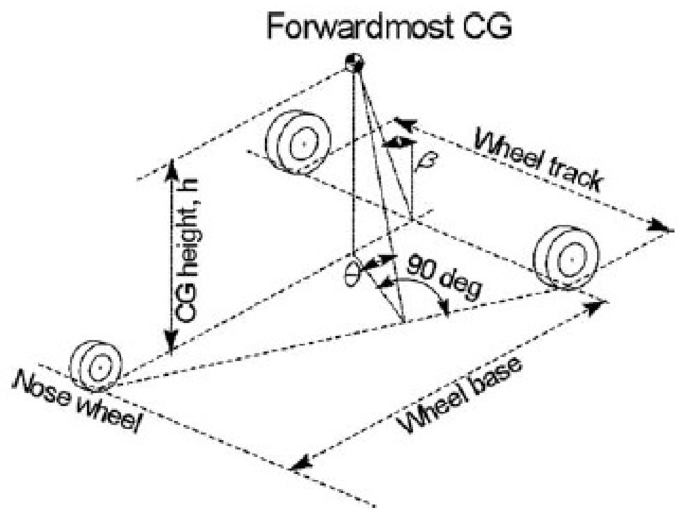

Figure 2.13: Position of the center of gravity of the aircraft relative to the landing gear [8].

Forwardmost position of the center of gravity of the aircraft determines the overturn characteristics of the aircraft. Overturning occurs about the axis joining the nose wheel and main wheel ground contact point, when the leading edge is about to hit the ground. There is a maximum angle for a tilted aircraft which has its center of gravity on top of a main wheel, beyond which the aircraft would turn over on its side, called the overturn angle, θ. An aircraft can also tip backwards if the rearmost center of gravity is behind the main wheel, in the case of a tricycle landing gear, or forwards if its center of gravity is in front of the main wheels, in the case of a tail–wheeled landing gear, as seen in figure 2.14. Most aircraft have θ between 40° and 50° [8].

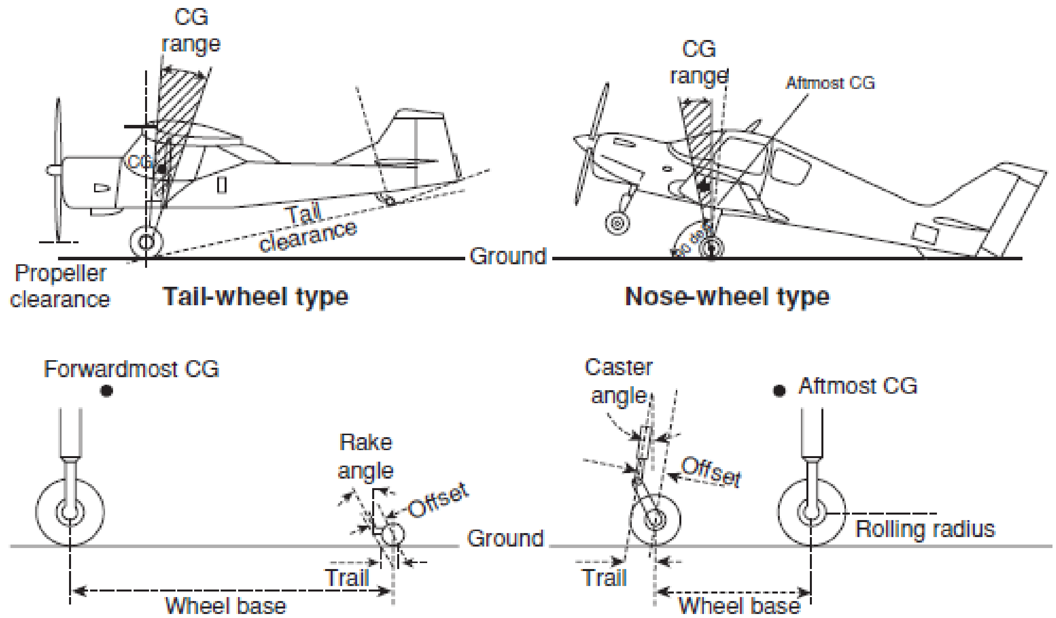

Figure 2.14: Landing gear layout [8].

Fuselage clearance angle γ is an important design consideration. Center of gravity of an aircraft should not be behind the wheel contact point at rotation during take–off. If β is the angle between the vertical and the line joining the wheel contact point with the center of gravity of the aircraft, then β must be greater than γ so that the center of gravity is not behind the wheel contact point, as seen in figure 2.15. Generally, β should be greater than or equal to 15° and γ should be between 12° and 16° [8].

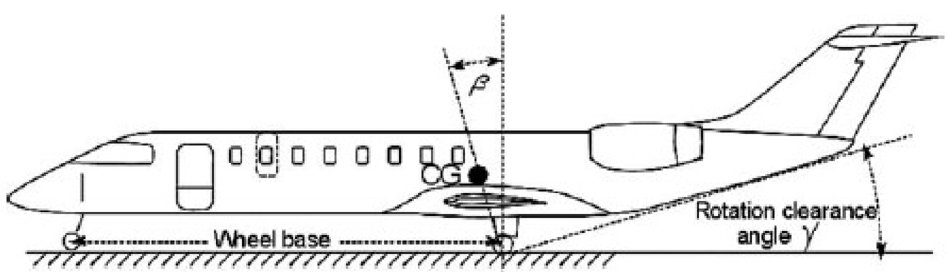

Figure 2.15: Rotation clearance angle [8].

Definitions of some parameters related to the nose wheel and strut are given below [7,8].

- Caster or rake angle: Angle between the caster axis, also known as the wheel swivel axis or the spindle axis, and a vertical line through the ground contact point of the swivel axis, as seen in figure 2.16. This parameter is important for the static and dynamic stability behavior of the wheel with respect to the strut.

- Caster length: Perpendicular distance from wheel contact point to ground and spindle axis.
- Trail: Distance from the point where the wheel contacts the ground to the point where the wheel swivel axis intersects the ground. In other words, it is the distance from the intersection of the shock absorber centerline with the ground to the center of the contact area of the wheel, measured along the ground. This parameter is important for the static and dynamic stability behavior of the wheel with respect to the strut. When the aircraft is static as in figure 2.17.a, the center of the contact area is directly under the strut centerline. When the wheel is moving, center of the contact area moves slightly backwards, as in figure 2.17.b, named as dynamic trail.
- Offset: Perpendicular distance from wheel axis and spindle axis.
- Loaded radius: Distance from wheel axis to ground contact point under static loading.
- Rolling radius: Distance from wheel axis to ground contact point under dynamic loading.

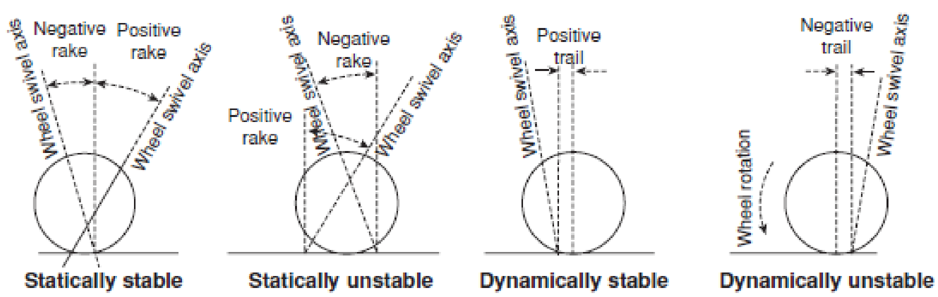

Figure 2.16: Rake angle and trail [8].

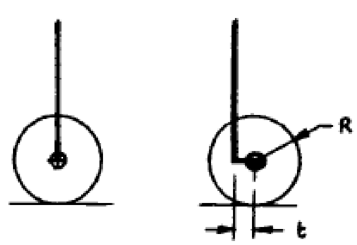

Figure 2.17: a. trail = 0 **b.** trail > 0 [8].

- Caster: Casters are wheels with pivoting arrangements allowing them to line up with the direction of motion. They are found on many steered wheels on cars, bicycles, motorcycles and aircraft and are intended to prevent the wheel from producing side forces so that the vehicle can move in a straight line in the absence of steering torques. A few powered vehicles have been constructed at the beginning of the age of powered vehicles with no caster at the steered wheels. It has been recognized soon that caster not only stabilizes the wheel, but also gives the wheel the ability to straighten out by itself during the absence of a steering torque. One disadvantage of using casters, however, is that they exhibit shimmy oscillations. There are various caster models, such as vertical axis caster, inclined axis caster and vertical axis caster with pivot flexibility, but they will not be included here for purposes of refraining from digression [12].

2.4 Components of Landing Gear

Most important components of a landing gear are the shock absorber, tires and the brakes. Based on the type of spring used, shock absorbers can be classified as those using a solid spring made of steel or rubber and those using gas or oil or a mixture of the two, called oleo–pneumatic shock absorbers.

Oleo–pneumatic systems, combining oil and air, are pneumatic shock absorbers, acting like springs, combined with hydraulic dampers. An oleo–pneumatic system acts as a damper by dissipating kinetic energy of the vertical velocity, and also as a spring for the lateral ground friction load. Oleo–pneumatic absorbers are preferred in modern aircraft due to their high efficiency under dynamic loading conditions in terms of energy absorption and dissipation.

Landing gear of most passenger aircraft consist of an oleo–pneumatic shock absorber (oleo), disk brakes and a multi–tire combination [2,5]. Other types of shock absorbers will also be mentioned in 2.4.1 for purposes of completeness.

2.4.1 Shock Absorbers

Energy absorption during landing is an important function of the landing gear. Shock absorbers are of significant importance to aircraft performance and also of significant cost. Shock absorbers are the most complex part of the landing gear. Function of a shock absorber is to absorb and dissipate kinetic energy so that the accelerations acting upon the airframe are reduced to an acceptable level. Landing is sometimes referred to as a "controlled crash", but it would actually be a disaster without the shock absorbing mechanism. A shock absorber with a large stroke within the range 0.3–0.6 m is required to limit the forces occurring during landing impact. For this reason, shock absorber is the most important component in the landing gear [7].

Main types of shock absorption used in aircraft are rigid axle absorbers, solid spring absorbers, levered bungee and oleo–pneumatic shock struts. The first three of these systems are mainly historical and are almost never considered in modern commercial aircraft designs. They only appear in light civil aircraft where the cost of the oleo–pneumatic shock absorber is not desirable. In such cases, solid spring elements are often preferred.

Shock absorbing elements are exposed to larger loads in cases of wind gusts, surface irregularities and human errors, such that design sink speeds are exceeded. In such cases, reserve energy dissipation devices, fitted between the shock absorbing element and the aircraft, absorb energy by deforming plastically.

2.4.1.1 Rigid axle shock absorber

Rigid axle shock absorbers were used in the early days of aviation history and relied on the absorption of the tires and the axle they are fitted to, as in figure 2.18. They are still used in light aircraft, such as Cessna, due to their simplicity and low cost.

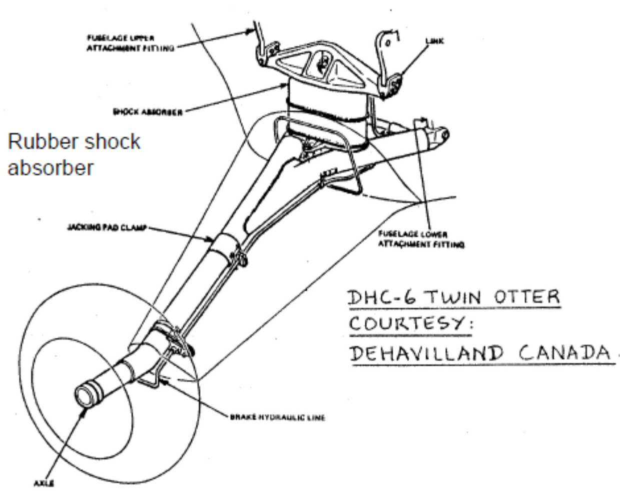

Figure 2.18: Rigid axle shock absorber [5].

2.4.1.2 Solid spring shock absorber

A solid spring arrangement uses a solid but flexible strut to connect the wheel arrangement to the fuselage, enabling shock absorption by allowing vertical displacement of the aircraft through bending. A disadvantage present in such systems is that they are suitable only for light aircraft having low sink speeds as the strut reverberates up and down like an undamped spring, causing the aircraft to bounce up and down. In addition, this motion causes excess wear on the tires, known as scrubbing. Such a system is shown in figure 2.19.

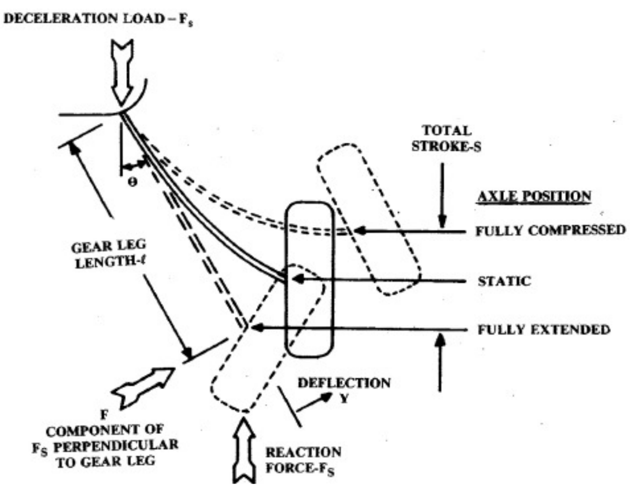

Figure 2.19: Solid spring shock absorber [5].

2.4.1.3 Levered bungee shock absorber

A levered bungee system engages a rubber shock cord along with a metal strut. Although this system is similar to a solid spring arrangement, the levered bungee system has improved energy absorption and damping characteristics, due to the rubber shock cord. Like in a solid spring arrangement, vertical displacement of the aircraft causes tire scrubbing through an outward movement of the landing gear. Such a system is shown in figure 2.20.

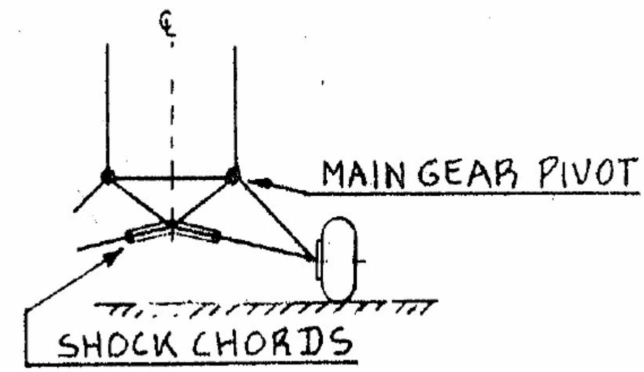

Figure 2.20: Levered bungee shock absorber [5].

2.4.1.4 Oleo–pneumatic shock absorber

A shock absorber either uses a solid steel or rubber spring or a fluid spring with gas or oil. The mixture of the two results in an oleo–pneumatic shock absorber. Such absorbers have high efficiency in terms of energy absorption and dissipation. Oleo–pneumatic shock absorbers are the most common shock absorber system in medium to large aircraft, since they provide the best shock absorption ability and effective damping. In other words, landing gear employing oleo–pneumatic shock absorbers provide the most efficient shock absorption. Shock absorber characteristics are validated by drop tests and landing tests.

Landing gear shock absorbers on most commercial aircraft consist of two interconnecting cylinders containing oil and nitrogen. Nitrogen is a substitute for a spring, while oil absorbs the energy of the shock. This is accomplished by forcing oil through an orifice and compressing air. Vertical energy dissipation is taken over mostly by an oleo–pneumatic shock absorber, combining a gas spring with oil and additional friction damping. Damping force is provided by oil flow forced through an orifice whose cross section is different for negative or positive stroke to achieve good efficiency. Oil flow is controlled by a pin such that the orifice area depends on the displacement of the shock absorber. Since the hydraulic damping force is proportional to the compression speed and inversely proportional to the cross section of the orifice, damping force, and thus the vertical load, increases prominently if the orifice does not expand immediately.

Oleo–pneumatic shock absorbers are highly efficient due to the combination of the spring force and the flow of hydraulic fluid through the orifice element. Spring force is the result of the compression of gas and the damping force is the result of the hydraulic fluid flow. As a result, the system can both absorb and remove vertical kinetic energy. Passive oleo–pneumatic shock absorbers can reach efficiencies of up to 80–90 %, as seen in table 2.2, where efficiencies of various types of shock absorbers are presented. Such an absorber has two components.

- A chamber filled with compressed gas, acting as a spring and absorbing the vertical shock.
- Hydraulic fluid forced through a small orifice, forming friction, slowing the oil and causing damping.

Table 2.2: Shock absorber efficiencies [5].

type	efficiency
steel leaf spring	0.50
steel coil spring	0.62
air spring	0.45
rubber block	0.60
rubber bungee	0.58
oleo pneumatic (fixed orifice)	0.65–0.80
oleo pneumatic (metered orifice)	0.75–0.90
tire	0.47

Disadvantage of passive shock absorbers is that their performance might decline in certain operation conditions, resulting in the transmission of high loads to the aircraft structure. Semi–active control, on the other hand, is a means to reduce the transmitted load. This is achieved by varying the viscosity, and thus damping of the shock absorber. An active system acts on both the stiffness and the damping, but is a heavy and expensive system. Semi–active control can be employed to achieve high absorption efficiencies. Passive, semi–active and control strategies will be described in 2.11 and discussed in depth in 7.2.

Figure 2.21 shows the schematic of an oleo–pneumatic shock absorber. Lower chamber contains hydraulic fluid and the upper chamber contains nitrogen under pressure. Oil and gas can be separate or mixed during compression, depending on the design. Most aircraft use nitrogen as the springing medium and oil flow through orifices provides damping [1].

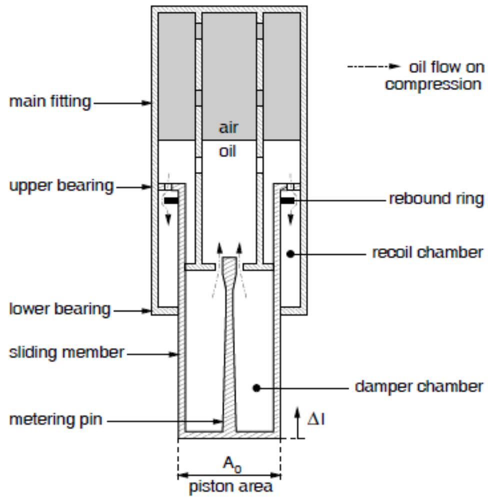

Figure 2.21: Schematic of an oleo–pneumatic shock absorber [1].

Working principle of oleo–pneumatic shock absorbers is that the chamber of oil is forced against the chamber of air or nitrogen, and then both the oil and the gas are compressed. As the strut compresses, the piston moves up and oil flows through into the upper chamber. The hydraulic pressure drop generated across the orifice resists the telescoping of the strut and the turbulence created provides a means of absorbing impact energy on landing. Energy is dissipated after the initial impact as the air pressure forces the oil back into its chamber through orifices.

Orifice area is constant in some struts, while most designs use a metering pin or a rod to control the orifice area as a function of stroke, and thus govern the damping effect of the strut. By varying the diameter of the pin, the strut load is kept almost constant under dynamic loading. Keeping this load constant would result in 100 % efficiency of the gear, but in reality this is 80 to 90 % [7,13,14].

The outer cylinder of an oleo–pneumatic shock absorber remains static with respect to the airframe and must withstand the internal pressure created by the gas and oil during operation. The inner cylinder is free to move in the axial direction with respect to the outer cylinder and must withstand the internal pressure. The inner cylinder is filled with hydraulic fluid while the outer cylinder contains a combination of hydraulic fluid and compressed gas, often nitrogen. The inner cylinder is extended with respect to the outer cylinder, when not loaded. When the landing load is applied, the inner is cylinder is forced to move in the longitudinal direction. This exerts a pressure on the hydraulic fluid in the inner cylinder and the fluid is forced upwards, through the orifice. Vertical kinetic energy is converted into heat within the hydraulic fluid and majority of the landing energy is absorbed through this damping process. When the hydraulic fluid passes through the orifice, volume of the gas within the outer cylinder is reduced. This forces the fluid back through the orifice, removing more energy and acting like a spring.

2.4.2 Tires

Tires play an important role for aircraft dynamics on the ground. They act as springs connecting the aircraft to the ground and their properties are essential in predicting landing gear shimmy. Tires are subject to severe static and dynamic loads during taxiing, take–off and landing rolls and constitute the boundary conditions between the runway and the rest of the landing gear.

Aircraft tires have much more strength and durability than the tires used in automotive industry, since aircraft tires are subjected to large shock loads during landing and take–off and landing speeds that are twice as high as automobile tire speeds. As aircraft tires have to sustain large deflections at pressures between 12000 and 16000 hPa (12 to 16 bar)and take–off speeds of up to 360km/h, their designs must ensure that tires do not blow off during take–off and landing. Static deflection of aircraft tires can be up to 30 % of the unloaded radius. During its service, a tire expands as its fabric stretches because of the heat generated during ground operations and the centrifugal force of spinning [5].

Tires are graded in terms of ply rating, maximum allowable static loading, recommended unloaded inflation pressure and maximum allowable runway speed. These terms are defined as the following [5].

- Ply rating is the maximum recommended static load that a tire may carry and the corresponding internal pressure, and is an indicator of tire strength. A tire with, for example, only 18 plies may have a ply rating of 32.
- Maximum allowable static loading is the maximum load the tire can carry when the aircraft is stationary and is smaller than the maximum allowable dynamic loading. This is because the tire experiences greater loads during landing, associated with shock absorption. Each tire is designed to operate at

a maximum allowable static load and this load depends on the type of tire and its ply rating.

- Recommended unloaded inflation pressure is the maximum recommended pressure of the unloaded tire. Pressure increases in loaded conditions, so the unloaded inflation pressure is not the maximum allowable pressure that the tire can withstand. It must be borne in mind that inappropriate inflation can result in uneven tire wear, as in figure 2.22. Tire inflation pressures vary, depending on the application. For instance, older aircraft employ low pressure, high volume tires for softer landings, while most new aircraft employ high pressure, low volume tires.
- Maximum allowable runway speed of a tire depends on the application for which the tire will be used. Heavier aircraft need greater take–off speeds to achieve the required lift, thus the maximum allowable runway speed should be higher for the tires to be employed in heavier aircraft.

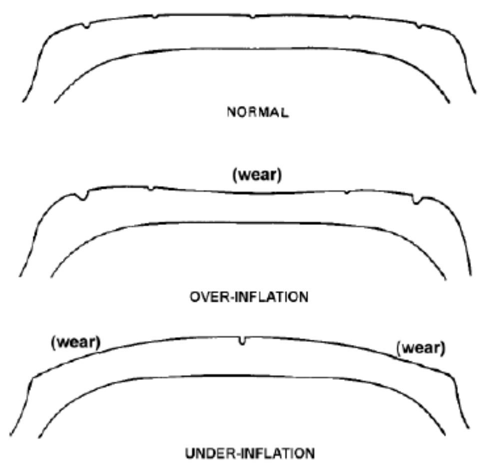

Figure 2.22: Uneven tire wear due to incorrect inflation [5].

Aircraft are equipped with pressurized tires, consisting of an inner and an outer tire. The air–pressurized inner tire carries the weight of the aircraft and is subject to landing shocks, while the outer tire protects the inner tire, maintains the shape of the tire and deforms during braking. Aircraft tires provide a cushion of air helping to absorb the shocks formed during take–off and landing. They also support the weight of the aircraft when it is on the ground and provide the necessary traction for braking. Some brake systems produce high temperatures during braking, heating the inner tire. Structure of the outer tire is shown in figure 2.23 [3,4].

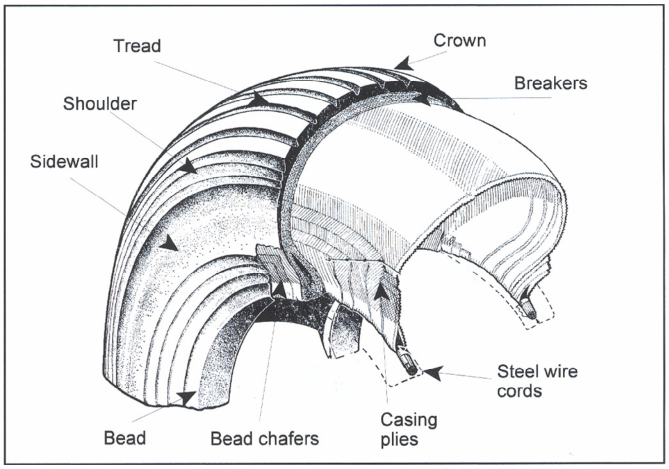

Figure 2.23: Outer tire [4].

2.4.2.1 Tire sizes and pressures

Tire information comprises size, ply, speed in mph, load in pounds, maximum braking in pounds, inflation pressure in psf, tire weight in pounds, maximum inflated outside diameter and width in inches and aspect ratio, while wheel information comprises size, width and diameter in inches. These terms, some of which were mentioned in 2.4.2, are defined as the following.

- Size is given as the outside diameter × section width and rim diameter.
- Ply is an index of the tire strength and does not necessarily give the number of cord plies.
- Speed is the maximum speed the tire is qualified to.
- Load is the maximum load for the ply rating of the tire.
- Maximum braking is the maximum steady braking that may be applied to the tire during landing.
- Inflation pressure is the pressure required to support the load.
- Aspect ratio is the ratio of the tire section height to the tire section width.

Differences in landing velocity, loads, runway and structure of the landing gear necessitate the use of different tire sizes and pressures. There are four basic categories of tire pressures, as seen in table 2.3. A dangerous but expected situation is that the tires tend to slide when first placed on the rim. This will be alleviated when the tires start rolling on the ground. Tires should be at the correct pressure level when in use. Incorrectly pressurizing tires at levels lower than the prescribed levels causes sliding over the rim. 90 % of the incidents related to tires are caused by incorrect pressurization of the tires. In modern aircraft, tire pressures can be seen through electronic displays in the control panel. Tires also need to be protected from excessive heating, humidity, sunlight, oil, fuel and hydraulic fluid.

Table 2.3: Aircraft tire pressures.

Classification	**Description**	**Pressure**
Low pressure	Grass fields	25–35 psi (1.73–2.42 bar)
Medium pressure	Grass and compressed fields	35–70 psi (2.42–4.83 bar)
High pressure	Conventional runways	70–90 psi (4.83–6.21 bar)
Very high pressure	Conventional runways	> 90 psi (6.21–24.2 bar)

Tires are force and moment generating structures. Their primary functions are transmitting forces in three directions and to cushion the vehicle against road irregularities. Vehicle dynamics investigates the complex structure and mechanical behavior of tires.

2.4.2.2 Tire designs

There are two types of tires, cross–ply or bias ply tires and radial tires. Radial tires have become the standard design due to their advantages. Main advantages of radial tires over cross–ply tires are weight reduction up to 25 % and longer life. Tires are fabricated not only from rubber, since that would make them too flexible and weak. There are a series of plies of cord within the rubber, acting as reinforcement. All common tires are made of layers of rubber and cords of polyester or steel, and this network of cords that gives the tire its strength and shape is called the carcass.

Radial tires have been patented by Michelin in 1946 and have gained acceptance in aviation since they were first introduced. Other major tire manufacturers for aviation are Goodyear, Goodrich, Dunlop, Michelin and Bridgestone.

In cross ply tires, cords are placed at an angle of about ±60° from the direction of travel, so they cross over each other. In comparison, radial tires lay all cord plies at 90° to the direction of travel, avoiding the rubbing of the plies against each other as the tire flexes, reducing the rolling friction of the tire. This allows vehicles with radial tires to achieve better fuel economy than vehicles with cross ply tires.

Another difference in construction is that in radial tires there is a steel fiber belt nearly the width of the tire, running the entire circumference. This belt reduces wear. A radial tire can stand 100000 miles of wear while a bias ply tire can stand 30000 miles. Due to the placement of the plies, sidewalls have a bulging look which causes the tire to look as if it is under inflated. Steel wires in radial tires become magnetic as the tires rotate, creating an alternating magnetic field. It is quite measurable with an EMF (electromagnetic field) meter close to the wheel well when a car is moving and has a spectrum of harmonic strengths from 10 to several hundred Hertz [3,6,16].

Combination of heavy loading, high speed and high deflection percentages make operating conditions of aircraft tires extremely severe. Shear stresses in the rubber matrix are minimized in radial construction and loads are distributed efficiently throughout the tire, resulting in weight savings. Improved wear performance is due to the minimized slippage between the tire and the contact surface. Some radial tires achieve twice as many landings as conventional cross ply tires. Experience has also shown that radial tires have higher overloading capacity and can withstand being under–inflated. Their additional advantages are long life, resistance to cuts, puncture and tears, excellent traction, improved handling and fuel economy, smooth ride and comfort [17].

Vertical loads allowed for aircraft tires exceed the values for truck tires of similar size, so aircraft tires should have larger contact areas. A 10 % increase in the footprint area improves flotation characteristics and reduces hydroplaning. The terms flotation and hydroplaning will explained in sections 2.6.1 and 2.6.2, respectively [13].

2.4.2.3 Categorization of tires

Tires are described in terms of certain geometric parameters. Sizing is done to establish nominal section width, W_G, height, H, and diameter, D. These terms are demonstrated in figure 2.24. Rim diameter of the hub is symbolized by d and the radius of the lower half under loading is symbolized by R_{load}. Load bearing capacity of a tire for inflation pressure and the airfield load classification number LCN

determine the number of wheels and tire size. LCN is a number representing the amount of load that a runway can accommodate based on construction characteristics. For heavy aircraft, the load is distributed over the high number of wheels and tires. Tire standard are regulated by FAA. Tire types are given in table 2.4, where tire aspect ratio is defined as H/W_G and lift ratio is defined as D/d [8].

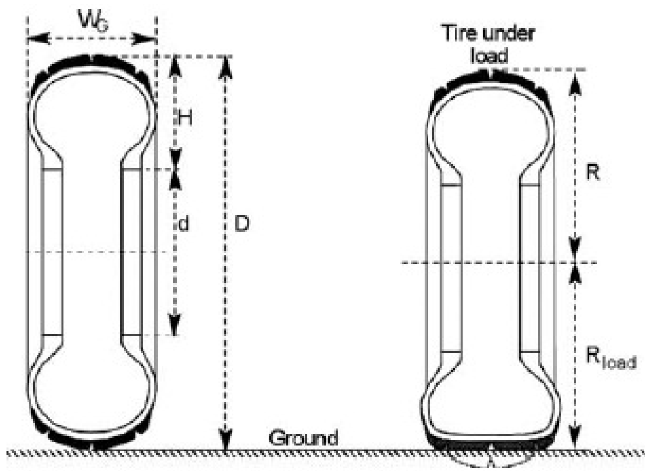

Figure 2.24: Tire designations [8].

Table 2.4: Tire types [8].

size	11.00–12	6.50–10	22×5.5	22×7.7–12
type	III	III	VII	VIII
lift ratio	2.67	2.17	1.81	1.83
aspect ratio	0.90	0.91	0.89	0.67

Tires are categorized based on the unloaded inflation pressure, ply ratings for holding shape under pressure, maximum static load for the maximum take–off weight $MTOW$, and the maximum aircraft speed on the ground [8]. Out of nine categories, mainly three are in use, which are type III, type VII and new design tires using three-part nomenclature. Type I tires had been intended for fixed landing gear. Type I, II, IV, V and VI tires are no longer produced.

Type III tires include low pressure tires providing a larger footprint or flotation effect [8]. Flotation is the capability of the runway and other surfaces such as taxiways and aprons, to support the aircraft and can be increased by keeping the contact pressure low [13]. These tires have a relatively small rim diameter d, compared to overall tire diameter, and are used when the speed is limited to less than 160 mph. Tire designation is expressed by the section width W_G and rim diameter d. Dimensions are in inches, meaning a tire designation of 6.00–6 means the tire has a width of 6.00 inches and a rim diameter hub of 6 inches

Type VII tires are high pressure tires that are relatively narrower, widely used in aircraft with pressure levels from 100 to more than 250 psi (6.89 to more than 17.23 bar). Tire designation is expressed by the overall diameter D and the section width W_G in inches, with the × sign in between. For example, a tire designation of 22×5.5 means the tire has an overall section diameter of 22 inches and a section width of 5.5 inches [8].

New design tires are intended for high–speed aircraft with high tire inflation pressures. They have a three–part designation as the outside diameter D, section width W_G and rim diameter d, with × and – signs in between, respectively. Dimensions of the diameter and section width may be in inches or mm, depending on whether FPS or SI units are used, but the rim diameter is always given in inches. For example a Boeing 747 tire has designation of 49×19.0–20, meaning the tire has an outside diameter of 49 inches, a section width of 19.0 inches and a rim diameter of 20 inches [8].

Tire pressures for a range of aircraft weights are given in table 2.5. Maximum tire deflection under a static load is typically one third of the maximum height H. Load increases on dynamic loading as the speed of the aircraft increases. Deflection is higher during impact landing but will recover soon, since the tire acts as a shock absorber. Tire sizing depends on the static and dynamic loads it should sustain. Higher the pressure of a tire, the smaller is its size. Main and nose gear tires of a Boeing 747–200 has size 49×19–20, with an unloaded inflation pressure of 195 psi [8].

Table 2.5: Tire pressures for a range of aircraft weights [8].

weight (kg)	pressure (psi)	pressure (bar)
< 3000	50	3.44
5000	25 to 50	1.72 to 3.44
10000	25 to 90	1.72 to 6.20
20000	45 to 240	3.10 to 16.52
50000	60 to 240	4.13 to 16.52
100000	75 to 240	5.17 to 16.52
200000	100 to 240	6.89 to 16.52
300000	110 to 240	7.58 to 16.52
>50000	150 to 240	10.34 to 16.52

Friction is experienced between the tires and the ground during ground movement and is considered as drag, consuming engine power during take–off run. Value of the ground rolling friction coefficient μ depends on the aircraft speed and the runway surface condition, depending on whether it is dry, wet or covered with snow, ice or slush. Figure 2.25 shows the dependence of μ on aircraft speed for various runway surface conditions. Braking friction coefficient μ_b is higher, depending on the runway surface condition. A typical value is 0.5. Locked wheels skid and wear the tire out and might possibly blow it out. To prevent this, most aircraft touching down above 80 knots have antiskid devices for μ_b as high as 0.7 [8].

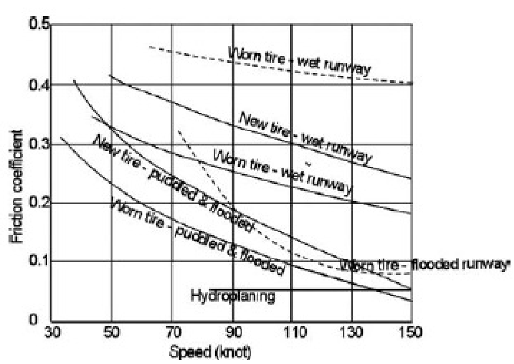

Figure 2.25: Ground rolling friction coefficient versus aircraft speed for various types of runways [8].

2.4.3 Modeling of tires

Function of the tire model is to represent the forces and moments occurring at the contact patch and resolving these to the wheel center and the aircraft. Tire modeling is a science in itself. Representation of tire dynamics is an important part of the aircraft landing gear model. Tires are the most difficult part to model in an automobile, and likewise in the landing gear of an aircraft. They support the aircraft and damp irregularities on the runway, in addition to providing longitudinal and lateral forces needed to change the speed and direction of the aircraft. These forces are produced by the deformation of the tire at the contact patch [18].

Although shimmy can be related to both the elasticity of the tire and that of the suspension system, elasticity of pneumatic tires is often much greater than lateral elasticity of the suspension systems. For this reason, tire modeling is an important issue. Modeling of aircraft tires presents similar challenges to those involved in modeling automotive tires in ground vehicle dynamics, on a much larger scale in terms size and loads on the tire [19,20].

If side forces are not present, a tire keeps travelling straight ahead along the wheel plane. Slip, on the other hand, occurs when the tire contact patch slips while rolling such that its motion is no longer in the direction of the wheel plane, as in figure 2.26. Slip angle is the angle between the direction of motion and the wheel plane. It is generated because the rim cannot change its plane of motion whereas an angle between the wheel and the direction of motion can be generated due to tire deflection. Slip generates a lateral force F_y at the tire–ground interface. This force allows a vehicle to be steered or negotiate a turn. Obviously, no lateral force is needed when a vehicle is traveling on a straight and level path without any external loads [12]. The aligning moment M_z is formed because the lateral force acts slightly behind the center of the wheel and tends to align the wheel in the direction of rolling.

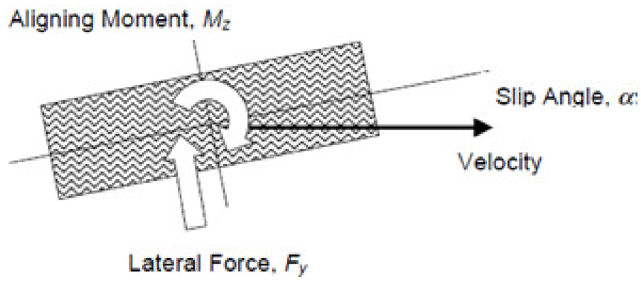

Figure 2.26: Slip angle [18].

Engineers and scientists have been trying to model the forces and moments generated in the tire contact patch, representing the physical behavior of the interaction of an aircraft tire in contact with the runway since the middle of the last century. These efforts were due to the occurrence wheel shimmy, often manifested as a violent and sudden vibration in the nose landing gear during landing. Tire modeling is important in both aerospace and automotive industries. Behavior of an aircraft when in contact with the runway during landing, take–off or taxiing may be considered as a vehicle dynamics problem [19].

There are two trends in modeling tires. One of them is the elastic string model and the other one is the point contact model. First tire models implemented the single contact point approach. The most widely used model in engineering is the von Schlippe stretched string model, based on the concept of a stretched elastic string with a finite contact patch length to describe the mechanics of a rolling tire. The tire is considered as a massless string of infinite length under a constant tension force, uniformly supported elastically in the lateral direction. Cornering force and aligning torque are defined in terms of the tire deflection. Smiley, Pacejka, Kluiters and Rogers models also depend on the stretched string model.

There exist a number of tire models for the analysis of shimmy instability. Linear models take only small slip angles into account and are restricted to lateral dynamics. Von Schlippe straight string model, straight tangent method developed by Pacejka by replacing the string in the von Schlippe stretched string model by a beam and the rigid ring method are the most renowned ones [21]. A low parameter mathematical model representing the force and moment components generated in aircraft tires for use in the computer simulation of take–off, landing and taxiing maneuvers is described in [19]. Low parameter model means a low number of model parameters have been obtained from a limited data range.

Interaction between the tire and the road or the runway is a complex problem. Forces and moments developed at the contact patch are due to the relative motion between the tire and the road. Generally, the tire and the wheel are considered as a disk coinciding with the plane of symmetry of the tire, as in figure 2.27. Forces generated by the tire are assumed to act at the contact center C, point of intersection between the wheel plane, road plane and plane through the wheel spin axis and normal to the road. Distance from the wheel center to C is called the loaded radius and is designated by R. A local reference system is defined to express forces, moments and velocities where the x axis is parallel to the line of intersection of the road and the wheel plane, y axis is perpendicular to this line and parallel to the road plane and the z axis is normal to the road.

In a vehicle dynamics approach, a tire input vector comprises the radial deflection ρ, longitudinal slip κ, speed of revolution Ω, lateral slip angle α, spin or turnslip φ and camber angle γ, whereas the output vector comprises longitudinal force F_x, cornering or side force F_y, normal load F_z, overturning moment M_x, rolling resistance moment M_y and the self aligning moment M_z. Related forces and moments are the longitudinal braking or traction force F_x, lateral cornering force or side force F_y, vertical force F_z, overturning moment M_x, rolling resistance moment M_y and the self aligning moment M_z. All of these quantities are functions of tire parameters, inflation pressure, road roughness and temperature [1,15].

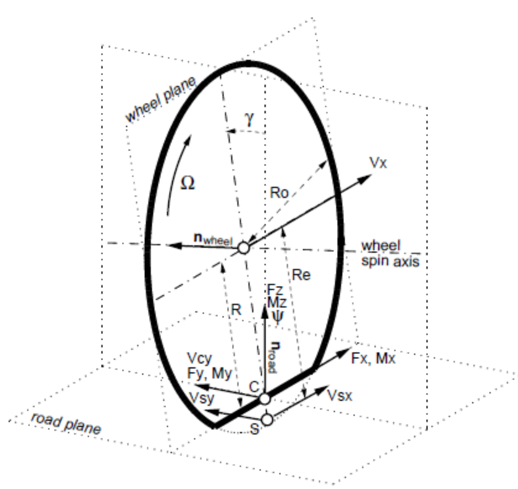

Figure 2.27: Representation of a wheel and a tire [1].

Both M_x and M_y occur because there is an offset between the vertical force in the actual tire and the contact point. Longitudinal braking or traction force F_x is generated between the tire and the road surface upon the application of a braking or driving torque. It is common to assume that the side force, or lateral cornering force, F_y is proportional to the normal force F_z. Tires often generate lateral and longitudinal forces simultaneously as turning and braking or accelerating happens at the same time.

There are difficulties in obtaining aircraft tire test data for a wide range of conditions. An aircraft tire model that can capture the main contact patch force and moment characteristics from limited data is needed. Complexity of models can be increased as more data become available. There are models that have been developed specifically for aircraft, as reported in [19].

2.4.3.1 Point contact model

Point contact tire model assumes the tire and the road have a contact point. Works of Keldysh and Moreland are based on this approach [22]. These models have been developed to analyze dynamic behavior of vehicles. Although published in 1945, the Keldysh model remained unknown to the Western world for many years, since the publication was in the Russian language. Moreland's point contact model, developed in 1954, considers all forces and torques to act at the center of the tire contact patch. The idea is that there is a time delay before the tire responds to a lateral force.

Schematic of the Keldysh point contact tire model is given in figure 2.28, although its equations of motion will not be presented for purposes of conciseness.

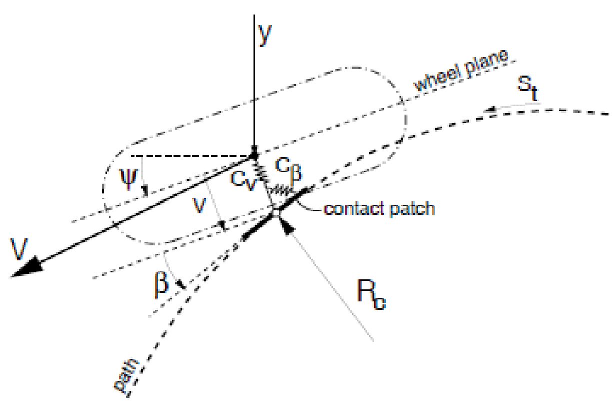

Figure 2.28: Tire coordinate system.

2.4.3.2 Stretched string model

The first tire models were based on the idea that the ground–tire interface is reduced to a single contact point. In 1942, von Schlippe introduced the concept of a stretched string with a finite contact length and many tire models, such as those of Smiley, Pacejka, Kluiters and Rogers, have been based on this idea.

In the stretched string approach, the tire is assumed to be a massless string of infinite length uniformly supported elastically in the lateral direction, as in figure 2.29 where a is the half of the length of the contact area of the tire with the road, σ is the relaxation length, and c_c is the lateral stiffness per unit length between the string and the wheel plane. This approach assumes that no sliding occurs in the contact area and as a result, the trailing contact point follows the same path as the leading contact point with a time delay. Contact line is approximated by forming a straight line connection between the leading and trailing contact point [21].

Derivation of the stretched string tire model is presented in detail in [1], [21] and [15] and in 5.2. It is assumed that points in contact with the road do not slide with respect to the road. Another assumption is that the angles remain small. Boundary conditions assume that during rolling, the string forms a continuously varying slope around the leading contact point, whereas at the rear end, the absence of bending stiffness may cause a discontinuity in the slope.

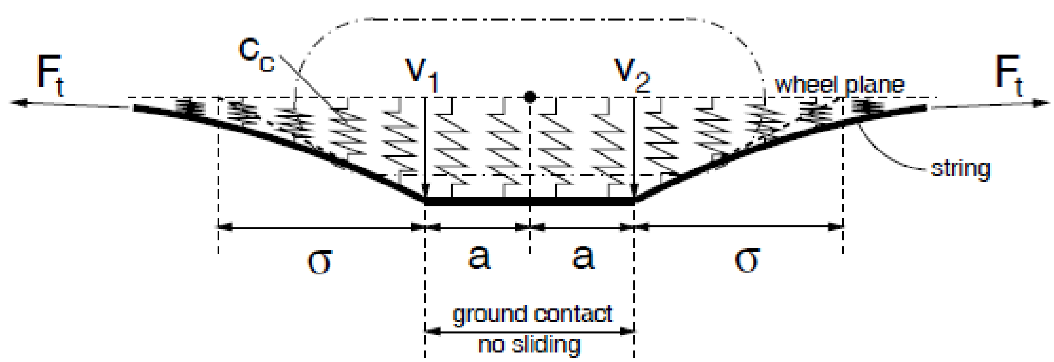

Figure 2.29: Stretched string model [1].

2.4.3.3 Straight tangent model

Straight tangent tire model is a linear approximation of the stretched string approach. It uses only the deflection in the leading contact point of the tire to calculate the lateral force and self aligning moment generated by the tire and is proven in [1] to be less accurate at low speeds [21]. Radial forces act on the circular shape of the string due to tension. These forces cause a moment around the vertical axis because of the lateral deflection of the string. In the straight tangent model, contact line is governed solely by the deflection v_1 at the leading contact point, as seen in figure 2.30. Derivation of the equations of motion of the straight tangent model will not be included here but can be found in literature.

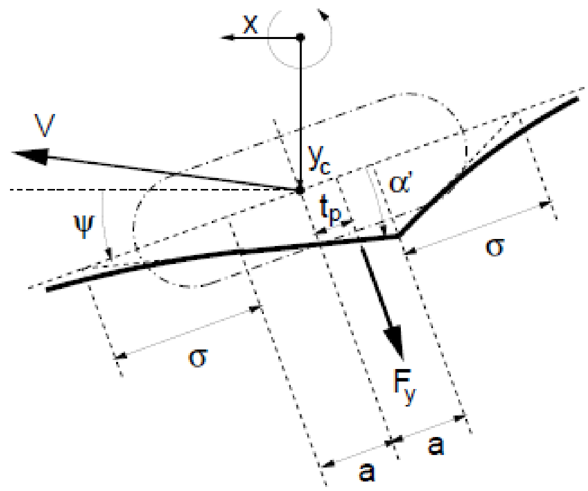

Figure 2.30: Straight tangent tire model [1].

2.4.3.4 Rigid ring model

The recently developed rigid ring model includes the dynamics of the belt and contact patch and is therefore capable of showing gyroscopic effects and resonances of the belt. It consists of three masses corresponding to a rim, belt and contact patch. The belt is elastically suspended with respect to the rim which represents the flexible carcass. Out–of–plane relative motion between the rim and the belt has three degrees of freedom. They are lateral translational degree of freedom and rotational degrees of freedom about the vertical and longitudinal axes, namely yaw and roll or camber.

Figure 2.31 shows a rigid ring tire model where ψ is the yaw angle, γ is the roll angle and Ω is the angular velocity of the wheel. Equations of motion pertaining to the dynamics of a rigid ring tire model will not be included here.

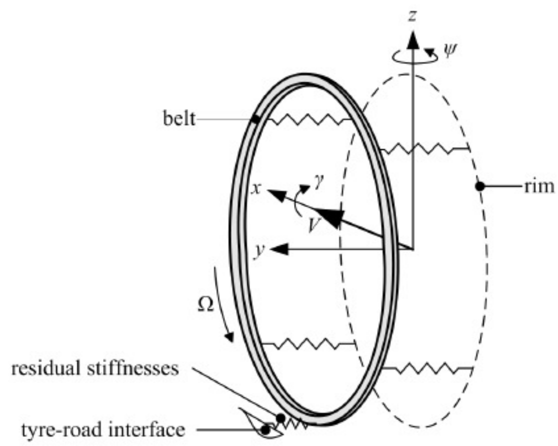

Figure 2.31: Rigid ring tire model [21].

2.4.3.5 State–of–the–art models

There exist newer tire models such as FTire, SWIFT, RMOD–K, used in automobile engineering. They have not yet been applied in modeling the aircraft landing gear tires, however they may be applied in the future as they are reported to be accurate models, providing good correlation with measurements.

Development of FTire, Flexible Structure Tire Model, began in 1998 and is currently the most widely used tire simulation model in automotive engineering. It is a nonlinear simulation model based on finite elements and has interfaces to software packages such as ADAMS, SIMPACK, Matlab/Simulink, RecurDyn and CarSim [23]. SWIFT is an extension of the rigid ring tire model. RMOD–K is a collection of tire models including rigid and flexible tire models. Rigid models need to be considered in the case of high–frequency disturbances [24].

2.4.4 Brakes

A brake must stop the aircraft within a specified distance, smoothly and repeatedly over its life. Brakes also control speed while taxiing, steer the aircraft through differential action and hold it stationary when parked and during engine start–up.

Almost all modern aircraft use disc brakes. There is an effort to reduce their weight by the use of advanced materials. Carbon brakes are 40 % lighter than conventional brakes with cost twice that of conventional brakes. Most aircraft use carbon disk brakes along with anti–skid systems.

Brakes turn kinetic energy of the forward motion of the aircraft into heat energy due to friction. This heat is dissipated to the surrounding environment of the brake, namely the wheels, tires and the surrounding air. Generally, brakes function based on the principle of conversion of the kinetic energy generated between sliding of a moveable surface across a static surface into heat. Building 6–8 km long runways would prevent excessive heating in the brakes of large aircraft, however this is not a physically feasible solution. Heavy–duty brakes cause the temperature to reach high levels, so there is a potential risk of fire, as was the case in the Concorde crash of 2000. Heavy braking requires heavy–duty tires that are quickly worn out and need to be replaced.

Brakes are often fixed only to the main landing gear and have an enormous weight. For example, brakes of the Airbus A300 weigh 24 % of the 3626 kg total mass of the landing gear legs. Brakes either stop an aircraft or steer it by differential braking. Differential braking means right or left brake can be applied individually.

Modern aircraft use hydraulically operating disc brakes, as shown in figure 2.32. Number of plates in the brake depends on the design and tire size.

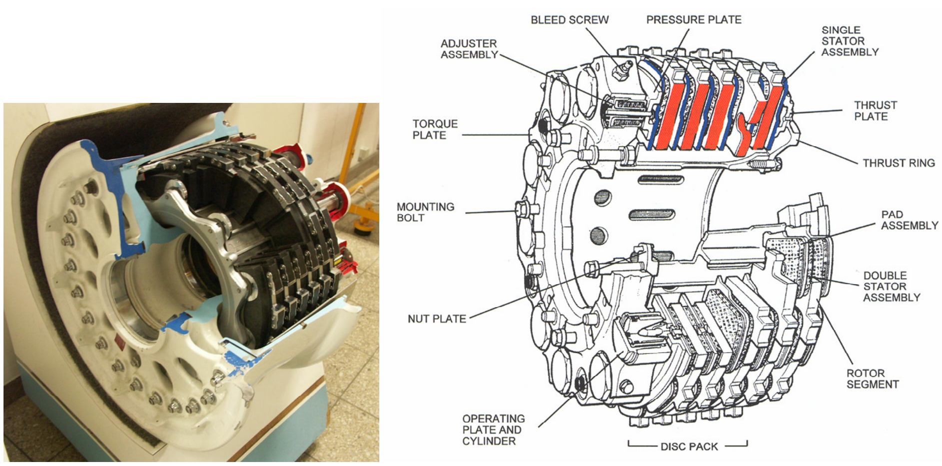

Figure 2.32: a. An aircraft disc brake. **b.** Schematic of an aircraft disc brake [4].

Aircraft need to be steered on the ground. The steering feature on most aircraft is a steerable nose gear. Steering might be accompanied by differential braking of the main landing gear or the use of differential thrust [3]. Combined nose and main landing gear steering systems have been developed for newer large aircraft like Boeing 747 and 777, since sharp turns cannot be achieved with a conventional nose steering system alone [13].

A braking torque is applied to the wheel center but there is an upper limit for the braking torque to prevent undesirable slipping. This limit depends on the translational speed of the wheel center with respect to the ground. Friction coefficient varies with respect to the translational speed during braking. Braked friction coefficient depends on the ground speed, as well. Friction coefficient decreases when braking on wet surfaces [25].

Skidding causes a tire to blow in less than 100 ft (3 km). Skid control systems are used to minimize stopping distance and reduce tire wear caused by skidding. This is accomplished by sensing the friction coefficient and providing an almost constant force up to the skidding point. Such systems provide control over resonance problems of the landing gear and shimmy oscillations [3,7,13].

2.5 Boeing 757 and Cessna 172 Aircraft as Examples

Cessna 172 is the most built aircraft to date, with more than 35000 of them produced in over 50 years. It has a high-wing, is powered by a single engine and may carry 4 people and 1 crew. Its maximum take–off weight is 1110 kg. A Cessna 172 is seen in figure 2.33.

Figure 2.33: Cessna 172 aircraft [5].

Main landing gear of the Cessna 172 aircraft consists of a solid spring and a single wheel, offering no shock absorption. As a result, the aircraft tends to bounce. The nose landing gear, on the other hand, implements a telescopic, oleo–pneumatic shock absorber, offering superior shock absorption, as it must support the engine.

Boeing 757 is a medium range airliner and a total of 1050 were manufactured from 1982 to 2004. It has a maximum take–off mass of 123600 kg and may carry 186 to

289 passengers. It is one of the first in its class to meet extended range twin–engine performance standards. A Boeing 757 is seen in figure 2.34.

Figure 2.34: Boeing 757 aircraft [26].

Landing gear of the Boeing 757 aircraft has a retractable tricycle configuration. It comprises of main landing gear located under each wing and a twin wheel nose landing gear. Main landing gear comprise of dual tandem wheels and telescopic oleo–pneumatic shock absorbers, while the nose landing gear has a smaller oleo–pneumatic shock absorber. Multi tires do not only distribute the load and pressure within each tire, but also increase shock absorption and help protect the runway surface. Nose landing gear contains fewer wheels since smaller loads are induced in the nose landing gear.

Cessna 172 has a smaller nose landing gear shock absorber than Boeing 757 due to its lower mass and design touchdown rate. Main landing gear stroke length of the Boeing 757 aircraft with a design touchdown rate of 3.6 m/s and a shock absorber efficiency of 0.75 is 35 cm, while the stroke length of the Cessna 172 aircraft with a design touchdown rate of 3.6 m/s and a shock absorber efficiency of 0.5 is 24 cm [5].

Since relatively smaller loads are induced in the nose landing gear of commercial aircraft, compared to the main landing gear, nose landing gear contain smaller oleo–pneumatic shock absorbers. Due to the importance of energy dissipation in commercial aircraft, shock absorbers need to have relatively high stroke distances.

As an example, table 2.6 gives information on the loads occurring in the Airbus A380 landing gear struts. Airbus A380has a *MTOW* of 560000 kg.

Table 2.6: Airbus A380 loads [8].

	Tire pressure	Maximum load per strut
nose gear	11.8 bar	77100 kg
wing gear	13.6 bar	112500 kg
body gear	13.6 bar	168750 kg

2.6 Flotation

Flotation refers to the capacity of the pavement on the runway, taxiways and aprons to support an aircraft. Configuration of the landing gear has a direct effect on ground flotation. Number and pattern of the wheels, weight of the aircraft and its distribution among the nose and main wheel assemblies imposes a requirement for the pavement thickness. The type of pavement found at the airports that the aircraft will serve need to be considered as different airfield surfaces allow different loads per tire to be applied. Large aircraft are equipped with multi–wheel/multi–axis configurations so that maximum allowed load is not exceeded. Inappropriate combinations of surface and landing gear might restrict the operation of aircraft on certain airfields.

Runway and apron pavements can be categorized as flexible and rigid pavements, as seen in figure 2.35. Flexible pavements are also known as asphalt because that is the surfacing material and multiple layers of compacted materials are used beneath the surface. Thickness of a flexible pavement is the total thickness of all the materials involved and is characterized as 8 to 60 inches. Rigid pavements are concrete made with cement. Thickness of a rigid pavement is the thickness of the concrete which is commonly 8 to 14 inches. Each layer must be thick enough so that the applied loads do not damage the surface or the underlying layers. Excessive tire loads may cause failure on the surface. To avoid these damages, tire pressures should not exceed the maximum allowable tire pressure for each type of surface [3,7,13].

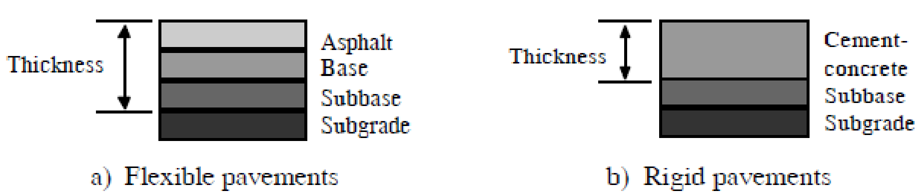

Figure 2.35: Pavement cross sections [13].

To prevent the gear from damaging surfaces, LCN (Load Classification Number) method has been suggested by ICAO (International Civil Aviation Organization). The main idea is to classify each runway in the world with a LCN and make sure that the LCN of a landing gear does not exceed the lowest runway LCN at which it is intended to operate [3].

Similarly, ACN (Aircraft Classification Number), is another standard imposed by ICAO, referring to the pavement load imposed by an aircraft. PCN (Pavement Classification Number) classifies surfaces at airports. In other words, ACN expresses the pavement load intensity of an aircraft while PCN expresses the load carrying capacity of a pavement. ICAO directs that runways, taxiways and aprons of each runway should have enough strength to stand the load of the heaviest aircraft operating at it [27–29].

2.7 Landing Gear Design

Landing gear may be defined as the "essential intermediary between the aeroplane and catastrophe"[13], thus its design is one of the most fundamental aspects in aircraft design. Design and integration phases include many engineering disciplines such as structure, determination of weights, runway design and economics. Configuring the landing gear geometry, load estimation and tire sizing is an important process.

Kinematics, structural sizing and brake requirements are some of the steps to be considered in landing gear design. This is a complex process due to conflicting requirements such as maximum strength, minimum weight, high reliability, low cost and airfield compatibility. If the computer model is updated as test results become available, it can be used for verification and certification purposes in the final design phases.

Weight of the landing gear including wheels and tires ranges from 6 to 10 % of the maximum take–off weight according to [1] and from 3 to 6 % according to [13]. Weight is a design consideration, but recent advances in flight science technologies imply reduced structural and mission fuel weights, which means the landing gear may become a greater weight percentage in future large aircraft. A major reduction in landing gear weight may be hard to realize since the landing gear is not a redundant structure, thus any reduction from the fail–safe standard is not acceptable. Parameters that should be considered when designing an aircraft are its size, weight, type of mission, placement of the wings and efficiency [1,4,7,8,13].

Many computer models regarding the computation of loads, verification of stress levels, fatigue life and retraction analysis are used during the development. Simulation models need to be validated in test facilities. Newly designed landing gear are tested in drop tests where the landing impact is simulated. These tests are conducted to validate spring and damper characteristics at high speeds.

Institutions that have large test facilities are the Wright Laboratory LGDF (Landing Gear Development Facility) at Wright Patterson Air Force Base, NASA Langley Research Center, CEAT (Centre d'Etudes Aerodynamiques et Thermiques, Center for Aerodynamic and Thermal Studies) at the University of Poitiers in France, IABG, an analysis and testing organization for the aeronautics industry and the Ministry of Defence in Germany and Cranfield University, a wholly postgraduate university in England that has conducted many tire tests within the LAGER project. Landing gear manufacturers in Europe conduct fatigue tests [1,2].

2.8 Landing Gear Simulation and Control

For many years, landing gear have been tested in drop test facilities which allow deduction of limited information about the interaction between the aircraft and the landing gear, but is a costly and time consuming procedure. Since tests on real aircraft are expensive and have risks, drop tests are performed by dropping one leg with tires spinning.

Behavior of an aircraft can be investigated and its design can be optimized by simulation at a reasonable cost. Simulation is needed to evaluate and ensure shimmy stability of a landing gear because that may pose several design constraints on the stiffness and geometry of the landing gear. If the computer model is updated as test results become available, it can be used for verification and certification purposes in the final design phases. The amount of simulation required in landing gear structural analysis has increased tremendously over the past ten years. The use of finite element modeling makes it possible to model detailed components accurately [2,31].

DLR (Deutsche Zentrum für Luft– und Raumfahrt, German Aerospace Center) is working on the international ELGAR (European Landing Gear Advanced Research) project and the German National Aerospace Research Program to improve passenger comfort and aircraft safety by modifications of the landing gear. The work also aims at reducing the loads on the airframe during taxiing and take–off and the vibrations that can cause fatigue.

DLR has developed SIMPACK, a general purpose multibody simulation software, to use in the analysis and simulation of dynamic systems for aerospace and vehicle applications. In this software, equations of motion are generated and solved using numerical integration. Numerical analysis methods such as linearization, eigenvalue analysis, root locus and frequency response analyses can also be performed [2,32].

Multibody codes, such as ADAMS (Automatic Dynamic Analysis of Mechanical Systems) or Motion Solve, are applied for the prediction of landing gear dynamic behavior over the past few years [33].

VI–Aircraft, which used to be ADAMS/Aircraft until the recent purchase of the module by the VI Grade company, makes it possible to model an aircraft or any of its subsystems and conduct simulations. It is therefore possible to model a landing gear and perform shimmy analyses. Many parameters can be changed in such a model, as landing gear flexibility, flexibility of the attachment between the landing gear and the aircraft, friction, freeplay, stiffness and damping of the steering system and tire characteristics including relaxation length, which has a direct effect on landing gear shimmy characteristics [34].

2.9 Definitions of Passive, Semi–Active and Active Control Systems

Landing gear shimmy damping is currently based on passive hydraulic damping, with a single–valued damping function. Impact loads experienced in aircraft with passive control are large because the design parameters cannot adjust to meet different landing and runway conditions.

One way to improve the performance of landing gear is to introduce active or semi–active control. Fully active suspension is a suspension that controls the forces acting in the shock absorber by generating an additional force, while semi–active suspension can only modulate the damping force by changing the damping coefficient.

Semi–active systems consist of a damper with a controllable orifice cross section to limit the oil flow. Since the orifice cross section is responsible for the damping effect, changing its cross section has an effect on the damping coefficient and reduces vibration. Semi–active control does not need a large external power supply and its implementation is simpler and more practical than active control [2,35].

The disadvantage of using actively controlled landing gear is that they require a heavy and costly force generation device, so they are unlikely to be accepted by aircraft manufacturers. Semi–active suspensions are less complicated, lighter and are easily designed fail–safe.

Semi–active control can achieve desirable performance, compared to passive control, and consumes much less power than active control. In other words, it combines the advantages of active and passive suspensions. In addition, the semi–active system can still work as a passive controller upon a failure.

No aircraft is yet equipped with an actively controlled landing gear, although the first proposals have been made in the 1970s. Active and semi–active controls have attracted attention by researchers over the last decade due to their advantages. Active and semi–active control is applied to landing gear systems only in theory and experiments and no active or semi–active oleo has been reported to be utilized in aircraft, although many semi–active ones have been designed for cars and trucks. NASA has investigated active control in the landing gear of A–10 and F–106B aircraft and performed drops tests for the latter [36].

The disadvantage of passive suspensions consisting of spring and damping devices is that they perform satisfactorily only within a frequency range. An aircraft’s response to runway excitations is in the range between 1 and 10 Hz and the human body is most sensitive to acceleration in the range between 4 and 8 Hz, thus it is important for accelerations in this range to be damped [2].

2.10 Landing Gear Manufacturers

Messier–Bugatti–Dowty is the global leader in aircraft landing, breaking and steering system design, manufacture and support. Based in France, it has sites in the UK, USA and Canada and other locations across the world and is partner to 33 commercial, business and military airframers. It equips more than 20000 aircraft making more than 35000 landings per day and is the world leader in carbon brakes, holding 50 % of the market share. Recently, the group, called the Safran group, won a wheel and carbon brake contract for the Boeing next–generation 737 twinjets and delivered the first set of Airbus A350–900 main landing gear [37].

Messier–Bugatti led the DRESS project with the goal of developing nose landing gear with electrical steering systems. Replacing hydraulic actuation by electrical actuation will reduce system weight and improve aircraft safety. DRESS is a 3 year STREP (Specific Targeted Research Project). Partners from European aeronautics industry taking part in the project are given in table 2.7. Major findings of the projects have been published in various papers in the years 2008 and 2009. First and second year activity reports and various technical reports may be found on the project website. Assessment report related to the final year of the project is not yet available online [38].

Table 2.7: Partners of the DRESS project.

<table>
<tr><th>Institution</th><th>Location</th><th>Description</th></tr>
<tr><td>Airbus</td><td>UK</td><td>aircraft manufacturer</td></tr>
<tr><td>Messier–Dowty</td><td>France</td><td>landing gear manufacturer</td></tr>
<tr><td>SAAB</td><td>Sweden</td><td rowspan="2">systems and equipment manufacturer</td></tr>
<tr><td>Messier–Bugatti</td><td>France</td></tr>
<tr><td>Instytut Lotnictwa
(Institute of Aviation)</td><td>Warsaw, Poland</td><td>research institution</td></tr>
<tr><td>INSA (Institut National des Sciences Appliques)</td><td>Toulouse, France</td><td rowspan="5">university</td></tr>
<tr><td>UHA (Universite de Haute Alsace)</td><td>Mulhouse, France</td></tr>
<tr><td>UCL (Universite Catholique de Louvain)</td><td>Louvain, Belgium</td></tr>
<tr><td>UCV (University of Craiova)</td><td>Romania</td></tr>
<tr><td>BUTE (Budapest University of Technology and Economics)</td><td>Hungary</td></tr>
<tr><td>TTTech Computertechnik AG</td><td>Vienna, Austria</td><td rowspan="3">SME (Small and Medium Sized Enterprise)</td></tr>
<tr><td>EAT (Equip Aero Technique)</td><td>France</td></tr>
<tr><td>SPAB (Stridsberg Powertrain AB)</td><td>Bandhagen, Sweden</td></tr>
</table>

GE Aviation, formerly called Smiths Aerospace, is a provider of jet engines and components as well as avionics, electric power and mechanical systems for aircraft and has customers around the world. It has over 40 years of experience in the design, development and manufacture of landing gear components and assemblies [39].

Grove Aircraft Company is an aircraft landing gear systems manufacturer, on a smaller scale. It is based in California and can manufacture custom landing gear for individual aircraft. Voss Aerospace, based in Cleveland, Ohio, is another small–scale manufacturer [40,41].

3. SHIMMY

3.1 Definition of Shimmy

Vibration of aircraft steering systems has been a problem of great concern since the production of first airplanes. Shimmy is an oscillatory motion of the landing gear in lateral and torsional directions, caused by the interaction between the dynamics of the tire and the landing gear, with a frequency range of 10–30 Hz. Though it can occur in both nose and main landing gear, the first one is more common. It is difficult to stiffen the nose gear against shimmy since it must be steerable and retractable. Vibration of aircraft steering systems deserves and has gained attention since shimmy is one of the most important problems in landing gear design.

Basic cause of shimmy is energy transfer from tire–ground contact force and vibration modes of the landing gear system. Shimmy is a dangerous condition of self–excited oscillations driven by the interaction between the tires and the ground that can occur in any wheeled vehicle. Problem of shimmy occurs in ground vehicle dynamics and aircraft during landing and taxiing.

Shimmy is driven by the kinetic energy of the forward motion of the aircraft and is a combined motion of the wheel in lateral and torsional directions, caused by the interaction of the landing gear and structural dynamics of the tire, as shown in figure 3.1. Shimmy may lead to instabilities degrading comfort, but it can also affect visibility of the pilot and cause more dangerous results such as loss of control, excessive tire wear, failure of mechanical components or even collapse of the landing gear.

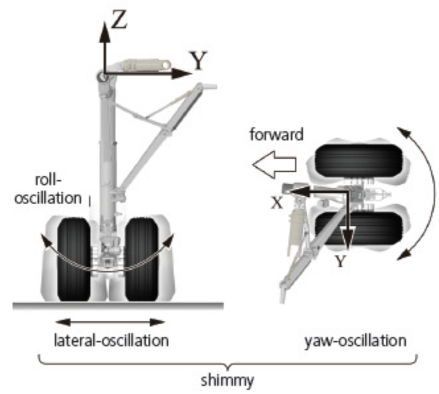

Figure 3.1: Shimmy oscillations [42].

Shimmy oscillations are unwanted self–excited vibrations of a rolling wheel about an almost vertical steering axis. Steering axis is also called the caster axis or the king–pin axis. Shimmy can occur in taxiing aircraft, as well as steerable wheels of cars, trucks, motorcycles, trailers and tea carts. In the case of landing gear, shimmy is the result of the coupling between tire forces and landing gear bending and torsion. In the case of a shopping cart wheel, it is caused by the coupling between transverse and pivot degrees of freedom of the wheel.

3.2 Causes of Shimmy

Basic cause of shimmy is energy transfer from tire–ground contact force and vibration modes of the landing gear system. Shimmy is reported to be due to the forces produced by runway surface irregularities and nonuniformities of the wheels [2,3,43,44].

Shimmy is an unstable phenomenon occurring with a certain combination of parameters such as mass, elastic quantities, damping, geometrical quantities, speed, excitation forces and nonlinearities such as friction and freeplay. It is difficult to determine shimmy analytically since it is a very complex phenomenon, as factors such as wear and ground conditions are hard to model.

Shimmy is a complex phenomenon influenced by many parameters. Causes of shimmy can be listed as follows [1,3,7,11,21,44,45].

- Insufficient overall torsional stiffness of the gear about the swivel axis
- Inadequate trail, since positive trail reduces shimmy

- Improper wheel mass balancing about the swivel axis
- Excessive torsional freeplay
- Flexibilities in the design of the suspension
- Surface irregularities
- Nonuniformities of the wheels
- Worn parts
- Steering system characteristics

Small differences in physical conditions can lead to extremely different results. For example, it is reported in [46] that a new small fighter aircraft whose name is withheld, has displayed no vibrations during low and high speed taxi tests and first several take–offs and landings, but shimmy vibrations with frequencies in the range 22–26 Hz were experienced during next several take–offs and landings at certain speeds, especially during landing. This demonstrates the effect of wear on landing gear shimmy.

In a journal paper dating to 1954, shimmy has been defined as the term used to describe the self–induced swiveling of the nosegear of an airplane. In the same paper, it is also stated that millions of dollars have been spent because of shimmy problems since 1950. Even as early as 1951, a program was initiated at the Wright Air Development Center to study the problem of shimmy by developing a theory and conducting experimental research on fighter, bomber and cargo aircraft. Several accidents on the runway have been reported to be caused due to shimmy [47].

Table 3.1 gives trail and strut inclination values of some aircraft. More can be found in [7].

Table 3.1: Nose gear mechanical trail and gear inclination values [7].

Aircraft	Trail (m)	Strut inclination (degrees)
Boeing 707	0.075	0
Boeing 727	0.075	0
Boeing 737	0.050	5
Boeing 747	0.127	0
Boeing 757	0.075	0
Boeing 767	0.075	0

Forces and moments developed between the wheel and the ground cause the wheel tend to deviate in the torsional ψ direction, which is the direction between the central plane of the wheel and the vertical plane of motion. The wheel deviates in the direction of the angle between the central plane of the wheel and the vertical plane of motion. Vibration in the ψ direction and deviation of the wheel are dependent on each other. Frequency of the rotations about the vertical swivel axis and oscillations in the lateral direction are in the range 10 to 30 Hz [1,3,21,43,44,48].

Normal load on the tires depend on the deflection of the shock absorber. Normal load on the tires cause changes in the tire characteristics. Thus, shimmy stability depends on shock absorber deflection due to changes in tire properties, as well [1].

3.3 An aircraft Accident Related to Shimmy

Shimmy is not catastrophic but it can lead to problems such as excessive wear, shortened life of landing gear components, discomfort for passengers and inconvenience for pilots.

For instance, in 1995, the left main landing gear of a Fokker F28 began shimmying after touchdown in Calgary, Canada. Oscillations continued until both left wheels and brakes were separated from the axles, although brakes were applied to slow down the aircraft and control shimmy. Examination revealed that upper torque links failed 6 km from touchdown and wheels were separated 44 km after touchdown. Passengers and crew were evacuated, but there was enormous damage to the wheels, tires, brakes and left flaps. This accident was reported to be the 29th recorded in the manufacturer's database up to that time [35].

3.4 Gear Walk

Another instability regarding a landing gear is the brake–induced instability called gear walk, low frequency fore–and–aft oscillation of the landing gear, as shown in figure 3.2. It occurs due to the coupling between the anti–skid system of the brake and the structural dynamics of the leg and involves the main landing gear.

When brakes are applied, a horizontal ground load develops and the leg curves backwards. When the brakes are released due to the detection of a skid, the leg curves forwards. The entire cycle repeats itself because the release of brakes accelerates the wheels and so on. Although the frequency range of gear walk depends on the landing gear, it is placed in the range 10–50 Hz. Effects of gear walk can be felt through the structure of the aircraft and can reach high amplitudes. Unlike shimmy, gear walk has not been extensively investigated in literature [33].

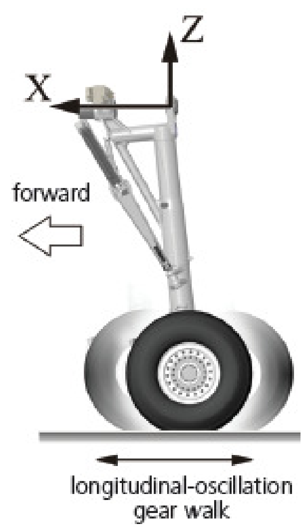

Figure 3.2: Gear walk [42].

3.5 Suppression of Shimmy

Shimmy is a great concern in aircraft landing gear design and maintenance. Prediction of nose landing gear shimmy is an essential step in landing gear design because shimmy oscillations are often detected during the taxi or runway tests of an aircraft, when it is no longer feasible to make changes on the geometry or stiffness of the landing gear.

Currently, effective measures to abate shimmy are to use a shimmy damper, as in figure 3.3, and to improve optimization of the landing gear design, but these methods cannot completely attenuate shimmy.

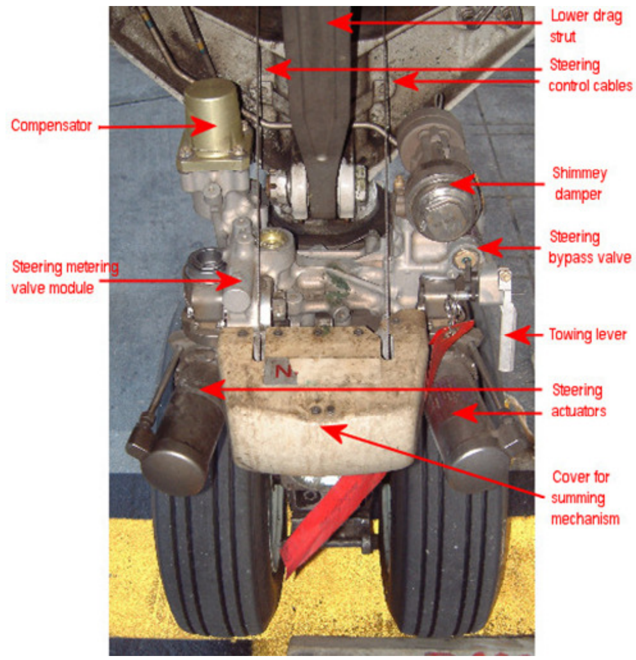

Figure 3.3: Placement of the shimmy damper [4].

Corotating wheels and inclining the shock absorber also have a stabilizing effect. Corotating wheels are formed by interconnecting two wheels by a shaft. This type of wheels on a common rotating shaft cause additional yaw stiffness and are very effective in increasing shimmy stability. They increase steering torque and even if one of the tires is burst, shimmy occurring with the remaining tire is tolerable. Many nose gear are designed with dual corotating wheels to prevent shimmy [1,49].

Hydraulic damping is the usual method to suppress shimmy. A traditional hydraulic shimmy damper has a single valued damping function. Oil viscosity cannot be changed and is affected by temperature and oil compressibility. For a long time, parameters of passive suspension systems are tried to be optimized so as to make the suspension system work better, but there are limitations such that the improvement is only effective in a certain frequency range.

Semi–active control can achieve desirable performance, compared to passive control, and consumes much less power than active control. In other words, it combines the advantages of active and passive suspensions. It provides good performance, is economical and safe and does not require high–power actuators or a large power supply. When the semi–active system fails, it can still work as a passive controller. Employment of semi–active suspension in aircraft landing gear is still subject to research and such devices have not been implemented on aircraft yet. Using semi–active control devices in aircraft landing gear will suppress of shimmy more effectively, as research indicates [50,51].

Addition of a mass ahead of the strut tends to attenuate shimmy, as well.

Another common cure is to replace the tires even though they may not be worn out.

It has been reported in [11] that torsional freeplay of less than 0.75° results in absolute stability in analytical shimmy tests of an aircraft.

Although shimmy was observed in earlier aircraft as well, there were no extra shimmy damping equipments installed. Historically, France and Germany tended to deal with shimmy in the design phase, while in United States, the trend was to solve the problem after its occurrence. Currently, the general methodology is to employ a shimmy damper and structural damping [35,45,52].

The following basic conclusions are listed in [30] regarding shimmy.

- Caster length is a critical shimmy parameter and sufficient caster length eliminates shimmy.
- Increasing loads on the wheel increases shimmy.
- Decreasing structural rigidity of the wheel and the fuselage increases shimmy.
- Main landing gear configurations involving bogies are less prone to shimmy instability than twin– wheeled designs due to increased wheelbase.

3.6 Shimmy Dampers

A shimmy damper, acting like a shock absorber in a rotary manner, is often installed in the steering degree of freedom to damp shimmy. It is a hydraulic damper with stroke limited to a few degrees of yaw, reducing the effects of shimmy by restraining the movement of the nose wheel, which prevents or reduces the amplitude of shimmy limit cycle oscillations. It allows the wheel to be steered by moving it slowly, but does not allow it to move back and forth rapidly. A shimmy damper consists of a hollow tube filled with hydraulic fluid, a shaft and piston causing velocity dependent viscous damping when moved through the fluid.

Shimmy dampers are used in the Boeing 737 and Airbus A320 as a preventive measure to improve stability, with the disadvantage of additional weight and maintenance. At speeds close to the critical shimmy velocity, small motions may grow, resulting in instabilities that the pilot may not be able to correct. To prevent such occurrences, there should be enough margin between taxi speeds and critical shimmy velocity [1,3,11,35,45,52].

Shimmy stability is a function of many design parameters involving the dynamic behavior of the tire and landing gear structure. Traditionally, shimmy stability analysis in linear systems is performed using Hurwitz criterion or an eigenvalue analysis. It is possible to develop analytical expressions for shimmy stability if the Hurwitz criterion is used so that behavior of the system can be approximated analytically for the parameters close to the critical ones [1].

Tire parameters, stiffness, entire operating range of the aircraft on the ground, freeplay, friction, stiffness modifications, geometry changes, steering system, friction plates, mass balance and shimmy dampers have to be considered when analyzing shimmy [2]. Many combinations of the vertical force and aircraft forward velocity should be considered. Length of the mechanical trail, tire wear and inflation pressure are other important parameters affecting shimmy stability.

Freeplay is caused by manufacturing tolerances and wear and has an effect on shimmy stability. Although tight tolerances might solve the problem of freeplay in the prototype, the problem will reoccur after the aircraft is in service. Damping can be improved by adding masses connected to the wheel axle and in front of the shock absorber.

3.7 Landing Gear Models

In general, a landing gear is modeled by three vibratory degrees of freedom, which are the torsional, lateral and longitudinal degrees of freedom.

Torsional or yaw degree of freedom is related to the rotation of the wheel assembly about the vertical axis, lateral degree of freedom is related to the lateral displacement of the strut and roll degree of freedom is related to the rotation about the fore and aft axis.

3.7.1 The simple trailing wheel system with torsional degree of freedom

The simplest system capable of exhibiting unstable shimmy vibrations is the simple trailing wheel system with yaw degree of freedom. The trailing wheel model seen in figure 3.4 is often used to illustrate shimmy instability and to evaluate the differences between tire models.

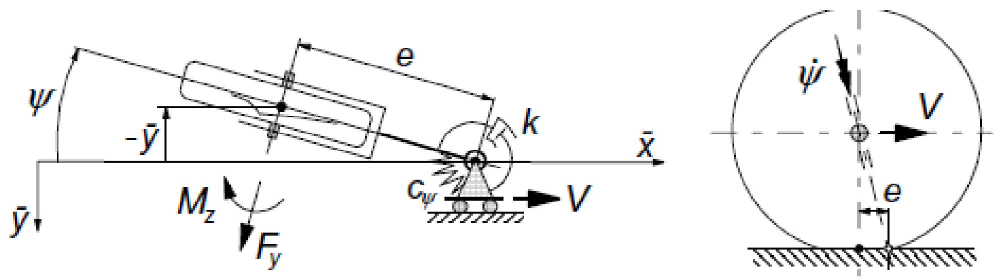

Figure 3.4: Simple trailing wheel system [15].

To reflect the landing gear more closely, yaw stiffness, lateral compliance of the support and roll may be added to the model [1,15].

In this model, the wheel and the tire are mounted on a trailing arm which can swivel about a vertical axis that moves with velocity V . Motion variable is the yaw angle ψ of the wheel plane about the swivel axis. This axis intersects the road plane at a distance e , called mechanical caster or trail length, in front of the contact center. A torsional spring with linear stiffness k and a rotation damper with viscous damping coefficient c are introduced for yaw motion. The hinge joint moves forward along a straight line with constant velocity V .

Equations of motion for the trailing wheel system will be presented in 5.1.

A simple bogie consisting of two wheels is introduced in [1], by adding a second deformation angle for the front tire. Such a simple bogie model is seen in figure 3.5. Its equations of motion are given in [1] but will not be presented here for purposes of conciseness.

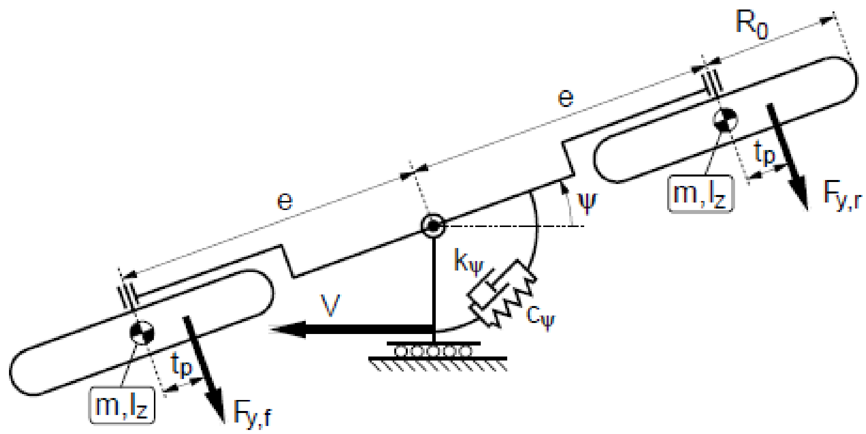

Figure 3.5: Top view of a bogie with two wheels [1].

3.7.2 Systems with torsional and lateral degrees of freedom

Lateral support of the hinge is rigid in the models presented in 3.6.1, but this might not always be the assumption when modeling a landing gear. Lateral flexibility of the support may be taken into consideration as a next step. The simplest way is to introduce lateral stiffness c_y as in figure 3.6. The additional degree of freedom allowing the steering axis to move sideways leads to a fifth order system [1,15].

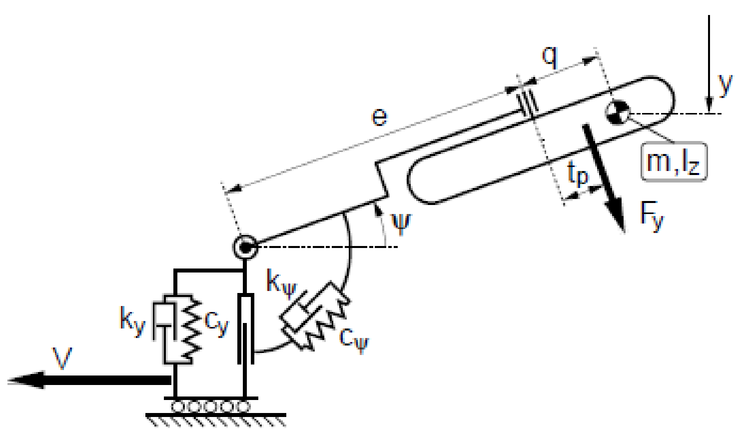

Figure 3.6: Trailing wheel system with lateral flexibility [1].

This system has independent lateral and yaw degrees of freedom y and ψ, respectively. Its equations of motion are given in [1] and [53] but will not be presented here for purposes of conciseness.

3.7.3 Systems with torsional, lateral and longitudinal degrees of freedom

All three modes of vibration of a landing gear may be considered in a model with torsional, lateral and longitudinal degrees of freedom, however it has been concluded in [54] that the longitudinal mode does not contribute much to the landing gear dynamics. Equations of motion of this model are given in [54] but will not be presented here for purposes of conciseness.

4. LITERATURE SURVEY ON LANDING GEAR SYSTEMS AND SHIMMY

A thorough review of the literature on landing gear shimmy, the wheel shimmy problem, tire models, solution techniques, the trend in treating shimmy in aviation industry, semi–active and active control of shimmy, software development, multibody dynamics approach, landing gear structural analysis and design, aeroacoustics and noise prediction and flight simulators has been conducted.

Selected books on aircraft analysis and design, landing gear design and tire and vehicle dynamics have been reported. The few dissertations on shimmy are also mentioned.

4.1 Landing Gear Shimmy

Number of publications available in literature on landing gear shimmy is limited because many developments are proprietary and are not published in literature. There even exist studies in literature where most figures are removed since the information is considered confidential, but the verbal sections are published in full [31].

Shimmy started being investigated in 1920's both theoretically and experimentally and soon it became clear that it is caused not by a single parameter but by the relationships between parameters. One of the earliest papers on shimmy dates back to 1954 and develops a theory for landing gear shimmy [47]. It is desired to obtain a stable gear with minimum artificial damping. Similarly, [55], dating to early 1960's, presents the nonlinear equations of motion of a four degree of freedom nose gear for an investigation of shimmy amplitude for proper design of damping devices. Likewise, [49], published in the same period, presents the equations of motion of a dual–wheeled landing gear with corotating wheels and shows the role of the tire in determining shimmy characteristics is more important in the dual–wheeled corotating system than in the conventional designs.

Effects of acceleration and deceleration on shimmy have been reported to be examined, and the accelerating system is found to be slightly less stable [22]. It is reported in [1] that although Douglas DC–9, BAC 1–11, Boeing 737 and Fokker F28, designed with very similar specifications, all had main wheel shimmy problems, none of the companies reported their work in literature. The general approach is to perceive shimmy as a problem that has no solution that can be found using established engineering methodologies. This is because of the lack of specific knowledge in the field, suitable analysis tools and reliable data on tire characteristics. Even if suitable analysis tools exist, results will not be complete until the designs of both the landing gear and the airframe are complete. In short, landing gear shimmy is still a hot topic.

It has been shown 40 years ago that instability of certain nosegear can result from wheel and tire imperfections such as unbalances and flat spots, and this self–excited instability called shimmy is similar to parametric resonance [56]. The major difference between this type of resonance and the ordinary resonance caused by an external periodic function is that the major instability occurs when the wheel rotation frequency is twice any natural frequency of the system. This has been shown on a very simple model with only camber and yaw degrees of freedom. It is stated in [1] and [2] that twin–wheeled cantilevered landing gear, which are more prone to shimmy oscillations than other configurations, have been dealt with the most in literature.

[57] is a valuable work in the sense that it applies different linear and nonlinear mathematical methods to investigate the shimmy of a torsional nosegear model, such as computing eigenvalues, obtaining stability curves in the parameter space, obtaining limit cycles and performing numerical simulation to obtain time histories. Nonlinear model is solved in the time domain to obtain time histories and limit cycles and the linearized model is used to obtain eigenvalues and stability boundaries. It is found that increasing velocity, decreasing damping coefficients and increasing vertical force increase the tendency for shimmy.

A dynamic model of an aircraft nosegear is developed in [44] and effects of design parameters such as energy absorption coefficient of the shimmy damper, the location of the center of gravity of the landing gear, shock strut elasticity, tire compliance, friction between the tire and the runway surface and the forward speed on shimmy are investigated. It is shown in [48] that dry friction is one of the principal causes of shimmy.

Lateral dynamics of nose landing gear shimmy models has gained some attention. Lateral response of a nose landing gear has been investigated in [45] where nonlinearities arise due to torsional freeplay. In [58], lateral response to ground–induced excitations due to runway roughness is taken into consideration as well. Both studies show that freeplay causes a very significant reduction in the critical shimmy velocity, however a combination of freeplay and runway roughness has an adverse effect. Lateral stability of a nose landing gear with a closed loop hydraulic shimmy damper is presented in [52]. Closed form analytical expressions for shimmy velocity and shimmy frequency are derived in regard to the lateral dynamics of a nose landing gear in [59].

Bifurcation analysis of a nosegear with torsional and lateral degrees of freedom is performed in [53]. Shimmy is considered as a function of the forward velocity of the aircraft and the vertical force on the landing gear. Similarly, bifurcation analysis of a nosegear with torsional, lateral and longitudinal modes is performed in [54] and shimmy is again considered as a function of the forward velocity and the vertical force. Contribution of each mode to shimmy is studied. Time histories, frequency spectra and the dependence of shimmy on torsion are presented.

[1] deals with the shimmy stability of twin–wheeled cantilevered aircraft main landing gear. A number of methods ranging from simple linear models of the landing gear structure and the tire to detailed nonlinear models are covered. Theories describing tire behavior are given. Analytical expressions for stability in terms of gear and tire parameters are derived, the effect of various parameters are investigated and the base configuration is optimized for a simple trailing wheel, a two wheel bogie and a trailing wheel with a flexible support.

Dependence of shimmy oscillations in the nose landing gear of an aircraft on tire inflation pressure are investigated in [60]. The model derived in [53] is used and it is concluded that landing gear is less susceptible to shimmy oscillations at inflation pressures higher than the nominal.

[30] proposes a new, computationally efficient and accurate tire model for aircraft landing gear dynamics where the aircraft tire is modeled as a set of individually

linked thin cylinders. Tire responses are investigated with increasing velocity, acceleration, inflation pressure and vertical load.

It is stated in [1] that analytical expressions are preferred to describe shimmy stability. Eigenvalues can be computed or the Hurwitz criterion can be applied to obtain analytical expressions to evaluate shimmy stability. The second has been applied in [1] and [15]. Eigenvalues have been calculated as a function of the mechanical trail. Stability boundaries have been obtained in the (e,V) parameter plane with and without a damper. It is shown that the unstable area is reduced with the introduction of damping and disappears when the damping is sufficiently high. At moderate values of yaw damping, stability has been found to depend on the velocity.

4.2 Wheel Shimmy Problem

Theoretical research on shimmy has a long history, with the initial focus on tire dynamic behavior because tires play an important role in causing shimmy instability. Over the years, a number of tire models have been developed for application to the shimmy problem but the question of which model is most accurate in predicting shimmy has not been answered.

Aircraft landing gear dynamics and vehicle dynamics can be considered similar in the sense that tire models are crucial for both. Shock absorbers and suspension designs have similar considerations and the flexibility of the vehicle is becoming a point of interest in both. In the case of aircraft, ground loads exerted by the landing gear are often design drivers for the aircraft as a whole. Determination of landing gear loads is a difficult task because the applied forces and torques, comfort requirements, cost, weight and maintainability constraints interact in a complicated way [2].

Many papers have been published addressing shimmy as a vehicle dynamics problem. In that perspective, tire is the most important item, and tire models have been investigated. The underlying idea is that dynamics of the vehicle or the aircraft can be solved to a certain extent by the development of multibody dynamics and commercial software. Wheel–ground contact problem, however, requires more attention. Existing models have been compared and progressed so that models that represent the behavior of tires more realistically can be obtained, and tires that are less prone to shimmy can be developed.

[22] examines the wheel shimmy problem and its relationship with longitudinal tire forces, vehicle motions and normal load oscillations using the von Schlippe model. Effects of system characteristic and operating conditions such as a constant braking–traction force, oscillations of the vertical tire load and oscillations of the forward velocity on wheel shimmy have been considered. The system taken into consideration represents an aircraft landing gear, front wheel of a motorcycle, or a bicycle. Results indicate that braking–traction forces and acceleration do not need to be taken into consideration. It is suggested that the system should be designed so that resonances occur only at velocities that are out of the operating range of the system. This can be achieved by modification of system parameters, such as the caster angle or tire–wheel combination. If this is not possible, a large trail might minimize shimmy resonance.

[43] is an investigation of tire parameter variations in wheel shimmy, by considering the shimmy resulting from the elasticity of a pneumatic tire, particularly in taxiing aircraft, by using the stretched string tire model. Stability boundaries for various tire and system parameters are given in terms of mechanical trail and forward velocity. Some of these parameters are tire relaxation length, tire pneumatic trail, tire half contact length and tire lateral stiffness. Effects of torsional damping, torsional stiffness, lateral damping, pivotal damping and pivotal stiffness have been considered. Experimental data obtained through the use of a scaled model has been presented.

It is concluded that mechanical trail is a parameter since shimmy does not occur for large trail. Due to space reasons, however, actual wheel struts must operate at small values of mechanical trail. Negative trail seems to be more desirable for most systems with torsional stiffness.

Results indicate that there should be an optimum ratio of the lateral to torsional stiffness, where the torsional natural frequency has a larger value minimizing the shimmy region. Results also show that tire length parameters have a little effect on the shimmy region. For small values of mechanical trail, the lateral stiffness of the tire also does not have much effect. Reduction of mass and inertia raises the value of the velocity defining the boundary of the stability region and damping always reduces the shimmy region. It is also stated it is hoped that some of the trends are fundamental enough to hold for any system model although actual systems may exhibit different behavior. System models that accurately predict shimmy regions can be constructed and results obtained from the model can be useful in the preliminary design of struts to avoid or minimize the possibility of shimmy. Effect of parametric excitation on tire shimmy is found to be small, and even negligible in some cases.

[61] is on the application of perturbation methods to investigate the limit cycle amplitude and stability of the wheel shimmy problem. Multiple time scale technique is applied to an aircraft landing gear with nonlinear damping, as well. Analytical expressions for the limit cycle amplitude and frequency are obtained in terms of the forward velocity of the aircraft and system parameters.

In another mathematical study, incremental harmonic balance method is applied to an aircraft wheel shimmy system with Coulomb and quadratic damping [75] and amplitudes of limit cycles are predicted.

4.3 Tire Models

Basic difficulties in analyzing and predicting shimmy are in modeling the tire–ground contact and description of transmission of the forces and moments generated at the contact region.

Theories on tire models can be divided into stretched string models and point contact models. Although the two models agree with each other under steady state conditions, differences exist in describing transient behavior [1,11].

The point contact method assumes the effects of the ground on the tire act at a single contact point and is much easier to implement in an analytical model.

In the stretched string model proposed by von Schlippe, the tire centerline is represented as a string in tension, the tire sidewalls are represented by a distributed spring where the string rests and the wheel is represented by a rigid foundation for the spring. Pacejka has proposed replacing the string by a beam.

Moreland and von Shlippe landing gear tire shimmy models have been compared in [62]. Parameters used in each model have been defined and their equivalence has been shown. Relaxation length and tire half footprint length are the two critical components in the von Schlippe model. Time constant and the yaw coefficient are the two critical components in the Moreland model.

Regardless of the model used, it is important to use accurate values for all parameters. Measurement techniques are used to obtain tire parameters and measurements on aircraft tires lead to empirical formulas. Construction of radial tires in the last decade brought up a difference in characterization of tire models. While the initial models to evaluate shimmy instability were linear, nonlinear models were used later on for both the tire and the suspension when analyzing the shimmy of the front wheel of a light truck [1,11].

[21] compares different dynamic tire models for the analysis of shimmy instability. Straight tangent tire model, von Schlippe tire model and the rigid ring tire model have been assessed and their equations have been validated using measurements.

[63] is on tire dynamics and is a development to deal with large camber angles and inflation pressure changes. [64] is another study on tire dynamics, where stability charts show the behavior of the system in terms of certain parameters such as speed, caster length, damping coefficient and relaxation length. [20] is an experimental study on wheel shimmy where system parameters are identified, stability boundaries and vibration frequencies are obtained on a test rig for an elastic tire.

[65] studies the periodic shimmy vibrations and chaotic vibrations of a simplified wheel model using bifurcation theory. Development of transient chaos has been analyzed. Routh–Hurwitz criterion has been applied to find the limits of stability.

4.4 Solution Techniques

The standard solution techniques used in shimmy analysis are either the application of stability criterion to linear systems or direct integration of the nonlinear equations of motion. In this respect, a different approach has been employed in [65] and [61] by employing the perturbation method.

Conventional techniques such as Routh–Hurwitz criteria or inspection of the real parts of the eigenvalues can only be applied if nonlinearities such as freeplay, Coulomb friction are neglected. In reality, however, nonlinearities due to torsional and lateral freeplay, dry friction and the use of nonlinear hydraulic dampers must be included for the model to adequately represent the shimmy behavior. The nose gear steering system is usually utilized as a shimmy damper in addition to its steering function, making the system an extremely complex nonlinear mechanism.

A full description of the steering system is very complex to model and the high order system of equations increases the time and costs required to solve them. The usual procedure to follow when analyzing nonlinear systems is to obtain time histories for a given forward velocity of the aircraft and a particular set of initial conditions. Parametric studies must be made to specify the required values of parameters such as damper coefficients, allowable freeplay and stiffness. Various initial conditions should be considered, as well. Limit cycle amplitudes should also be compared with allowable deflections and rotations of landing gear components.

4.5 Trend in Treating Shimmy in Aviation Industry

Landing gear designs need to meet JAR (Joint Aviation Requirements) in Europe and FAR (Federal Aviation Regulations) in USA to obtain an airworthiness certificate. Although the requirements are very extensive with respect to calculation of static loads, regulations do not include dynamic stability analysis or a shimmy analysis. Therefore, shimmy analysis seems to be a missed point in civil aviation requirements.

As a number of experts have stated, shimmy is ignored in the design process because of lack of specific knowledge of the shimmy phenomenon, suitable analysis tools and reliable data on structural stiffness or tire characteristics. Situation is even more complicated because even if the best tools are available, analysis results may not be expected until the design of both the landing gear and the airframe are advanced.

Shimmy is ignored up to the point when problems occur on the prototype aircraft or the aircraft already in service and a symptomatic treatment is provided if shimmy occurs [2]. Potential for shimmy is often revealed during runway taxi tests and the only option available at this point is to add a shimmy damper. This is similar to adding masses to the body of a passenger car to suppress resonance.

A shimmy free landing gear has not been built yet. Trend in the industry is to develop shimmy models when the problem occurs but the problem is that structural parameters cannot be changed for shimmy suppression once the design is complete.

It will be useful to develop models that have no shimmy problems in the first place. For this purpose, various existing landing gear designs need to be evaluated for shimmy stability. This will improve the general understanding of the shimmy phenomenon any may also provide additional confidence in the simulation techniques [1].

In 1995, a conference devoted to landing gear shimmy was organized by AGARD (NATO Advisory Group for Aerospace Research and Development), showing the attention paid and importance given to the shimmy phenomenon.

4.6 Semi–Active and Active Shimmy Control

Control and damping of shimmy has also gained attention, due to the risks involved in the case of shimmy. Passive controllers are currently used in most aircraft. Oil viscosity in conventional hydraulic shimmy dampers cannot be changed and is susceptible to temperature and compressibility.

Semi–active control can achieve more desirable performance when compared to passive control and consumes less power when compared to active control. Semi–active control is applied only in theory and has not been realized. It must be borne in mind, however, that design parameters of a shock absorber in a passive system cannot meet physical requirements for different landing and runway environments.

Semi–active control of landing gear shimmy using a magnetorheological damper is investigated in [50]. Variation of critical shimmy velocity with vertical force and caster length has been examined. Similarly, a magnetorheological damper is applied to a landing gear in [66].

Active control of shimmy in aircraft landing gear is investigated in [35]. Landing gear model is the one given in [57]. Limit cycle oscillations of the nonlinear model have been obtained with respect to varying parameters and shimmy stability variation with varying caster length and taxi velocity has also been analyzed after linearizing the system. Active control has been employed to suppress shimmy oscillations.

Another investigation of active shimmy damping can be found in [36], where the active control strategy incorporates a PID (Proportional Integral Derivative) controller. Active control is reported to reduce impact and fatigue loads and vertical displacements by adjusting the stiffness and damping values.

The model in [57] is also used in [67] to analyze the influence of structural parameters on shimmy. Robust model predictive control is applied to suppress shimmy during landing and taxiing. An adaptive shock absorber with two cavities and dual damping is designed in [10] and simulated on the ADAMS software.

A direct adaptive output feedback controller is proposed in [68] for active shimmy damping, as part of the DRESS (Distributed and Elecromechanical Nosegear Steering System) FP6 project. Dynamics of the shimmy phenomenon is modeled according to [57].

4.7 Software Development

The objective in [11] is to develop software on assessing shimmy stability of a general class of landing gear designs using linear and nonlinear landing gear shimmy models. The linear model combines the finite element model of the landing gear with a point contact tire model and is analyzed with an eigenvalue approach to determine stability. The nonlinear model is integrated numerically to simulate the system response to a specified initial disturbance. The advantage of the nonlinear model is its ability to take care of nonlinear aspects such as freeplay, exponential damper and Coulomb friction.

An auto modeling program based on ADAMS software is developed in [69] with the aim of generating aircraft models to be incorporated in landing gear simulation.

4.8 Multibody Dynamics Approach

Dynamic analysis of a nose landing gear has been studied as a benchmark problem in [25] using the finite element method. The study focuses on rigid and flexible joint modeling using the finite element method. Beam elements, a spring damper representing the shock absorber and a flexible wheel have been used to model the landing gear. All joints have been considered to be the hinge type. The load is represented by a rigid body at the top node. Friction coefficient is assumed to vary with the slipping velocity and touchdown is followed by two bounces during simulation.

Cases of landing on flat and sinusoidal surfaces have been taken into consideration. Simulation results show the time histories of vertical position of the wheel center, lateral deformation of the wheel, radial contact force, angular velocity of the wheel and slipping velocity of the wheel.

In another study taking a multibody modeling approach, gear walk has been analyzed using a finite element model in terms of a wide range of operating conditions, aircraft payload distribution and runway surface characteristics [33].

4.9 Landing Gear Structural Analysis and Design

From an aircraft landing gear structural analysis perspective, there exists some work in literature regarding the dynamics of such mechanisms.

[70] takes a structural mechanics approach and investigates the calculated and measured strength of a composite undercarriage spar. Some of the papers are on the subject of failure analysis.

[71] conducts fracture analysis to search for the causes of the accident of a civil aircraft by investigating the causes of failure of its main landing gear by optical analysis and electron microscopy. The cause of the accident was found to be heavy landing, leading to shear failure of bolts of the locking linkages. [72] investigates the fatigue crack of a landing gear that failed during its landing by visual examination, metallographic examination, chemical analysis, tensile testing, fractography and fracture toughness testing. While no pre–failure cracks were discovered in the case in [71], some were discovered in [72].

[31] investigates analysis techniques for landing gear structural design, involving a balance of weight, cost and safety. Safety is the first objective and no compromise can be made in this regard in designing a landing gear, whereas weight and cost might involve tradeoffs, depending on the project.

Transverse vibrations of landing gear struts with respect to a hull of infinite mass have been studied theoretically in [73]. Transverse axis is defined as the hull longitudinal axis. Simplifying assumptions in this study are that the aircraft is represented by two bodies, a hull and main gear struts. It is stated that fatigue failure of landing gear components is mainly due to cyclic transverse loads. Similarly, [74] presents a nonlinear model describing the dynamics of the main gear wheels relative to the fuselage. The model accounts for yaw and roll degrees of freedom. Most shimmy models present at the time of publishing of this work consider the speed vector of the aircraft in the wheel plane as undisturbed motion, where the wheels move without slip. This is the situation of landing and taking off under no crosswind. The model studied in this work, however allows for a constant lateral fuselage speed, as well. It is concluded that increasing lateral speed has a decreasing effect on the critical shimmy speed of the main wheels.

On a different perspective, [27] investigates the relationship between pavement life cycle and aircraft loading depending on the type of the landing gear, using airfield pavement test data and updating historical records. Numerical analysis was performed to predict pavement thickness requirements and pavement life.

4.10 Aeroacoustics and Noise Prediction

Numerical simulation of noise around complex geometries like a landing gear is a challenge in the field of aeroacoustics. Prediction of airframe noise is difficult because of the complexity of the geometry and the sound field.

Considerable effort is given to noise reduction because the continuous increase in air travel requires attention must be paid to the environment around an airport. Similar to the shimmy phenomenon, most of the data is confidential.

Engine noise was the major source of aircraft noise in the past, but noise reduction techniques have reduced engine noise significantly over the past decades. Noise from the landing gear, flaps and slats, called airframe noise, can exceed the engine noise when the engines are at low power. There is a minimum noise an aircraft must not exceed to pass certification [75].

Flow around a two–wheel main landing gear is investigated in [76] since landing gear noise is one of the most dominant sources of noise during the approach phase of an aircraft when the engines are operating at low thrust.

[77] is another study on landing gear noise prediction, aiming at predicting noise radiation from basic geometries and a simplified landing gear model, using CFD and computational aeroacoustic simulation. It is concluded that removing a small part of the geometry leads to significant changes in the radiated sound.

Prediction of noise from isolated or installed landing gear geometry, including aeroacoustic and aerodynamic interactions involved in noise generation is undertaken experimentally and numerically by the use of the FLUENT software in [75] to aid designers in creating low noise landing gear. Main and nose landing gear of Boeing 777 have been taken as example cases.

4.11 Flight Simulators

Flight simulators are an essential part of flight training since they reduce the costs and risks involved in training for normal and extreme operating conditions. Pilots need to be trained for situations that are too dangerous to practice in real aircraft and too important to ignore. Major airlines, manufacturers and research institutes operate flight simulators ranging from purely visual systems to 6 degree of freedom hydraulic simulators.

Dynamic behavior of a simulator should be realistic enough for scenarios in flight and on the ground. The simulator and the aircraft need to be compared and matched so that the behavior of the simulator is verified and the training is realistic for conventional and dangerous maneuvers. Ground handling modes generally respond incorrectly because the landing and bouncing of aircraft are not yet well understood. Transition from aerodynamics to landing gear dynamics needs attention if pilots are to be trained adequately for zero height scenarios.

[14] develops a piecewise simulator model to replicate nonlinear aircraft behavior during taxiing, flight and landing. Time histories of the model show good consistence with the instrumented data from a Boeing 747. Tires are modeled as nonlinear mass spring systems subject to forces during landing and taxiing, resulting in longitudinal, lateral and normal deformations. Tire characteristics such as relaxation length, pneumatic caster or trail, shape constant, distortion factors, normal tire sinking due to deformation, change in stiffness due to tire velocity and tire type are included in the tire model. Runway unevenness and pilot inputs such as steering and braking are included in the model as inputs. Outputs of the tire model are the resulting forces and deformation.

Landing gear models to be used during landing and take–off of the aircraft on a 6 degree of freedom platform are derived in [78] and [79]. The landing gear is modeled on a 6 degree of freedom platform so that the landing gear model is valid for cases other than landing on steady ground, considering aircraft landing on and taking off from carriers. Dynamic model of landing gear of aircraft landing on carriers is derived in [80]. The deck has six degrees of freedom of motion in the model, therefore the damper in the landing gear is more complex to model than in the case of landing on the ground.

4.12 Selected Books

4.12.1 Aircraft analysis and design

There are some, if not many, books written on aircraft design with chapters devoted to landing gear analysis and design.

[8], published in 2010, has sections on the basics of landing gear design including a classification of landing gear, nomenclature, definitions of various declared lengths and angles, design drivers, calculation of loads on wheels and shock absorbers, classification of runway pavement and tires. There are also worked out examples of landing gear design for a civil and a military aircraft. These might be helpful in providing background information on landing gear analysis and design.

[3] is part of a series of books on airplane design, focusing on landing gear systems, published in 2000. The book includes sections on landing gear design, with subsections on tires, struts and shock absorbers, brakes and braking capability, landing gear geometry, design considerations for carrier airplanes, retraction kinematics and examples on unconventional landing gear designs. There are also sections related to military applications, such as weapons integration. The book also includes many figures and data tables regarding various components and subsystems.

[13] is a comprehensive technical report written by researchers at the Multidisciplinary Analysis and Design Center for Advanced Vehicles at Virginia Polytechnic Institute and State University in 1996 on landing gear integration in aircraft conceptual design, prepared with the support of NASA Ames Research Center. Similar to the sections mentioned above, this report has sections on aircraft center of gravity, concept selection, tires, wheels, brakes, shock absorber design, kinematics, flotation analysis, weight estimation, analysis package, parametric studies, cost and future considerations.

4.12.2 Landing gear design

[7] is solely on landing gear design. Although printed more than 20 years ago, it is helpful in providing insight about landing gear design principles. It has sections on the design process, requirements, shock absorbers, tires, wheels, brakes, skid control, steering systems, locks, kinematics of retraction and extension mechanisms, cockpit requirements, maintenance, strength, weight and airfield considerations. It also has sections on unconventional landing gear such as those with skis or skids.

4.12.3 Tire and vehicle dynamics

[15] is on tire and vehicle dynamics, and has detailed sections devoted to tire characteristics, vehicle handling, tire modeling and the shimmy phenomenon. Tire plays an important role in the operational properties of road vehicles. Earlier research on tire models has been reviewed.

4.13 Dissertations

Only a few dissertations on shimmy vibrations exist in literature. They will be mentioned for purposes of completeness and to provide the reader with an idea of which institutions in the world are interested in working on shimmy vibrations.

Dissertations related to shimmy oscillations are presented in table 4.1, while dissertations related to landing gear are presented in table 4.2. The names of the institutions and their years of publication are also presented in the tables. Dissertations submitted in Turkey that are related to landing gear are presented in table 4.3.

A study of table 4.3 reveals that the dissertations submitted in Turkey are mostly related to the design and structure of landing gear, rather than their dynamics or shimmy analyses. All of the studies listed in table 4.3 are M.Sc. theses, rather than Ph.D. studies.

Table 4.1: Dissertations related to shimmy oscillations.

Number of reference	Title of Dissertation	Institution	Year of publication
[43]	Investigation of Tire Parameter Variations in Wheel Shimmy	University of Michigan, Engineering Mechanics	1973
[22]	The Wheel Shimmy Problem, Its Relationship to Longitudinal Tire Forces, Vehicle Motions and Normal Load Oscillations	Cornell University, Engineering Mechanics	1974
[61]	A Perturbation Method for Predicting Amplitudes of Nonlinear Wheel Shimmy	University of Washington, Mechanical Engineering	1977
[11]	Aircraft Landing Gear Shimmy	University of Missouri, Rolla, Mechanical Engineering	1992
[1]	Shimmy of Aircraft Main Landing Gears	Technical University of Delft	2000
[21]	A Comparison of Dynamic Tire Models for Vehicle Shimmy Stability Analysis	Eindhoven University of Technology, Department of Mechanical Engineering	2009

Table 4.2: Dissertations related to landing gear.

Number of reference	Title of Dissertation	Institution	Year of publication
[30]	A New Tire Model for Aircraft Landing Gear Dynamics	University of Akron, Graduate Faculty	1999
[35]	Active Control of Shimmy Oscillation in Aircraft Landing Gear	Concordia University, Department of Mechanical and Industrial Engineering	2006
[31]	Resolution of Indeterminate Landing Gear Structure Design	Ryerson University, Mechanical Engineering	2007
[75]	A New Approach to Complete Aircraft Landing Gear Noise Prediction	Pennsylvania State University, Aerospace Engineering	2009

Table 4.3: Dissertations submitted in Turkey related to landing gear.

Number of reference	Title of Dissertation	Institution	Year of publication
[81]	Burun tekerlekli hafif nakliye uçağı iniş takımı ön tasarımı ve boyutlandırılması (in Turkish)	Anadolu Üniversitesi, Graduate School of Science	1995
[82]	F–16 burun iniş takımının pist pürüzlülüğüne karşı davranışının analizi (in Turkish)	Erciyes Üniversitesi, Graduate School of Science	1996
[83]	İki kişilik hafif askeri uçağı burun iniş takımı (in Turkish)	Istanbul Technical University, Graduate School of Science, Engineering and Technology	1996
[84]	İki kişilik hafif askeri uçağı ana iniş takımı (in Turkish)	Istanbul Technical University, Graduate School of Science, Engineering and Technology	1996
[85]	Uçakların iniş takımları tasarımında dikkat edilecek hususlar (in Turkish)	Eskişehir Osmangazi Üniversitesi, Graduate School of Science	2002
[86]	Design and analysis of landing gear of a transport aircraft	Istanbul Technical University, Graduate School of Science, Engineering and Technology	2003
[87]	Bir insansız hava aracının kompozit iniş takımının tasarımı, üretimi ve testleri (in Turkish)	Istanbul Technical University, Graduate School of Science, Engineering and Technology	2009

5. SHIMMY ANALYSIS OF A TORSIONAL NOSE LANDING GEAR MODEL

In this section, a landing gear model with torsional degree of freedom is analyzed.

Equations of motion of the torsional landing gear model and the von Schlippe stretched string tire model are derived in 5.1 and 5.2, respectively.

Nonlinear equation of motion of the landing gear model is linearized in 5.3 to compute eigenvalues and perform linear stability analysis.

Characteristic equation and eigenvalues are obtained for variation of caster length and velocity in 5.4.

Application of the Routh–Hurwitz criterion to the linearized model is presented in 5.6 to obtain stability boundaries. Stability boundaries in the $e - v$ plane are presented in 5.6.1 for different values of k, while stability boundaries in the $c - v$ plane are presented in 5.6.3 for different values of σ and F_z.

Effects of increasing and decreasing the caster length e and half contact length a on stability boundaries are investigated in 5.7.

Time domain simulation of the linear model is performed in 5.8. Time histories of the torsion angle ψ and lateral tire deformation y are obtained through numerical integration using the fourth order Runge–Kutta algorithm.

Time domain simulation of the nonlinear system is performed and limit cycles are obtained in 5.9. Shimmy is presented as a limit cycle phenomenon. Effects of the damping constant c and taxiing velocity v on shimmy are investigated in 5.9.3 and 5.9.5, respectively.

5. 1 Torsional Nose Landing Gear Model

Landing gear models present in the literature have been summarized in section 3.6.

The model to be incorporated throughout the rest of this study is the torsional landing gear model presented in [35,57,67,68]. This model has been used extensively in literature to analyze the dynamics of landing gear as it has been found adequate in modeling the dynamics of nose landing gear. It will be used in this thesis as it is sufficient to perform the aforementioned analyses.

Torsional dynamics of the lower parts of the nose landing gear mechanism is modeled by a nonlinear ordinary differential equation of second order for the torsion or yaw angle ψ about the vertical axis z, while the dynamics of the elastic tire is modeled using the von Schlippe stretched string tire model, comprising of one ordinary differential equation of first order for the tire deflection y and an algebraic condition.

Landing gear dynamics is a technical issue, meaning researchers and scientists working in this area are more interested in stability and shimmy suppression, rather than developing complex mathematical models. For this reason, the torsional nose landing gear model will be used in this thesis, as well.

Figure 5.1 shows side and top views of the shimmy dynamics model.

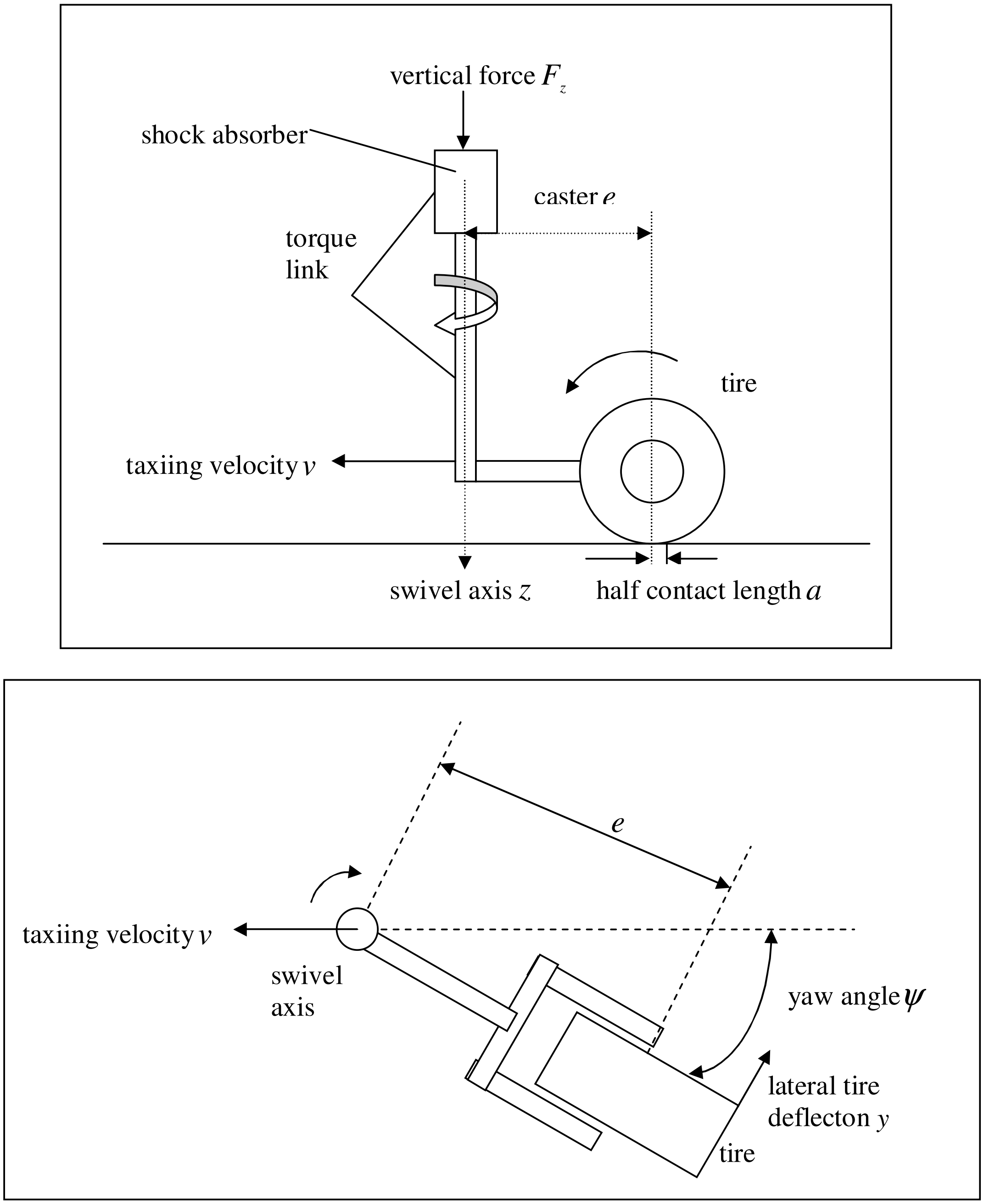

Figure 5.1: Shimmy dynamics model. **a.** Side view. **b.** Top view.

A few changes have been made to the model presented in [57] for clarification.

1) In [57], torsional spring rate is denoted by c while the torsional damping constant is denoted by k. This is not in agreement with the usual convention of using k to denote the torsional spring rate and c to denote the torsional damping constant. The convention in the model given in [57] is changed.

2) Constants k and c take negative values in [57]. This is confusing, so equation (5.1) is formed by modifying the corresponding equation in the above reference such that k and c take positive values.

$$I_z\ddot{\psi} + M_1 + M_2 + M_3 + M_4 = 0 \tag{5.1}$$

where I_z is the moment of inertia about the z axis,

M_1 is the linear spring moment between the turning tube and the torque link,

M_2 is the combined damping moment from viscous friction in the bearings of the oleo–pneumatic shock absorber and from the shimmy damper,

M_3 is the tire moment about the z axis and

M_4 is the tire damping moment due to tire tread width..

M_2 and M_4 are external moments.

M_3 and M_4 are caused by lateral tire deformations due to side slip.

M_3 is composed of M_z, tire aligning moment about the tire center, and tire cornering moment eF_y. F_y is the wheel cornering force or the sideslip force acting with caster e as the lever arm.

$$M_1 = k\psi \tag{5.2}$$

$$M_2 = c\dot{\psi} \tag{5.3}$$

$$M_3 = M_z - eF_y \tag{5.4}$$

$$M_4 = \frac{\kappa}{v}\dot{\psi} \tag{5.5}$$

where k is the torsional spring rate, c is the torsional damping constant, v is the taxiing velocity and κ is the tread width moment constant defined as

$$\kappa = -0.15\, a^2 c_{F\alpha}\, F_z \tag{5.6}$$

F_y and M_z depend on the vertical force F_z and slip angle α. Tire sideslip characteristics are nonlinear, as seen in the plot of F_y/F_z versus α in figure 5.2.

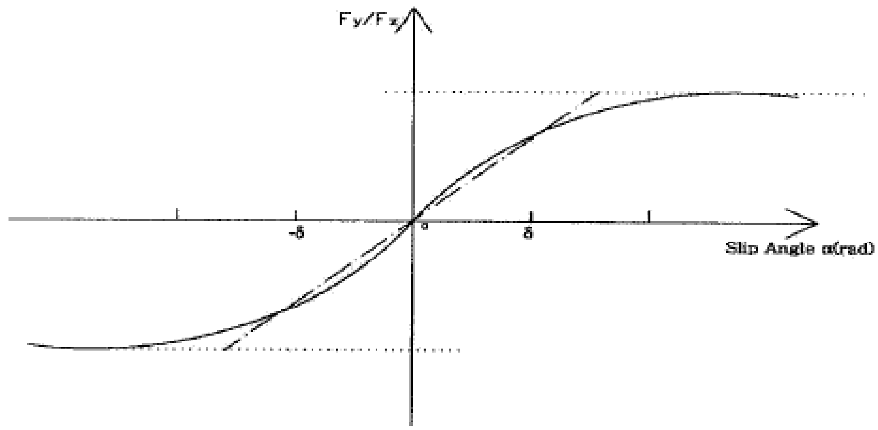

Figure 5.2: F_y/F_z versus α [35]

Cornering force F_y and vertical force F_z are related as

$$F_y/F_z = c_{F\alpha}\alpha, \text{ for } |\alpha| \le \delta \tag{5.7}$$

$$F_y/F_z = c_{F\alpha}\delta\, sign(\alpha), \text{ for } |\alpha| > \delta \tag{5.8}$$

where δ is the limiting slip angle or the limit angle of tire force and $sign(\alpha)$ is the sign function defined as

$$sign(\alpha) = \begin{cases} 1, \text{if } \alpha > \delta \\ -1, \text{if } \alpha \le \delta \end{cases} \tag{5.9}$$

Slip angle may be caused by either pure yaw or pure sideslip. Pure yaw occurs when the yaw angle ψ is allowed to vary while the lateral deflection y is held at zero. Pure sideslip, on the other hand, occurs when the lateral deflection y is allowed to vary as the yaw angle ψ is held zero [35].

An expression is given for the nonlinear sideslip characteristic by the widely used Magic Formula [1,35,63] as the following

$$F_y = D\sin[C\arctan\{B\alpha - E(B\alpha - \arctan(B\alpha))\}] \tag{5.10}$$

where B, C, D and E are functions of the wheel load, slip angle, slip ratio and camber. B and E are related to vertical force F_z, C is the shape factor and D is the peak value of the curve. The plot of F_y/F_z versus α according to the Magic Formula is seen in figure 5.3.

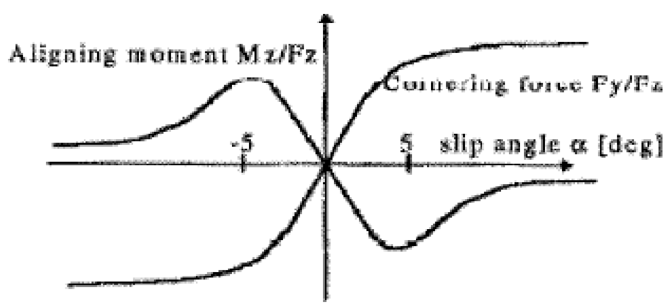

Figure 5.3: F_y/F_z and M_z/F_z versus α according to the Magic Formula [35]

It is clear that figures 5.2 and 5.3 have similar characteristics, thus the simple approximations given by (5.7) and (5.8) are used instead of the complicated Magic Formula. Only force and moment derivatives are needed as parameters for (5.7) and (5.8).

Aligning moment M_z is defined using a half–period sine. M_z/F_z is approximated by a sinusoidal function and the constant zero given by (5.11) and (5.12). The plot of M_z/F_z versus α is seen in figure 5.4.

$$M_z/F_z = c_{M\alpha}\frac{\alpha_g}{180}\sin\left(\frac{180}{\alpha_g}\alpha\right), \text{ for } |\alpha| \le \alpha_g \tag{5.11}$$

$$M_z/F_z = 0, \text{ for } |\alpha| > \alpha_g \tag{5.12}$$

where α_g is the limiting angle of tire moment.

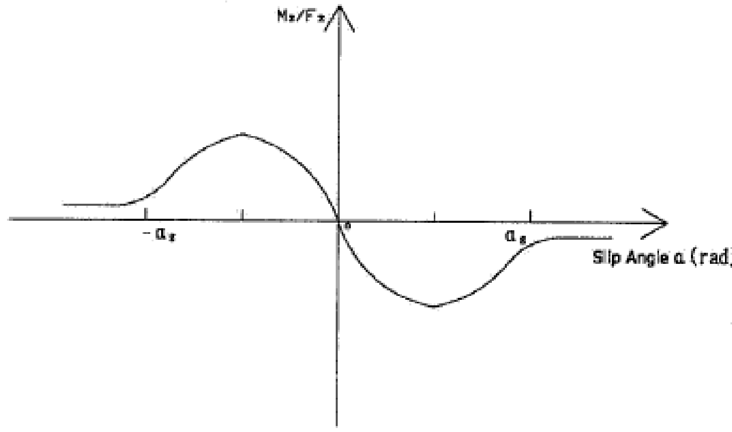

Figure 5.4: M_z / F_z versus α [35]

5.2 Tire Model

Tire is modeled using the von Schlippe stretched string model. Stretched string theory states that lateral deflection y of the leading contact point of the tire with respect to tire plane can be described as a first order differential equation [35,57]

$$\dot{y} + \frac{v}{\sigma} y = v\psi + (e - a)\dot{\psi} \tag{5.13}$$

Derivation of (5.13) is as follows.

Tire sideslip velocity V_t is expressed as

$$V_t = \dot{y} + \frac{y}{\tau} \tag{5.14}$$

where $\tau = \dfrac{\sigma}{V}$ is the time constant, σ is the relaxation length, which is the ratio of the slip stiffness to longitudinal force stiffness.

The tire also undergoes yaw motion, leading to a yaw velocity V_r which is approximated as

$$V_r = v\psi + (e - a)\dot{\psi} \tag{5.15}$$

As the wheel rolls on the ground,

$$V_t = V_r \tag{5.16}$$

Substituting (5.14) and (5.15) into (5.16) yields (5.13).

An equivalent side slip angle caused by lateral deflection is used to compute cornering force F_y and aligning moment M_z and is approximated as

$$\alpha \approx \arctan\alpha = \frac{y}{\sigma} \tag{5.17}$$

Equations (5.1), (5.13) and (5.17) constitute the governing equations of the torsional landing gear and include nonlinear tire force and moment.

Parameters of a light aircraft taken from literature and used in the computations are given in table 5.1. Since technical data of aircraft landing gear is often proprietary, it was decided to work on the geometrical and structural parameters found in literature because the real focus of this study is an analysis of landing gear shimmy, rather than finding real aircraft data.

Table 5.1: Parameters used in the torsional dynamics.

Parameter	Description	Value	Unit
v	velocity	0…80	m/s
a	half contact length	0.1	m
e	caster length	0.1	m
I_z	moment of inertia	1	kg m^2
F_z	vertical force	10000	N
k	torsional spring rate	100000	Nm/rad
$c_{F\alpha}$	side force derivative	20	1/rad
$c_{M\alpha}$	moment derivative	-2	m/rad
c	torsional damping constant	0…50	Nm/rad/s
κ	tread width moment constant	-270	Nm^2/rad
$\sigma = 3a$	relaxation length	0.3	m
α_g	limit angle of tire moment	10	deg
δ	limit angle of tire force	5	deg

5.3 Linearization of the Model

In order to use linear analysis tools, the nonlinear landing gear model presented in section 5.1 has to be linearized. Following from this, eigenvalues will be obtained and linear stability analysis will be performed.

Figures 5.2 and 5.4 show that within a small range of the side slip angle α, cornering force F_y and the ratio M_z / F_z can be approximated proportional to the side slip angle. Based on this assumption, substituting equations (5.7), (5.8), (5.11) and (5.12) into (5.4) yields (5.20), the complete expression for the tire moment M_3.

$$F_y = \begin{cases} c_{F\alpha} \alpha F_z, & |\alpha| \le \delta \\ c_{F\alpha} \delta \, sign(\alpha), & |\alpha| > \delta \end{cases} \tag{5.18}$$

$$M_z = \begin{cases} c_{M\alpha} \dfrac{\alpha_g}{180} \sin\left(\dfrac{180}{\alpha_g} \alpha \right) F_z, & |\alpha| \le \alpha_g \\ 0, & |\alpha| \ge \alpha_g \end{cases} \tag{5.19}$$

$$M_3 = \begin{cases} -ec_{F\alpha} \delta \, sign(\alpha) \, F_z, & \alpha \le -\alpha_g \\ c_{M\alpha} \dfrac{\alpha_g}{180} \sin\left(\dfrac{180}{\alpha_g} \alpha \right) F_z - ec_{F\alpha} \delta \, sign(\alpha) \, F_z, & -\alpha_g < \alpha < -\delta \\ c_{M\alpha} \dfrac{\alpha_g}{180} \sin\left(\dfrac{180}{\alpha_g} \alpha \right) F_z - ec_{F\alpha} \delta \, F_z, & -\delta < \alpha < \delta \\ c_{M\alpha} \dfrac{\alpha_g}{180} \sin\left(\dfrac{180}{\alpha_g} \alpha \right) F_z - ec_{F\alpha} \delta \, sign(\alpha) \, F_z, & \delta < \alpha < \alpha_g \\ ec_{F\alpha} \delta \, sign(\alpha) \, F_z, & \alpha > \alpha_g \end{cases} \tag{5.20}$$

Substituting (5.17) into (5.20) and expressing M_3 in the neighborhood of $\alpha = 0$ or $y = 0$ yields

$$M_3 = c_{M\alpha} \frac{\alpha_g}{180} \sin\left(\frac{180}{\alpha_g} \frac{y}{\sigma} \right) F_z - ec_{F\alpha} \frac{y}{\sigma} F_z \tag{5.21}$$

M_3 can be linearized using the Taylor series expansion as

$$\left.\frac{\partial M_3}{\partial y}\right|_{y=0} = c_{M\alpha}\frac{\alpha_g}{180}\cos\left(\frac{180}{\alpha_g}\frac{y}{\sigma}\right)F_z\frac{180}{\alpha_g\sigma} - ec_{F\alpha}\frac{1}{\sigma}F_z\Bigg|_{y=0} = \frac{F_z}{\sigma}\left(c_{M\alpha} - ec_{F\alpha}\right) \qquad \textbf{(5.22)}$$

Defining the state variables as $(\psi, \dot{\psi}, y)$ gives the linearized model in state–space form as three ordinary differential equations of first order as

$$\begin{bmatrix} \dot{\psi} \\ \ddot{\psi} \\ \dot{y} \end{bmatrix} = \begin{bmatrix} 0 & 1 & 0 \\ c_1 & c_2 & c_3 \\ v & c_4 & c_5 \end{bmatrix} \begin{bmatrix} \psi \\ \dot{\psi} \\ y \end{bmatrix} \qquad \textbf{(5.23)}$$

where

$$c_1 = \frac{-k}{I_z} \qquad \textbf{(5.24)}$$

$$c_2 = \frac{-c}{I_z} + \frac{\kappa}{vI_z} \qquad \textbf{(5.25)}$$

$$c_3 = \frac{\left(c_{M\alpha} - ec_{F\alpha}\right)F_z}{I_z\sigma} \qquad \textbf{(5.26)}$$

$$c_4 = e - a \qquad \textbf{(5.27)}$$

$$c_5 = \frac{-v}{\sigma} \qquad \textbf{(5.28)}$$

5.4 Characteristic Equation and Eigenvalues

According to stability theory, characteristic equation is obtained based on the idea that the solution to the system is an exponential function. From here, characteristic equation for eigenvalues λ is formed by letting

$$\left|A - \lambda I\right| = 0 \qquad \textbf{(5.29)}$$

where A is the system matrix in equation (5.23).

An n^{th} order system has n eigenvalues that are roots of the characteristic equation. Stability of the system can be judged based on the eigenvalues. Each eigenvalue contributes to a part of the free response in the form of $e^{\lambda t}$ where λ is the eigenvalue in question.

Contribution of a real and negative eigenvalue is in the form of a decaying exponential function. Contribution of a real and positive eigenvalue, however, is in the form of an exponentially increasing function of time, thus the system will be unstable if any one or more of its eigenvalues is real and positive.

Eigenvalues that are complex conjugate pairs contribute sinusoidal components multiplied by an exponential. If the real part is negative, the contribution is an oscillating function with decreasing amplitude. If the real part is positive, however, the contribution is an oscillating function with increasing amplitude, thus the system will be unstable if the complex conjugate eigenvalues have positive real parts.

In short, all eigenvalues must either be real and negative or complex conjugate pairs with negative real parts for system stability. In this system, eigenvalues vary with varying taxiing velocity v and caster length e. This affects stability of the system.

$$\begin{aligned}
&\begin{vmatrix} -\lambda & 1 & 0 \\ c_1 & c_2-\lambda & c_3 \\ v & c_4 & c_5-\lambda \end{vmatrix} \\
&= -\lambda \begin{vmatrix} c_2-\lambda & c_3 \\ c_4 & c_5-\lambda \end{vmatrix} - \begin{vmatrix} c_1 & c_3 \\ v & c_5-\lambda \end{vmatrix} \\
&= -\lambda\left(c_2c_5 - c_5\lambda - c_2\lambda + \lambda^2 - c_3c_4\right) - \left(c_1c_5 - c_1\lambda - vc_3\right) \\
&= -c_2c_5\lambda + c_5\lambda^2 + c_2\lambda^2 - \lambda^3 + c_3c_4\lambda - c_1c_5 + c_1\lambda + vc_3
\end{aligned} \quad \textbf{(5.30)}$$

Characteristic equation is obtained as

$$\lambda^3 - \left(c_2 + c_5\right)\lambda^2 + \left(c_2c_5 - c_1 - c_3c_4\right)\lambda + \left(c_1c_5 - vc_3\right) = 0 \quad \textbf{(5.31)}$$

In this section, caster length e varies between -0.4 m and 0.4 m and the velocity v varies between 5 and 85 m/s. Torsional damping constant c is taken as 10 Nm/rad/s.

It can be seen from figure 5.5 that the system shows instability due to positive real parts of the complex roots for caster lengths between -0.07 and 0.35 m and velocities above 25 m/s. Eigenvalues of the system are stable for caster lengths below -0.07 m and above 0.35 m.

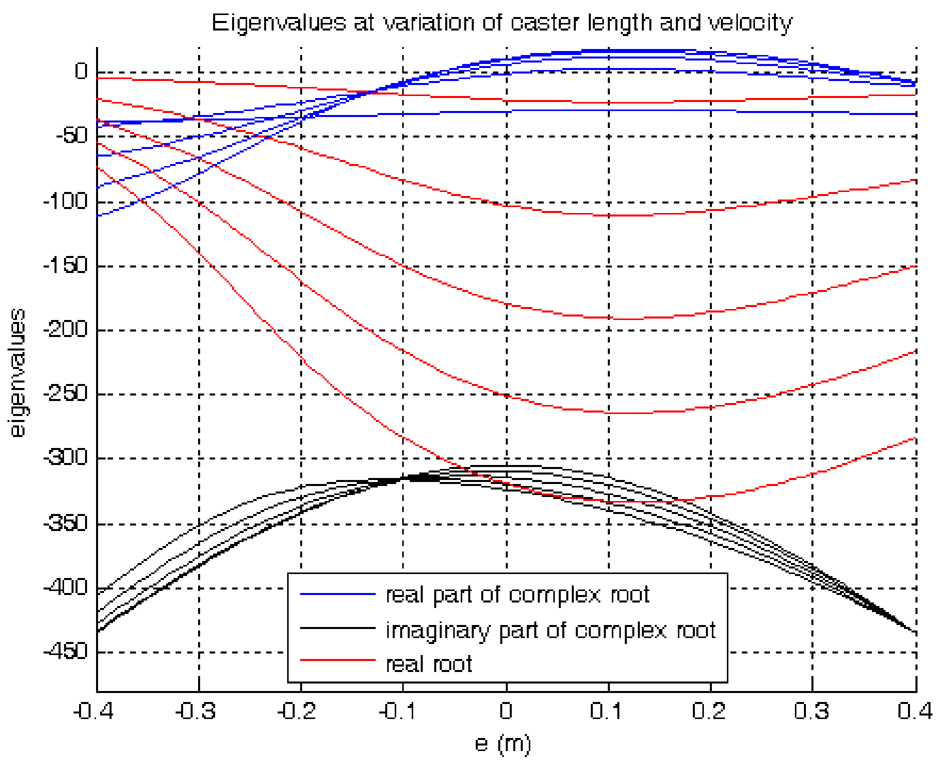

Figure 5.5: Eigenvalues at variation of caster length and velocity.

5.5 Conclusions about the Eigenvalues at Variation of Caster Length e and Velocity v

- Eigenvalues are computed for e in the range -0.4 m and 0.4 m and v in the range 5 m/s and 85 m/s.
- The linear system has a pair of complex eigenvalues and a real eigenvalue.
- The system is unstable due to positive real parts of the complex eigenvalues for caster lengths between -0.1m and 0.35 m and for velocities above 25 m/s.

5.6 Routh–Hurwitz Criterion and Stability Boundaries

It is important to study the stability of the linear system since instability of the linear system causes shimmy in the nonlinear system. Routh–Hurwitz criterion is applied to determine stability boundaries of the linear model. Routh–Hurwitz criterion is a technique to decide on the stability of the system without computing the eigenvalues. The importance of Routh–Hurwitz criterion is in its ability to find algebraic conditions for stability in terms of the coefficients of the equation of motion, meaning the physical parameters of the system. Complex, high–order models are hard to analyze using Routh–Hurwitz criterion, however low–order models can be analyzed effectively using this criterion.

Although the stability analysis based on linearized models may not reveal all the dynamic problems of the real problem, it is very likely that unstable behavior in the linear model will imply unstable behavior in the nonlinear model, as well.

Routh–Hurwitz criterion will not be given here in detail for an n^{th} order system, however conditions for a third order system described by a third order polynomial

$$a_3 s^3 + a_2 s^2 + a_1 s + a_0 = 0 \tag{5.32}$$

to be stable are that all coefficients of the characteristic equation must be positive and the Hurwitz determinant must be positive as

$$a_n > 0 \tag{5.33}$$

and

$$a_2 a_1 > a_3 a_0 \tag{5.34}$$

.By inspecting the characteristic equation (5.31)

$$a_3 = 1 \tag{5.35}$$

$$a_2 = -(c_2 + c_5) \tag{5.36}$$

$$a_1 = c_2 c_5 - c_1 - c_3 c_4 \tag{5.37}$$

$$a_0 = c_1 c_5 - v c_3 \qquad \textbf{(5.38)}$$

Thus, for the landing gear model to be stable

$$-(c_2 + c_5) > 0 \qquad \textbf{(5.39)}$$

$$c_2 c_5 - c_1 - c_3 c_4 > 0 \qquad \textbf{(5.40)}$$

$$c_1 c_5 - v c_3 > 0 \qquad \textbf{(5.41)}$$

$$-(c_2 + c_5)(c_2 c_5 - c_1 - c_3 c_4) > c_1 c_5 - v c_3 \qquad \textbf{(5.42)}$$

Explicit expressions for $c_1 - c_5$ given in (5.24)–(5.28) are substituted in (5.39)–(5.42) to plot stability regions in the parameter space.

In the following sections, stability regions are plotted in the $e - v$ and $c - v$ planes. Stability analysis in the $e - v$ plane is performed for various values of the torsional spring rate k while stability analysis in the $c - v$ plane is performed for various values of the relaxation length σ and vertical force F_z. Stable regions are shown in blue while unstable regions are shown in red.

5.6.1 Stability boundaries in the $e - v$ plane for different values of k

Stability regions are plotted in the $e - v$ plane for different values of the torsional spring rate k.

In figures 5.6–5.8, caster length e varies between -0.1 and 0.4 m, while the velocity v varies between 0 and 250 m/s. k takes the values 0, 50000 and 100000 Nm/rad. Torsional damping constant c is taken as 50 Nm/rad/s.

Table 5.2 shows the percentages of the areas of the stable regions in the $e - v$ plane for the values of k considered.

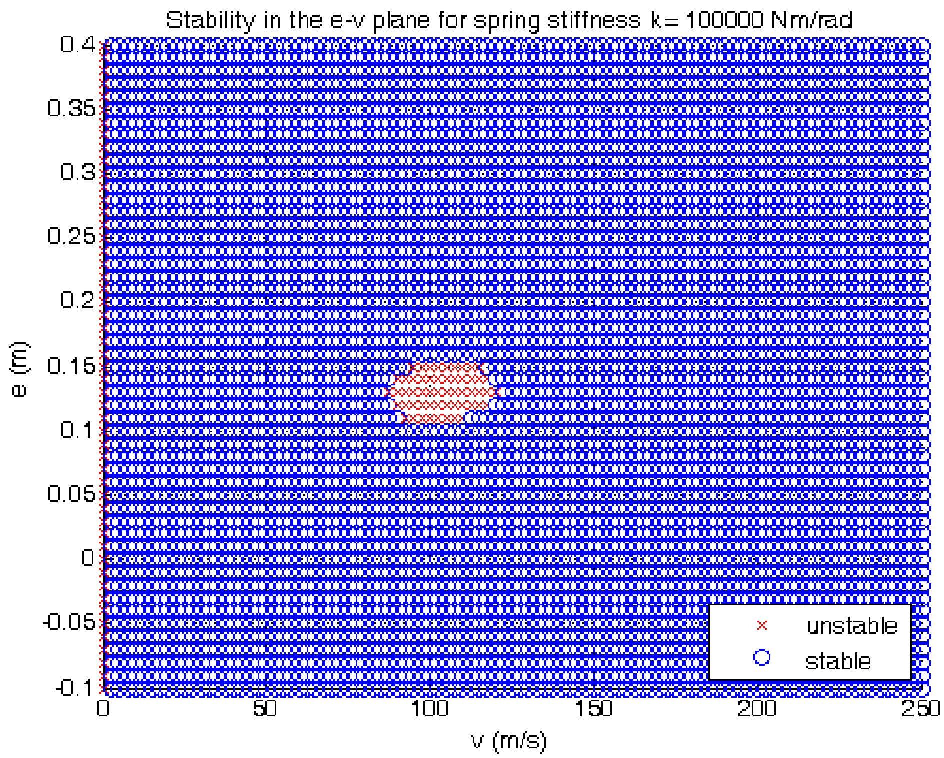

Figure 5.6: Stability in the $e - v$ plane for k =100000 Nm/rad.

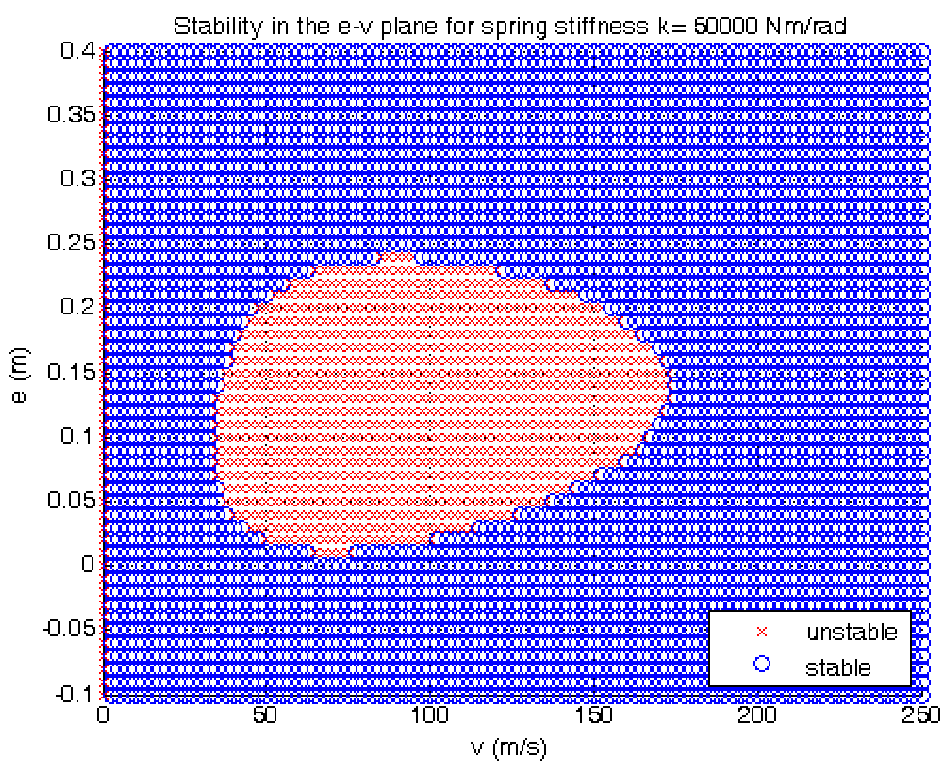

Figure 5.7: Stability in the $e - v$ plane for k =50000 Nm/rad.

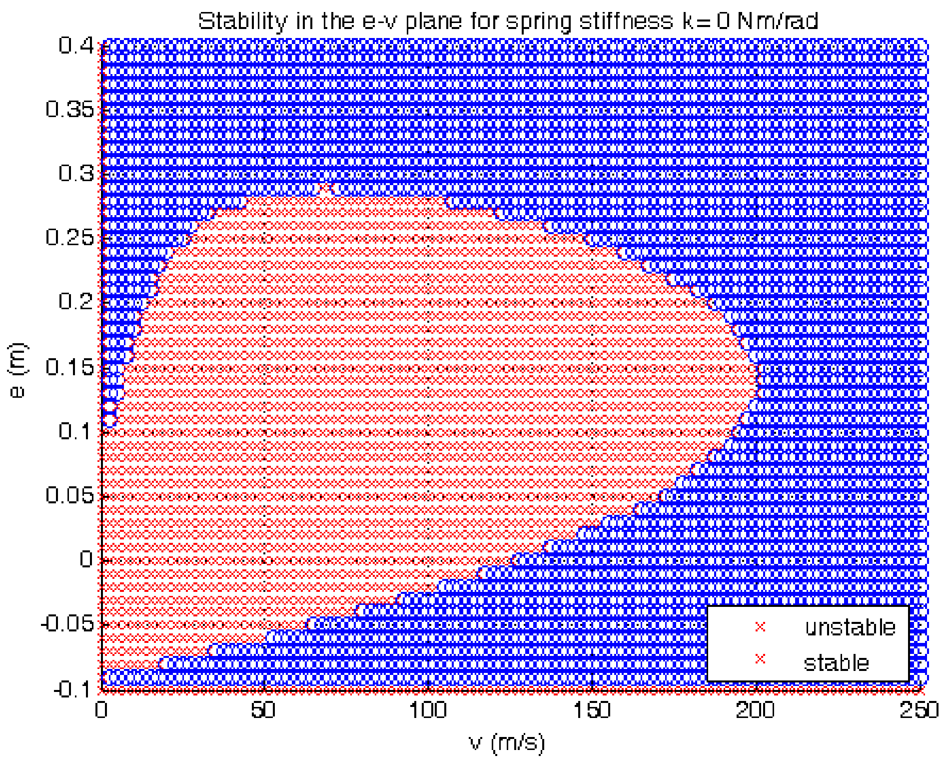

Figure 5.8: Stability in the $e-v$ plane for k =0 Nm/rad.

Table 5.2: Percentages of stable region in the $e-v$ plane for different values of k.

	percentage of stable region
k **=100000 Nm/rad**	97.9 % stable
k **=50000 Nm/rad**	79.7 % stable
k **=0 Nm/rad**	56.3 % stable

5.6.2 Conclusions about stability boundaries in the $e-v$ plane for different values of k

- Stability is analyzed for e in the range -0.1 m and 0.4 m and v in the range 0 m/s and 250 m/s.
- Increasing the torsional spring rate k increases stability.
- For the parameters considered, the most risky configuration is having a caster length e in the range 0.1–0.15 m and velocity v in the range 90–120 m/s, as

this region is unstable even for a high spring constant k of 100000 Nm/rad. For this value of k, there seem to be no shimmy problems if the caster length is outside the range 0.1–0.15 m or if the velocity is outside the range 90–120 m/s.

- For $k < 100000$, there is more instability at small velocities and more stability at large velocities.
- The system is stable for $e > 0.3$ and $e < -0.1$.

5.6.3 Stability boundaries in the $c - v$ plane for different values of σ and F_z

Stability regions are plotted in the $c - v$ plane for different values of the relaxation length σ and vertical force F_z.

In figures 5.9–5.18, torsional damping constant c varies between 0 and 100 Nm/rad/s while the velocity v varies between 0 and 250 m/s. σ takes the values 0.02, 0.07, 0.12, 0.17, 0.22, 0.27 and 0.32 m in figures 5.9–5.15 and F_z takes the values 5000, 10000 and 15000 N in figures 5.16–5.18.

Tables 5.3 and 5.4 show the percentages of the areas of the stable regions in the $c - v$ plane for the values of σ and F_z considered, respectively.

It is seen by inspecting figures 5.9–5.15 that for $\sigma < 0.1$, there is more instability at small velocities and more stability at large velocities, while for $\sigma > 0.1$, there is more stability at small velocities and more instability at large velocities. Figures 5.16–5.18 reveal that larger values of F_z and v require larger values of c for stability and there is no instability below 16 m/s. Generally speaking, shimmy occurs under a certain damping value, depending on the velocity. There is stability for all values of the damping constant c for velocities below 16 m/s.

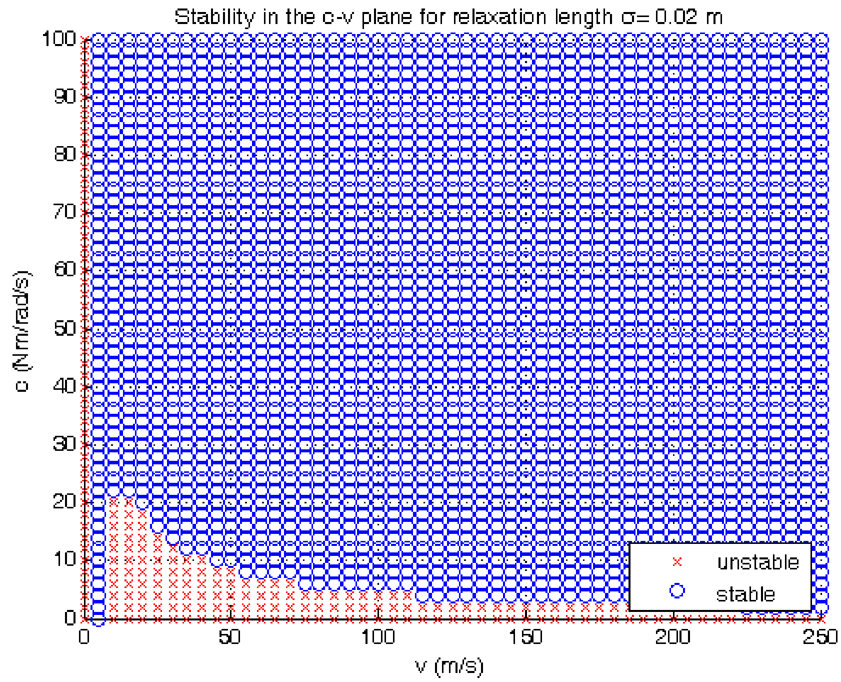

Figure 5.9: Stability in the $c - v$ plane for σ =0.02 m.

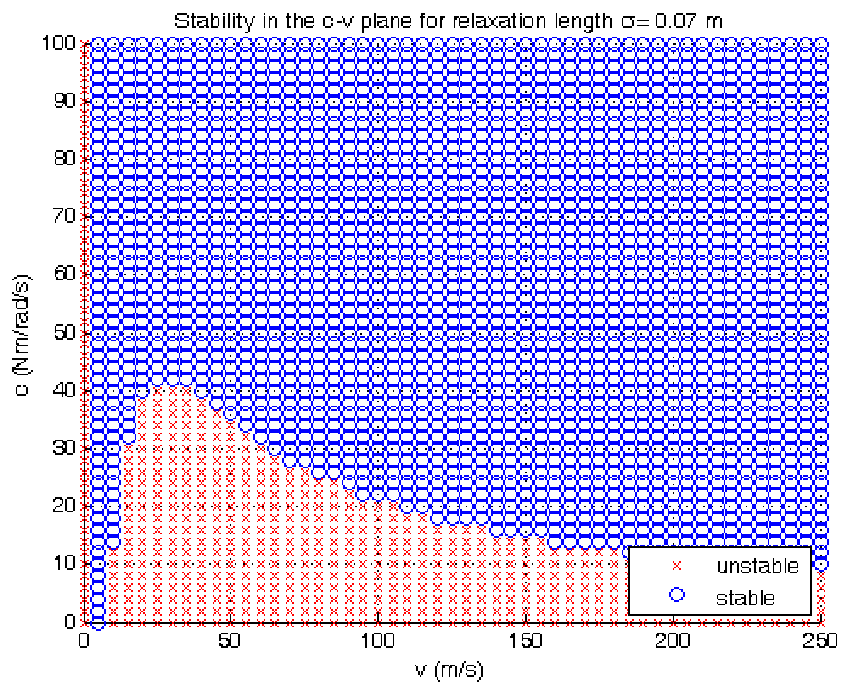

Figure 5.10: Stability in the $c - v$ plane for σ =0.07 m.

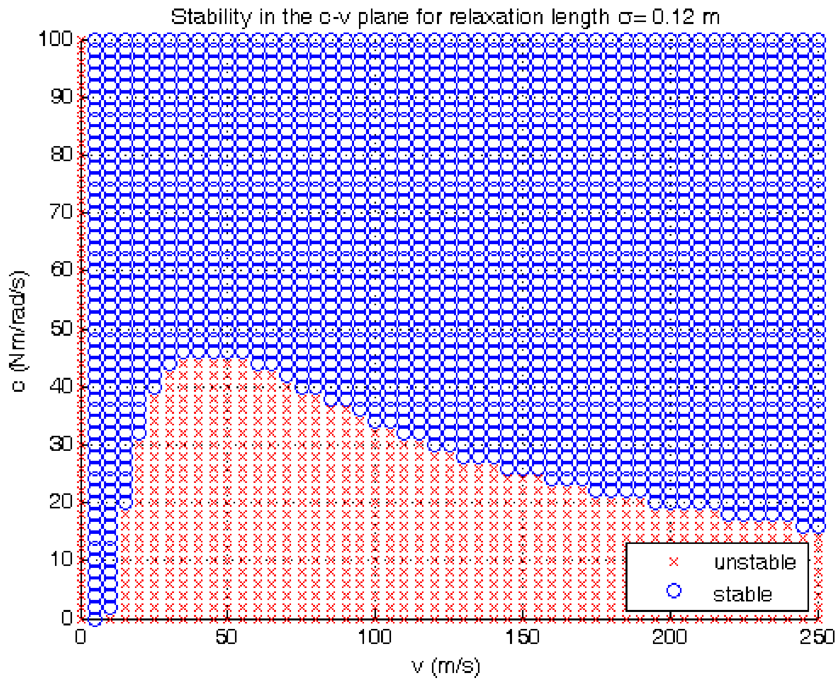

Figure 5.11: Stability in the $c-v$ plane for σ =0.12 m.

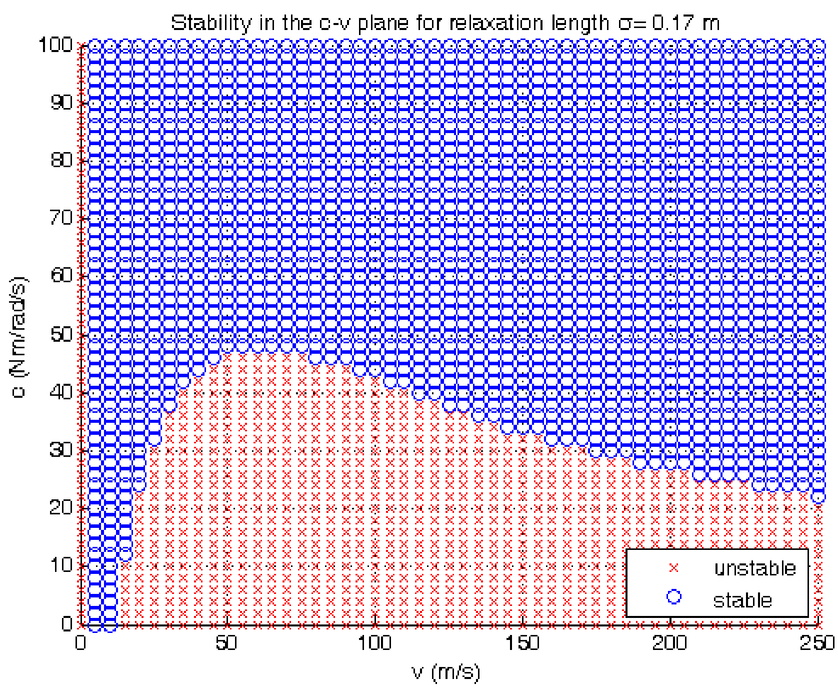

Figure 5.12: Stability in the $c-v$ plane for σ =0.17 m.

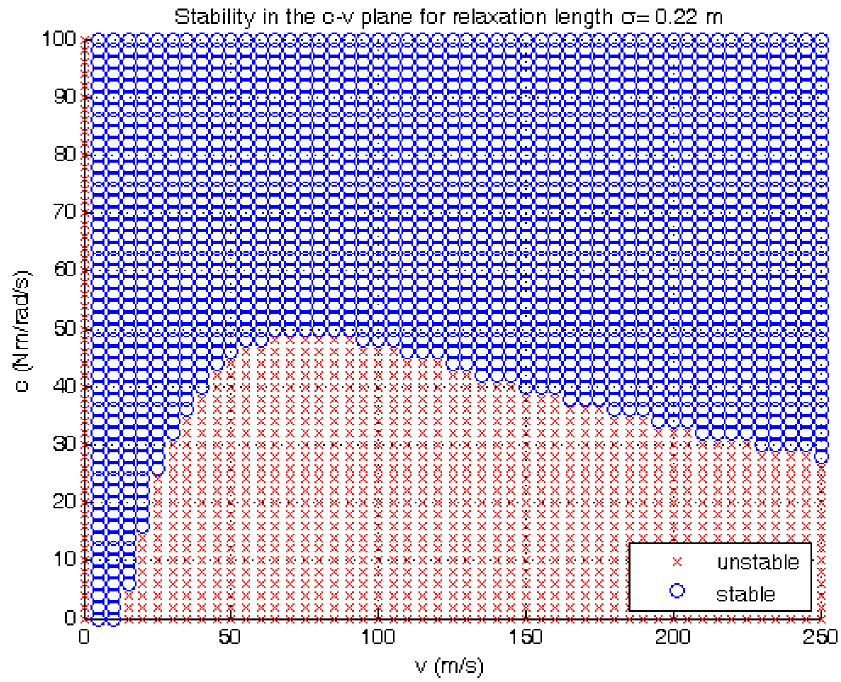

Figure 5.13: Stability in the $c - v$ plane for σ =0.22 m.

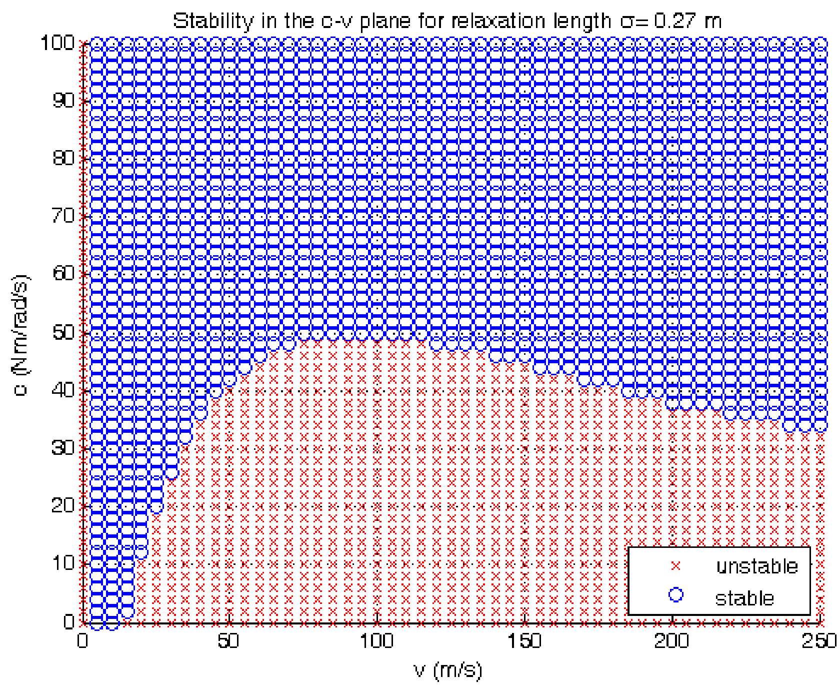

Figure 5.14: Stability in the $c - v$ plane for σ =0.27 m.

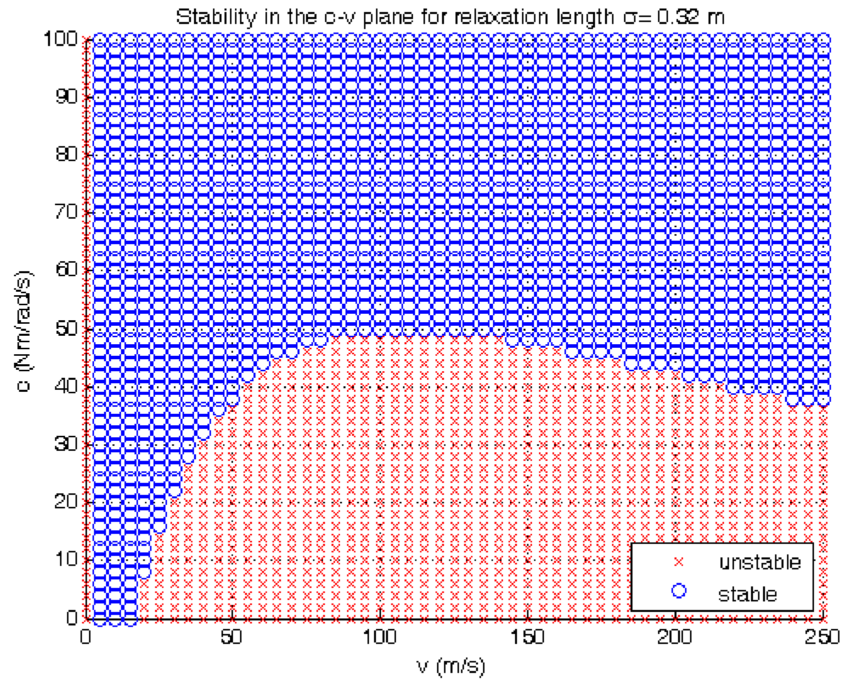

Figure 5.15: Stability in the $c - v$ plane for σ =0.32 m.

A study of figures 5.9–5.15 reveals that increasing the relaxation length σ decreases stability.

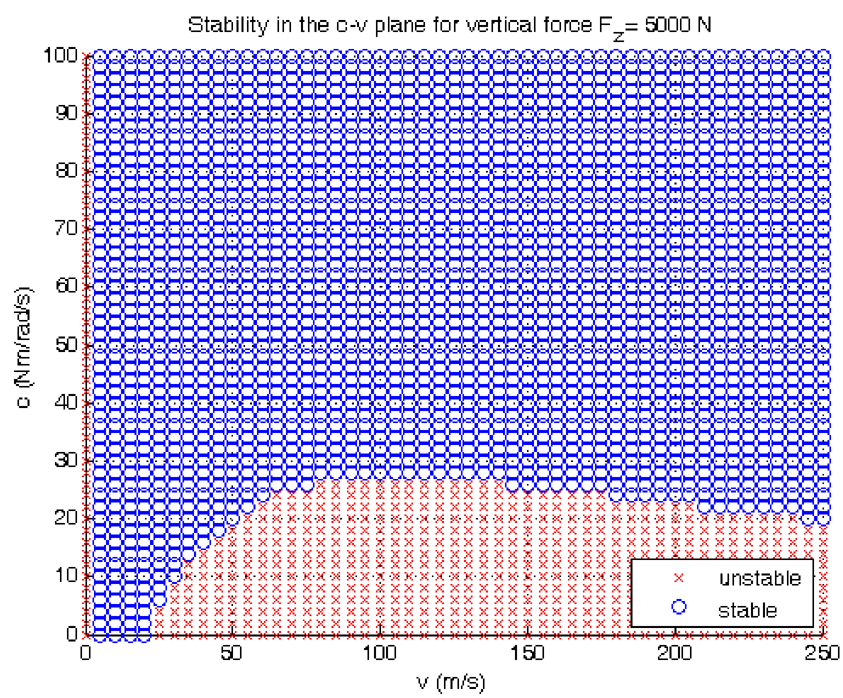

Figure 5.16: Stability in the $c - v$ plane for F_z =5000N.

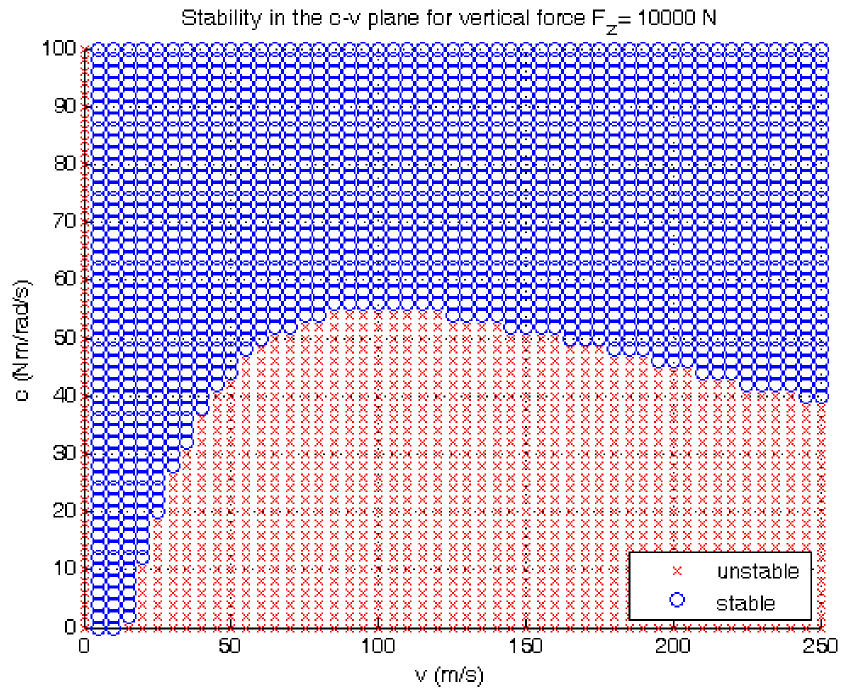

Figure 5.17: Stability in the $c - v$ plane for F_z =10000N.

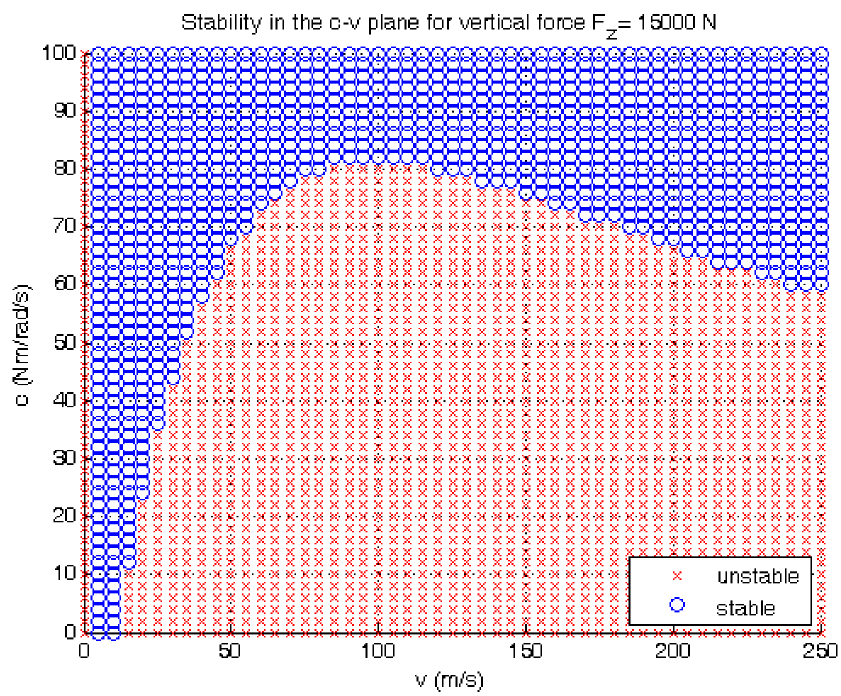

Figure 5.18: Stability in the $c - v$ plane for F_z =15000N.

A study of figures 5.16–5.18 reveals that an increase in the vertical force F_z decreases stability.

Table 5.3: Percentages of stable regions in the $c-v$ plane for different values of σ.

	percentage of stable region
σ **=0.02 m**	91.9 % stable
σ **=0.07 m**	78.3 % stable
σ **=0.12 m**	70.6 % stable
σ **=0.17 m**	65.6 % stable
σ **=0.22 m**	62.3 % stable
σ **=0.27 m**	60.5 % stable
σ **=0.32 m**	59.4 % stable

Table 5.4: Percentages of stable regions in the $c-v$ plane for different values of F_z.

	percentage of stable region
F_z **=5000 N**	77.1 % stable
F_z **=10000 N**	55.5 % stable
F_z **=15000 N**	34.9 % stable

5.6.4 Conclusions about stability boundaries in the $c-v$ plane for different values of σ and F_z

- Stability is analyzed for c in the range 0 and 100 Nm/rad/s and v in the range 0 m/s and 250 m/s.
- For $\sigma < 0.1$, there is more instability at small velocities and more stability at large velocities.
- For $\sigma > 0.1$, there is more stability at small velocities and more instability at large velocities.
- Increasing the relaxation length σ decreases stability. Since $\sigma = 3a$, where a is the half contact length, using stiffer tires or tires with smaller contact patches help increase stability of the system.

- An increase in the vertical force F_z decreases stability.
- Although stability has been analyzed for different values of σ and F_z, it must be borne in mind that aircraft designers do not have a lot of freedom in choosing the size of the tire contact patch. Likewise, the vertical load that an aircraft needs to withstand is more or less known and there is not much freedom in choosing the vertical force. In other words, contact patch size and vertical force cannot be main design driver.

5.7 Effects of Increasing and Decreasing the Caster Length e and Half Contact Length a on Stability Boundaries

Effects of the variation of the caster length e, half contact length a and their ratio on stability boundaries are analyzed. Increments and decrements in the stable portions of the $e-v$ and $c-v$ planes are presented quantitatively in tabular form in the results section.

5.7.1 Effects of increasing and decreasing the caster length e and half contact length a on stability boundaries in the $e-v$ plane for different values of k

This part of the stability analysis of the linear model is conducted in the $e-v$ plane, thus the effect of the caster length e is already contained within the plots. For this reason, only the effect of the half contact length a on stability of the model will be analyzed.

In figures 5.6–5.8, a is taken as 0.1 m. Effects of 5 % and 10 % increase and decrease of the half contact length a are analyzed in this section.

5 % increase in the half contact length a from 0.1 m to 0.105 m leads to an increase in the unstable region in the $e-v$ plane, as can be seen by comparing figures 5.19–5.21 with figures 5.6–5.8 and by inspecting table 5.5.

It is observed that there is a greater increase in the unstable region for a torsional spring rate k of 100000 Nm/rad, than for 50000 Nm/rad.

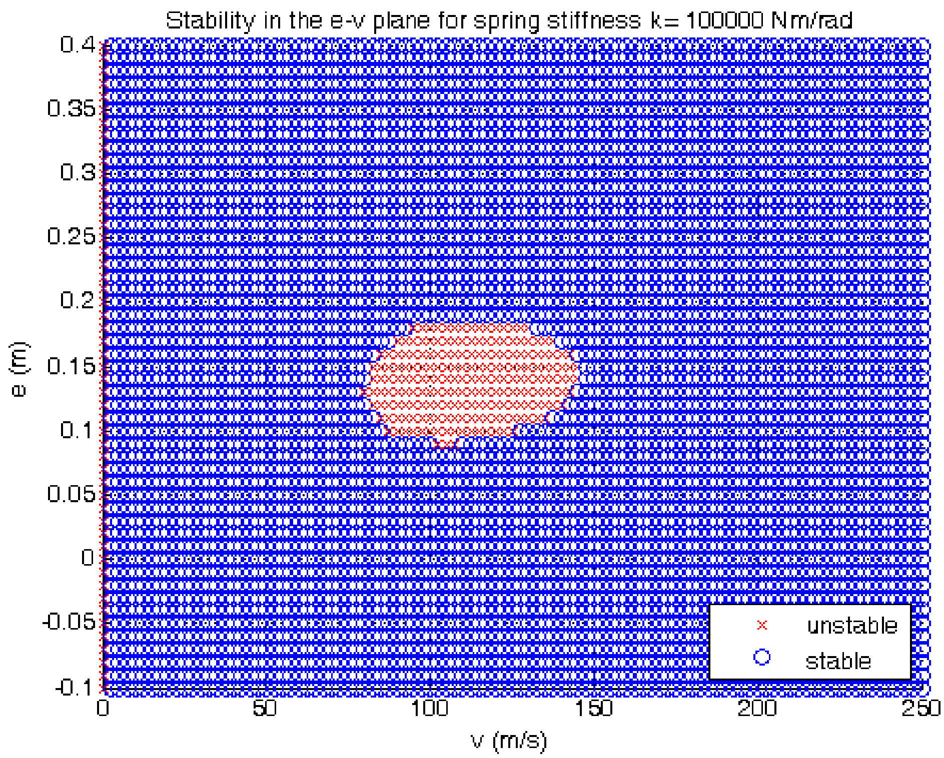

Figure 5.19: Stability in the $e - v$ plane for k =100000 Nm/rad and a =0.105 m.

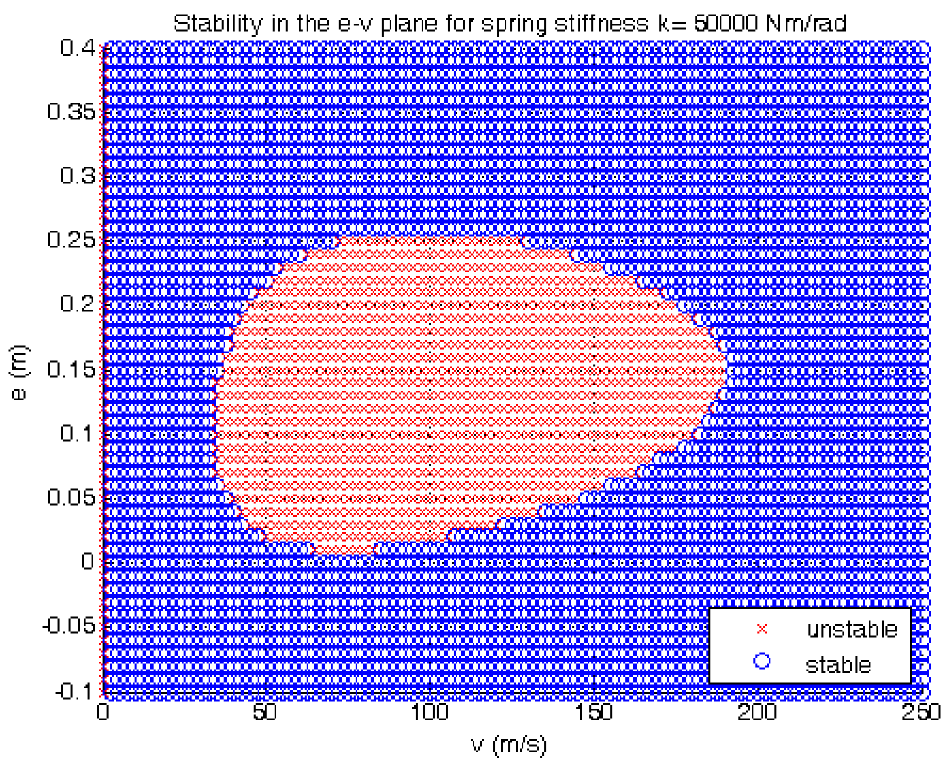

Figure 5.20: Stability in the $e - v$ plane for k =50000 Nm/rad and a =0.105 m.

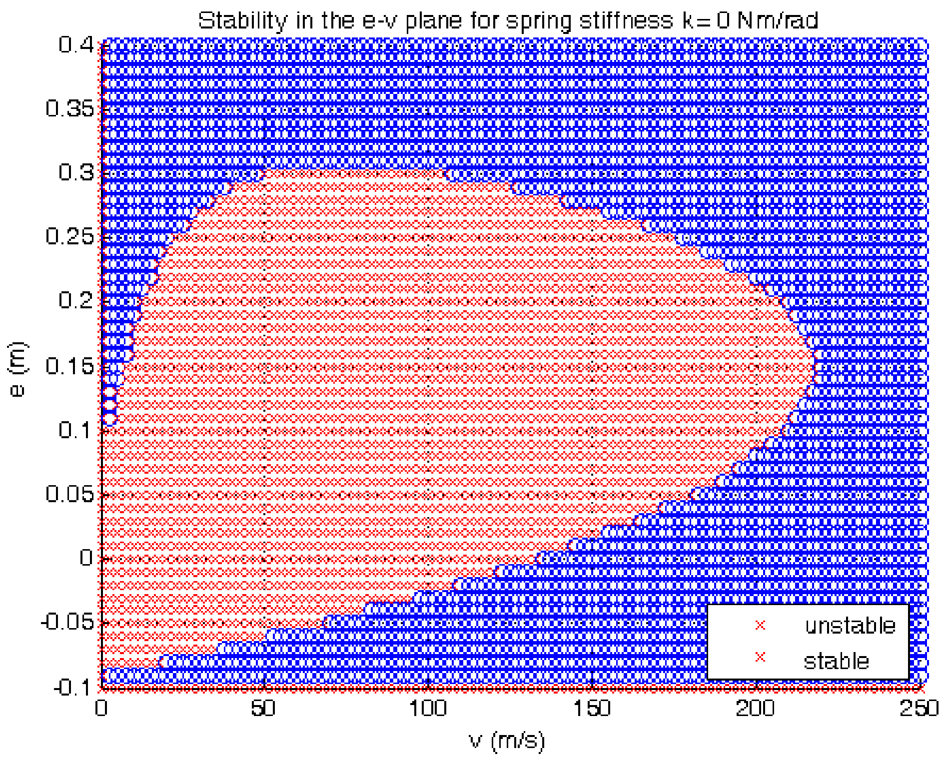

Figure 5.21: Stability in the $e-v$ plane for k =0 Nm/rad and a =0.105 m.

10 % increase in the half contact length a from 0.1 m to 0.11 m leads to a further increase in the unstable region in the $e-v$ plane, as can be seen by comparing figures 5.22–5.24 with figures 5.6–5.8 and by inspecting table 5.5.

As was the case for a half contact length of 0.105 m, there is a greater increase in the unstable region for a torsional spring rate k of 100000 Nm/rad, than for 50000 Nm/rad.

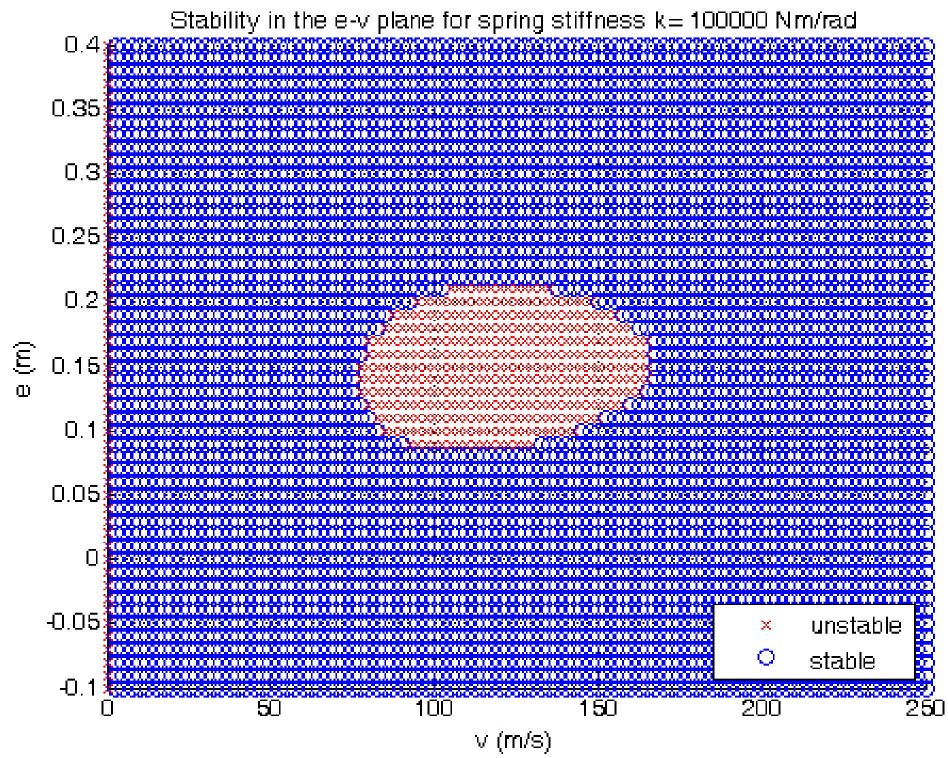

Figure 5.22: Stability in the $e - v$ plane for k =100000 Nm/rad and a =0.11 m.

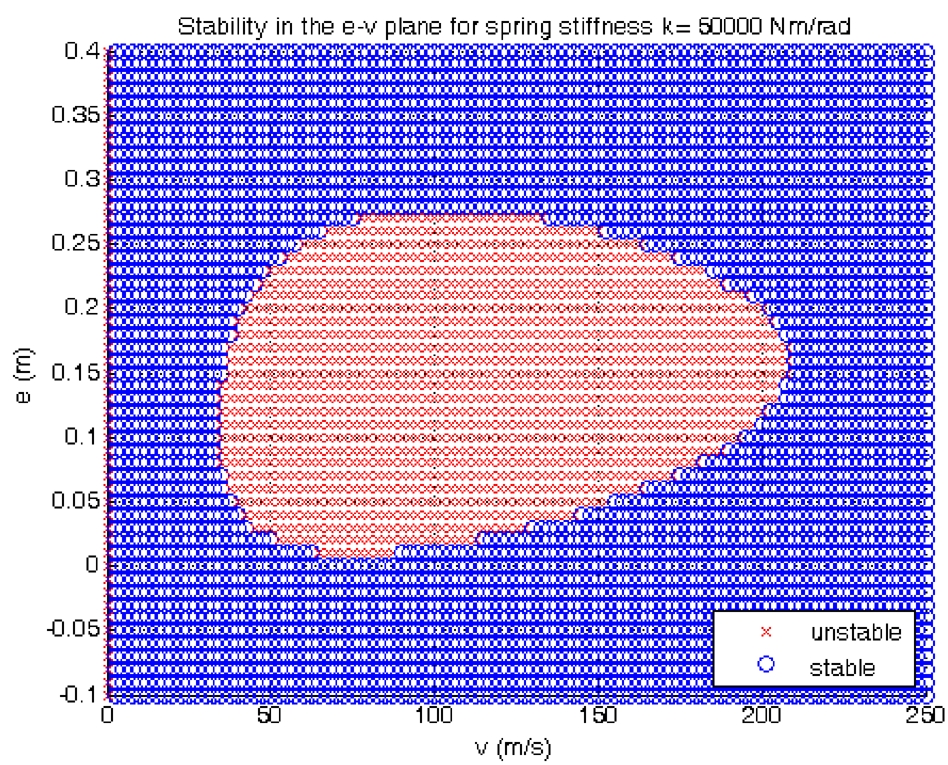

Figure 5.23: Stability in the $e - v$ plane for k =50000 Nm/rad and a =0.11 m.

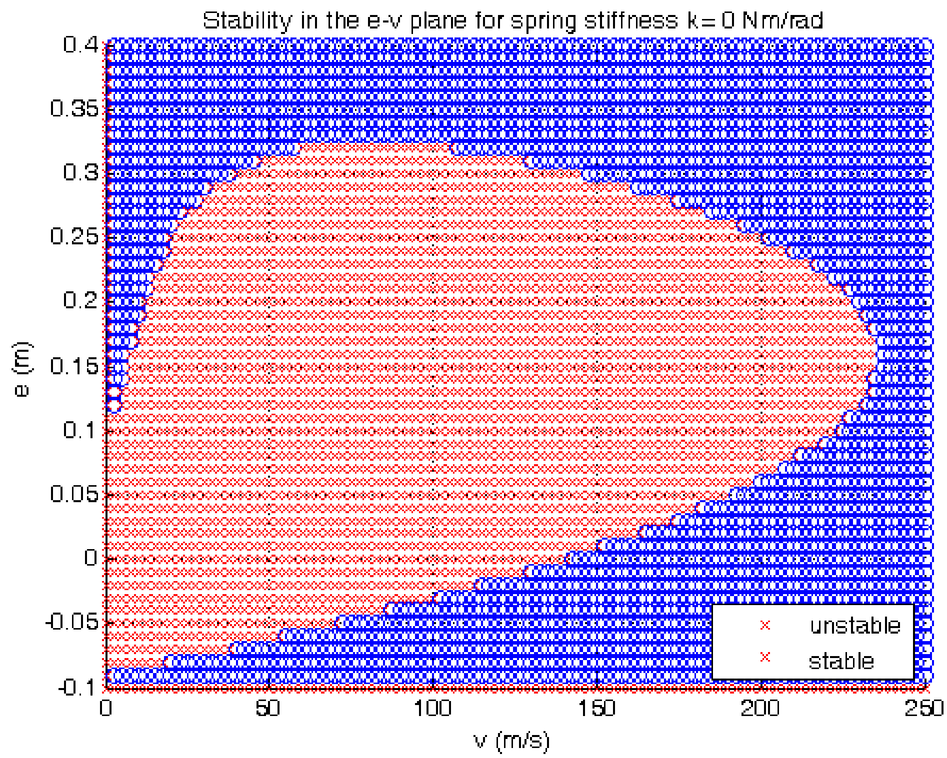

Figure 5.24: Stability in the $e-v$ plane for k =0 Nm/rad and a =0.11 m.

5 % decrease in the half contact length a from 0.1 m to 0.095 m leads to an increase in the stable region in the $e-v$ plane, as can be seen by comparing figures 5.25–5.27 with 5.6–5.8 and by inspecting table 5.5.

There are no instabilities in the $e-v$ plane for a high torsional spring rate k of 100000 Nm/rad.

It observed that there is a greater increase in the stable region for a torsional spring rate k of 100000 Nm/rad, than for 50000 Nm/rad.

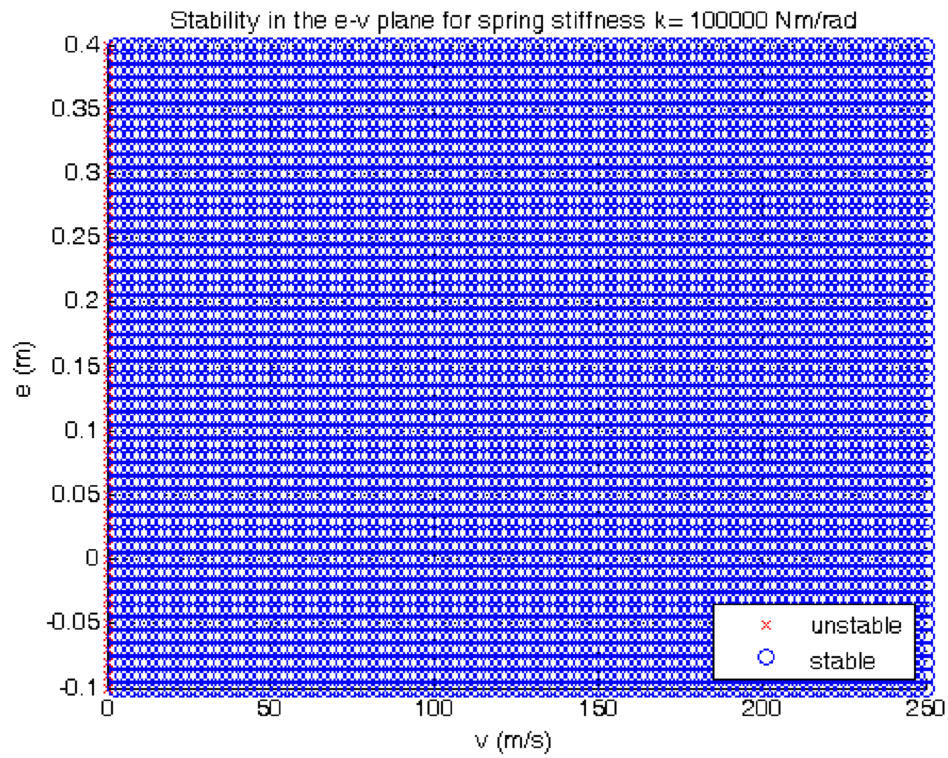

Figure 5.25: Stability in the $e-v$ plane for k =100000 Nm/rad and a =0.095 m.

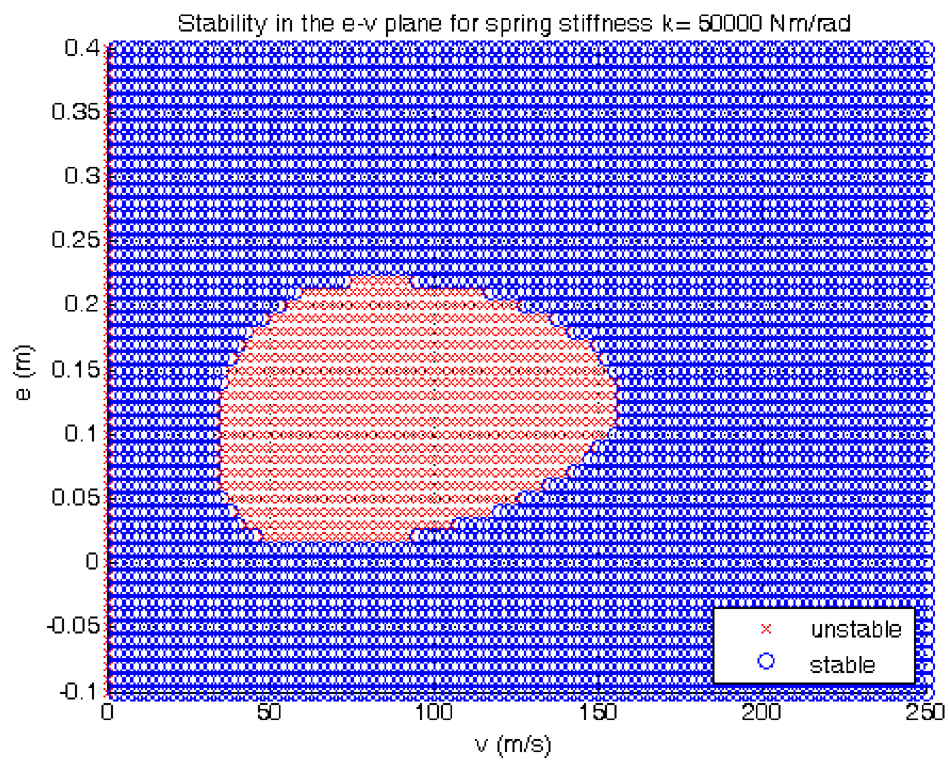

Figure 5.26: Stability in the $e-v$ plane for k =50000 Nm/rad and a =0.095 m.

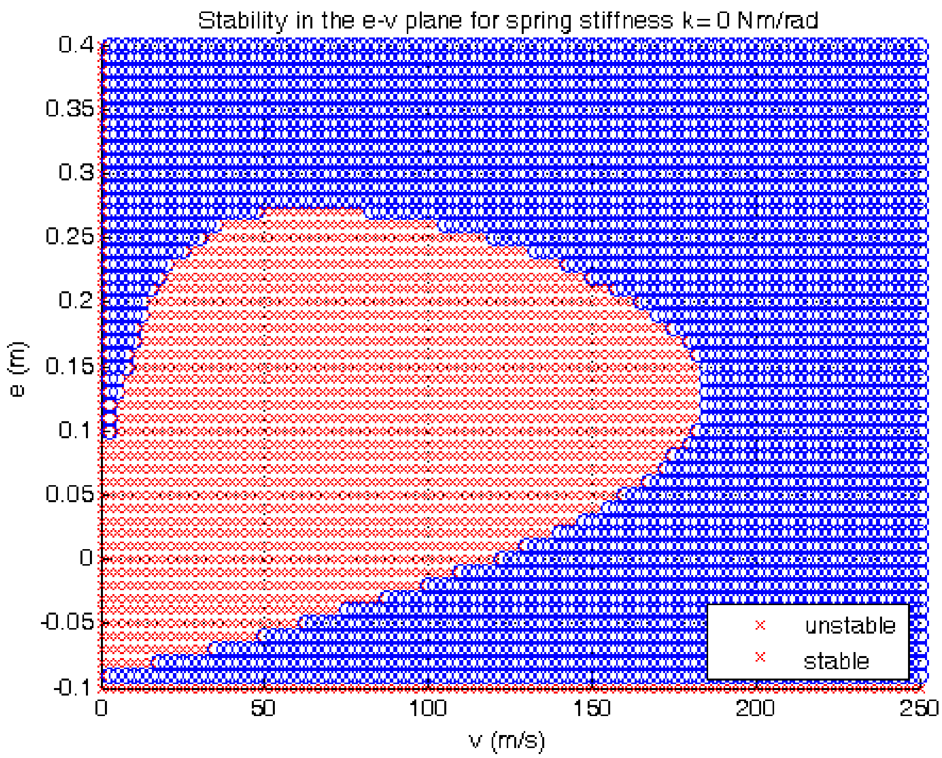

Figure 5.27: Stability in the $e-v$ plane for k =0 Nm/rad and a =0.095 m.

10 % decrease in the half contact length a from 0.1 m to 0.09 m leads to a further increase in the stable region in the $e-v$ plane, as can be seen by comparing figures 5.28–5.30 with figures 5.6–5.8 and by inspecting table 5.5.

As was the case for a half contact length of 0.095 m, there are no instabilities in the $e-v$ plane for a high torsional spring rate k and there is a greater increase in the stable region for a torsional spring rate k of 100000 Nm/rad, than for 50000 Nm/rad.

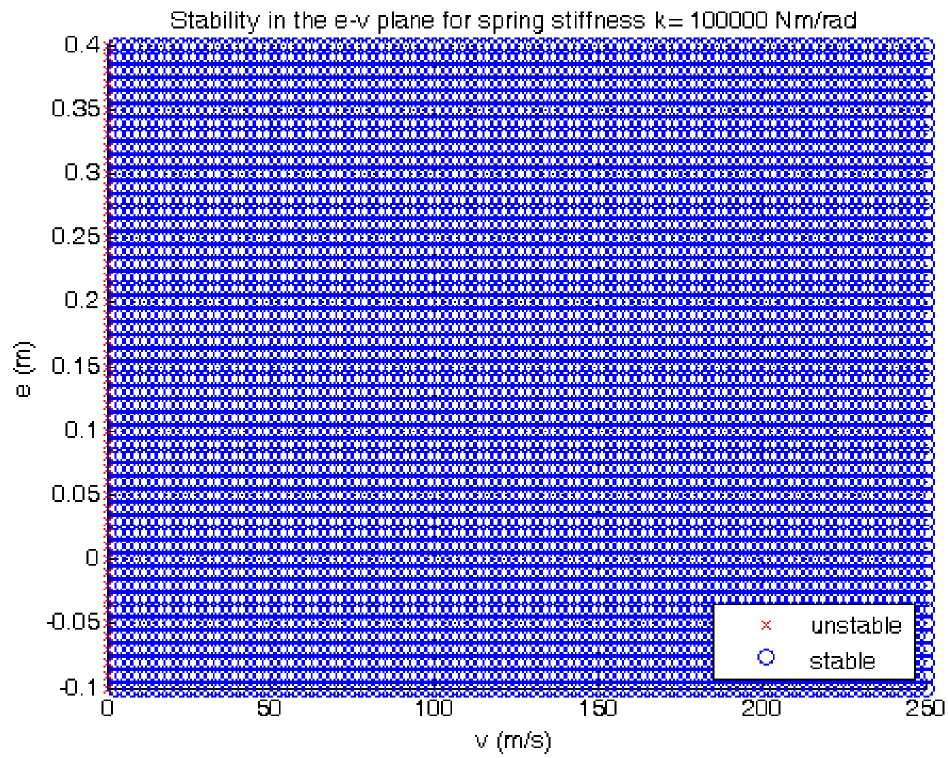

Figure 5.28: Stability in the $e-v$ plane for k =100000 Nm/rad and a =0.09 m.

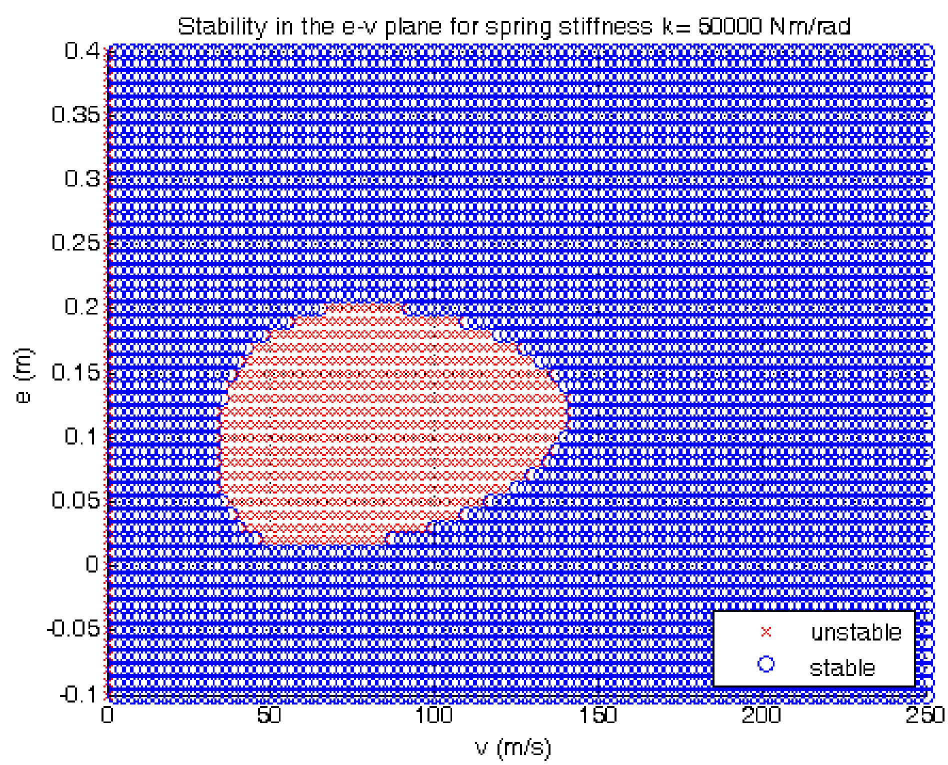

Figure 5.29: Stability in the $e-v$ plane for k =50000 Nm/rad and a =0.09 m.

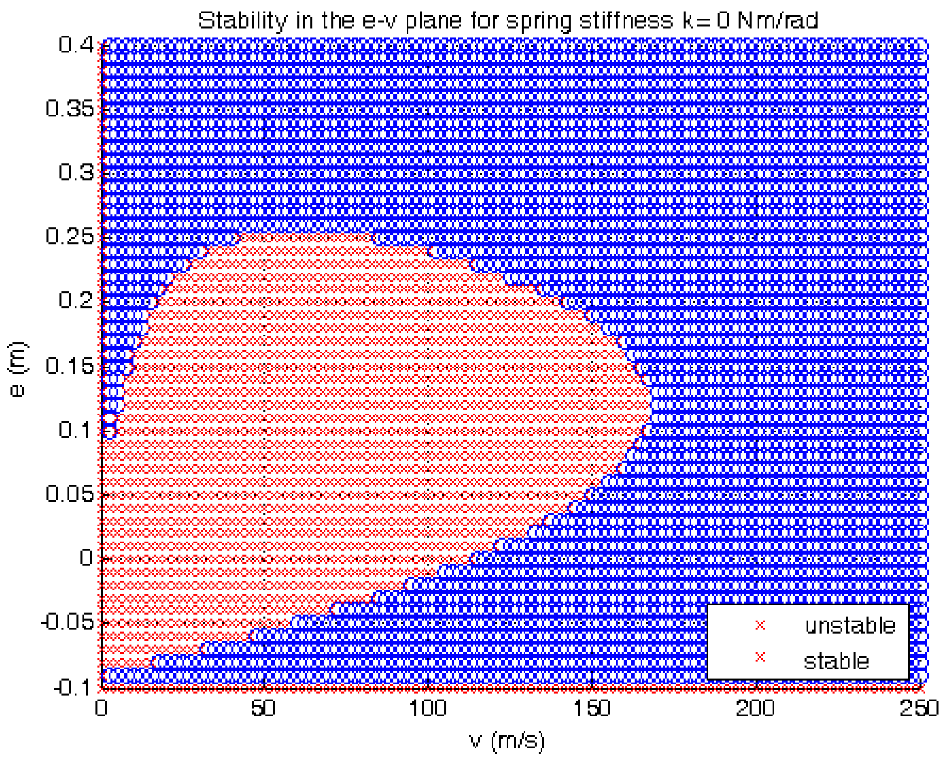

Figure 5.30: Stability in the $e-v$ plane for k =0 Nm/rad and a =0.09 m.

5.7.2 Conclusions about the effects of increasing and decreasing the caster length e and half contact length a on stability boundaries in the $e-v$ plane for different values of k

- Since this part of the analysis is conducted in the $e-v$ plane, the effect of the caster length e is already contained within the plots. For this reason, only the effect of the half contact length a on stability has been analyzed.

- 5 % increase in the half contact length a leads to an increase in the unstable region in the $e-v$ plane.

- 10 % increase in the half contact length a leads to a further increase in the unstable region in the $e-v$ plane.

- 5 % decrease in the half contact length a leads to an increase in the stable region in the $e-v$ plane. For the parameters considered, there were no instabilities in the $e-v$ plane for a high torsional spring rate k of 100000 Nm/rad.

- 10 % decrease in the half contact length a leads to a further increase in the stable region in the $e-v$ plane. For the parameters considered, there were no instabilities in the $e-v$ plane for a high torsional spring rate k of 100000 Nm/rad.

- Increments in the stable and unstable regions are greater for a smaller value of 50000 Nm/rad of the torsional spring rate k than for 100000 Nm/rad.

- Increments in the half contact length lead to increments in the unstable region in the $e-v$ plane. In other words, increasing the half contact length decreases stability.

- Decrements in the half contact length lead to increments in the stable region in the $e-v$ plane. In other words, decreasing the half contact length increases stability.

- The following table quantifies the amounts of increments and decrements in the stability of the $e-v$ plane for variations of the half contact length a. Values given for a half contact length of 0.1 m show how much of the analyzed region in the $e-v$ plane is stable. Values given in the following lines for half contact lengths of 0.105 m, 0.11 m, 0.095 m and 0.09 m show how much of the analyzed region are stable and how much increment or decrement exists with respect to the stability of the system having a half contact length of 0.1 m.

- It is seen by inspecting table 5.5 that the directions of decreasing torsional spring rate k and increasing half contact length a are also the direction of decreasing stability.

- Most stable results are obtained for a half contact length a of 0.09 m and a spring rate k of 100000 Nm/rad. This is in accordance with the previous results as increasing k and decreasing a were shown to increase stability.

Table 5.5: Effect of variation of the half contact length a on stability in the $e - v$ plane.

<table>
<tr><td colspan="2" rowspan="2"></td><td colspan="3">→ direction of decreasing torsional spring rate</td></tr>
<tr><td>k =100000 Nm/rad</td><td>k =50000 Nm/rad</td><td>k =0 Nm/rad</td></tr>
<tr><td></td><td>a =0.1 m</td><td>97.9 % stable</td><td>79.7 % stable</td><td>56.3 % stable</td></tr>
<tr><td rowspan="4">increment in the half contact length</td><td rowspan="2">a =0.105 m</td><td>95.1 % stable</td><td>75.7 % stable</td><td>50.7 % stable</td></tr>
<tr><td>2.8 % decrement</td><td>5.0 % decrement</td><td>9.9 % decrement</td></tr>
<tr><td rowspan="2">a =0.11 m</td><td>91.8 % stable</td><td>71.0 % stable</td><td>44.6 % stable</td></tr>
<tr><td>6.2 % decrement</td><td>10.9 % decrement</td><td>20.7 % decrement</td></tr>
<tr><td rowspan="4">decrement in the half contact length</td><td rowspan="2">a =0.095 m</td><td>100 % stable</td><td>83.4 % stable</td><td>61.3 % stable</td></tr>
<tr><td>2.1 % increment</td><td>4.6 % increment</td><td>8.8 % increment</td></tr>
<tr><td rowspan="2">a =0.09 m</td><td>100 % stable</td><td>86.7 % stable</td><td>66.0 % stable</td></tr>
<tr><td>2.1 % increment</td><td>8.7 % increment</td><td>17.2 % increment</td></tr>
</table>

5.7.3. Effects of increasing and decreasing the caster length e and half contact length a on stability boundaries in the $c - v$ plane for different values of σ and F_z

This part of the stability analysis of the linear model is conducted in the $c - v$ plane. Effects of the caster length e, half contact length a and their ratio on stability of the model will be analyzed.

In figures 5.9–5.18, both e and a are taken as 0.1 m. Effects of 5 % and 10 % increase and decrease of e and a and variation of their ratio are analyzed in this section. σ takes values 0.02 m–0.32 m in figures 5.9–5.15 and F_z takes values 5000 N–15000 N in figures 5.16–5.18. These values will be retained to provide a good comparison with figures 5.9–5.18.

5.7.3.1 Effects of increasing and decreasing the caster length e and half contact length a on stability boundaries in the $c - v$ plane for different values of σ

This part of the stability analysis of the linear model is conducted for different values of the relaxation length σ, thus the effect of the half contact length a is already contained within the plots since $\sigma = 3a$. For this reason, only the effect of the caster length e on stability of the model will be analyzed. In figures 5.9–5.15, e is taken as 0.1 m. Effects of 5 % and 10 % increase and decrease of e are analyzed in this section.

5 % increase in the caster length e from 0.1 m to 0.105 m leads to an increase in the stable region in the $c - v$ plane, as can be seen by comparing figures 5.31–5.37 with figures 5.9–5.15 and by inspecting table 5.6.

It is observed that there is a smaller increase in the stable region for large values of the relaxation length σ. Increase in the stable region is almost unnoticeable for a relaxation length of 0.22 m and there is a slight decrease in the stable region for relaxation lengths of 0.27 and 0.32 m.

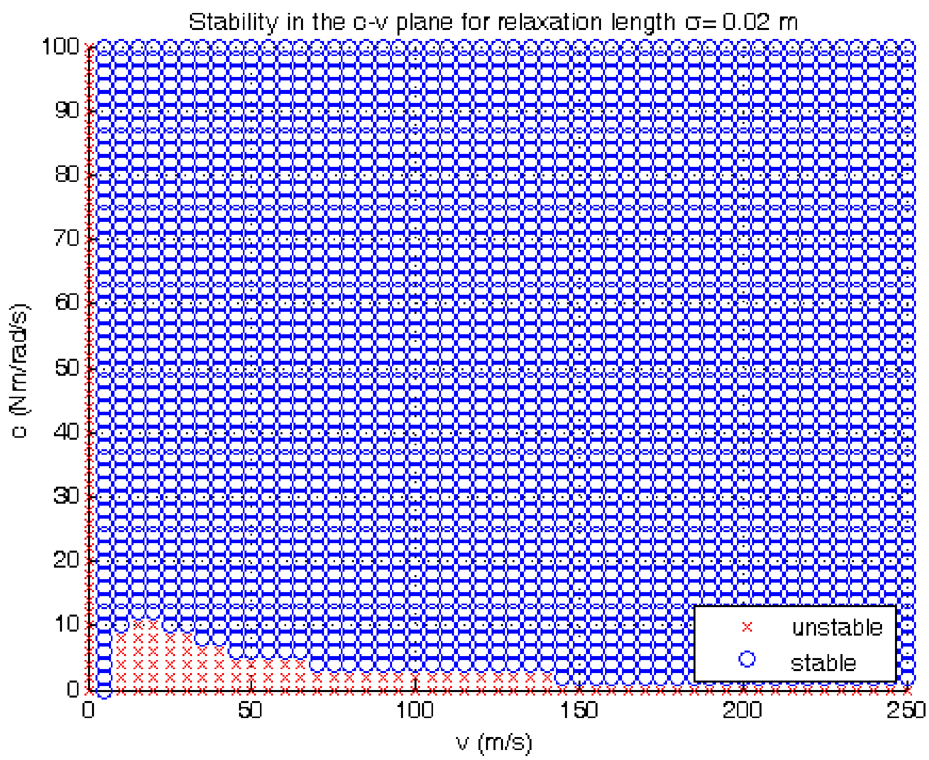

Figure 5.31: Stability in the $c - v$ plane for σ =0.02 m and e =0.105 m.

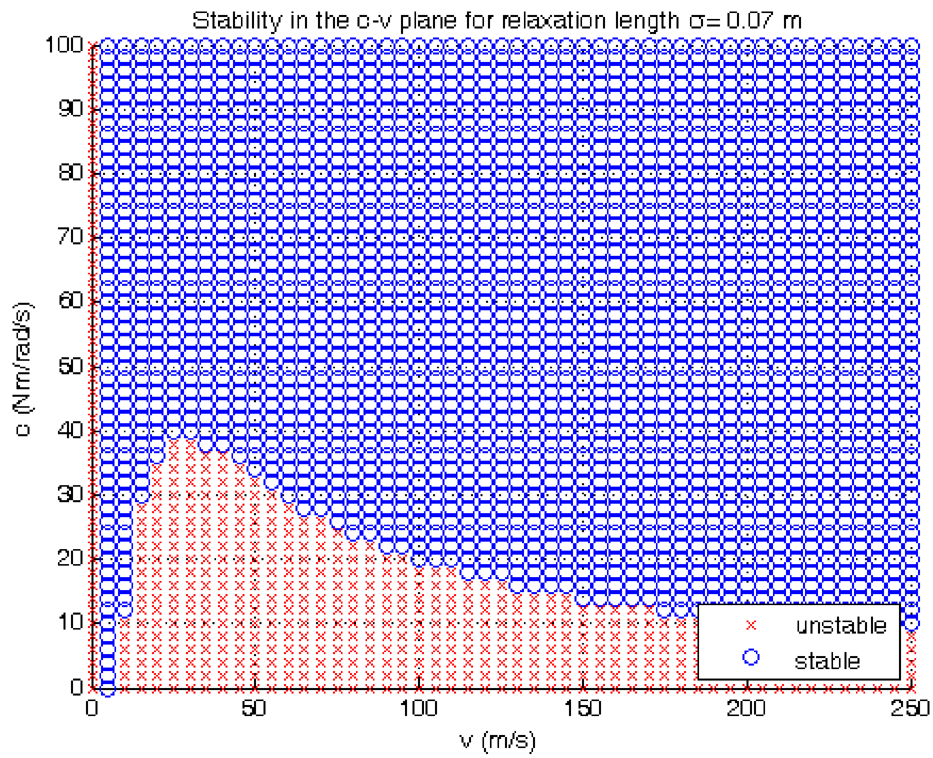

Figure 5.32: Stability in the $c-v$ plane for σ =0.07 m and e =0.105 m.

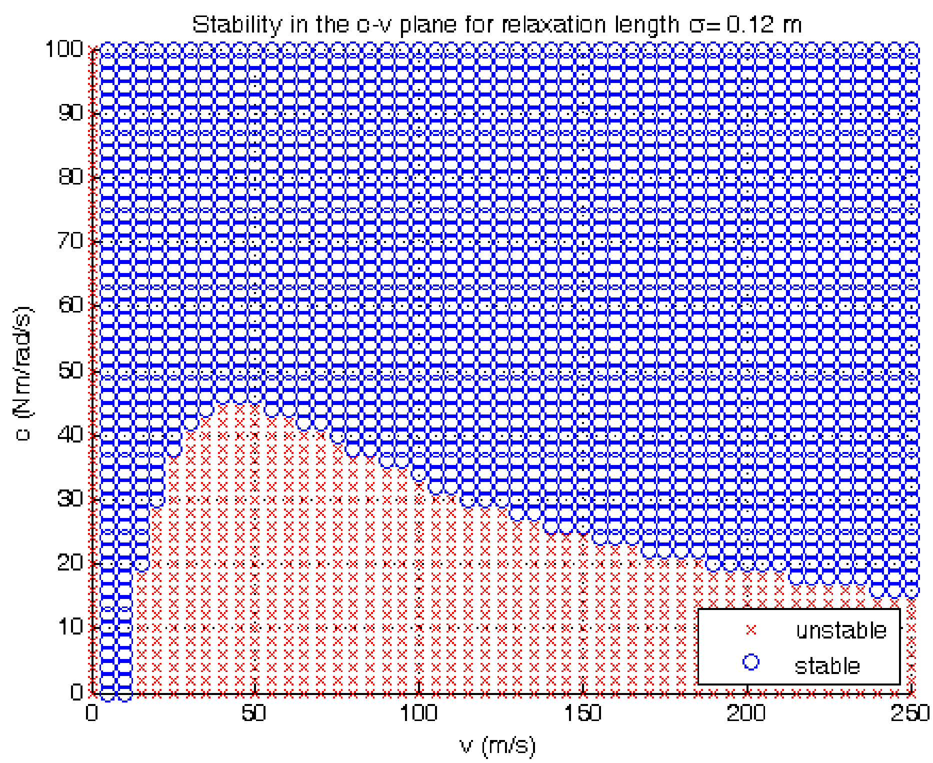

Figure 5.33: Stability in the $c-v$ plane for σ =0.12 m and e =0.105 m.

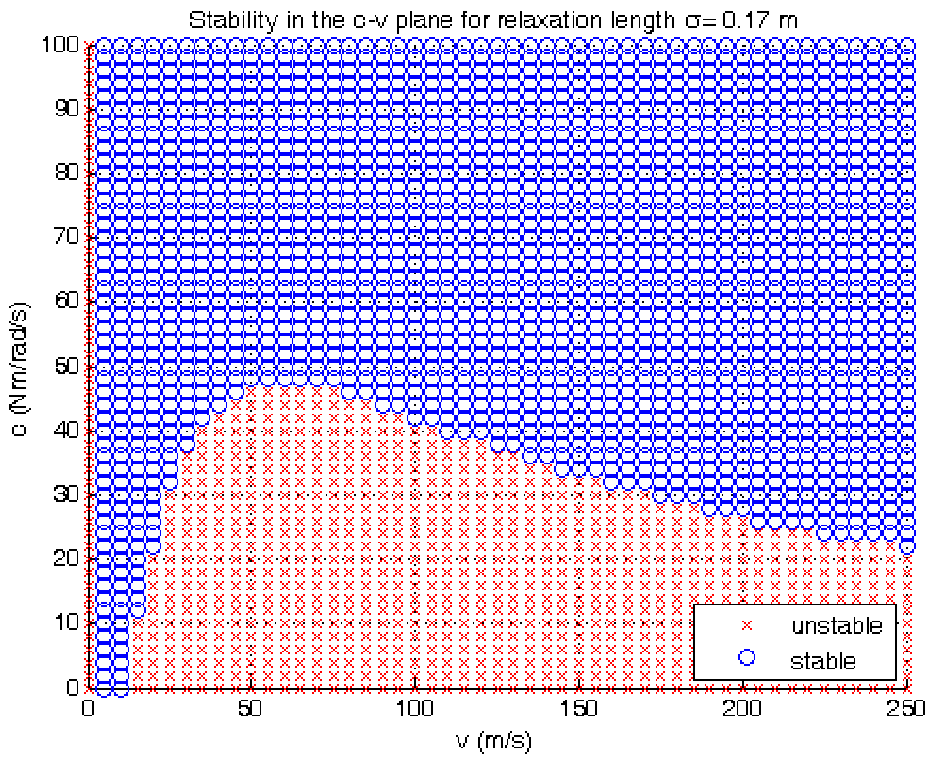

Figure 5.34: Stability in the $c-v$ plane for σ =0.17 m and e =0.105 m.

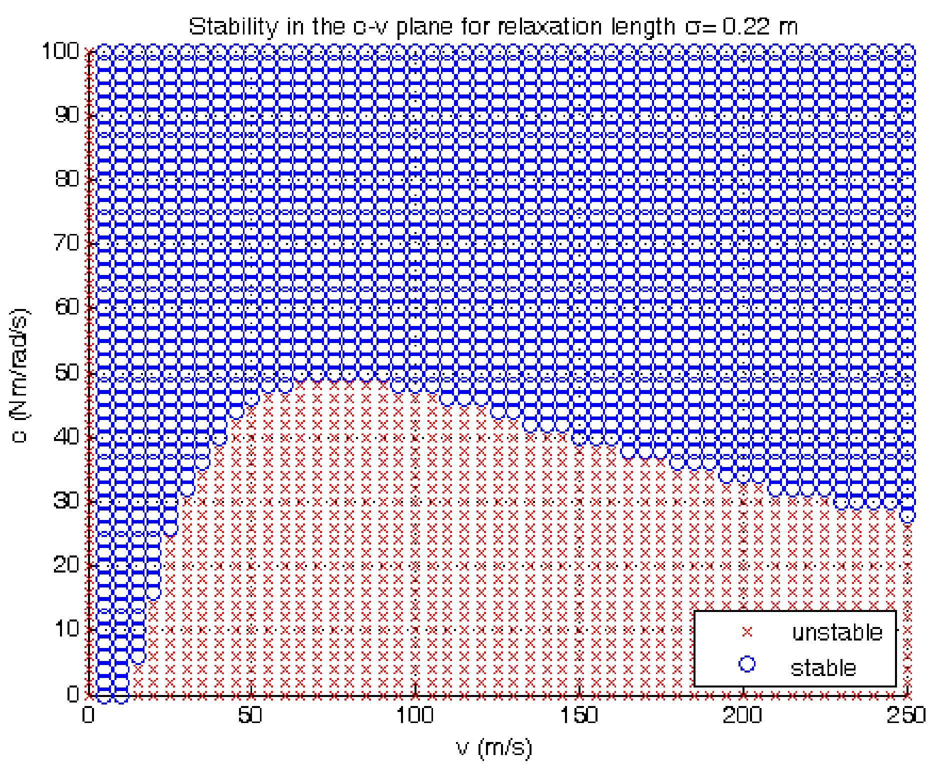

Figure 5.35: Stability in the $c-v$ plane for σ =0.22 m and e =0.105 m.

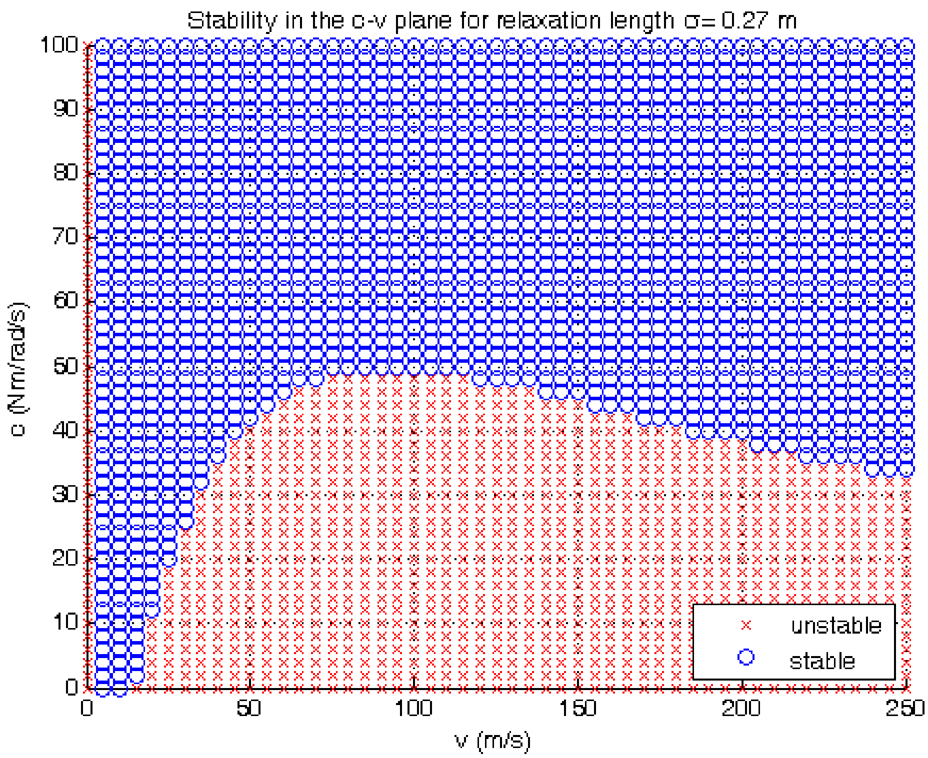

Figure 5.36: Stability in the $c - v$ plane for σ =0.27 m and e =0.105 m.

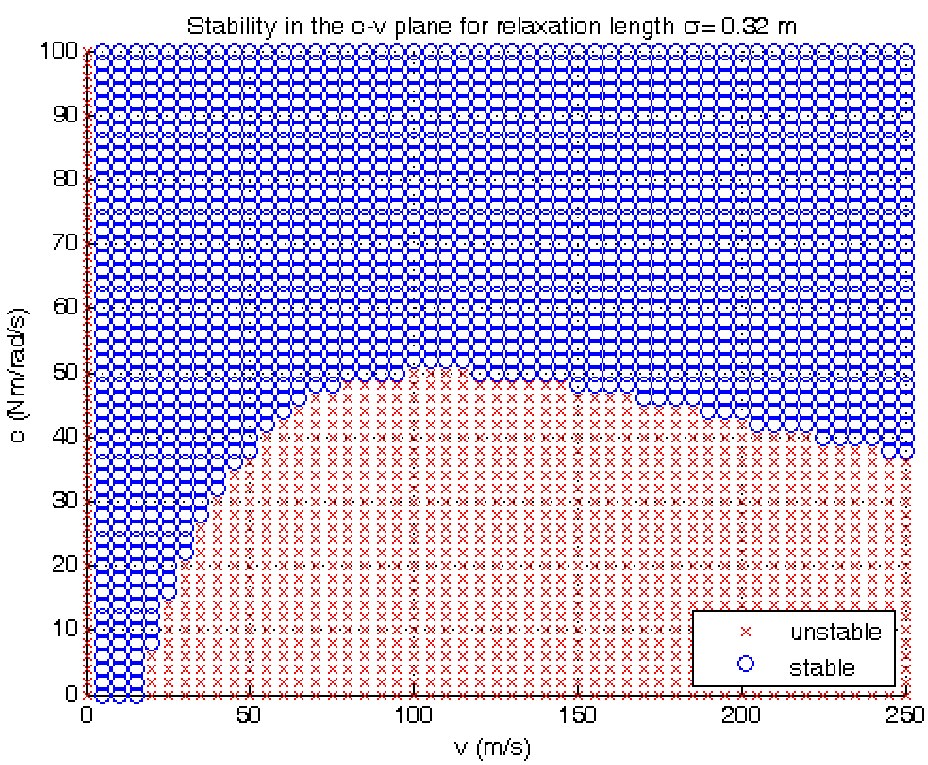

Figure 5.37: Stability in the $c - v$ plane for σ =0.32 m and e =0.105 m.

10 % increase in the caster length e from 0.1 m to 0.11 m leads to a further increase in the stable region in the $c - v$ plane, as can be seen by comparing figures 5.38–5.44 with figures 5.9–5.15 and by inspecting table 5.6.

As was the case for a caster length of 0.105 m, there is a smaller increase in the stable region for large values of relaxation length σ. The increase in the stable region is almost unnoticeable for a relaxation length of 0.22 m and there is a slight decrease in the stable region for relaxation lengths of 0.27 and 0.32 m.

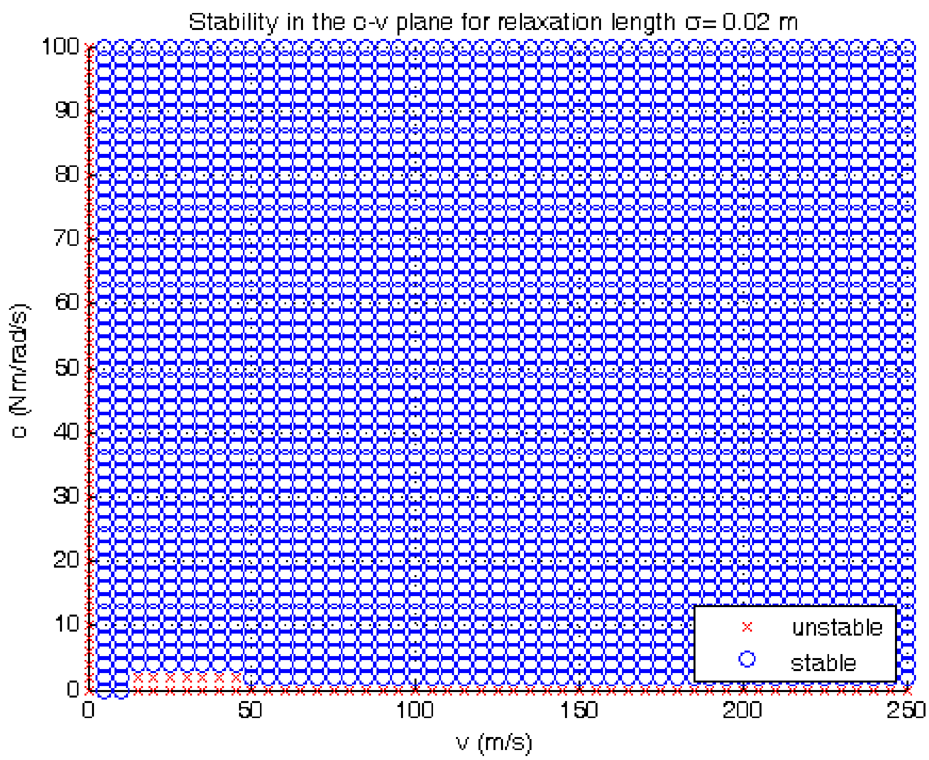

Figure 5.38: Stability in the $c - v$ plane for σ =0.02 m and e =0.11 m.

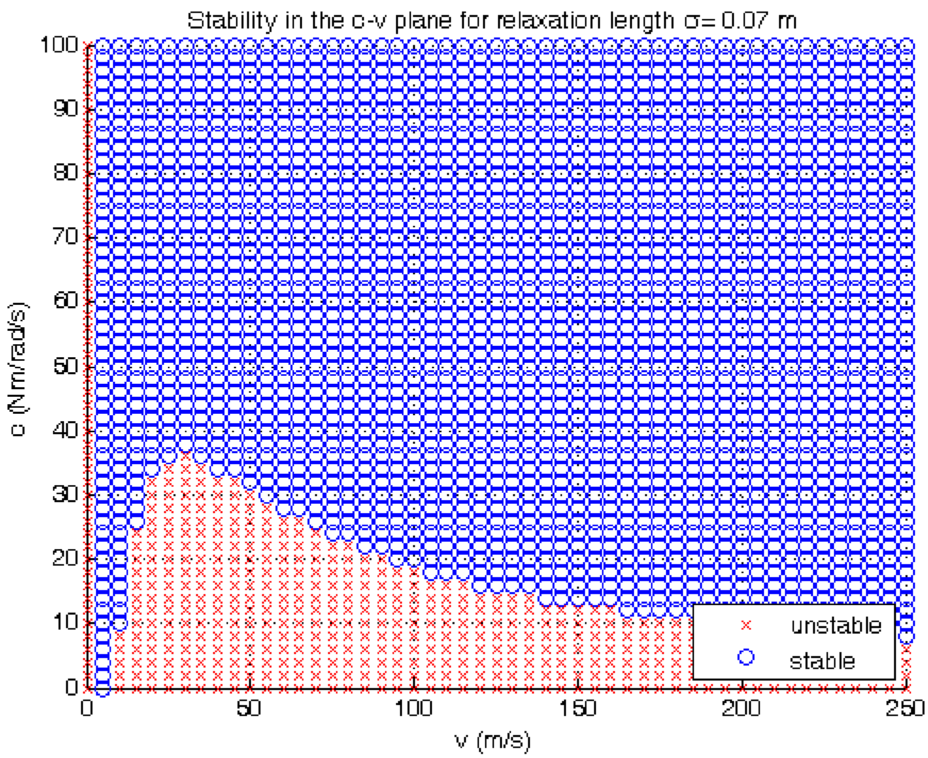

Figure 5.39: Stability in the $c-v$ plane for σ=0.07 m and e=0.11 m.

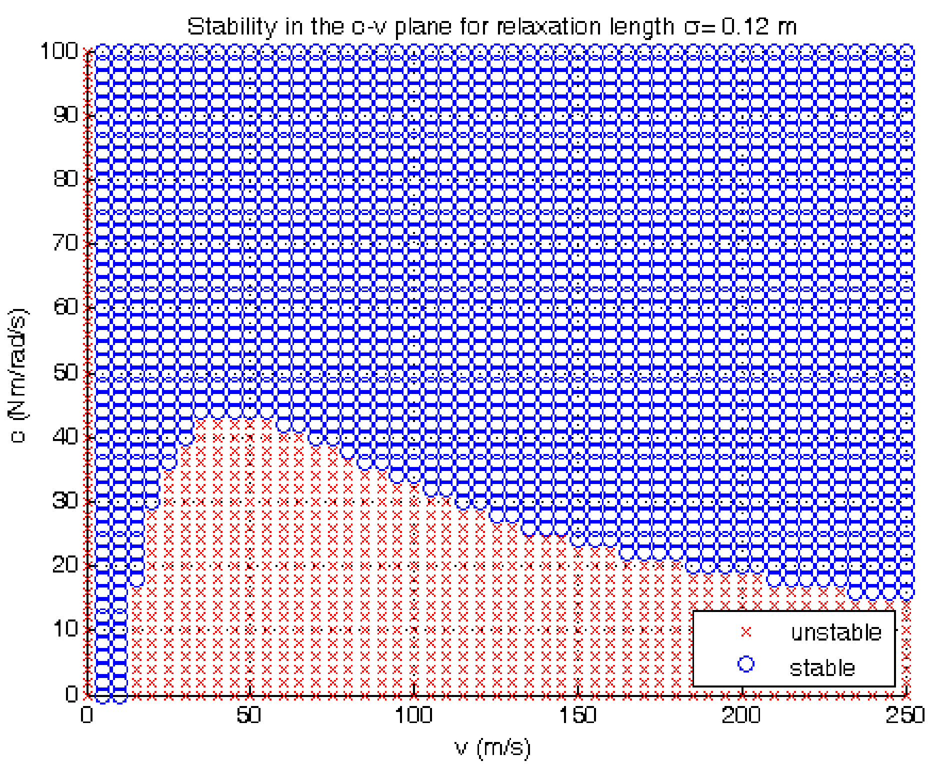

Figure 5.40: Stability in the $c-v$ plane for σ=0.12 m and e=0.11 m.

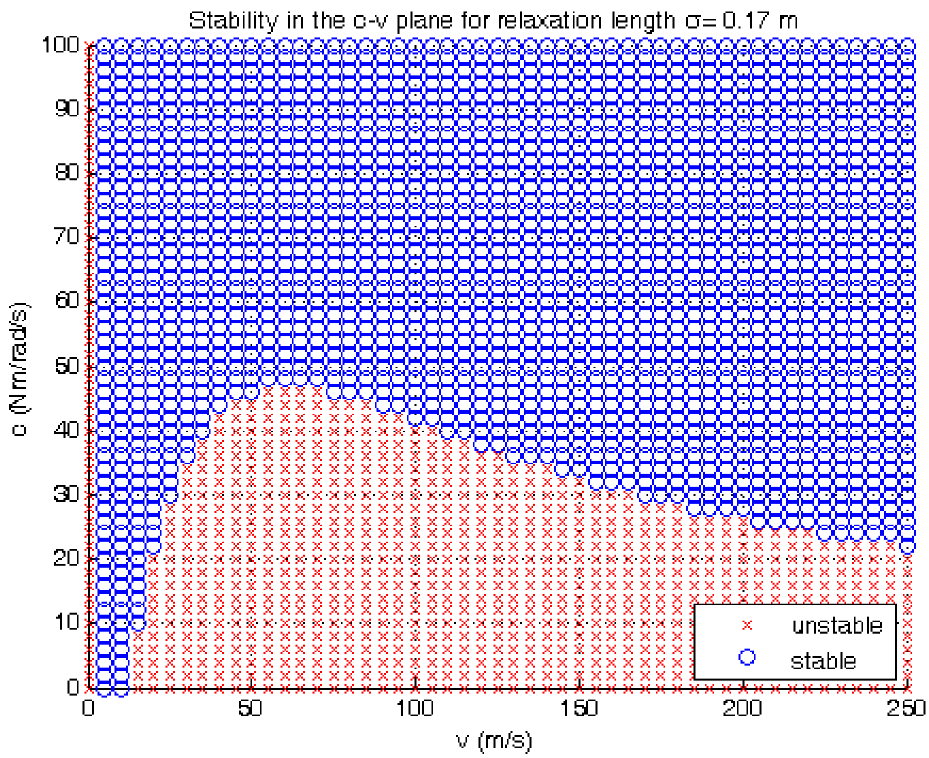

Figure 5.41: Stability in the $c - v$ plane for σ =0.17 m and e =0.11 m.

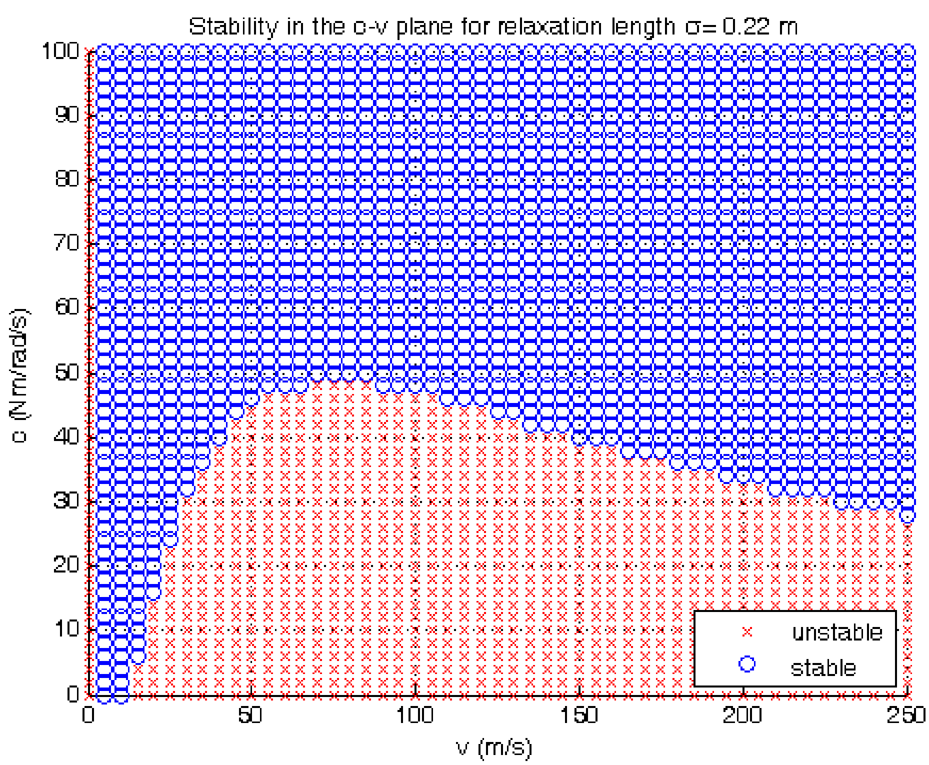

Figure 5.42: Stability in the $c - v$ plane for σ =0.22 m and e =0.11 m.

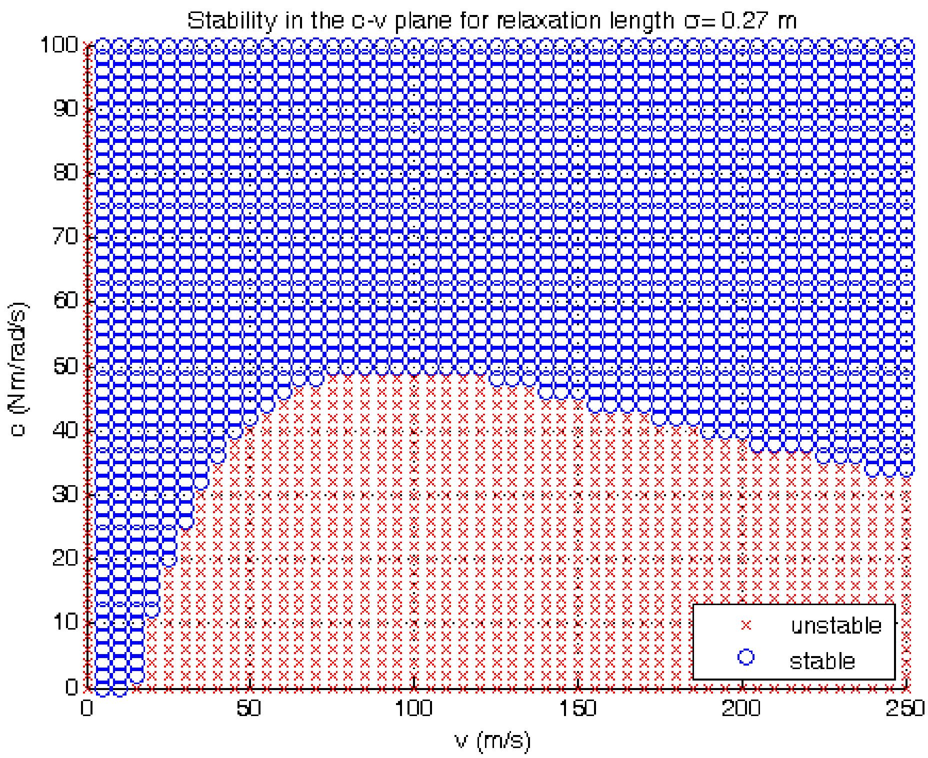

Figure 5.43: Stability in the $c - v$ plane for σ =0.27 m and e =0.11 m.

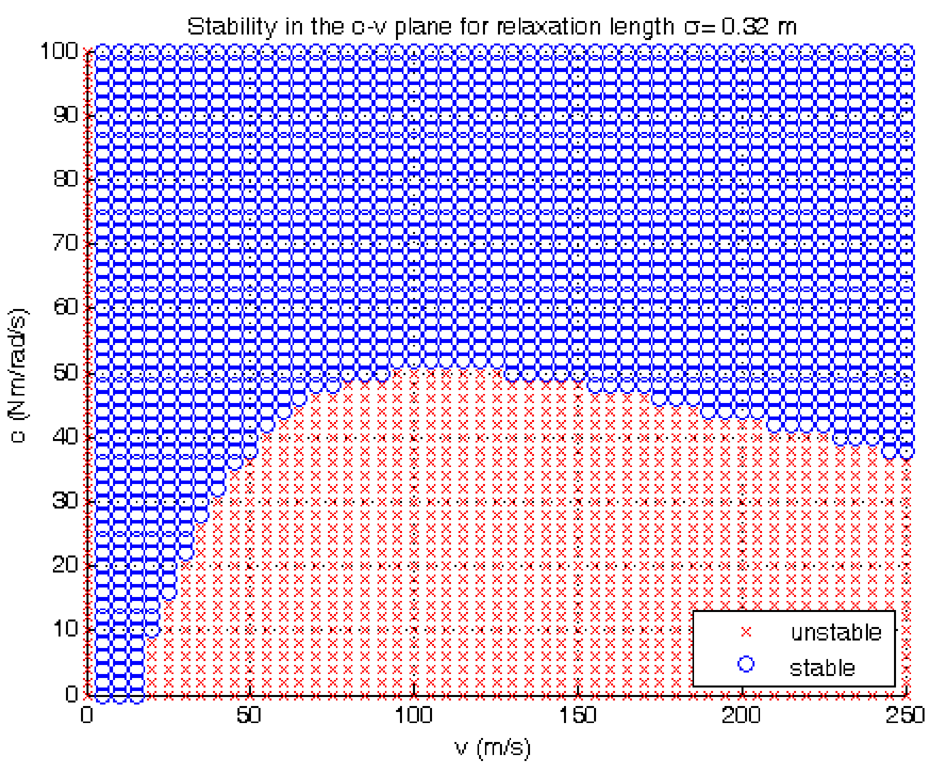

Figure 5.44: Stability in the $c - v$ plane for σ =0.32 m and e =0.11 m.

5 % decrease in the caster length e from 0.1 m to 0.095 m leads to an increase in the unstable region in the $c-v$ plane, especially for low velocities, as can be seen by comparing figures 5.45–5.51 with figures 5.9–5.15 and by inspecting table 5.6.

It is observed that there is a smaller increase in the unstable region for large values of the relaxation length σ. Decrease in the stable region is unnoticeable for relaxation lengths of 0.22 and 0.27 m and there is a slight increase in the stable reason for a relaxation length of 0.32 m.

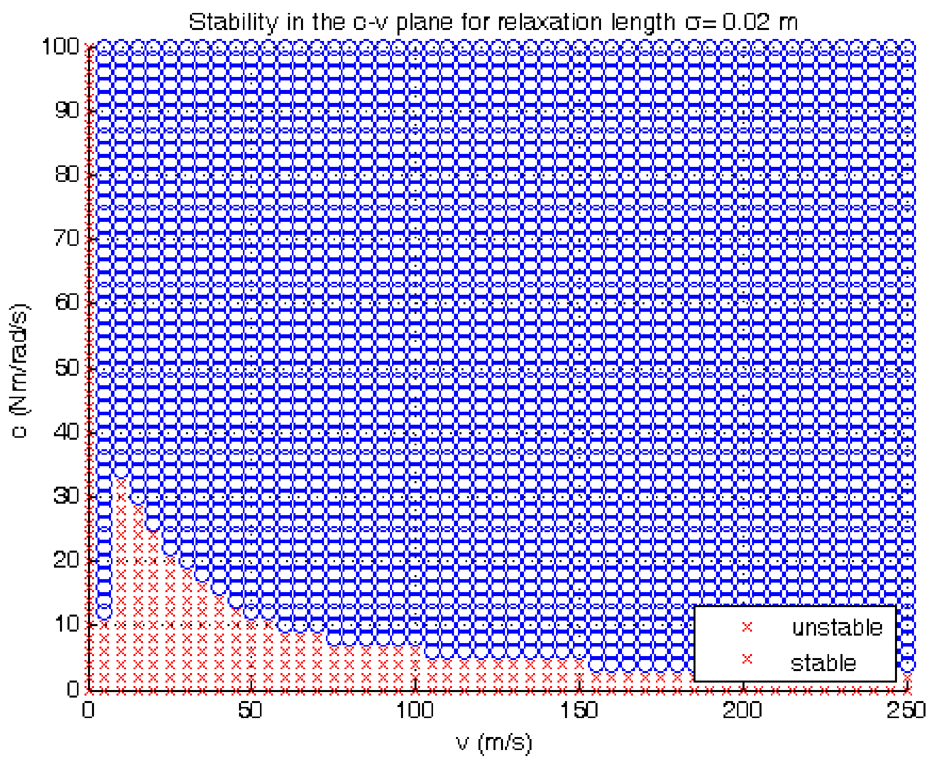

Figure 5.45: Stability in the $c-v$ plane for σ =0.02 m and e =0.095 m.

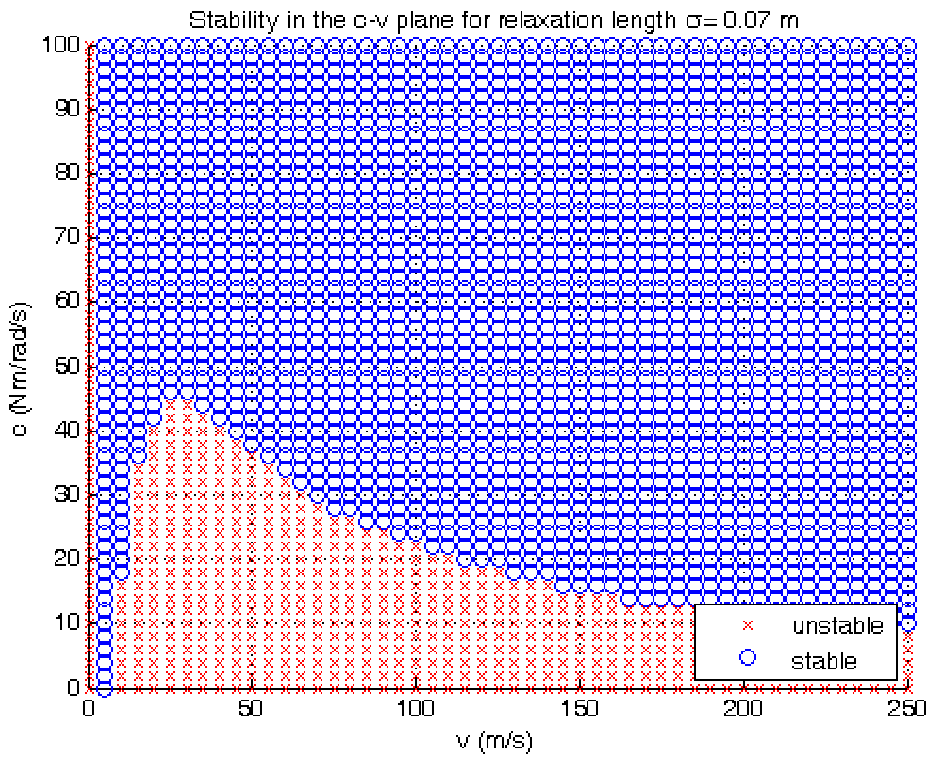

Figure 5.46: Stability in the $c-v$ plane for σ =0.07 m and e =0.095 m.

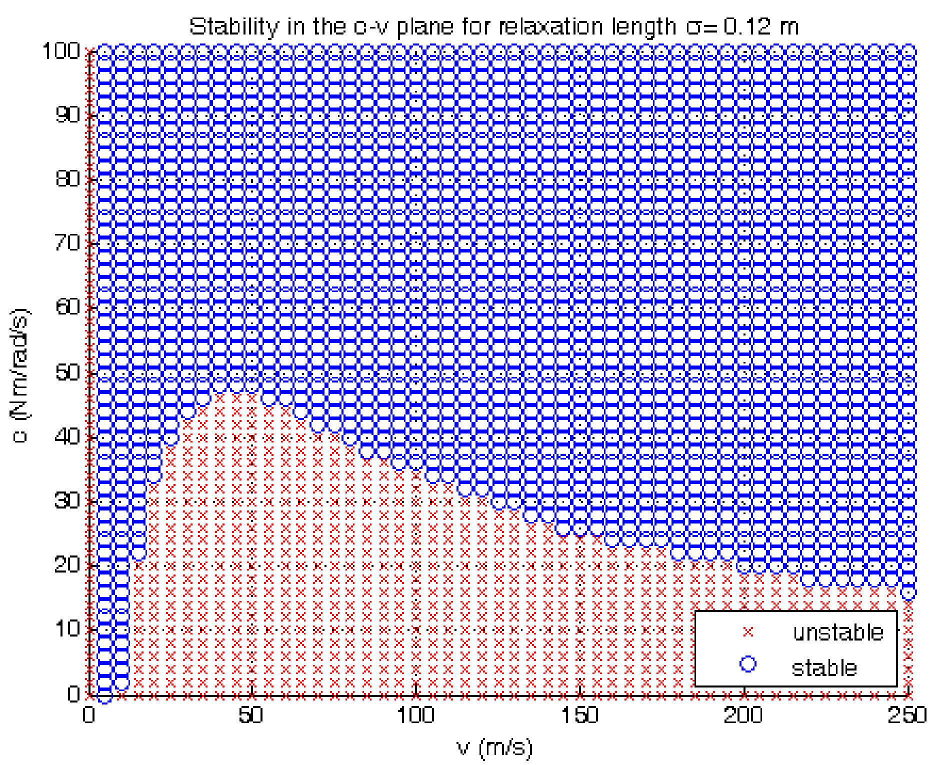

Figure 5.47: Stability in the $c-v$ plane for σ =0.12 m and e =0.095 m.

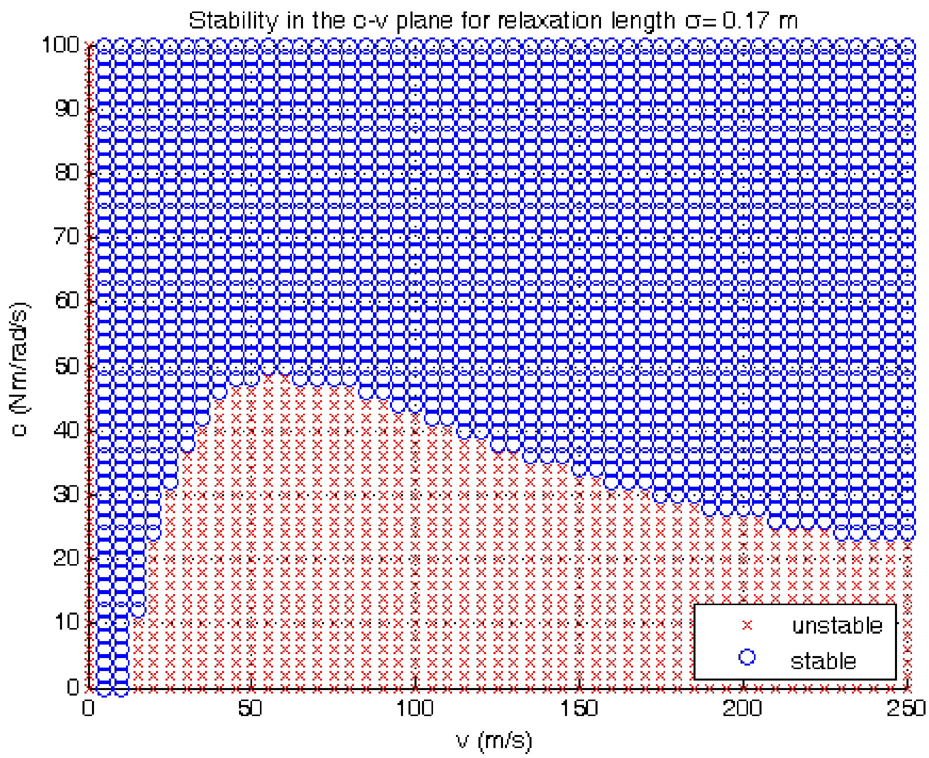

Figure 5.48: Stability in the $c - v$ plane for σ =0.17 m and e =0.095 m.

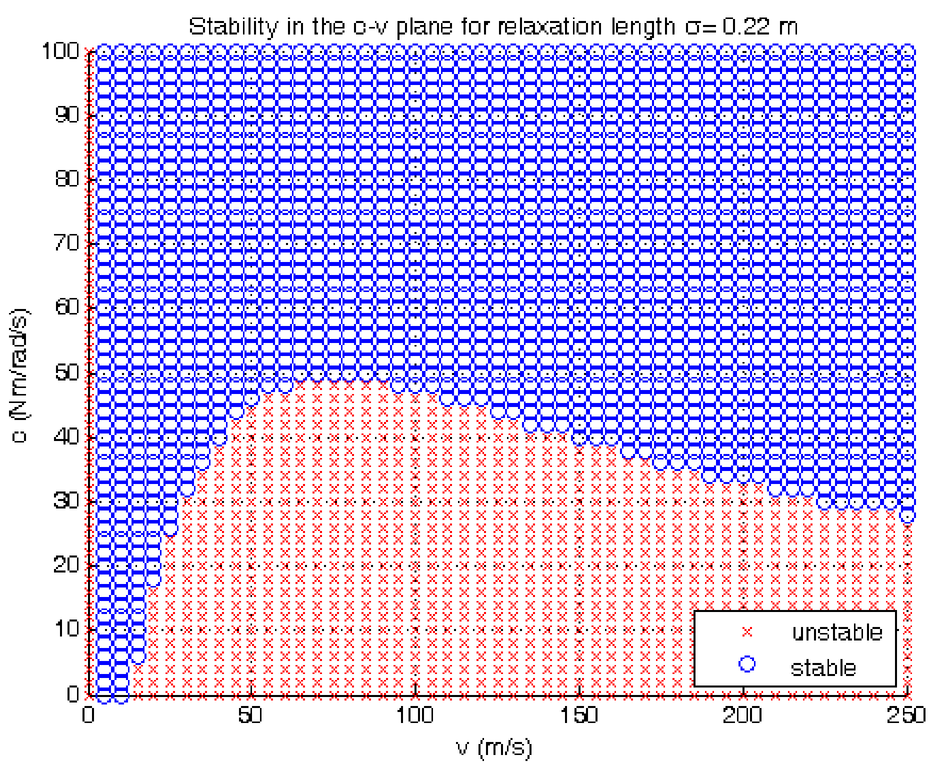

Figure 5.49: Stability in the $c - v$ plane for σ =0.22 m and e =0.095 m.

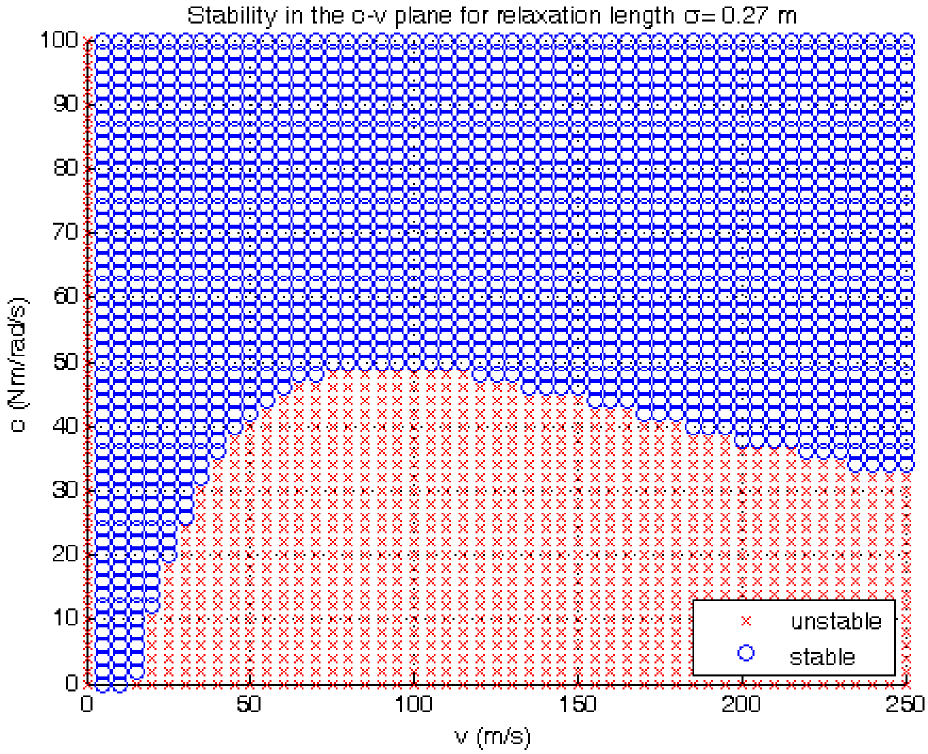

Figure 5.50: Stability in the $c - v$ plane for σ =0.27 m and e =0.095 m.

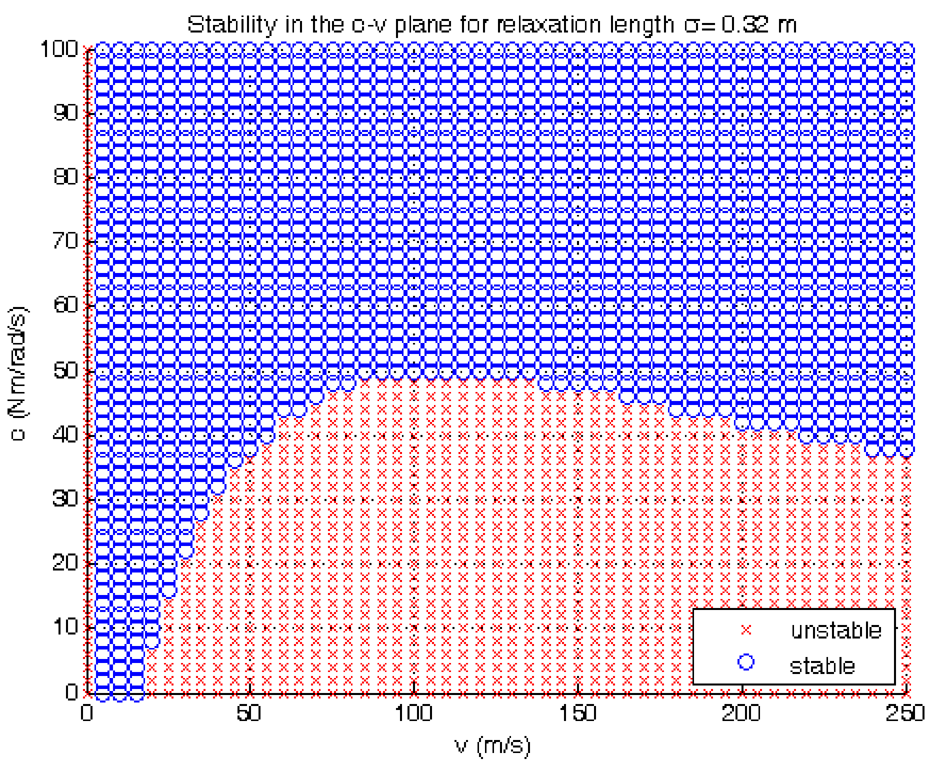

Figure 5.51: Stability in the $c - v$ plane for σ =0.32 m and e =0.095 m.

10 % decrease in the caster length e from 0.1 m to 0.09 m leads to a further increase in the unstable region in the $c - v$ plane, especially for low velocities, as can be seen by comparing figures 5.52–5.58 with figures 5.9–5.15 and by inspecting table 5.6.

As was the case for a caster length of 0.095 m, there is a smaller increase in the unstable region for large values of the relaxation length σ and there is a slight increase in the stable reason for relaxation lengths above 0.17 m.

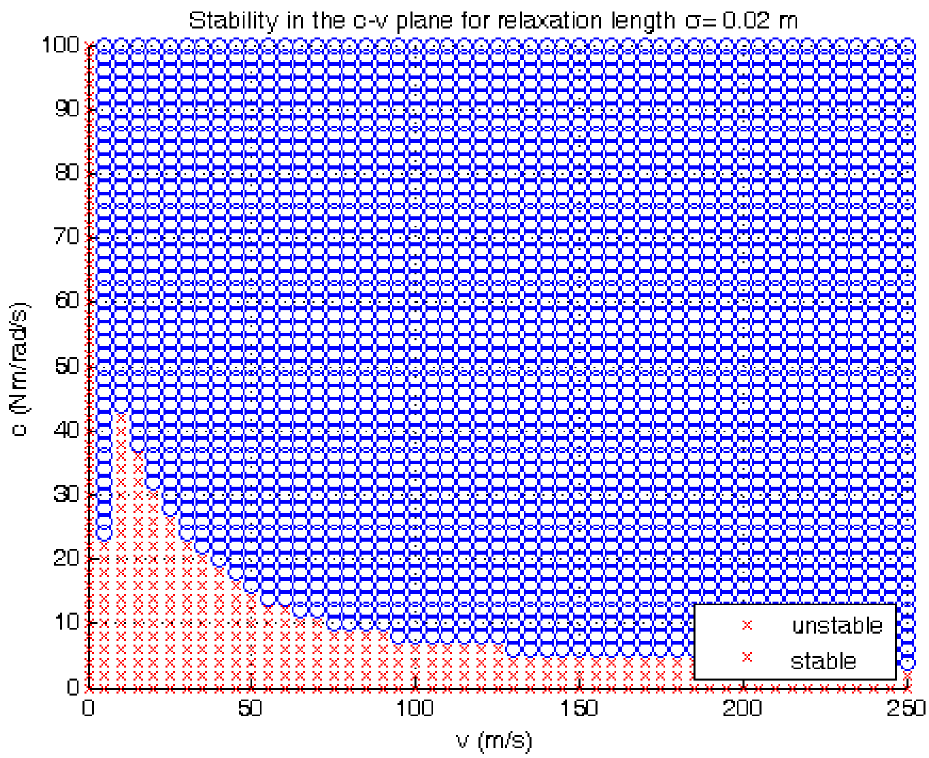

Figure 5.52: Stability in the $c - v$ plane for σ =0.02 m and e =0.09 m.

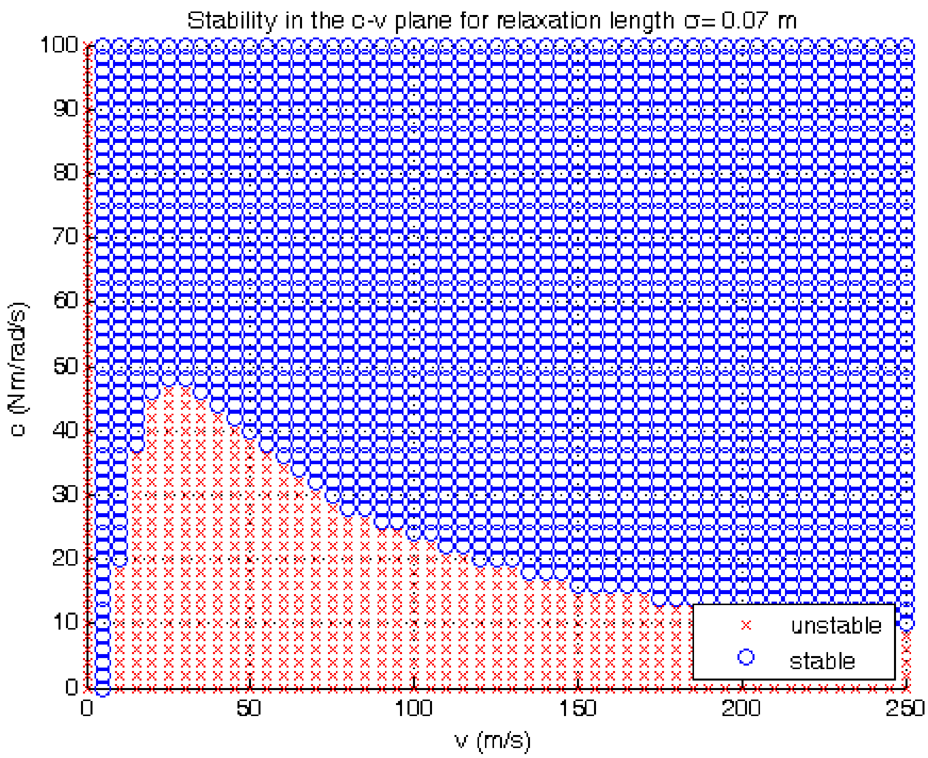

Figure 5.53: Stability in the $c - v$ plane for σ =0.07 m and e =0.09 m.

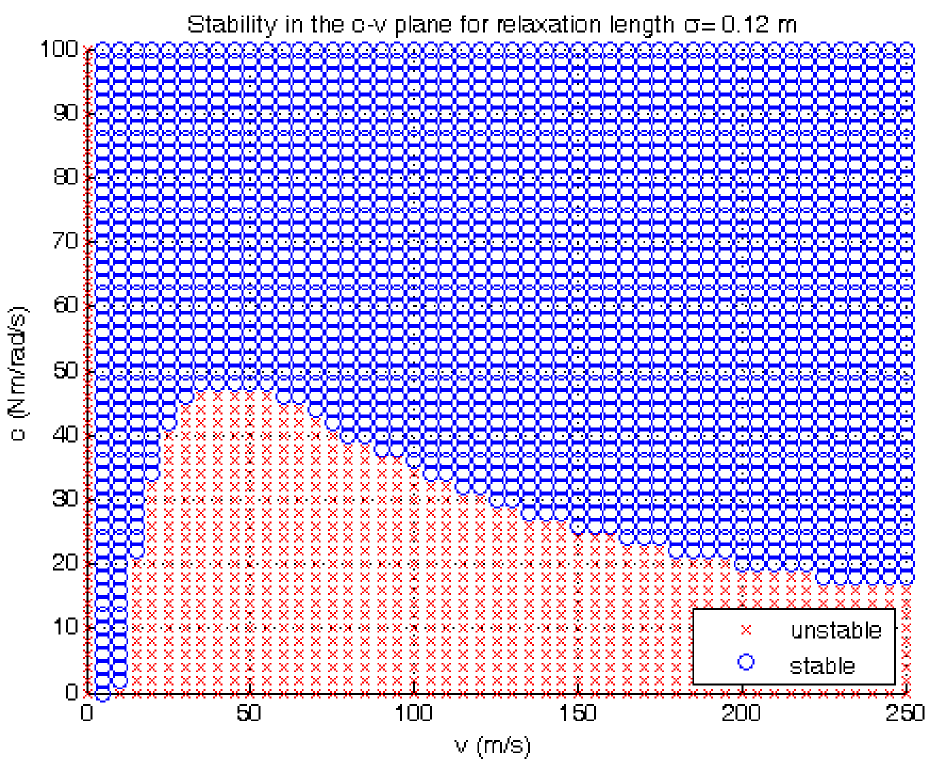

Figure 5.54: Stability in the $c - v$ plane for σ =0.12 m and e =0.09 m.

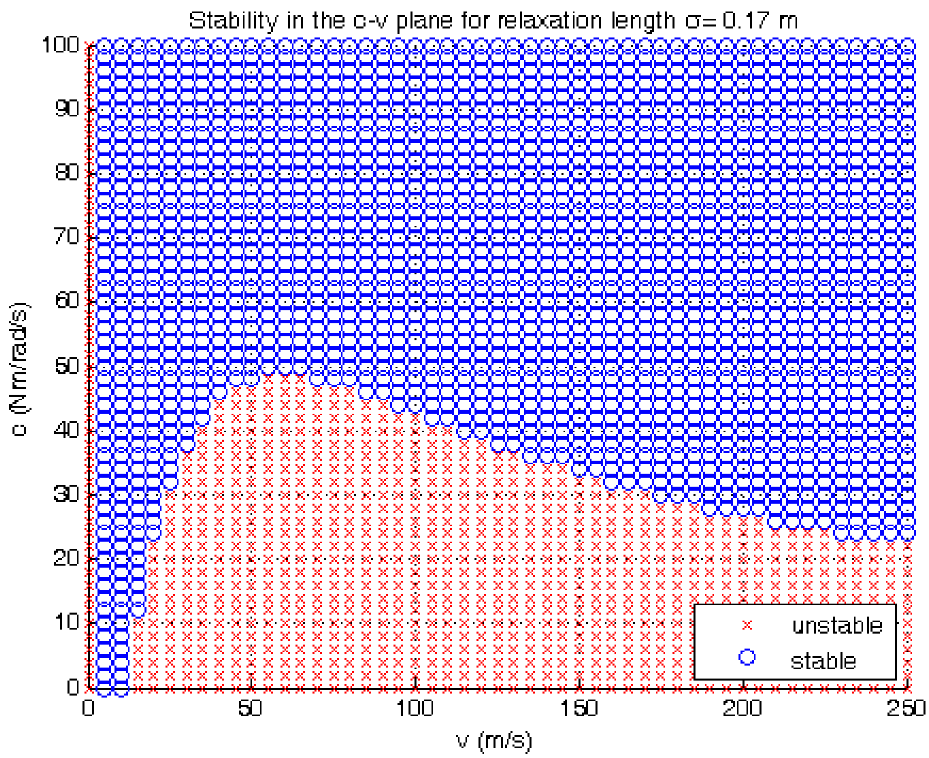

Figure 5.55: Stability in the $c - v$ plane for σ =0.17 m and e =0.09 m.

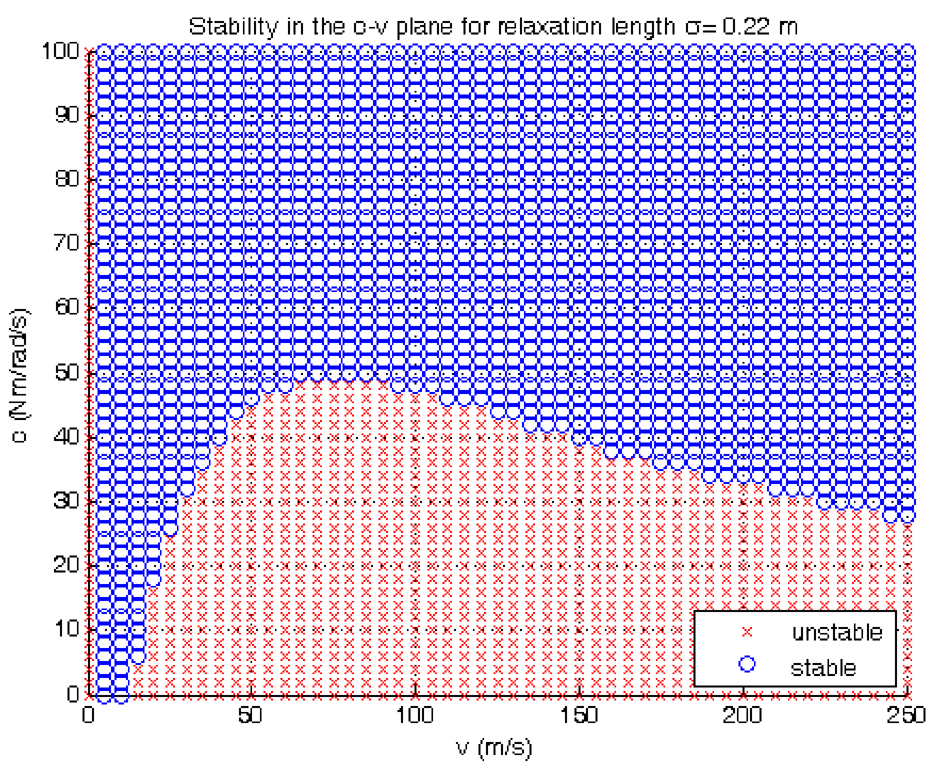

Figure 5.56: Stability in the $c - v$ plane for σ =0.22 m and e =0.09 m.

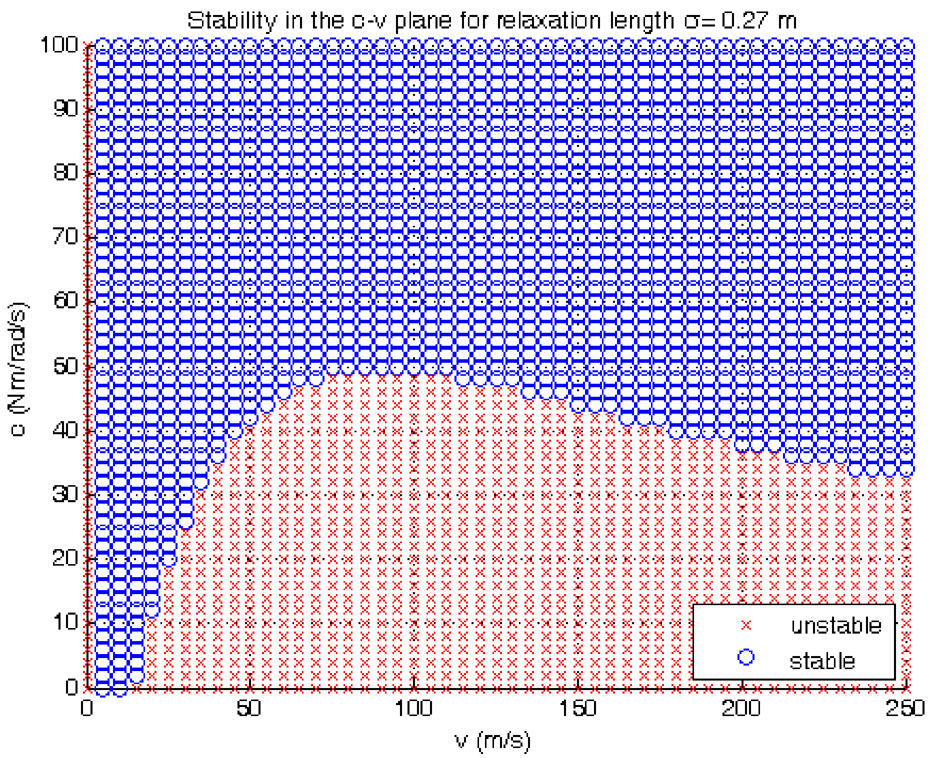

Figure 5.57: Stability in the $c - v$ plane for σ =0.27 m and e =0.09 m.

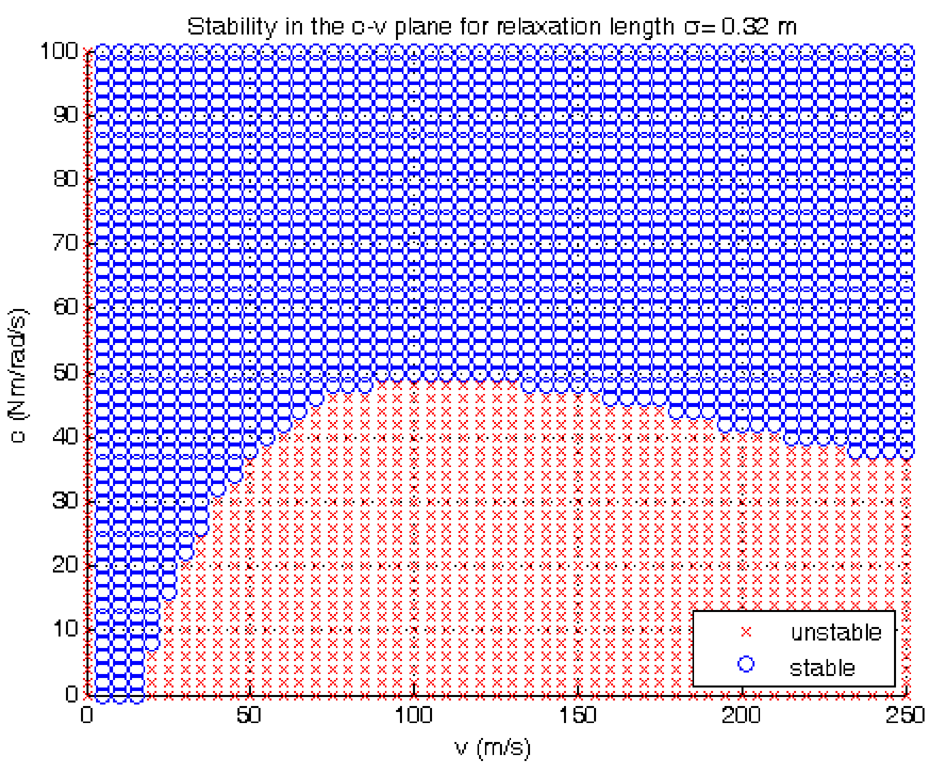

Figure 5.58: Stability in the $c - v$ plane for σ =0.32 m and e =0.09 m.

5.7.3.2 Conclusions about the effects of increasing and decreasing the caster length e and half contact length a on stability boundaries in the $c-v$ plane for different values of σ

- 5 % increase in the caster length e leads to an increase in the stable region in the $c-v$ plane. There is a smaller increase in the stable region for large values of the relaxation length σ. Increase in the stable region is almost unnoticeable for a relaxation length of 0.22 m and there is a slight decrease in the stable region for relaxation lengths of 0.27 and 0.32 m.
- 10 % increase in the caster length e leads to a further increase in the stable region in the $c-v$ plane. There is a smaller increase in the stable region for large values of the relaxation length σ. Increase in the stable region is almost unnoticeable for a relaxation length of 0.22 m and there is a slight decrease in the stable region for relaxation lengths of 0.27 and 0.32 m.
- 5 % decrease in the caster length e leads to an increase in the unstable region in the $c-v$ plane, especially for low velocities. There is a smaller increase in the unstable region for large values of the relaxation length σ. Decrease in the stable region is unnoticeable for relaxation lengths of 0.22 and 0.27 m and there is a slight increase in the stable reason for a relaxation length of 0.32 m.
- 10 % decrease in the caster length e from leads to a further increase in the unstable region in the $c-v$ plane, especially for low velocities. As was the case for a caster length of 0.095 m, there is a smaller increase in the unstable region for large values of the relaxation length σ and there is a slight increase in the stable reason for relaxation lengths above 0.17 m.
- Increments in the caster length e lead to increments in the stable region in the $c-v$ plane. In other words, increasing the caster length increases stability.
- Decrements in the relaxation length σ lead to increments in the stable region in the $c-v$ plane. In other words, decreasing the relaxation length σ or the half contact length increases stability.
- Increments in the stable and unstable regions are smaller for large values of the relaxation length σ.

- Table 5.6 quantifies the amounts of increments and decrements in the stability of the $c-v$ plane for variations of the caster length e. Values given for a caster length of 0.1 m show how much of the analyzed region in the $c-v$ plane is stable. Values given in the following lines for caster lengths of 0.105 m, 0.11 m, 0.095 m and 0.09 m show how much of the analyzed region are stable and how much increment or decrement exists with respect to the stability of the system having a caster length of 0.1 m.
- It is seen by inspecting table 5.6 that the directions of increasing relaxation length and decreasing the caster length are also the direction of decreasing stability.
- Most stable result is obtained for a caster length e of 0.11 m and a relaxation length σ of 0.02 m. This is in accordance with the previous results as increasing e and decreasing σ were shown to increase stability.

Table 5.6: Effect of variation of the caster length on stability in the $c - v$ plane.

		→ direction of increasing relaxation length						
		σ =0.02 m	**σ =0.07 m**	**σ =0.12 m**	**σ =0.17 m**	**σ =0.22 m**	**σ =0.27 m**	**σ =0.32 m**
	e =0.1 m	91.9 % stable	78.3 % stable	70.6 % stable	65.6 % stable	62.3 % stable	60.5 % stable	59.4 % stable
increment in the caster length	**e =0.105 m**	94.1 % stable	79.5 % stable	71.2 % stable	65.8 % stable	62.3 % stable	60.4 % stable	59.0 % stable
		2.3 % increment	1.5 % increment	0.8 % increment	0.3 % increment	0 % increment	0.1 % decrement	0.6 % decrement
	e =0.11 m	95.9 % stable	80.6 % stable	71.9 % stable	66.2 % stable	62.4 % stable	60.3 % stable	58.7 % stable
		4.3 % increment	2.9 % increment	1.8 % increment	0.9 % increment	0.1 % increment	0.3 % decrement	1.1 % decrement
decrement in the caster length	**e =0.095 m**	89.6 % stable	77.2 % stable	70.0 % stable	65.3 % stable	62.3 % stable	60.5 % stable	59.6 % stable
		2.5 % decrement	1.4 % decrement	0.8 % decrement	0.4 % decrement	0 % decrement	0 % decrement	0.3 % increment
	e =0.09 m	87.6 % stable	76.2 % stable	69.6 % stable	65.3 % stable	62.4 % stable	60.7 % stable	60.0 % stable
		4.67 % decrement	2.6 % decrement	1.4 % decrement	0.4 % decrement	0.1 % increment	0.3 % increment	1 % increment

5.8 Time Histories of the Linear Model

5.8.1 Time histories of the torsion angle ψ and lateral tire deformation y

Time histories of the torsion angle ψ and lateral tire deformation y are obtained for 1 s for various values of the velocity v and damping constant c. v takes values in the range 20–50 m/s, while c takes values in the range 10–90 Nm/rad/s.

A Runge–Kutta algorithm with timestep 0.001 s has been employed. Superiority of the fourth order Runge–Kutta algorithm over the Euler and improved Euler methods and the ode functions of the Matlab software are proven in Appendix A by application to the Lorenz attractor problem, thus this algorithm will be used in numerical simulations in this study.

Figures 5.59–5.72 show the time histories of the torsion angle ψ, while figures 5.73–5.86 show the time histories of the lateral tire deformation y. Initial conditions employed in obtaining figures 5.59–5.86 are $\psi(0)=0.01, \dot{\psi}(0)=0$ and $y(0)=0.001$.

Clearly, increasing the velocity v increases the amplitude of the torsion angle ψ, while increasing the damping constant c decreases the amplitude of the torsion angle.

Table 5.7 gives root mean squares of the amplitudes of the torsion angle and lateral tire deformation in 0–1 s and qualitative observations about the presented time histories.

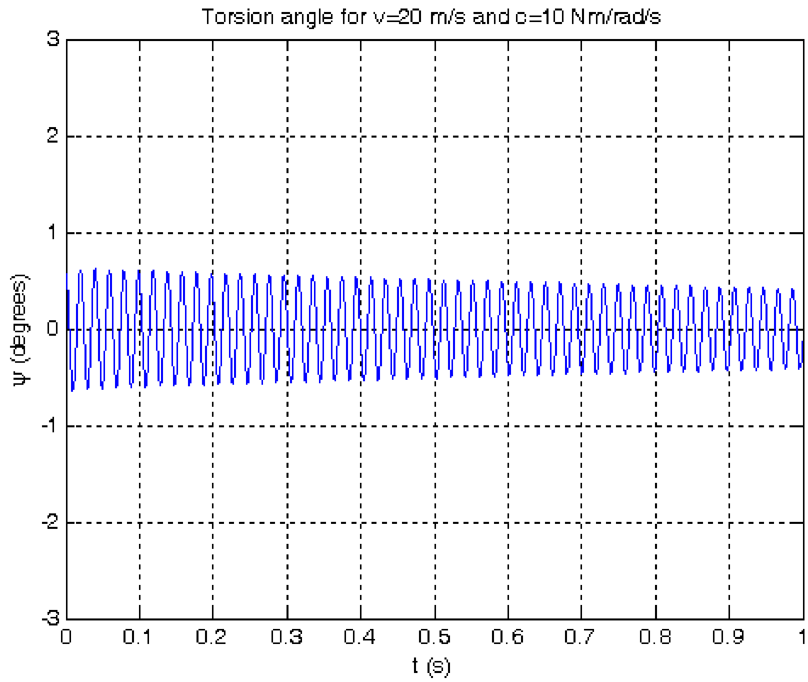

Figure 5.59: Torsion angle for v =20 m/s and c =10 Nm/rad/s.

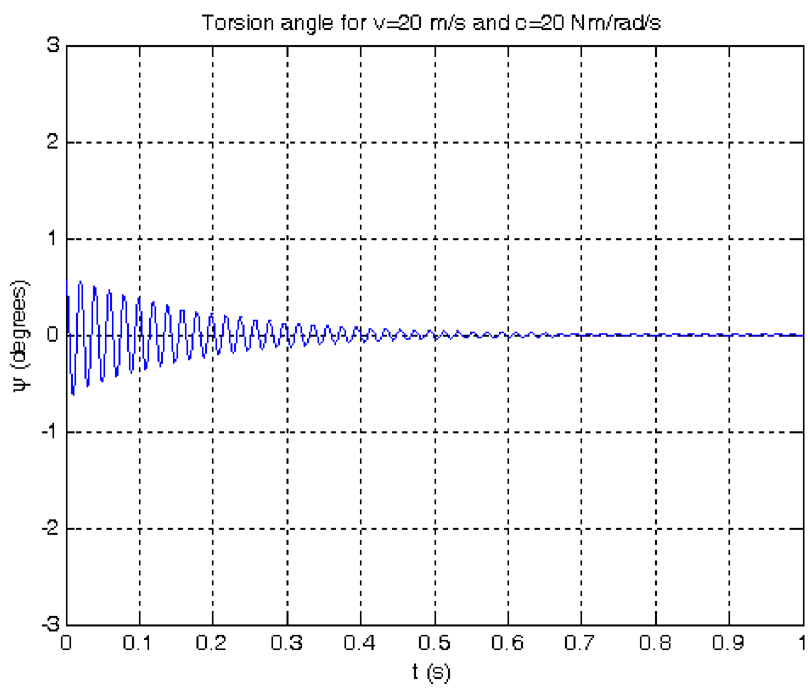

Figure 5.60: Torsion angle for v =20 m/s and c =20 Nm/rad/s.

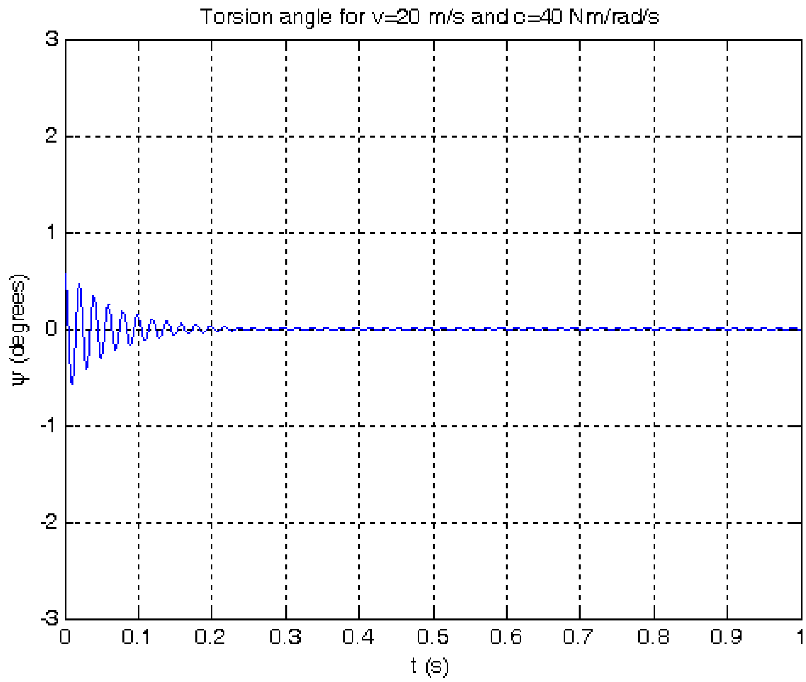

Figure 5.61: Torsion angle for v =20 m/s and c =40 Nm/rad/s.

A comparison of figures 5.59–5.61 reveals that increasing the damping constant c decreases the amplitude of the torsion angle.

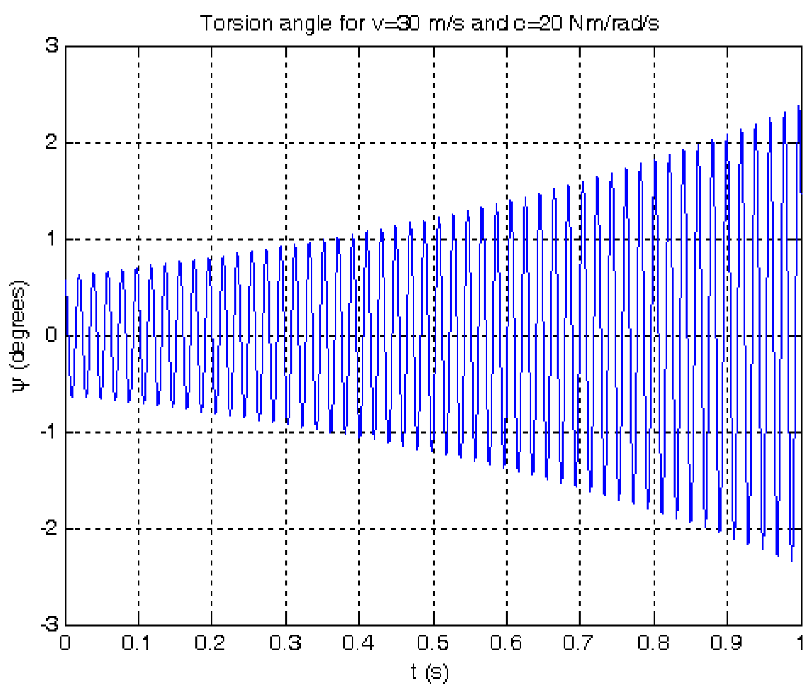

Figure 5.62: Torsion angle for v =30 m/s and c =20 Nm/rad/s.

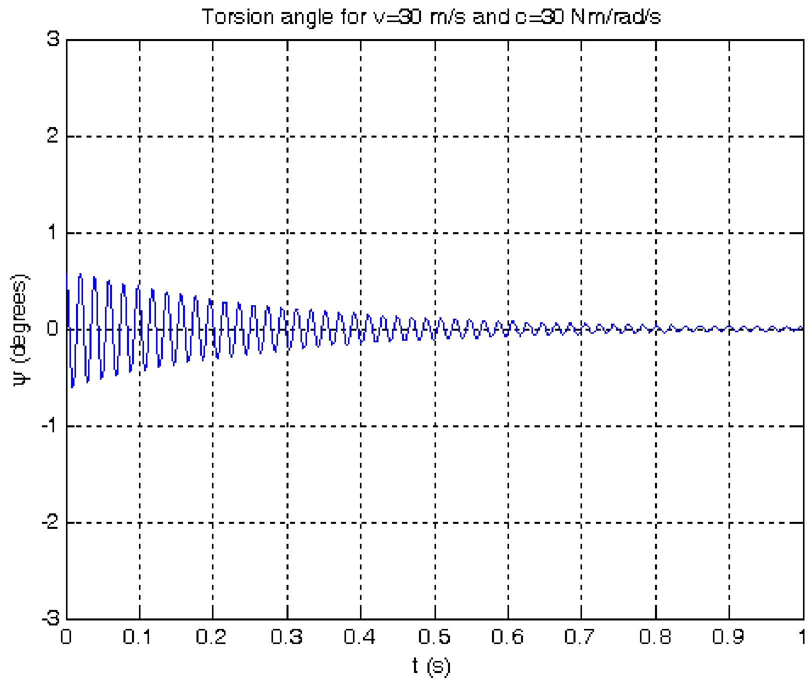

Figure 5.63: Torsion angle for v =30 m/s and c =30 Nm/rad/s.

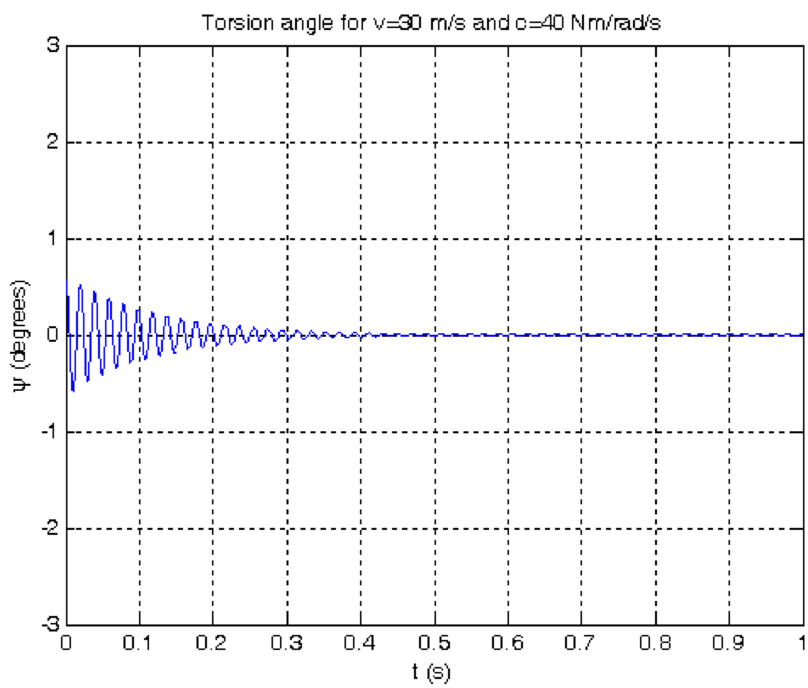

Figure 5.64: Torsion angle for v =30 m/s and c =40 Nm/rad/s.

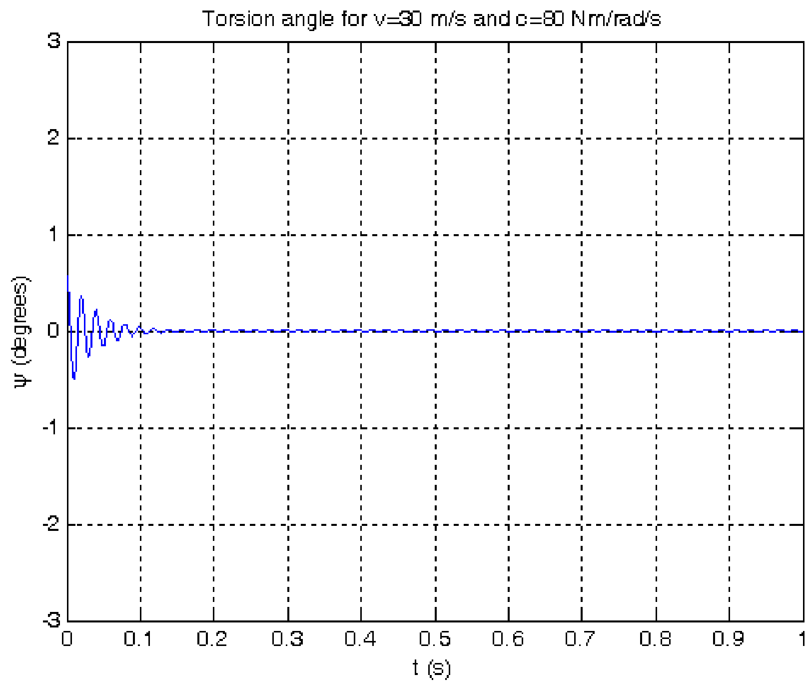

Figure 5.65: Torsion angle for v =30 m/s and c =80 Nm/rad/s.

A comparison of figures 5.62–5.65 reveals that increasing the damping constant c decreases the amplitude of the torsion angle.

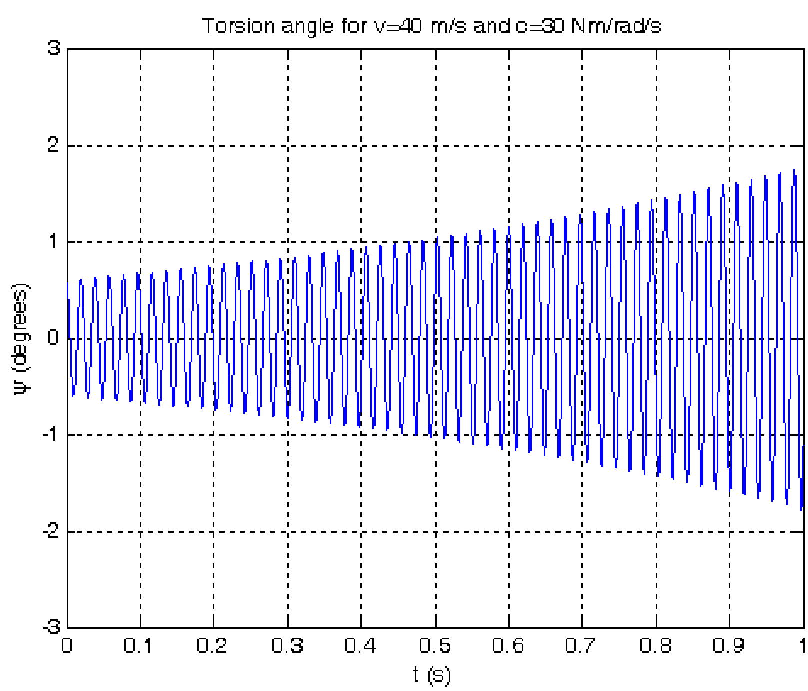

Figure 5.66: Torsion angle for v =40 m/s and c =30 Nm/rad/s.

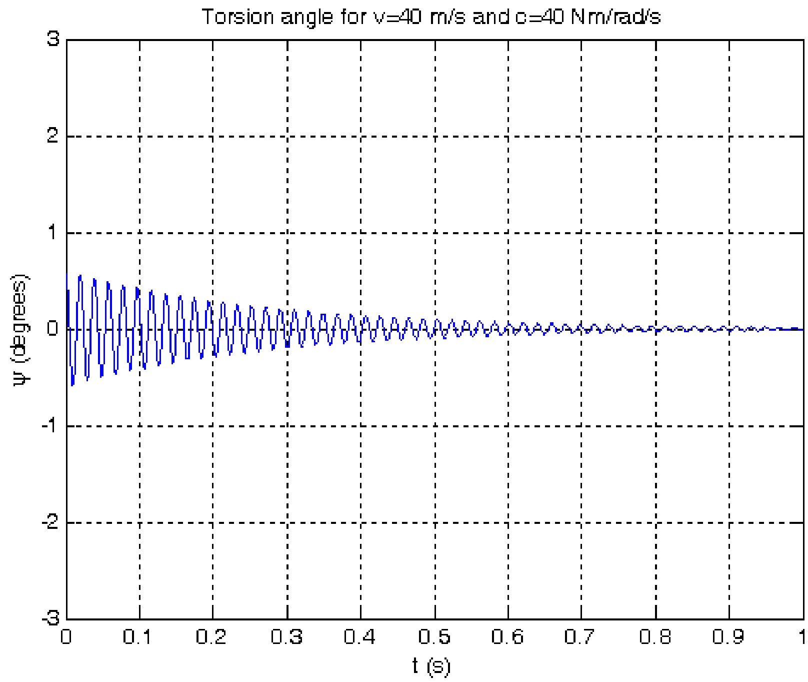

Figure 5.67: Torsion angle for v =40 m/s and c =40 Nm/rad/s.

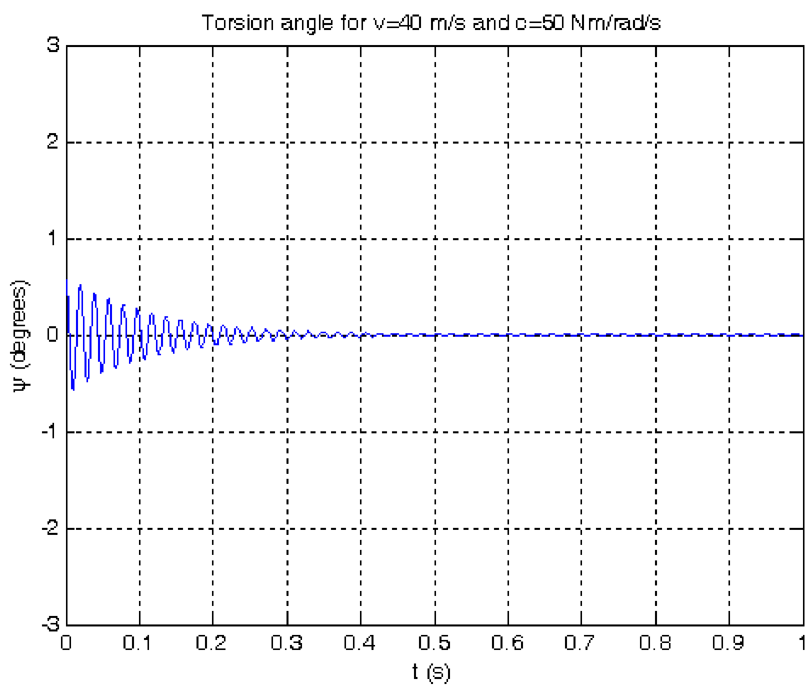

Figure 5.68: Torsion angle for v =40 m/s and c =50 Nm/rad/s.

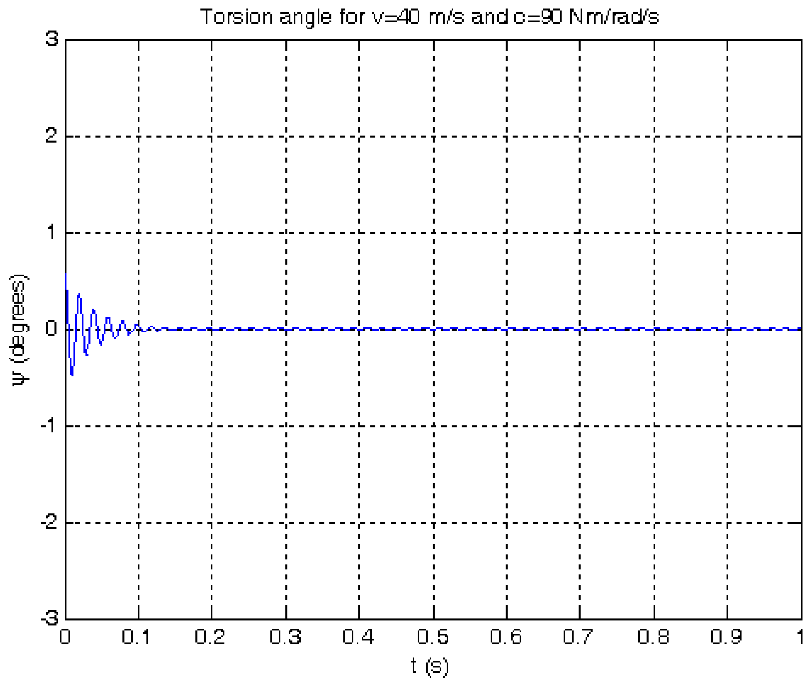

Figure 5.69: Torsion angle for v =40 m/s and c =90 Nm/rad/s.

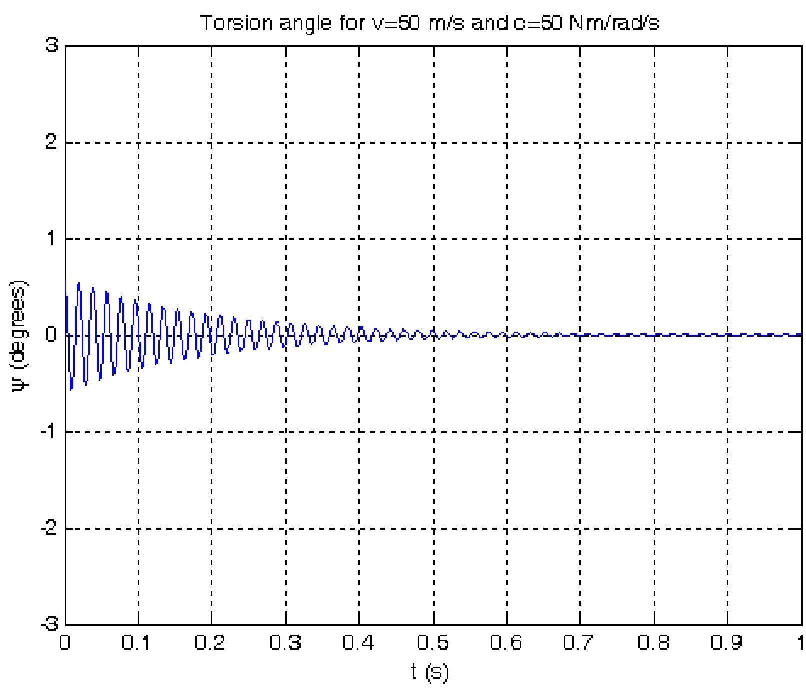

Figure 5.70: Torsion angle for v =50 m/s and c =50 Nm/rad/s.

A comparison of figures 5.68 and 5.70 reveals that increasing the velocity v increases the amplitude of the torsion angle.

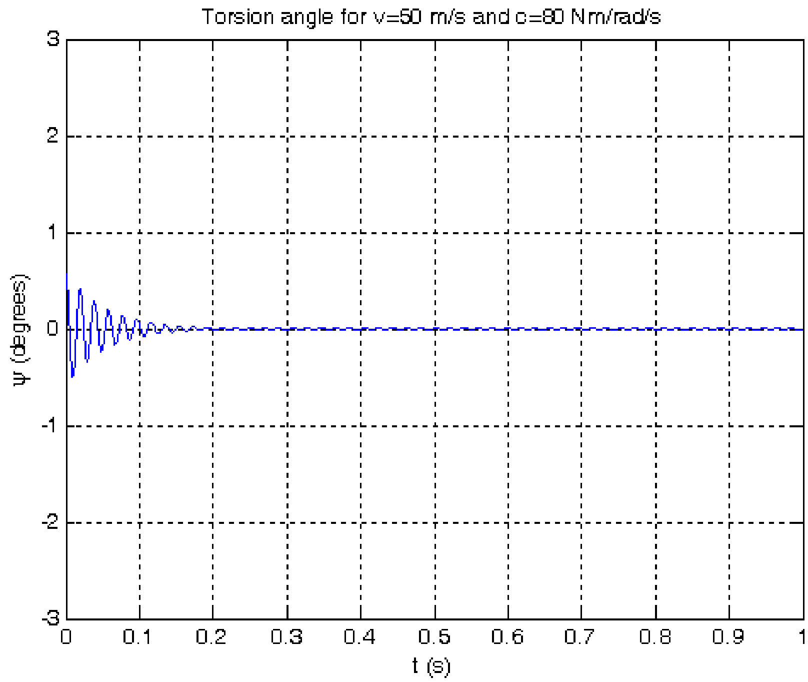

Figure 5.71: Torsion angle for $v = 50$ m/s and $c = 80$ Nm/rad/s.

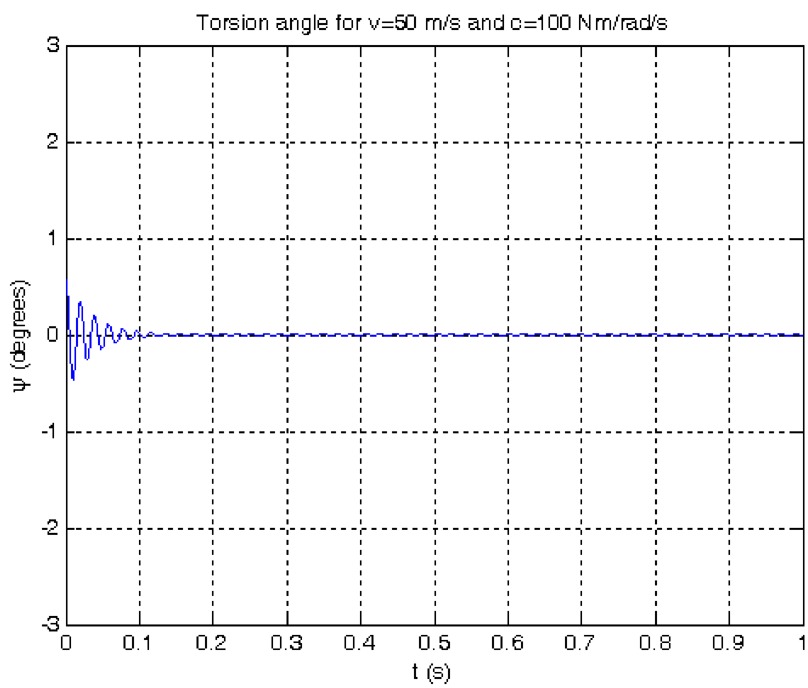

Figure 5.72: Torsion angle for $v = 50$ m/s and $c = 100$ Nm/rad/s.

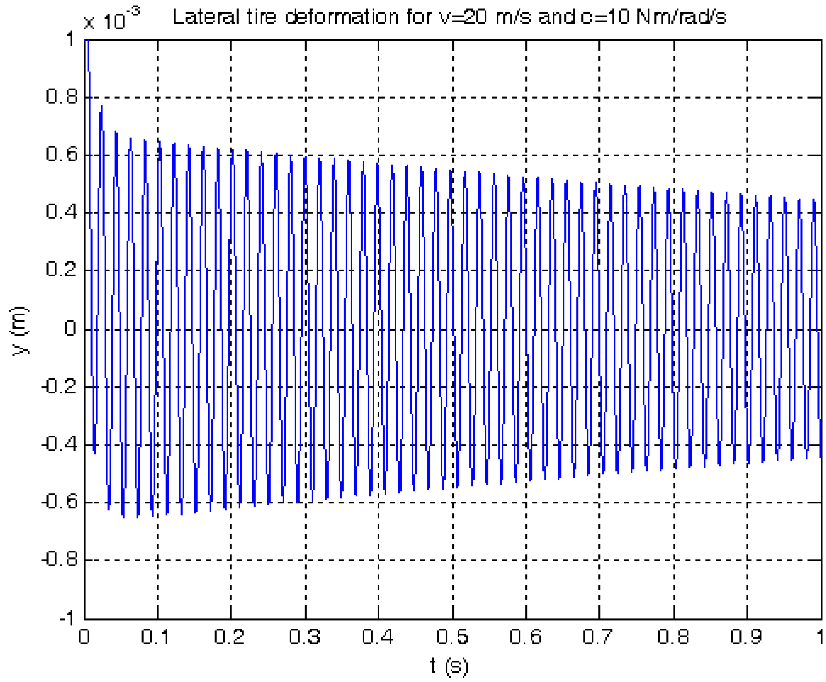

Figure 5.73: Lateral tire deformation for v =20 m/s and c =10 Nm/rad/s.

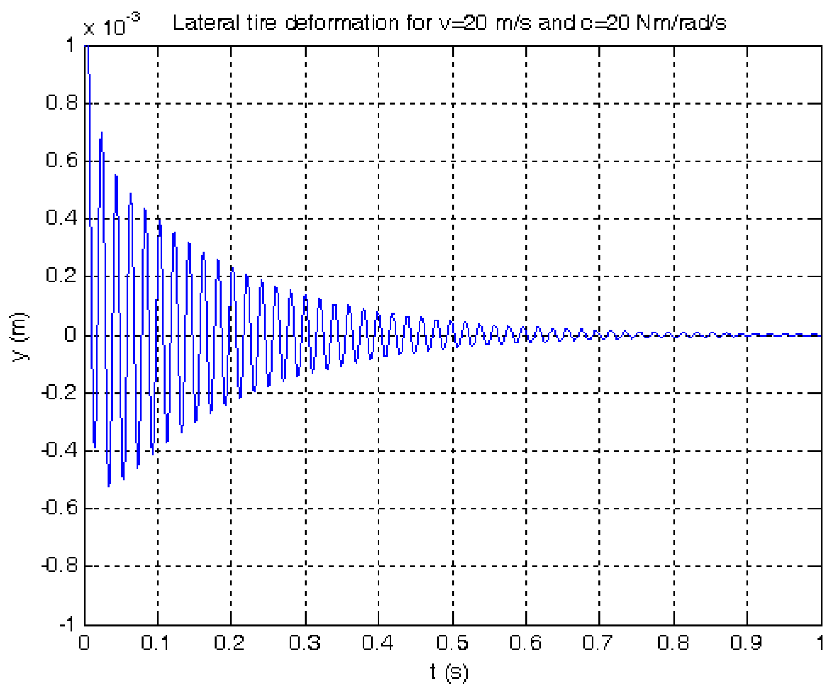

Figure 5.74: Lateral tire deformation for v =20 m/s and c =20 Nm/rad/s.

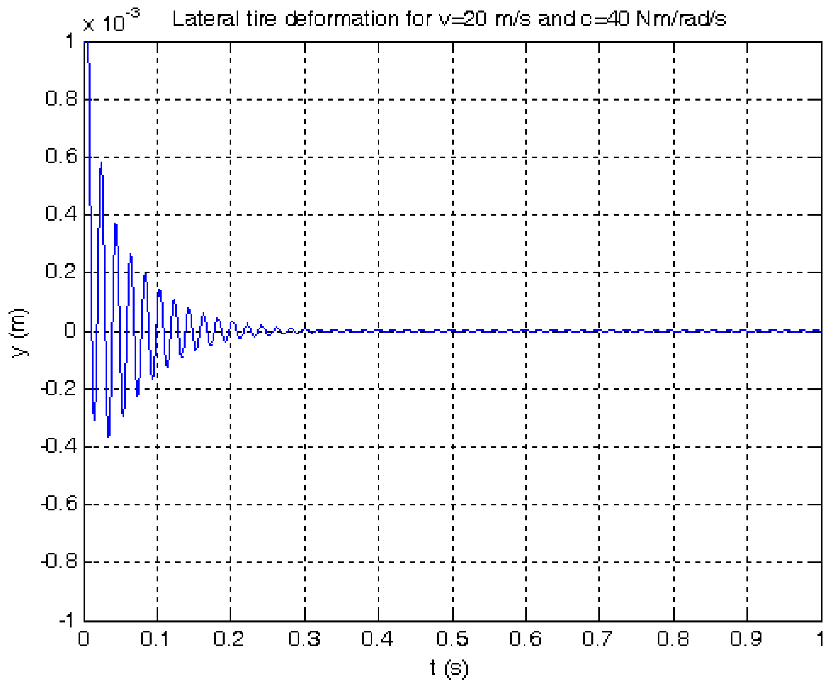

Figure 5.75: Lateral tire deformation for v =20 m/s and c =40 Nm/rad/s.

A comparison of figures 5.73–5.75 reveals that increasing the damping constant c decreases the amplitude of the lateral tire deformation.

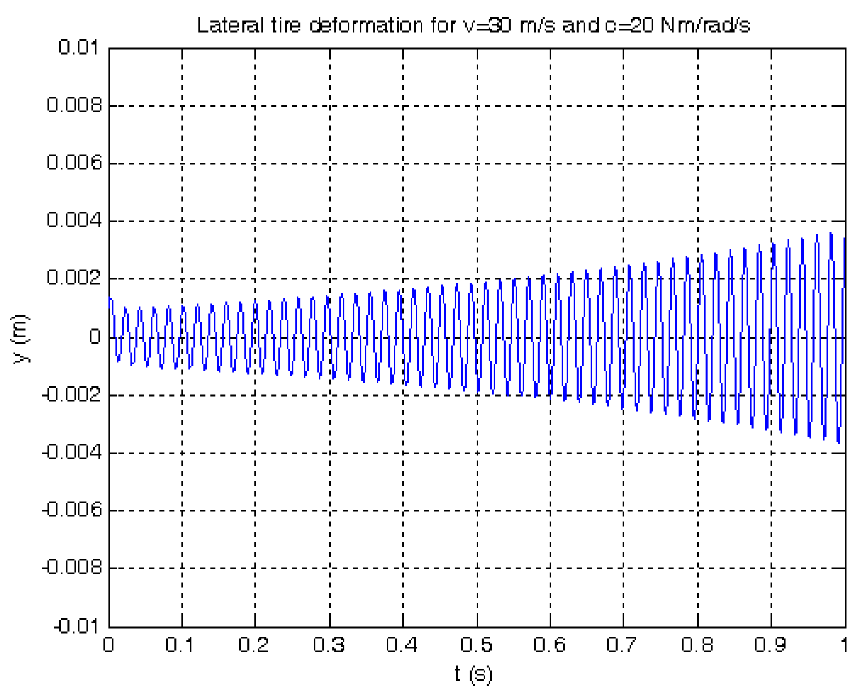

Figure 5.76: Lateral tire deformation for v =30 m/s and c =20 Nm/rad/s.

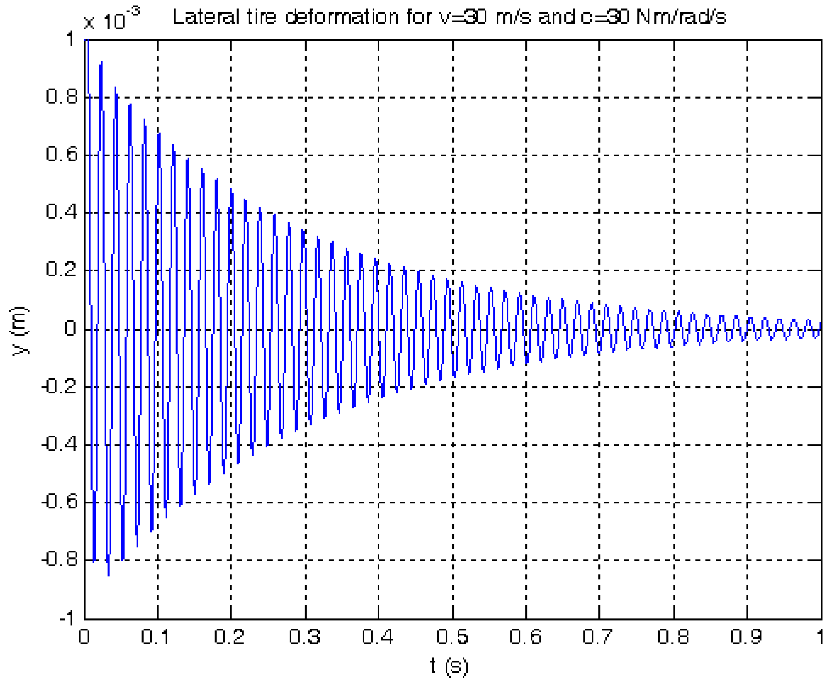

Figure 5.77: Lateral tire deformation for v =30 m/s and c =30 Nm/rad/s.

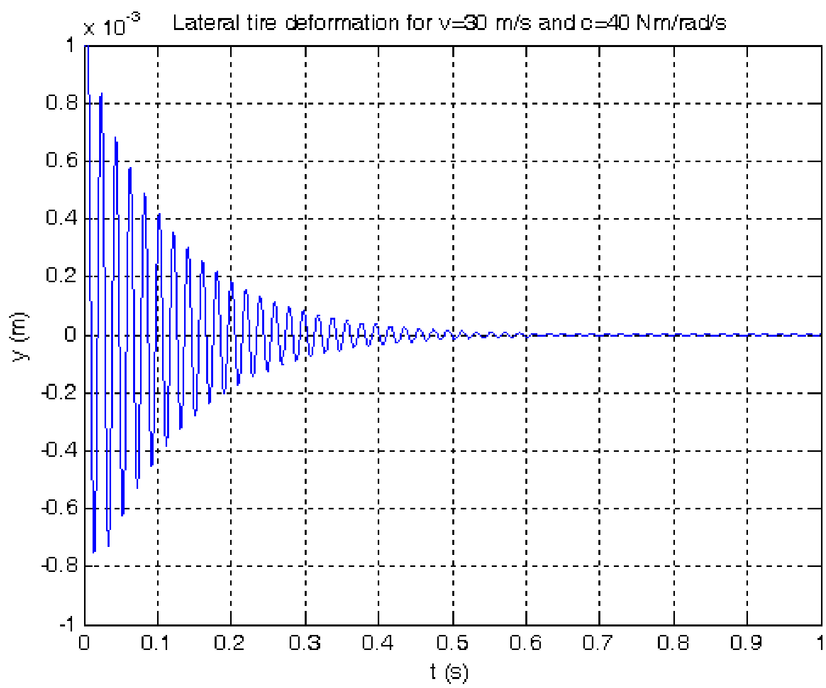

Figure 5.78: Lateral tire deformation for v =30 m/s and c =40 Nm/rad/s.

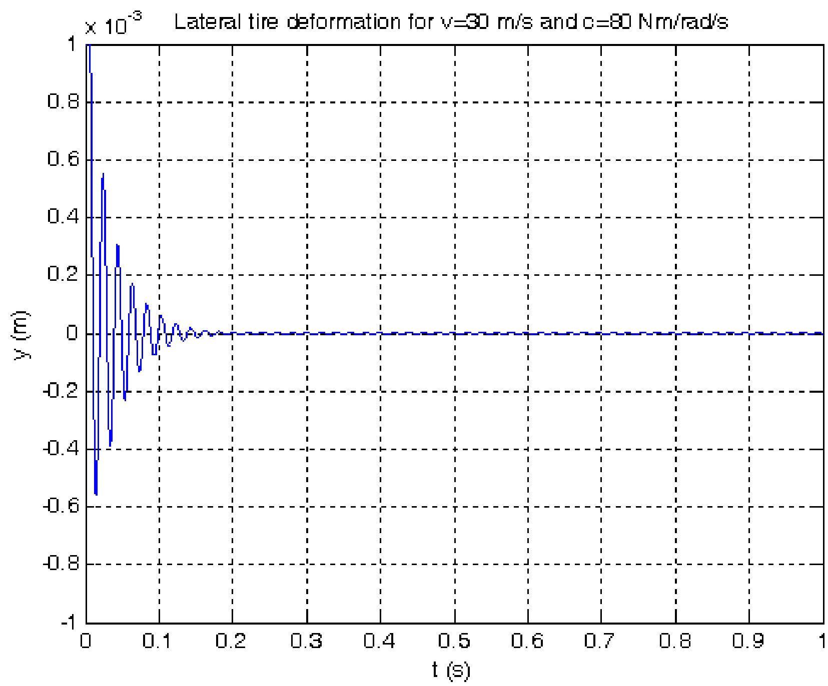

Figure 5.79: Lateral tire deformation for v =30 m/s and c =80 Nm/rad/s.

A comparison of figures 5.76–5.79 reveals that increasing the damping constant c decreases the amplitude of the lateral tire deformation.

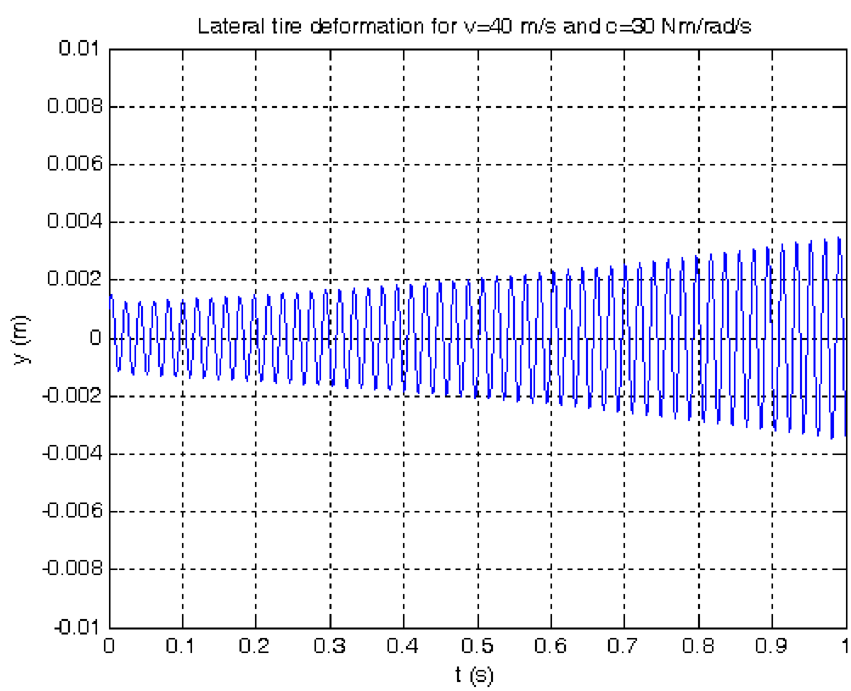

Figure 5.80: Lateral tire deformation for v =40 m/s and c =30 Nm/rad/s.

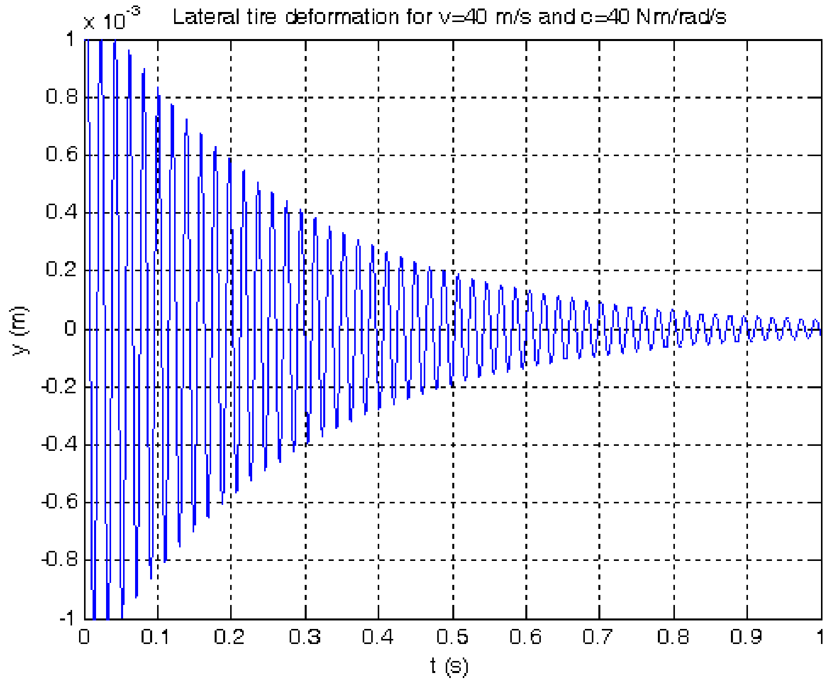

Figure 5.81: Lateral tire deformation for v =40 m/s and c =40 Nm/rad/s.

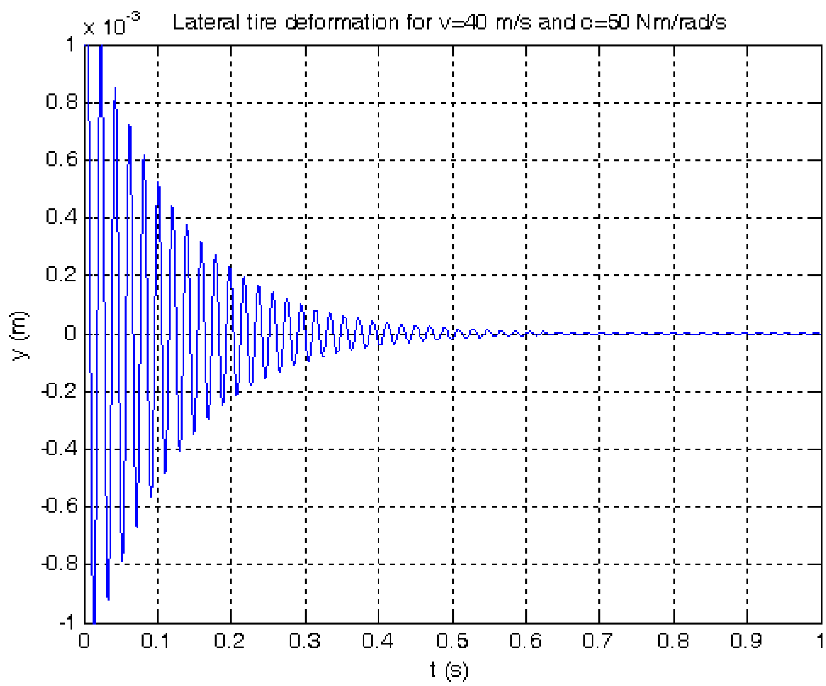

Figure 5.82: Lateral tire deformation for v =40 m/s and c =50 Nm/rad/s.

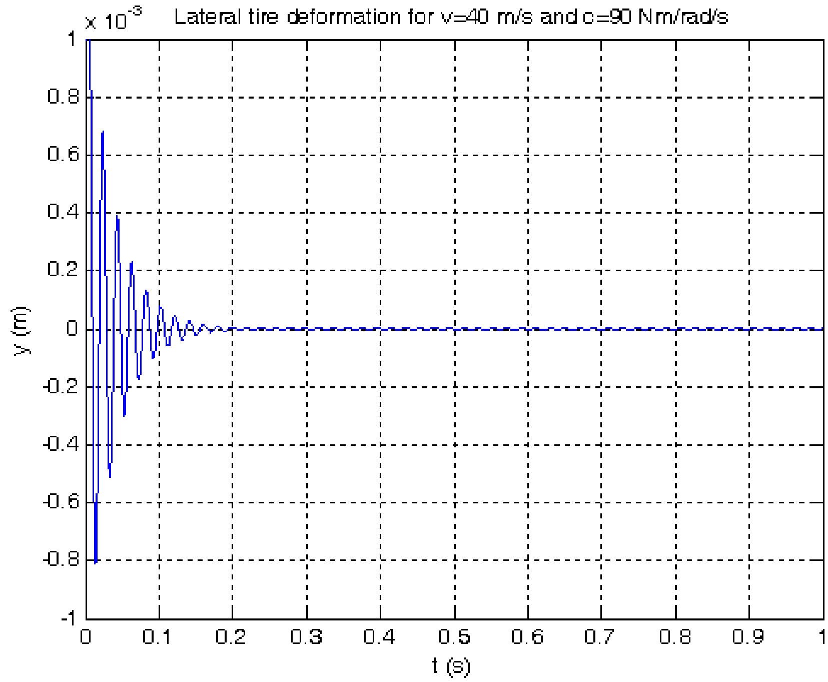

Figure 5.83: Lateral tire deformation for v =40 m/s and c =90 Nm/rad/s.

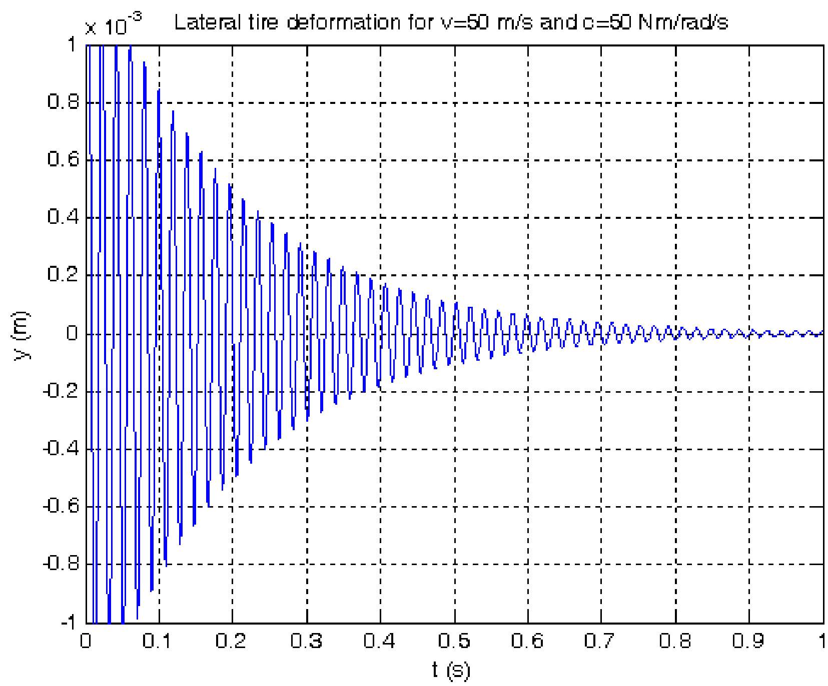

Figure 5.84: Lateral tire deformation for v =50 m/s and c =50 Nm/rad/s.

A comparison of figures 5.82 and 5.84 reveals that increasing the velocity v increases the amplitude of the lateral tire deformation.

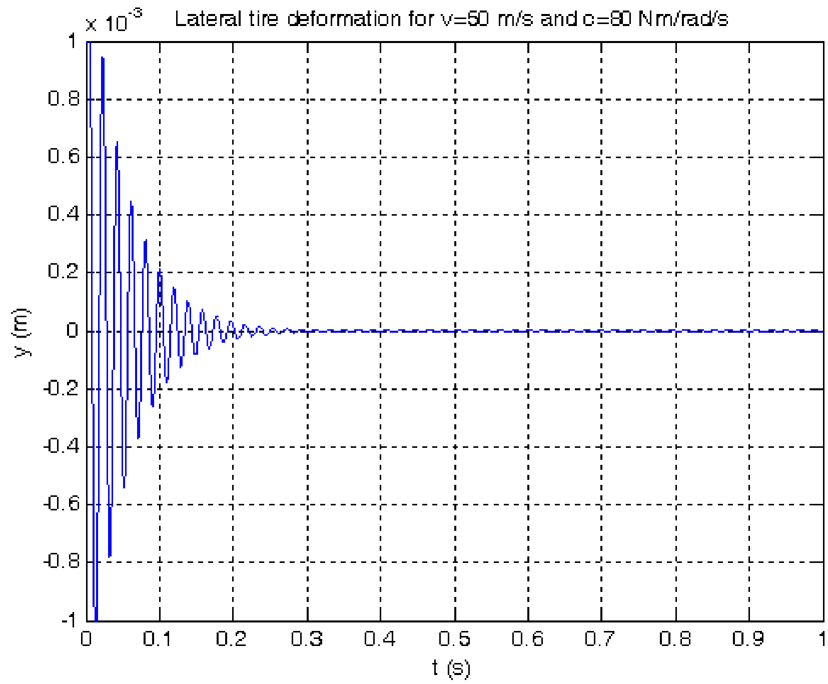

Figure 5.85: Lateral tire deformation for v =50 m/s and c =80 Nm/rad/s.

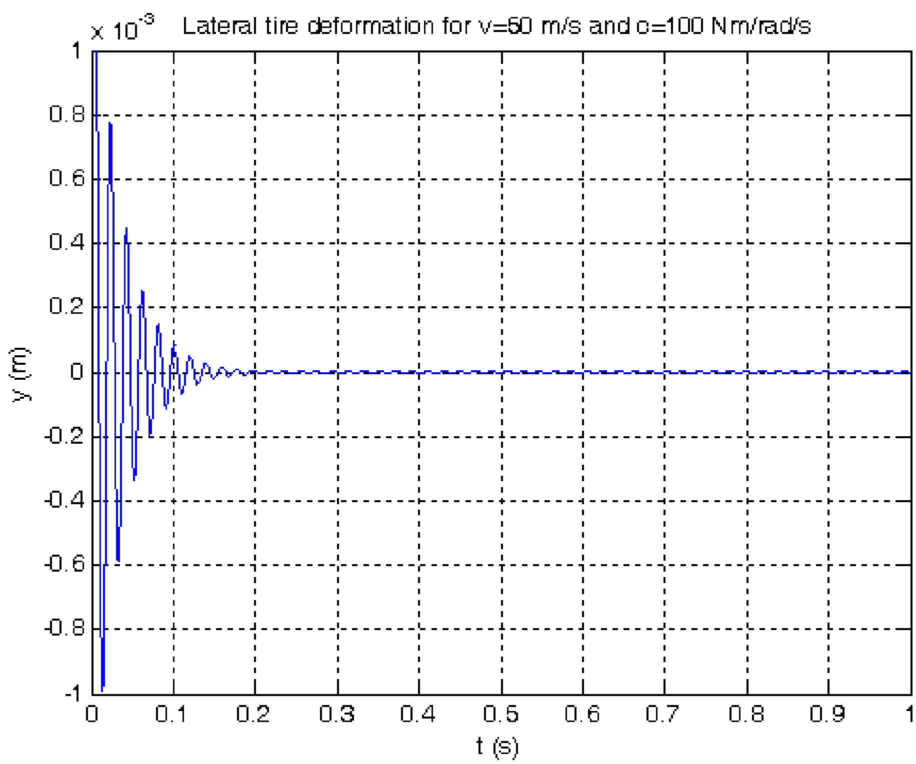

Figure 5.86: Lateral tire deformation for v =50 m/s and c =100 Nm/rad/s.

Table 5.7: Observations about the time histories of the torsion angle ψ and lateral tire deformation y.

	velocity v **(m/s)**	**torsional damping constant** c **(Nm/rad/s)**	**root mean square of the amplitude**	**qualitative description**
Torsion angle	20	10	0.0064	weak damping
	20	20	0.0024	oscillation is damped in 0.7 s
	20	40	0.0014	oscillation is damped in 0.2 s
	30	20	0.0173	amplitude grows
	30	30	0.0029	oscillation is almost damped in 1 s
	30	40	0.0019	oscillation is damped in 0.4 s
	30	80	0.0010	oscillation is damped in 0.1 s
	40	30	0.0141	amplitude grows
	40	40	0.0027	oscillation is almost damped in 1 s
	40	50	0.0018	oscillation is damped in 0.4 s
	40	90	0.0010	oscillation is damped in 0.1 s
	50	50	0.0023	oscillation is almost damped in 1 s
	50	80	0.0012	oscillation is damped in 0.2 s
	50	100	9.874×10^{-4}	oscillation is damped in 0.1 s
Lateral tire deformation	20	10	4.02×10^{-4}	weak damping
	20	20	1.717×10^{-4}	oscillation is almost damped in 1 s
	20	40	1.271×10^{-4}	oscillation is damped in 0.3 s
	30	20	0.0015	amplitude grows
	30	30	2.701×10^{-4}	oscillation is almost damped in 1 s
	30	40	1.867×10^{-4}	oscillation is damped in 0.5 s
	30	80	1.285×10^{-4}	oscillation is damped in 0.2 s

	40	30	0.0016	amplitude grows
	40	40	3.231×10^{-4}	oscillation is almost damped in 1 s
	40	50	2.223×10^{-4}	oscillation is damped in 0.6 s
	40	90	1.444×10^{-4}	oscillation is damped in 0.2 s
	50	50	3.182×10^{-4}	oscillation is almost damped in 1 s
	50	80	1.803×10^{-4}	oscillation is damped in 0.3 s
	50	100	1.570×10^{-4}	oscillation is damped in 0.2 s

5.8.2 Conclusions about the time histories of the torsion angle ψ and lateral tire deformation y

- Increasing the damping constant c gives better damping characteristics either by damping the oscillation that would not be damped with a lower damping constant or helps the oscillation be damped faster.
- Increasing the velocity v results in the requirement for a higher damping constant.
- Table 5.7 gives qualitative observations about the time histories of the torsion angle ψ and lateral tire deformation y in figures 5.59 – 5.86.
- It is observed from table 5.7 that there is a correlation between the oscillatory and damping characteristics of the torsion angle and that of the lateral tire deformation.

5.9 Nonlinear Model and Limit Cycles

5.9.1 Computation of limit cycles

Limit cycle oscillations are periodic oscillations of nonlinear systems and shimmy is a typical limit cycle phenomenon of a nonlinear system. Limit cycle phenomenon is presented in appendix B and van der Pol's equation, a system exhibiting limit cycles, is presented in appendix C.

Landing gear may exhibit limit cycle oscillations in the existence of nonlinearities. Nonlinearities found in landing gear systems are dry friction between sliding surfaces, nonlinear tire stiffness and damping and freeplay in the torsional degree of freedom. The model considered in this study accounts for nonlinear tire force and moments.

Kinetic energy of the forward motion of the aircraft is the source of the energy required for the self–excited shimmy oscillations. Such oscillations occur even when the aircraft is taxiing on the runway with little external disturbance. Unstable landing gear experience damage when such oscillations grow. In some cases, when the instability grows to some amplitude, oscillations are limited to remain within some response envelope. This kind of oscillations is named as limit cycle oscillations.

Dynamics of the nonlinear system in equations (5.1), (5.13) and (5.17) are integrated numerically using the Runge–Kutta algorithm.

In stable cases where high damping constants are involved, time histories of the nonlinear model are very similar to the linear ones, as figure 5.87 is very similar to figure 5.86. Figure 5.87 shows the lateral tire deformation y of the tire for the nonlinear system, while figure 5.86 shows the same time history for the linear system. Both have employed a high damping constant of 100 Nm/arad/s.

Limit cycles occur in unstable cases where a weak damping constant of 10 or 20 Nm/rad/s is employed. Limit cycles of the nonlinear model are computed numerically. Limit cycles for various velocities and damping constants are seen in figures 5.88–5.99. Approach direction of limit cycles varies with different initial conditions. It is seen that the limit cycle is approached from inside in figures 5.88–5.93 for a small initial condition such as $\psi(0)=0.01$ and from outside in figures 5.94–5.99 for a large initial condition such as $\psi(0)=1$.

Figures 5.88–5.93 show the 3 dimensional and 2 dimensional plots of limit cycle oscillations, $(\psi,\dot{\psi},t)$ and $(\psi,\dot{\psi})$, respectively, time histories of the torsion angle ψ and lateral tire deformation y for various velocities and damping coefficients for $\psi(0)=0.01$ and k =100000Nm/rad.

Figures 5.94–5.99 show the same plots for the same velocities and damping coefficients but for $\psi(0)=1$.

Table 5.8 gives limit cycle amplitudes of the torsion angle ψ, rate of change of the torsion angle $\dot{\psi}$ and lateral tire deformation y for $\psi(0) = 0.01$ and k =100000Nm/rad, while table 5.9 gives the same amplitudes for the same initial condition but for k =75000Nm/rad.

Table 5.10 gives limit cycle amplitudes of the torsion angle ψ, rate of change of the torsion angle $\dot{\psi}$ and lateral tire deformation y for $\psi(0) = 1$ and k =100000Nm/rad, while table 5.11 gives the same amplitudes for the same initial condition but for k =75000Nm/rad.

Same velocities and damping constants have been used in obtaining figures 88–99 and tables 5.8–5.11 so that correct comparisons can be made.

Plots have not been included for the lower spring constant k of 75000Nm/rad for purposes of saving space. It is seen that the possibility of shimmy increases with increasing velocity and vertical force and decreasing damping coefficients.

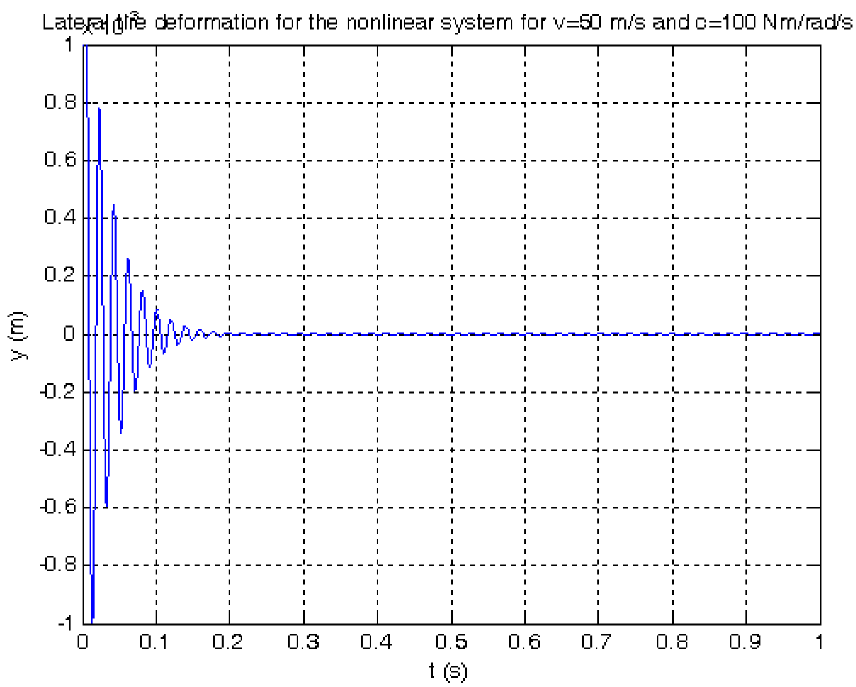

Figure 5.87: Lateral tire deformation in the nonlinear system for v =50 m/s and c =100 Nm/rad/s.

Figure 5.88 shows the 3 and 2 dimensional limit cycles and time histories of the torsion angle and tire deformation for v =30 m/s, c =10 Nm/rad/s and $\psi(0) = 0.01$.

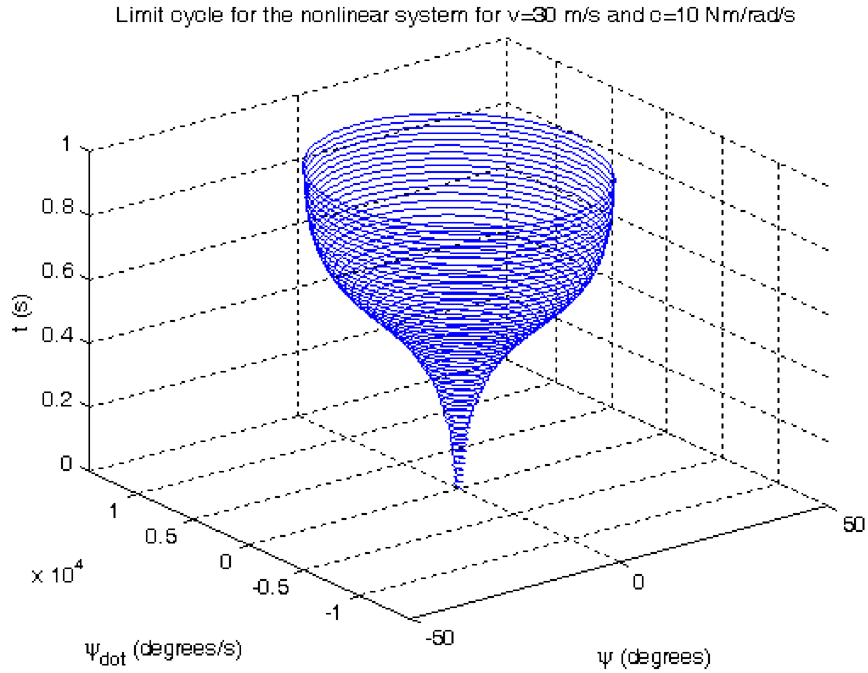

Figure 5.88: a. 3D limit cycle for v =30 m/s, c =10 Nm/rad/s and $\psi(0) = 0.01$.

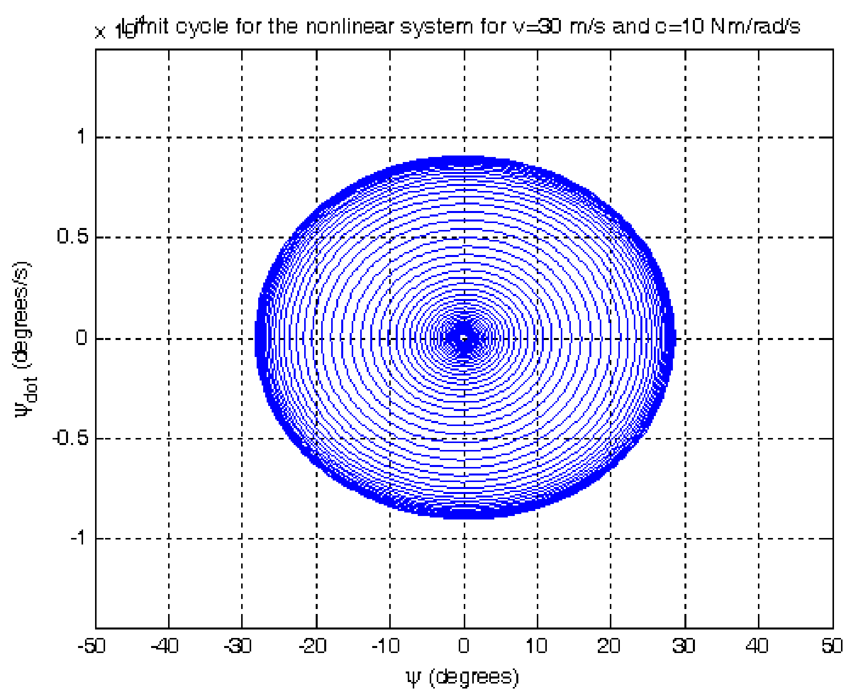

Figure 5.88:b. 2D limit cycle for v =30 m/s, c =10 Nm/rad/s and $\psi(0) = 0.01$.

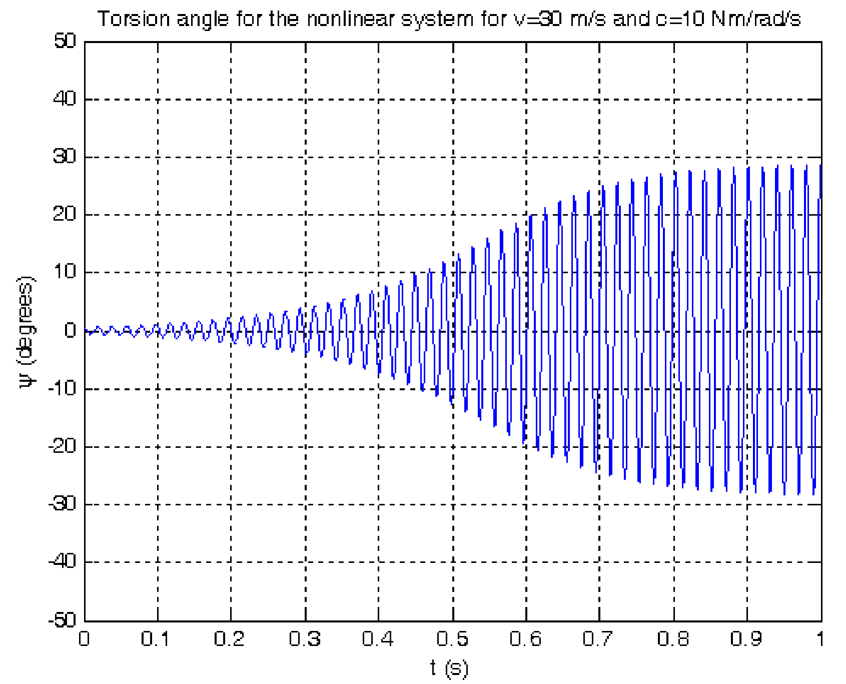

Figure 5.88: c. ψ for v =30 m/s, c =10 Nm/rad/s and $\psi(0) = 0.01$ (nonlinear model).

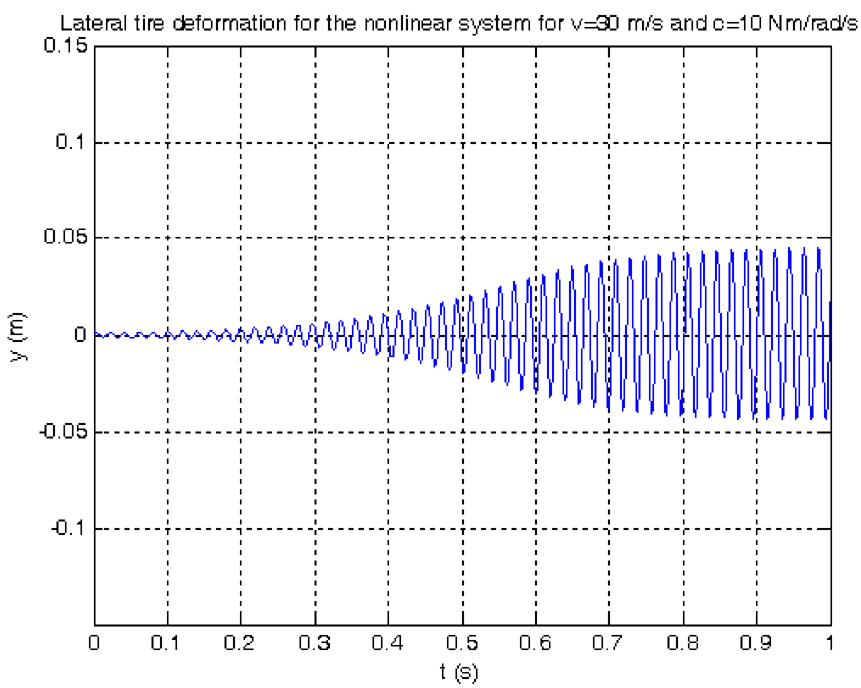

Figure 5.88: d. y for v =30 m/s, c =10 Nm/rad/s and $\psi(0) = 0.01$ (nonlinear model).

Figure 5.89 shows the 3 and 2 dimensional limit cycles and time histories of the torsion angle and tire deformation for v =40 m/s, c =10 Nm/rad/s and $\psi(0) = 0.01$.

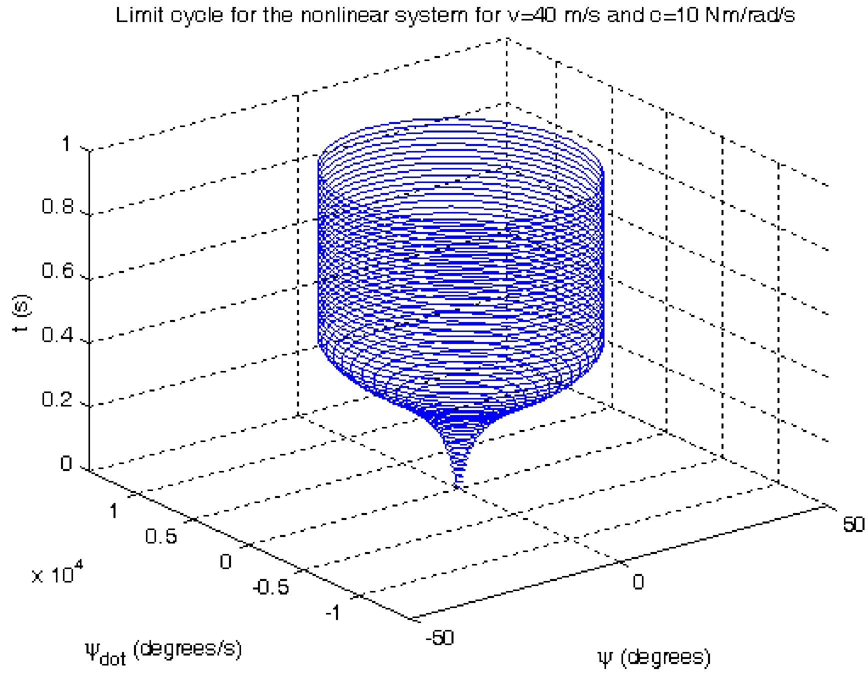

Figure 5.89: a. 3D limit cycle for v =40 m/s, c =10 Nm/rad/s and $\psi(0) = 0.01$.

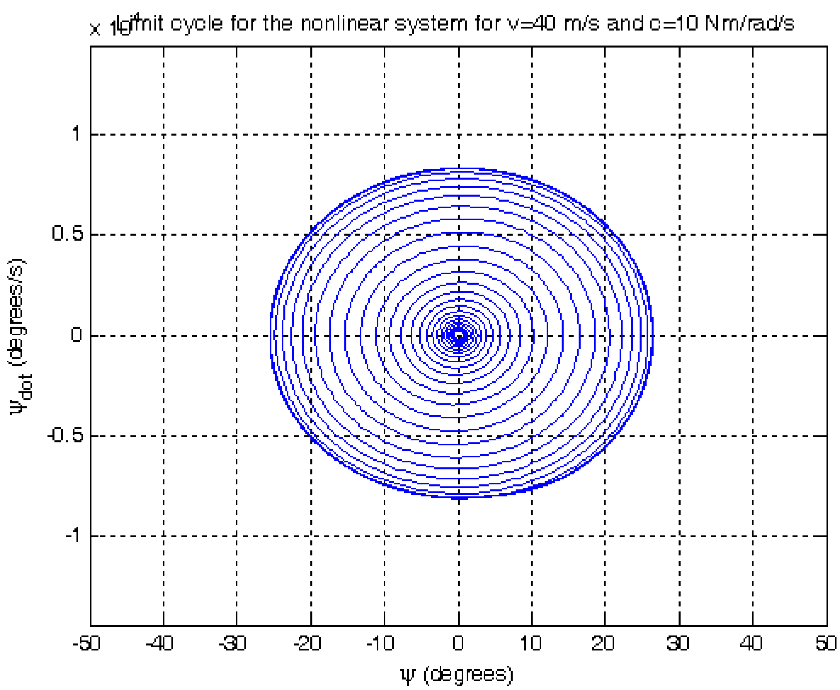

Figure 5.89: b. 2D limit cycle for v =40 m/s, c =10 Nm/rad/s and $\psi(0) = 0.01$.

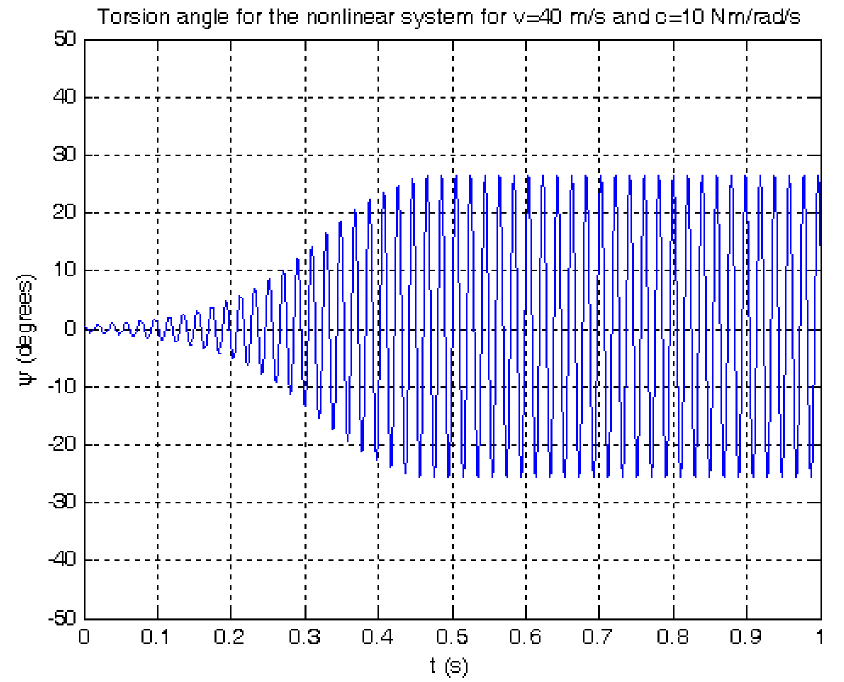

Figure 5.89: c. ψ for v =40 m/s, c =10 Nm/rad/s and $\psi(0) = 0.01$ (nonlinear model).

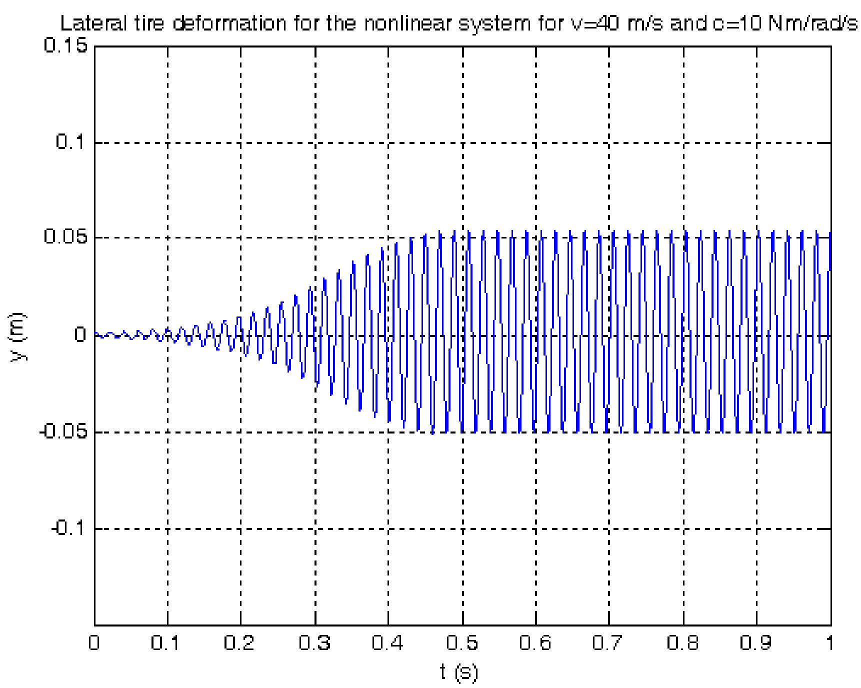

Figure 5.89: d. y for v =40 m/s, c =10 Nm/rad/s and $\psi(0) = 0.01$ (nonlinear model).

Figure 5.90 shows the 3 and 2 dimensional limit cycles and time histories of the torsion angle and tire deformation for v =50 m/s, c =10 Nm/rad/s and $\psi(0) = 0.01$.

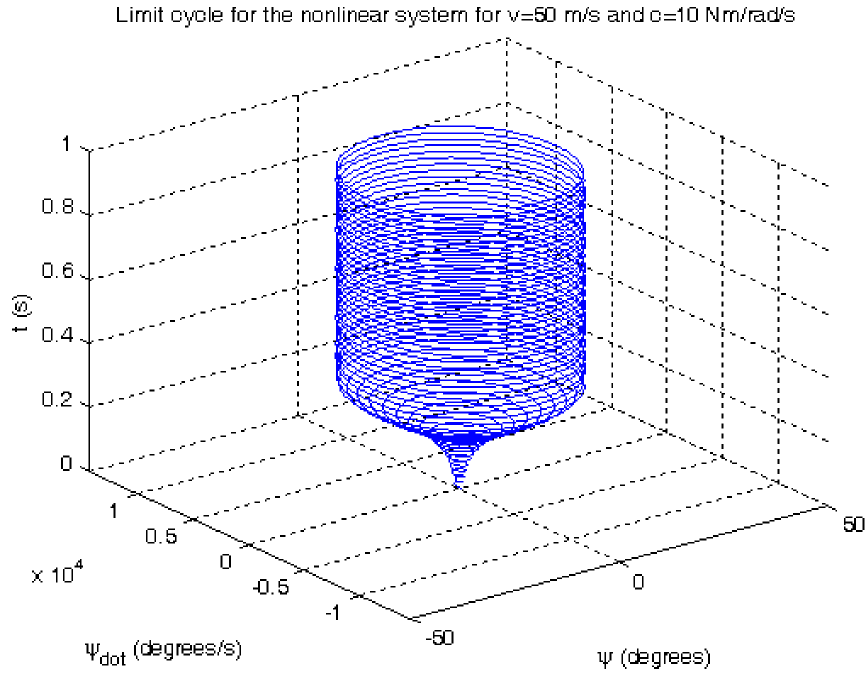

Figure 5.90: a. 3D limit cycle for $v = 50$ m/s, $c = 10$ Nm/rad/s and $\psi(0) = 0.01$.

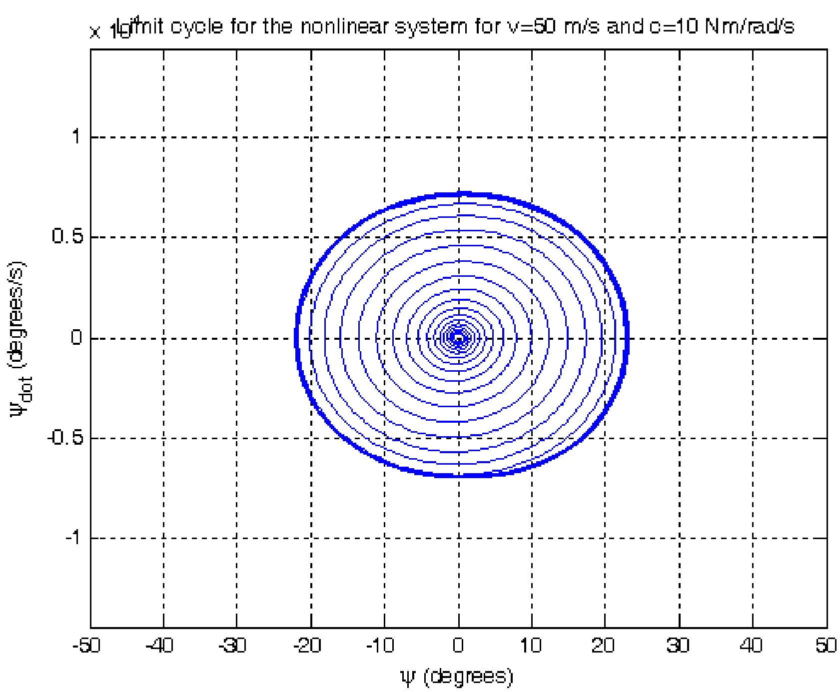

Figure 5.90: b. 2D limit cycle for $v = 50$ m/s, $c = 10$ Nm/rad/s and $\psi(0) = 0.01$.

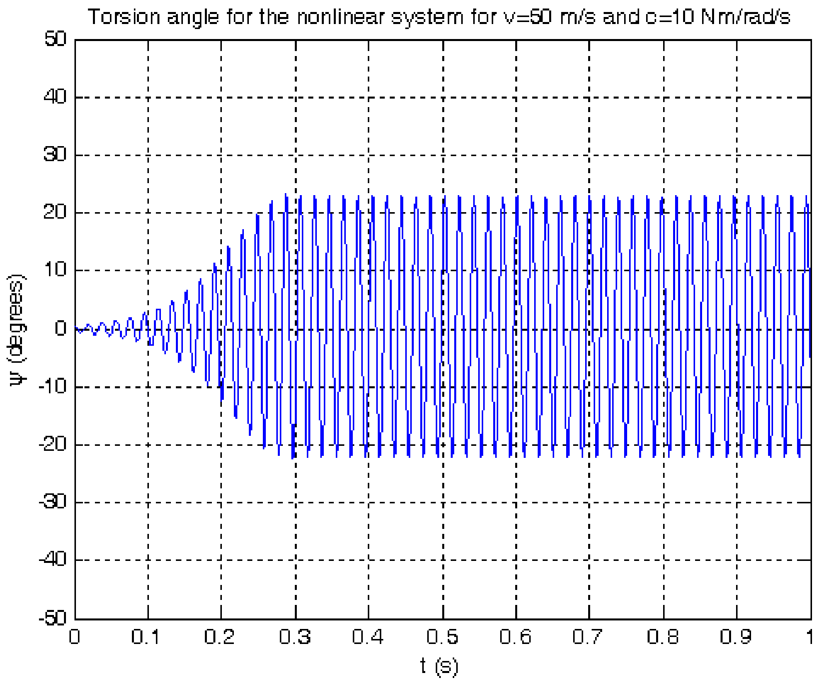

Figure 5.90: c. ψ for v =50 m/s, c =10 Nm/rad/s and $\psi(0) = 0.01$ (nonlinear model).

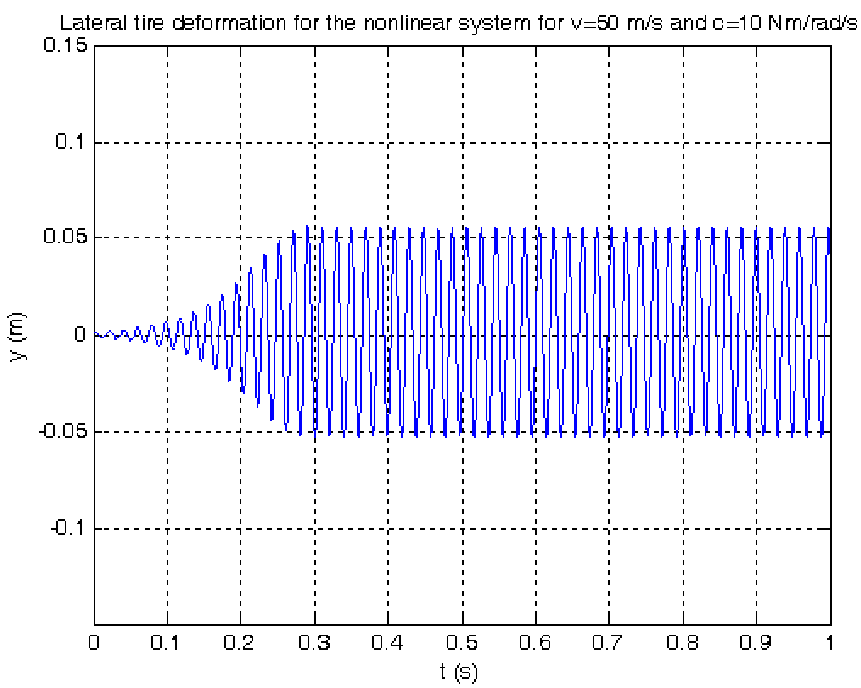

Figure 5.90: d. y for v =50 m/s, c =10 Nm/rad/s and $\psi(0) = 0.01$ (nonlinear model).

Figure 5.91 shows the 3 and 2 dimensional limit cycles and time histories of the torsion angle and tire deformation for v =50 m/s, c =20 Nm/rad/s and $\psi(0) = 0.01$.

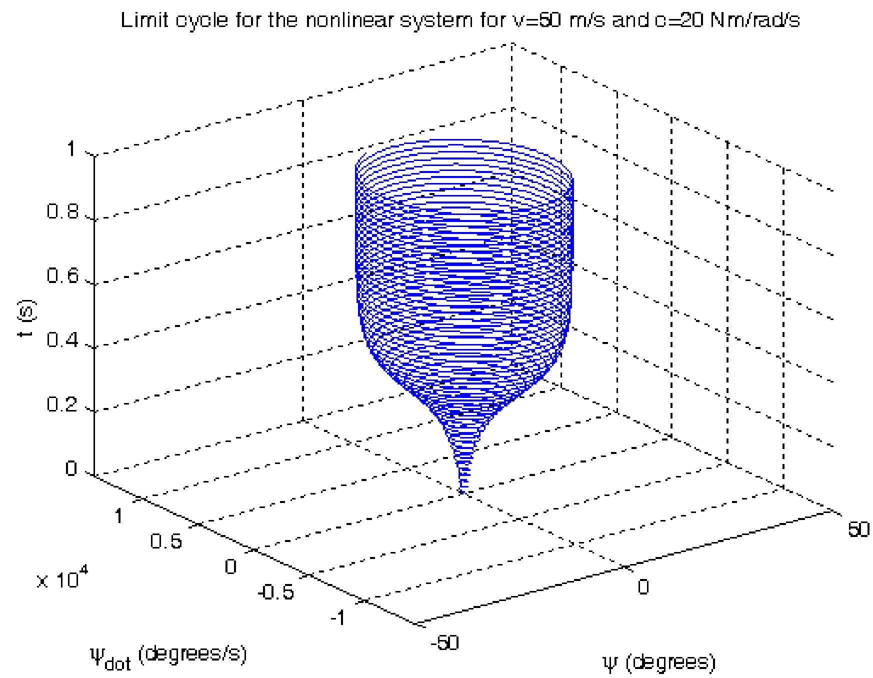

Figure 5.91: a. 3D limit cycle for v =50 m/s, c =20 Nm/rad/s and $\psi(0) = 0.01$.

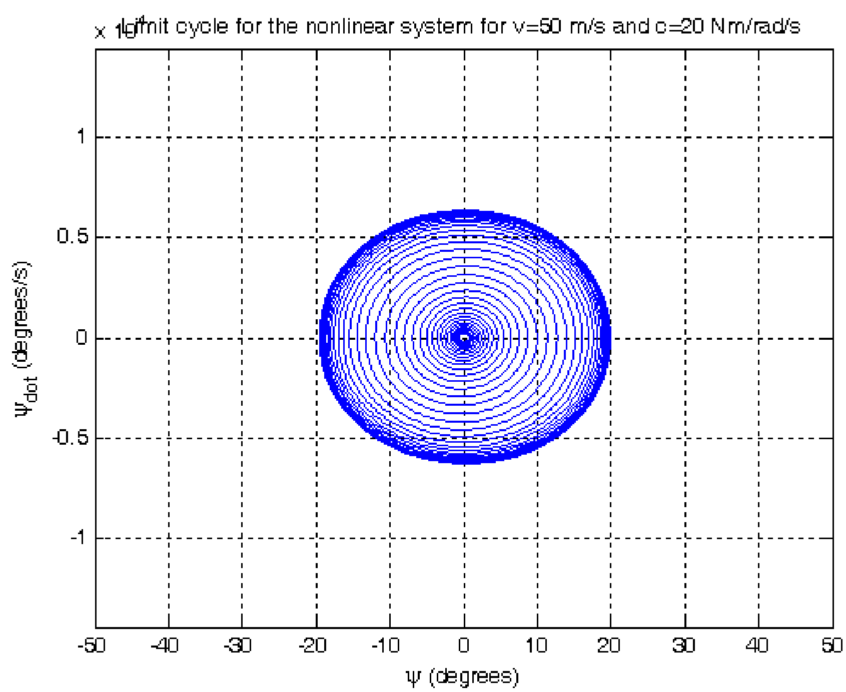

Figure 5.91: b. 2D limit cycle for v =50 m/s, c =20 Nm/rad/s and $\psi(0) = 0.01$.

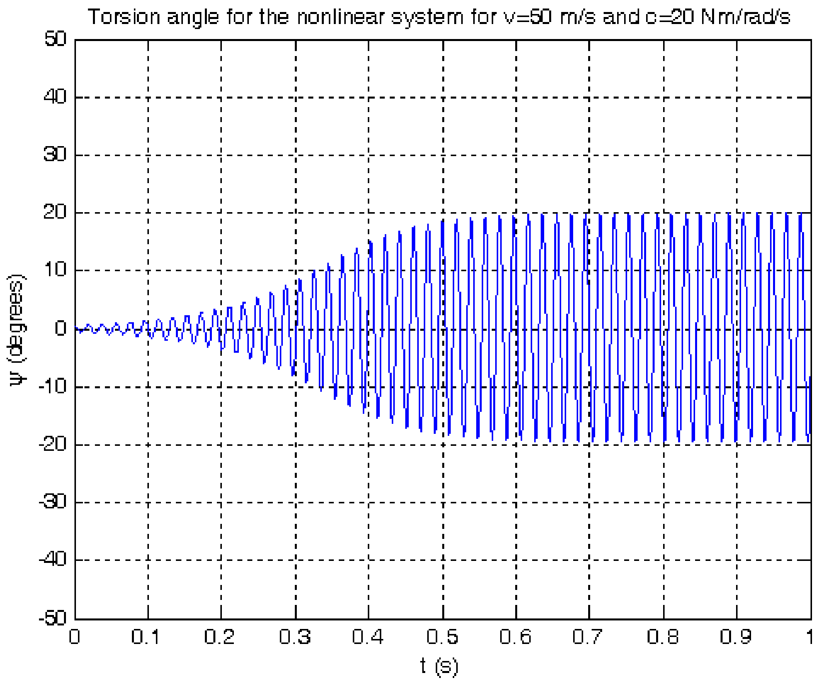

Figure 5.91: c. ψ for v =50 m/s, c =20 Nm/rad/s and $\psi(0)=0.01$ (nonlinear model).

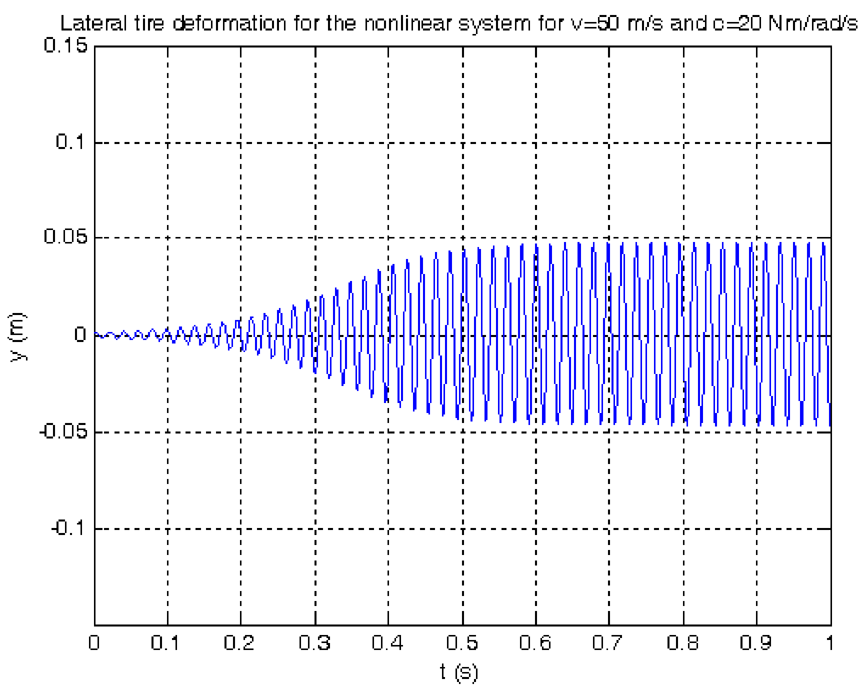

Figure 5.91: d. y for v =50 m/s, c =20 Nm/rad/s and $\psi(0)=0.01$ (nonlinear model).

Figure 5.92 shows the 3 and 2 dimensional limit cycles and time histories of the torsion angle and tire deformation for v =70 m/s, c =20 Nm/rad/s and $\psi(0)=0.01$.

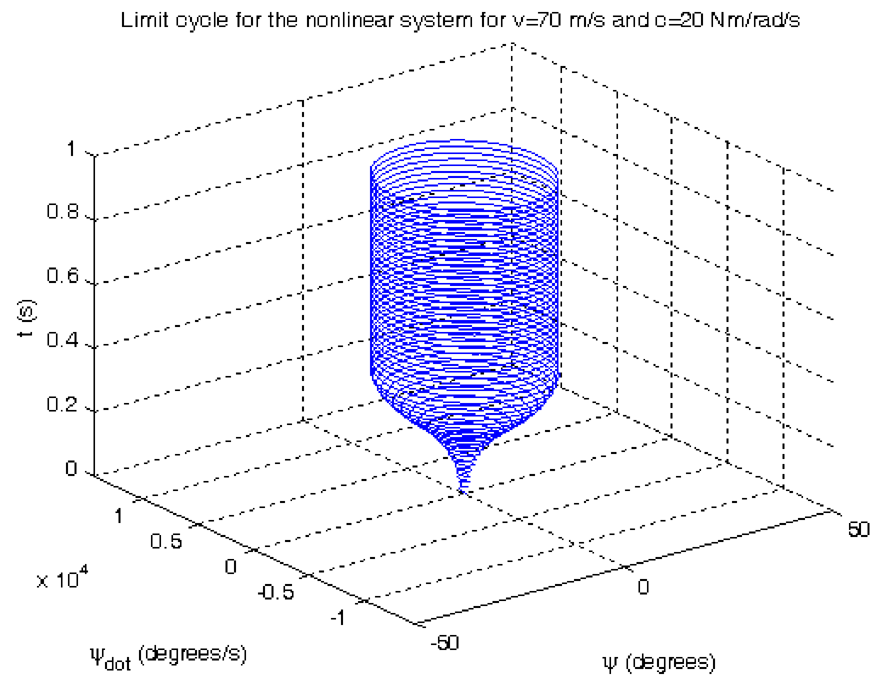

Figure 5.92: a. 3D limit cycle for v =70 m/s, c =20 Nm/rad/s and $\psi(0) = 0.01$.

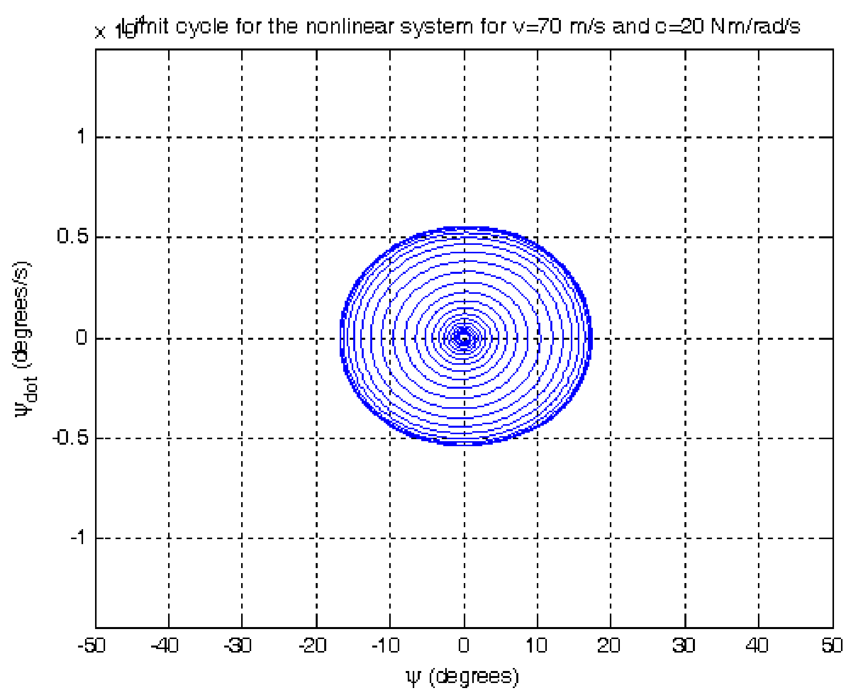

Figure 5.92: b. 2D limit cycle for v =70 m/s, c =20 Nm/rad/s and $\psi(0) = 0.01$.

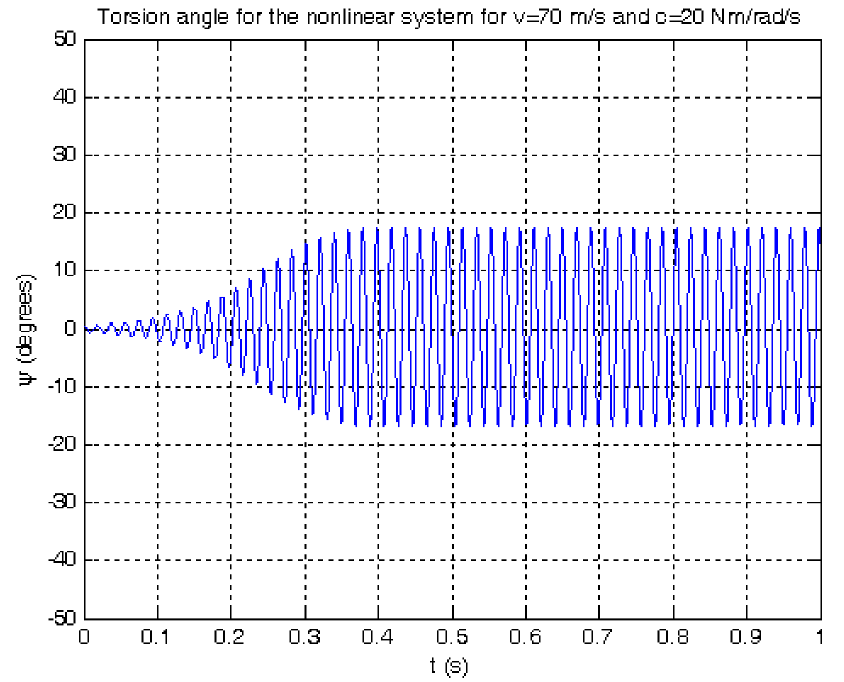

Figure 5.92: c. ψ for v =70 m/s, c =20 Nm/rad/s and $\psi(0) = 0.01$ (nonlinear model).

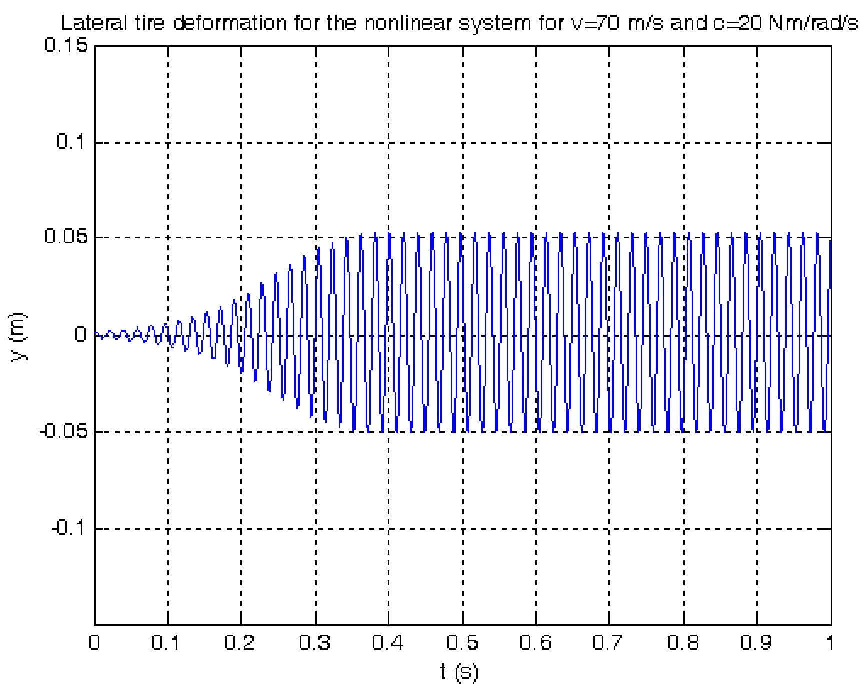

Figure 5.92: d. y for v =70 m/s, c =20 Nm/rad/s and $\psi(0) = 0.01$ (nonlinear model).

Figure 5.93 shows the 3 and 2 dimensional limit cycles and time histories of the torsion angle and tire deformation for v =100 m/s, c =20 Nm/rad/s and $\psi(0) = 0.01$.

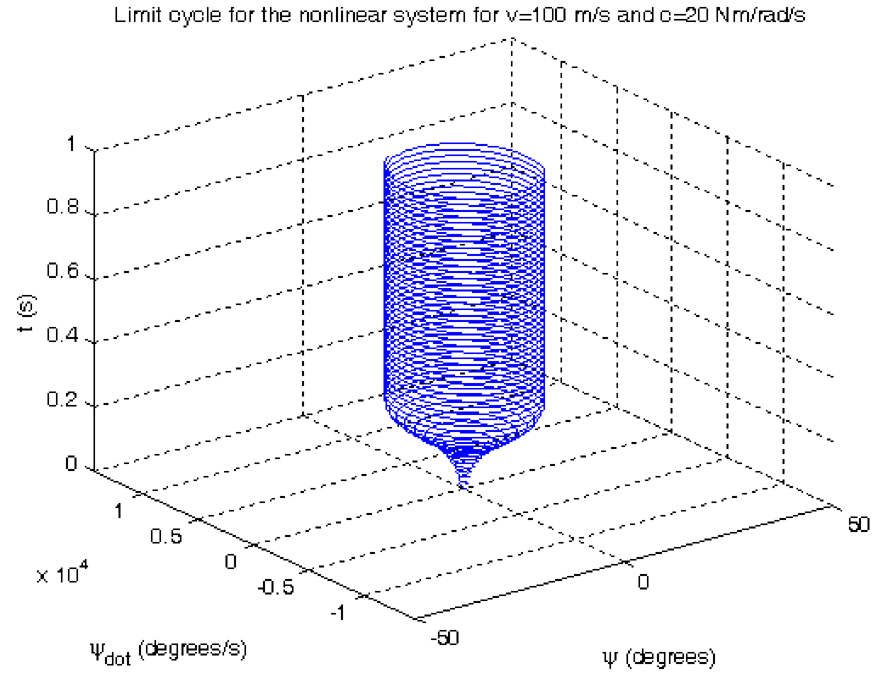

Figure 5.93: a. 3D limit cycle for v =100 m/s, c =20 Nm/rad/s and $\psi(0) = 0.01$.

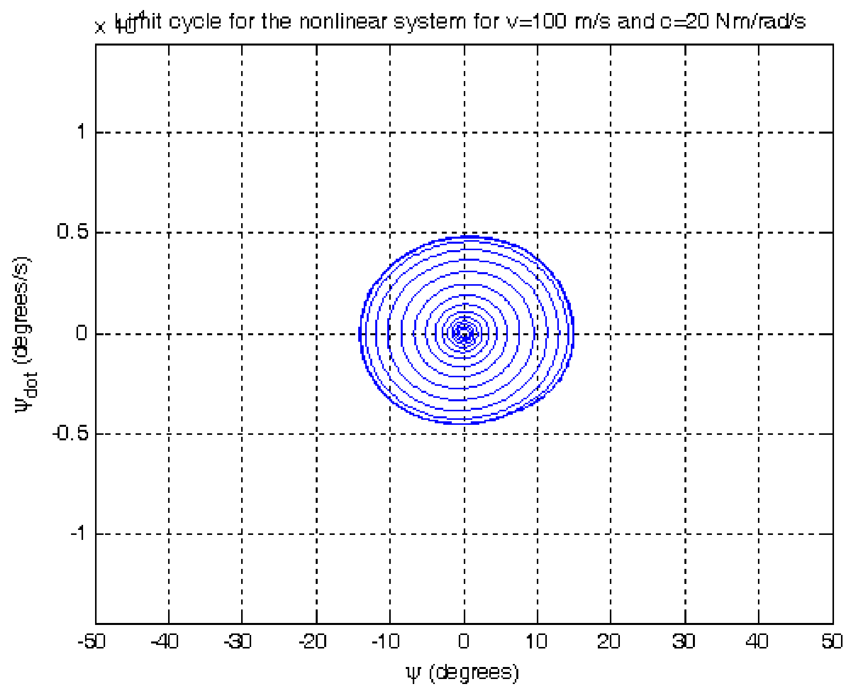

Figure 5.93: b. 2D limit cycle for v =100 m/s, c =20 Nm/rad/s and $\psi(0) = 0.01$.

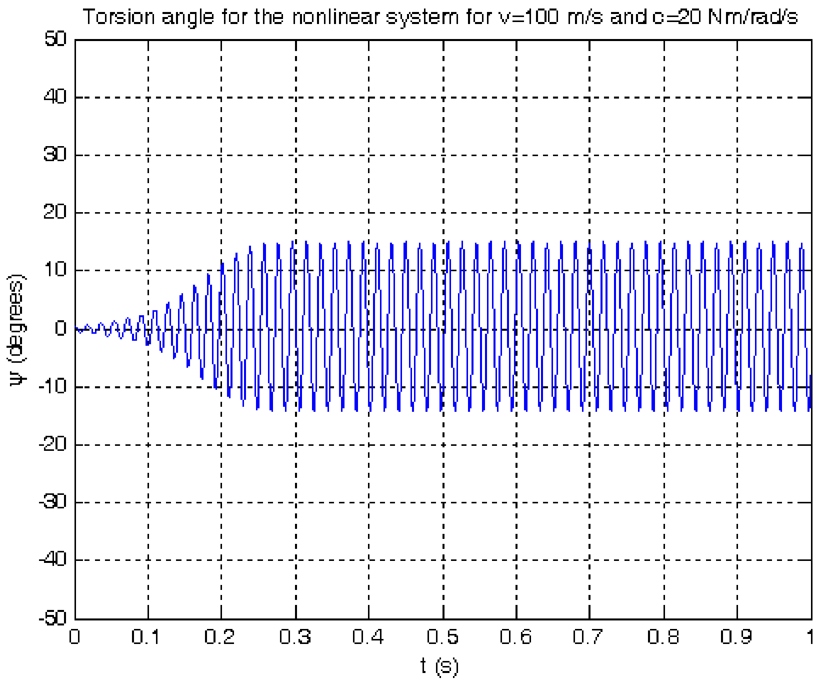

Figure 5.93: c. ψ for v =100 m/s, c =20 Nm/rad/s and $\psi(0) = 0.01$ (nonlinear model)

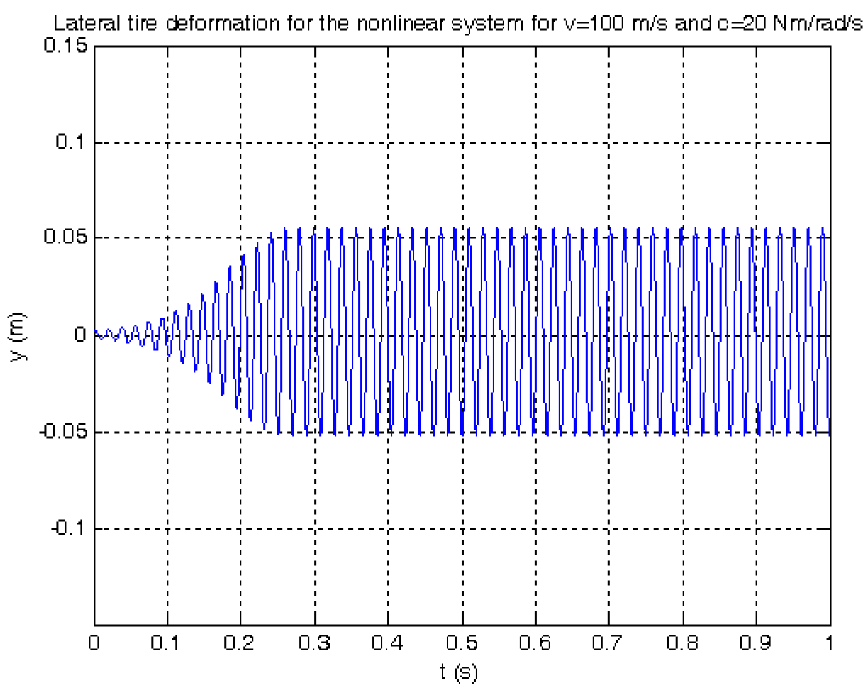

Figure 5.93: d. y for v =100 m/s, c =20 Nm/rad/s and $\psi(0) = 0.01$ (nonlinear model).

Table 5.8: Limit cycle amplitudes of the torsion angle ψ **,** rate of change of the torsion angle $\dot{\psi}$ and lateral tire deformation y for $\psi(0) = 0.01$ and k =100000Nm/rad.

Velocity v **(m/s)**	**Torsional damping constant** c **(Nm/rad/s)**	**Torsion angle** ψ **(degrees)**	$\dot{\psi}$ **(degrees/s)**	**Lateral tire deformation** y **(m)**
		amplitude	**amplitude**	**amplitude**
30	10	28.59	9045.9	0.045
40	10	26.43	8301.3	0.054
50	10	23.19	7250.9	0.056
50	20	19.88	6333.9	0.047
70	20	17.38	5544.6	0.053
100	20	14.50	4680.7	0.054

Table 5.9: Limit cycle amplitudes of the torsion angle ψ **,** rate of change of the torsion angle $\dot{\psi}$ and lateral tire deformation y for $\psi(0) = 0.01$ and k =75000Nm/rad.

Velocity v **(m/s)**	**Torsional damping constant** c **(Nm/rad/s)**	**Torsion angle** ψ **(degrees)**	$\dot{\psi}$ **(degrees/s)**	**Lateral tire deformation** y **(m)**
		amplitude	**amplitude**	**amplitude**
30	10	29.43	8016.7	0.052
40	10	25.13	6783.5	0.057
50	10	21.14	5681.9	0.057
50	20	19.94	5485.2	0.053
70	20	16.60	4594.4	0.055
100	20	14.22	4020.8	0.056

Figure 5.94 shows the 3 and 2 dimensional limit cycles and time histories of the torsion angle and tire deformation for v =30 m/s, c =10 Nm/rad/s and $\psi(0) = 1$.

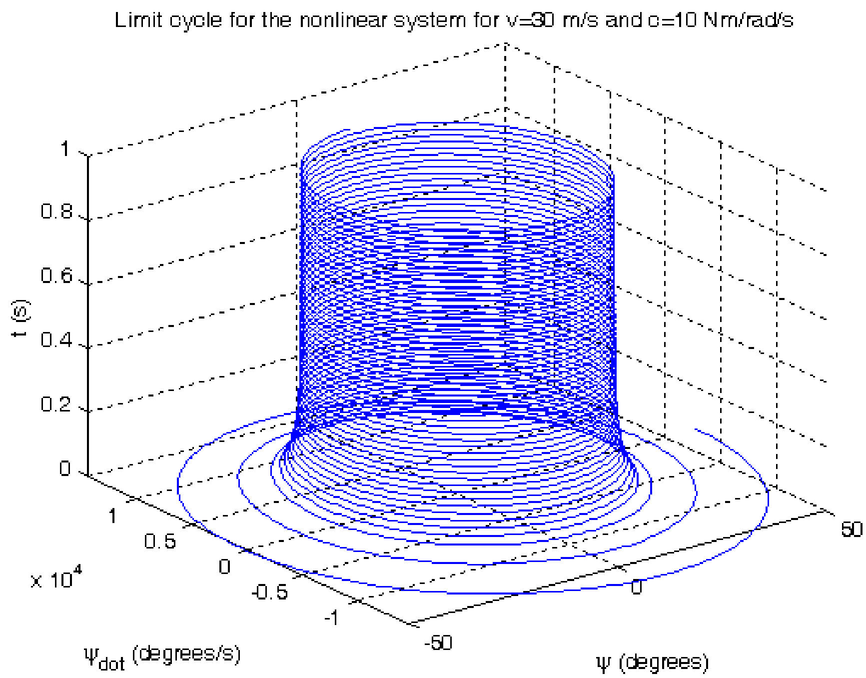

Figure 5.94: a. 3D limit cycle for v =30 m/s, c =10 Nm/rad/s and $\psi(0)=1$.

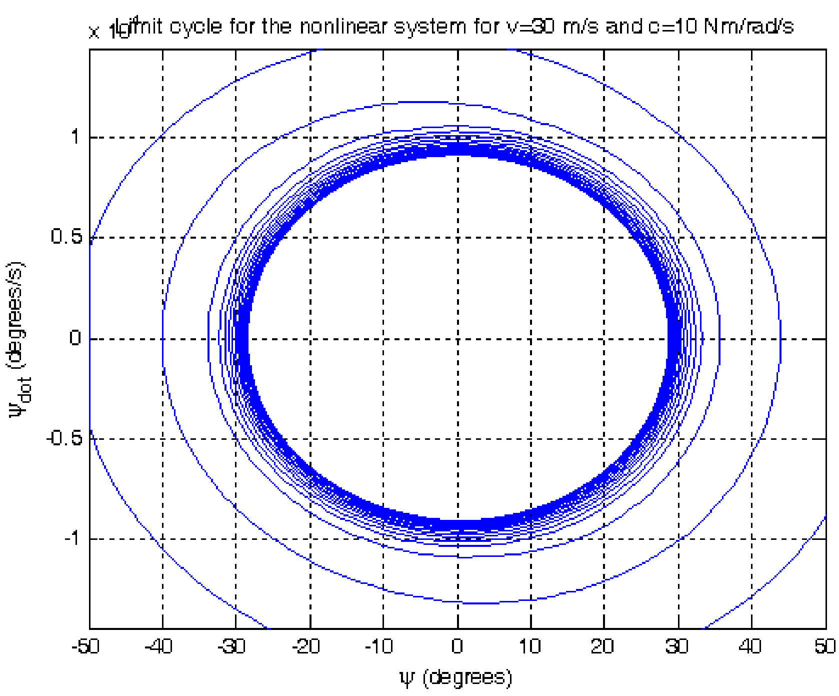

Figure 5.94: b. 2D limit cycle for v =30 m/s, c =10 Nm/rad/s and $\psi(0)=1$.

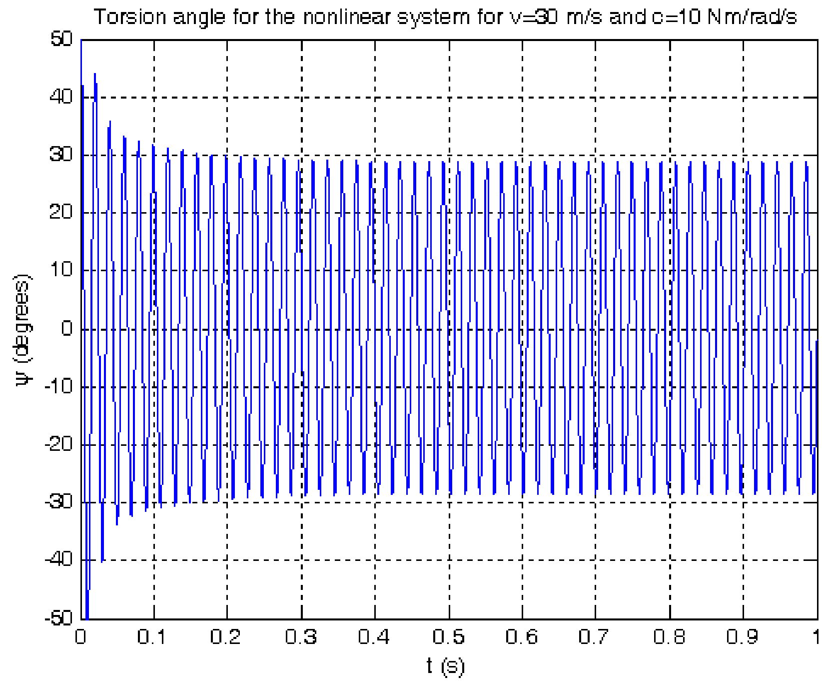

Figure 5.94: c. ψ for v =30 m/s, c =10 Nm/rad/s and $\psi(0)=1$ (nonlinear model).

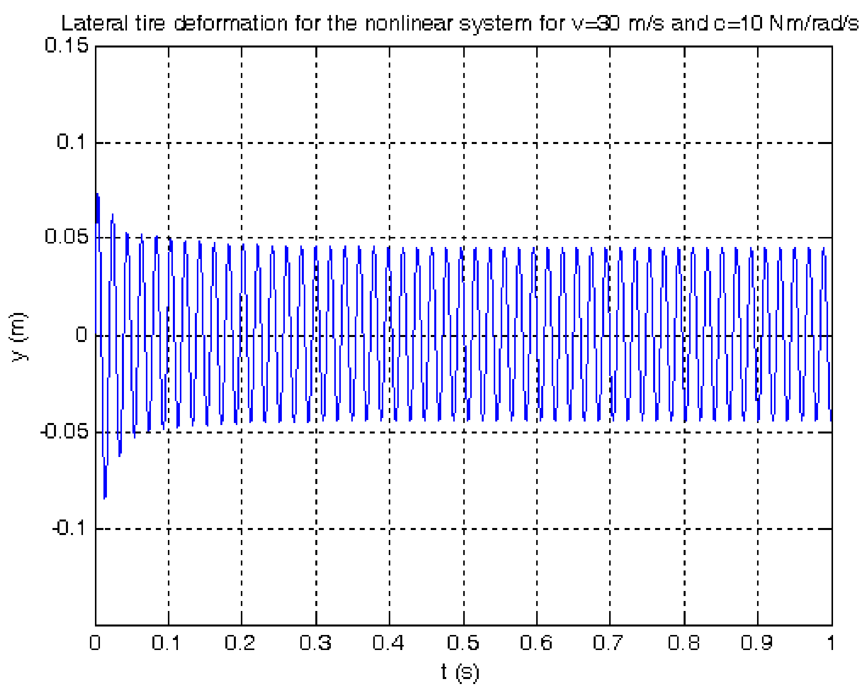

Figure 5.94: d. y for v =30 m/s, c =10 Nm/rad/s and $\psi(0)=1$ (nonlinear model).

Figure 5.95 shows the 3 and 2 dimensional limit cycles and time histories of the torsion angle and tire deformation for v =40 m/s, c =10 Nm/rad/s and $\psi(0)=1$.

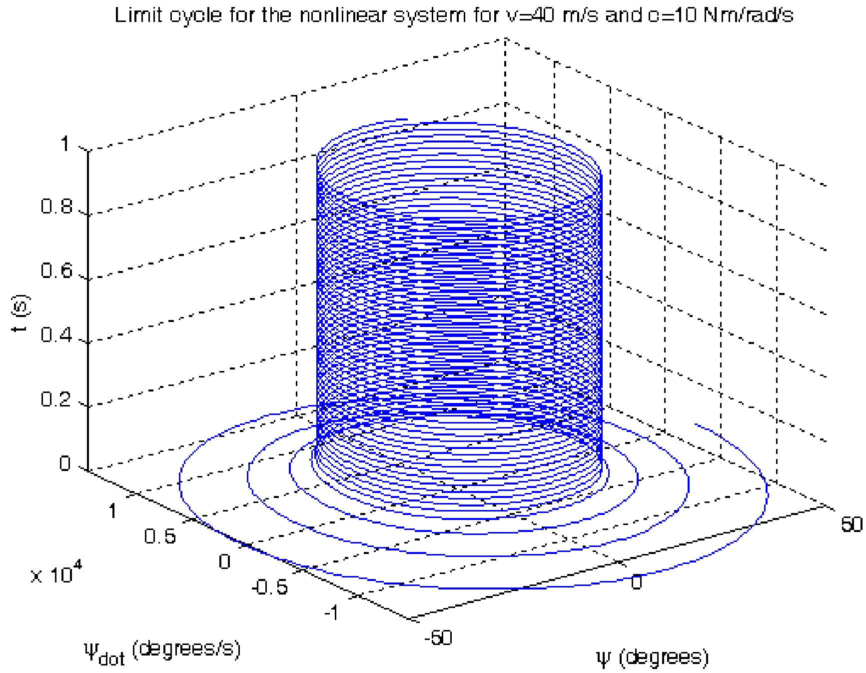

Figure 5.95: a. 3D limit cycle for v =40 m/s, c =10 Nm/rad/s and $\psi(0)=1$.

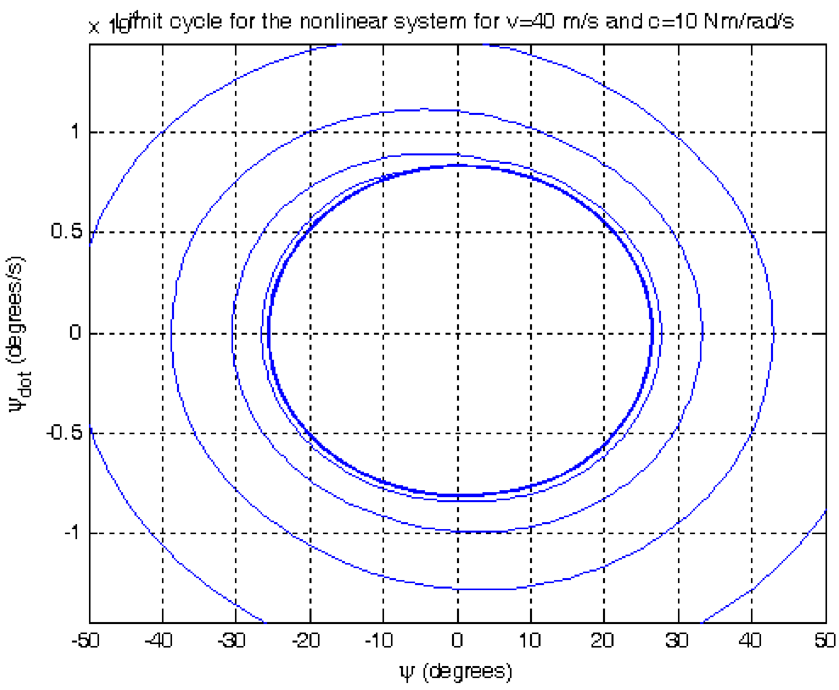

Figure 5.95: b. 2D limit cycle for v =40 m/s, c =10 Nm/rad/s and $\psi(0)=1$.

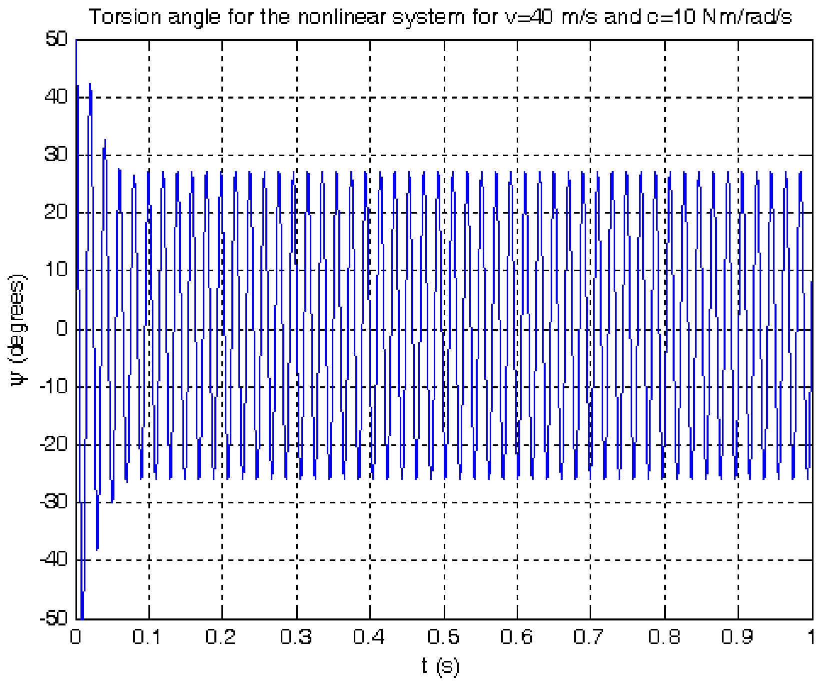

Figure 5.95: c. ψ for v =40 m/s, c =10 Nm/rad/s and $\psi(0)=1$ (nonlinear model).

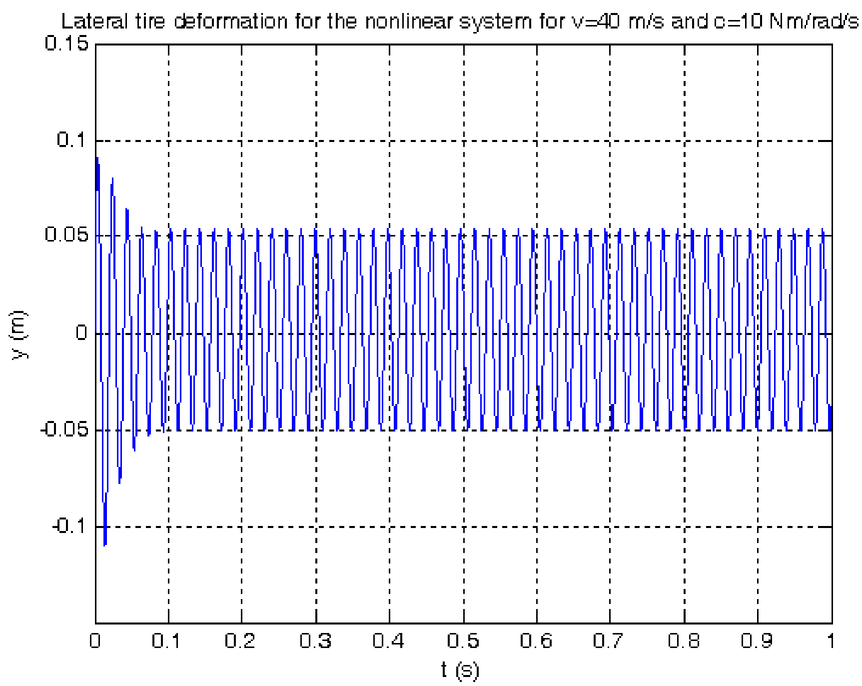

Figure 5.95: d. y for v =40 m/s, c =10 Nm/rad/s and $\psi(0)=1$ (nonlinear model).

Figure 5.96 shows the 3 and 2 dimensional limit cycles and time histories of the torsion angle and tire deformation for v =50 m/s, c =10 Nm/rad/s and $\psi(0)=1$.

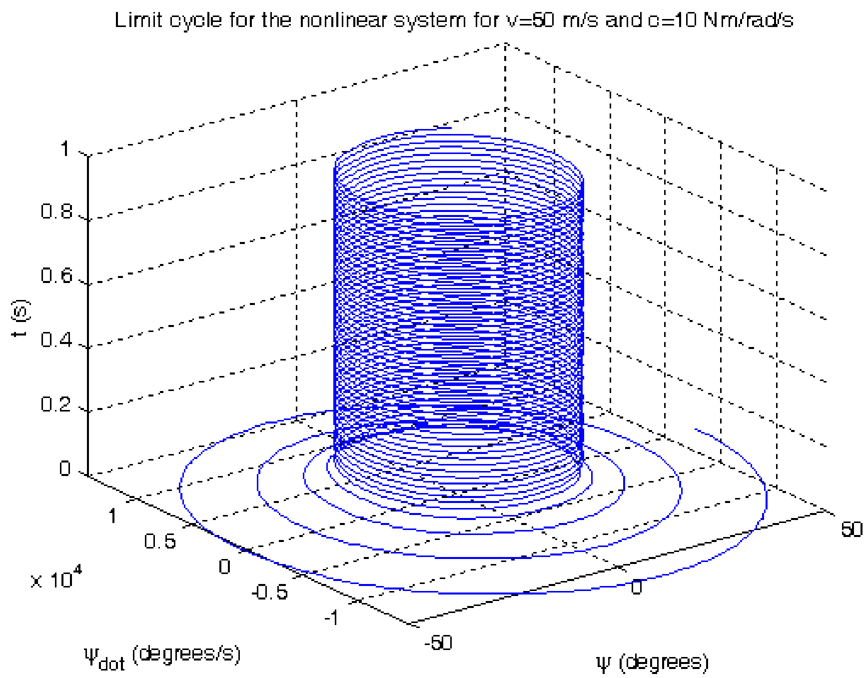

Figure 5.96: a. 3D limit cycle for $v = 50$ m/s, $c = 10$ Nm/rad/s and $\psi(0) = 1$.

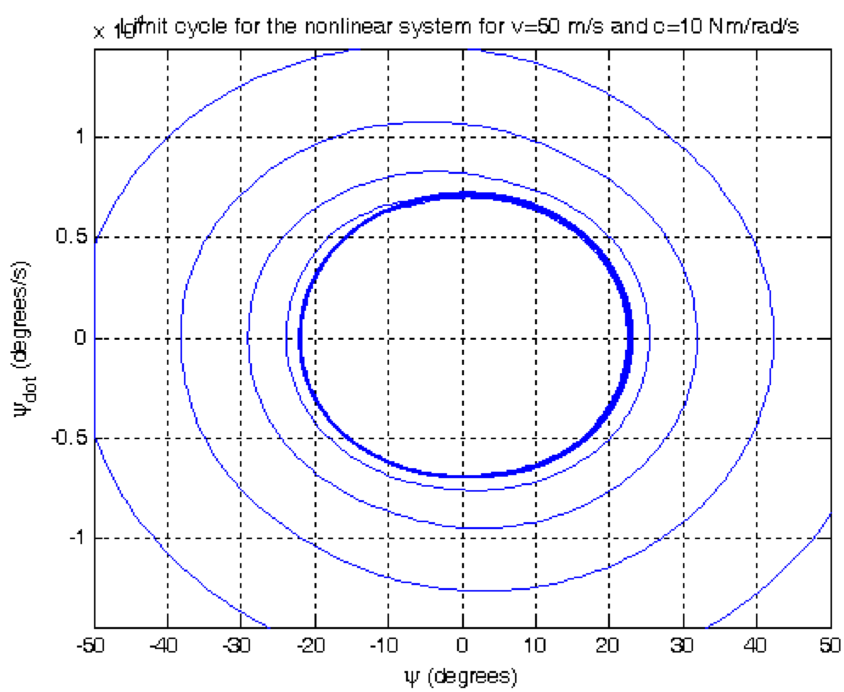

Figure 5.96: b. 2D limit cycle for $v = 50$ m/s, $c = 10$ Nm/rad/s and $\psi(0) = 1$.

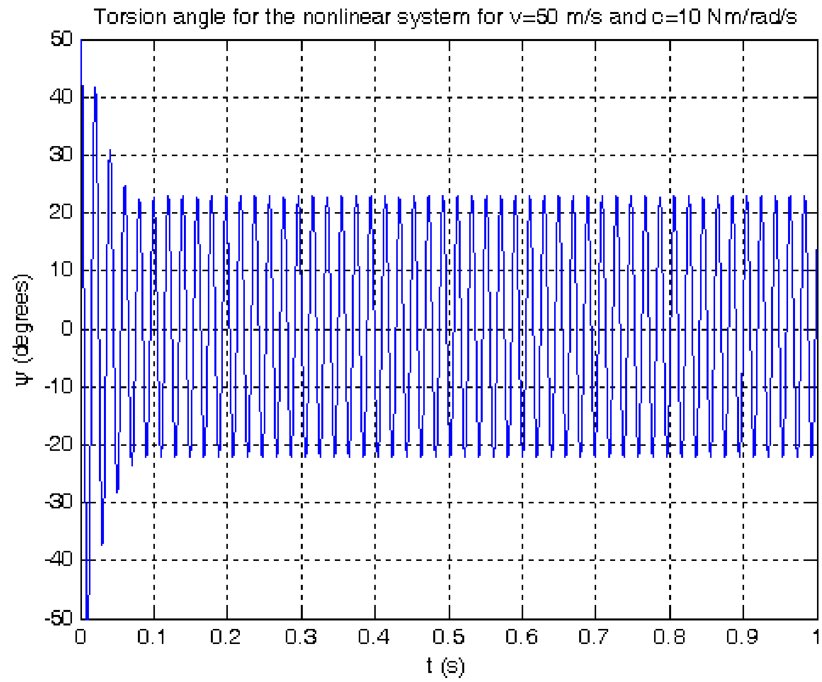

Figure 5.96: c. ψ for v =50 m/s, c =10 Nm/rad/s and $\psi(0)=1$ (nonlinear model).

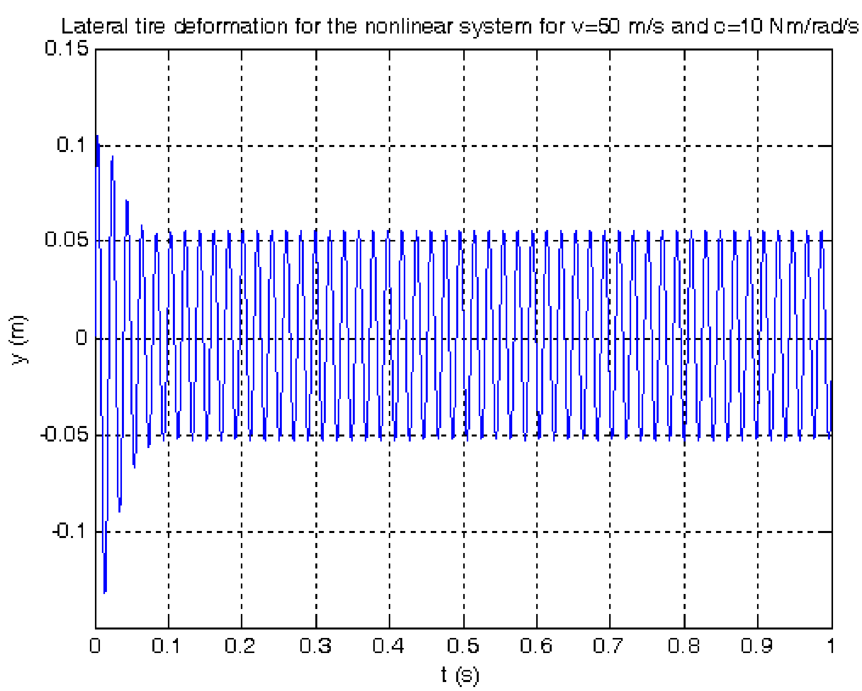

Figure 5.96: d. y for v =50m/s, c =10 Nm/rad/s and $\psi(0)=1$ (nonlinear model).

Figure 5.97 shows the 3 and 2 dimensional limit cycles and time histories of the torsion angle and tire deformation for v =50 m/s, c =20 Nm/rad/s and $\psi(0)=1$.

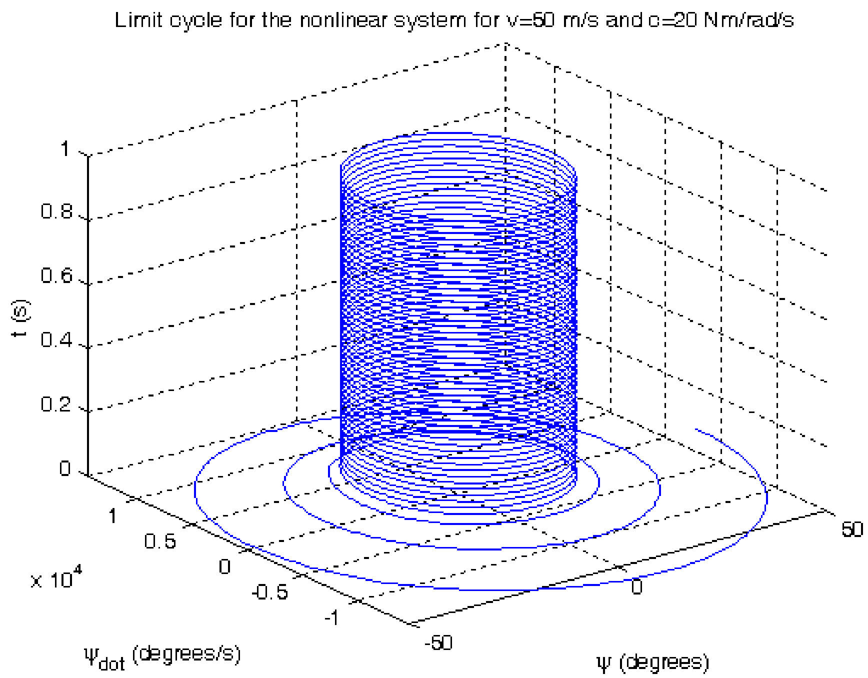

Figure 5.97: a. 3D limit cycle for v =50 m/s, c =20 Nm/rad/s and $\psi(0)=1$.

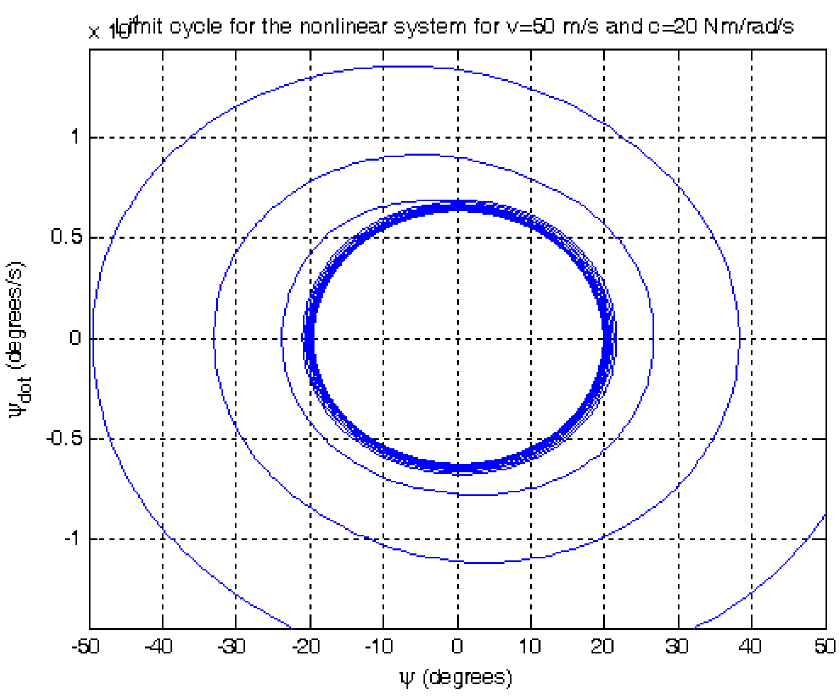

Figure 5.97: b. 2D limit cycle for v =50 m/s, c =20 Nm/rad/s and $\psi(0)=1$.

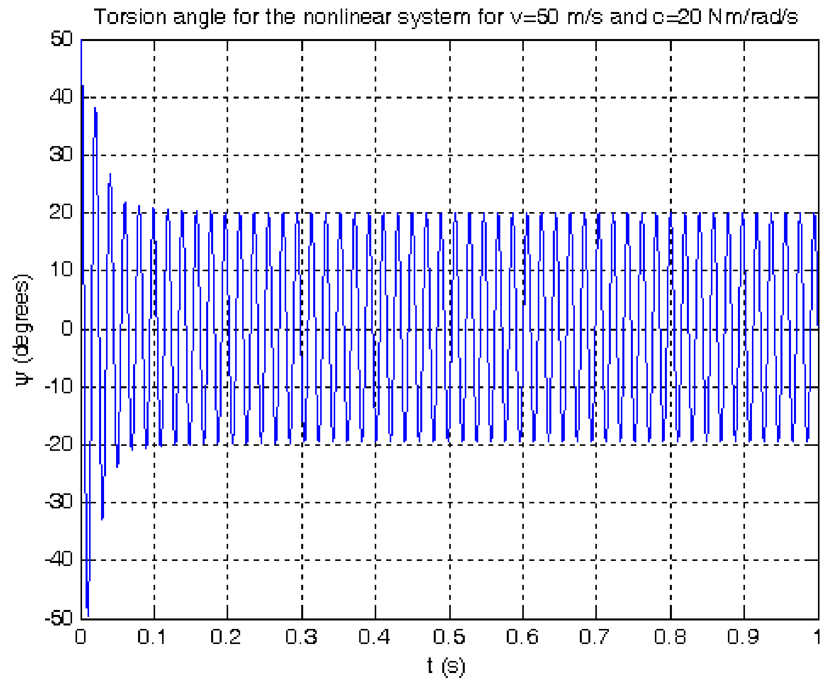

Figure 5.97: c. ψ for v =50 m/s, c =20 Nm/rad/s and $\psi(0)=1$ (nonlinear model).

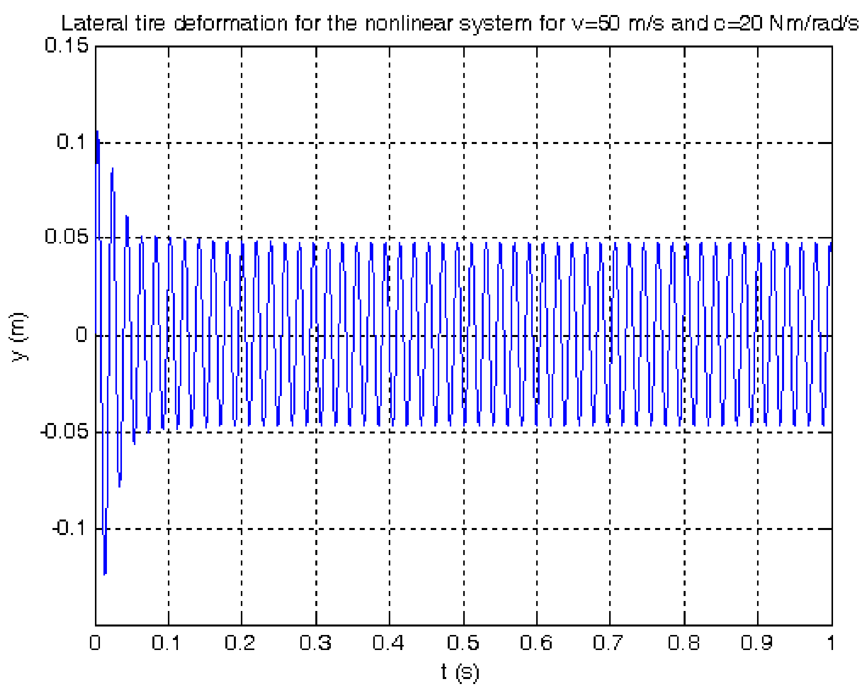

Figure 5.97: d. y for v =50 m/s, c =20 Nm/rad/s and $\psi(0)=1$ (nonlinear model).

Figure 5.98 shows the 3 and 2 dimensional limit cycles and time histories of the torsion angle and tire deformation for v =70 m/s, c =20 Nm/rad/s and $\psi(0)=1$.

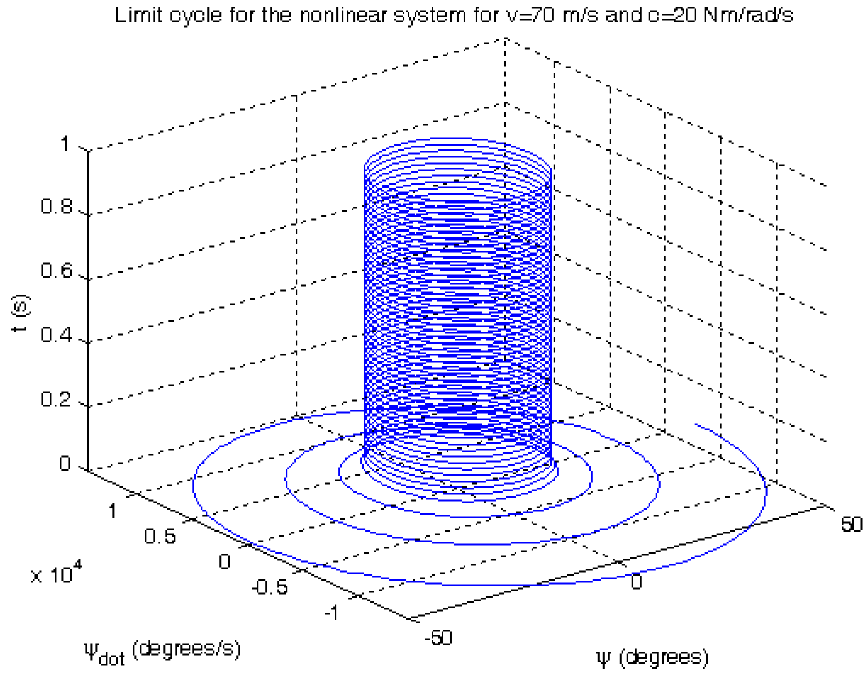

Figure 5.98: a. 3D limit cycle for v =70 m/s, c =20 Nm/rad/s and $\psi(0)=1$.

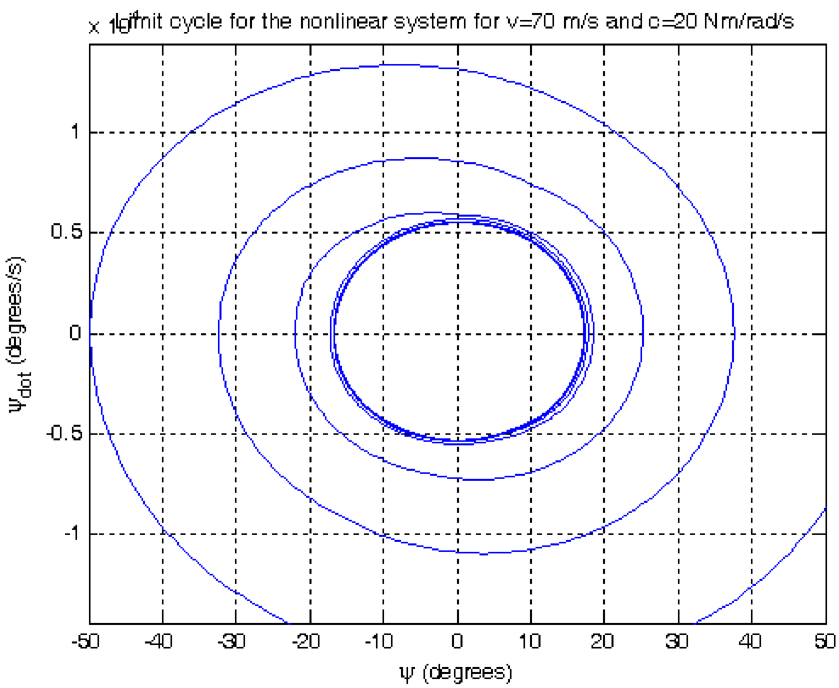

Figure 5.98: b. 2D limit cycle for v =70 m/s, c =20 Nm/rad/s and $\psi(0)=1$.

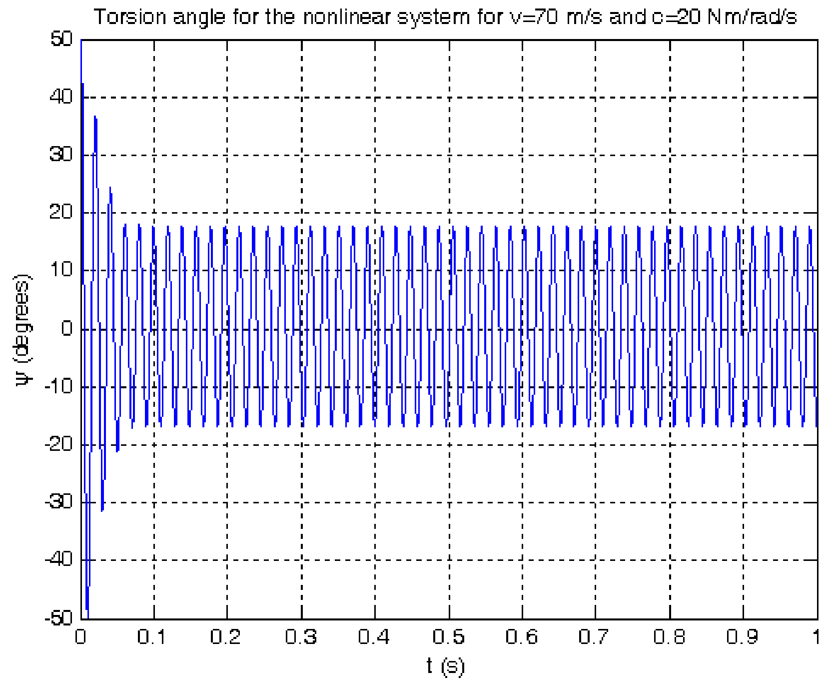

Figure 5.98: c. ψ for v =70 m/s, c =20 Nm/rad/s and $\psi(0)=1$ (nonlinear model).

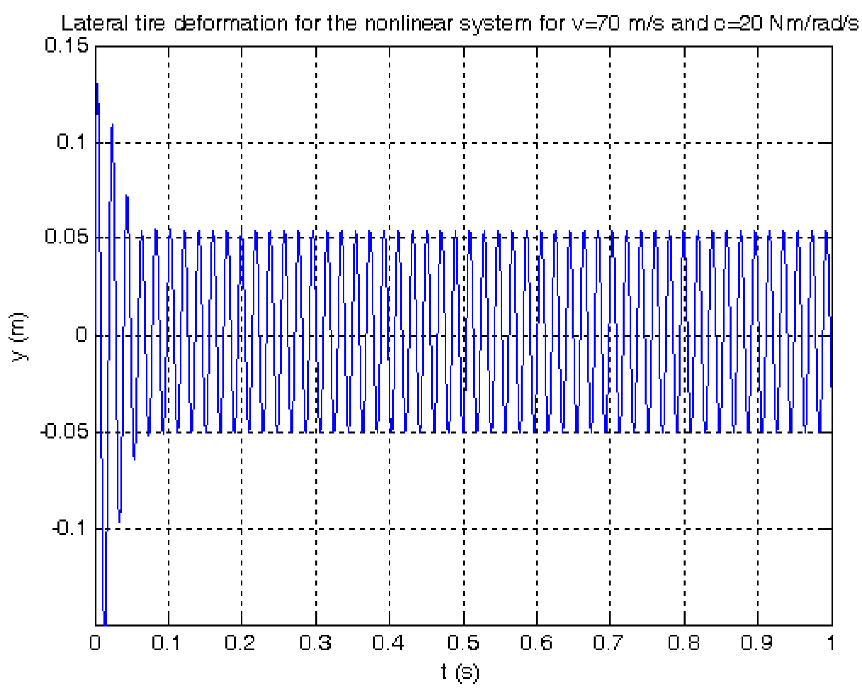

Figure 5.98: d. y for v =70 m/s, c =20 Nm/rad/s and $\psi(0)=1$ (nonlinear model).

Figure 5.99 shows the 3 and 2 dimensional limit cycles and time histories of the torsion angle and tire deformation for v =100 m/s, c =20 Nm/rad/s and $\psi(0)=1$.

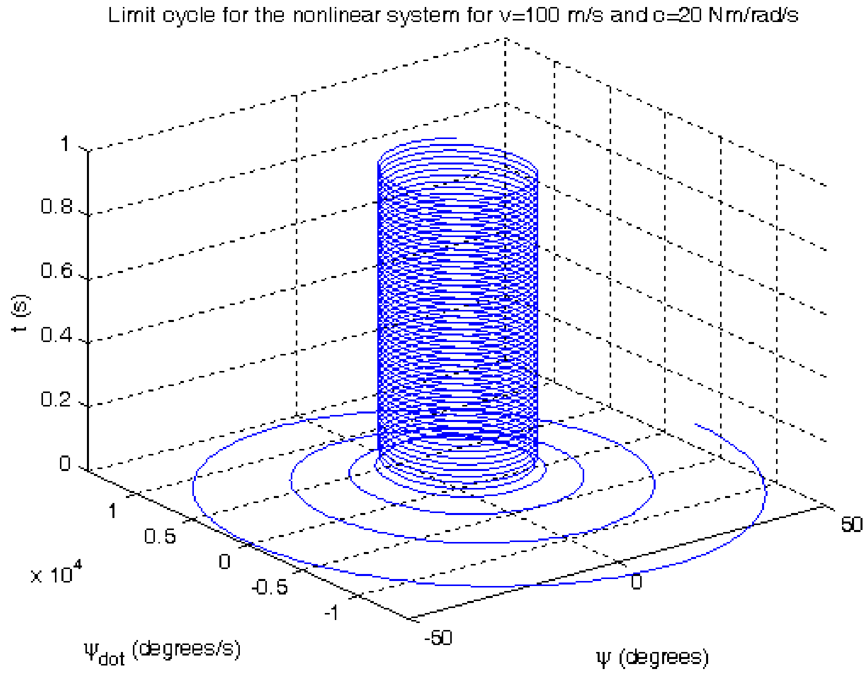

Figure 5.99: a. 3D limit cycle for v =100 m/s, c =20 Nm/rad/s and $\psi(0)=1$.

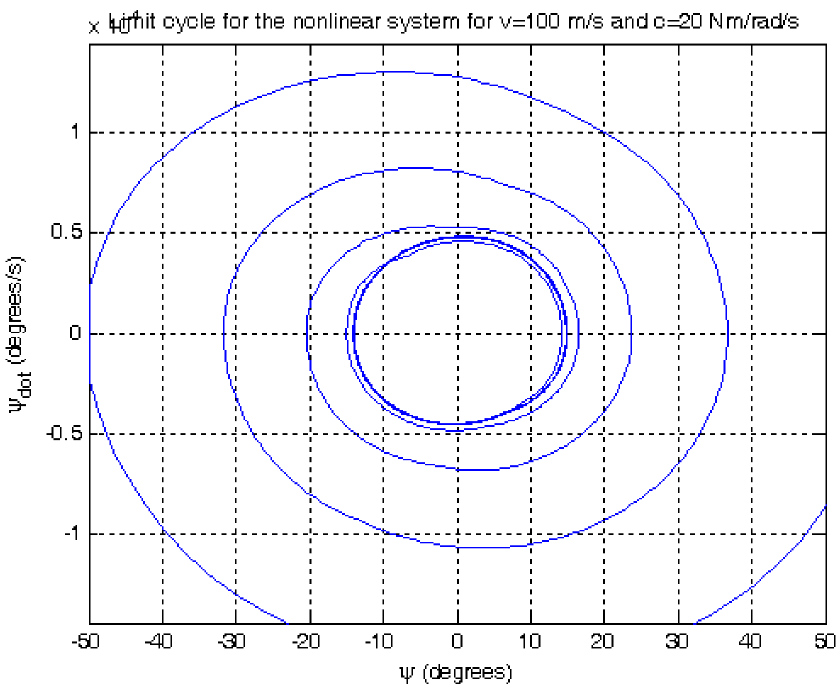

Figure 5.99: b. 2D limit cycle for v =100 m/s, c =20 Nm/rad/s and $\psi(0)=1$.

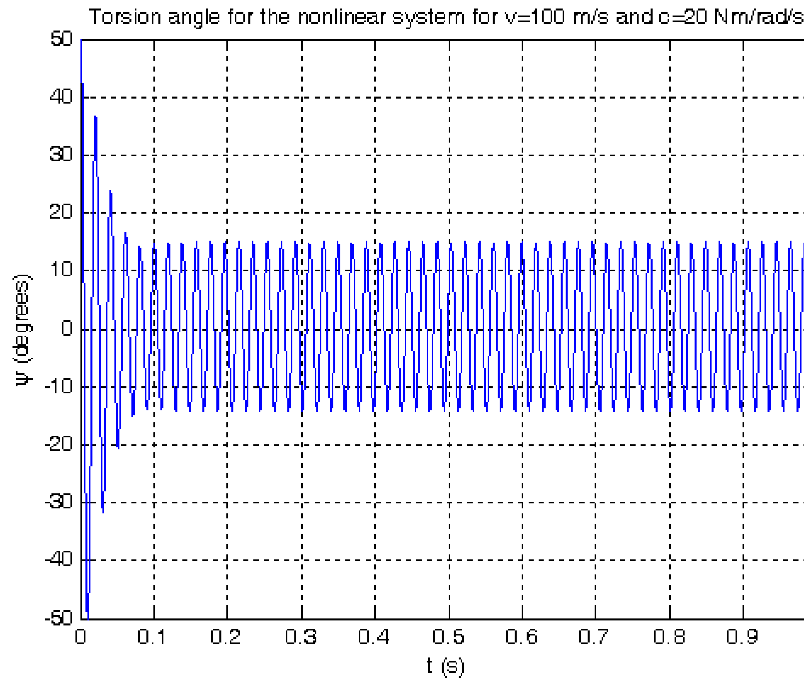

Figure 5.99: c. ψ for v =100 m/s, c =20 Nm/rad/s and $\psi(0)=1$ (nonlinear model).

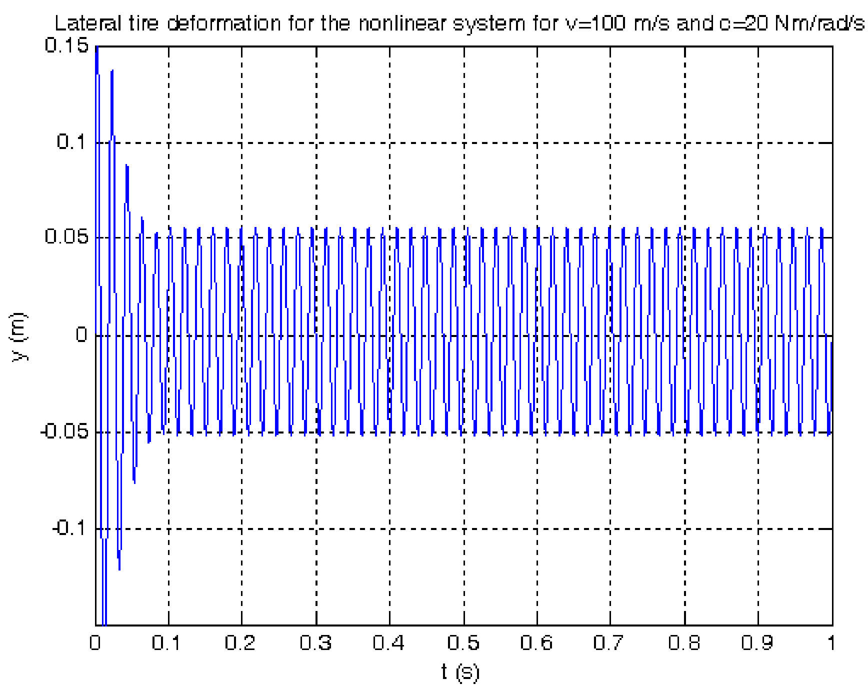

Figure 5.99: d. y for v =100 m/s, c =20 Nm/rad/s and $\psi(0)=1$ (nonlinear model).

Table 5.10: Limit cycle amplitudes of the torsion angle ψ **,** rate of change of the torsion angle $\dot{\psi}$ and lateral tire deformation y for $\psi(0)=1$ and k =100000Nm/rad.

Velocity v **(m/s)**	**Torsional damping constant** c **(Nm/rad/s)**	**Torsion angle** ψ **(degrees)**	$\dot{\psi}$ **(degrees/s)**	**Lateral tire deformation** y **(m)**
		amplitude	**amplitude**	**amplitude**
30	10	28.8	9117.5	0.045
40	10	26.4	8294.7	0.053
50	10	23.1	7231.5	0.056
50	20	19.8	6334.8	0.048
70	20	17.3	5517.9	0.053
100	20	14.5	4672.6	0.054

Table 5.11: Limit cycle amplitudes of the torsion angle ψ **,** rate of change of the torsion angle $\dot{\psi}$ and lateral tire deformation y for $\psi(0)=1$ and k =75000Nm/rad.

Velocity v **(m/s)**	**Torsional damping constant** c **(Nm/rad/s)**	**Torsion angle** ψ **(degrees)**	$\dot{\psi}$ **(degrees/s)**	**Lateral tire deformation** y **(m)**
		amplitude	**amplitude**	**amplitude**
30	10	29.3	8003.2	0.052
40	10	25.0	6771.3	0.057
50	10	20.9	5614.4	0.056
50	20	19.7	5438.5	0.053
70	20	16.5	4590.0	0.055
100	20	14.1	4006.8	0.056

5.9.2 Conclusions about time histories of the nonlinear model and limit cycles

- In stable cases such as c=100 Nm/rad/s, time histories of the nonlinear model are very similar to the linear ones, as figure 5.86 is very similar to figure 5.87.
- Limit cycles occur in unstable cases where a weak damping constant of 10 or 20 Nm/rad/s is employed.
- 3 dimensional and 2 dimensional plots of limit cycle oscillations, time histories of the torsion angle ψ and lateral tire deformation y are plotted for various velocities and damping constants in figures 88–99. $\psi(0)=0.01$ is employed in figures 88–93 and $\psi(0)=1$ is employed in figures 94–99.
- Approach direction of limit cycles varies with initial conditions. Limit cycle is approached from inside for small initial yaw angles such as $\psi(0)=0.01$ and from outside for large initial conditions such as $\psi(0)=1$.
- Limit cycle amplitude is independent of the initial condition.
- Tables 5.8–5.11 reveal that increasing the velocity v decreases the limit cycle amplitudes of the torsion angle ψ, rate of change of the torsion angle $\dot{\psi}$ and the lateral tire deformation y. The onset of shimmy happens faster with higher velocities.
- Tables 5.8–5.11 reveal that increasing the damping constant c decreases the limit cycle amplitudes of the torsion angle ψ, rate of change of the torsion angle $\dot{\psi}$ and the lateral tire deformation y.
- Tables 5.8–5.11 reveal that decreasing the torsional spring constant k decreases the limit cycle amplitudes of the torsion angle ψ and rate of change of the torsion angle, $\dot{\psi}$, while increasing the limit cycle amplitude of the lateral tire deformation y. Decreasing k also has an effect of decreasing the limit cycle frequency. The only exception is that for the case of v=30

m/s, c =10 Nm/rad/s, decreasing the torsional spring rate has increased the limit cycle amplitude of the torsion angle.

- Shimmy amplitude increases with increased velocities and decreased damping constants.

5.9.3 Effect of the damping constant c on shimmy

Torsional damping constant c is an important parameter in landing gear design because it is critical for shimmy oscillation analysis. In this section, effect of the damping constant is observed by varying the torsional damping constant c and keeping the taxiing velocity v constant.

For this purpose, 2 and 3 dimensional plots of the limit cycles, $(\psi, \dot{\psi}, t)$ and $(\psi, \dot{\psi})$, and time histories of the of the torsion angle ψ and lateral tire deformation y are obtained for a taxiing velocity v of 80 m/s, $\psi(0) = 0.01$ and a varying torsional damping constant c of 10, 20, 30, 40, 50, and 70 Nm/rad/s and presented in figures 5.100–5.105.

It is shown that the increase of torsional damping constant helps suppress shimmy. Limit cycle oscillations exist in the case of weak damping, such as in figure 5.100, however shimmy oscillations become smaller and weaker as the damping constant increases.

Deflection of the tire also decreases by increasing the damping constant. In the case of a very strong damping constant of 100 Nm/rad/s as in figure 5.106, which is impossible in practice, torsion angle and tire deflection quickly converge to 0. This demonstrates that the increase of the torsional damping constant helps suppress shimmy.

Table 5.12 gives limit cycle amplitudes of the torsion angle ψ **,** rate of change of the torsion angle $\dot{\psi}$ and lateral tire deformation y for v =80 m/s and a varying damping constant c .Simulation was performed for 1 s for lower values of c such as 10, 20, 30 and 40 Nm/rad/s, but for higher values of c such as 50 and 70 Nm/rad/s, 2 s were needed for the onset of the limit cycle.

Figure 5.100 shows the 3 and 2 dimensional limit cycles and time histories of the torsion angle and tire deformation for v =80 m/s, c =10 Nm/rad/s and $\psi(0) = 0.01$.

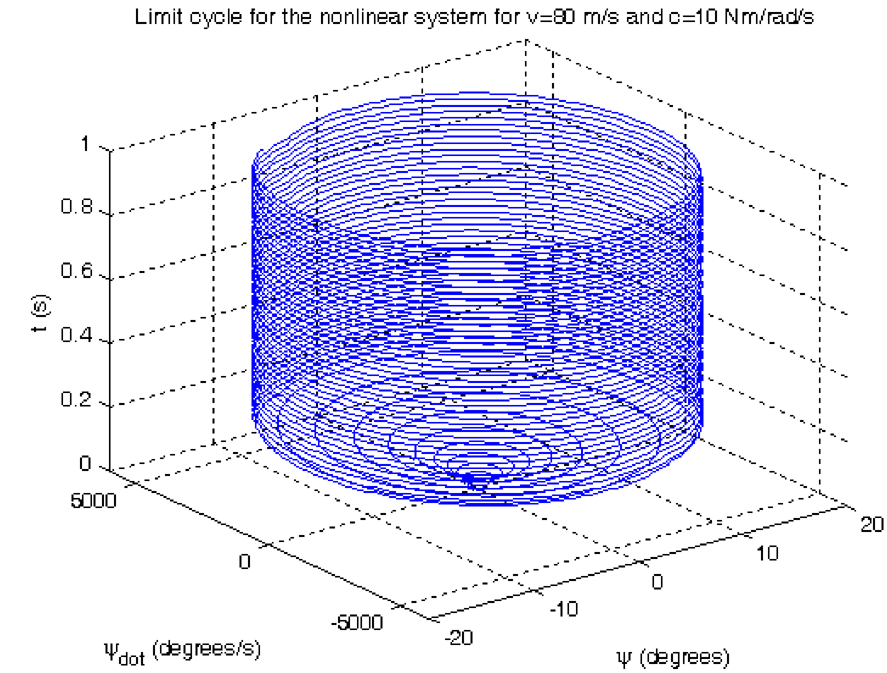

Figure 5.100: a. 3D limit cycle for v =80 m/s, c =10 Nm/rad/s and $\psi(0) = 0.01$.

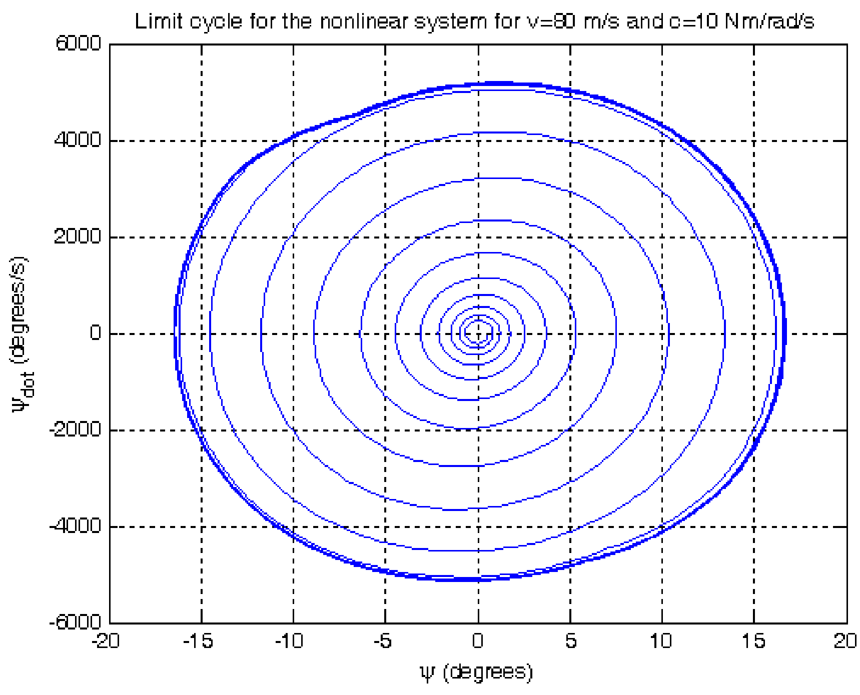

Figure 5.100: b. 2D limit cycle for v =80 m/s, c =10 Nm/rad/s and $\psi(0) = 0.01$.

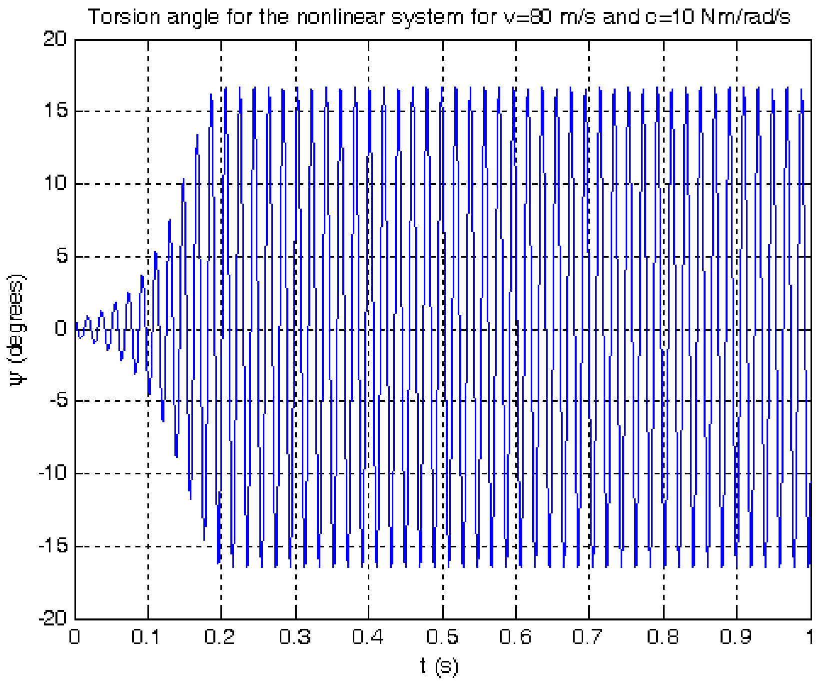

Figure 5.100: c. ψ for v =80 m/s, c =10 Nm/rad/s, $\psi(0)=0.01$ (nonlinear model).

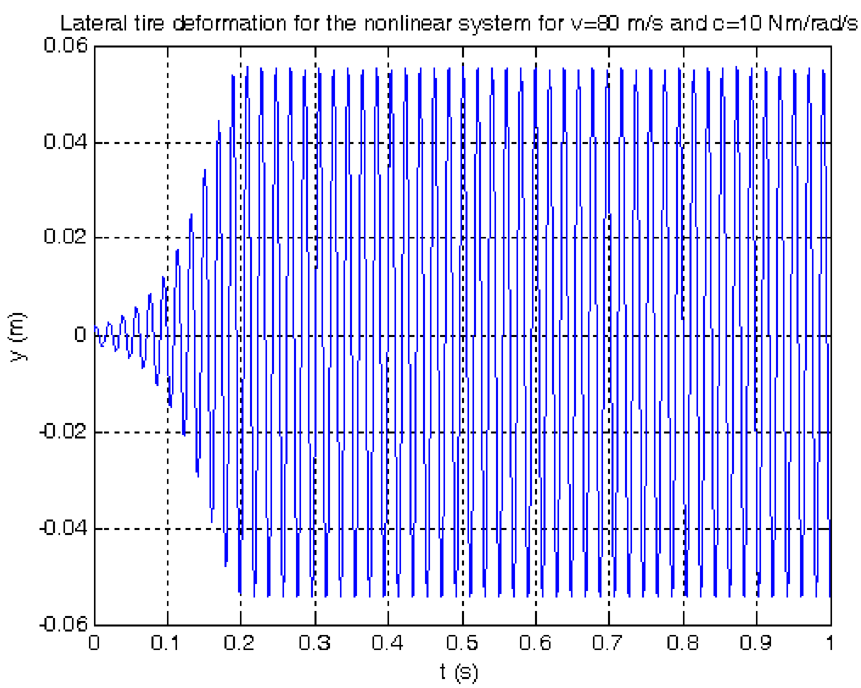

Figure 5.100: d. y for v =80 m/s, c =10 Nm/rad/s, $\psi(0)=0.01$ (nonlinear model).

Figure 5.101 shows the 3 and 2 dimensional limit cycles and time histories of the torsion angle and tire deformation for v =80 m/s, c =20 Nm/rad/s and $\psi(0)=0.01$.

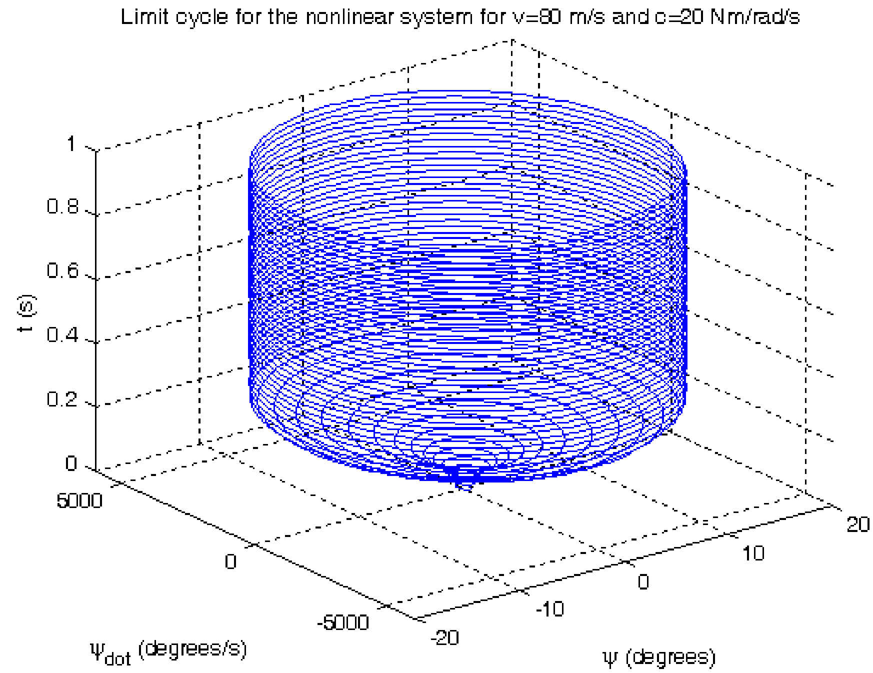

Figure 5.101: a. 3D limit cycle for v =80 m/s, c =20 Nm/rad/s and $\psi(0) = 0.01$.

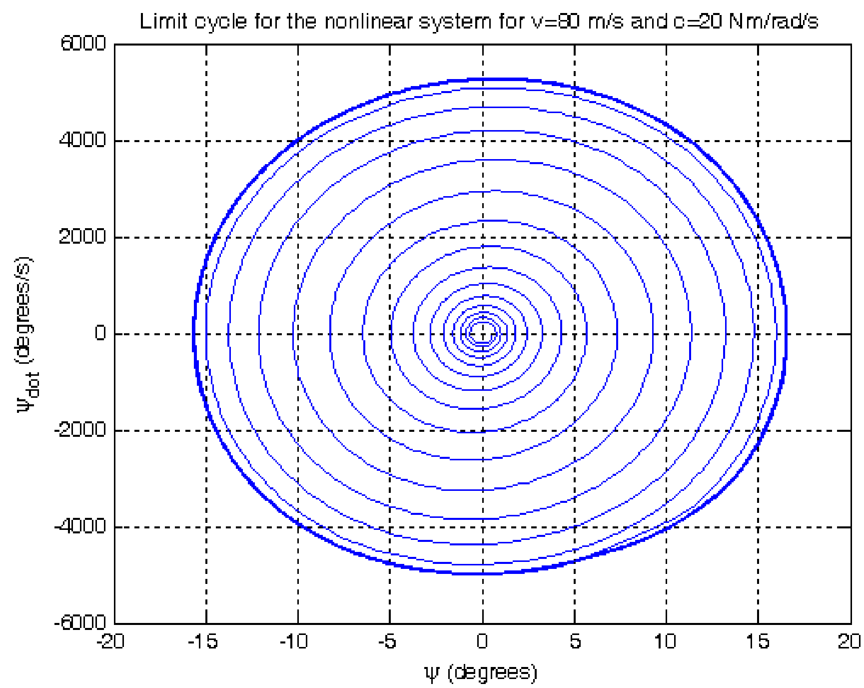

Figure 5.101: b. 2D limit cycle for v =80 m/s, c =20 Nm/rad/s and $\psi(0) = 0.01$.

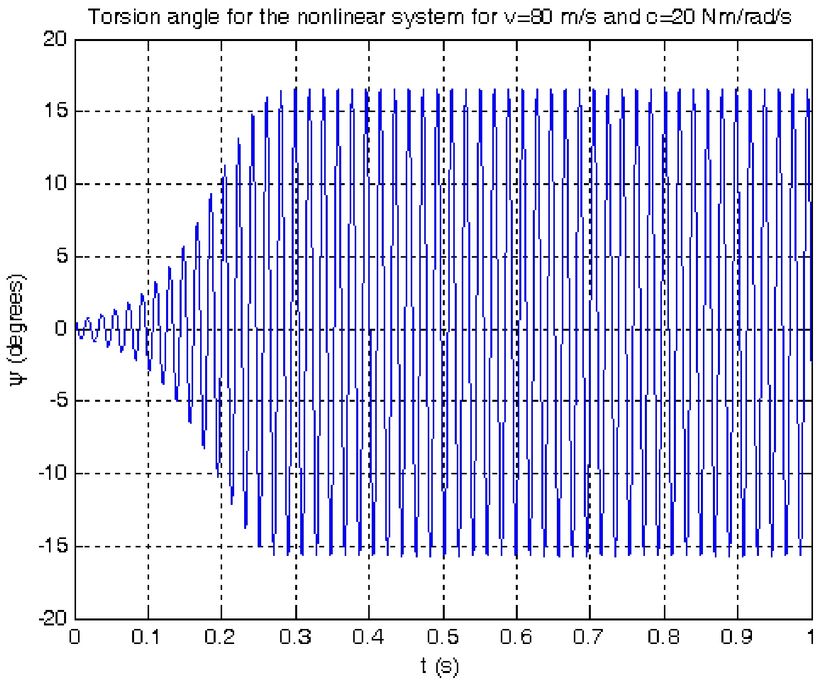

Figure 5.101: c. ψ for v =80 m/s, c =20 Nm/rad/s, $\psi(0)=0.01$ (nonlinear model).

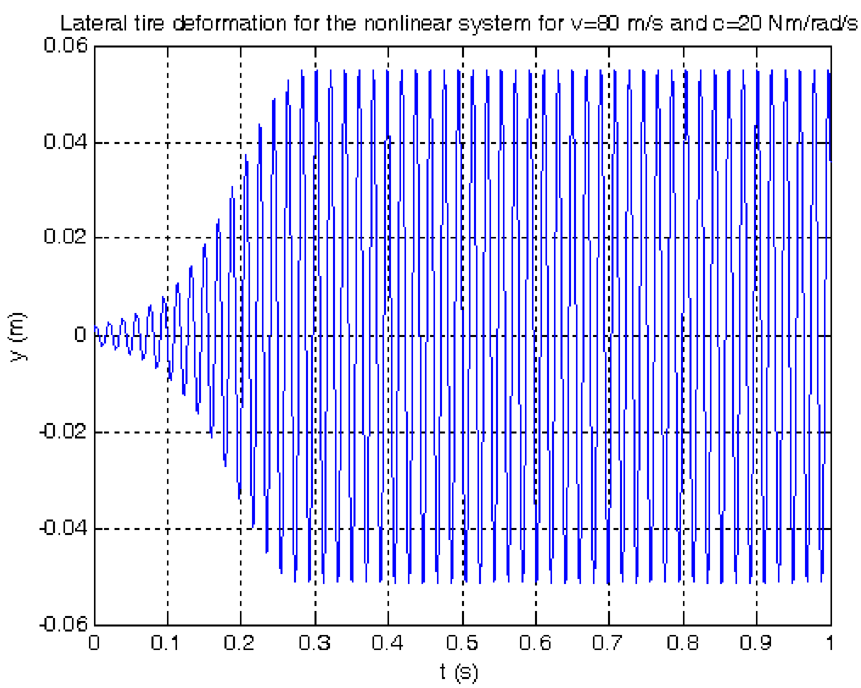

Figure 5.101: d. y for v =80 m/s, c =20 Nm/rad/s, $\psi(0)=0.01$ (nonlinear model).

Figure 5.102 shows the 3 and 2 dimensional limit cycles and time histories of the torsion angle and tire deformation for v =80 m/s, c =30 Nm/rad/s and $\psi(0)=0.01$.

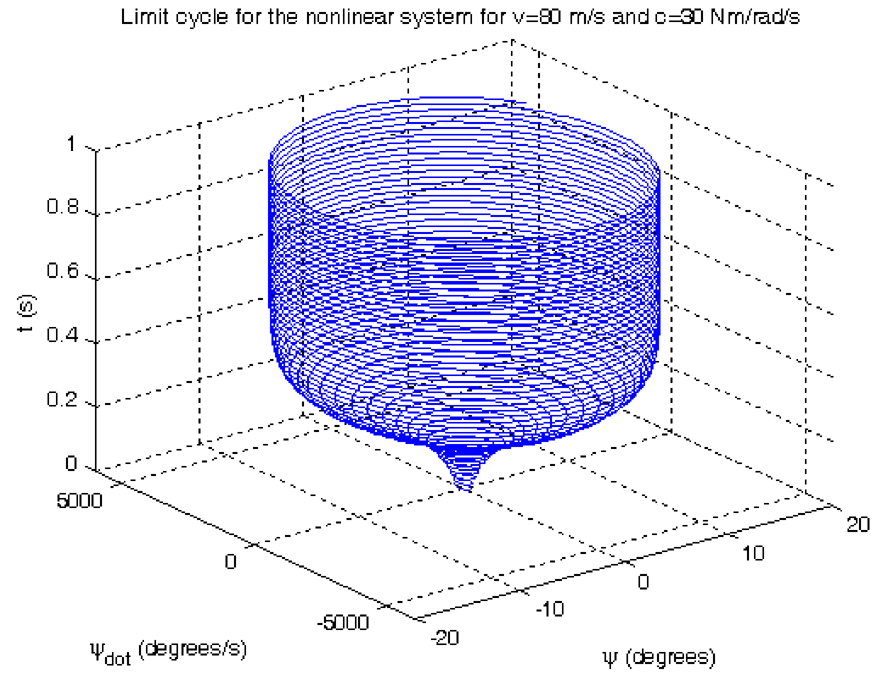

Figure 5.102: a. 3D limit cycle for v =80 m/s, c =30 Nm/rad/s and $\psi(0) = 0.01$.

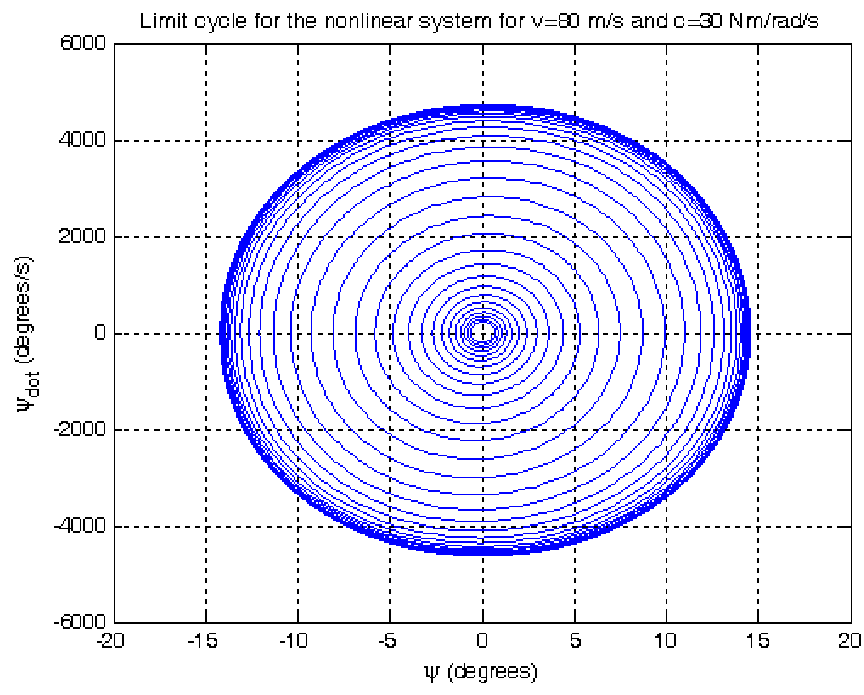

Figure 5.102: b. 2D limit cycle for v =80 m/s, c =30 Nm/rad/s and $\psi(0) = 0.01$.

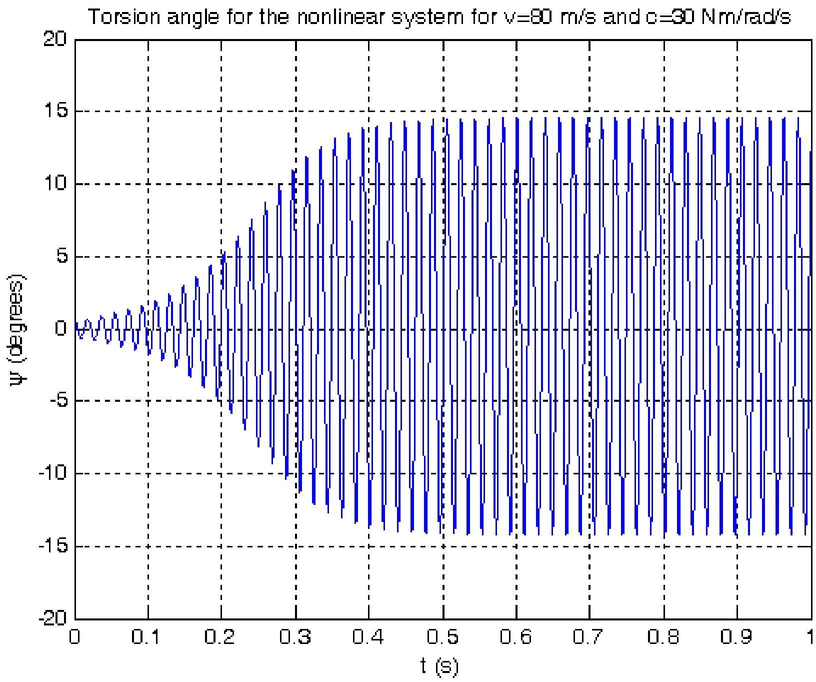

Figure 5.102: c. ψ for v =80 m/s, c =30 Nm/rad/s, $\psi(0) = 0.01$ (nonlinear model).

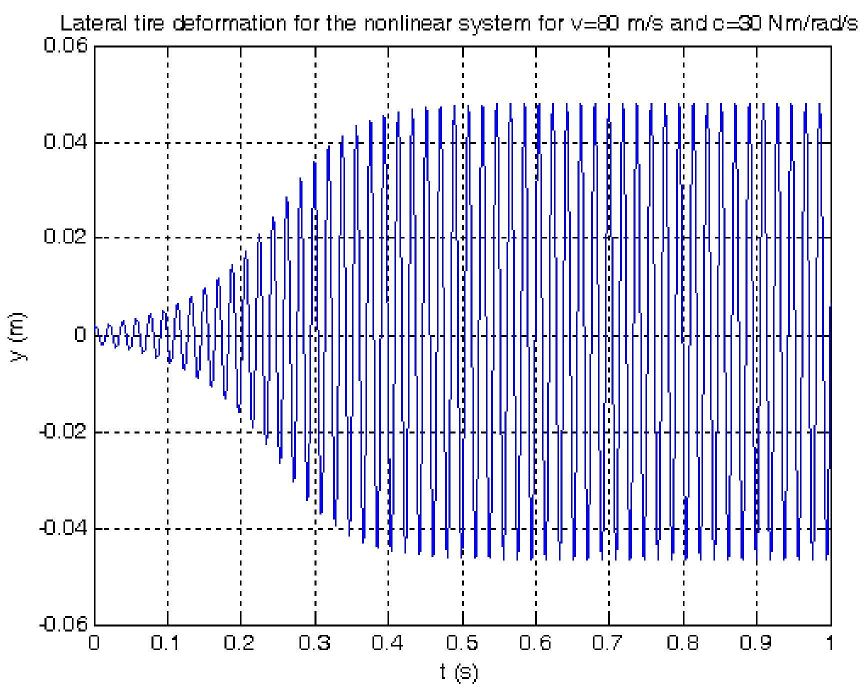

Figure 5.102: d. y for v =80 m/s, c =30 Nm/rad/s, $\psi(0) = 0.01$ (nonlinear model).

Figure 5.103 shows the 3 and 2 dimensional limit cycles and time histories of the torsion angle and tire deformation for v =80 m/s, c =40 Nm/rad/s and $\psi(0) = 0.01$.

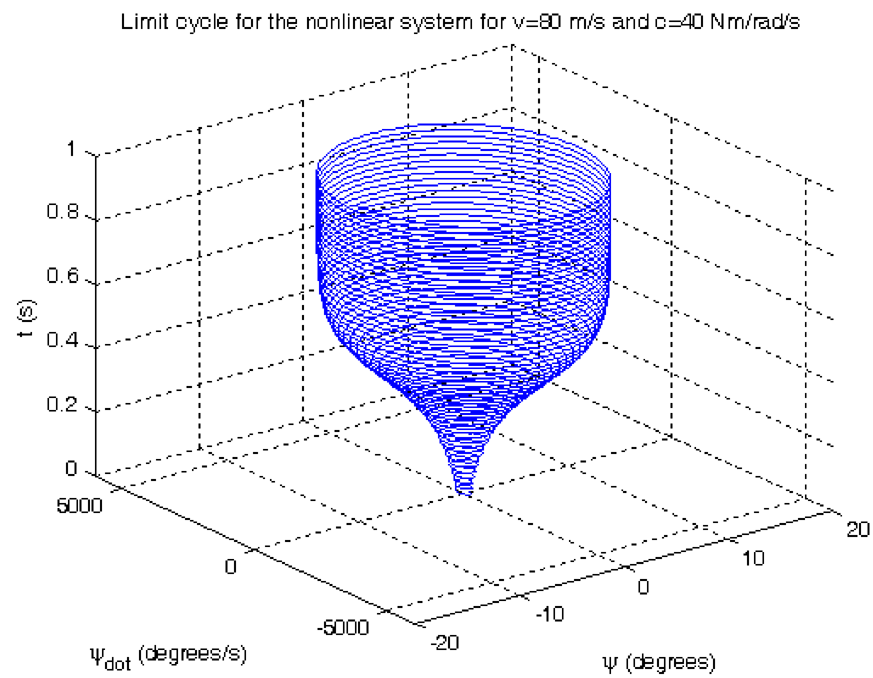

Figure 5.103: a. 3D limit cycle for v =80 m/s, c =40 Nm/rad/s and $\psi(0) = 0.01$.

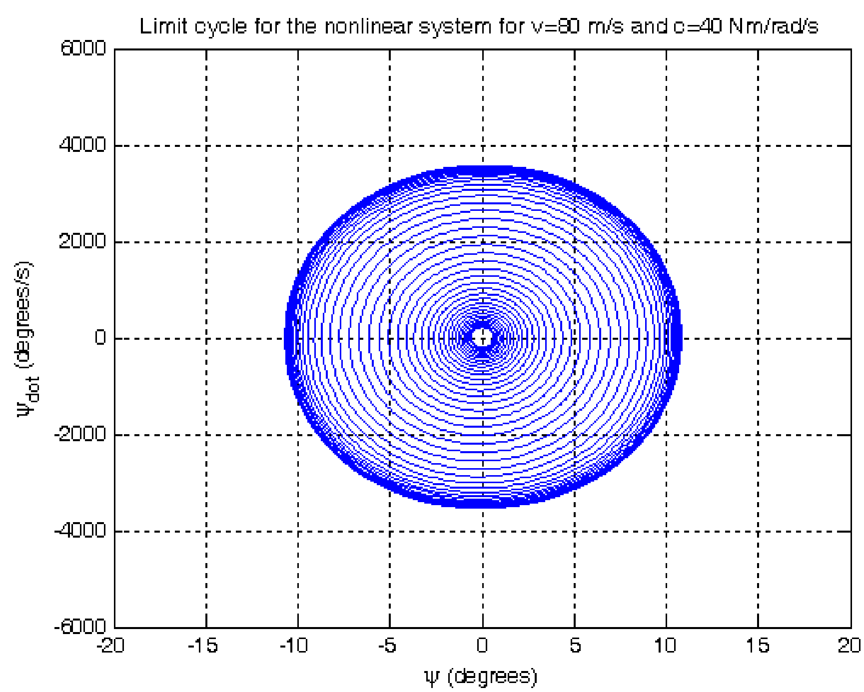

Figure 5.103: b. 2D limit cycle for v =80 m/s, c =40 Nm/rad/s and $\psi(0) = 0.01$.

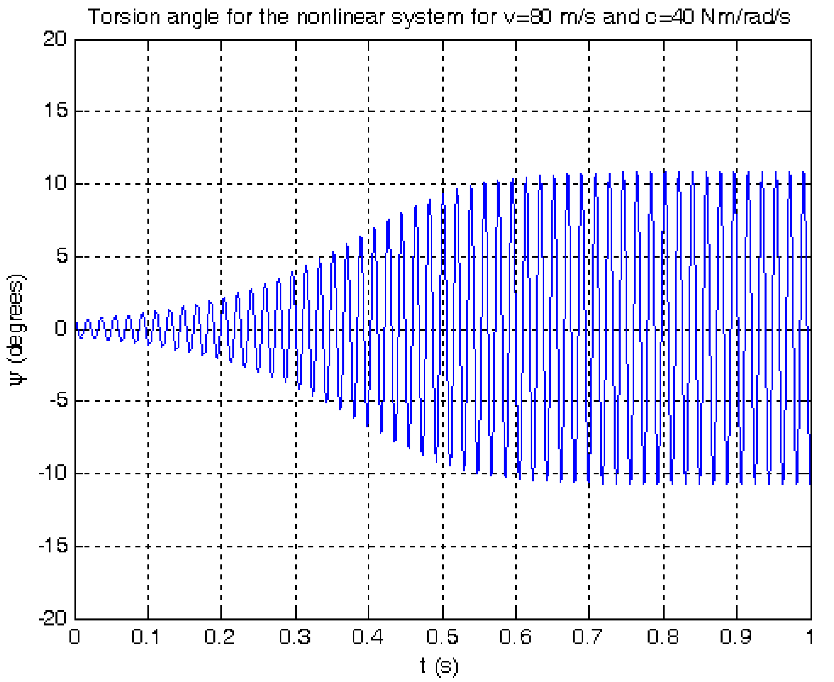

Figure 5.103: c. ψ for v =80 m/s, c =40 Nm/rad/s, $\psi(0) = 0.01$ (nonlinear model).

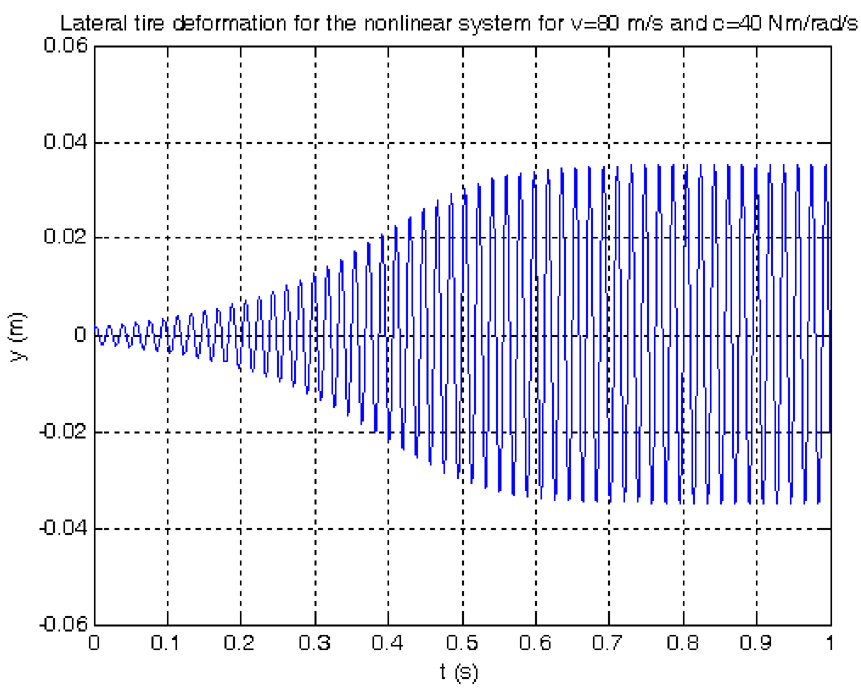

Figure 5.103: d. y for v =80 m/s, c =40 Nm/rad/s, $\psi(0) = 0.01$ (nonlinear model).

Figure 5.104 shows the 3 and 2 dimensional limit cycles and time histories of the torsion angle and tire deformation for v =80 m/s, c =50 Nm/rad/s and $\psi(0) = 0.01$.

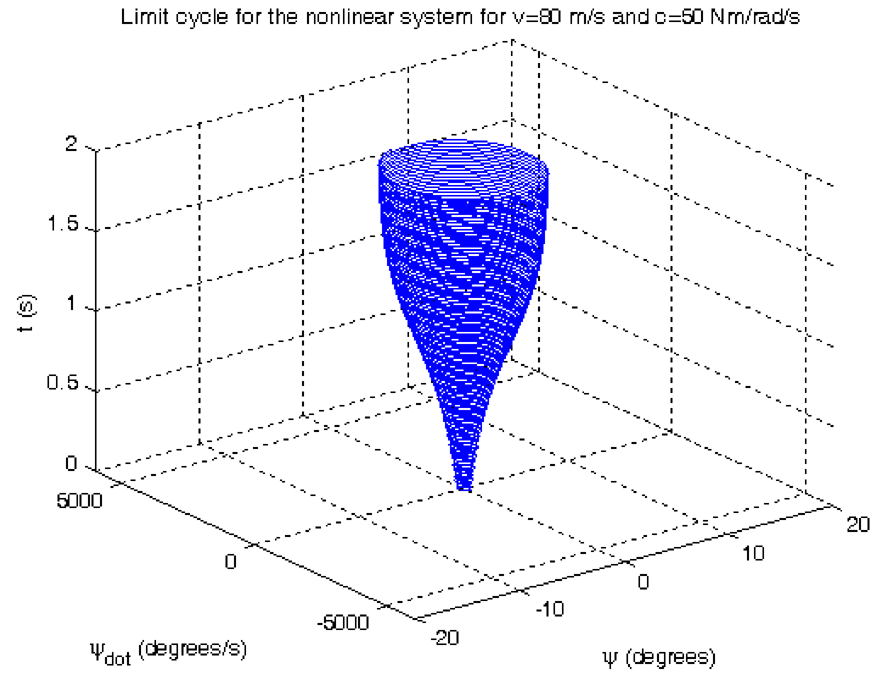

Figure 5.104: a. 3D limit cycle for v =80 m/s, c =50 Nm/rad/s and $\psi(0) = 0.01$.

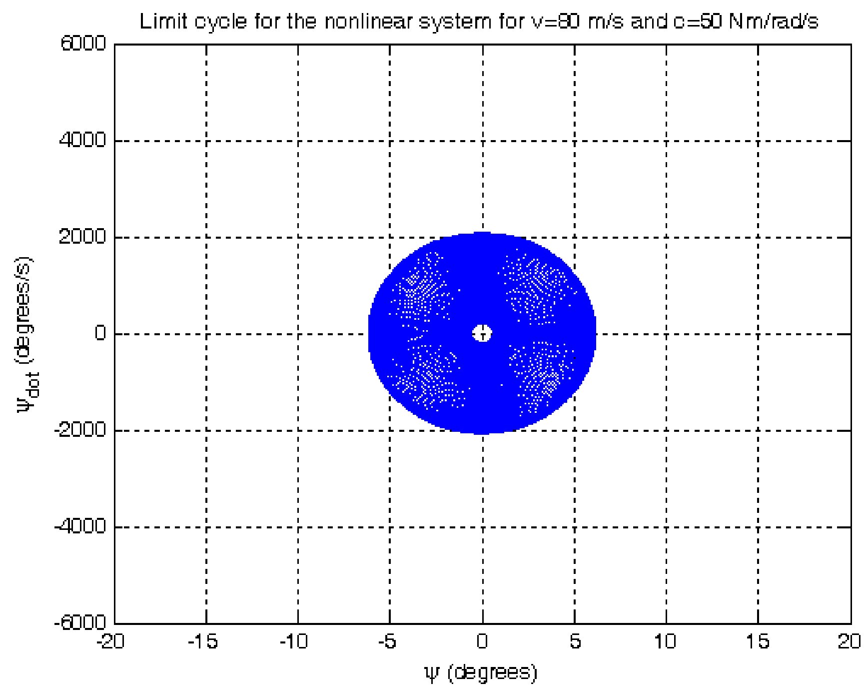

Figure 5.104: b. 2D limit cycle for v =80 m/s, c =50 Nm/rad/s and $\psi(0) = 0.01$.

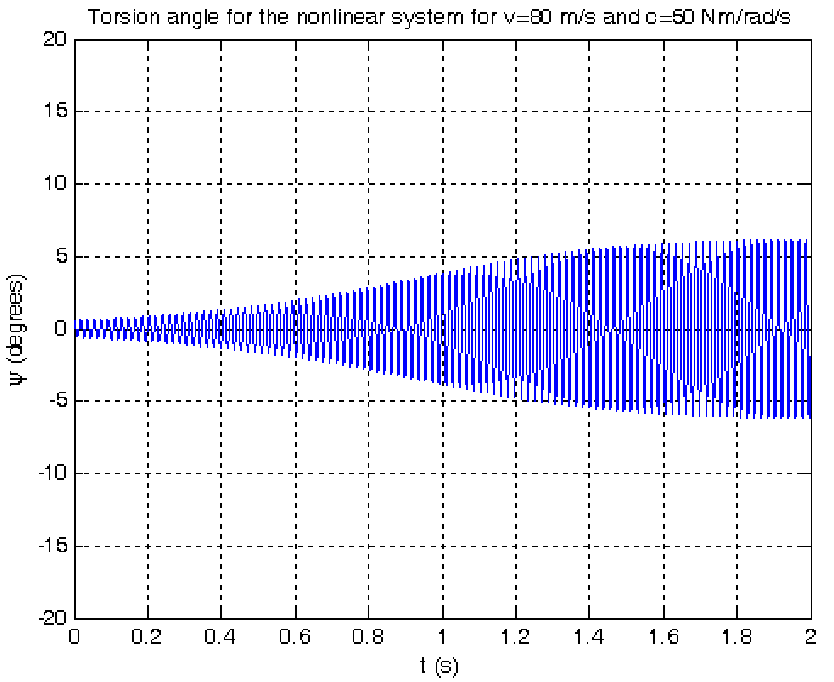

Figure 5.104: c. ψ for v =80 m/s, c =50 Nm/rad/s, $\psi(0)=0.01$ (nonlinear model).

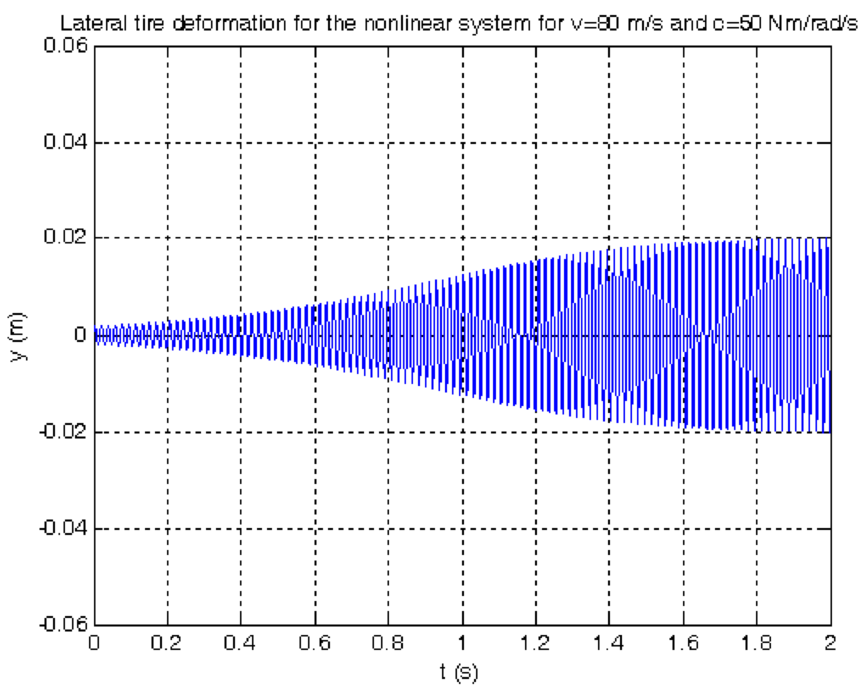

Figure 5.104: d. y for v =80 m/s, c =50 Nm/rad/s, $\psi(0)=0.01$ (nonlinear model).

Figure 5.105 shows the 3 and 2 dimensional limit cycles and time histories of the torsion angle and tire deformation for v =80 m/s, c =70 Nm/rad/s and $\psi(0)=0.01$.

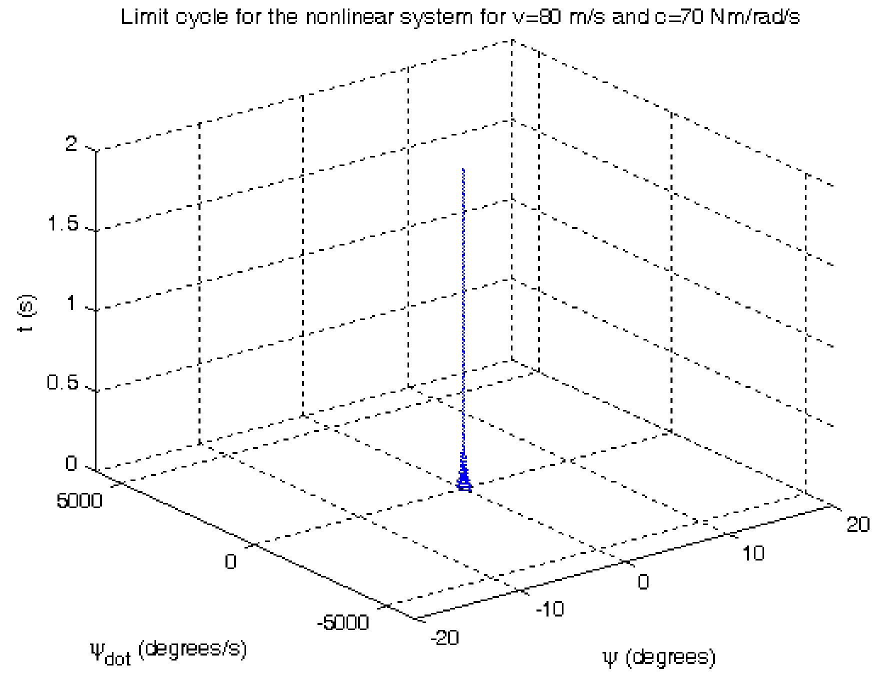

Figure 5.105: a. 3D limit cycle for v =80 m/s, c =70 Nm/rad/s and $\psi(0) = 0.01$.

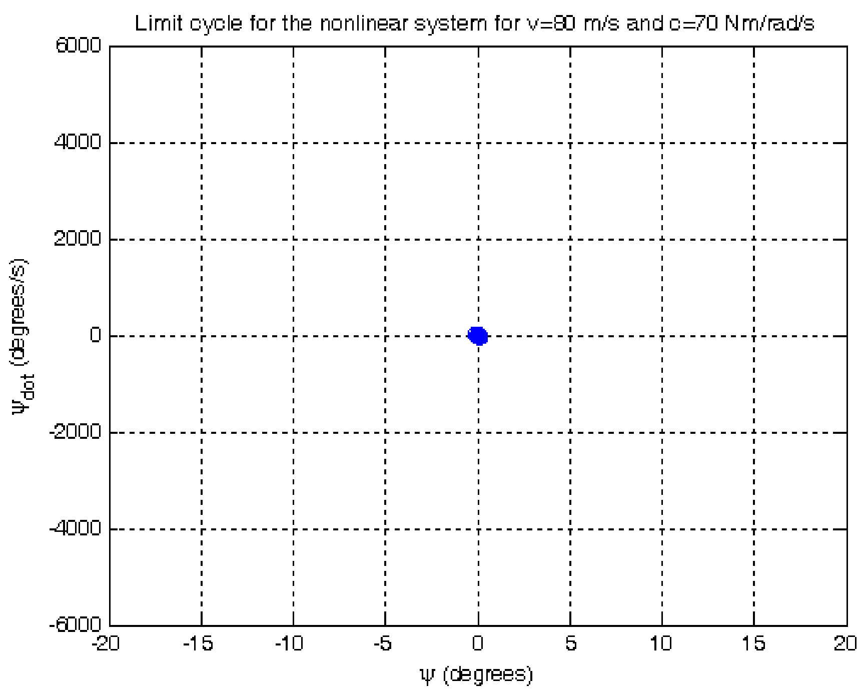

Figure 5.105: b. 2D limit cycle for v =80 m/s, c =70 Nm/rad/s and $\psi(0) = 0.01$.

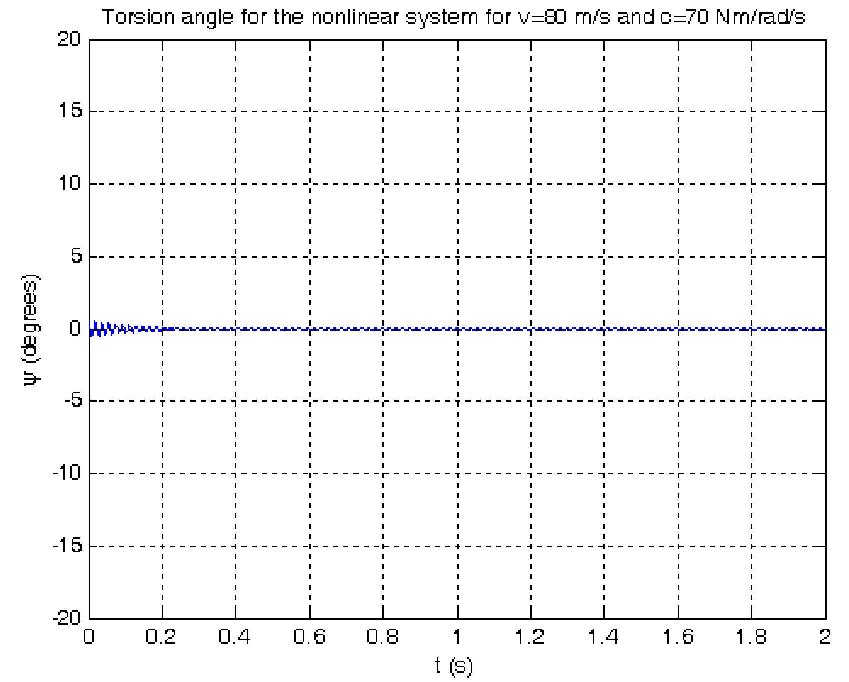

Figure 5.105: c. ψ for v =80 m/s, c =70 Nm/rad/s, $\psi(0)=0.01$ (nonlinear model).

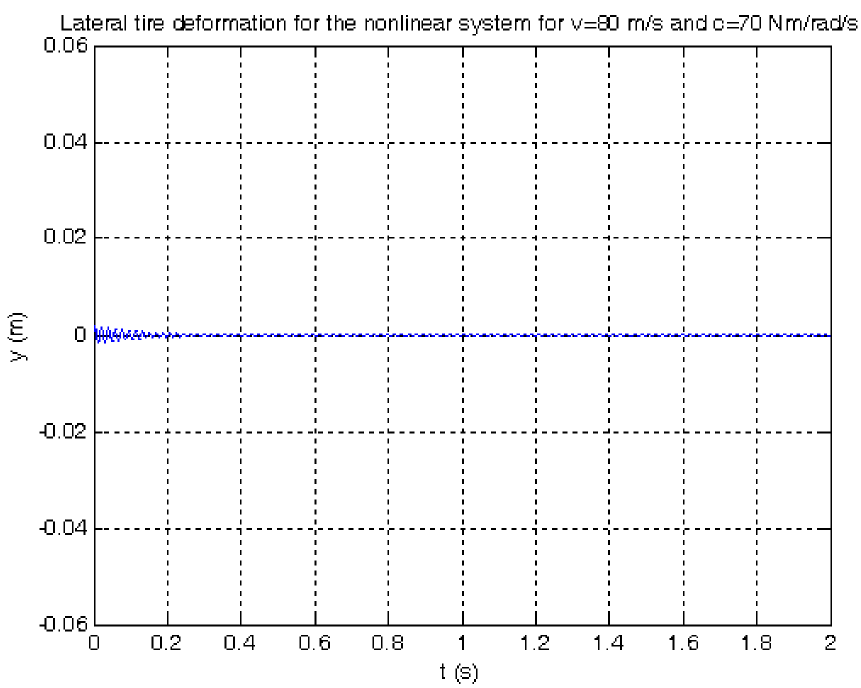

Figure 5.105: d. y for v =80 m/s, c =70 Nm/rad/s, $\psi(0)=0.01$ (nonlinear model).

Table 5.12: Limit cycle amplitudes of the torsion angle ψ, rate of change of the torsion angle $\dot{\psi}$ and lateral tire deformation y for v =80m/s and a varying damping coefficient c.

Velocity v **(m/s)**	**Torsional damping coefficient** c **(Nm/rad/s)**	**Torsion angle** ψ **(degrees)**	$\dot{\psi}$ **(degrees/s)**	**Lateral tire deformation** y **(m)**
80	10	16.6	5193.3	0.055
80	20	16.2	5200.1	0.054
80	30	13.1	4278.2	0.043
80	40	8.9	2982.7	0.029
80	50	0.57	190.4	0.0018
80	70	0.57	167.5	0.0018

5.9.4 Conclusions about the effect of the damping constant c on shimmy

- Tables 5.21 reveals that increasing the damping constant c decreases the limit cycle amplitudes of the torsion angle ψ, rate of change of the torsion angle $\dot{\psi}$ and the lateral tire deformation y.
- Simulation was performed for 1 s for lower values of c such as 10, 20, 30 and 40 Nm/rad/s, but for higher values of c such as 50 and 70 Nm/rad/s, 2 s were needed for the onset of the limit cycle.

5.9.5 Effect of the taxiing velocity v on shimmy

Taxiing velocity is one of the major parameters in a landing gear model and is always changing during the landing and take–off processes. In this section, effect of the taxiing velocity is observed by varying the taxiing velocity and keeping torsional damping constant.

For this purpose, phase plots of the yaw angle and time histories of the lateral tire deformation are obtained for a damping constant c of 30 Nm/rad/s, $\psi(0)=0.01$ and a varying taxiing velocity of 80, 70, 60, 50, 40 and 30 m/s. Lateral deflection of the tire and phase plots of the yaw angle are presented in figures 5.106–5.112.

It is shown that amplitudes of limit cycle oscillations are lower for lower taxiing velocities. Deflection of the tire also decreases by decreasing the taxiing velocity. This demonstrates that lower taxiing velocities lead to higher stability, as reported in literature. Amplitudes and frequencies of lateral tire deformation are presented in table 5.13.

Figure 5.106 shows the 3 and 2 dimensional limit cycles and time histories of the torsion angle and tire deformation for v =80 m/s, c =30 Nm/rad/s and $\psi(0) = 0.01$.

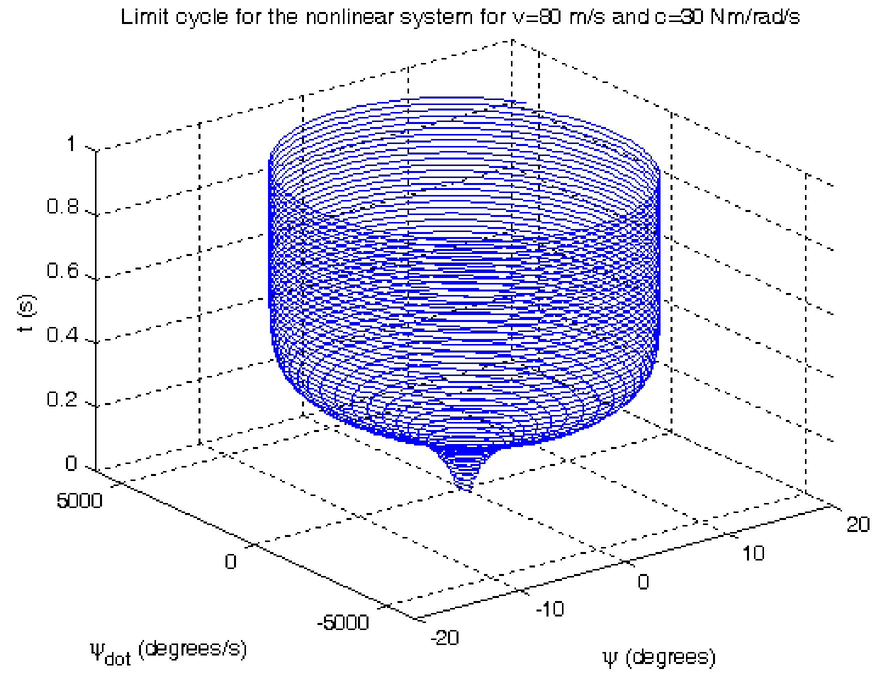

Figure 5.106: a. 3D limit cycle for v =80 m/s, c =30 Nm/rad/s and $\psi(0) = 0.01$.

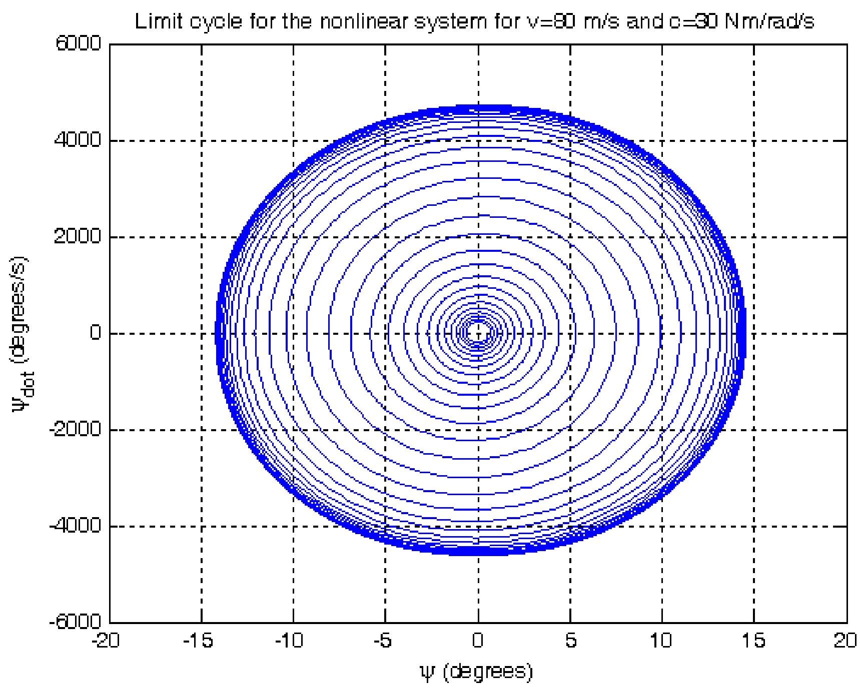

Figure 5.106: b. 2D limit cycle for v =80 m/s, c =30 Nm/rad/s and $\psi(0) = 0.01$.

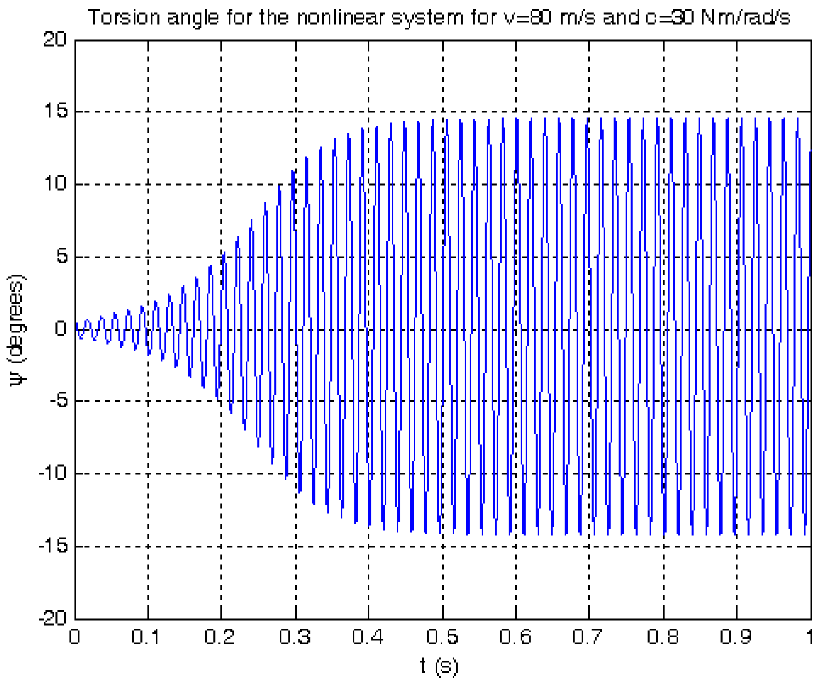

Figure 5.106: c. ψ for v =80 m/s, c =30 Nm/rad/s, $\psi(0)=0.01$ (nonlinear model).

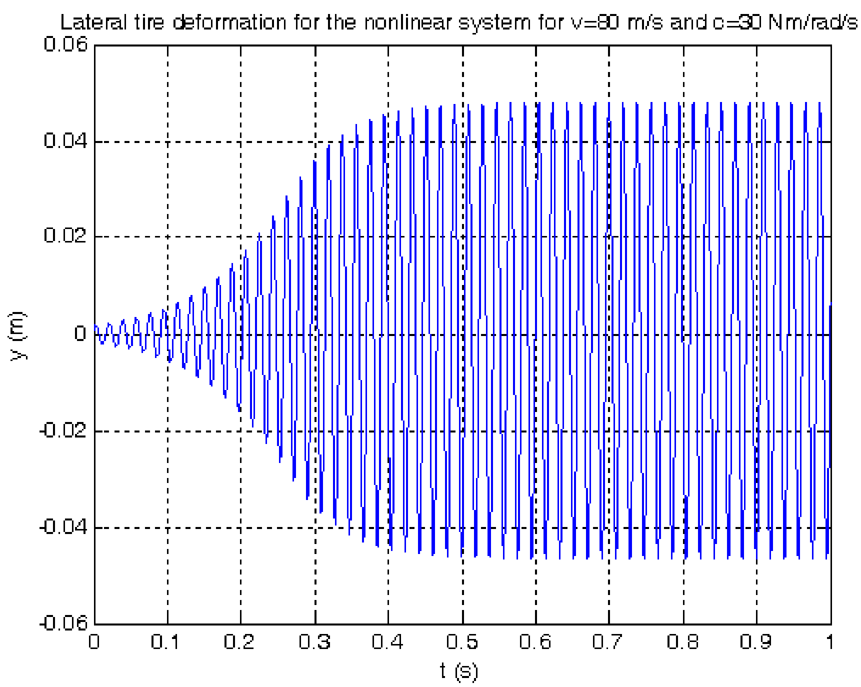

Figure 5.106: d. y for v =80 m/s, c =30 Nm/rad/s, $\psi(0)=0.01$ (nonlinear model).

Figure 5.107 shows the 3 and 2 dimensional limit cycles and time histories of the torsion angle and tire deformation for v =70 m/s, c =30 Nm/rad/s and $\psi(0)=0.01$.

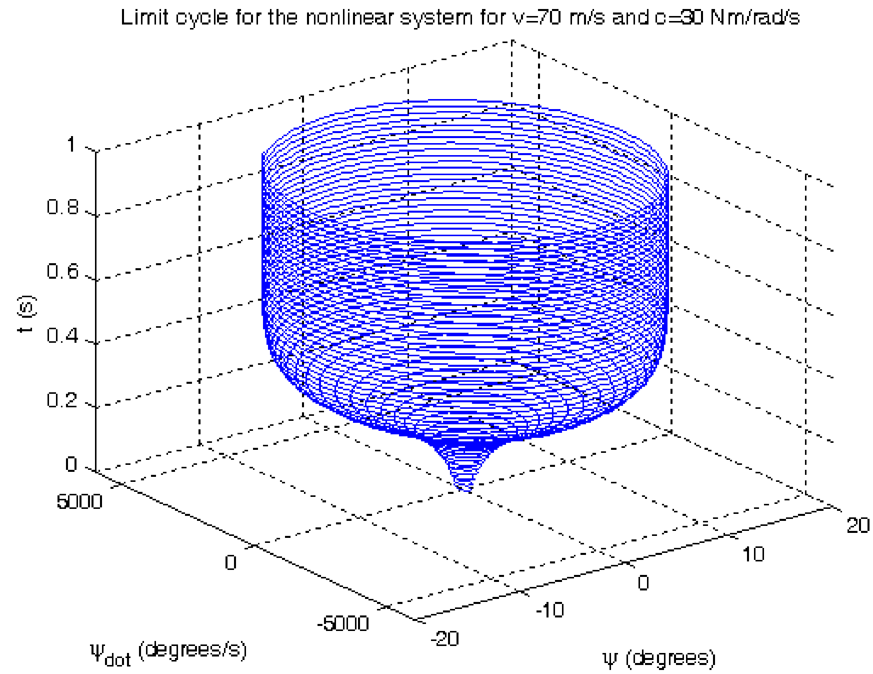

Figure 5.107: a. 3D limit cycle for v =70 m/s, c =30 Nm/rad/s and $\psi(0) = 0.01$.

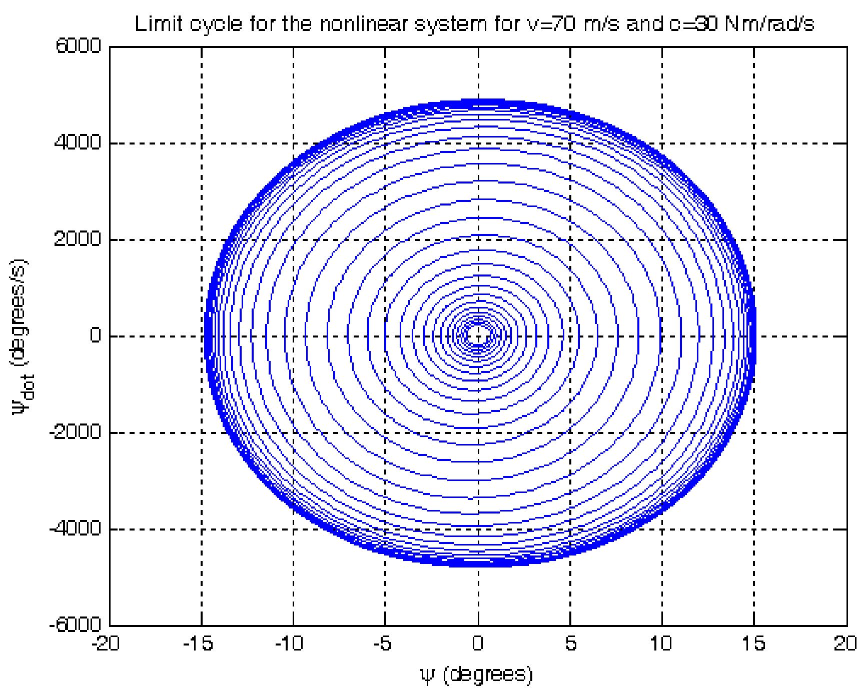

Figure 5.107: b. 2D limit cycle for v =70 m/s, c =30 Nm/rad/s and $\psi(0) = 0.01$.

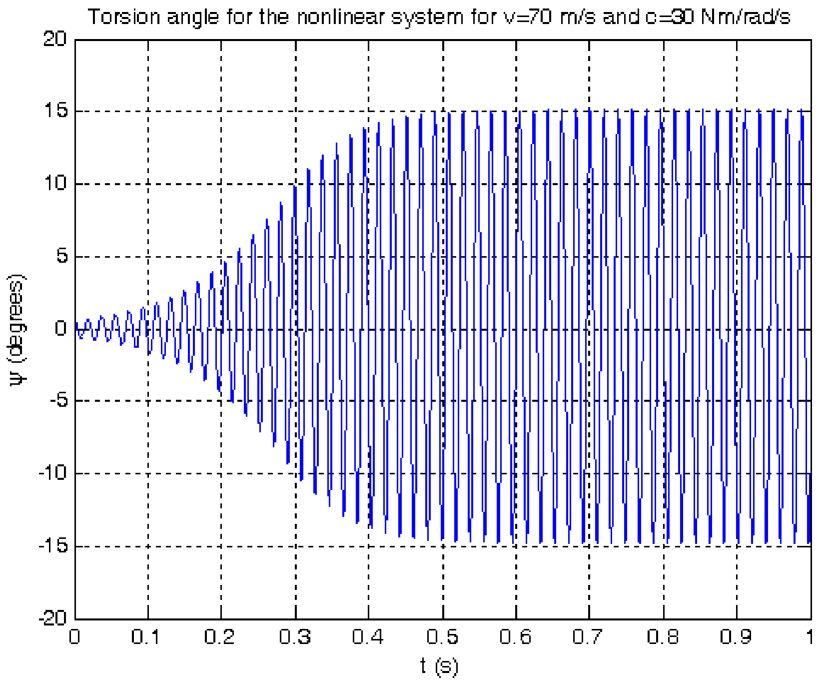

Figure 5.107: c. ψ for v =70 m/s, c =30 Nm/rad/s, $\psi(0)=0.01$ (nonlinear model).

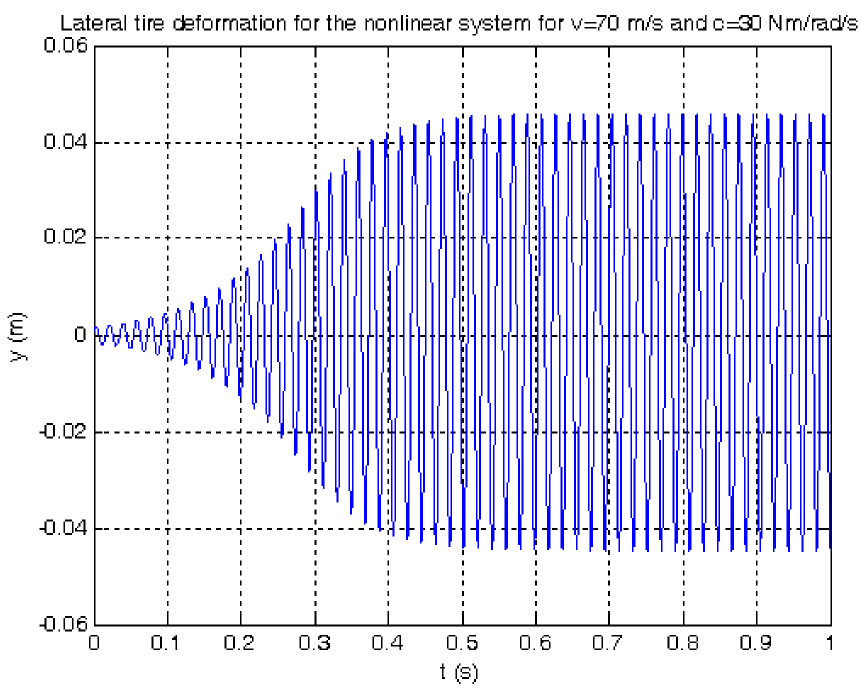

Figure 5.107: d. y for v =70 m/s, c =30 Nm/rad/s, $\psi(0)=0.01$ (nonlinear model).

Figure 5.108 shows the 3 and 2 dimensional limit cycles and time histories of the torsion angle and tire deformation for v =60 m/s, c =30 Nm/rad/s and $\psi(0)=0.01$.

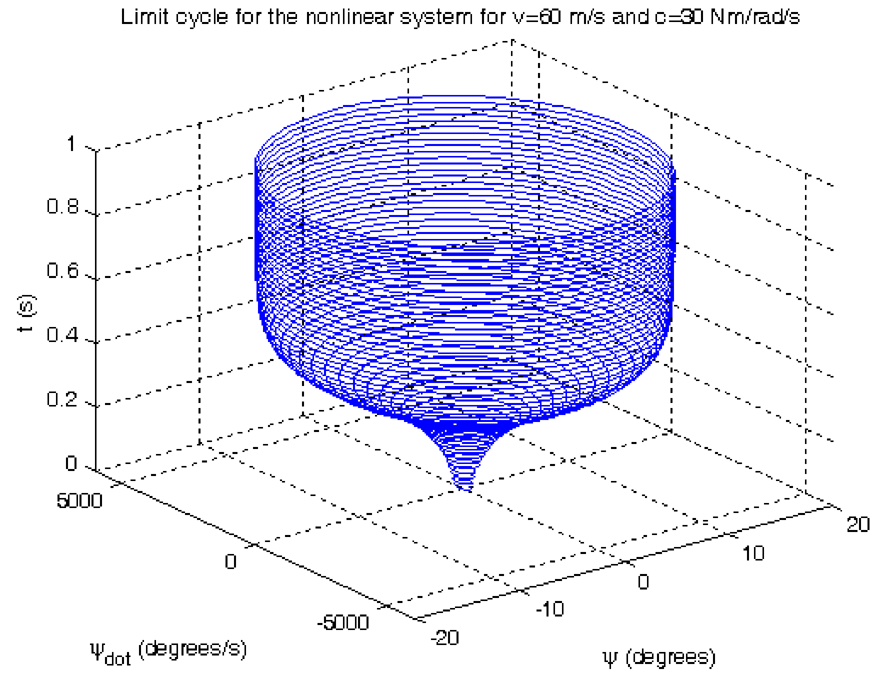

Figure 5.108: a. 3D limit cycle for v =60 m/s, c =30 Nm/rad/s and $\psi(0) = 0.01$.

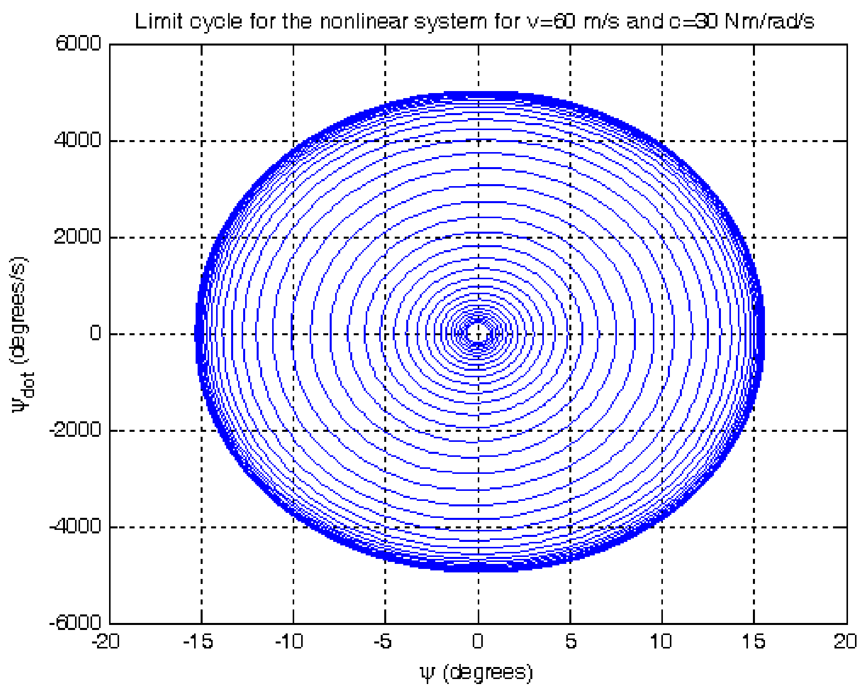

Figure 5.108: b. 2D limit cycle for v =60 m/s, c =30 Nm/rad/s and $\psi(0) = 0.01$.

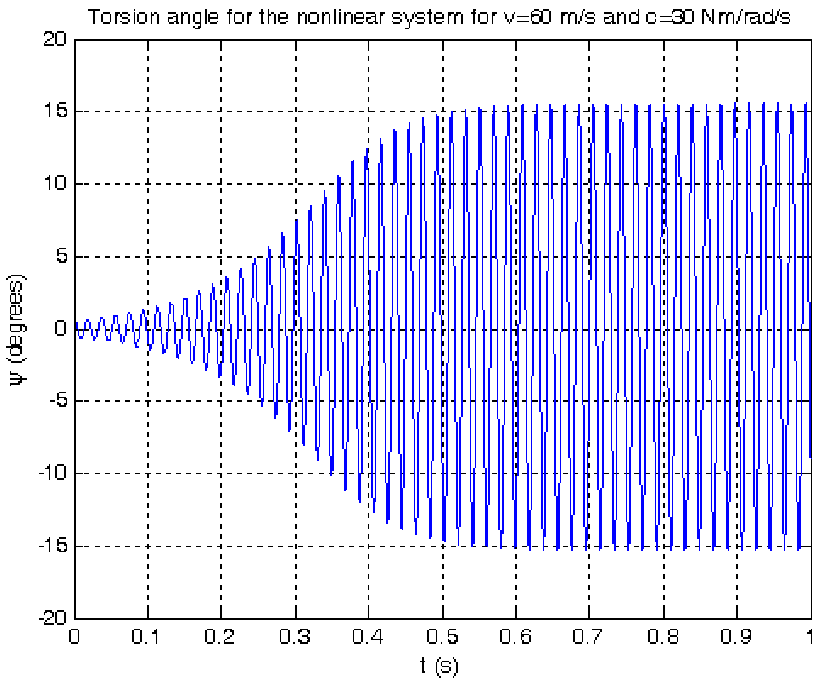

Figure 5.108: c. ψ for v =60 m/s, c =30 Nm/rad/s, $\psi(0)=0.01$ (nonlinear model).

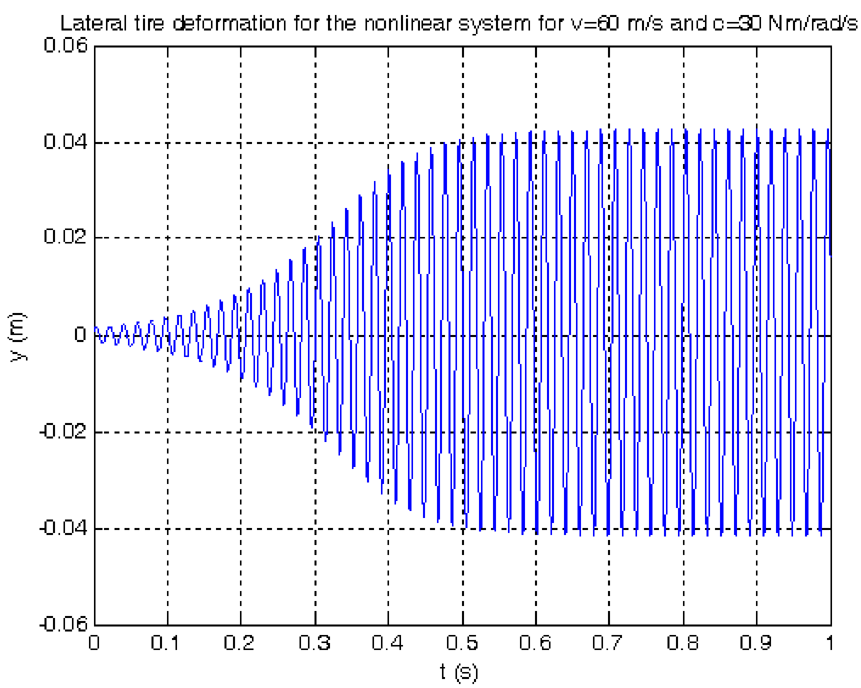

Figure 5.108: d. y for v =60 m/s, c =30 Nm/rad/s, $\psi(0)=0.01$ (nonlinear model).

Figure 5.109 shows the 3 and 2 dimensional limit cycles and time histories of the torsion angle and tire deformation for v =50 m/s, c =30 Nm/rad/s and $\psi(0)=0.01$.

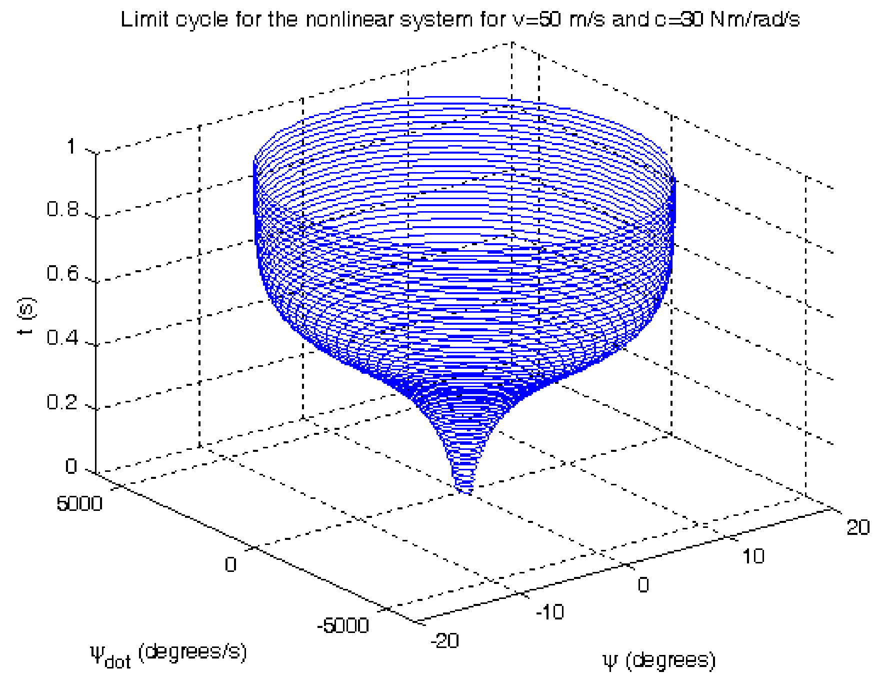

Figure 5.109: a. 3D limit cycle for v =50 m/s, c =30 Nm/rad/s and $\psi(0) = 0.01$.

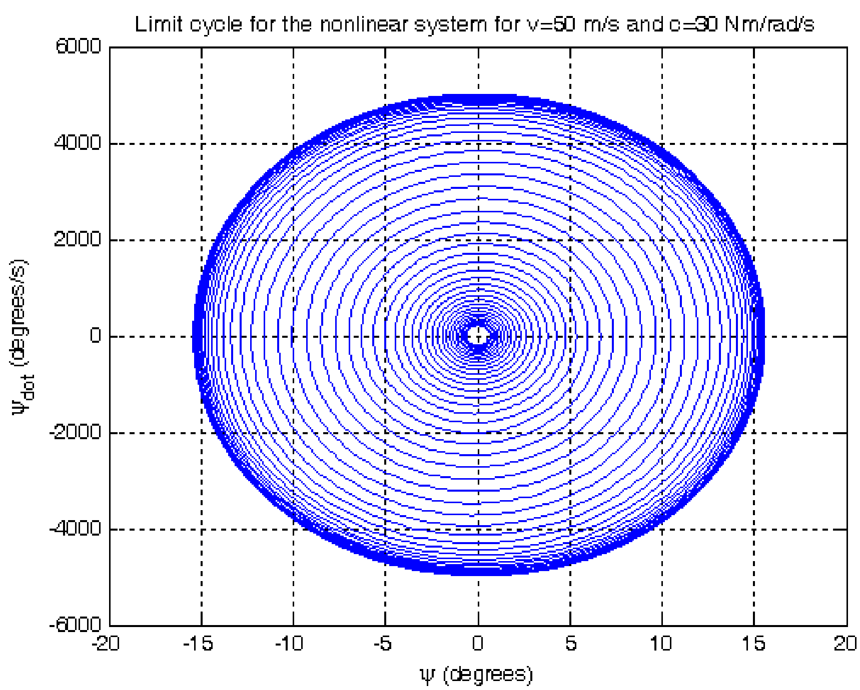

Figure 5.109: b. 2D limit cycle for v =50 m/s, c =30 Nm/rad/s and $\psi(0) = 0.01$.

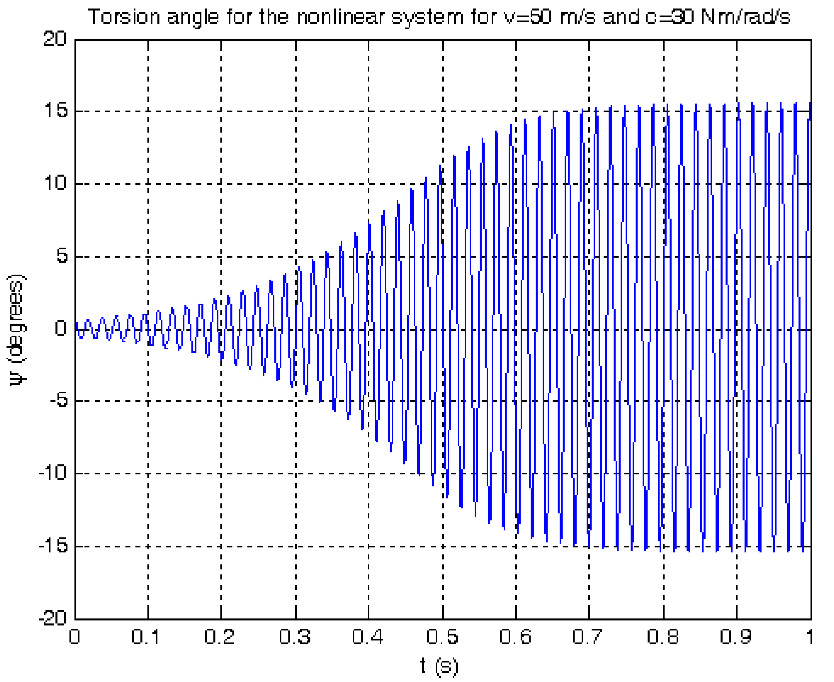

Figure 5.109: c. ψ for v =50 m/s, c =30 Nm/rad/s, $\psi(0)=0.01$ (nonlinear model).

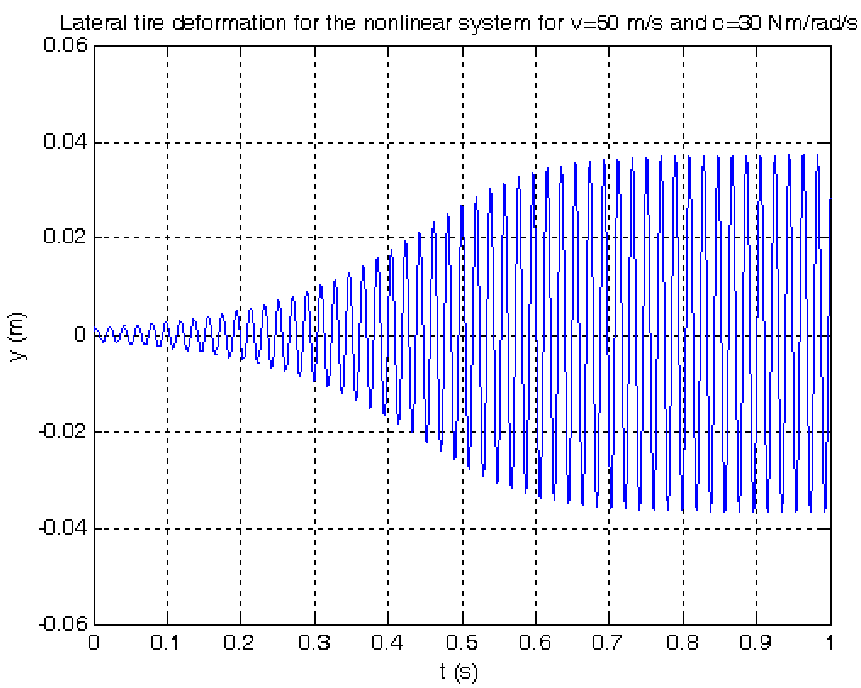

Figure 5.109: d. y for v =50 m/s, c =30 Nm/rad/s, $\psi(0)=0.01$ (nonlinear model).

Figure 5.110 shows the 3 and 2 dimensional limit cycles and time histories of the torsion angle and tire deformation for v =40 m/s, c =30 Nm/rad/s and $\psi(0)=0.01$.

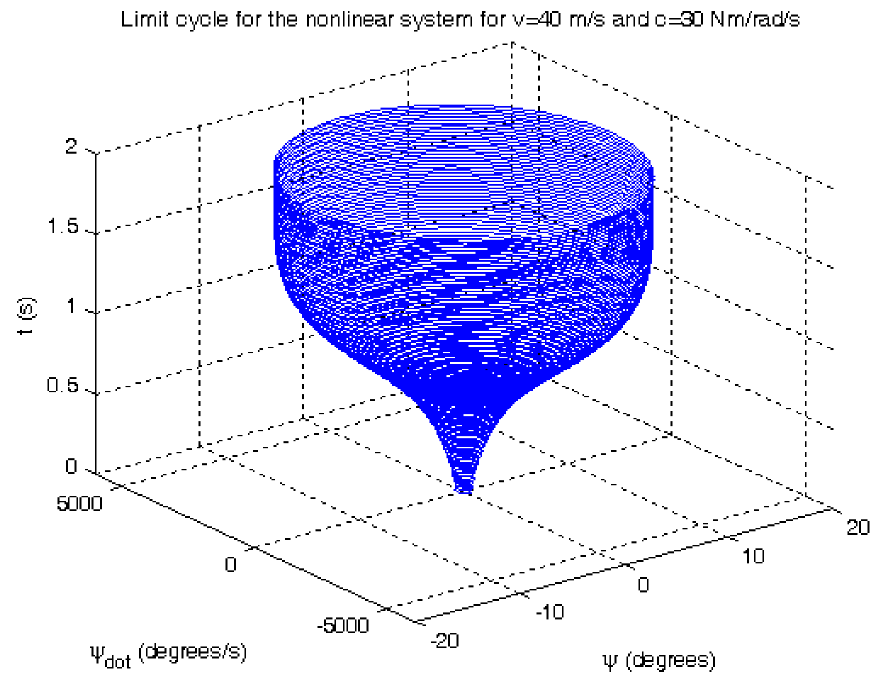

Figure 5.110: a. 3D limit cycle for v =40 m/s, c =30 Nm/rad/s and $\psi(0) = 0.01$.

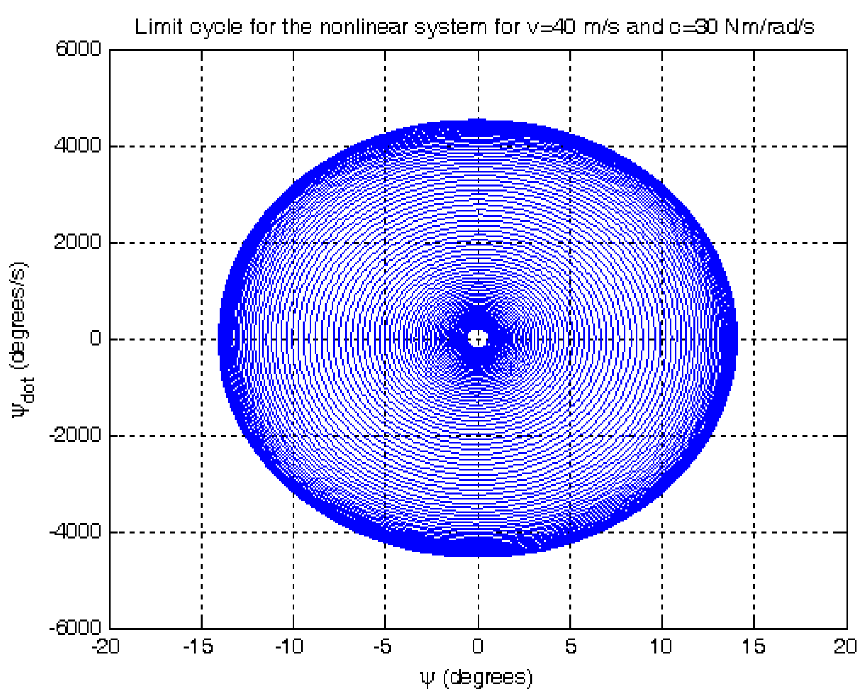

Figure 5.110: b. 2D limit cycle for v =40 m/s, c =30 Nm/rad/s and $\psi(0) = 0.01$.

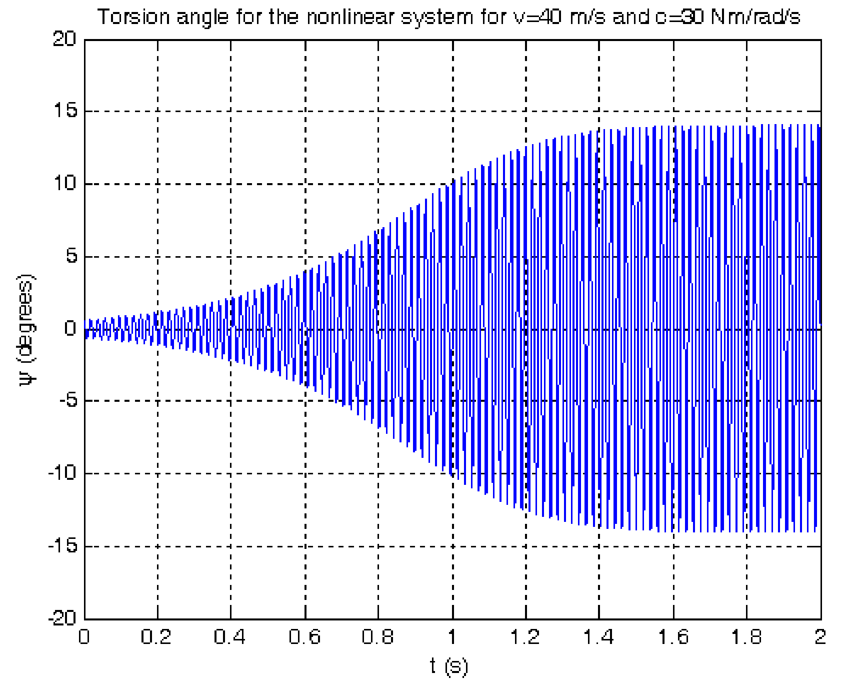

Figure 5.110: c. ψ for v =40 m/s, c =30 Nm/rad/s, $\psi(0) = 0.01$ (nonlinear model).

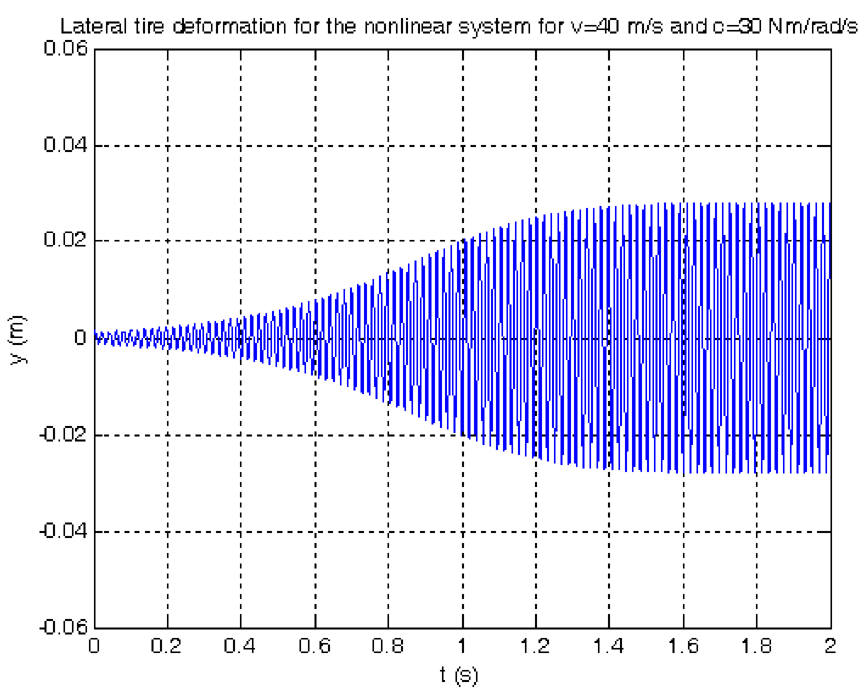

Figure 5.110: d. y for v =40 m/s, c =30 Nm/rad/s, $\psi(0) = 0.01$ (nonlinear model).

Figure 5.111 shows the 3 and 2 dimensional limit cycles and time histories of the torsion angle and tire deformation for v =30 m/s, c =30 Nm/rad/s and $\psi(0) = 0.01$.

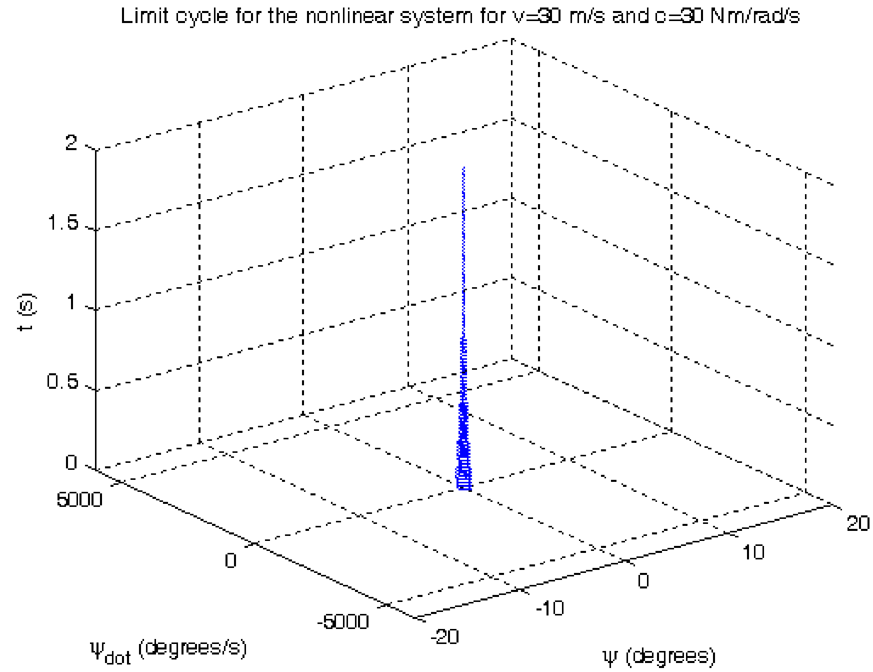

Figure 5.111: a. 3D limit cycle for v =30 m/s, c =30 Nm/rad/s and $\psi(0) = 0.01$.

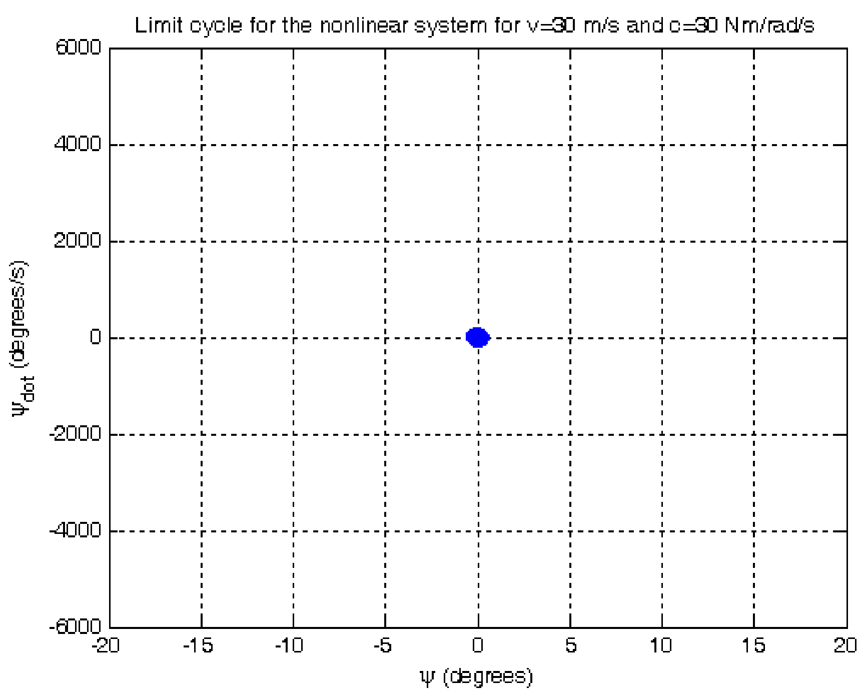

Figure 5.111: b. 2D limit cycle for v =30 m/s, c =30 Nm/rad/s and $\psi(0) = 0.01$.

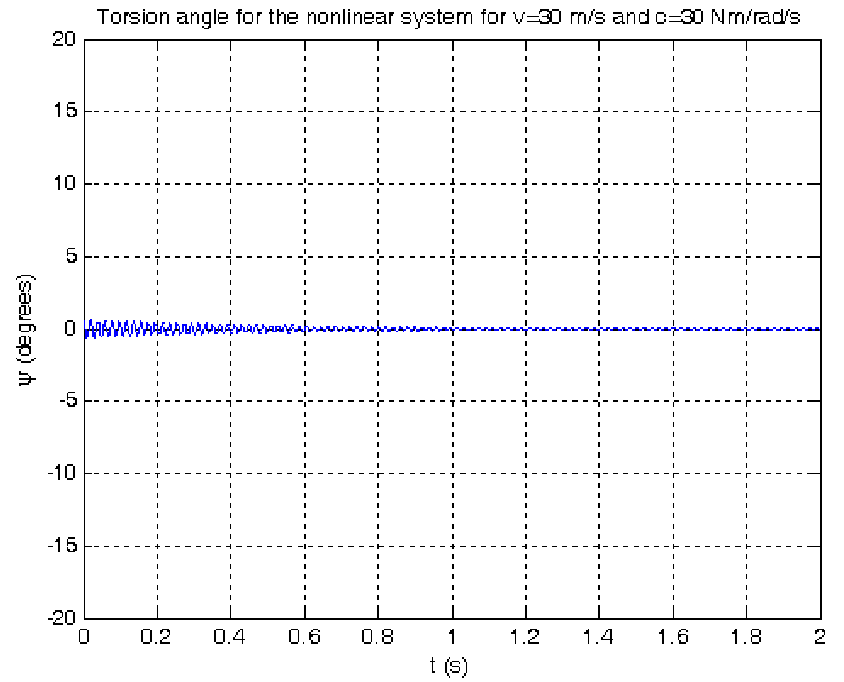

Figure 5.111: c. ψ for v =30 m/s, c =30 Nm/rad/s, $\psi(0) = 0.01$ (nonlinear model).

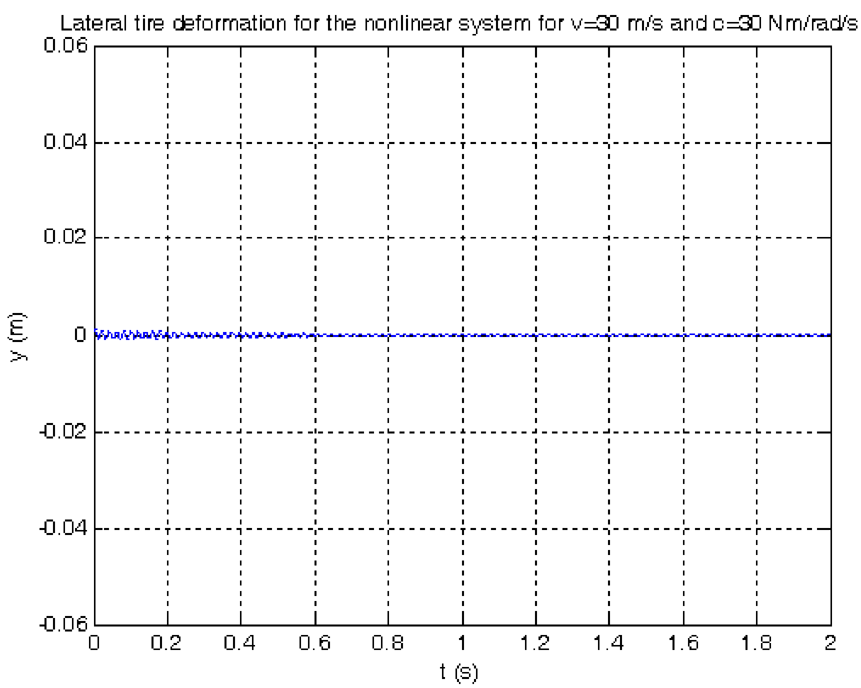

Figure 5.111: d. y for v =30 m/s, c =30 Nm/rad/s, $\psi(0) = 0.01$ (nonlinear model).

Table 5.13: Limit cycle amplitudes of the torsion angle ψ **,** rate of change of the torsion angle $\dot{\psi}$ and lateral tire deformation y for c =30Nm/rad/s and a varying taxiing velocity v .

Velocity v **(m/s)**	**Torsional damping coefficient** c **(Nm/rad/s)**	**Torsion angle** ψ **(degrees)**	$\dot{\psi}$ **(degrees/s)**	**Lateral tire deformation** y **(m)**
80	30	13.1	4278.2	0.043
70	30	13.5	4401.7	0.041
60	30	13.7	4460.3	0.037
50	30	13.0	4230.8	0.031
40	30	1.98	640.8	0.004
30	30	0.57	189.0	0.0014

5.9.6 Conclusions about the effect of the taxiing velocity v on shimmy

- Table 5.13 reveals that decreasing the taxiing velocity v decreases the limit cycle amplitudes of the torsion angle ψ , rate of change of the torsion angle $\dot{\psi}$ and the lateral tire deformation y .
- Simulation was performed for 1 s for higher values of v such as 80, 70, 60 and 50 m/s, but for lower values of v such as 40 and 30 m/s, 2 s were needed for the onset of the limit cycle.

6. FREEPLAY

6.1 Definition of Freeplay

Freeplay is a type of concentrated structural nonlinearity inherent in many mechanical systems. It exists in the hinge part of the control surfaces of most flight vehicles and is generated from loose or worn hinge connections, joint slippage and manufacturing tolerances.

Freeplay is hard to avoid in loose or old joints. Its existence may affect the system response, however harmful results can be avoided if possible limit cycle oscillations are known in advance. Therefore, it is important to determine the possibility of the existence of such motions before they occur [88–90].

Freeplay may cause limit cycle oscillations during flight, leading to structural damage due to fatigue. Thus, it is crucial to incorporate freeplay into the equations of motion and to predict its effects in advance.

Cyclic loading occurs during taxi due to runway surface irregularities, which may lead to wear in mechanical components of the landing gear, including freeplay in the steering system, interlinkages of the torque link, fuselage attachment points, steering collar and wheel axle [45].

Freeplay will increase with the number of flights. Application of tight tolerances might help in solving shimmy problems in the prototype phase, however, the problem will reoccur when the aircraft is in service, due to wear [1].

Various parts of the landing gear move with respect to each other during landing impact and when retracted. Freeplay at the wheel axle due to the contributions from various connections are less than one degree in yaw and in the order of millimeters in the lateral and fore/aft directions.

Freeplay will have an effect on the response of the system to a control law designed for the linear model [91]. Although freeplay is often linearized or ignored in calculations, it is necessary to compare the responses of the systems with and without freeplay. Amount of freeplay present in the studies in literature are in the range 0.1º–2.12º.

Most of the literature considering the effect of freeplay concentrates on problems of aeroelasticity. Missile control surfaces, moveable aircraft lifting surfaces such as horizontal tails or rotatable pylons on aircraft with variable sweep exhibit freeplay that can be potentially dangerous from an aeroelastic perspective, in terms of flutter conditions.

Additionally, freeplay may cause instabilities both above and below the flutter speed predicted by the linear theory. Responses to freeplay include nonlinear phenomena such as limit cycle oscillations and even chaotic responses. Limit cycle oscillations are likely to occur in the presence of freeplay nonlinearities, leading to fatigue and damage in the long run. The possibility of even small freeplay angles leading to severe instabilities dangerous fatigue conditions are shown in literature [88–90,92–95].

Concentrated structural nonlinearities, such as cubic, freeplay and hysteresis stiffnesses, have significant effects on aeroelastic responses of airfoil surfaces. Freeplay gives the most critical flutter condition among the three and is inevitable for control surfaces due to wear and manufacturing errors.

6.2 Literature Survey on Freeplay

A literature survey on freeplay reveals that freeplay has been investigated much, mostly by researchers working on the fluid–structure interaction problem. A few researchers have studied freeplay in control surface hinges.

Freeplay has been incorporated into the equations of motion of landing gear mechanisms in very few studies literature. Dynamics of a landing gear mechanism with torsional and lateral degrees of freedom and freeplay in the torsional degree of freedom is analyzed in [45]. Unfortunately, data on the geometry and structure of the landing gear employed in the study have not been presented.

Hinges of control surfaces often demonstrate freeplay nonlinearity. [96] is a study examining the limit cycle oscillations of a combination of an airfoil and an aileron, resulting in three degrees of freedom, with freeplay in the aileron hinge. Aeroelastic response of other two dimensional systems having control surface freeplay nonlinearity are studied using the harmonic balance approach in [97] and both numerically and experimentally in [91].

A three dimensional control surface with freeplay is investigated in [98] to demonstrate the effects of angle of attack and Mach number. Flutter analysis of a missile wing having freeplay in it the rotation degree of freedom of the wing control mechanism is conducted in [90] by investigating limit cycles and chaotic motion. Results state that the system response depends on the amount of freeplay and initial conditions.

A study on a mechanical system exhibiting freeplay nonlinearity is studied both numerically and experimentally in [94] where the problem of developing a mathematical model and performing a simulation of the dynamics of systems exhibiting freeplay nonlinearity is addressed. Contact due to freeplay is considered, constraints are formulized and the stability of an aircraft wing displaying freeplay in the hinge supporting a control surface is investigated. Freeplay is considered as one of the rotor faults in the simulation of helicopter structural damages in [99].

A dissertation was presented to Duke University in 2000, covering the dynamics of a two dimensional aeroelastic system with control surface freeplay nonlinearity, both experimentally and mathematically, where limit cycle oscillations are observed [100]. The system is very similar to the one given in [96], a combination of an airfoil with an aileron.

Flutter analysis of airfoils with freeplay nonlinearities in pitch degree of freedom subject to incompressible flow have gained some attention. Limit cycle oscillations of airfoils having two degrees of freedom and freeplay nonlinearities in pitch, placed in transonic and supersonic flows are investigated in [88] and [89], respectively. Similar numerical studies investigating the same model are [101], where the model is placed in subsonic and transonic flows, [95], where the model is placed in transonic and low supersonic flows, and [102], where the model is placed in turbulent flow. Bifurcation analysis of the same system with two degrees of freedom is conducted in [103].

Mathematical analysis of the behavior of a two dimensional aeroelastic system with freeplay nonlinearity is presented in [104] and two formulations are developed. Formulations are extended to a hysteresis model in [105].

Bifurcation analysis an airfoil having two degrees of freedom with both freeplay and cubic stiffness nonlinearities in pitch placed in supersonic flow has been conducted in [93]. Bifurcation analysis of an aircraft with freeplay nonlinearity is conducted in [106]. Limit cycle oscillations of an airfoil with two degrees of freedom having freeplay in the pitching degree of freedom are examined experimentally and theoretically in [92]. An experimental delta wing model with freeplay at the attachment points is designed and tested in [107], and its gust response is investigated in [108]. Effect of freeplay on the aerodynamic response, such as limit cycle flutter, has been examined. It has been found that the amplitude and position of the limit cycle varies with the magnitude of freeplay. Effects of variations in parameters have been examined for both the damped and limit cycle oscillations. Critical flutter speeds are predicted.

6.3 Modeling of Freeplay

Freeplay model used in this study is based on the ones in [45] and [88]. Freeplay nonlinearity in both studies are modeled using the same principle and formulation, although the two studies are in two very distinct disciplines. Same formulation as in [88] is employed in [98,101], and mathematical models given in [89,90,93,95,96,102,103,104] are also similar .

Freeplay is modeled as a nonlinear spring as in figure 6.1, where some deflection is possible before a force develops and the spring force is zero if the amplitude remains within the freeplay band. Formulations have been suggested in literature to determine an equivalent linear stiffness.

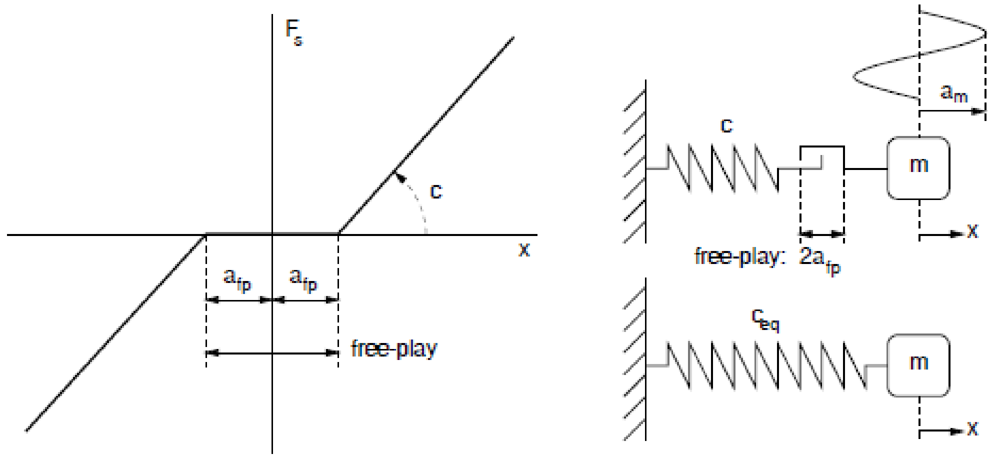

Figure 6.1:. Modeling of freeplay [11].

Freeplay nonlinearity causes structural stiffness to become piecewise continuous. Equation (6.1) gives the piecewise continuous restoring moment function that describes the concentrated nonlinearity at the torsional degree of freedom.

$$M(\psi) = \begin{cases} k(\psi - \psi_{fp}) & \text{if } \psi \geq \psi_{fp} \\ 0 & \text{if } -\psi_{fp} \leq \psi \leq \psi_{fp} \\ k(\psi + \psi_{fp}) & \text{if } \psi \leq -\psi_{fp} \end{cases} \tag{6.1}$$

where k is the torsional spring rate and ψ_{fp} is the freeplay angle.

6.4 Incorporation of Freeplay into the Torsional Landing Gear Model

In this ection, torsional freeplay is incorporated into the equations of motion of the landing gear. Results are displayed for various values of the freeplay angle ψ_{fp} within the range 0º–2º, as this is the range employed in literature.

Freeplay model given in (6.1) can be incorporated in the equations of motion in two ways. One of them, is to linearize the model as in (5.23)–(5.28) and substitute $M(\psi)$ given by (6.1) into $k\psi$. This way, the only nonlinearity in the model is freeplay nonlinearity such that the second equation in (5.23) becomes

$$\ddot{\psi} = \frac{M(\psi)}{I_z} + c_2\dot{\psi} + c_3 y \tag{6.2}$$

Second way of incorporating freeplay nonlinearity in the model is to obtain a more realistic model by substituting (6.1) directly into the nonlinear model. This is accomplished by replacing the linear spring moment M_1 given in (5.2) by the freeplay term given in (6.1) and this is the approach taken in this study.

$$I_z\ddot{\psi} + M(\psi) + M_2 + M_3 + M_4 = 0 \qquad \textbf{(6.3)}$$

(5.13), equation describing the lateral tire dynamics and (5.17), equation describing the equivalent slip angle, remain unchanged.

Thus, equations (6.3), (5.13) and (5.17) describe the dynamics of the torsional landing gear model with freeplay.

6.5 Effect of Freeplay on the Torsion Angle, Lateral Tire Deformation and Limit Cycles

Equations (6.3), (5.13) and (5.17) will be solved to observe the effect of freeplay on the torsion angle, lateral tire deformation and limit cycles. Freeplay angles of 0º, 0.5º, 1º and 1.5º have been incorporated in the numerical computations.

It has been observed that the existence of freeplay contributes to an increase in the amplitude of the torsion angle ψ and lateral tire deformation y. It has also been observed that an aircraft having torsional freeplay in its landing gear becomes less susceptible to shimmy if its velocity increases.

6.5.1 Effect of freeplay on the torsion angle ψ

Time histories of the torsion angle are presented for a taxiing velocity v of 50 m/s and freeplay angles of 0º, 0.5º, 1º and 1.5º in figures 6.2–6.5 for $\psi(0) = 0.01$ and in figures 6.6–6.9 for $\psi(0) = 0.1$. Time histories are also obtained for a taxiing velocity of 80 m/s and the same freeplay angles to see the effect of taxiing velocity on shimmy characteristics in the existence of freeplay, in figures 6.10–6.12 for $\psi(0) = 0.1$.

Amplitude and frequency of the torsion angle ψ with varying ψ_{fp} are presented in table 6.1 for $\psi(0) = 0.01$ and in table 6.2 for $\psi(0) = 0.1$.

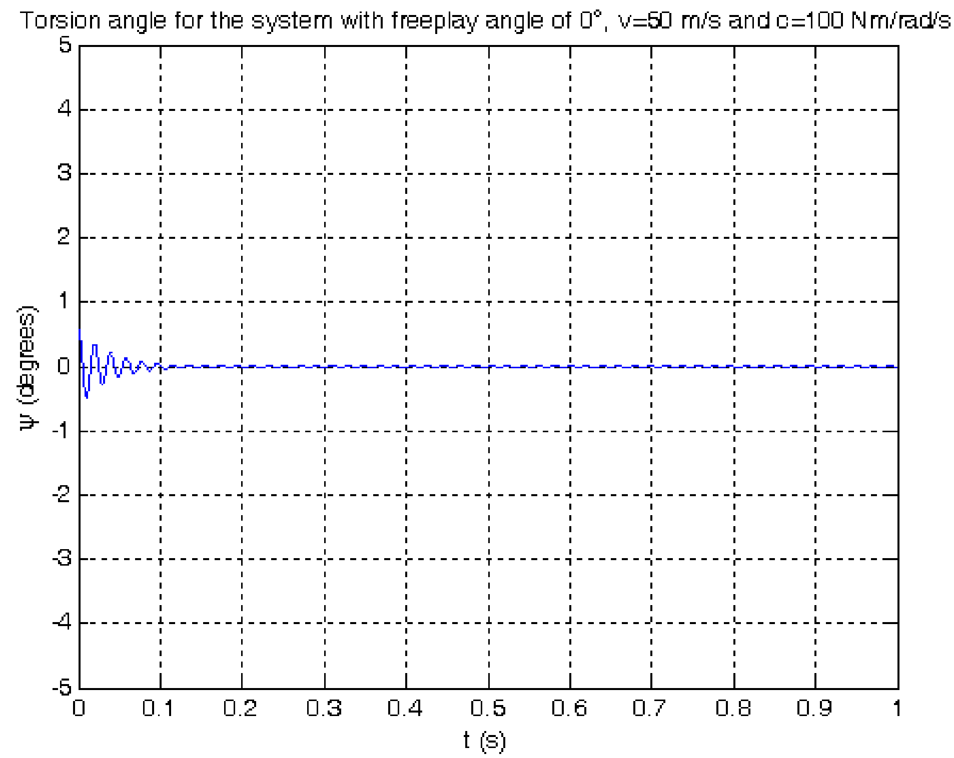

Figure 6.2: ψ for ψ_{fp} =0°, v =50 m/s, c =100 Nm/rad/s and $\psi(0) = 0.01$.

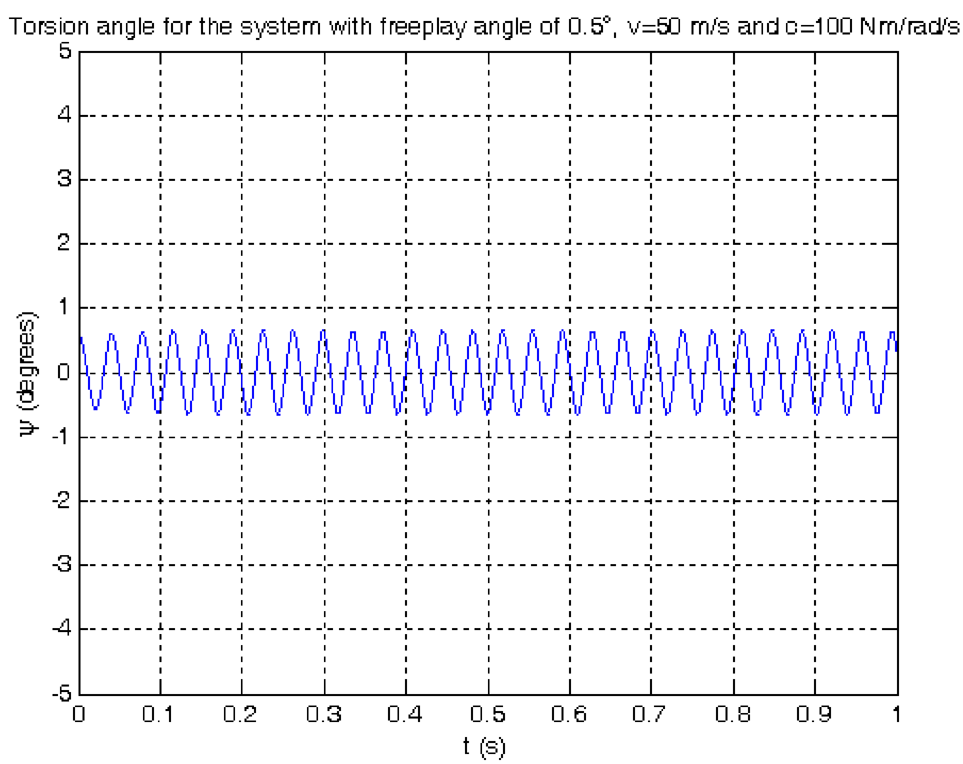

Figure 6.3: ψ for ψ_{fp} =0.5°, v =50 m/s, c =100 Nm/rad/s and $\psi(0) = 0.01$.

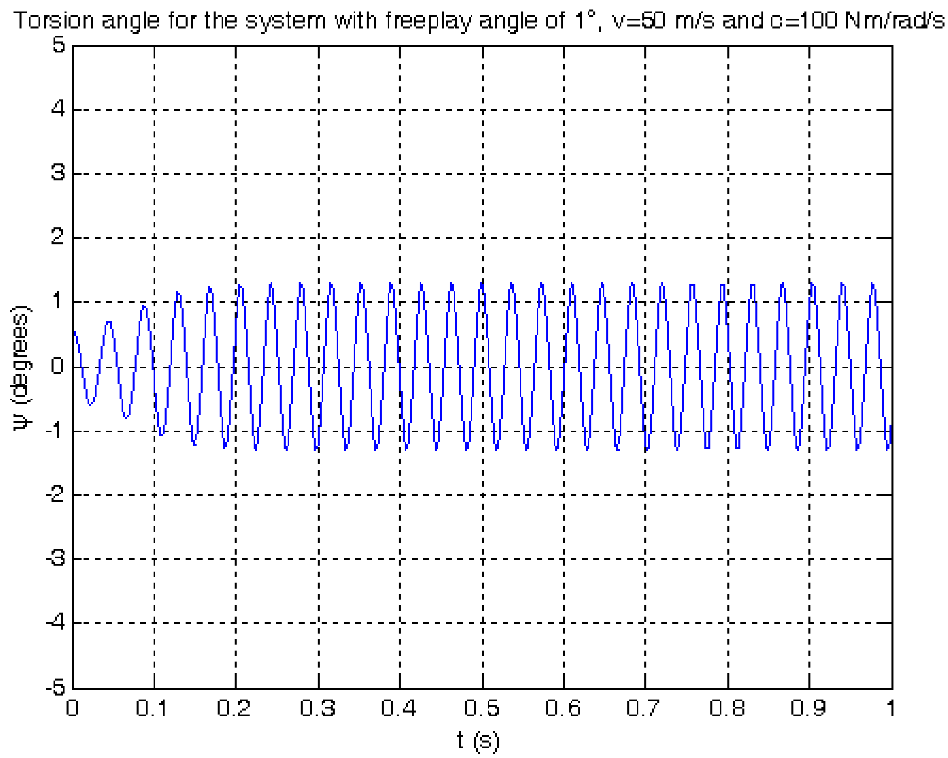

Figure 6.4: ψ for ψ_{fp} =1°, v =50 m/s, c =100 Nm/rad/s and $\psi(0) = 0.01$.

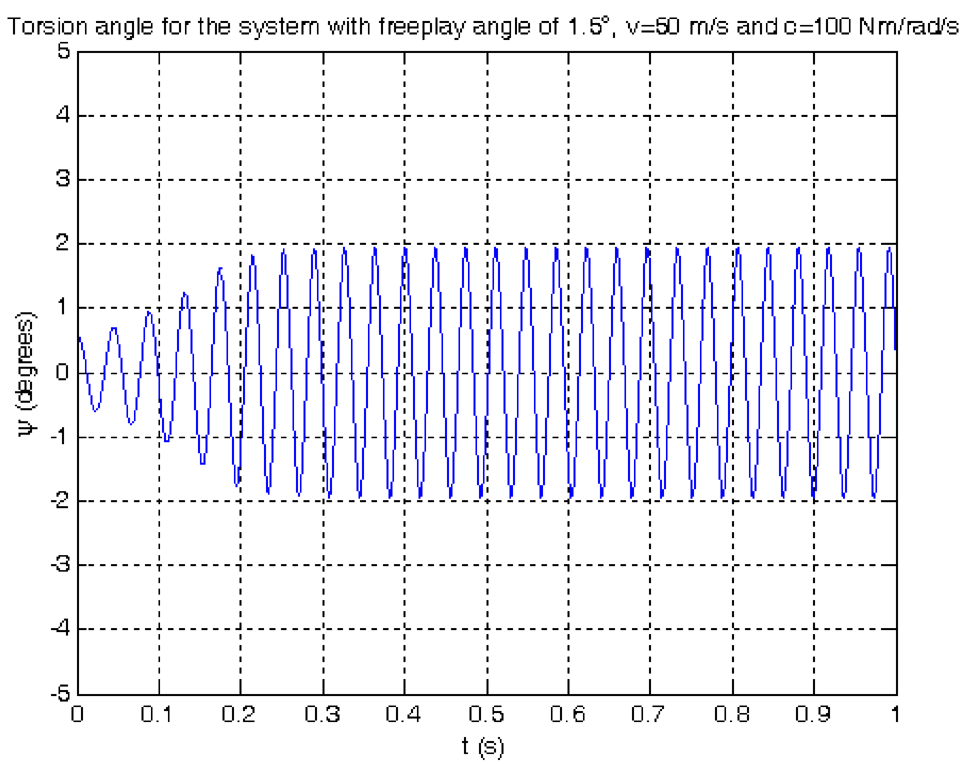

Figure 6.5: ψ for ψ_{fp} =1.5°, v =50 m/s, c =100 Nm/rad/s and $\psi(0) = 0.01$.

Table 6.1: Effect of freeplay angle ψ_{fp} on the amplitude of the torsion angle ψ for v =50 m/s, c =100 Nm/rad/s and $\psi(0) = 0.01$.

velocity v (m/s)	**ψ_{fp} (degrees)**	**limit cycle amplitude of ψ (degrees)**
50	0	oscillation is damped in 0.1 s
	0.5	0.65
	1	1.30
	1.5	1.94

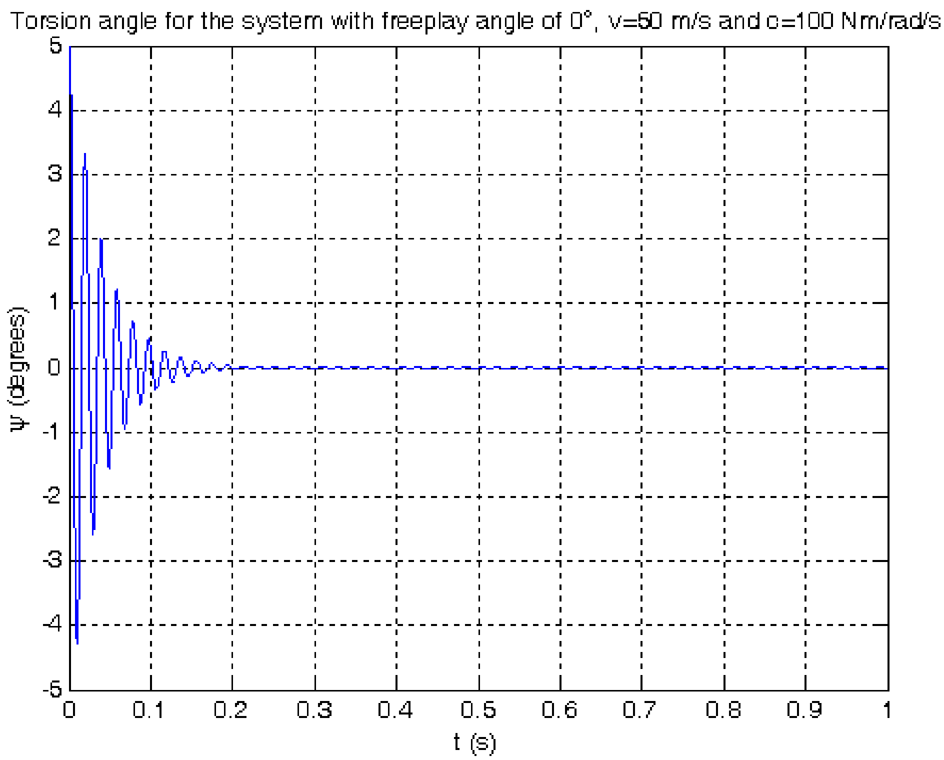

Figure 6.6: ψ for ψ_{fp} =0°, v =50 m/s, c =100 Nm/rad/s and $\psi(0) = 0.1$.

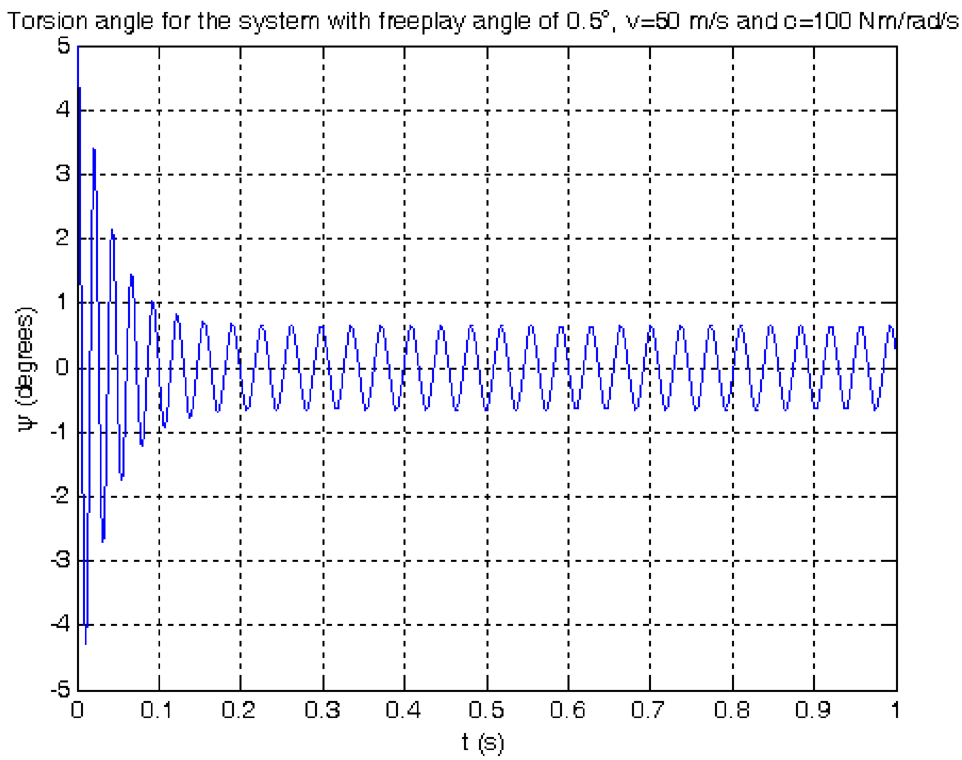

Figure 6.7: ψ for ψ_{fp} =0.5°, v =50 m/s, c =100 Nm/rad/s and $\psi(0) = 0.1$.

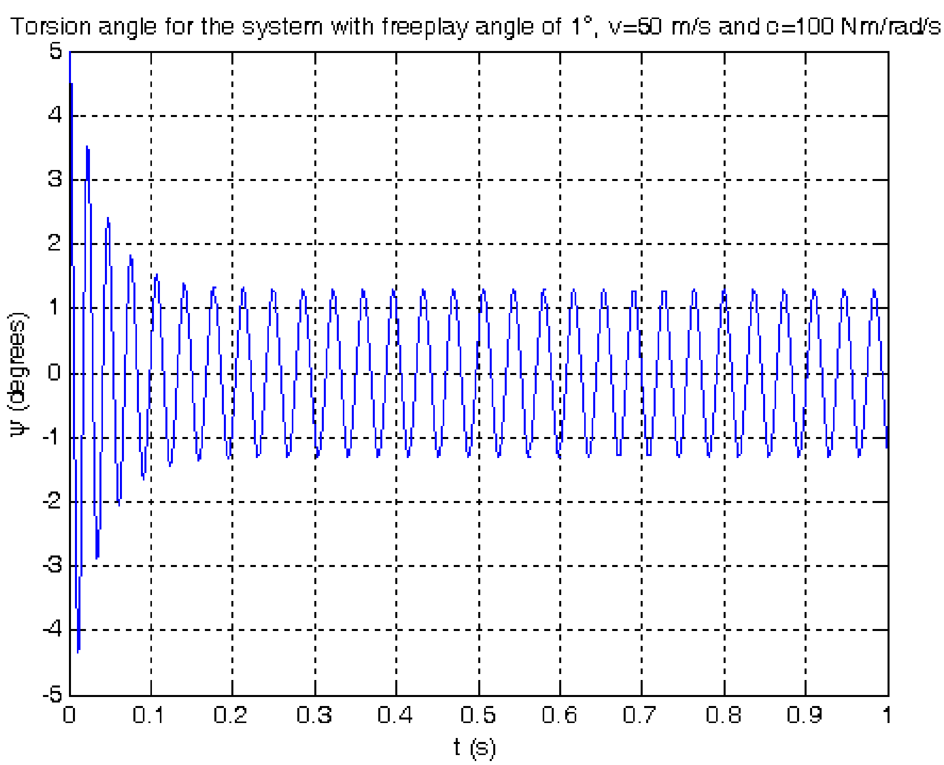

Figure 6.8: ψ for ψ_{fp} =1°, v =50 m/s, c =100 Nm/rad/s and $\psi(0) = 0.1$.

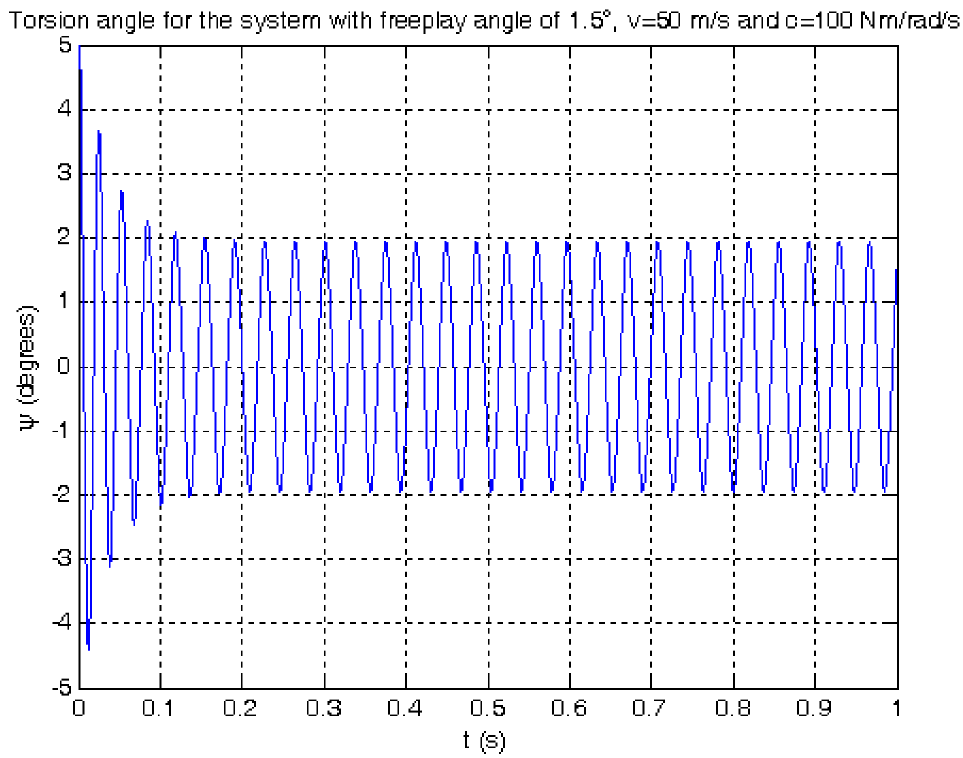

Figure 6.9: ψ for ψ_{fp} =1.5°, v =50 m/s, c =100 Nm/rad/s and $\psi(0) = 0.1$.

Table 6.2: Effect of freeplay angle ψ_{fp} on the amplitude of the torsion angle ψ for v =50 m/s, c =100 Nm/rad/s and $\psi(0) = 0.1$.

velocity	ψ_{fp} **(degrees)**	**limit cycle amplitude of** ψ **(degrees)**
50	0	oscillation decays in 0.1 s
	0.5	0.65
	1	1.30
	1.5	1.94

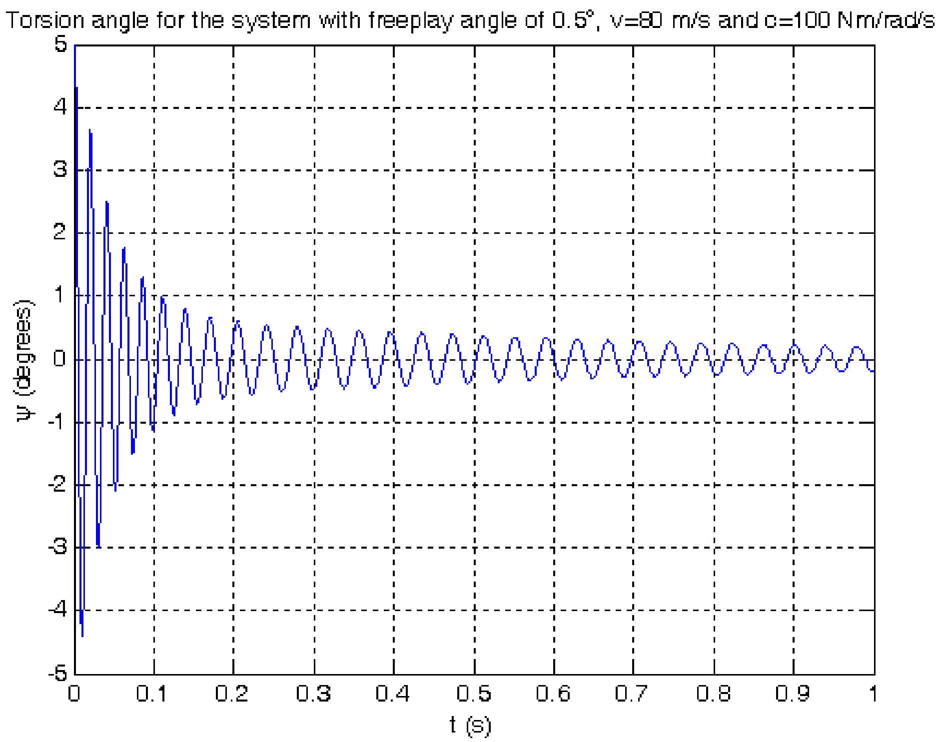

Figure 6.10: ψ for ψ_{fp} =0.5°, v =80 m/s, c =100 Nm/rad/s and $\psi(0) = 0.1$.

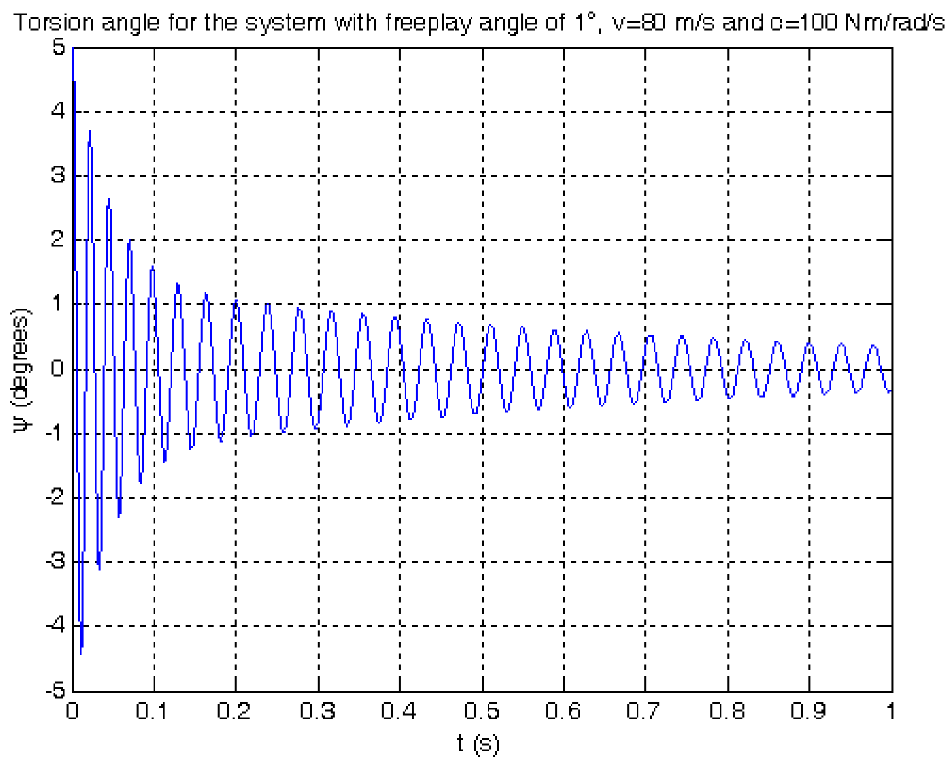

Figure 6.11: ψ for ψ_{fp} =1°, v =80 m/s, c =100 Nm/rad/s and $\psi(0) = 0.1$.

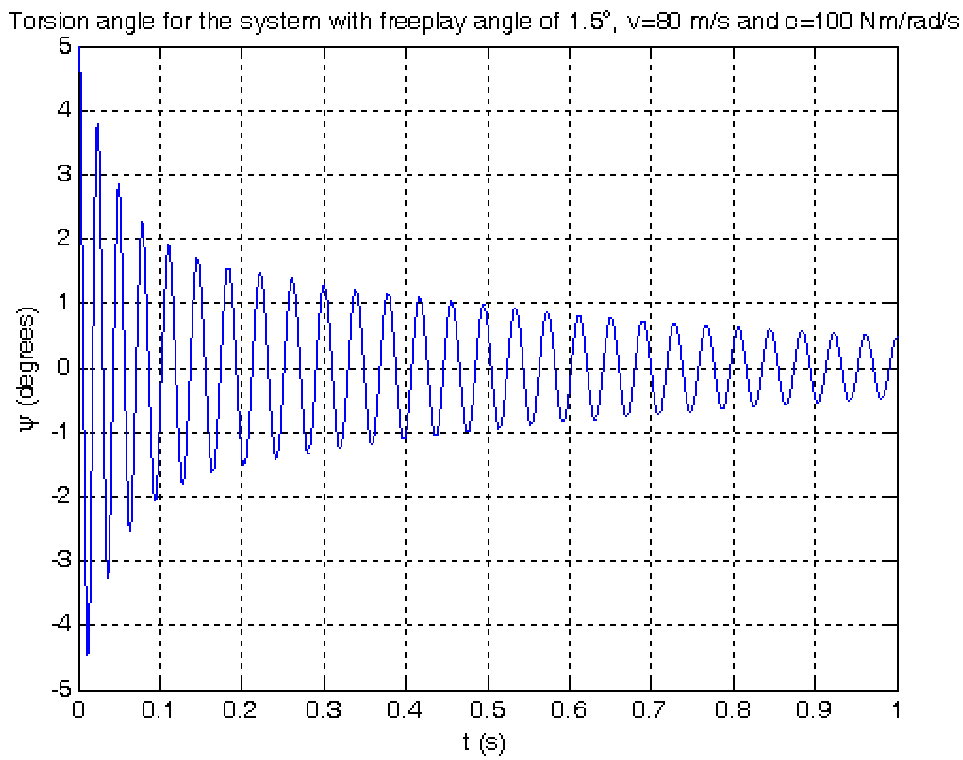

Figure 6.12: ψ for ψ_{fp} =1.5°, v =80 m/s, c =100 Nm/rad/s and $\psi(0)=0.1$.

6.5.2 Conclusions about the effect of freeplay on the torsion angle

- Time histories of the torsion angle are obtained for v =50 m/s with freeplay angles of 0º, 0.5º, 1º and 1.5º for $\psi(0)=0.01$ and $\psi(0)=0.1$, also for v =80 m/s with freeplay angles of 0.5º, 1º and 1.5º for $\psi(0)=0.1$. c =100 Nm/rad/s in all cases.

- Tables 6.1 and 6.2 reveal that limit cycle amplitudes increase with increasing freeplay angle.

- A comparison of figures 6.7–6.9 with figures 6.10–6.12 reveals that an aircraft having torsional freeplay in its landing gear becomes less susceptible to shimmy if its velocity increases.

- Initial condition $\psi(0)$ does not have a significant effect on the limit cycle amplitude of the torsion angle.

- Existence of freeplay prevents shimmy damping of the system that would have been damped without freeplay.

6.5.3 Effect of freeplay on the lateral tire deformation *y*

Time histories of the lateral tire deformation are presented for freeplay angles of 0º, 0.5º, 1º and 1.5º in figures 6.13–6.16 for $\psi(0) = 0.01$ and in figures 6.17–6.20 for $\psi(0) = 0.1$. Amplitudes of the lateral tire deformation y are presented for varying freeplay angles in table 6.3 for $\psi(0) = 0.01$ and in table 6.4 for $\psi(0) = 0.1$.

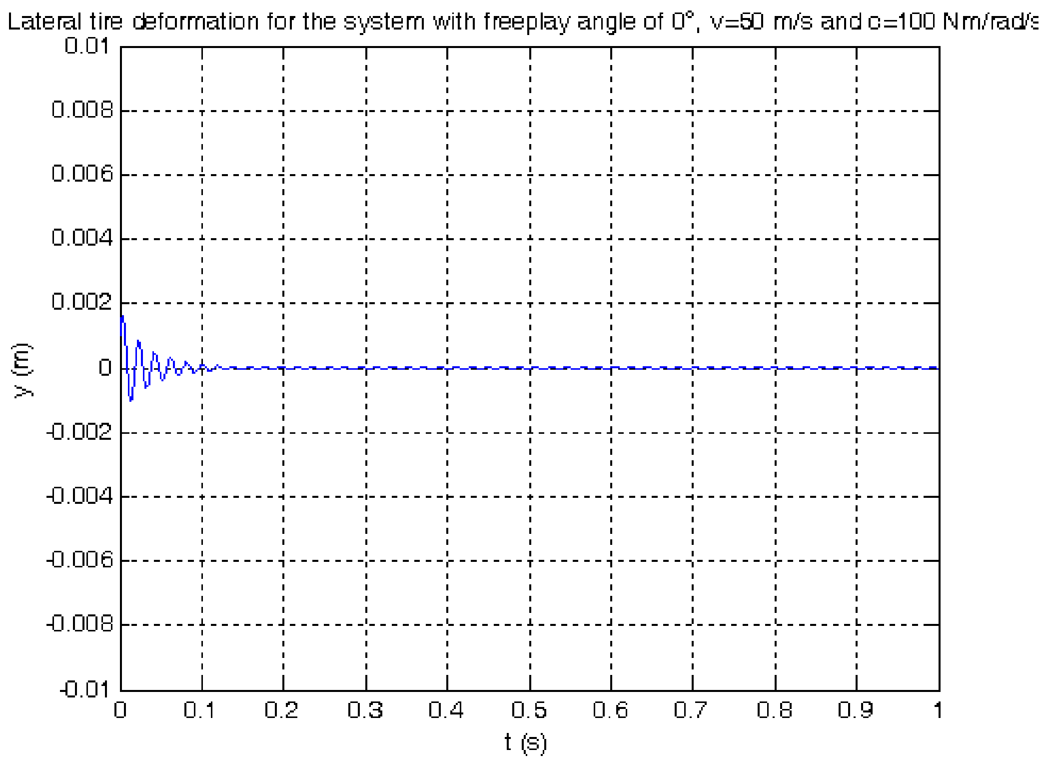

Figure 6.13: y for ψ_{fp} =0°, v =50 m/s, c =100 Nm/rad/s and $\psi(0) = 0.01$.

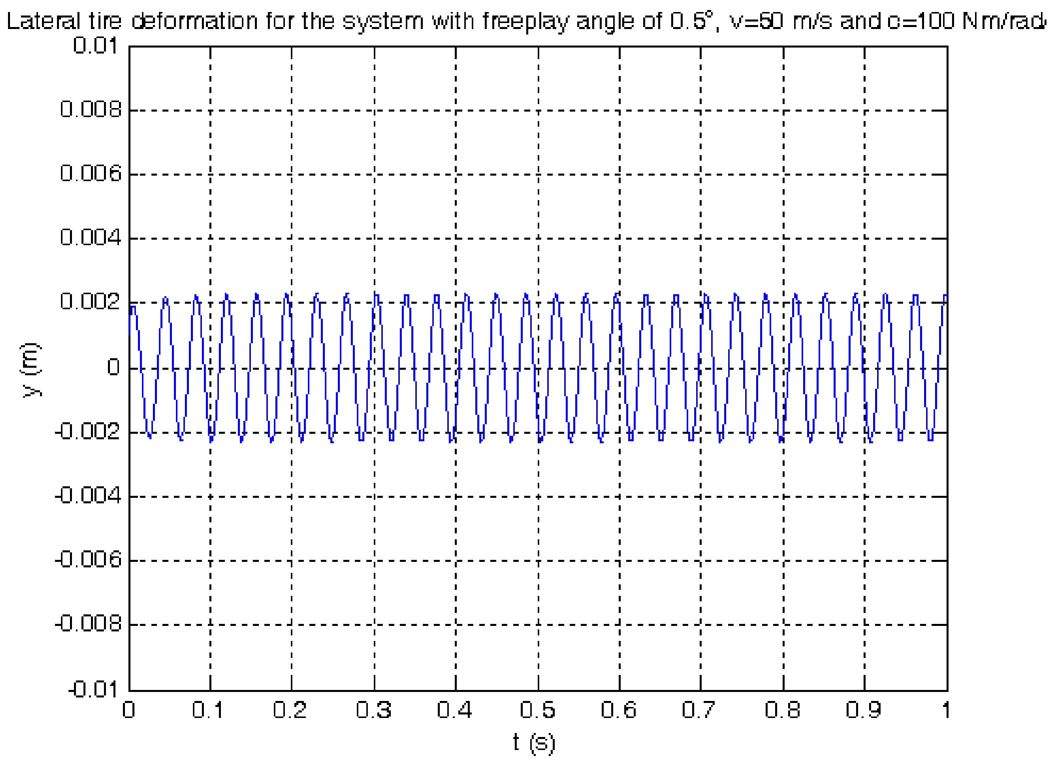

Figure 6.14: y for ψ_{fp} =0.5°, v =50 m/s, c =100 Nm/rad/s and $\psi(0) = 0.01$.

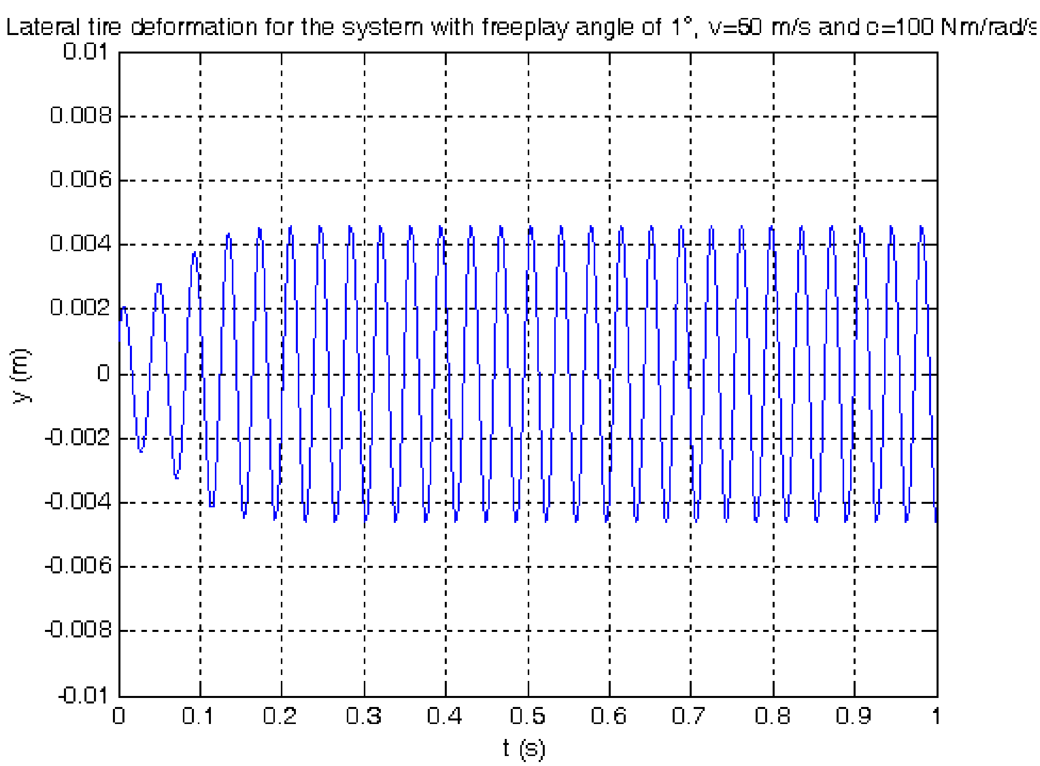

Figure 6.15: y for ψ_{fp} =1°, v =50 m/s, c =100 Nm/rad/s and $\psi(0) = 0.01$.

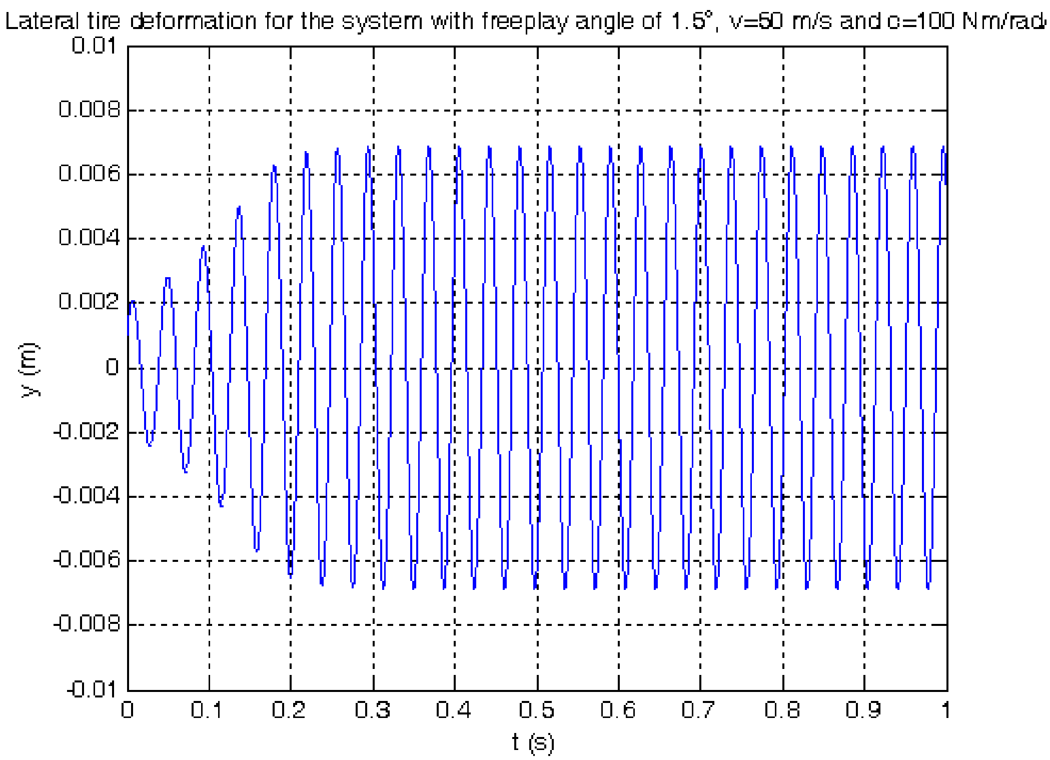

Figure 6.16: y for ψ_{fp} =1.5°, v =50 m/s, c =100 Nm/rad/s and $\psi(0)=0.01$.

Table 6.3: Effect of freeplay on the amplitude of the lateral tire deformation y for v =50 m/s, c =100 Nm/rad/s and $\psi(0)=0.01$.

ψ_{fp} **(degrees)**	y **(m)**
0	oscillation decays in 0.2 s
0.5	0.0023
1	0.0046
1.5	0.0069

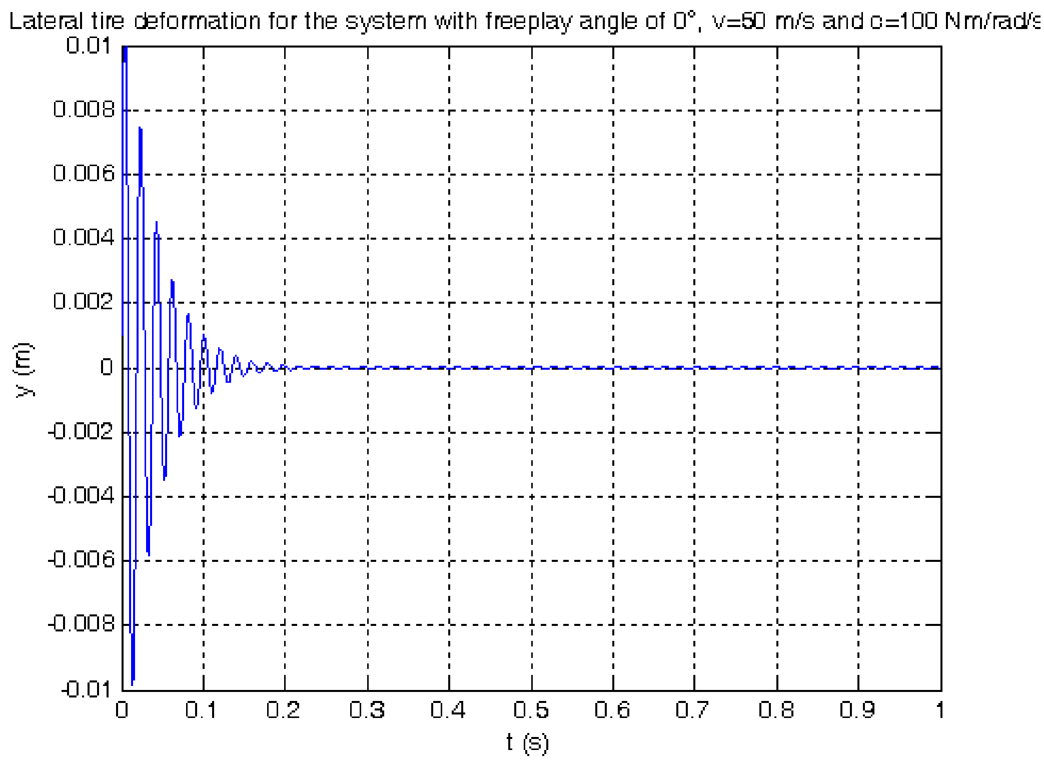

Figure 6.17: y for ψ_{fp} =0°, v =50 m/s, c =100 Nm/rad/s and $\psi(0) = 0.1$.

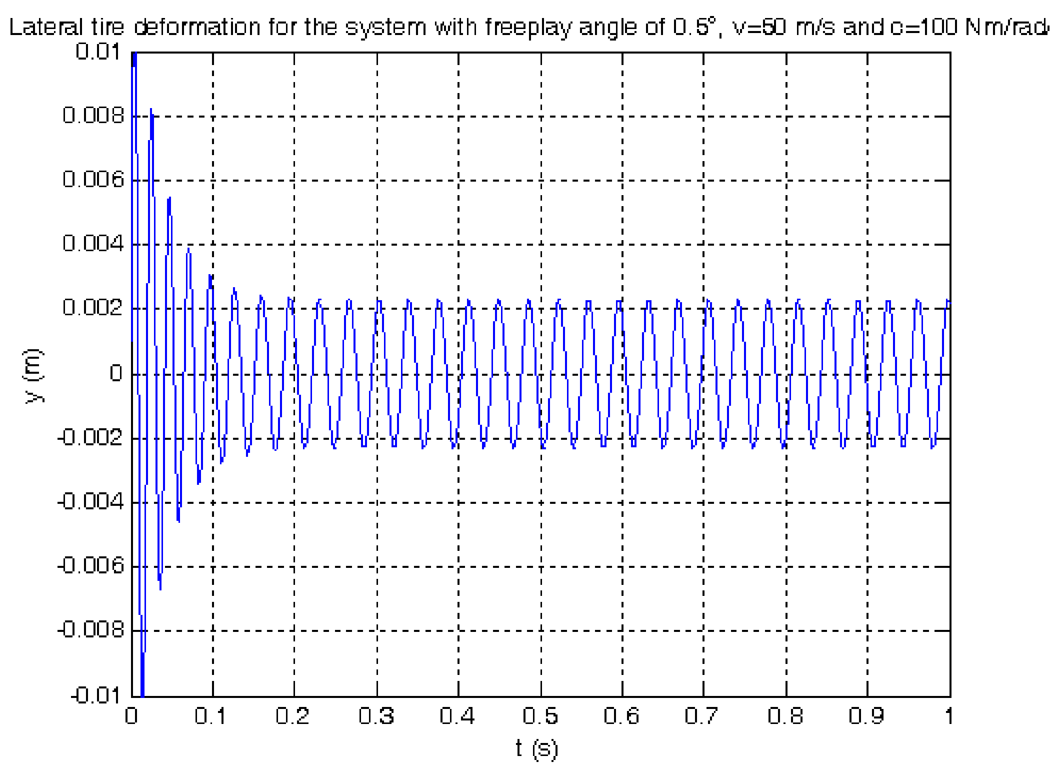

Figure 6.18: y for ψ_{fp} =0.5°, v =50 m/s, c =100 Nm/rad/s and $\psi(0) = 0.1$.

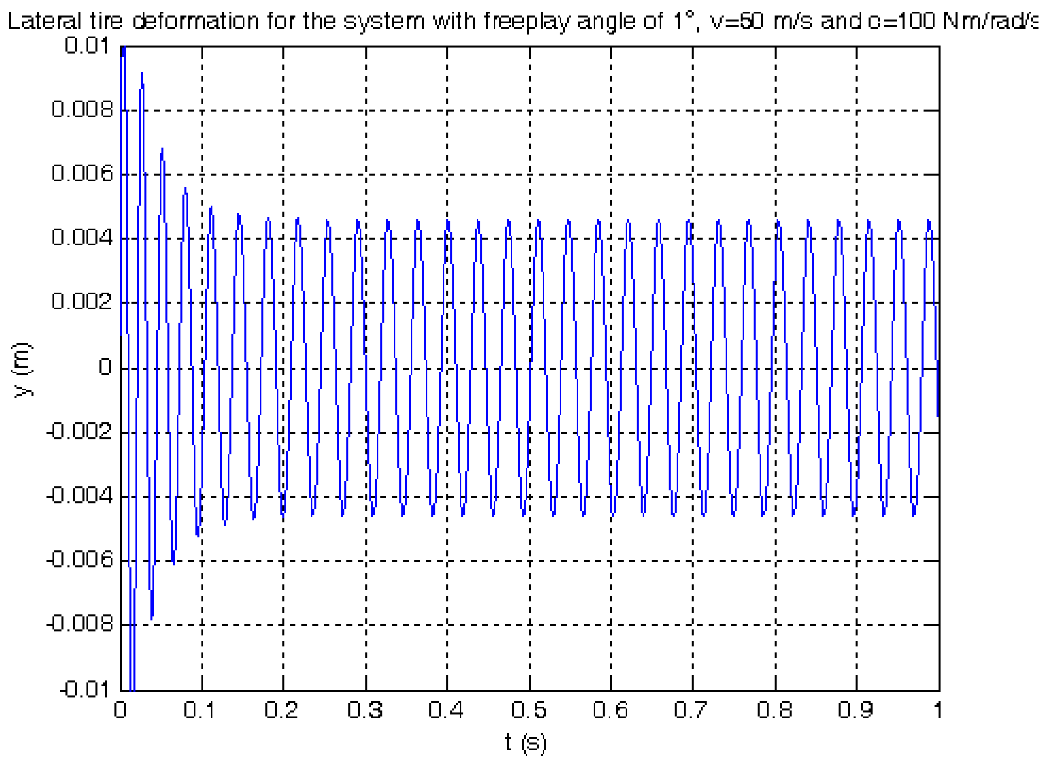

Figure 6.19: y for ψ_{fp} =1°, v =50 m/s, c =100 Nm/rad/s and $\psi(0)=0.1$.

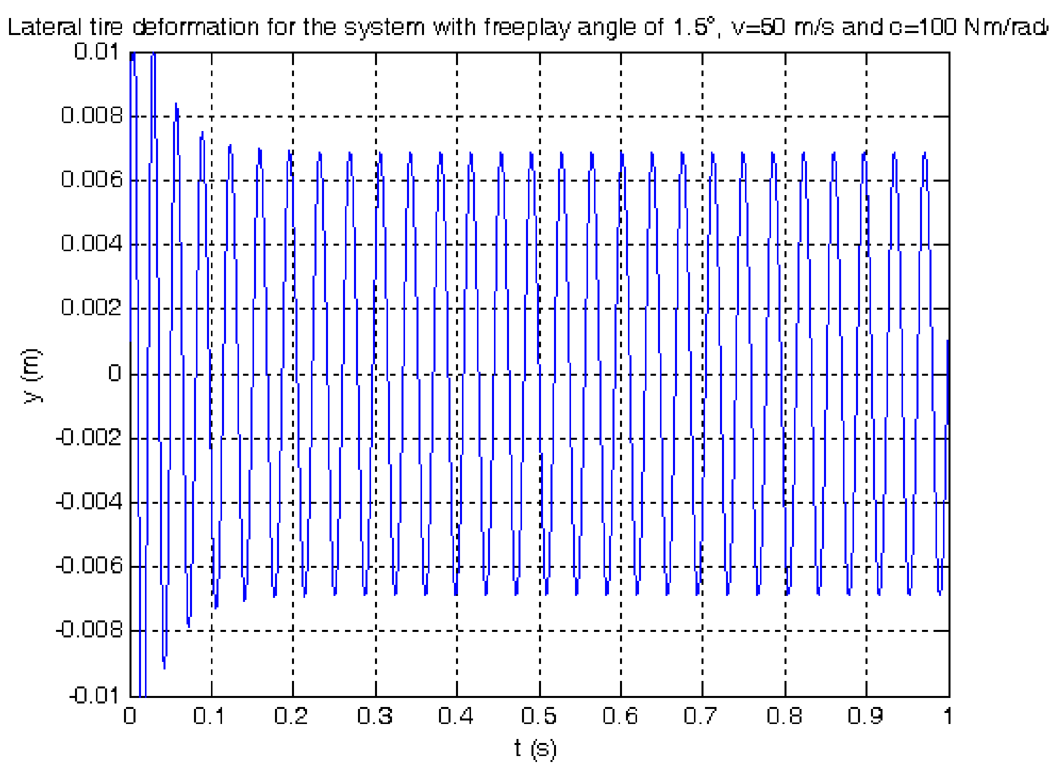

Figure 6.20: y for ψ_{fp} =1.5°, v =50 m/s, c =100 Nm/rad/s and $\psi(0)=0.1$.

Table 6.4: Effect of freeplay on the amplitude of the lateral tire deformation y for v=50 m/s, c=100 Nm/rad/s and $\psi(0)=0.1$.

ψ_{fp} **(degrees)**	y **(m)**
0	oscillation decays in 0.2 s
0.5	0.0023
1	0.0046
1.5	0.0069

6.5.4 Conclusions about the effect of freeplay on the lateral tire deformation

- Time histories of the lateral tire deformation are obtained for v=50 m/s, c=100 Nm/rad/s and freeplay angles of 0º, 0.5º, 1º and 1.5º for $\psi(0)=0.01$ and $\psi(0)=0.1$.
- Tables 6.3 and 6.4 reveal that an increase in the freeplay angle leads to an increase in the lateral tire deformation.
- Initial condition $\psi(0)$ does not have a significant effect on the limit cycle amplitude of the lateral tire deformation.
- Existence of freeplay prevents shimmy damping of the system that would have been damped without freeplay.

6.5.5 Effect of freeplay on limit cycles

Figures 6.21–6.24 show the 3 dimensional and 2 dimensional plots of limit cycle oscillations, $(\psi,\dot{\psi},t)$ and $(\psi,\dot{\psi})$, for v=50 m/s, c=30 Nm/rad/s, $\psi(0)=0.01$ and freeplay angles of 0º, 0.5º, 1º and 1.5º. Limit cycle amplitudes of the torsion angle ψ and $\dot{\psi}$ are presented in table 6.5 for varying freeplay angles.

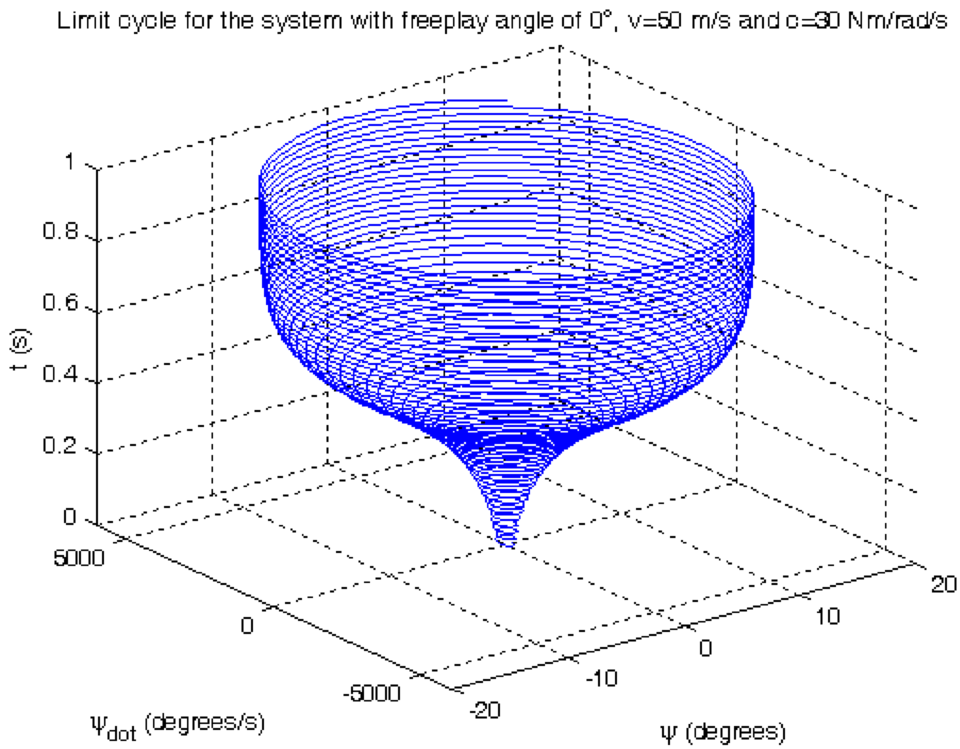

Figure 6.21: a. 3D limit cycle for v =50 m/s, c =30 Nm/rad/s, ψ_{fp} =0º, $\psi(0)=0.01$.

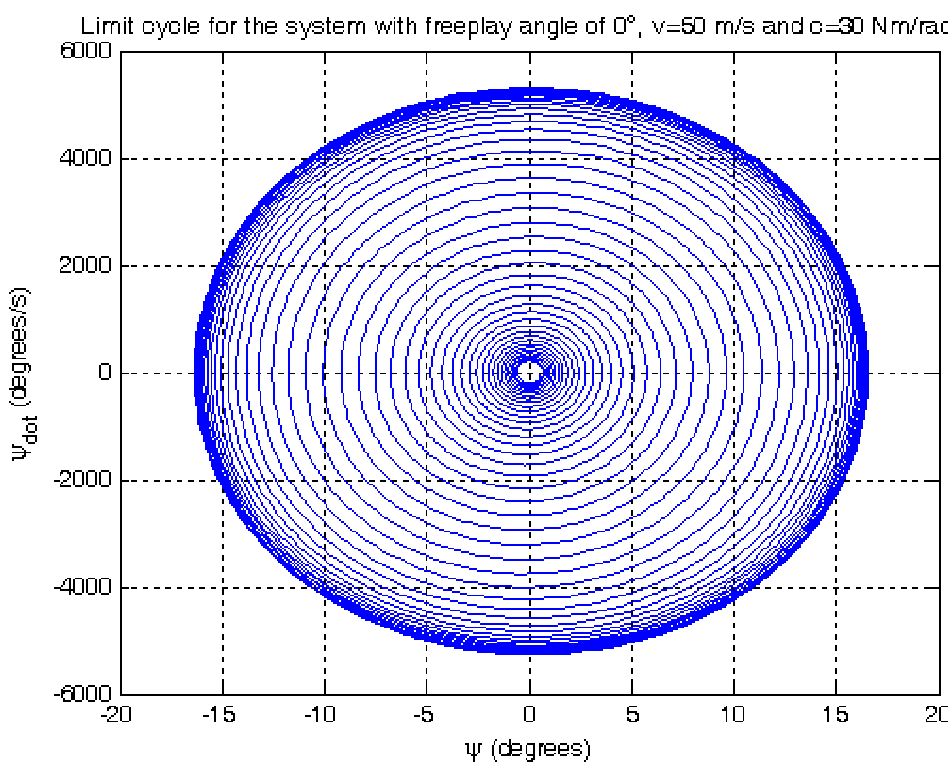

Figure 6.21: b. 2D limit cycle for v =50 m/s, c =30 Nm/rad/s, ψ_{fp} =0º, $\psi(0)=0.01$.

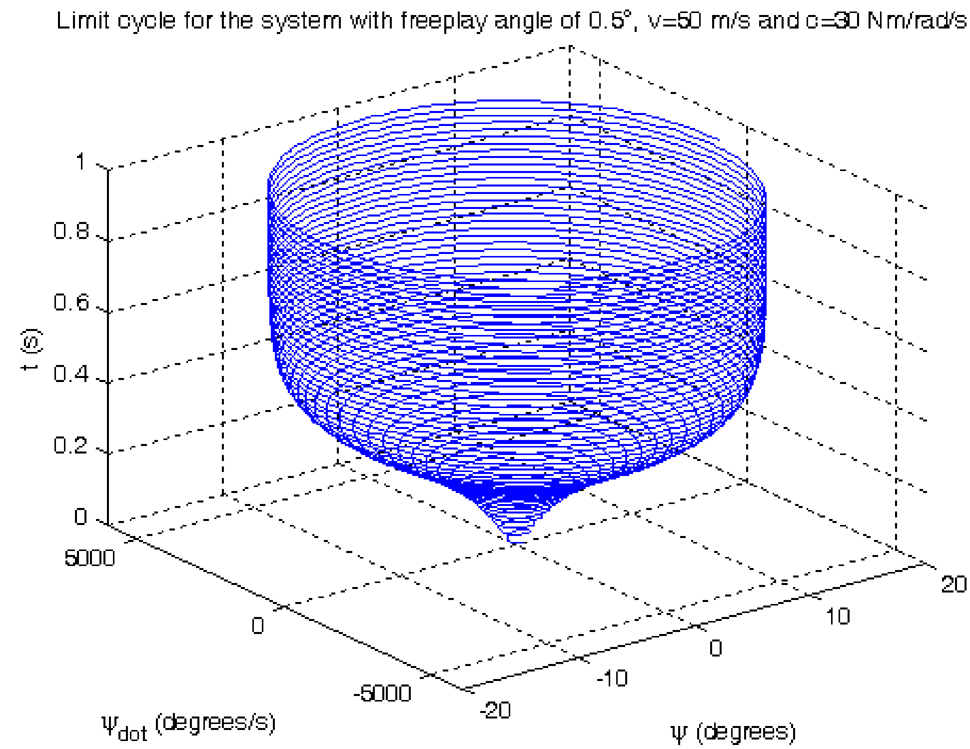

Figure 6.22: a. 3D limit cycle for v =50 m/s, c =30Nm/rad/s, ψ_{fp} =0.5°, $\psi(0) = 0.01$

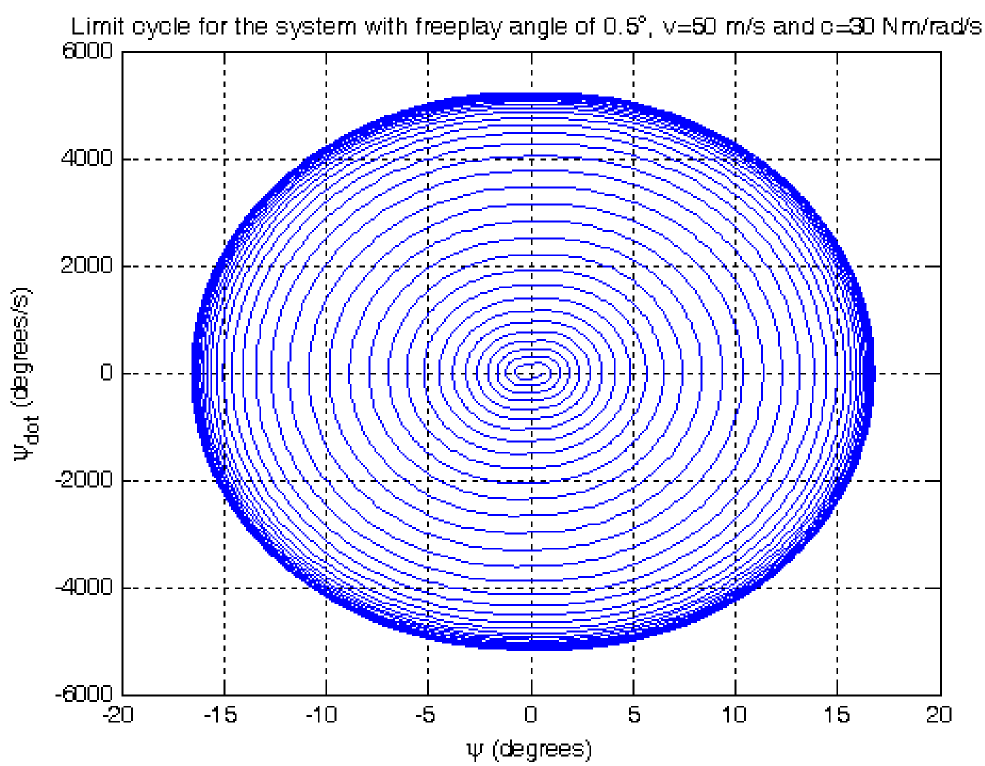

Figure 6.22:b.2Dlimit cycle for v =50 m/s, c =30 Nm/rad/s, ψ_{fp} =0.5°, $\psi(0) = 0.01$.

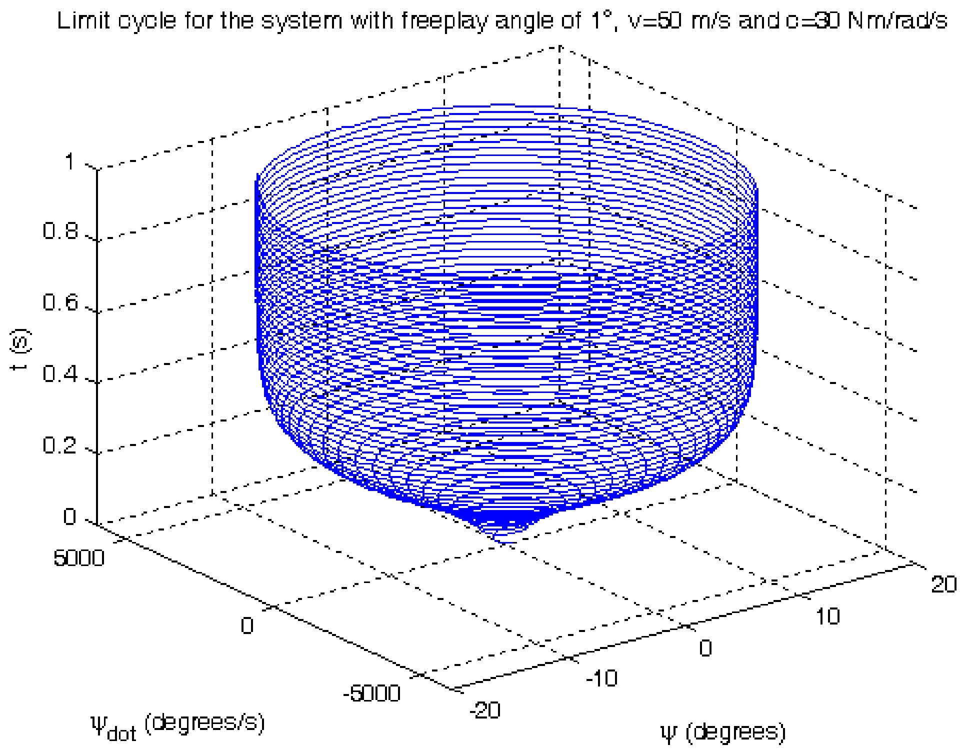

Figure 6.23: a. 3D limit cycle for v =50 m/s, c =30Nm/rad/s, ψ_{fp} =1°, $\psi(0) = 0.01$

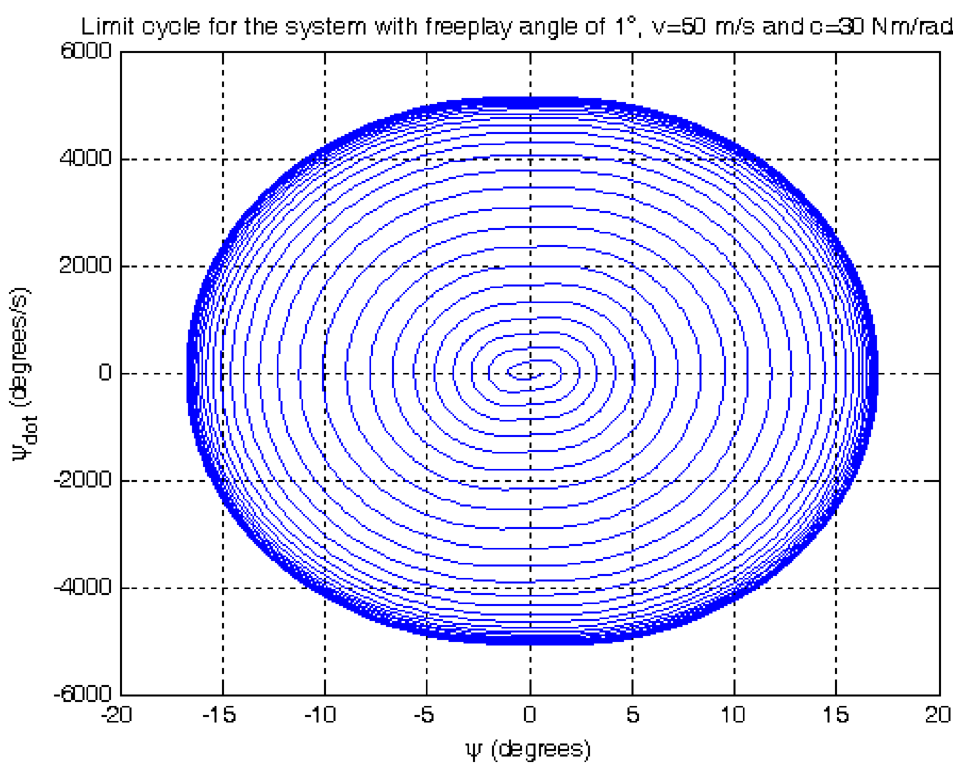

Figure 6.23: b. 2D limit cycle for v =50 m/s, c =30 Nm/rad/s, ψ_{fp} =1°, $\psi(0) = 0.01$.

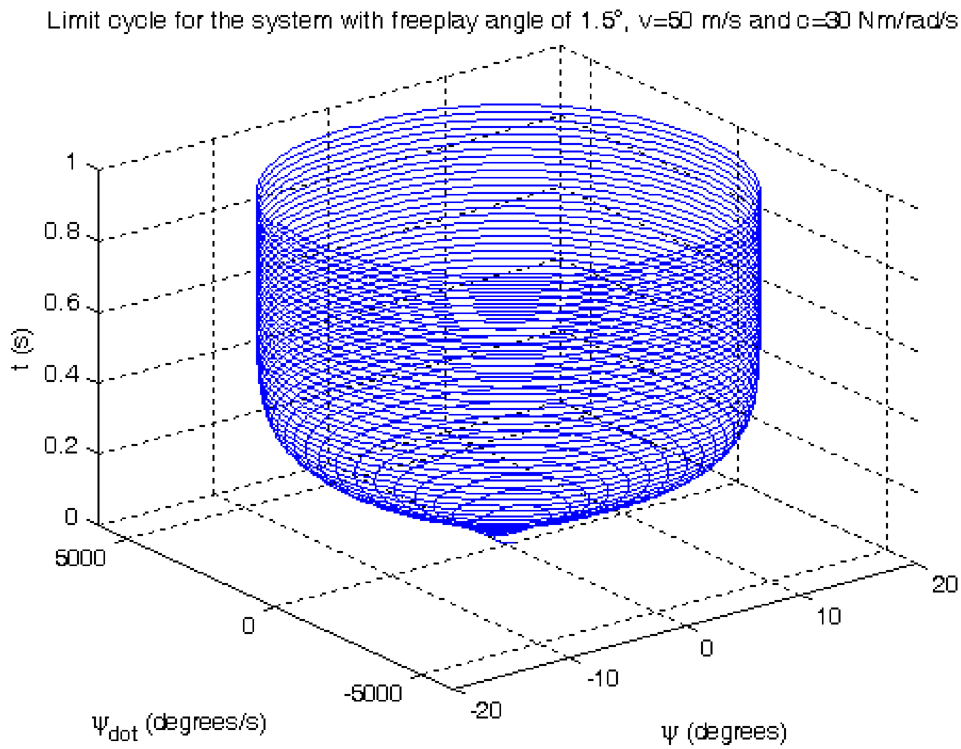

Figure 6.24: a. 3D limit cycle for v =50 m/s, c =30Nm/rad/s, ψ_{fp} =1.5º, $\psi(0) = 0.01$

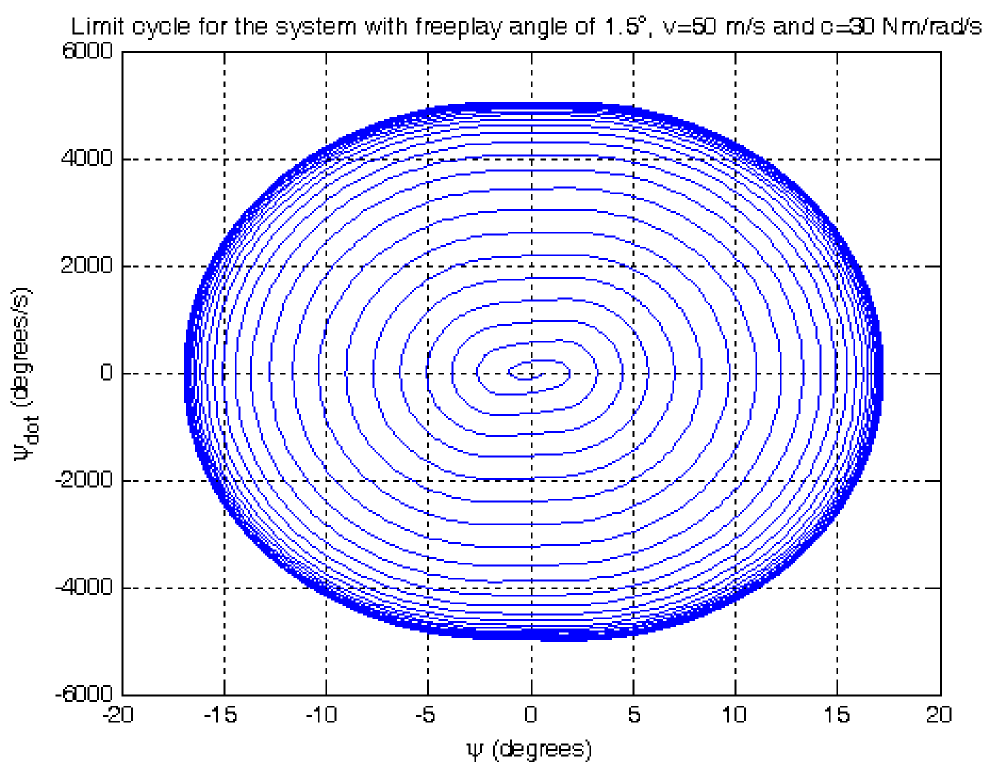

Figure 6.24: b.2D limit cycle for v =50 m/s, c =30Nm/rad/s, ψ_{fp} =1.5º, $\psi(0) = 0.01$

Table 6.5: Effect of freeplay angle ψ_{fp} on the limit cycle amplitudes of the torsion angle ψ and rate of change of the torsion angle $\dot{\psi}$ for v =50 m/s, c =30 Nm/rad/s and $\psi(0) = 0.01$.

ψ_{fp} **(degrees)**	ψ **(degrees)**	$\dot{\psi}$ **(degrees/s)**
0	16.5	5307.2
0.5	16.7	5225.2
1	16.9	5138.0
1.5	17.2	5048.2

6.5.6

Conclusions about the effect of freeplay on the limit cycle amplitudes of the torsion angle ψ and rate of change of the torsion angle $\dot{\psi}$

- 3 dimensional and 2 dimensional plots of the limit cycle oscillations are obtained for v =50 m/s, c =30 Nm/rad/s and freeplay angles of 0°, 0.5°, 1° and 1.5° for $\psi(0) = 0.01$.
- Table 6.5 reveals that an increase in the freeplay angle leads to an increase in the limit cycle amplitude of the torsion angle but a decrease in the limit cycle amplitude of the rate of change of the torsion angle.

7. SEMI–ACTIVE CONTROL VIA A MAGNETORHEOLOGICAL DAMPER

7.1 Introduction to Suspension Systems

Any suspension system is designed and built for providing isolation from the forces transmitted by external excitation. Suspension systems are composed of spring elements in parallel with dissipative elements. Spring element is the elastic element of a suspension system while the damping element is generally a viscous damper. A viscous damper achieves damping by the flow of viscous fluid through orifices, depending on the viscosity of the fluid and the geometry of the orifices and the damper. This technology has been used extensively since the beginning of the last century [109].

Suspension systems are employed in mobile applications as vehicles, as well as non–mobile applications as vibrating machinery or civil structures.

Effective measures to abate shimmy are to use a shimmy damper and to improve landing gear design, but these methods cannot completely attenuate shimmy. A traditional hydraulic shimmy damper has a single–valued damping function with respect to velocity. In addition, oil viscosity cannot be changed and is affected by temperature and oil compressibility. Passive oil dampers have simplicity in design and are cost–effective, but their performance is limited due to the uncontrollable damping force.

7.2 Passive, Semi–Active and Active Suspension Systems

Vibration control is an important aspect in the design of mechanisms as they become more precise and thus less tolerant to transient vibrations. Passive, semi–active and active suspensions are shown schematically in figure 7.1. Controlled suspension systems employ feedback controlled actuators to control the elastic and damping characteristics of the suspension system.

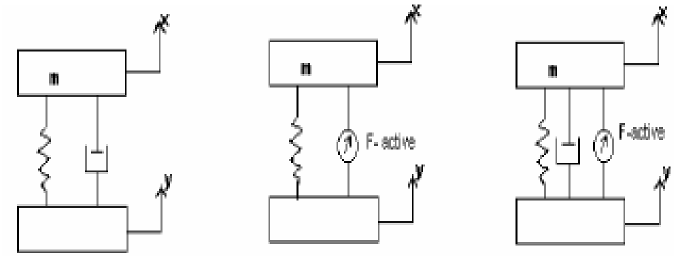

Figure 7.1: a. Passive suspension, **b.** active suspension, **c.** semi–active suspension.

Passive suspensions have limitations as a consequence of the choice of the spring rate and damping characteristics. In other words, behavior of a passive system is not equally acceptable over the whole range of working frequencies.

Active damper technologies started gaining attention in the 1980's. A fully active system should be able to produce the appropriate force for the entire range of inputs. The damping force can be changed and thus the damping characteristics of the system can be controlled. However, these systems are complex and expensive as they require force actuators. The active force generator, depicted as F_{active} in figure 7.1, is a complex hydraulic system, requiring a large control power. Active systems replace the damper with a hydraulic actuator and achieve optimum control at a high cost. Moreover, the system may collapse if the force generator fails. Active control of shimmy is still and open problem [35,68].

Semi–active damping technology is a practical and economical solution as it produces only dissipative forces by increasing or decreasing the effective damping coefficient of the damper, rather than controlling the force output of the damper. Semi–active dampers need less control power, very few moving parts and thus simpler construction and rapid response to control signals. They can achieve desirable levels of shimmy suppression.

Semi–active control systems have the reliability of active systems without requiring large power sources, since semi–active control systems do not input mechanical energy into the controlled system, in contrast to active control systems. Examples of such systems are variable orifice dampers and dampers with controllable fluids, such as electrorheological and magnetorheological fluids [109].

7.3 Magnetorheological Dampers

The heart of a semi–active suspension system is the controllable damper. Magnetorheological (MR) dampers are currently the most popular method of achieving semi–active control. An MR damper is filled with an MR fluid that increases its viscosity when subjected to a magnetic field to the point of acting like a viscoelastic solid. The magnetic field is usually formed by an electromagnet. Thus, the damping characteristics of the shock absorber are controlled continuously by varying the power of the electromagnet. Fluid responds in less than 10 milliseconds, allowing for the design of devices with high bandwidth. MR dampers enable semi–active control by varying the damping force in real time [110–112].

Magnetorheological (MR) fluid dampers are capable of changing their damping force, in response to the current input. They are continuously–controlled semi–active control devices using MR fluids to produce controllable dampers and are not very different from conventional viscous dampers, except for the MR oil and the presence of a solenoid embedded inside the damper, producing a magnetic field. Dynamic response of the damper is created by factors such as construction of the damper and properties of the fluid and the electromagnet.

The damping force cannot be controlled in MR dampers directly but the input voltage can be adjusted. MR dampers can be considered as fail–safe in the sense that they become passive dampers in case of a hardware malfunction. They have attracted interest because they can provide a simple and rapid response interface between electronic controls and mechanical systems [109,112,113].

MR dampers have been applied to vehicle technologies and civil engineering. They are employed in automotive shock absorbers to control the motion of the sprung mass and are available in several high segment cars including Audi TT and R8, Buick Lucerne, Chevrolet Corvette and certain models of Cadillac and Ferrari. Improved ride and handling is achieved by semi–active control of the suspension through changing the damping characteristics of the damper, without the additional cost and complication required in active damper systems. The dampers found in these cars are produced by the Delphi Corporation and BWI, Beijing West Industries, that owns the Chassis Division of Delphi as of November 2009 [114].

Employment of MR dampers in seismic hazard mitigation has been the subject of many studies. An MR damper was installed between the ground and the first floor of a model building, as a first step [115]. The damper was a product of the Lord Company, designed for use in large on and off–road vehicle seats. It required 4 watts at the maximum design current of 1 A.

Large scale MR dampers to be used in civil engineering applications for protection against earthquakes and wind loading have been analyzed and designed and one with a maximum damping force of 200000 N has been constructed at the University of Notre Dame [115–117]. This damper was used as a step towards actually installing an MR damper in a building.

First application of semi–active control to a building was in the year 2001 in Japan [118]. Two 30 ton MR dampers were installed between the third and fifth buildings at the National Museum of Emerging Science and Innovation. The dampers were built by the Sanwa Tekki Corporation and the MR fluid was manufactured by the Lord Corporation.

Active structural control has been applied to over twenty commercial building and ten bridges for seismic hazard mitigation, but semi–active control will be particularly useful in seismic events when low power requirements are an advantage.

7.4 Physics of MR Dampers

Earlier damper technologies suggested regulating the damping force by changing the orifice area in the damper and thus changing the fluid flow, but the changing of speed was too slow. Later on, electrorheological (ER) and MR fluids were investigated.

ER and MR fluids are smart materials formed by mixing fine particles into a liquid having low viscosity. In the presence of an electric or magnetic field above certain strength, the particles form chain–like structures and solidify the suspension. On the contrary, the suspension is liquefied upon the removal of the electric or magnetic field. The solidified suspension has high yield strength. This process takes less than a few milliseconds and can be easily controlled. In other words, rheological properties of an MR fluid can be continuously and reversely changed within milliseconds by the application and removal of external magnetic field. Energy consumption is very small, as a semi–actively controlled MR damper requires only a battery for power.

Although ER fluids received more attention in the beginning, MR fluids were found to be more suited for most applications as MR fluids exhibit a much higher increase in viscosity, and thus yield strength, compared to ER fluids. Physical properties are important factors in choosing the fluid suitable for the application. Physical properties of ER and MR fluids are compared in table 7.1, revealing that maximum yield stresses of ER fluids are in the range 2–5 kPa, while those of MR fluids are in the range 50–100 kPa. Additionally, power requirement of an MR damper is lower than that of an equivalent ER damper. Due to these reasons, MR technology is more attractive and MR fluids are being used extensively in shock absorbers, vibration insulation systems, brakes, clutches, land vehicles, helicopter rotor systems, seismic hazard mitigation, aerospace, civil and automotive engineering. MR dampers are present on a number of high–segment cars [118–124].

Table 7.1: Properties of ER and MR fluids [109,114].

Property	ER fluid	MR fluid
Response time	milliseconds	milliseconds
Plastic viscosity at 25º	0.2–0.3 Pa s	0.2–0.3 Pa s
Operable temperature range	+10 to +90℃ (ionic, DC) -25 to +125℃ (non–ionic, AC)	-40 to +150℃
Maximum yield stress	2–5 kPa (at 3–5 kV/mm)	50–100 kPa (at 150–250 kA/m)
Maximum field	4 kV/mm	250 kA/m
Power supply	2–5 kV 1–10 mA (2–50 W)	2–25 V 1–2 A (2–50 W)
Density	1×10^3–2×10^3 kg/m^3	3×10^3–4×10^3 kg/m^3
Maximum energy density	10^3 J/m^3	10^5 J/m^3
Stability	cannot tolerate impurities	unaffected by most impurities

Power requirements of an MR damper can be exemplified through the technical data of the MR damper used in the experiments conducted for [114]. The damper used in the experiments is 21.5 cm long in extended position with ±2.5 cm stroke and its main cylinder has a diameter of 3.8 cm. The device houses 50 ml of MR fluid and can generate forces of up to 3000 N. The electromagnet is supplied with a current of 0–1 A and the peak power requirement is less than 10 Watts.

7.5 Working Principles of MR Dampers

MR dampers have control over the output force. MR fluids change their apparent viscosity upon the application of a magnetic field. An MR fluid is a non–colloidal solution composed of a non–conductive carrier fluid containing 20–40 % by volume iron particles, with dimensions 3–10 microns in diameter. The carrier fluid is often a passive damper fluid. Some additives may also be used to keep the iron particles suspended.

The fluid behaves like a Newtonian fluid when the magnetic field is absent. When the magnetic field passes through the fluid, however, iron particles act as dipoles and align along the constant flux lines, increasing apparent viscosity. The chains of iron particles have a yield strength that increases the force needed to achieve the same flow as an unactivated fluid. Viscosity of the base or carrier fluid remains unchanged.

An MR fluid has yield strength of 50–100 kPa for magnetic fields of 150–250 kA/m, which is much higher than that of ER fluids. In addition, MR fluids are not affected by temperature or contaminates.

A typical MR damper is seen in figure 7.2. Top of the damper is seen at the right side of the figure. It can be seen that its construction is similar to a passive damper and that the activated region is very small compared to the volume of the fluid. The valve sets the major difference with a passive damper. The valve has a long, narrow fluid gap instead of a small orifice. Flow effects such as turbulence and possibility of cavitation at the entrance and exit exist, like a valve in a passive damper.

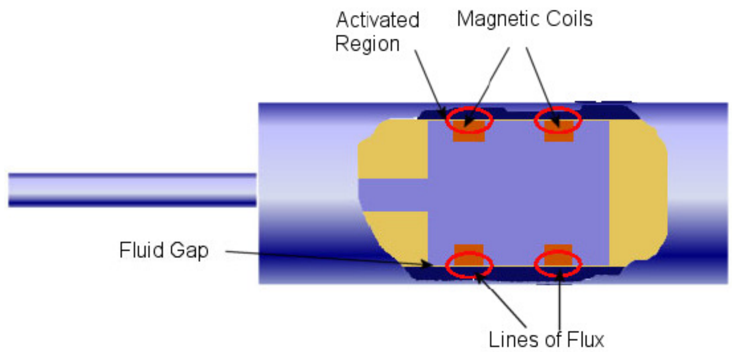

Figure 7.2: Schematic of an MR damper [112,124].

Damping force is controlled by two electromagnetic coils in the piston. When an external current is applied to the electromagnetic coils, the coils create a corresponding magnetic field passing through the MR fluid, radially across the gap, perpendicular to the fluid flow. Iron particles align where magnetic field lines of constant flux are perpendicular to the flow, and cause the fluid to exhibit yield strength, increasing effective damping. When iron particles align as in figure 7.3, they resist being moved out of their flux lines and act as a barrier to the flow of fluid.

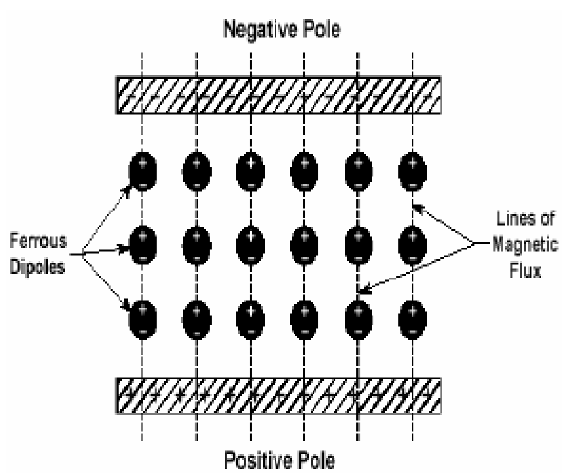

Figure 7.3: Dipole arrangements [121].

Viscosity of the MR fluid can be increased by increasing the electric current through the electromagnet, thus resisting the MR fluid flow through the valve and increasing the damping force of the MR damper. In other words, yield stress of the MR fluid changes depending on the magnetic field intensity. When the magnetic field is absent, damping occurs only due to the viscosity of the MR fluid, however, in the presence of a magnetic field, an additional damping force occurs due to the MR effect of the MR fluid [112,119,120].

As a result of the polarizing magnetic field, particles form chains, modifying the oil yield stress. In such a state, rheological properties of the oil change and the fluid is in semi–solid state. Thus, continuously variable damping can be achieved by controlling the current in the solenoid, without using moving parts such as variable orifices. In such a case, energy requirements are extremely low. Rheological properties of MR fluids are independent of temperature and contamination, making MR dampers reliable and letting them provide excellent performance over a wide range of operating conditions [109,114,125].

7.6 MR Damper Technology

Dampers, also known as shock absorbers, are used in vehicle applications to prevent excessive motion of the vehicle by dissipating energy in the vertical direction. First dampers were implemented on automobiles in 1910 and were frictional or Coulomb dampers. By 1925, hydraulic dampers were in extensive use. Active dampers started being used in the 1980's. Today, dampers are often hydraulic with telescopic construction, with the three basic types shown in figure 7.4.

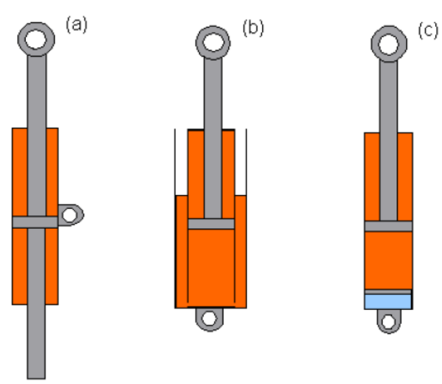

Figure 7.4: Telescopic dampers. **a.** through–rod **b.** double tube **c.** monotube [112].

A mono tube, seen in detail in figure 7.5, is the most common MR damper design. A mono tube has one reservoir for the MR fluid and an accumulator mechanism to compensate for the change in volume resulting from the movement of the piston rod. The accumulator piston acts as a barrier between the MR fluid and a compressed gas, which is usually nitrogen, used to accommodate the volume changes occurring when the piston rod enters the housing.

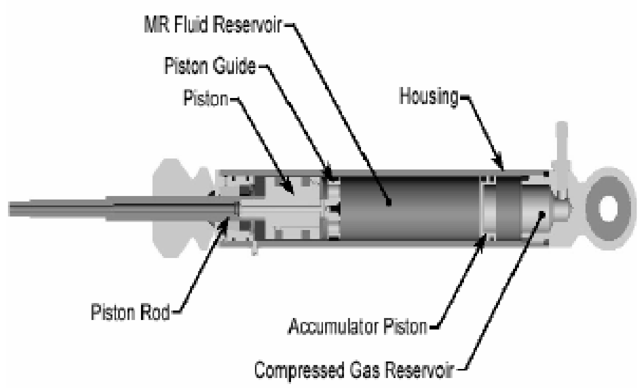

Figure 7.5: Monotube MR damper [121].

An MR fluid valve has a flow channel that the MR fluid is forced to move through, under a pressure applied at the channel inlet. Upon the application of the magnetic field, viscosity of the MR fluid increases and thus a higher pressure needs to be exerted to have the same flow rate. In short, the hydraulic resistance of the valve can be adjusted using the magnetic field. Optimization of MR valves is in the direction of decreasing their dimensions. The drawback is that small electromagnetic parts require complicated and expensive technologies. Thus, there have been attempts towards optimizing the channel geometry [112,126].

7.7 Literature Survey on MR Dampers

7.7.1 MR models and design, fabrication and testing of MR dampers

[125] is a review on the parametric methods found in literature that model force–displacement and force–velocity behavior of MR dampers. [112] examines three different models to fit experimental data of current, velocity and force. The linear model depends only on the current. One of the nonlinear models depends on both the current and velocity, while the second nonlinear model includes a filter affecting the force response of the model with time. Another model based on the Bouc–Wen model is proposed in [124], with the improvement of having parameters that incorporate current, amplitude and frequency of excitation as variables, enabling the prediction of the hysteresis force for changing excitation conditions.

An experimental study on the design, fabrication and testing of MR dampers is carried out in [121]. In another experimental study, sensitivity analysis is of the Bouc–Wen model is performed to assess the influence of each parameter on the model, some parameters are proven to be redundant, a simplified Bouc–Wen model is proposed and its parameters are identified using genetic algorithms [122].

Parameter identification and sensitivity analysis of an MR damper hysteresis model is done using genetic algorithms in [127]. Parameter sensitivity analyses determine and eliminate insignificant parameters of the original model and the simplified Bouc–Wen model is obtained by giving fixed values to insensitive parameters. Modeling of an MR fluid damper is accomplished using neural networks in [128].

A prototype MR damper produced by the Lord Corporation is controlled using clipped optimal control for seismic hazard mitigation purposes in [114]. Another MR damper produced by the same company is used for verification of adaptive control strategy.

Hysteretic characteristics of MR dampers are modeled in [129] and a generalized model is proposed so as to characterize the hysteretic force/velocity relationship of an MR damper under a range of excitation conditions and magnitudes of current. In similar study, [130], an MR damper hysteresis model is proposed and validated with experimental data. A simple hysteresis model that can predict the damping force based on the velocity and current inputs has been proposed for an MR damper in [113]. The model can also be used to obtain an inverse dynamics model to determine the necessary input voltage to produce the desired damper force.

Dynamic behavior of hysteresis elements in mechanical systems has been investigated in [131] and [132].

7.7.2 Applications of MR dampers in landing gear and other systems

Semi–active control has been applied to landing gear [50,120,133] and vehicle suspension systems [119]. It is stated that ride quality and drive stability are two conflicting criteria in vibration control. MR damper technology has been applied in earthquake hazard mitigation in [114].

Semi–active control of landing gear shimmy is investigated in [50] and it is found that the performance of the controllable MR damper is superior to that of the hydraulic shimmy damper during taxiing. A torsional MR damper has been applied to shimmy vibration control of a nose landing gear in [133] and effects of various parameters on shimmy behavior have been examined. A skyhook controller is applied to a landing gear system with an MR damper for attenuating undesired shock and vibration during landing and taxiing in [120] and is found to be effective. Descriptions of the skyhook, groudhook and balance control algorithms can be found in Appendix D.

A semi–active skyhook control system with an MR damper has been applied to a vehicle suspension system in [119] and it is seen that semi–active control performs well in vibration suppression. Experimental studies have shown that the damping coefficient increases with electric current but decreases with excitation amplitude.

[109] is a book on semi–active suspension systems, with a chapter devoted to MR dampers and individual chapters on theoretical and experimental design of semi–active control systems, with an emphasis on automotive applications.

MR fluids have been applied in automobile brake systems in [134] and [135], where the disc brakes are immersed in MR fluid and enclosed by an electromagnet. A brake system is proposed and optimized and a sliding mode controller is designed in [135]. An MR brake has been characterized using a simplified Bouc–Wen model, experimental data has been gathered and an optimization has been performed to determine the parameters of the model in [136]. Design, fabrication and optimization of a semi–active suspension system is undertaken as a project in Sakarya University, as well [137].

7.7.3 Optimization of MR dampers

Optimization of MR and ER valves and dampers within a constrained cylindrical volume is performed in [123] and the optimal design is selected on the basis of damping performance. Performance of the MR damper is proven to be superior to that of a geometrically similar ER damper. Geometry and dimensions of the flow channel of an MR fluid valve is optimized in [126]. Performance analysis of ER and MR dampers is conducted using the plastic shear model in [118]. Effect of the flow behavior on the damper is investigated.

Multidisciplinary design optimization of the brake system proposed in [135] is performed in [134] for the selection of MR fluid, magnetic circuit design, torque requirements, weight, dimensions and temperature. Geometry optimization of a passenger vehicle MR damper has been undertaken in [138], to find the optimal dimensions of the electromagnetic circuit in order to maximize the damping force.

Interactive design optimization of MR brakes has been performed in [139] using the Taguchi method, taking into consideration parameters such as number of coil turns, wire diameter and current that directly affect the output torque of the MR brake.

7.8 MR Damper Models

One of the most challenging aspects of MR dampers is the development of accurate dynamic models. Dynamic models of MR dampers relate the damper force to the displacement and applied current or voltage. Dynamic characteristics of MR dampers need to be understood perfectly when implementing them in real applications. Application of acceptable MR damper models will enable implementation of better control strategies and computer models that can accurately predict the force response of the damper.

An MR damper model is usually associated with the displacement and/or velocity of the piston and electric current applied to the coil as inputs and the force generated on the piston as the output. Parametric MR damper models are reviewed in [125]. Parametric models are able to characterize an MR damper accurately and a number of them have been proposed. In general, a nonlinear mathematical model is required as strong nonlinearity exists in the rheological process.

Despite the advantages of using MR dampers, they have complex mechanical characteristics and the nonlinearity in the rheological process makes them hard to model. Experimental studies have shown that MR dampers display remarkably hysteretic characteristics [122,127]. Modeling of force/velocity and force/displacement responses of MR dampers is cumbersome as these responses exhibit hysteresis. Different approaches have been proposed to model and simulate the hysteretic force response of MR dampers [112,119,121,122,124,125,127].

Hysteresis is the term used to describe the nonlinear effects depending on the previous position and velocity of the damper. In other words, it is the “lagging after” effect, first observed in ferromagnetism, and occurring in other phenomena such as optics or friction. “Lagging behind” implies that the state of a system depends on the history of motion, that the output depends on the history of the input or that the system has a memory [131,132].

Bouc–Wen model is the most commonly used hysteresis based dynamic model. Bouc–Wen model will be discussed in depth in 7.9, as it is the model that will be incorporated in the numerical simulations.

As hysteresis is a prominent property of MR dampers, some models are based on hysteresis operators. Other than the Bouc–Wen model, Dahl model and LuGre model are also based on the hysteresis operator. Models based on the hyperbolic tangent function and sigmoid function also exist in literature [125].

Bingham model and modified Bingham model combine a Coulomb friction element in parallel with a viscous dashpot. Bingham behavior of MR dampers are derived from the Bingham plastic model for MR fluids. Various extensions of the Bingham model can be found in literature. Other models such as biviscous models and viscoelastic–plastic models have been studied in detail, as well. Biviscous models assume that the MR fluid is plastic in both the pre–yield and post–yield conditions. Viscoelastic–plastic models, on the other hand, assume that the pre–yield region exhibits a strong hysteresis, as is typical of viscoelastic materials, while the post–yield region is plastic [125].

7.9 Bouc–Wen Model

Bouc–Wen model, proposed in by Bouc in 1971 and developed by Wen in 1976, is popular as it includes hysteresis in the yield characteristics of the damper fluid. The model is able to capture a wide range of force–displacement and force–velocity hysteresis cycles matching the behavior of a wide class of hysteretic systems. Developments of the Bouc–Wen model are presented in literature. Bouc–Wen model consists of a set of differential equations with parameters that need to be estimated simultaneously [113,122,124,125,127,].

Bouc–Wen model is based on a nonlinear ordinary differential equation containing a memory variable z, representing the hysteretic restoring force, whose position is identified by the variable x and parameters that need to be estimated simultaneously. Optimization techniques can be used to identify the parameters that are adequate in simple problems. The restoring force and deformation are connected through a nonlinear differential equation containing unspecified parameters. It is possible to obtain a variety of hysteresis loops by changing these parameters.

Restoring force in a nonlinear hysteretic system can be expressed as

$$F(x,\dot{x}) = g(x,\dot{x}) + \alpha\ z(x) \qquad \textbf{(7.1)}$$

where $g(x,\dot{x})$ is the nonhysteretic component, α is the scaling value and $z(x)$ is the hysteretic component. Evolutionary component z is governed by

$$\dot{z} = -\gamma\, z\, |\dot{x}|\, |z|^{n-1} - \beta\, \dot{x}\, |z|^{n} + A\dot{x} \qquad \textbf{(7.2)}$$

where γ, n, β and A are parameters related to the shape of the hysteresis loop. Characteristic shape of the force–velocity curve can be altered by adjusting these parameters. These characteristic parameters define the shape and amplitude of the hysteresis loop, such that the model can portray a wide range of hysteretic behavior, depending on the choice of coefficients.

Modifications of the classical Bouc–Wen model have been made by various researchers to accurately capture the force–displacement and force–velocity hysteresis loops [112,119,125].

7.9.1 Simple Bouc–Wen model

Hysteretic behavior of MR dampers can be described using the simple Bouc–Wen model shown in figure 7.6, where the damper force is expressed as [109,119,122,124]

$$f = c_o\dot{x} + k_o(x - x_o) + \alpha z \qquad \textbf{(7.3)}$$

where x is the damper displacement or material deformation, x_o is the initial displacement, c_o is the coefficient of viscosity, k is the coefficient of stiffness, α is a scaling factor and z is the evolutionary shape variable or the imaginary hysteretic displacement given by (7.2).

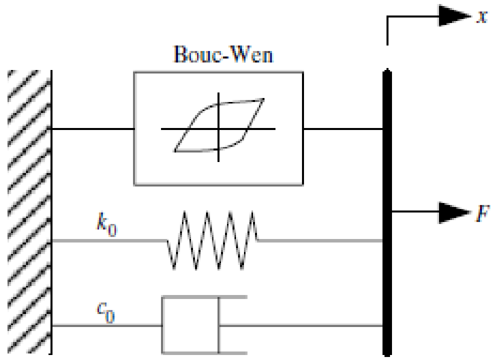

Figure 7.6: Simple Bouc–Wen model [125].

The damper force in the Bouc–Wen model consists of three components. $c_o\dot{x}$, the dashpot component, is associated with viscous dissipation, $k_o x$ represents the linear spring force due to the compressed gas in the accumulator and αz is the evolutionary force due to hysteretic component of the restoring force. c_o, coefficient of viscosity describes the relationship between force and velocity, k_o, coefficient of stiffness describes the relationship between force and displacement and also gives information about the rigidity of the MR damper fluid and α is the hysteretic coefficient. When the hysteresis scaling factor α is zero, the MR damper behaves like a spring connected in parallel to a dashpot. Parameter n represents sharpness, having values from 1 to 3. The remaining parameters do not have physical meanings and are responsible for the shape of the hysteresis curves. Stiffness is very small, compared to viscosity.

In order to accurately characterize the behavior of MR dampers using the simple Bouc–Wen model described by equations (7.2) and (7.3), a set of eight parameters need to be identified to relate the shape parameters to the current excitation. These parameters are $[c_o, k_o, \alpha, x_o, \gamma, \beta, A, n]$.

7.9.2 Modified Bouc–Wen model

The model seen in figure 7.7 can accurately predict the behavior of MR dampers over a broad range of inputs. The model is governed by

$$f = c_1\dot{y} + k_1(x - x_o) \tag{7.4}$$

where y is the internal displacement of the damper governed by

$$\dot{y} = \frac{1}{c_o + c_1}(\alpha z + c_o \dot{x} + k_o(x - y)) \quad \textbf{(7.5)}$$

where z is the evolutionary variable given as

$$\dot{z} = -\gamma z |\dot{x} - \dot{y}| |z|^{n-1} - \beta (\dot{x} - \dot{y}) |z|^n + A(\dot{x} - \dot{y}) \quad \textbf{(7.6)}$$

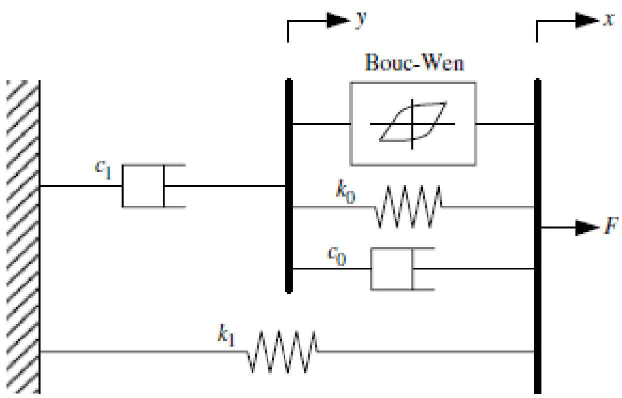

Figure 7.7: Modified Bouc–Wen model [129].

In order to acccurately characterize the behavior of MR dampers using the modified Bouc–Wen model described by equations (7.4)–(7.6), a set of ten parameters need to be identified. These parameters are $[c_o, c_1, k_o, k_1, \alpha, x_o, \gamma, \beta, A, n]$.

Parameters are assumed to be dependent on the applied current I, which is dependent on the applied voltage v, so that a model valid for varying magnetic field strengths is obtained. The following relationships between the applied voltage and parameters have been proposed.

7.9.2.1 Linear current relationship

The following linear relationships between the applied voltage and parameters have been adopted [125].

$$\alpha = \alpha(u) = \alpha_a + \alpha_b u \quad \textbf{(7.7)}$$

$$c_1 = c_1(u) = c_{1a} + c_{1b} u \quad \textbf{(7.8)}$$

$$c_o = c_o(u) = c_{oa} + c_{ob} u \quad \textbf{(7.9)}$$

where c_{oa} and α_a are the damping coefficient and Coulomb force of the MR damper at 0V, respectively, and u is a variable used to determine the dependence of the parameters on the voltage.

The relationship between u and v is modeled as

$$\dot{u} = -\eta(u - v) \tag{7.10}$$

where η reflects the response time of the MR damper.

In order to accurately characterize the behavior of MR dampers using the current–dependent Bouc–Wen model described by equations (7.4)–(7.10), a set of 14 parameters need to be identified. These parameters are $[c_{oa}, c_{ob}, c_{1a}, c_{1b}, k_o, k_1, \alpha_a, \alpha_b, x_o, \gamma, \beta, A, n, \eta]$.

Modified Bouc–Wen model has improved accuracy, however the increased number of parameters increases the complexity of the model, which makes it harder to identify the parameters. Still, the model has potential inaccuracies due to the linear current relationship. Experimental studies in literature suggest a nonlinear dependence of the damper force on the applied current.

7.9.2.2 Nonlinear current relationship

Third order polynomials have been assumed for α, c_o and c_1 when modeling the large scale MR damper that has been constructed so as to produce a maximum damping force of 200000 N [116,117]. Identified equations are given as [125]

$$\alpha = \alpha(I) = \alpha_a + \alpha_b I + \alpha_c I^2 + \alpha_d I^3 \tag{7.11}$$

$$c_1 = c_1(I) = c_{1a} + c_{1b} I + c_{1c} I^2 + c_{1d} I^3 \tag{7.12}$$

$$c_o = c_o(I) = c_{oa} + c_{ob} I + c_{oc} I^2 + c_{od} I^3 \tag{7.13}$$

7.9.3 Current–dependent Bouc–Wen model

The simple Bouc–Wen model described by equations (7.3) and (7.2) does not incorporate current as a variable, which implies that the characteristic parameters need to be evaluated for each current excitation separately, which is an expensive task. In order to overcome this, the model can be modified such as [125]

$$f = c_o(I)\,\dot{x} + k_o(I)\,x + \alpha(I)\,z \qquad \textbf{(7.14)}$$

where z is the evolutionary variable defined by the following differential equation.

$$\dot{z}(I) = -\gamma(I)\,z\,|\dot{x}|\,|z|^{n-1} - \beta(I)\,\dot{x}\,|z|^{n} + A(I)\,\dot{x} \qquad \textbf{(7.15)}$$

If $A(I)$ is set as unity and $\beta(I)$ is set as zero, $z(I)$ becomes

$$z(I) = \frac{1}{\sqrt{\gamma(I)}}\tanh\left\{\sqrt{\gamma(I)}\left[\dot{x} + \frac{1}{\sqrt{\gamma(I)}}\,\mathrm{arctan\,h}\left(\frac{F_{zo}(I)\sqrt{\gamma(I)}}{\alpha(I)}\right)\right]\right\} \qquad \textbf{(7.16)}$$

for $x < 0$ and

$$z(I) = \frac{1}{\sqrt{\gamma(I)}}\tanh\left\{\sqrt{\gamma(I)}\left[\dot{x} + \frac{1}{\sqrt{\gamma(I)}}\,\mathrm{arctan\,h}\left(-\frac{F_{zo}(I)\sqrt{\gamma(I)}}{\alpha(I)}\right)\right]\right\} \qquad \textbf{(7.17)}$$

for $x \geq 0$ where the relationships between the current excitation and parameters c_o, k_o, α, γ and F_{zo} are

$$c_o(I) = c_1 + c_2\left(1 - e^{-c_3 I}\right) \qquad \textbf{(7.18)}$$

$$k_o(I) = k_1 + k_2 I \qquad \textbf{(7.19)}$$

$$\alpha(I) = \alpha_1 + \alpha_2\left(1 - e^{-\alpha_3 I}\right) \qquad \textbf{(7.20)}$$

$$\gamma(I) = -\gamma_1 + \gamma_2 I \qquad \textbf{(7.21)}$$

$$F_{zo}(I) = F_{zo1} + F_{zo2}\left(1 - e^{-F_{zo3} I}\right) \qquad \textbf{(7.22)}$$

Thus, a set of 13 parameters need to be identified in order to accurately characterize the behavior of MR dampers using the current–dependent Bouc–Wen model described by equations (7.14)–(7.22). These parameters are $[c_1, c_2, c_3, k_1, k_2, \alpha_1, \alpha_2, \alpha_3, \gamma_1, \gamma_2, F_{zo1}, F_{zo2}, F_{zo3}]$.

In addition to the simple Bouc–Wen model, modified Bouc–Wen models with linear and cubic current relationships and the current dependent Bouc–Wen model, there exist some other modifications of the Bouc–Wen model. Some of them are the modified Bouc–Wen model using the sigmoid function in the current functions, Bouc–Wen model for shear mode dampers, Bouc–Wen model for large scale dampers, current–frequency–amplitude– dependent Bouc–Wen model and the non–symmetrical Bouc–Wen model. They will not be included here but have been mentioned for completeness.

7.10 Parameter Identification

In literature, general strategy to identify parameters of parametric dynamic models is to estimate the parameter values to make the simulated behavior of the system as close to experimental data as possible. Various optimization methods such as nonlinear optimization, genetic algorithms, particle swarm optimization and adaptive algorithms are used for parameter identification.

Drawback of the Bouc–Wen model is the evaluation of the constant parameters so as to minimize the error between experimental and simulation results since there is a significantly large combination of these parameters and no unique solution. In addition, characteristic parameters in the Bouc–Wen model are not functions of current, amplitude and frequency of excitation, meaning the estimated parameters can only characterize the behavior the MR damper under specific excitation conditions and must be evaluated once again for different excitation conditions. This is a computationally expensive situation. It is important to have a model requiring the minimum number of input parameters.

Sensitivity analysis and parameter identification have been conducted in [121], [122] and [127] for this purpose of obtaining simpler models. Excitation conditions have been included as variables in [124] to remove the necessity to calculate system parameters for each excitation condition. Genetic algorithms have been applied in these studies for parameter identification in the hysteretic Bouc–Wen model. Neural networks are also applied in approximating the MR damper model, as in [128].

The methodology is to identify the parameters in the parametric dynamic models so that the hysteresis loop agrees with the experimental data. Parameter estimation is an optimization problem where the optimization algorithm is used to adjust model parameters to minimize the objective function. In experimental studies, quadratic or root mean square error between the simulated and measured damping forces are often used as objective functions.

7.11 Application of MR Dampers in Landing Gear Shimmy

Aircraft shock absorbers are generally passive shock absorbers designed to withstand the hardest expected landing conditions. In reality, however, working conditions are below these critical levels and the passive absorber is too stiff for optimal performance. There have been proposals to build additional hydraulic circuits pumping additional fluid in or out of the system so as to increase or decrease hydraulic pressure and eventually obtain a desired damping force, but such a system is not rapid enough to dissipate impact energy as a touchdown lasts only 200 ms. Aircraft landing gear require faster ways of changing the damping force. For this reason, researchers working on aircraft technologies consider the possibility of introducing active or semi–active control to aircraft landing gear. MR dampers have the capacity to change damper characteristics fast enough.

Very few studies in literature study the application of an MR damper in landing gear shimmy. Semi–active control of landing gear shimmy is investigated in [50] and it is found that the performance of the controllable MR damper is superior to that of the hydraulic shimmy damper during taxiing. A torsional MR damper has been applied to shimmy vibration control of a nose landing gear in [133] and effects of various parameters on shimmy behavior have been examined. A skyhook controller is applied to a landing gear system with an MR damper for attenuating undesired shock and vibration during landing and taxiing in [120] and is found to be effective. Description of skyhook control algorithm is given in Appendix D.

7.12 Introduction of an MR Damper into the Torsional Landing Gear Model

This section studies the effect of using an additional MR shimmy damper. An MR damper is introduced into the torsional landing gear model. Sections 7.12, 7.14 and 7.16 cover the application of an MR damper to the torsional landing gear model, the landing gear model with torsional freeplay and the landing roll of an aircraft, respectively. The MR damper has been modeled using the current–dependent Bouc–Wen model, as parameters in this model do not have to be determined for each current input. Genetic algorithms have been employed in identifying the parameters of the Bouc–Wen model.

The MR damper model has been applied as a supplementary torsional shimmy damper, in addition to the conventional hydraulic shimmy damper, however the damping constant of the hydraulic damper is kept at a very low level to better observe the effect of the MR damper. The MR damper has also been incorporated in the presence of torsional freeplay. Finally, the MR damper model has been applied in a landing scenario where the velocity of the aircraft decreases gradually.

Current–dependent Bouc–Wen model is selected due to its versatility to be incorporated with different current inputs. In the other models discussed in sections 7.9.1 and 7.9.2, parameters have to be identified for each current input. Due to their dependence on the current input, parameters in the current–dependent Bouc–Wen model do not have to be identified over and over for each current input, and thus the current–dependent model will be incorporated here.

Current–dependent Bouc–Wen model described by equations (7.14)–(7.22) is applied to the torsional landing gear model described by (5.1), (5.13) and (5.17). This is accomplished by adding an MR term to equation (5.1) that describes the torsional dynamics of the landing gear such as

$$I_z\ddot{\psi} + M_1 + M_2 + M_3 + M_4 + M_5 = 0 \qquad \textbf{(7.23)}$$

where I_z is the moment of inertia about the z axis,

M_1 is the linear spring moment between the turning tube and the torque link,

M_2 is the combined damping moment from viscous friction in the bearings of the oleo–pneumatic shock absorber and from the shimmy damper,

M_3 is the tire moment about the z axis,

M_4 is the tire damping moment due to tire tread width and

M_5 is the control moment provided by the magnetorheological damper given as

$$M_5 = fd \tag{7.24}$$

where f is the damper force and

d is the moment arm of the control force to suppress shimmy.

Thus, equation (7.14) is substituted into M_5 as the damper force.

When the current–dependent Bouc–Wen model is incorporated, equations (7.14)–(7.22) need to be considered and 13 parameters need to be identified. This is accomplished by the use of genetic algorithms.

Parameters involved in the current–dependent Bouc–Wen model are optimized using genetic algorithms. Details and working principles of genetic algorithms will not be included here for reasons of conciseness. Optimal values of the involved parameters, $[c_1, c_2, c_3, k_1, k_2, \alpha_1, \alpha_2, \alpha_3, \gamma_1, \gamma_2, F_{zo1}, F_{zo2}, F_{zo3}]$ are given in appendix E.

Current–dependent Bouc–Wen model described by equations (7.14)–(7.22) is applied to the torsional landing gear model described by (7.23), (5.13) and (5.17). In this application, as seen in equation (7.23), the hydraulic damper is not removed from the system when the MR damper is introduced. Damping constant of the initial, hydraulic damper is kept at a very low level to better observe the effect of the MR damper.

Parameters of the current–dependent Bouc–Wen model have been optimized using genetic algorithms. Fitness function of the genetic algorithm has been defined such that the optimization problem is a maximization of the MR damper force defined by (7.14).

As a general rule, shimmy oscillation amplitude should be reduced to one–third of the original disturbance within 3 seconds or there should be enough damping to reduce the amplitude to one–fourth or less of the original after three cycles.

Figures 7.8–7.12 show the result of applying currents of 0, 0.5, 0.75, 1 and 1.1 A to the MR damper in an aircraft taxiing at 30 m/s, while figures 7.13 and 7.14 show the result of applying currents of 1 and 1.1 A to the MR damper in an aircraft taxiing at 80 m/s. It is seen by inspecting figures 7.8–7.14 and table 7.2 that an MR damper added to the system is able to suppress shimmy, even at the existence of a very low hydraulic damping of 20 Nm/rad/s. It is further seen that a very low current of 1A is able to suppress shimmy in 0.1 s in a taxiing aircraft with velocity 30 m/s and in 0.2 s in a taxiing aircraft with velocity 80 m/s. Application of a current of 1.1 A suppresses shimmy in 0.05 s in both aircraft.

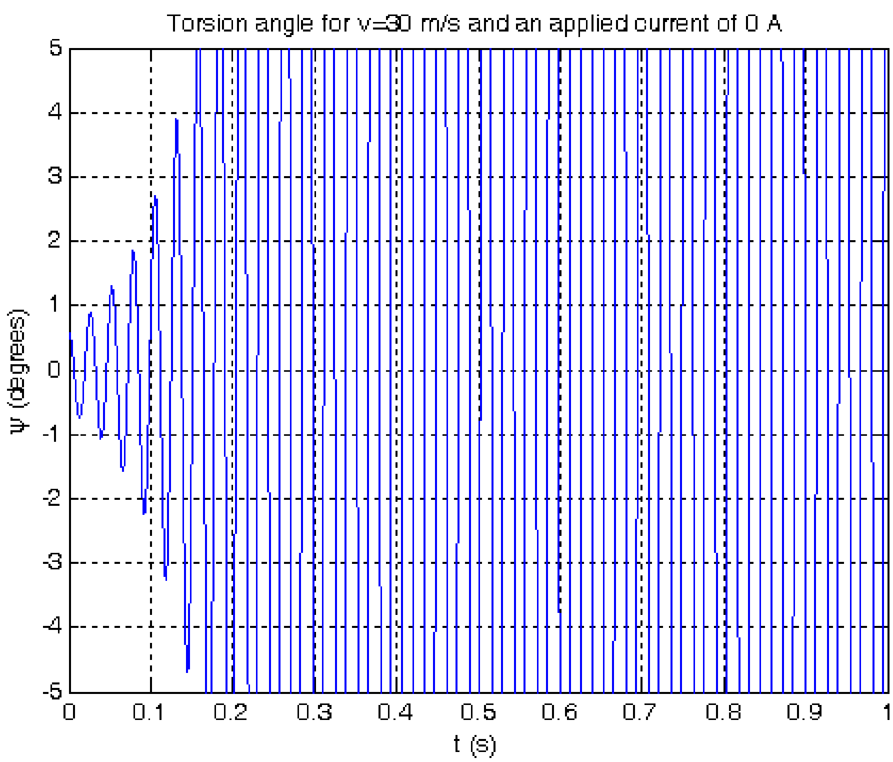

Figure 7.8: Torsion angle ψ for v =30 m/s and an applied current of 0 A.

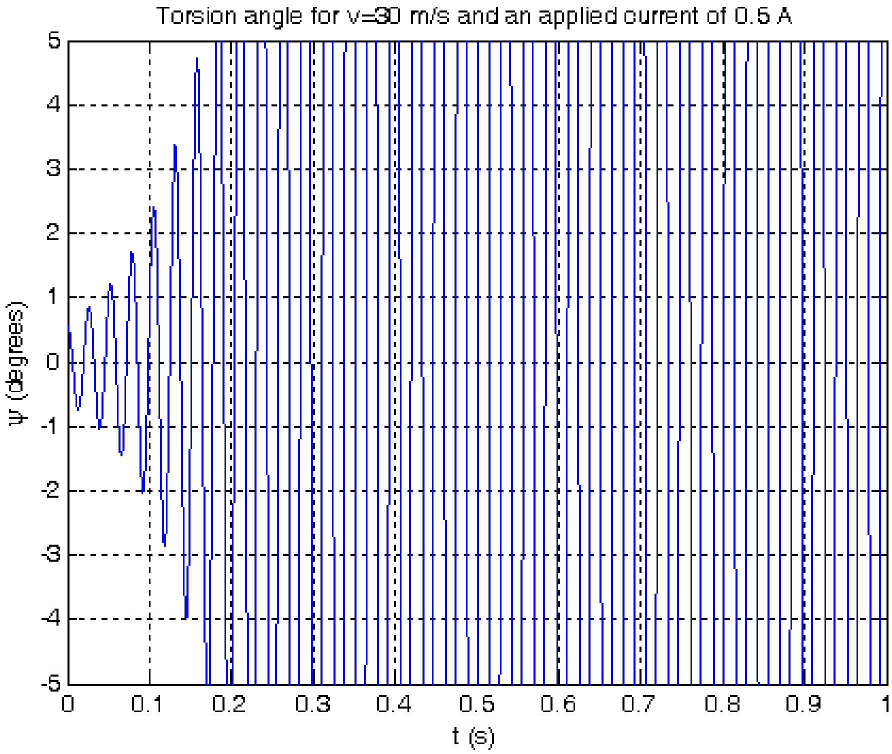

Figure 7.9: Torsion angle ψ for v =30 m/s and an applied current of 0.5 A.

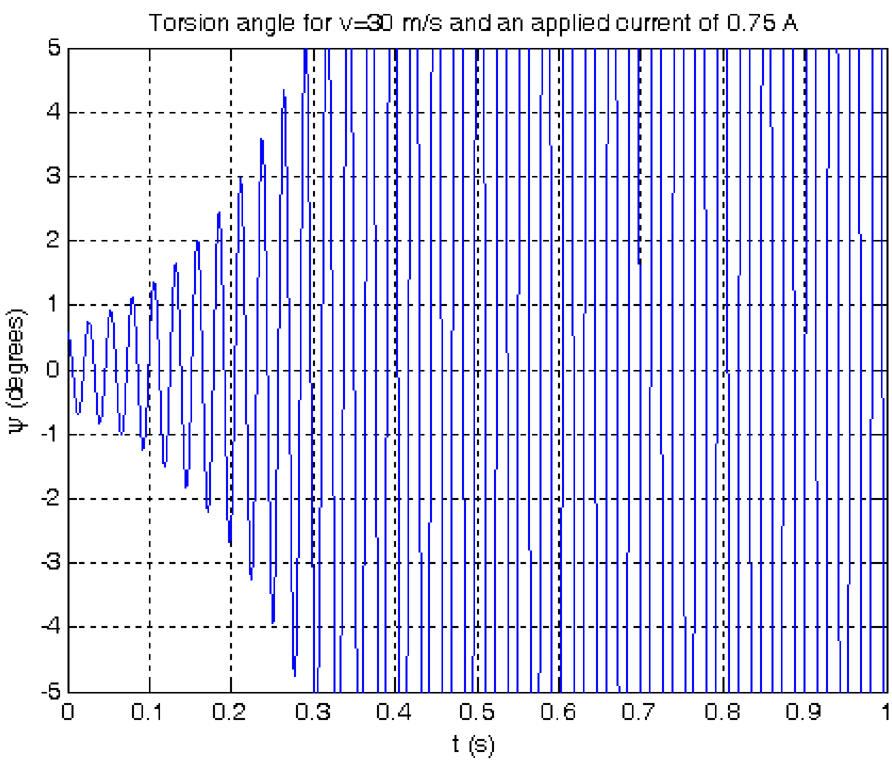

Figure 7.10: Torsion angle ψ for v =30 m/s and an applied current of 0.75 A.

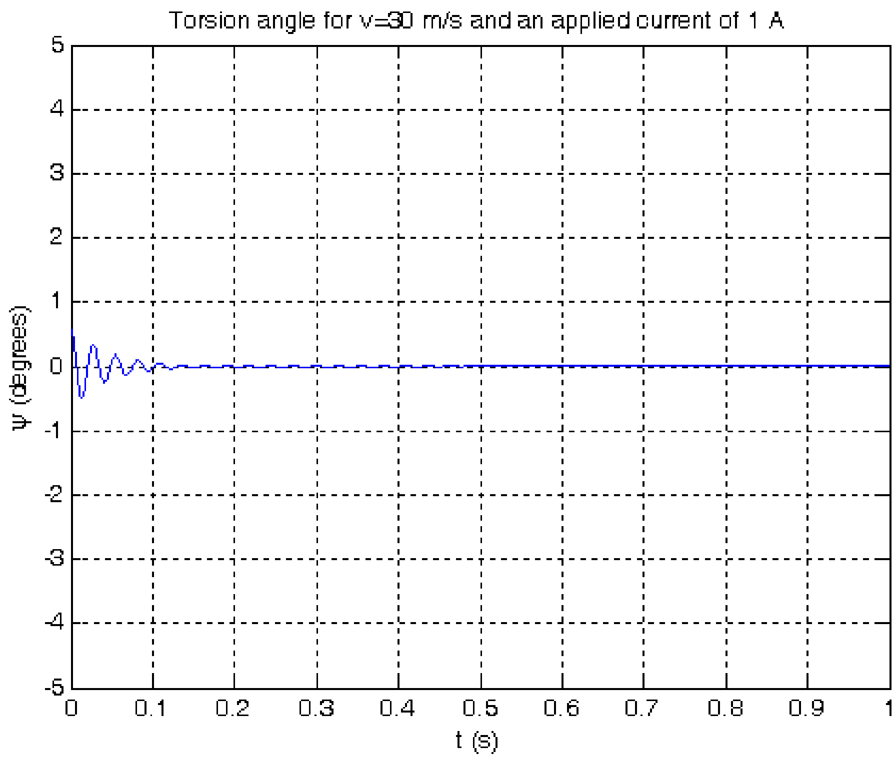

Figure 7.11: Torsion angle ψ for v =30 m/s and an applied current of 1 A.

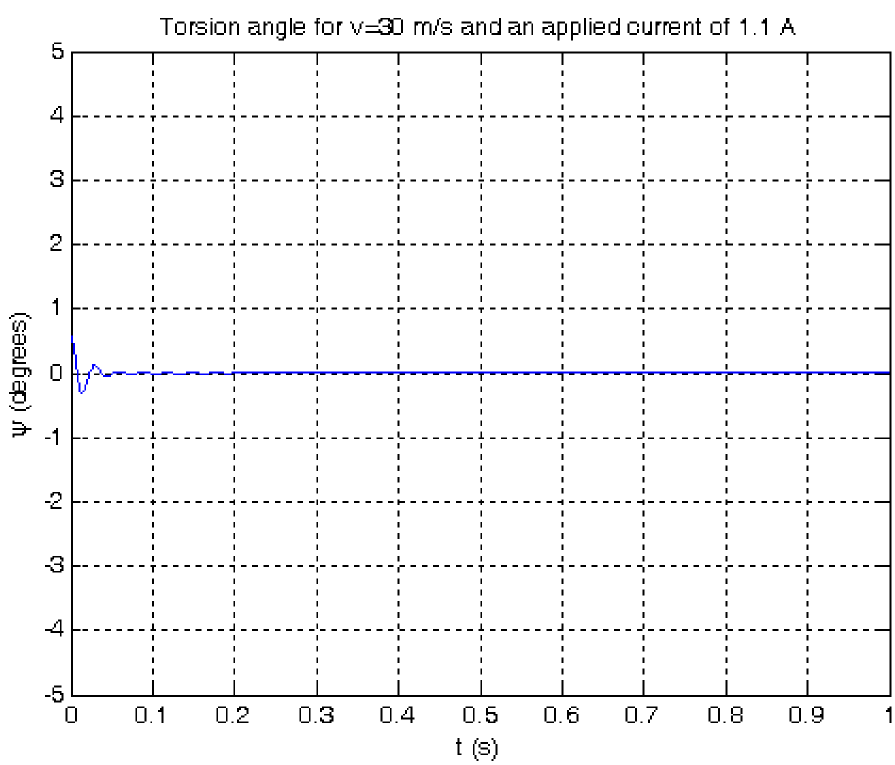

Figure 7.12: Torsion angle ψ for v =30 m/s and an applied current of 1.1 A.

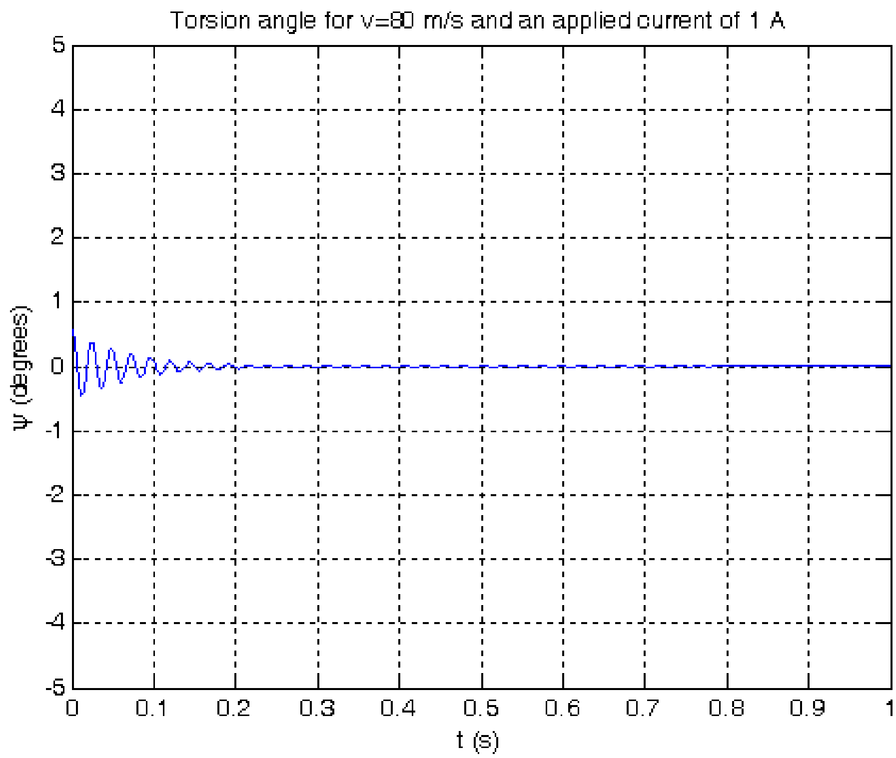

Figure 7.13: Torsion angle ψ for v =80 m/s and an applied current of 1 A.

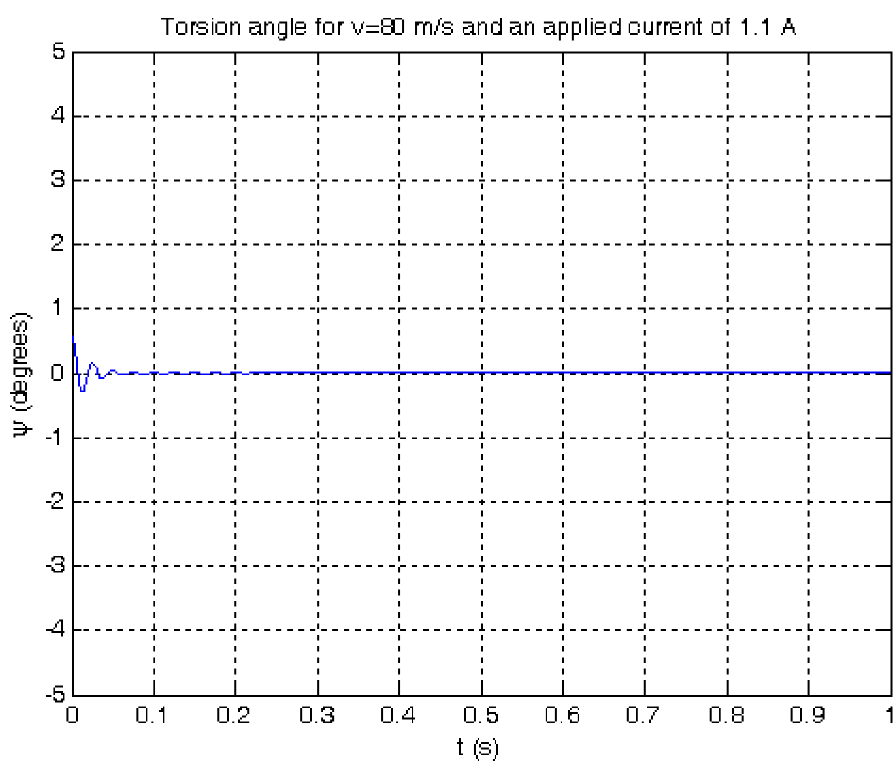

Figure 7.14: Torsion angle ψ for v =80 m/s and an applied current of 1.1 A.

Table 7.2: Application of an MR damper to the torsional landing gear model.

velocity v (m/s)	applied current I (A)	root mean square of the amplitude (degrees)	qualitative description
30	0	0.2579	amplitude grows
	0.5	0.2535	amplitude grows
	0.75	0.1641	amplitude grows
	1	0.0012	oscillation is damped in 0.1 s
	1.1	7.8×10^{-4}	oscillation is damped in 0.05 s
80	1	0.0013	oscillation is damped in 0.2 s
	1.1	7.6×10^{-4}	oscillation is damped in 0.05 s

7.13 Conclusions about Introduction of the MR damper into the Torsional Landing Gear Model

- An MR damper modeled by the current–dependent Bouc–Wen model is introduced into the torsional landing gear model.
- Currents of 0, 0.5, 0.75, 1 and 1.1 A have been applied to the MR damper in an aircraft taxiing at 30 m/s and currents of 1 and 1.1 A have been applied to the MR damper in an aircraft taxiing at 80 m/s.
- Time histories of the torsion angle ψ are plotted.
- An MR shimmy damper added to the system is able to suppress shimmy, even at the presence of a very low hydraulic damping constant of 20 Nm/rad/s.
- A low current of 1A is able to suppress shimmy in 0.1 s for a taxiing velocity of 30 m/s and in 0.2 s for that of 80 m/s.
- Application of a current of 1.1 A suppresses shimmy in 0.05 s for taxiing velocities of 30 m/s and 80 m/s.
- Figures 7.8–7.14 reveal that increasing the applied current decreases shimmy amplitude.

- Increasing the applied current damps the oscillation in a shorter amount of time.
- A comparison of figures 7.11–7.12 and 7.13–7.14 reveal that if the same current is applied to the MR dampers in two aircraft taxiing at different velocities, it will take longer for shimmy to be damped in the faster aircraft.

7.14 Introduction of the MR damper into the Torsional Landing Gear Model with Freeplay

An MR damper is introduced into the torsional landing gear model with freeplay. Torsional freeplay is incorporated by substituting (6.1) into (7.23) such as

$$I_z\ddot{\psi} + M(\psi) + M_2 + M_3 + M_4 + M_5 = 0 \qquad \textbf{(7.25)}$$

where $M(\psi)$ is the freeplay term.

Current–dependent Bouc–Wen model described by equations (7.14)–(7.22) is applied to the torsional landing gear model with freeplay described by (7.25), (5.13) and (5.17). As was the case in section 7.12 and as seen in equation (7.25), the torsional damper is not removed from the system when the MR damper is introduced. (7.14) is substituted into M_5 as the damper force, as in section 7.12. Optimal parameters found in section 7.12 have been utilized in this section, as well.

Results are displayed for freeplay angles ψ_{fp} within the range 0º–2º, as this is the range employed in literature, and various current inputs. Results are compared with those of section 7.12 to see the effect of having an MR damper at the existence of freeplay.

Time histories of the torsion angle ψ are obtained for freeplay angles ψ_{fp} of 0º, 0.5º, 1º and 1.5º and applied currents of1, 1.1 and 1.2 A.

Figures 7.15–7.24 are obtained for a taxiing velocity of 30 m/s while figures 7.25 and 7.26 are obtained for a taxiing velocity of 80 m/s. Figure 7.15 shows the time history of the torsion angle ψ for a freeplay angle ψ_{fp} of 0º and for an applied current of 1 A. Figures 7.16–7.18 show the time history of the torsion angle ψ for a freeplay angle ψ_{fp} of 0.5º and applied currents of 1, 1.1 and 1.2 A, respectively. Figures

7.19–7.21 show the time history of the torsion angle ψ for a freeplay angle ψ_{fp} of 1° and applied currents of 1, 1.1 and 1.2 A, respectively. Figures 7.22–7.24 show the time history of the torsion angle ψ for a freeplay angle ψ_{fp} of 1.5° and applied currents of 1, 1.1 and 1.2 A, respectively. Figures 7.25 and 26 show the time history of the torsion angle ψ for a freeplay angle ψ_{fp} of 0.5° and applied currents of 1 and 1.1 A, respectively. Limit cycle oscillations are observed for applied currents of 1 A for a taxiing velocity of 30 m/s.

It is seen by inspecting figures 7.16–7.26 and table 7.3 that a higher current input is necessary for shimmy damping in the case of freeplay.

Figure 7.15 shows the torsion angle for v=30 m/s and an applied current of 1 A in the absence of a freeplay angle.

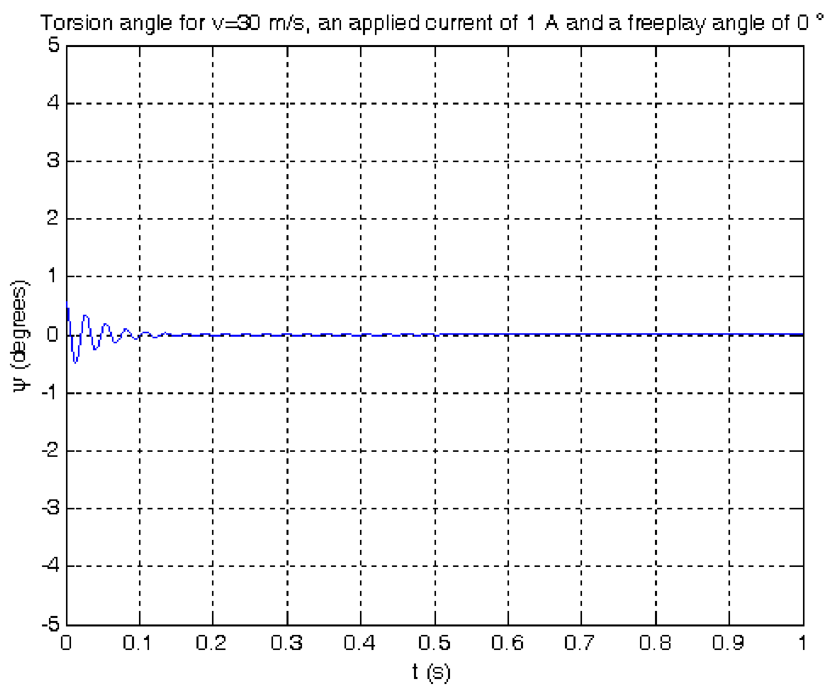

Figure 7.15: ψ for ψ_{fp} =0°, v=30 m/s and an applied current of 1 A.

Figures 7.16–7.18 show the torsion angle for v=30 m/s and a freeplay angle of 0.5° with applied currents of 1, 1.1 and 1.2 A, respectively.

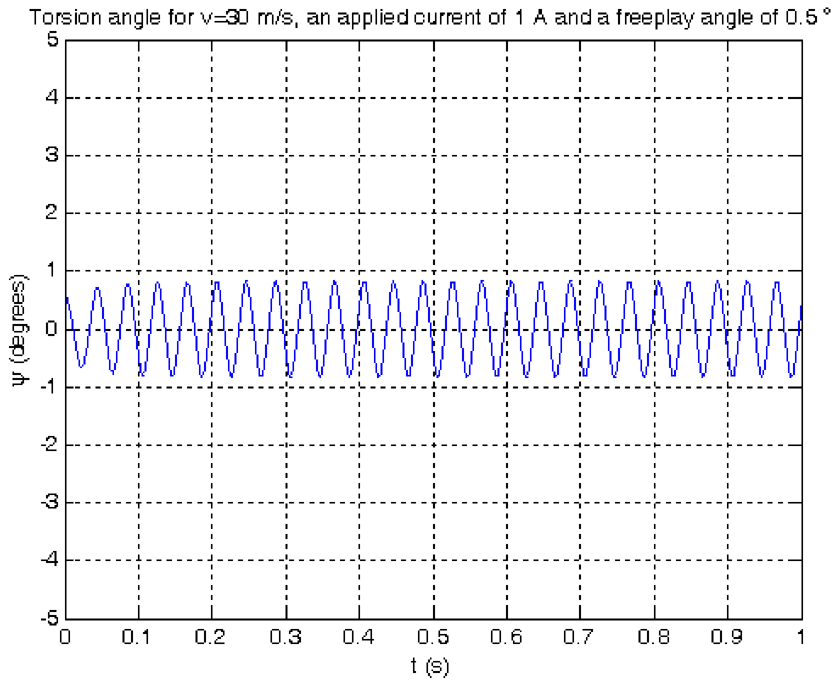

Figure 7.16: ψ for ψ_{fp} =0.5°, v =30 m/s and an applied current of 1 A.

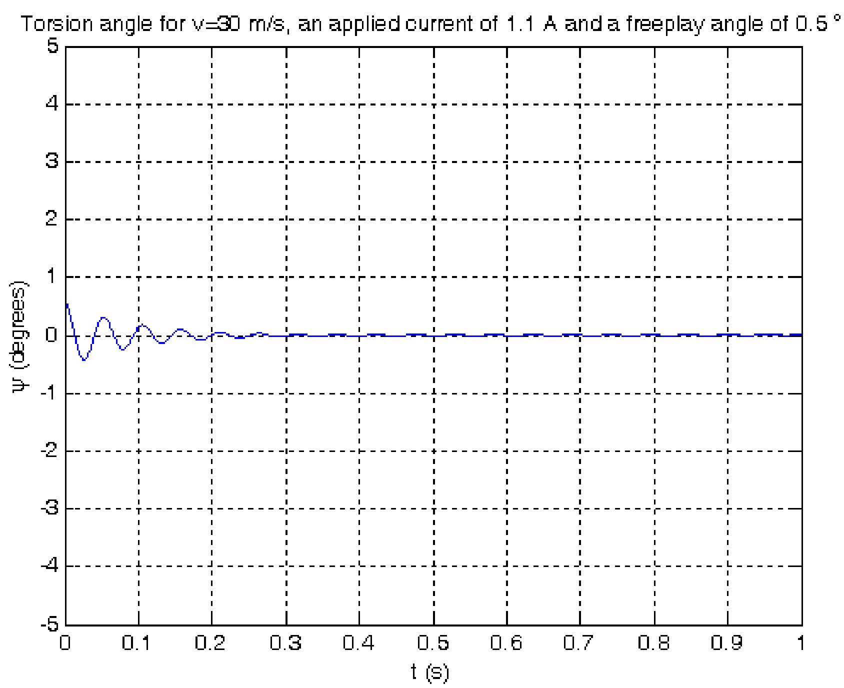

Figure 7.17: ψ for ψ_{fp} =0.5°, v =30 m/s and an applied current of 1.1 A.

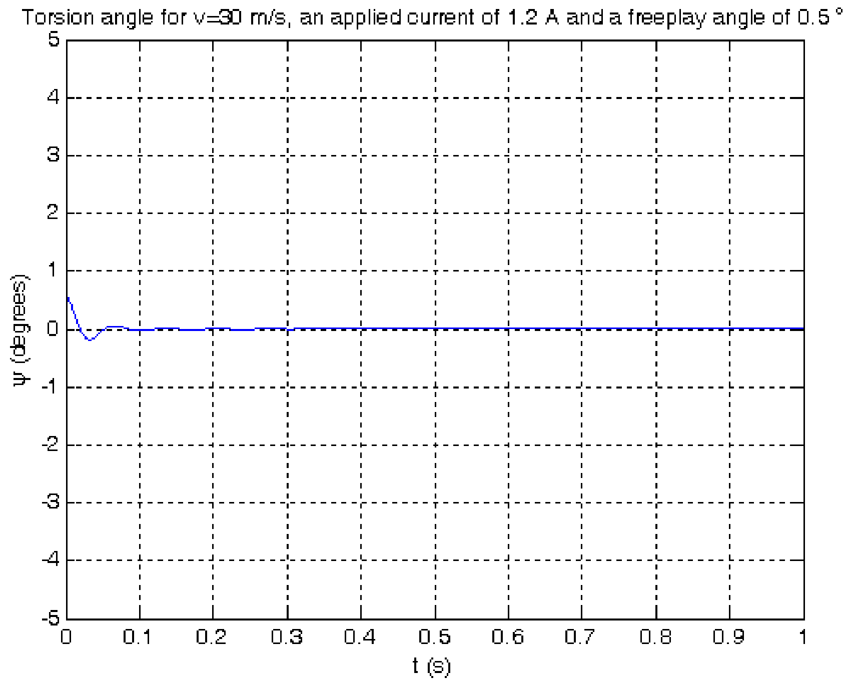

Figure 7.18: ψ for ψ_{fp} =0.5°, v =30 m/s and an applied current of 1.2 A.

Figures 7.19–7.21 show the torsion angle for v =30 m/s and a freeplay angle of 1° with applied currents of 1, 1.1 and 1.2 A, respectively.

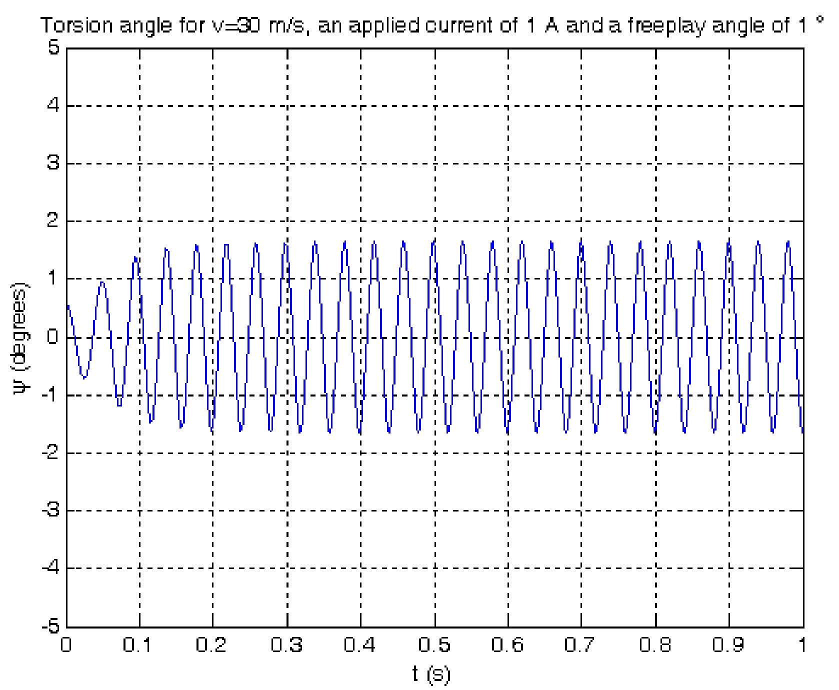

Figure 7.19: ψ for ψ_{fp} =1°, v =30 m/s and an applied current of 1 A.

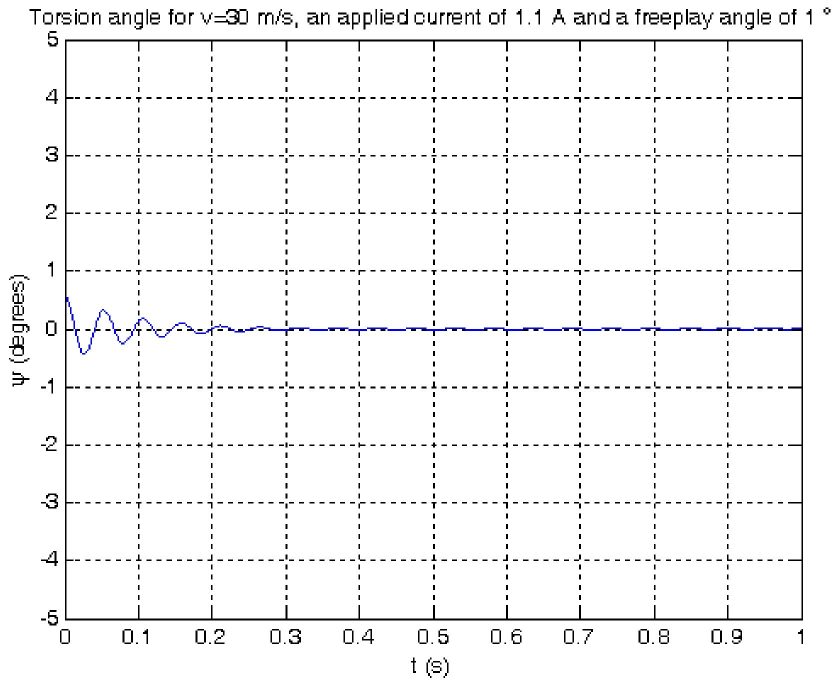

Figure 7.20: ψ for $\psi_{fp}=1°$, $v=30$ m/s and an applied current of 1.1 A.

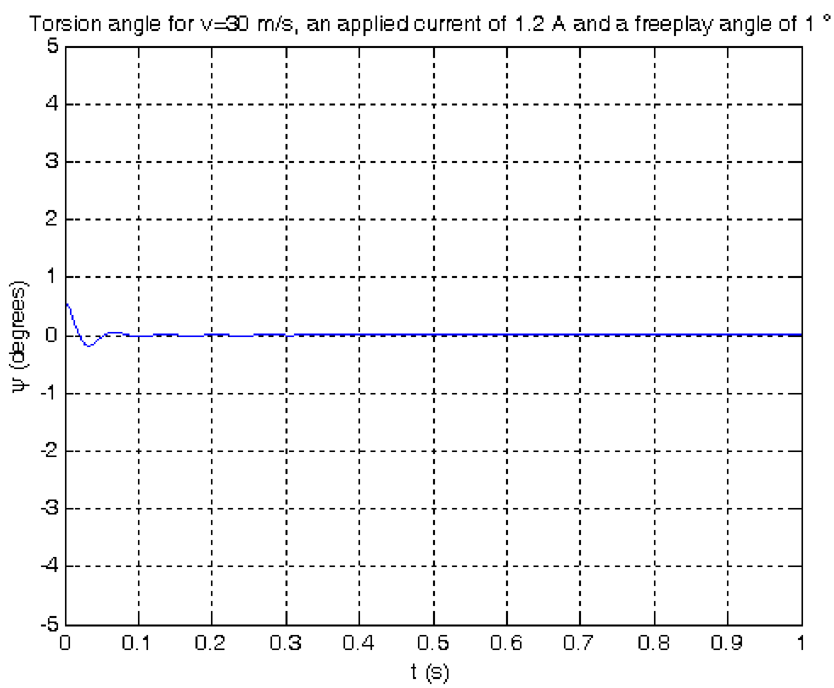

Figure 7.21: ψ for $\psi_{fp}=1°$, $v=30$ m/s and an applied current of 1.2 A.

Figures 7.22–7.24 show the torsion angle for $v=30$ m/s and a freeplay angle of 1.5° with applied currents of 1, 1.1 and 1.2 A, respectively.

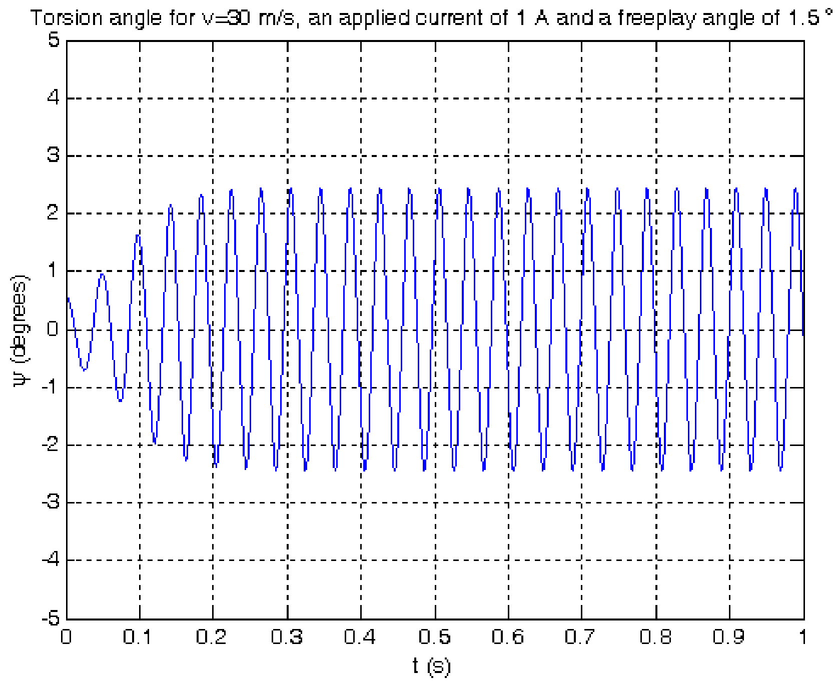

Figure 7.22: ψ for ψ_{fp} =1.5°, v =30 m/s and an applied current of 1 A.

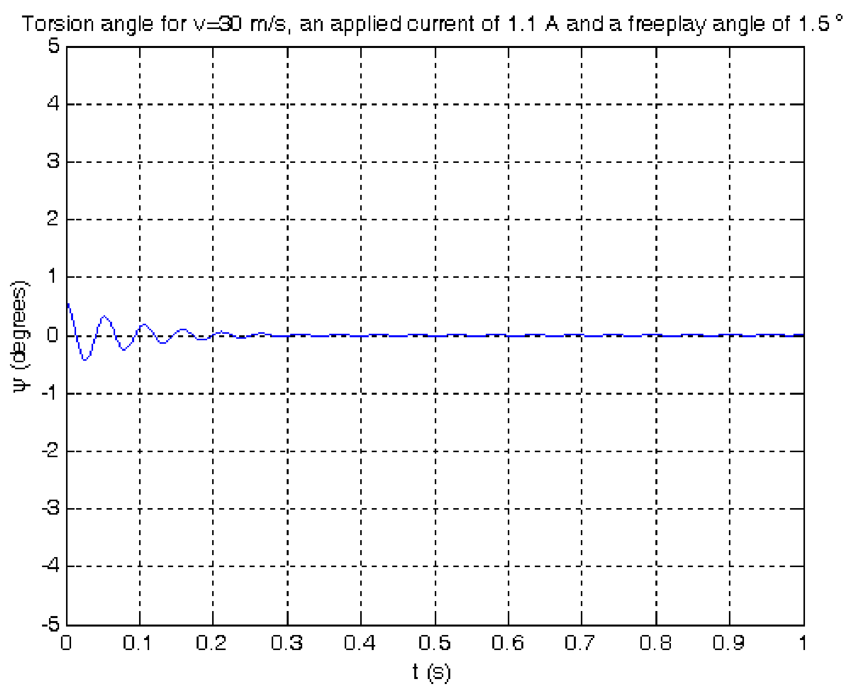

Figure 7.23: ψ for ψ_{fp} =1.5°, v =30 m/s and an applied current of 1.1 A.

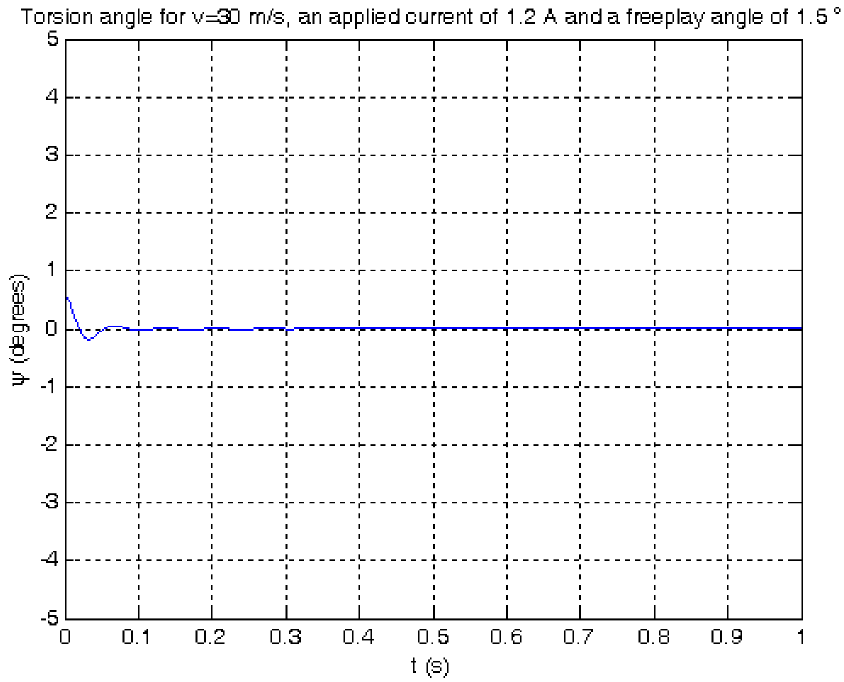

Figure 7.24: ψ for ψ_{fp} =1.5°, v =30 m/s and an applied current of 1.2 A.

Figures 7.25 and 7.26 show the torsion angle for v =80 m/s and a freeplay angle of 0.5° with applied currents of 1 and 1.1 A, respectively.

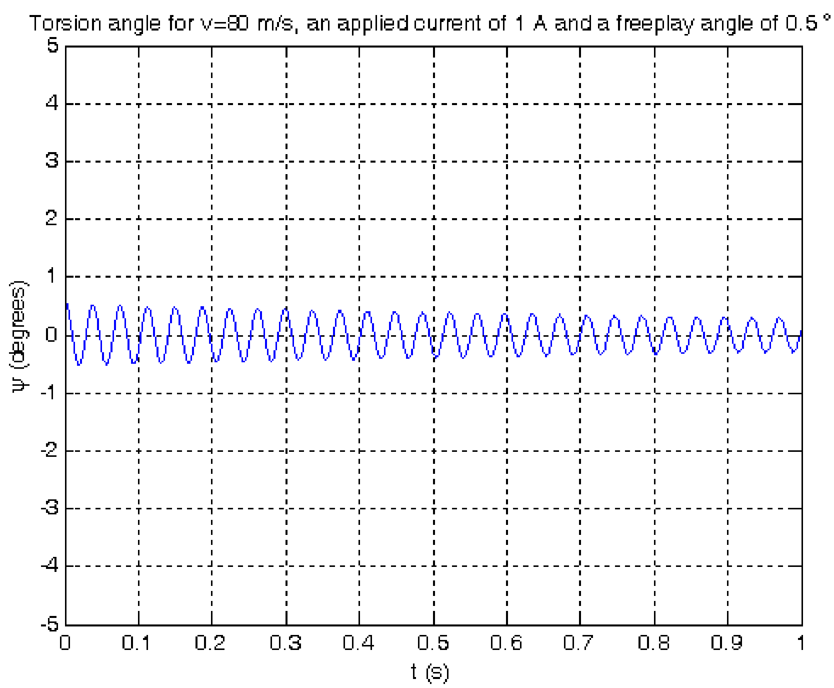

Figure 7.25: ψ for ψ_{fp} =0.5°, v =80 m/s and an applied current of 1 A.

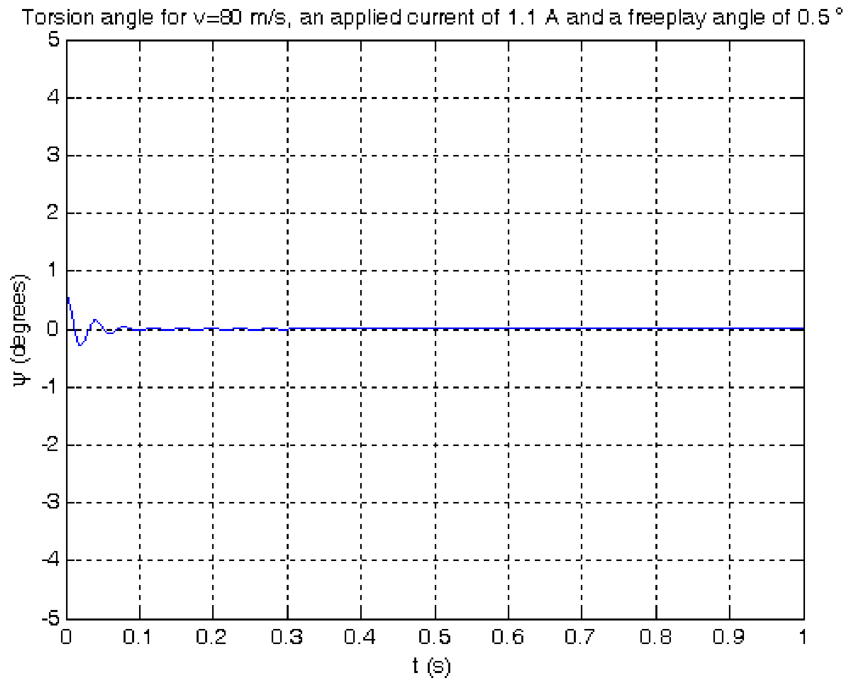

Figure 7.26: ψ for ψ_{fp} =0.5°, v =80 m/s and an applied current of 1.1 A.

Table 7.3: Application of an MR damper to the torsional landing gear model with freeplay.

velocity v **(m/s)**	**freeplay angle** ψ_{fp} **(degrees)**	**applied current** I **(A)**	**root mean square of the amplitude (degrees)**	**qualitative description**
30	0	1	0.0012	oscillation is damped in 0.1 s
	0.5	1	0.0097	limit cycle oscillation with amplitude 0.82°
		1.1	0.0015	oscillation is damped in 0.3 s
		1.2	9.8×10^{-4}	oscillation is damped in 0.1 s
	1	1	0.0189	limit cycle oscillation with amplitude 1.63°
		1.1	0.0016	oscillation is damped in 0.3 s
		1.2	0.0010	oscillation is damped in 0.1 s
	1.5	1	0.0277	limit cycle oscillation with amplitude 2.44°

		1.1	0.0016	oscillation is damped in 0.3 s
		1.2	0.0010	oscillation is damped in 0.1 s
80	0.5	1	0.0050	slowly decaying oscillation
		1.1	9.48×10^{-4}	oscillation is damped in 0.1 s

7.15 Conclusions about Introduction of an MR Damper into the Torsional Landing Gear Model with Freeplay

- Time histories of the torsion angle ψ are obtained for freeplay angles ψ_{fp} of 0°, 0.5°, 1° and 1.5° and applied currents of 1, 1.1 and 1.2 A in an aircraft taxiing at 30 m/s.
- Figures 7.15–7.24 and table 7.3 reveal that limit cycle oscillations are observed for an applied current of 1 A for freeplay angles of 0.5°, 1° and 1.5°.
- Limit cycle amplitudes increase with increasing freeplay angle, as stated in section 6.5.2.
- A comparison of tables 7.2 and 7.3 shows that a higher current input is necessary for shimmy damping in the case of freeplay.
- Existence of freeplay necessitates a higher current input to the MR damper for shimmy damping. 1.1 A was the sufficient current for shimmy damping for taxiing velocities of 30 and 80 m/s and a hydraulic damping coefficient c of 20 Nm/rad/s. In the case of freeplay, 1.2 A is sufficient for freeplay angles of 0.5°, 1° and 1.5°.
- 1.2 A is enough to suppress shimmy for a taxiing velocity of 30 m/s even for a freeplay angle of 5°. The necessary current to suppress shimmy for a taxiing velocity of 30 m/s is 1.2 A, regardless of the amount of freeplay.
- It was stated in section 6.5.2 that an aircraft having torsional freeplay in its landing gear becomes less susceptible to shimmy if its velocity increases. A comparison of figures 7.16 and 7.17 with 7.25 and 7.26 reveals the same information. Figures 7.16 and 7.17 show the time history of the torsion angle for a taxiing velocity of 30 m/s and applied currents of 1 and 1.1 A in the presence of 0.5° of freeplay, while figures 7.25 and 7.26 show the time

history of the torsion angle for a taxiing velocity of 80 m/s and applied currents of 1 and 1.1 A in the presence of 0.5° of freeplay. It is seen that the configuration with a taxiing velocity of 30 m/s is more prone to shimmy than the configuration with a taxiing velocity of 80 m/s.

7.16 A Landing Roll Scenario

In this section, landing roll of an aircraft is simulated with and without the MR damper model discussed above. For this purpose, slowing down of the aircraft on the runway from 80 m/s to 30 m/s in 10 s has been simulated. Cases with the MR damper are for currents of 0, 0.5, 0.75 and 1 A. The conventional hydraulic shimmy damper has been assigned damping constants of 20, 40, 60 and 70 Nm/rad/s. Time histories of the torsion angle ψ for all the landing combinations are seen in figures 7.27–7.42 and qualitative and quantitative observations about each of these cases have been summarized in table 7.4.

Figures 7.27–7.30 show the torsion angle for c =20 Nm/rad/s with applied currents of 0, 0.5, 0.75 and 1 A, respectively.

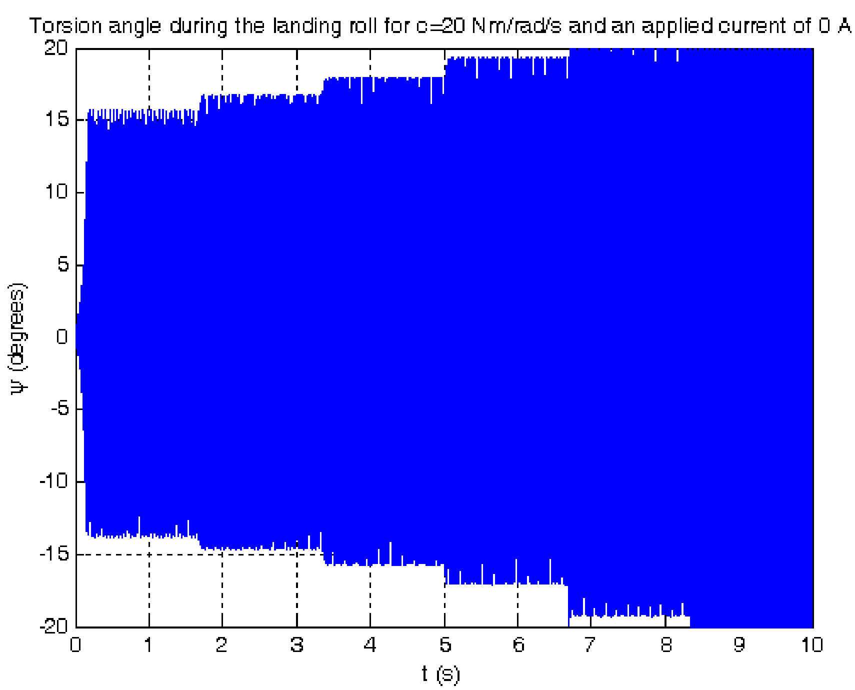

Figure 7.27: ψ during the landing roll for c =20 Nm/rad/s and a current of 0A.

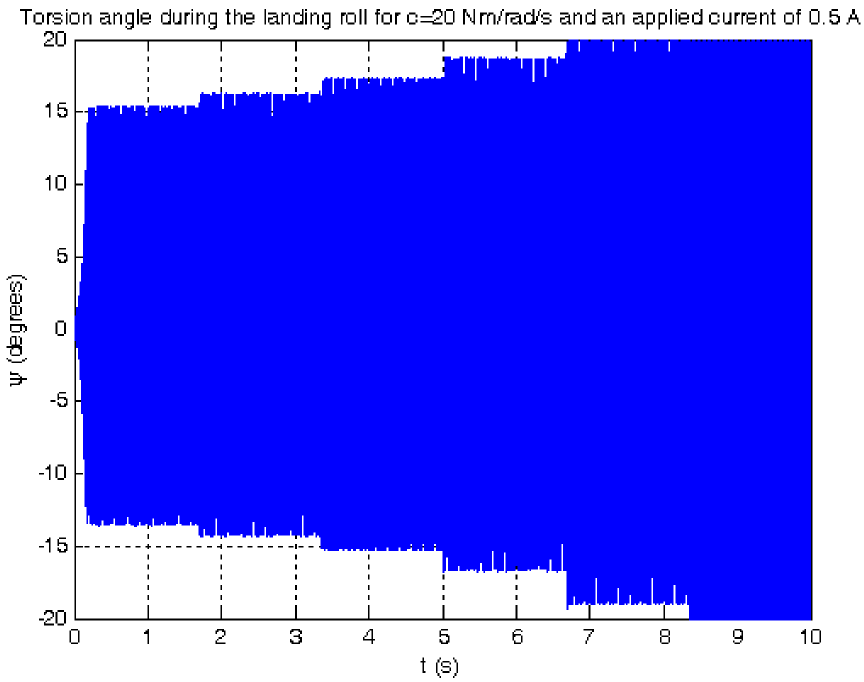

Figure 7.28: ψ during the landing roll for c =20 Nm/rad/s and a current of 0.5A.

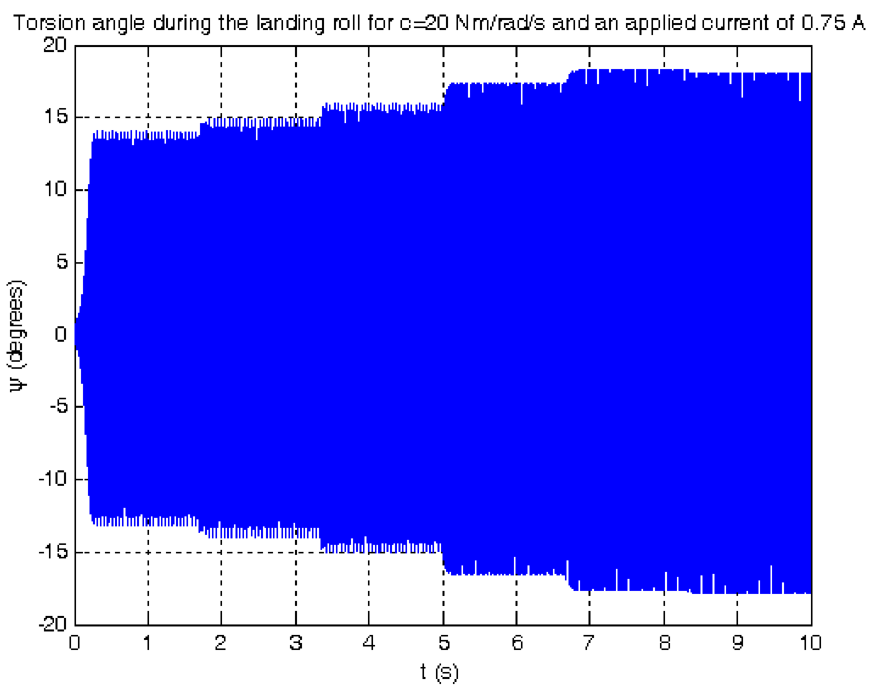

Figure 7.29: ψ during the landing roll for c =20 Nm/rad/s and a current of 0.75A.

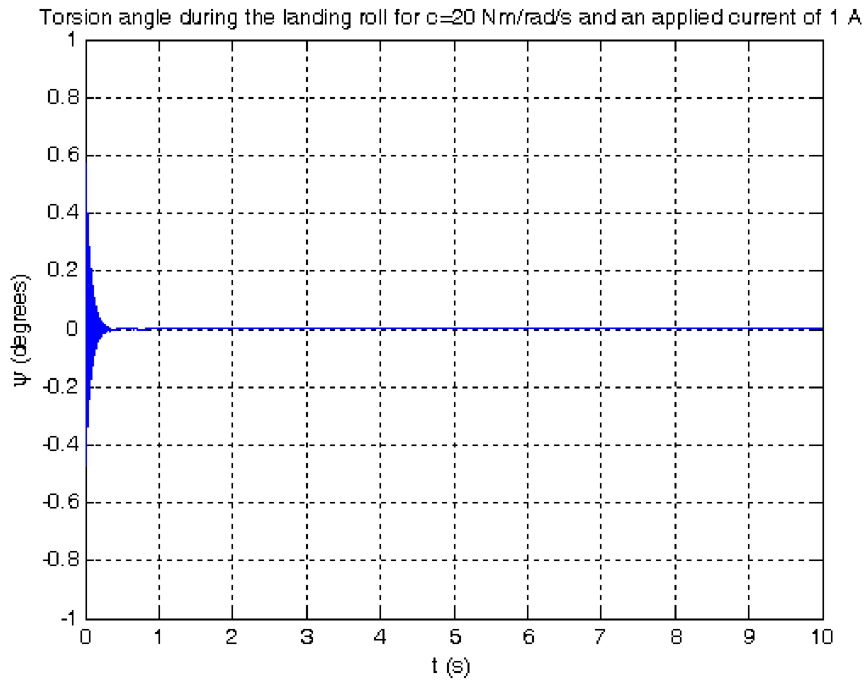

Figure 7.30: ψ during the landing roll for c =20 Nm/rad/s and a current of 1A.

Figures 7.31–7.34 show the torsion angle for c =40 Nm/rad/s with applied currents of 0, 0.5, 0.75 and 1 A, respectively°.

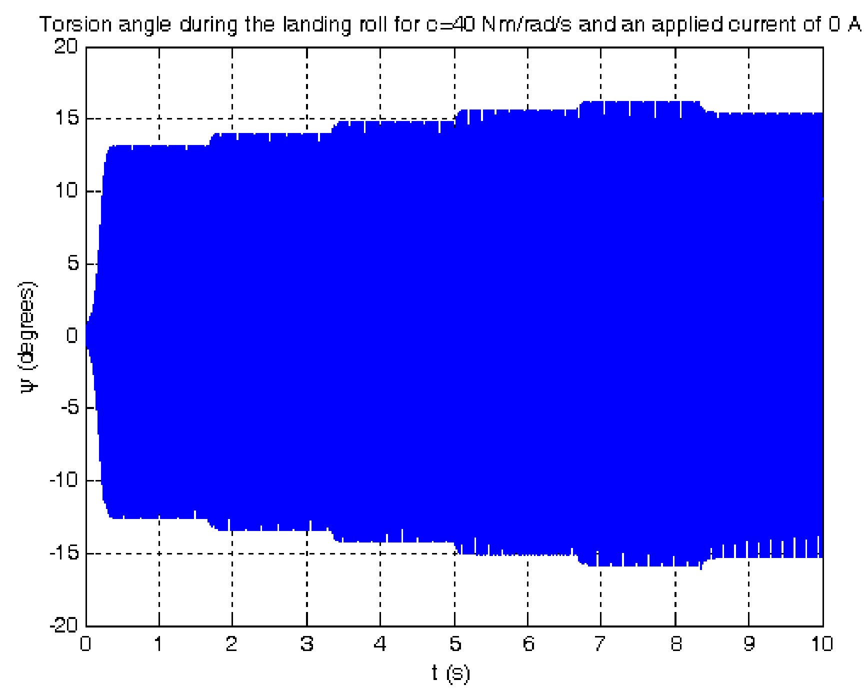

Figure 7.31: ψ during the landing roll for c =40 Nm/rad/s and a current of 0A.

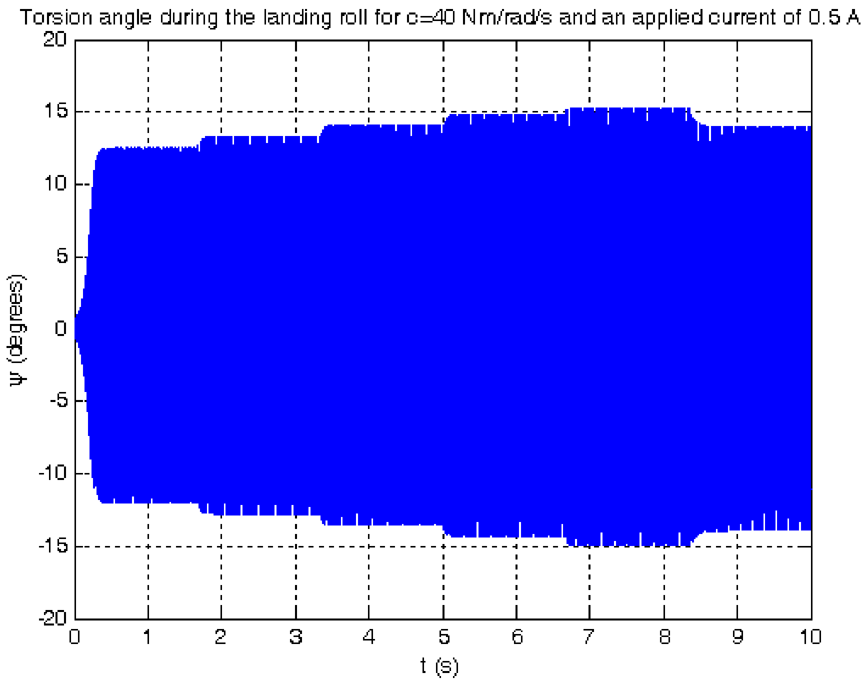

Figure 7.32: ψ during the landing roll for c =40 Nm/rad/s and a current of 0.5A.

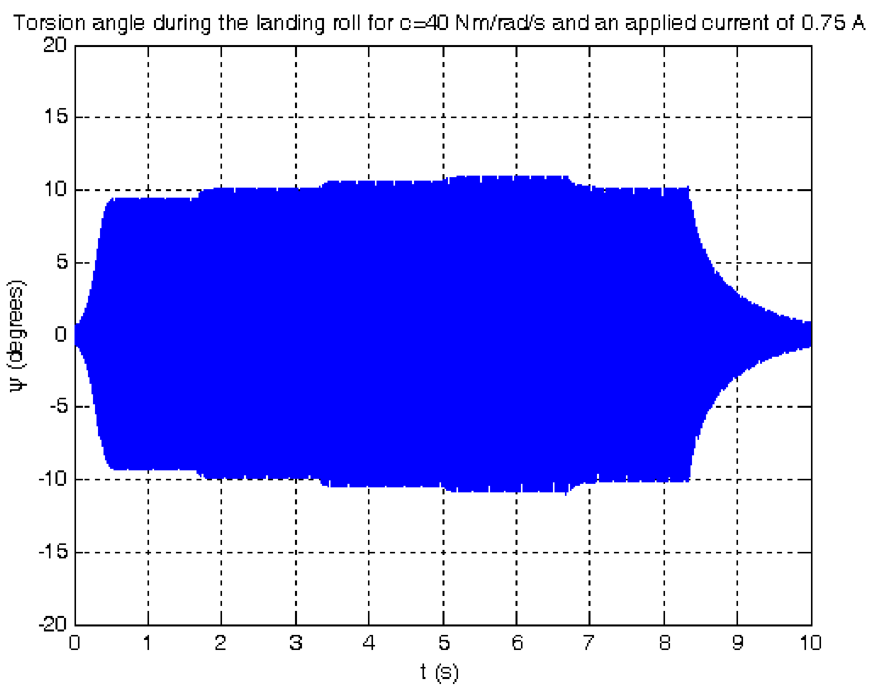

Figure 7.33: ψ during the landing roll for c =40 Nm/rad/s and a current of 0.75A.

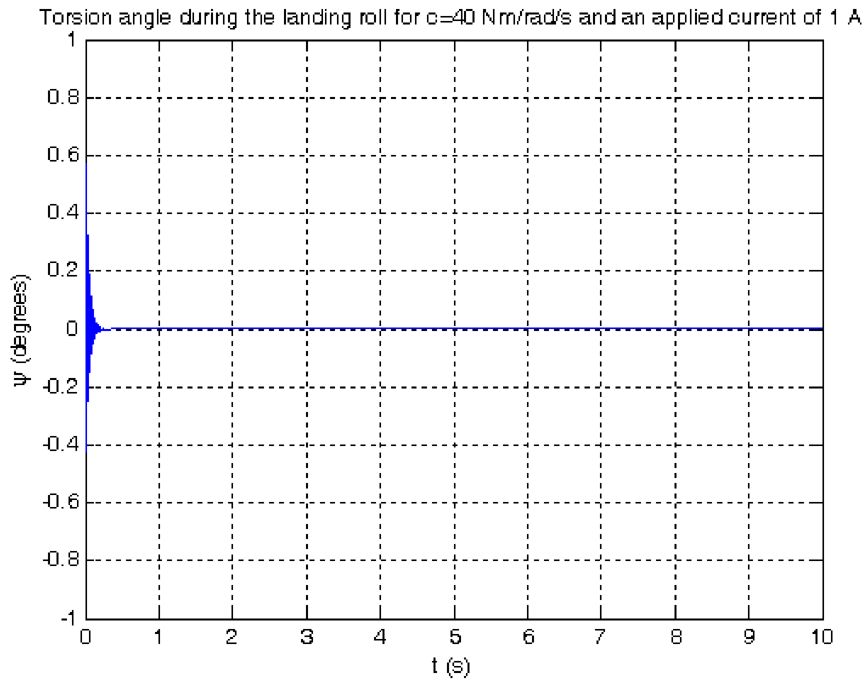

Figure 7.34: ψ during the landing roll for c =40 Nm/rad/s and a current of 1A.

Figures 7.35–7.38 show the torsion angle for c =60 Nm/rad/s with applied currents of 0, 0.5, 0.75 and 1 A, respectively°.

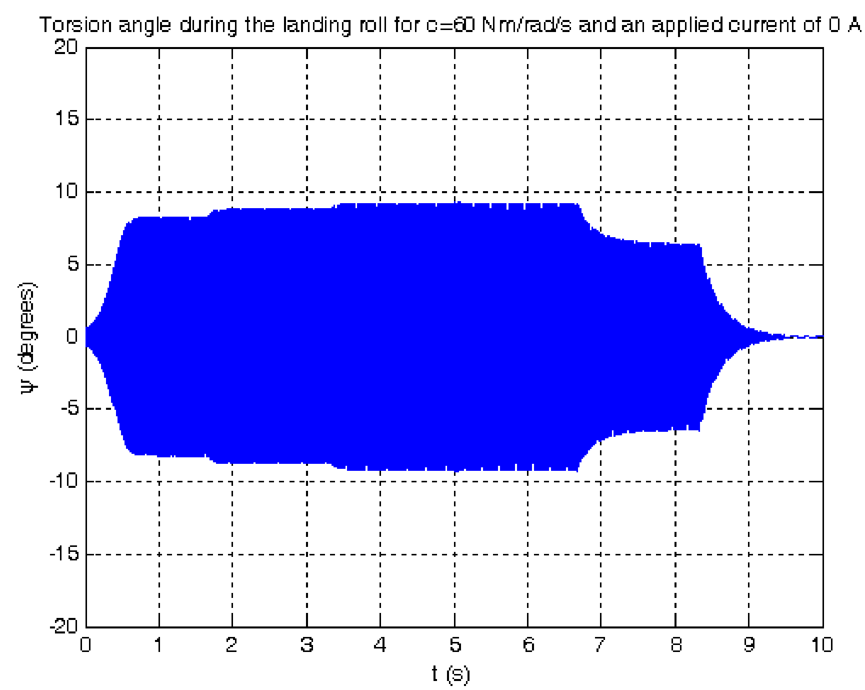

Figure 7.35: ψ during the landing roll for c =60 Nm/rad/s and a current of 0A.

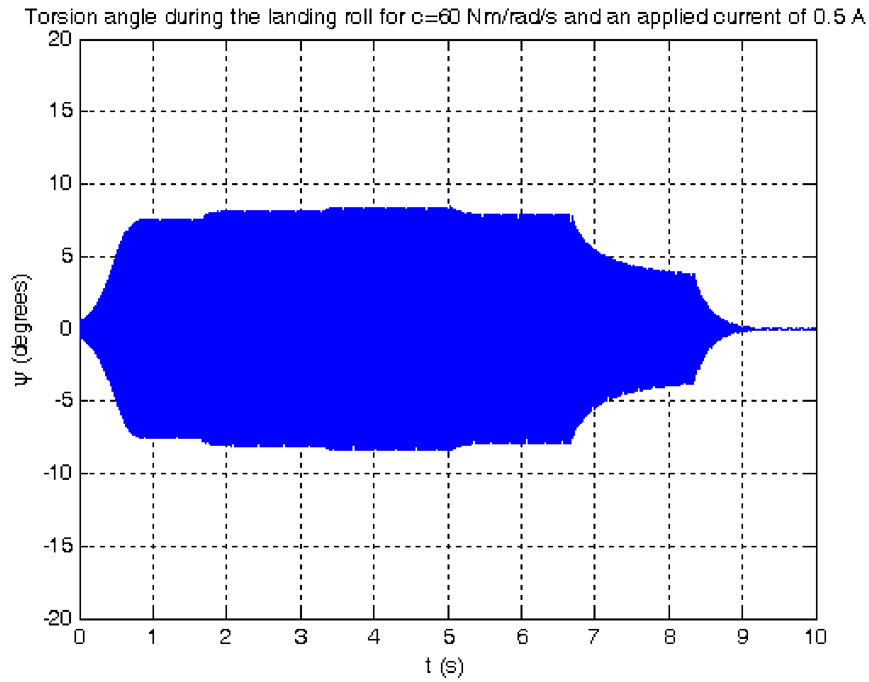

Figure 7.36: ψ during the landing roll for c =60 Nm/rad/s and a current of 0.5A.

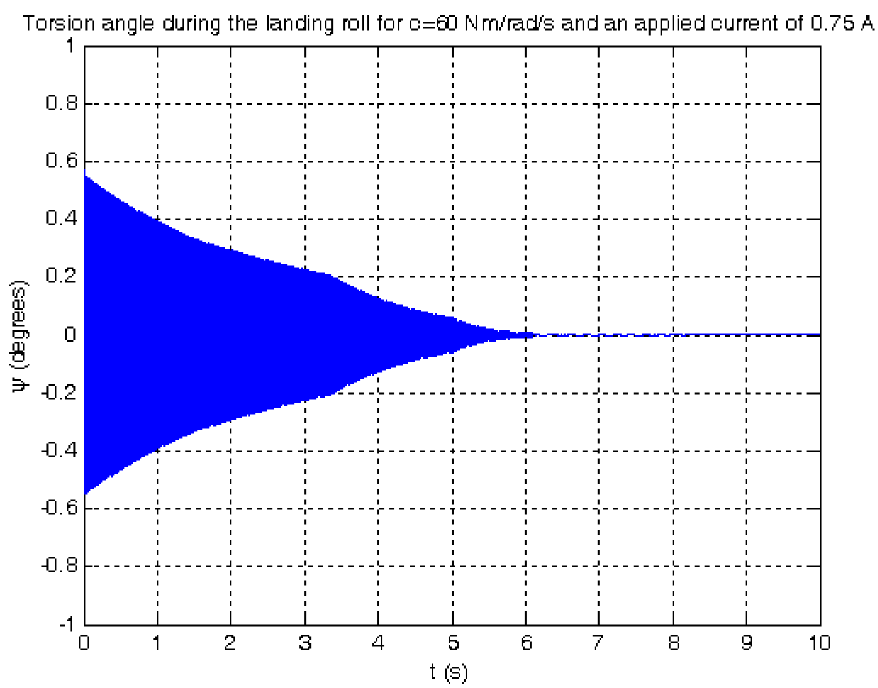

Figure 7.37: ψ during the landing roll for c =60 Nm/rad/s and a current of 0.75A.

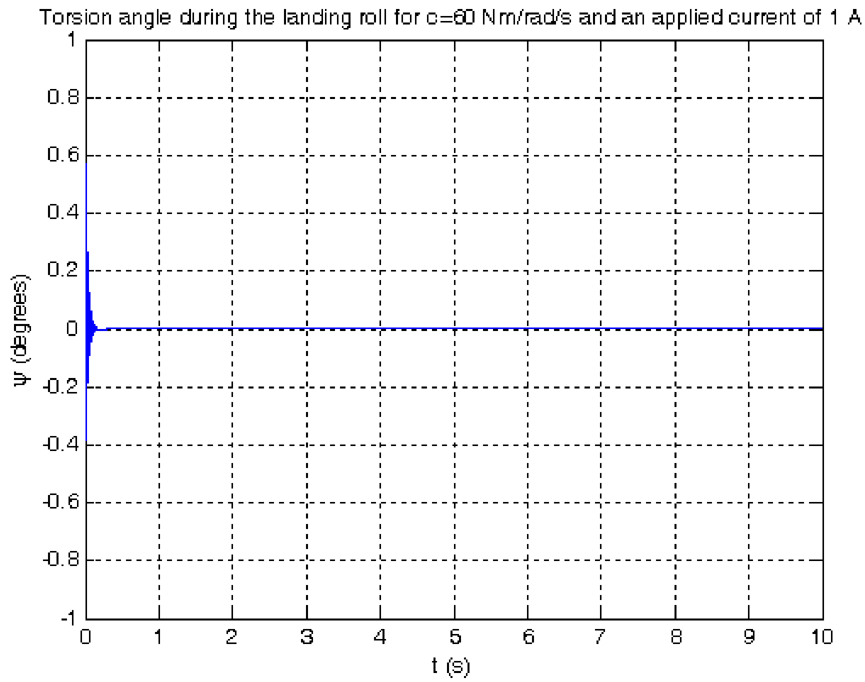

Figure 7.38: ψ during the landing roll for $c = 60$ Nm/rad/s and a current of 1A.

Figures 7.39–7.42 show the torsion angle for $c = 70$ Nm/rad/s with applied currents of 0, 0.5, 0.75 and 1 A, respectively°.

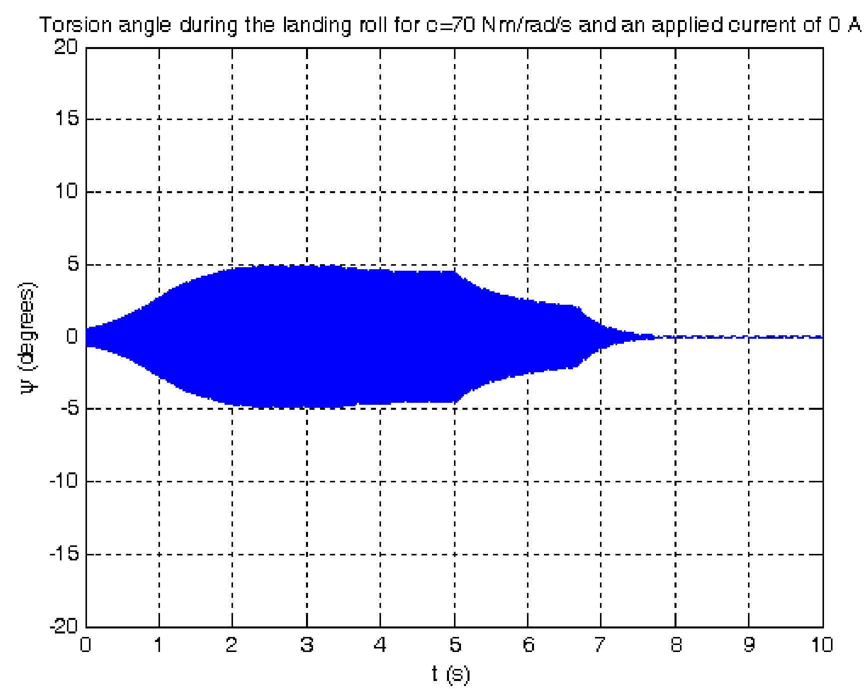

Figure 7.39: ψ during the landing roll for $c = 70$ Nm/rad/s and a current of 0A.

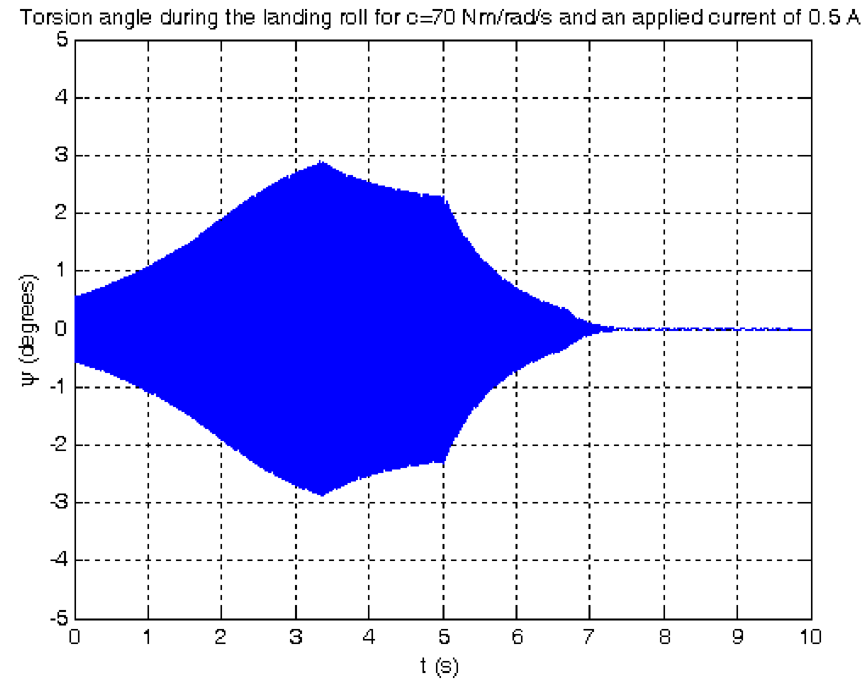

Figure 7.40: ψ during the landing roll for c =70 Nm/rad/s and a current of 0.5A.

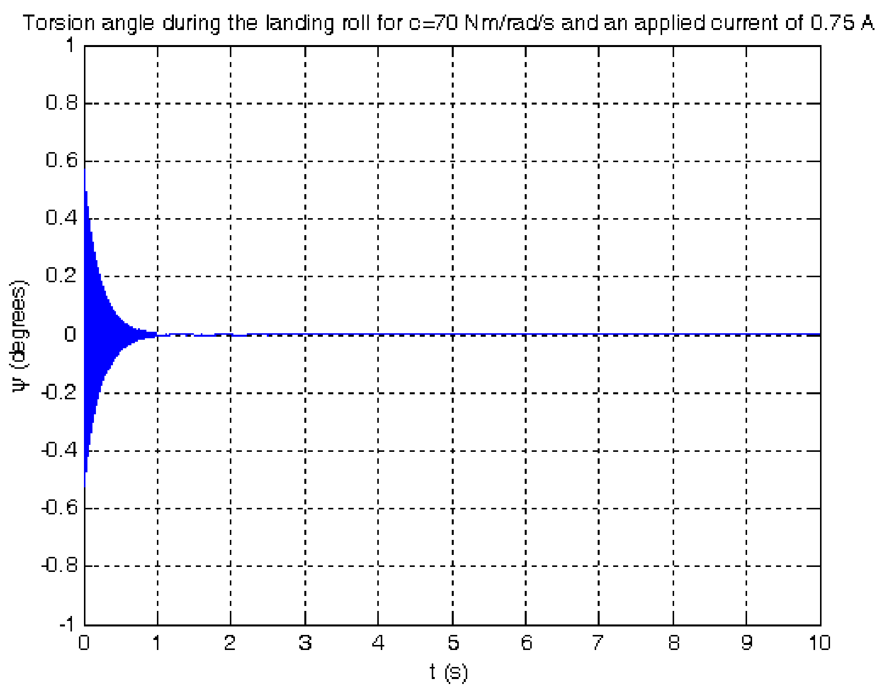

Figure 7.41: ψ during the landing roll for c =70 Nm/rad/s and a current of 0.75A.

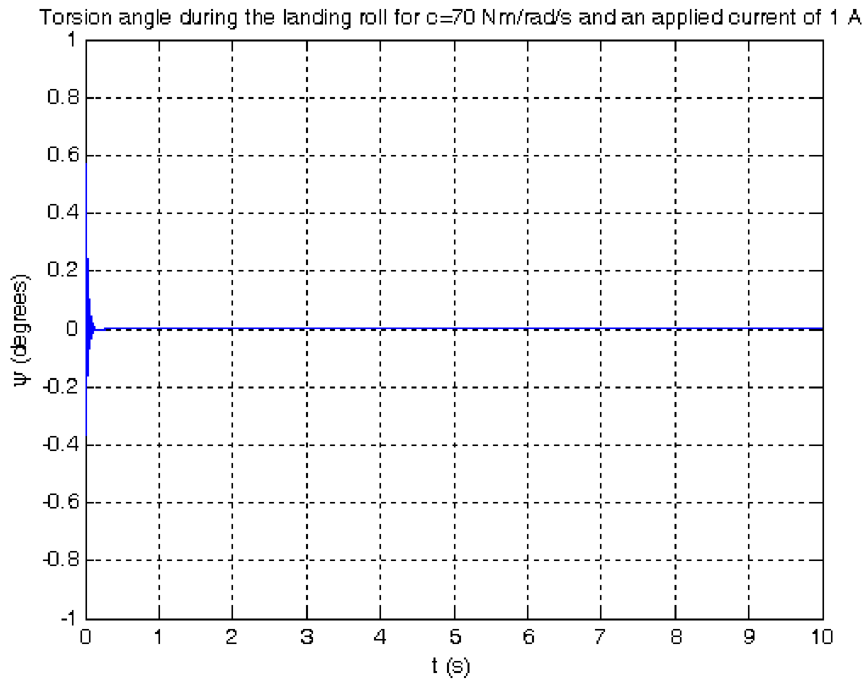

Figure 7.42: ψ during the landing roll for c =70 Nm/rad/s and a current of 1A.

Table 7.4: Effect of the MR damper during the landing roll.

hydraulic damping constant c **(Nm/rad/s)**	**applied current** I **(A)**	**root mean square of the amplitude (degrees)**	**qualitative description**
20	0	0.2260	oscillations with growing amplitudes
	0.5	0.2224	oscillations with growing amplitudes
	0.75	0.1951	oscillations with growing amplitudes
	1	4.19×10^{-4}	oscillation is damped in 0.25 s
40	0	0.1787	• oscillations with growing amplitudes • amplitude decreases at 8.3 s as the velocity drops to 30 m/s
	0.5	0.1683	• oscillations with growing amplitudes • amplitude decreases at 8.3 s as the velocity drops to 30 m/s

	0.75	0.1142	• oscillations with growing amplitudes • amplitude starts to decay at 8.3 s as the velocity drops to 30 m/s
	1	3.3×10^{-4}	oscillation is damped in 0.25 s
60	0	0.0934	• oscillations with growing amplitudes until 6.7 s • amplitude starts to decay at 6.7 s as the velocity drops to 40 m/s • amplitude starts to decay faster at 8.3 s as the velocity drops to 30 m/s • oscillation is damped in 9.5 s
	0.5	0.0815	• oscillations with growing amplitudes until 6.7 s • amplitude starts to decay at 6.7 s as the velocity drops to 40 m/s • amplitude starts to decay faster at 8.3 s as the velocity drops to 30 m/s • oscillation is damped in 9.1 s
	0.75	0.0026	• oscillations with decreasing amplitudes • oscillation is damped in 6.1 s
	1	2.9×10^{-4}	oscillation is damped in 0.2 s
70	0	0.0390	• oscillations with growing amplitudes until 3.3 s • amplitude starts to decay at 3.3 s as the velocity drops to 60 m/s • amplitude starts to decay faster at 5 s as the velocity drops to 50 m/s • amplitude starts to decay even faster at 6.6 s as the velocity drops to 40 m/s • oscillation is damped in 7.7 s
	0.5	0.0190	• oscillations with growing amplitudes until 3.3 s • amplitude starts to decay at 3.3 s as the velocity drops to 60 m/s • amplitude starts to decay faster at 5 s as the velocity drops to 50 m/s

			• oscillation is damped in 7.7 s
	0.75	7.14×10^{-4}	oscillation is damped in 1 s
	1	2.7×10^{-4}	oscillation is damped in 0.1 s

7.17 Conclusions about Introduction of the MR Damper during the Landing Roll

- Landing roll of an aircraft has been simulated with and without an MR damper, while the conventional hydraulic shimmy damper is maintained within the model.
- Slowing down of the aircraft on the runway from 80 m/s to 30 m/s in 10 s has been simulated. Cases with the MR damper are for currents of 0, 0.5, 0.75 and 1 A. The conventional hydraulic shimmy damper has been assigned damping constants of 20, 40, 60 and 70 Nm/rad/s.
- Time histories of the torsion angle ψ are plotted.
- Qualitative and quantitative results are summarized in table 7.4.
- Figures 7.27–7.42 reveal that increasing the applied current decreases shimmy amplitude.
- Increasing the applied current damps the oscillation in a shorter amount of time.
- For cases with damping coefficients c of 20, 40 and 60 Nm/rad/s, 1A is the required current for shimmy to be damped. In all three cases, shimmy is damped in less than 0.25 s.
- Since 60 Nm/rad/s is not a low damping coefficient, a current of 0.75 A damps shimmy in 6.1 s and a current of 0.5 A damps shimmy in 9.1 s. Shimmy is damped in 9.5 s even when no current is applied.
- In the case of a hydraulic damping coefficient c of 40 Nm/rad/s, if no current or a current of 0.5 or 0.75 A is applied to the MR damper, shimmy amplitude increases until 8.3 s when the aircraft slows down to 30 m/s and starts to decrease after 8.3 s. The amount of decay in amplitude increases with increasing current.

- In the case of a hydraulic damping coefficient c of 20 Nm/rad/s, shimmy amplitudes grow if no current or a current of 0.5 or 0.75 A is applied to the MR damper.
- In the case of a hydraulic damping coefficient c of 70 Nm/rad/s, shimmy is damped in 7.7 s even when no current or a current of 0.5 A is applied to the shimmy damper. Shimmy is damped in 1 s when a current of 0.75 A is applied.
- Application of 1 A damps shimmy in 0.25 s if the hydraulic damping coefficient is 20 or 40 Nm/rad/s, in 0.2 s if it is 60 Nm/rad/s and in 0.1 s if it is 70 Nm/rad/s.
- If the same current is applied to the MR dampers in two aircraft taxiing at different velocities, it will take longer for shimmy to be damped in the faster aircraft.
- If the same current is applied to the MR dampers in two aircraft taxiing with different hydraulic damping coefficients, it will take longer for shimmy to be damped in the aircraft with a smaller damping coefficient.

8. CONCLUSIONS AND RECOMMENDATIONS FOR FUTURE RESEARCH

Shimmy analysis of a torsional nose landing gear model is conducted in this study. Shimmy is the oscillatory motion of the landing gear, caused by the interaction between the dynamics of the tire and the landing gear, and is an important phenomenon as it may lead to damage to the landing gear or the aircraft itself.

Linear and nonlinear analysis tools have been used and the concept of freeplay and an MR damper have been incorporated into the model. Current–dependent Bouc–Wen model has been applied.

Shimmy stability of a landing gear is a function of many design variables regarding the landing gear structure and the tire. Stiffness and geometry of the landing gear are decisive factors for shimmy stability. The following conclusions have been drawn.

- Eigenvalues have been computed for e in the range -0.4 m and 0.4 m and v in the range 5 m/s and 85 m/s. The linear system was found to have a pair of complex eigenvalues and a real eigenvalue. The system was found to be unstable due to positive real parts of the complex eigenvalues for a range of caster lengths and velocities.
- Stability was analyzed in the $e-v$ plane for e in the range -0.1 m and 0.4 m and v in the range 0 m/s and 250 m/s. It was concluded that increasing the torsional spring rate k increases stability. The most and least risky ranges of e and v have been found for the parameters considered. It was concluded that for $k<100000$, there is more instability at small velocities and more stability at large velocities. The system was found to be stable for $e>0.3$ and $e<-0.1$.
- Stability was analyzed in the $c-v$ plane for c in the range 0 and 100 Nm/rad/s and v in the range 0 m/s and 250 m/s. It was concluded that for

$\sigma < 0.1$, there is more instability at small velocities and more stability at large velocities while for $\sigma > 0.1$, there is more stability at small velocities and more instability at large velocities.

- It was concluded that increasing the relaxation length σ decreases stability. Since $\sigma = 3a$, where a is the half contact length, using stiffer tires or tires with smaller contact patches help increase stability of the system.
- It was concluded that an increase in the vertical force F_z decreases stability.
- Although stability has been analyzed for different values of σ and F_z, it must be borne in mind that aircraft designers do not have a lot of freedom in choosing the size of the tire contact patch. Likewise, the vertical load that an aircraft needs to withstand is more or less known and there is not much freedom in choosing the vertical force. In other words, contact patch size and vertical force cannot be the main design driver.
- Increments in the half contact length led to increments in the unstable region in the $e-v$ plane. In other words, increasing the half contact length decreased stability. Decrements in the half contact length led to increments in the stable region in the $e-v$ plane. In other words, decreasing the half contact length increased stability. It was observed that increments in the stable and unstable regions are greater for a larger value of 100000 Nm/rad of the torsional spring rate k than for 50000 Nm/rad. It was seen that the directions of decreasing torsional spring rate k and increasing half contact length a are also the direction of decreasing stability.
- Increments in the caster length e led to increments in the stable region in the $c-v$ plane. In other words, increasing the caster length increased stability. Decrements in the relaxation length σ led to increments in the stable region in the $c-v$ plane. In other words, decreasing the relaxation length σ or the half contact length increased stability. Increments in the stable and unstable regions were smaller for large values of the relaxation length σ. It was seen that the directions of increasing relaxation length and decreasing the caster length are also the direction of decreasing stability.

- Increasing the damping constant c gave better damping characteristic. Increasing the velocity v resulted in the requirement for a higher damping constant. It was observed that there is a correlation between the oscillatory and damping characteristics of the torsion angle and that of the lateral tire deformation.
- In stable cases such as c =100 Nm/rad/s, time histories of the nonlinear model were observed to be very similar to the linear ones.
- Limit cycles occured in unstable cases where a weak damping constant of 10 or 20 Nm/rad/s is employed.
- Approach direction of limit cycles was observed to vary with initial conditions. Limit cycle is approached from inside for small initial yaw angles such as $\psi(0)=0.01$ and from outside for large initial conditions such as $\psi(0)=1$.
- Limit cycle amplitude is observed to be independent of the initial condition.
- Increasing the velocity v increased the limit cycle amplitudes of the torsion angle ψ and rate of change of the torsion angle $\dot{\psi}$, but decreased that of the lateral tire deformation y.
- Increasing the damping constant c decreased the limit cycle amplitudes of the torsion angle ψ, rate of change of the torsion angle $\dot{\psi}$ and the lateral tire deformation y.
- Decreasing the torsional spring constant k decreases the limit cycle amplitudes of the torsion angle ψ and rate of change of the torsion angle, $\dot{\psi}$, but increased the limit cycle amplitude of the lateral tire deformation y. Decreasing k also had an effect of decreasing the limit cycle frequency.
- It was observed that shimmy amplitude increases with increased velocities and decreased damping constants.
- It was concluded that limit cycle amplitudes increase with increasing freeplay angle. An aircraft having torsional freeplay in its landing gear becomes less susceptible to shimmy if its velocity increases. Initial condition $\psi(0)$ did not

have a significant effect on the limit cycle amplitude of the torsion angle. It was concluded that the existence of freeplay prevents shimmy damping of the system that would have been damped without freeplay.

- Increasing the freeplay angle led to an increase in the lateral tire deformation. Initial condition $\psi(0)$ did not have a significant effect on the limit cycle amplitude of the lateral tire deformation. It was concluded that existence of freeplay was prevents shimmy damping of the system that would have been damped without freeplay.

- An MR shimmy damper added to the system was able to suppress shimmy, even at the presence of a very low hydraulic damping constant of 20 Nm/rad/s. A low current of 1A was able to suppress shimmy in 0.1 s for a taxiing velocity of 30 m/s and in 0.2 s for that of 80 m/s. Application of a current of 1.1 A suppressed shimmy in 0.05 s for taxiing velocities of 30 m/s and 80 m/s. Increasing the applied current decreased shimmy amplitude. Increasing the applied current damped the oscillation in a shorter amount of time. When the same current was applied to the MR dampers in two aircraft taxiing at different velocities, it took longer for shimmy to be damped in the faster aircraft.

The following recommendations can be considered for future research on landing gear and shimmy.

- Aircraft landing gear and their interaction with the fuselage need to be improved. Guidelines to achieve a landing gear design free of vibrations are needed. Efforts should be given to find the right design the first time.

- All system parameters must be considered thoroughly to obtain a reliable design since there is no simple design rule for aircraft landing gear.

- Shimmy stability depends on tire characteristics and reliable data on aircraft tires are required. Effects of inflation pressure, wear and road texture can also be investigated, although wear and texture are hard to model and express quantitatively.

- Parametric studies can be conducted to study shimmy stability of a landing gear. It will be useful to determine the critical parameters effecting shimmy so that a straightforward design plan can be deduced.
- Situations such as accelerating during take–off or braking after landing may be considered. A vertical degree of freedom may be necessary in the case of a braking aircraft since the oleo may possibly be excited.
- Torsional and lateral bending modes of the fuselage may be included in the case of large commercial aircraft.
- A significant amount of testing is required.
- Dynamic conditions such as gear walk can also be considered.
- Effects of brake heating, tire inflation pressure and wear can be taken into account.
- Friction can be considered.

REFERENCES

[1] **Besselink, I. J. M.** (2000). S*himmy of Aircraft Main Landing Gears*, (Doctoral dissertation). Technical University of Delft.

[2] **Krüger, W., Besselink, I., Cowling, D., Doan, D. B., Kortüm, W. and Krabacher, W.** (1997). Aircraft Landing Gear Dynamics, Simulation and Control. *Vehicle System Dynamics,* **6**, 119–158.

[3] **Roskam, J.** (2000). Airplane Design, Part IV: Layout of Landing Gear and Systems, DAR Corporation.

[4] **Özkol, İ.** (2011). İniş Sistemi.

[5]<*ftp://ftp.uni-uisburg.de/FlightGear/Docs/Landing_Gear_Shock_Absorber.pdf*>, date retrieved November 23 2011

[6] <*http://en.wikipedia.org/wiki/Radial_tire*>, date retrieved March 19 2011

[7] **Currey, N. S.** (1988). Aircraft Landing Gear Design: Principles and Practices. AIAA Education Series.

[8] **Kundu, A. K.** (2010). Aircraft Design. Cambridge Aerospace Series, Cambridge University Press.

[9] <*http://en.wikipedia.org/wiki/Undercarriage*>, date retrieved March 15 2011

[10] **Zhu, S., Tong, M. and Xu, J.** (2008) Design of an adaptive shock absorber of landing gear and preliminary analysis on taxiing performance. *IEEE 7th International Conference on System Simulation and Scientific Computing*, October 10–12.

[11] **Baumann, J. A..** (1992). *Aircraft Landing Gear Shimmy* (Doctoral dissertation). University of Missouri.

[12] **Karnopp, D.** (2004). Vehicle Stability. Marcel Dekker, USA.

[13] **Chai, S. T. and Mason, W. H.** (1996). Landing Gear Integration in Aircraft Conceptual Design, Report, Multidisciplinary Analysis and Design Center for Advanced Vehicles Virginia Polytechnic Institute and State University Blacksburg, Virginia.

[14] **Kapadoukas, G. G. and Self, A.** (2000). A taxonomy of aircraft ground handling modes. *Aircraft Engineering and Aerospace Technology*, **72**, 4, 328–333.

[15] **Pacejka, H. B.** (2004). Tire and Vehicle Dynamics. Butterworth-Heinemann, Oxford.

[16] <*http://www.wisegeek.com/what-are-radial-tires.htm*>, date retrieved March 19 2011

[17] <*http://www.michelinag.com/agx/en-US/products/advantages/bias_radial/ bias_radial.jsp*>, date retrieved March 19 2011

[18] <*http://www-cdr.stanford.edu/dynamic/bywire/tires.pdf*>, date retrieved March 26 2011

[19] **Wood, G., Blundell, M. and Sharma, S.** (2012). A Low Parameter Tire Model for Aircraft Ground Dynamic Simulation, *Materials and Design*, **35**, 820–832.

[20] **Takacs, D. and Stepan, G.** (2009). Experiments on Quasiperiodic Wheel Shimmy, *Journal of Computational and Nonlinear Dynamics*, **4**.

[21] **Maas, J. W. L. H.** (2009). *A Comparison of Dynamic Tire Models for Vehicle Shimmy Stability Analysis* (Dissertation). Eindhoven University of Technology.

[22] **Podgorski, W. A.** (1974). *The Wheel Shimmy Problem, Its Relationship to Longitudinal Tire Forces, Vehicle Motions and Normal Load Oscillations* (Dissertation). Cornell University.

[23] <*http://www.cosin.eu*>, date retrieved March 7, 2012

[24] <*http://www.rmod-k.com*>, date retrieved March 7, 2012

[25] **Cardona, A., Geradin, M. and Doan, D.B.** (1991) Rigid and Flexible Joint Modeling in Multibody Dynamics Using Finite Elements. *Computer Methods in Applied Mechanics and Engineering*, **89**, 395– 418.

[26]<*http://www.boeing.com/companyoffices/gallery/images/commercial/757200-02.html*>, date retrieved March 12, 2012

[27] **Gervais, E. L., Hayhoe, G. F. and Garg, N.** (2003). Towards a permanent ACN solution for 6 wheel landing gear aircraft. *Proceedings of ASCE Airfield Pavements Specialty Conference*, 39–56.

[28] <*http://en.wikipedia.org/wiki/Aircraft_Classification_Number*>, date retreieved May 6 2011

[29]<*http://en.wikipedia.org/wiki/Pavement_Classification_Number*>, date retrieved May 6 2011

[30] **Lindsley, N. J.** (1999). *A New Tire Model for Aircraft Landing Gear Dynamics* (Dissertation). University of Akron.

[31] **Greenland, B. J.** (2007). *Resolution of Indeterminate Landing Gear Structure Design* (Dissertation). Ryerson University.

[32] **Eichberger, A. and Hofmann, G.** (2007). TMPT–Multibody package SIMPACK, *Vehicle System Dynamics*, **45**, 207–216.

[33] **Gualdi, S., Morandini, M. and Ghiringhelli, G. L.** (2008). Anti–skid induced aircraft landing gear instability, *Aerospace Science and Technology*, **12**, 627–637.

[34] <*http://www.vi-grade.com*>, date retrieved March 10, 2012

[35] **Long, S. H.** (2006). *Active Control of Shimmy Oscillation in Aircraft Landing Gear* (Dissertation). Concordia University.

[36] **Wang, H., Xing, J. T., Price, W. G. and Li, W.** (2008). An investigation of an active landing gear system to reduce aircraft vibrations caused by landing impacts and runway excitations, *Journal of Sound and Vibration*, **317**, 50–66.

[37] <*http://www.safranmbd.com/?lang=en*>, date retrieved May 6 2011

[38] <*http://www.dress-project.eu*>, date retrieved May 17 2011

[39] <*http://www.geaviationsystems.com*>, date retrieved May 10 2011

[40] <*http://www.groveaircraft.com*>, date retrieved May 10 2011

[41] <*http://www.vossind.com*>, date retrieved March 10, 2012

[42] **Lernbeiss, R.** (2010). Simulation of the Dynamic Behavior of Aircraft Landing Gear Systems. *SIMPACK News*.

[43] **Nybakken, G. H.** (1973). *Investigation of Tire Parameter Variations in Wheel Shimmy* (Dissertation). University of Michigan.

[44] **Esmailzadeh, E. and Farzaneh, K. A. (**1999). Shimmy Vibration Analysis of Aircraft Landing Gear, *Journal of Vibration and Control*, **5**, 45–56.

[45] **Sura, N. K. and Suryanarayan, S.** (2007). Lateral response of nonlinear nose–wheel landing gear models with torsional freeplay, *Journal of Aircraft*, **44**, 6, 1991–1997.

[46] **Hetreed, C.** Preliminary nose landing gear shimmy analysis using MSC ADAMS Aircraft. *MSC ADAMS North American User Conference*.

[47] **Moreland, W. J. (**1954). The Story of Shimmy, *Journal of the Aeronautical Sciences*, **21**, 12, 793–.

[48] **Zhuravlev, V. P. and Klimov, D. M.** (2009). The causes of the shimmy phenomenon, *Doklady Physics*, **54**, 10, 475–478.

[49] **Stevens, J. E.** (1960). Shimmy of a Nose Gear with Dual Corotating Wheels. 622–.

[50] **Dawei, C., Hongbin, G. and Hao, W.** (2010) Application of magnetorheological damper in landing gear shimmy. *IEEE 3rd International Symposium on Systems and Control in Aeronautics and Astronautics*, China, June 8–10.

[51] **Mikulowski, G. and Holnicki–Szulc, J.** (2004). Adaptive aircraft shock absorbers. *Proceedings of the Third European Conference on Structural Control*, Vienna, July 12–15.

[52] **Sura, N. K. and Suryanarayan, S.** (2009). Lateral stability of aircraft nose–wheel landing gear with closed loop shimmy damper, *Journal of Aircraft*, **46**, 2, 505–509.

[53] **Thota, P., Krauskopf, B. and Lowenberg, M.** (2009). Interaction of torsion and lateral bending in aircraft nose landing gear shimmy, *Nonlinear Dynamics*, **57**, 455–467.

[54] **Thota, P., Krauskopf, B. and Lowenberg, M.** (2010). Bifurcation analysis of nose landing gear shimmy with lateral and longitudinal bending, *Journal of Aircraft*, **47**, 1, 87–95.

[55] **Beery, R. W. and Tsien, V. C.** (1962). Mathematical Analysis of Corotating Nose Gear Shimmy Phenomenon. 1462–.

[56] **Ho, F.H. and Lai, J.L.** (1970). Parametric Shimmy of a Nosegear, *Engineering Notes*, July-August, 373 –.

[57] **Somieski, G.** (1997). Shimmy Analysis of a Simple Aircraft Nose Landing Gear Model Using Different Mathematical Methods, *Aerospace Science and Technology*, 8, 545–555.

[58] **Sura, N. K. and Suryanarayan, S.** (2007). Lateral response of nose–wheel landing gear system to ground induced excitation, *Journal of Aircraft*, **44**, 6, 1998–2005.

[59] **Sura, N. K. and Suryanarayan, S.** (2007). Closed form analytical solution for the shimmy instability of nose wheel landing gears, *Journal of Aircraft*, **44**, 6, 1985–1990.

[60] **Thota, P., Krauskopf, B., Lowenberg, M. and Coetzee, E.** (2010). Influence of tire inflation pressure on nose landing gear shimmy, *Journal of Aircraft*, **47**, 5, 1697–1706.

[61] **Gordon, J. T.** (1977). *A Perturbation Method for Predicting Amplitudes of Nonlinear Wheel Shimmy* (Dissertation). University of Washington.

[62] **Krabacher, W. E.** (1997) A Comparison of the Moreland and von Schlippe-Dietrich Landing Gear Tire Shimmy Models, *Vehicle System Dynamics*, **27**, 335–338.

[63] **Besselink, I. J. M., Schmeitz, A. J. C. and Pacejka, H. B.** (2010). An improved Magic Formula/Swift tire model that can handle inflation pressure changes, *Vehicle System Dynamics*, 48, 337–352.
[64] **Takacs, D., Orosz, G. and Stepan, G.** (2009). Delay effects in shimmy dynamics of wheels with stretched string–like tires, *European Journal of Mechanics A/Solids*, **28**, 516–525.
[65] **Stepan, G.** (1991). Chaotic Motion of Wheels, *Vehicle System Dynamics*, **20**, 6, 341–351.
[66] **Lee, D. Y., Nam, Y. J., Yamane, R. and Park, M. K.** (2009). Performance Evaluation on Vibration Control of MR Landing Gear, *Journal of Physics: Conference Series*, *11th Conference on Electrorheological Fluids and Magnetorheological Suspensions*, **149**.
[67] **Fallah, M. S., Long, S. H., Xie, W. F. and Bhat, R.** (2008) Robust model predictive control of shimmy vibration in aircraft landing gears, *Journal of Aircraft*, **45**, 6, 1872–1880.
[68] **Pouly, G., Huynh, T., Lauffenburger, J. and Basset, M.** (2008). Active Shimmy Damping Using Fuzzy Adaptive Output Feedback Control. *10th International Conference on Control, Automation, Robotics and Vision*, Vietnam, December 17–20.
[69] **Xiaopeng, W., Chi, H. and Meiying, Z.** (2009). Development of Auto Modeling Program Based on ADAMS Macros for Aircraft Landing Gear Dynamic Loads Simulation Analysis. *IEEE Second International Conference on Intelligent Computation Technology and Automation*, China, October 10–11.
[70] **Pompe, V.** (2010). Calculated and Measured Strength of a Composite Aircraft Undercarriage Spar. *Bulletin of Applied Mechanics*, **6**, 21, 12–15.
[71] **Ossa, E. A.** (2006). Failure Analysis of a Civil Aircraft Landing Gear. *Engineering Failure Analysis*, **13**, 1177–1183.
[72] **de Farias Azevedo, C. R. and Hippert Jr., E.** (2002). Fracture of an aircraft's landing gear. *Engineering Failure Analysis*, **9**, 265–275.
[73] **Plakhtienko, N. P. and Shifrin, B. M.** (2002). On Transverse Vibration of Aircraft Landing Gear. *Strength of Materials*, **34**, 6, 584–591.
[74] **Plakhtienko, N. P. and Shifrin, B. M.** (2006). Critical Shimmy Speed of Nonswiveling Landing Gear Wheels Subject to Lateral Loading. *International Applied Mechanics*, **42**, 9, 1077–1084.
[75] **Lopes, L. V.** (2009). *A new approach to complete aircraft landing gear noise prediction* (Dissertation). Pennsylvania State University.
[76] **Imamura, T., Hirai, T. and Amemiya, K.** (2010). Aerodynamic and Aeroacoustic Simulations of a Two–Wheel Landing Gear. *Procedia Engineering, IUTAM Symposium on Computational Aero–Acoustics for Aircraft Noise Prediction,* 293–302.
[77] **Drage, P., Wiesler, B., van Beek, P., van Lier, L., Parchen, R. and Tibaut, P.** (2007). Prediction of noise radiation from basic configurations of landing gears by means of computational aeroacoustics. *Aerospace Science and Technology*, **11**, 451–458.
[78] **Zhu, Q., Wu, X., Gao, S. and Wang, L.** (2007). Modeling of Undercarriage on 6dof Platform in Dynamics Simulation. *IEEE International Conference on Robotics and Biomimetics*, China, December 15–18.

[79] **Wu, X., Zhu, Q., Gao, S. and Wu, G.** (2007). Research on Undercarriage Model Based on 6dof Platform. *IEEE International Conference on Mechatronics and Automation*, China, August 5–8.
[80] **Wen, Z., Zhi, Z., Qidan, Z. and Shiyue, X.** (2008). Dynamics model of carrier–based aircraft landing gears landed on dynamic deck. *Chinese Journal of Aeronautics*, **22**, 371–379.
[81] **Erdem, M.** (1995). *Burun tekerlekli hafif nakliye uçağı iniş takımı ön tasarımı ve boyutlandırılması* (Dissertation). Anadolu Üniversitesi.
[82] **Taplak, H.** (1996). *F–16 burun iniş takımının pist pürüzlülüğüne karşı davranışının analizi* (Dissertation). Erciyes Üniversitesi.
[83] **Gündoğdu, E.** (1996). *İki kişilik hafif askeri uçağı burun iniş takımı* (Dissertation). İstanbul Teknik Üniversitesi.
[84] **Keskin, Z.** (1996). *İki kişilik hafif askeri uçağı ana iniş takımı* (Dissertation). İstanbul Teknik Üniversitesi.
[85] **Altun, C.** (2002). *Uçakların iniş takımları tasarımında dikkat edilecek hususlar* (Dissertation). Eskişehir Osmangazi Üniversitesi.
[86] **Tatçı, Ö. Y.** (2003). *Design and analysis of landing gear of a transport aircraft* (Dissertation). İstanbul Technical University.
[87] **Tugay, B. G.** (2009). *Bir insansız hava aracının kompozit iniş takımının tasarımı, üretimi ve testleri* (Dissertation). İstanbul Teknik Üniversitesi.
[88] **Dimitrijevic, Z., Mortchelewicz, G. D. and Poirion, F.** (2000). Nonlinear dynamics of a two dimensional airfoil with freeplay in an inviscid compressible flow. *Aerospace Science and Technology*, **4**, 125–133.
[89] **Zhao, H., Cao, D. and Zhu, X.** (2010). Aerodynamic flutter and limit cycle analysis for a 2d wing with pitching freeplay in the supersonic flow. *3rd International Symposium on Systems and Control in Aeronautics and Astronautics*, Harbin, China, June 8–10, 1105–1109.
[90] **Arevalo, F. and Garcia–Fogeda, P.** (2010). Aeroelastic characteristics of slender wing/bodies with freeplay nonlinearities. *Proceedings of the Institution of Mechanical Engineers*, *Journal of Aerospace Engineering*, **225**, 347–359.
[91] **Conner, M. D., Tang, D. M., Dowell, E. H. and Virgin, L. N.** (1997). Nonlinear behavior of a typical airfoil section with control surface freeplay: a numerical and experimental study. *Journal of Fluids and Structures*, **11**, 89–109.
[92] **Marsden, C. C. and Price, S. J.** (2005). The aeroelastic response of a wing section with a structural freeplay nonlinearity: An experimental investigation. *Journal of Fluids and Structures*, **21**, 257–276.
[93] **De–Min, Z. and Qi–Chang, Z.** (2010). Bifurcation and chaos analysis for aeroelastic airfoil with freeplay structural nonlinearity in pitch. *Chinese Physics B*, **19**, 3.
[94] **Zenthner, I. and Poirion, F**. (2006). Non–smooth dynamics and stability of mechanical systems featuring a freeplay nonlinearity. *International Journal of Nonlinear Mechanics*, **41**, 796–806.
[95] **Kim, D. and Lee, I.** (2000). Transonic and low–supersonic aeroelastic analysis of a two degree of freedom airfoil with a freeplay nonlinearity. *Journal of Sound and Vibration*, **234**, 5, 859–880.
[96] **Alighanbari, H.** (2002). Aeroelastic response of an airfoil–aileron combination with freeplay in aileron hinge. *Journal of Aircraft*, **39**, 4, 711–713.

[97] **Liu, L. and Dowell, E. H.** (2005). Harmonic Balance Approach for an Airfoil with a Freeplay Control Surface. *AIAA Journal*, **43**, 4, 802–815.

[98] **Park, Y., Yoo, J. and Lee, I.** (2006). Effects of angle of attack on the aeroelastic characteristics of a wing with freeplay. *Journal of Spacecraft and Rockets*, **43**, 6, 1419–1422.

[99] **Ganguli, R., Chopra, I. and Haas, D.** (1998). Simulation of helicopter rotor system structural damage, blade mistracking, friction and freeplay. *Journal of Aircraft*, **35**, 4, 591–597.

[100] **Trickey, S. T.** (2000). *Global and local dynamics of an aeroelastic system with a control surface freeplay nonlinearity* (Dissertation). Duke University.

[101] **Yoo, J., Park, Y., Lee, I. and Han, J.** (2005) Aeroelastic analysis of a wing with freeplay in the subsonic/transonic regions. *JSME International Journal Series B*, **48**, 2, 208–211.

[102] **Zhao, D., Zhang, Q. and Tan, Y.** (2009). Random flutter of a 2 dof nonlinear airfoil in pitch and plunge with freeplay in pitch. *Nonlinear Dynamics*, **58**, 643–654.

[103] **Chung, K. W., Chan, C. L. and Lee, B. H. K.** (2007). Bifurcation analysis of a two degree of freedom aeroelastic system with freeplay structural nonlinearity by a perturbation–incremental method. *Journal of Sound and Vibration*, **299**, 520–539.

[104] **Liu, L., Wong, Y. S. and Lee, B. H. K.** (2002) Nonlinear aeroelastic analysis using the point transformation method, part 1: freeplay model. *Journal of Sound and Vibration*, **253**, 2, 447–469.

[105] **Liu, L., Wong, Y. S. and Lee, B. H. K.** (2002) Nonlinear aeroelastic analysis using the point transformation method, part 2: hysteresis model. *Journal of Sound and Vibration*, **253**, 2, 471–483.

[106] **Dimitriadis, G.** (2008). Bifurcation analysis of aircraft with structural nonlinearity and freeplay using numerical continuation. *Journal of Aircraft*, **45**, 3, 893–905.

[107] **Tang, D. and Dowell, E. H.** (2006). Flutter and limit cycle oscillations for a wing store model with freeplay. *Journal of Aircraft*, **43**, 2, 487–503.

[108] **Tang, D. and Dowell, E. H.** (2006). Experimental and theoretical study of gust response for a wing–store model with freeplay. *Journal of Sound and Vibration*, 295, 659–684.

[109] **Guglielmino, E., Sireteanu, T., Stammers, C. W., Ghita, G. and Giuclea, M.** (2008). Semi–active Suspension Control, Springer–Verlag, London.

[110] <*http://en.wikipedia.org/wiki/Magnetorheological_damper*> date retrieved May 17 2011

[111] <*http://en.wikipedia.org/wiki/Magnetorheological_fluid*> date retrieved May 17 2011

[112] **Richards, R.** (2007). *Comparison of linear, nonlinear, hysteretic and probabilistic MR damper models* (Dissertation). Virginia Polytechnic Institute and State University.

[113] **Sakai, C., Ohmori, H. and Sano, A.** (2003) Modeling of MR damper with hysteresis for adaptive vibration control. *Proceedings of the 42nd IEEE Conference on Decision and Control*, Maui, Hawaii, December.

[114] **Dyke, S. J., Spencer, B. F., Sain, M. K. and Carlson, J. D.** (1996). Modeling and control of magnetorheological dampers for seismic response

reduction.
<*intranet.dei.polimi.it/users/Luigi.Piroddi/MRD/DykeSpencer96c.pdf*> date retrieved February 22, 2012.

[115] **Spencer, B. F., Carlson, J. D., Sain, M. K. and Yang, G.** (1997). On the current status of magnetorheological dampers–seismic protection of full scale structures. *Proceedings of the American Control Conference*, New Mexico, June.

[116] **Yang, G., Spencer, B. F., Carlson, J. D. and Sain, M. K.** (2002). Large scale MR fluid dampers–modeling and dynamic performance considerations. *Engineering Structures*, **24**, 309–323.

[117] **Yang, G., Spencer, B. F., Jung, H. and Carlson, J. D.** (2004). Dynamic modeling of large scale magnetorheological damper systems for civil engineering applications. *ASCE Journal of Engineering Mechanics*, September, 1107–1115.

[118] <*http://en.wikipedia.org/wiki/Magnetorheological_damper*> date retrieved February 22 12.

[119] **Yao, G. Z., Yap, F. F., Chen, G., Li, W. H. and Yeo, S. H.** (2002). MR damper and its application for semi–active control of vehicle suspension system. *Mechatronics*, **2**, 963–973.

[120] **Lee, D. Y., Nam, Y. J., Yamane, R., Park and M. K.** (2009). Performance Evaluation on Vibration Control of MR landing gear. *11th Conference on Electrorheological Fluids and Magnetorheological Suspensions, Journal of Physics: Conference Series*, **143**, 1–6.

[121] **Ashfak, A., Saheed, A., Abdul Rasheed, K. K. and Abdul Jaleel, J.** (2011). Design, fabrication and evaluation of MR damper. *International Journal of Aerospace and Mechanical Engineering*, **5**, 1, 27–32.

[122] **Xue, X., Sun, Q., Zhang, L., Wu, X. and Zhang, L.** (2010). Parameter identification of simplified Bouc–Wen model for a MR damper using efficient GA. *International Journal of Applied Electromagnetics and Mechanics*, **33**, 175–181.

[123] **Rosenfeld, N. C. and Wereley N. M.** (2004). Volume constrained optimization of magnetorheological and electrorheological valves and dampers. *Institute of Physics Publishing, Smart Materials and Structures*, **13**, 1303–1313.

[124] **Dominguez, A., Sedaghati, R. and Stiharu, I.** (2006). A new dynamic hysteresis model for magnetorheological dampers. *Institute of Physics Publishing, Smart Materials and Structures*, **15**, 1179–1189.

[125] **Wang, D. H. and Liao, W. H.** (2011). Magnetorheological fluid dampers–a review of parametric modeling. *Smart Materials and Structures*, **20**, 1–34.

[126] **Kuzhir, P., Bossis, G. and Bashtovoi, V.** (2005). Optimization of magnetorheological fluid valves. *International Journal of Modern Physics B*, **19**, 7, 8 and 9, 1229–1235.

[127] **Xiaomin, X., Qing, S., Ling, Z. and Bin, Z.** (2009). Parameter estimation and its sensitivity analysis of the MR damper hysteresis model using a modified genetic algorithm. *Journal of Intelligent Material Systems and Structures*, **20**, 2089–2100.

[128] **Ahn, K. K., Islam, M. A. and Truong, D. Q.** (2008). Hysteresis modeling of magnetorheological fluid damper by self–tuning fuzzy control.

International Conference on Control, Automation and Systems, Seoul, October 14–17.

[129] **Wang, E. R., Ma, X. Q., Rakhela, S. and Su, C. Y.** (2003). Modeling the hysteretic characteristics of a magnetorheological fluid damper. *Proceedings of the Instn Mech. Engrs, Part: D, Journal of Automobile Engineering*, **217**, 537–550.

[130] **Lozoya–Santos, J., Aubouet, S., Morales–Menendez, R., Sename, O., Ramirez–Mendoza, R. A. and Dugard, L.** (2010). Hysteresis modeling for a MR damper. *7th EUROSIM Congress on Modeling and Simulation*, Prague.

[131] **Symens, W., Al–Bender, F., Swevers, J. and van Brussel, H.** (2002). Dynamic characterization of hysteresis elements in mechanical systems. *Proceeding of the American Control Conference*, Anchorage, May 8–10.

[132] **Al–Bender, F., Symens, W., Swevers, J. and van Brussel, H.** (2004). Theoretical analysis of the dynamic behavior of hysteresis elements in mechanical systems. *International Journal of Nonlinear Mechanics*, **39**, 1721–1735.

[133] **Sateesh, B. and Maiti, D. K.** (2009). The analysis of shimmy instability of a typical nose landing gear using active torsional magnetorheological damper. *Proc. IMEch Part: G Journal of Aerospace Engineering*, **223**, 201–216.

[134] **Park, E. J., da Luz, L. F. and Suleman, A.** (2007). Multidisciplinary design optimization of an automotive magnetorheological brake design. *Computers and Structures*, **86**, 207–216.

[135] **Park, E. J., Stoikov, D., da Luz, L. F. and Suleman, A.** (2006). A performance evaluation of an automotive magnetorheological brake design with a sliding mode controller. *Mechatronics*, **16**, 405–416.

[136] **Vavreck, A. N. and Ho, C.** (2005). Characterization of a commercial magnetorheological brake/damper in oscillatory motion. *Smart Structures and Materials, Proceedings of SPIE*, **5760**, 256–267.

[137] **Engin, T., Şahin, İ., Soydan, Y., Morgül, Ö. K., Fırat, M., Öz, R., Çeşmeci, Ş., Yazıcı, İ. and Parlak, Z.** (2012). Design, fabrication and optimization of a new–generation semi–active suspension system, TÜBİTAK Project.

[138] **Sung, K., Choi, S. and Park, M.** (2011). Geometry optimizaiton of magnetorheological damper for vehicle suspension via finite element method. *Advanced Science Letters*, **4**, 805–809.

[139] **Erol, O. and Gurocak, H.** (2011). Interactive design optimizaiton of magnetorheological brake actuators using the Taguchi method. *Smart Materials and Structures*, **20**, 1–12.

[140] **Strogatz, S. H.** (2000). Nonlinear Dynamics and Chaos. Westview Press, USA.

[141] **Kreyszig, E.** (1999). Advanced Engineering Mathematics. John Wiley and Sons, USA.

APPENDICES

Appendix A: Lorenz Attractor
Appendix B: Limit Cycle
Appendix C: Van der Pol's Equation
Appendix D: Balance, Skyhook and Groundhook Algorithms
Appendix E: Optimal Values of the Parameters Involved in the MR Damper

Appendix A: Lorenz Attractor

Lorenz equations, derived from a simplified model of convection in the atmosphere, arising in models of lasers and dynamos, are [140]

$$\dot{x}_1 = \sigma(x_2 - x_1) \tag{A.1}$$

$$\dot{x}_2 = rx_1 - x_2 - x_1x_3 \tag{A.2}$$

$$\dot{x}_3 = x_1x_2 - bx_3 \tag{A.3}$$

where $\sigma > 0$ is the Prandtl number, $r > 0$ is the Rayleigh number and $b > 0$ is related to the aspect ratio in convection problems. It has been discovered that this simple–looking system can have unpredictable behavior. Solutions oscillate irregularly, never exactly repeating themselves, while remaining in a bounded region of the phase space. Lorenz showed that for a certain range of parameters, there are no stable fixed points and no stable limit cycles, while he also proved that all trajectories are confined in a bounded region and are eventually attracted to a limiting set called a strange attractor. The attractor exhibits sensitive dependence on initial conditions, meaning two trajectories starting out close to each other will rapidly diverge and have totally different futures. In practice, long–term prediction of such systems is impossible since small uncertainties are amplified. Although no definition of chaos is universally accepted, it can be said that chaos is aperiodic long–term behavior in a deterministic system exhibiting sensitive dependence on initial conditions [140].

Runge–Kutta algorithm has been employed to obtain figures A.1–A.5. Figure A.1 shows the three dimensional phase diagram of the Lorenz system for $\sigma = 10$, $r = 28$ and $b = 8/3$ and the initial conditions $(0,1,0)$. Figures A.2 and A.3 give the time histories of $x_2(t)$ and $z(t)$, respectively. It can be seen that the solution settles into an irregular oscillation after an initial transient. Superiority of the Runge–Kutta method over both Euler and improved Euler methods can be seen when compared with the results given in [140]. An inspection of figure A.4 reveals that the trajectory crosses itself repeatedly when $x(t)$ is plotted against $z(t)$. This happens only because the three–dimensional trajectory is projected onto a two–dimensional plane. No self– intersections occur in three dimensions. When figure A.4 is viewed in detail, it is seen that the trajectory spirals out on right and left sides indefinitely and the number of circuits on either side varies unpredictably from one cycle to the next in random sequence. Similarly, $z(t)$ is plotted against $y(t)$ in figure A.5.

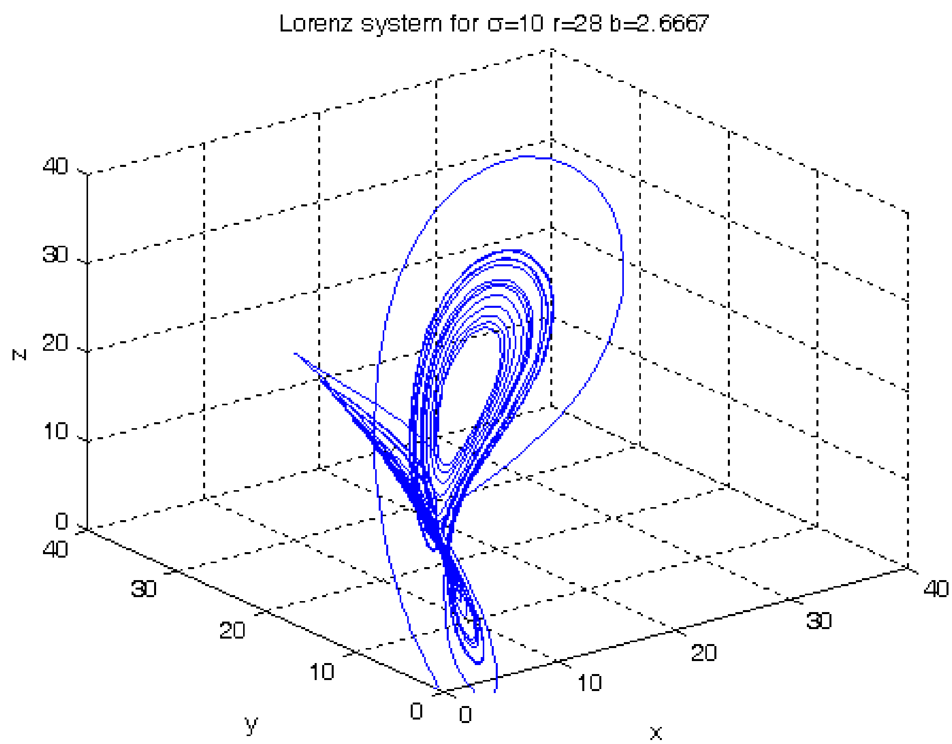

Figure A.1: Three–dimensional phase diagram of the Lorenz system.

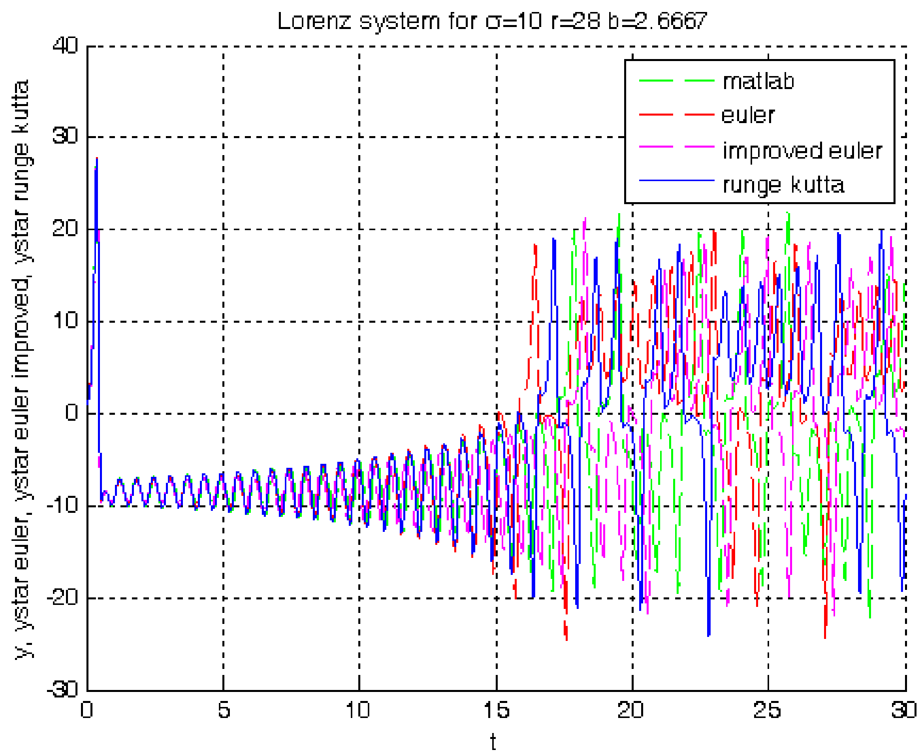

Figure A.2: Time history of $y(t)$.

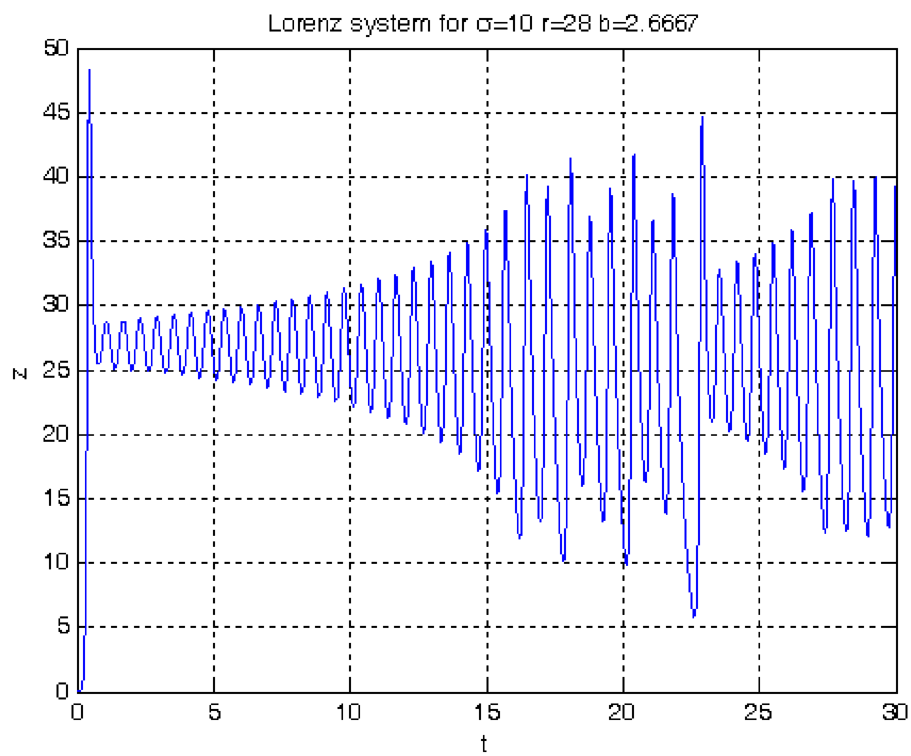

Figure A.3: Time history of $z(t)$.

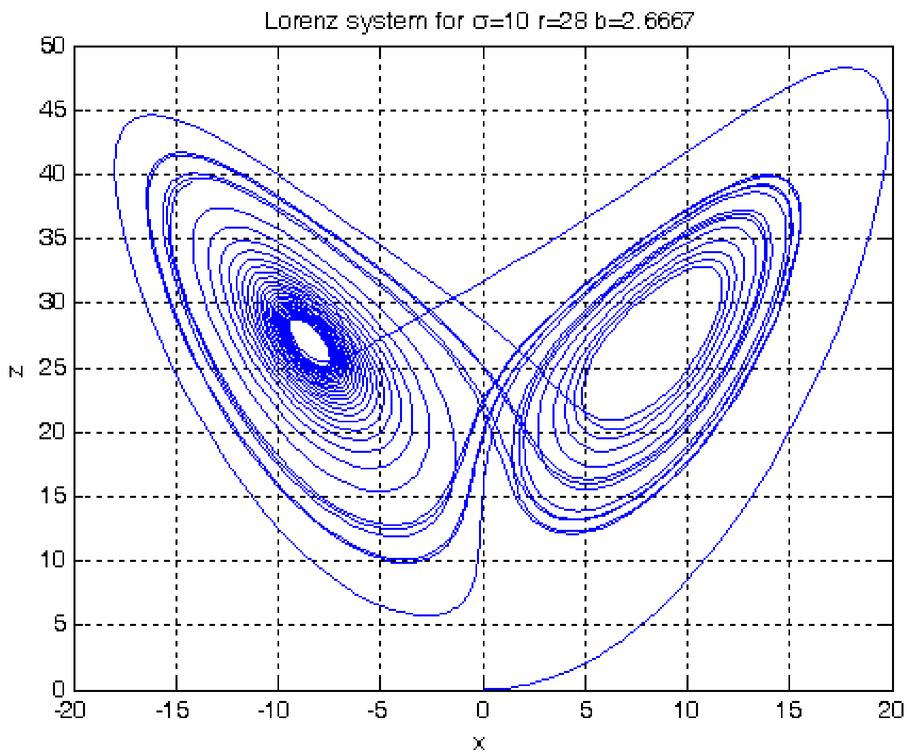

Figure A.4: $x(t)$ vs $z(t)$.

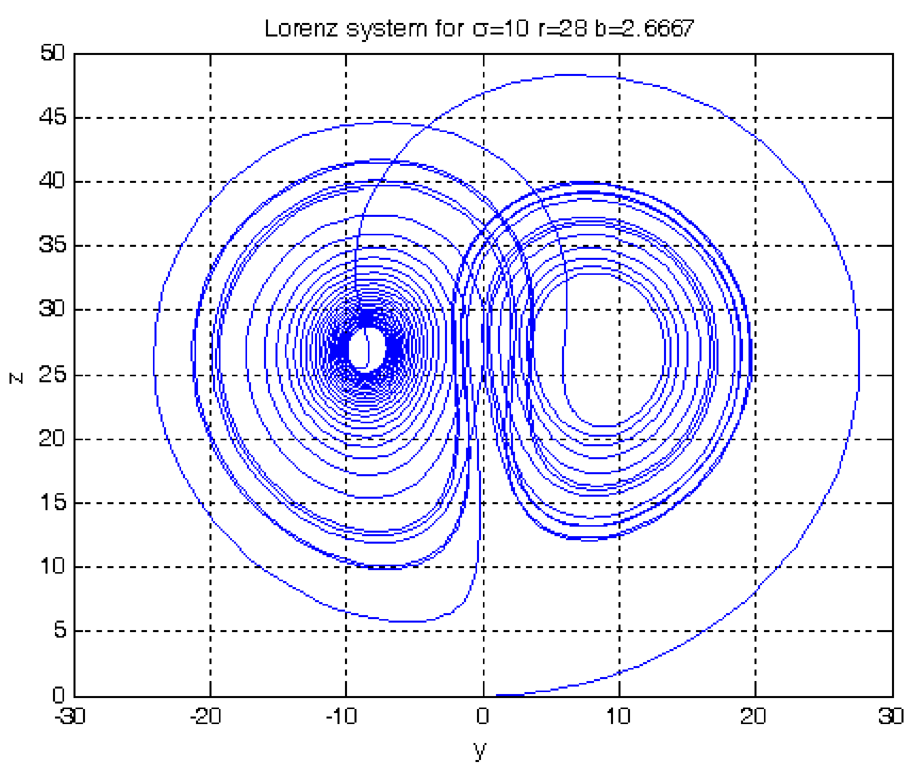

Figure A.5: $y(t)$ vs $z(t)$.

Appendix B: Limit Cycle

A limit cycle is an isolated closed trajectory, meaning neighboring trajectories spiral either towards or away from the limit cycle. If neighboring trajectories approach the limit cycle, the limit cycle is called stable, otherwise it is called unstable. Stable limit cycles represent systems exhibiting self–sustained oscillations. Limit cycles are nonlinear phenomena, which means they occur only in nonlinear systems. Examples of such systems that oscillate even in the absence of an external periodic forcing are the beating of the heart and self–excited vibrations in airplane wings. The connection between the system and the limit cycle is that the system always returns to the limit cycle after a slight perturbation. In simple terms, limit cycles are periodic oscillations of nonlinear systems [140,141].

A system governed by the differential equations

$$\dot{x}_1 = r - x_1 - \frac{4x_1 x_2}{1 + x_1^2} \tag{B.1}$$

$$\dot{x}_2 = s x_1 \frac{1 - x_2}{1 + x_1^2} \tag{B.2}$$

can have either of the two following phase portraits depending on the constants r and s. In figures B.1 and B.2, all trajectories spiral into a fixed point, whereas in figures B.3 and B.4, they are attracted to a limit cycle. Comparison of the results of using matlab ode45 function, Euler method, improved Euler method and Runge–Kutta method can be seen in figures B.1 and B.3.

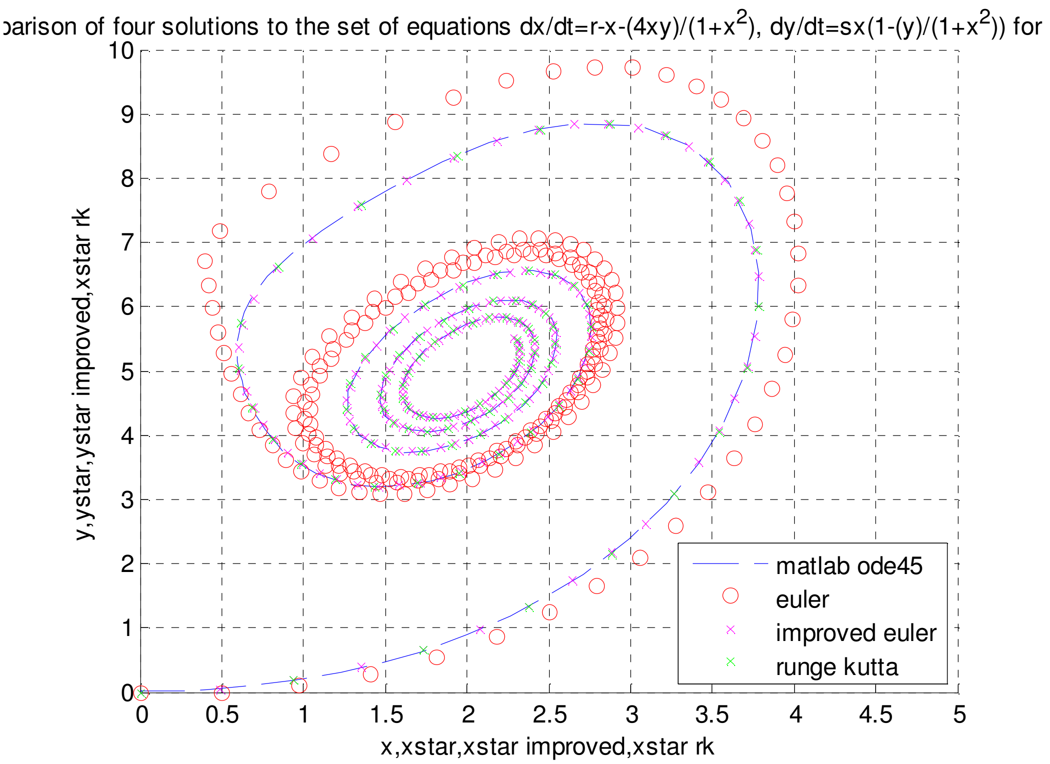

Figure B.1: Comparison of four solutions.

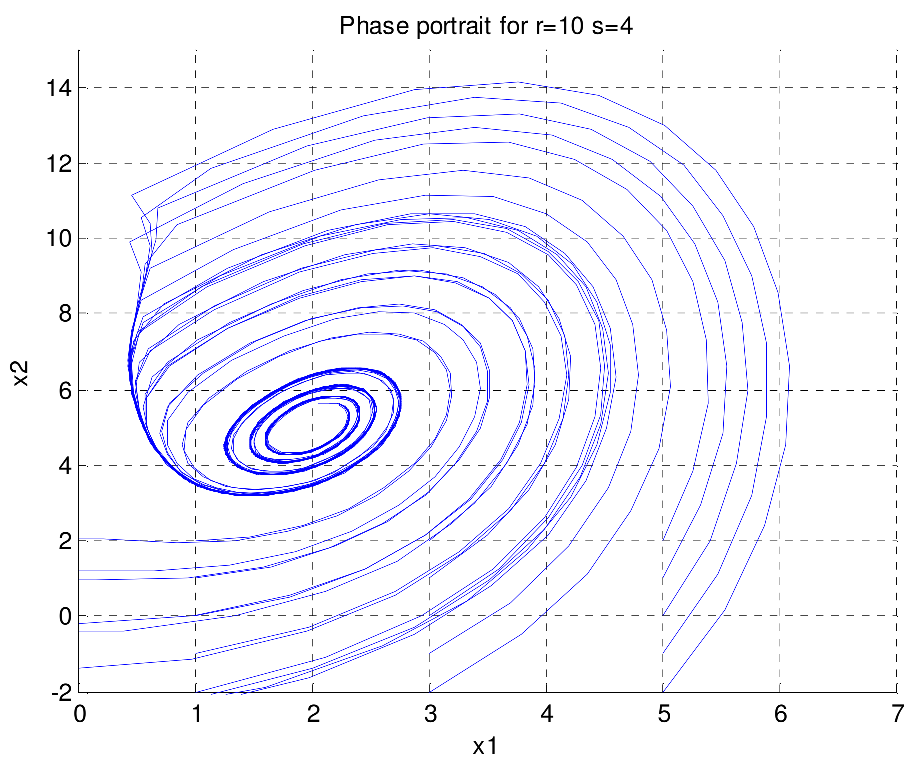

Figure B.2: Stable fixed point.

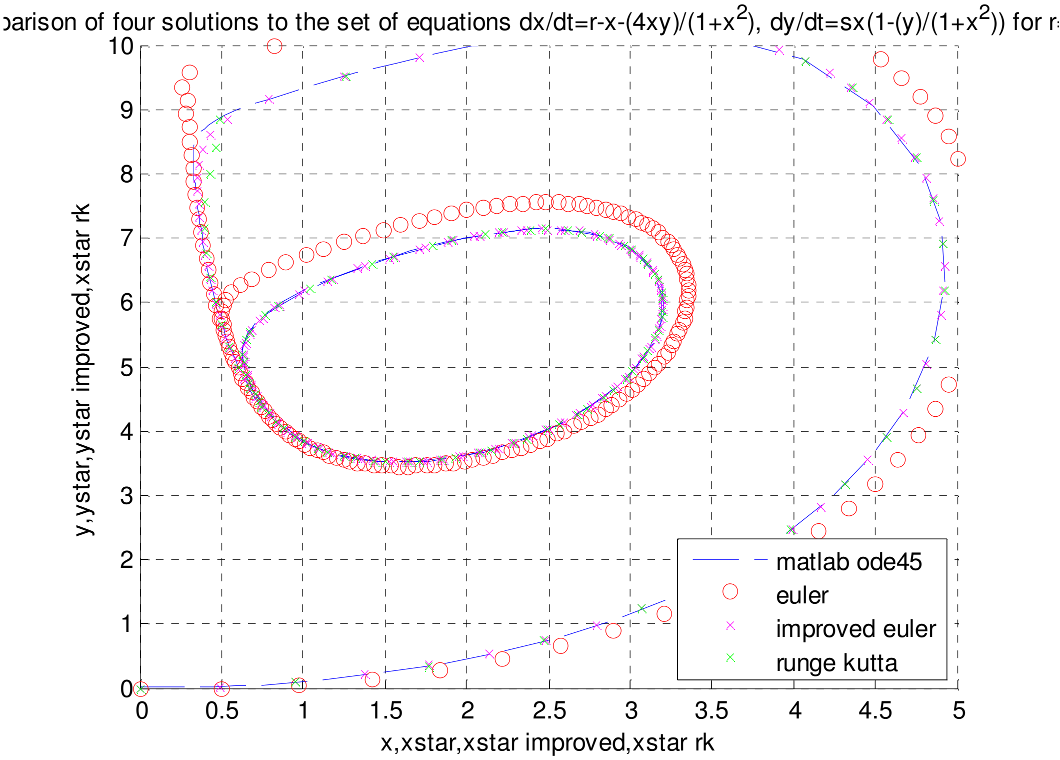

Figure B.3: Limit cycle.

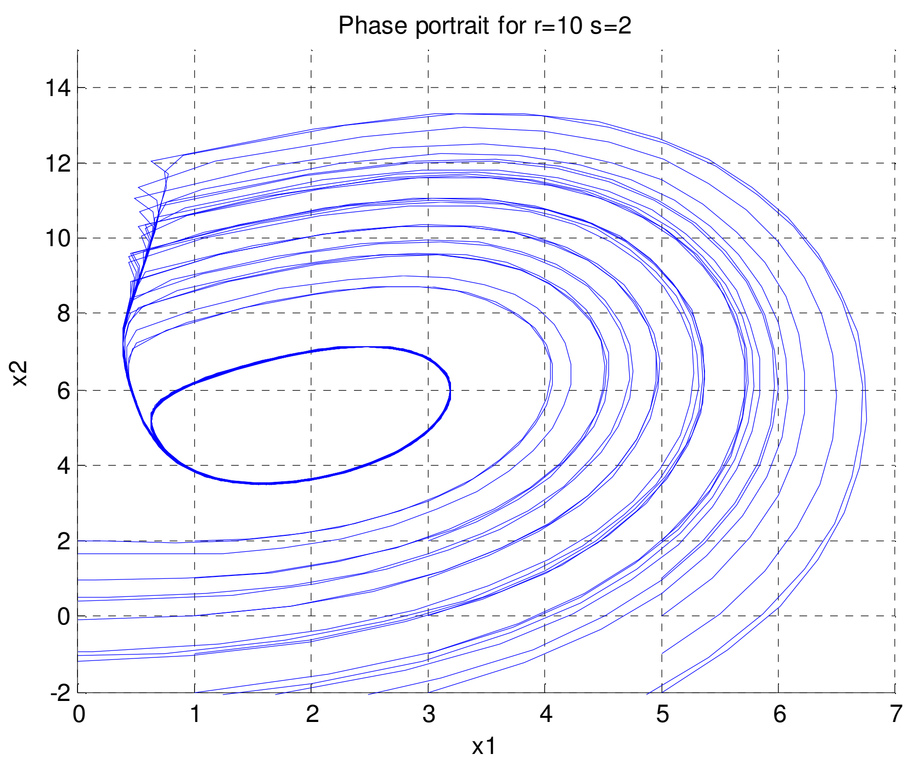

Figure B.4: Limit cycle.

Appendix C: Van der Pol's Equation

Some physical systems are such that energy is fed into the system for small oscillations and taken from the system for large oscillations, meaning large oscillations will be damped while there is negative damping for small oscillations. Such a system approaches a periodic behavior appearing as a closed trajectory in the phase plane, called a limit cycle [141]. A differential equation exhibiting such behavior is the van der Pol equation

$$\ddot{x} - \mu\left(1 - x^2\right)\dot{x} + x = 0 \tag{C.1}$$

where μ is a constant. Displacement and phase diagrams of the van der Pol oscillator for $\mu = 0$, $\mu = 0.1$ and $\mu = 1$ are given in figures C.1–C.6. For $\mu = 0$, the equation becomes $\ddot{x} + x = 0$, the equation of a simple harmonic oscillator, as seen in figures C.1 and C.2 . For $\mu > 0$ however, the damping term $-\mu\left(1 - x^2\right)$ is negative for small oscillations where $y^2 < 1$, meaning there is negative damping, is zero for $y^2 = 1$ and is positive if $y^2 > 1$, meaning there is positive damping and loss of energy. For small μ, the limit cycle is almost circular, as in figure C.4, because the equation differs only a little from $\ddot{x} + x = 0$. For larger μ, the limit cycle no longer resembles a circle, as figure C.6 shows. Trajectories approach the limit cycle is more rapidly for $\mu = 1$ than for $\mu = 0.1$.

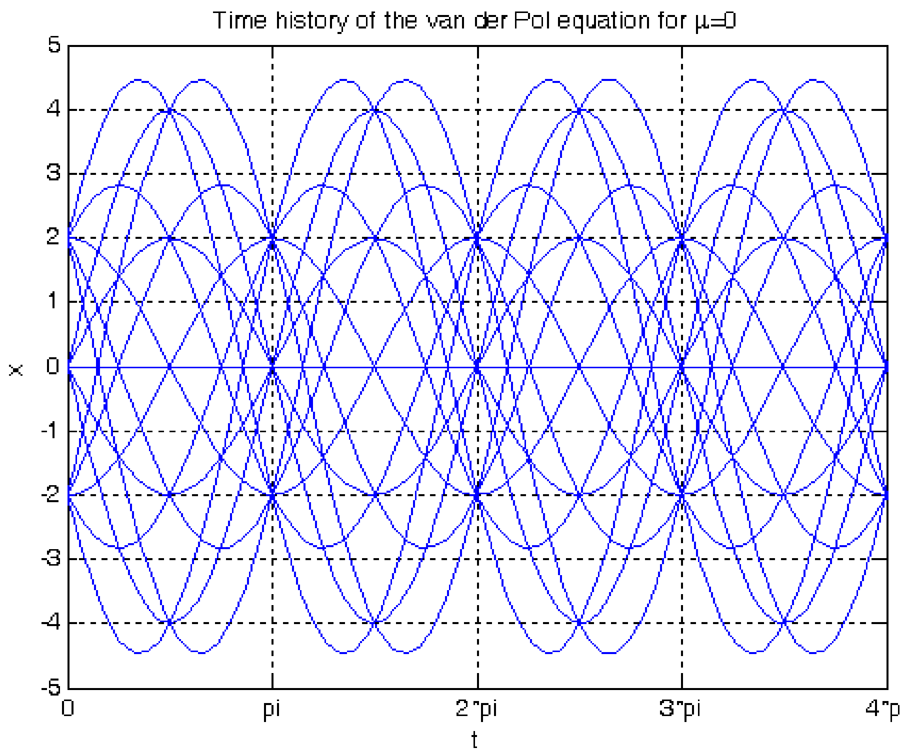

Figure C.1: Time history of the van der Pol oscillator for $\mu = 0$.

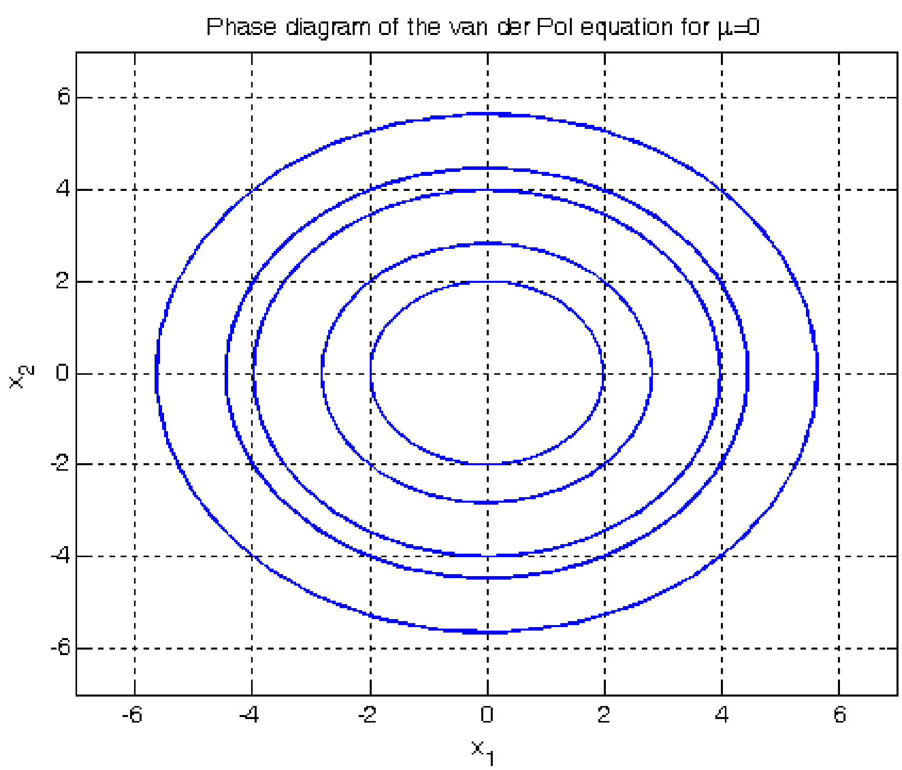

Figure C.2: Phase diagram of the van der Pol oscillator for $\mu = 0$.

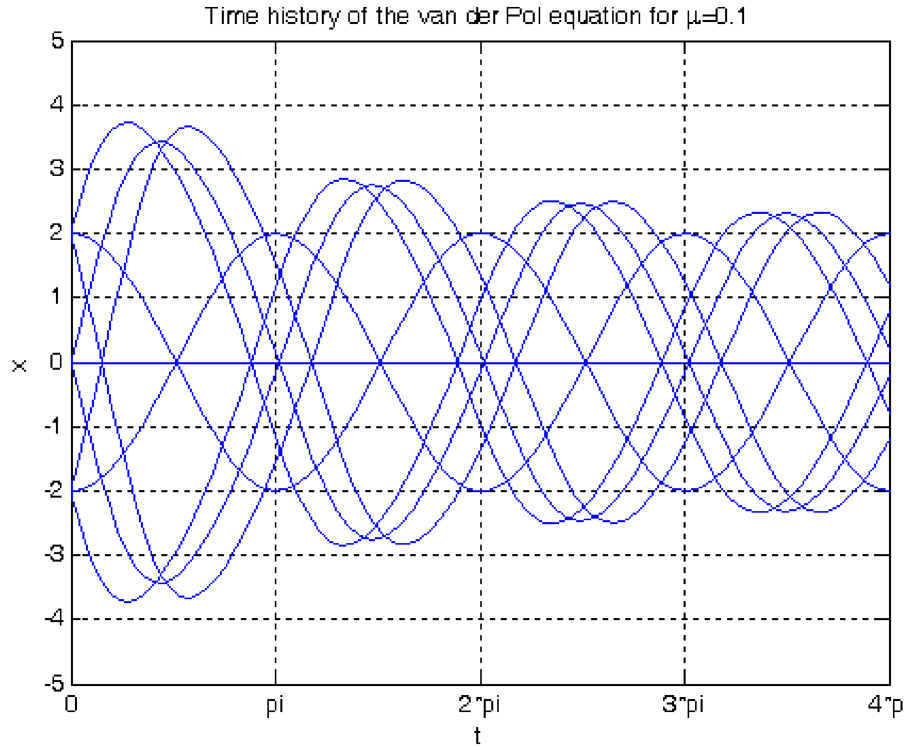

Figure C.3: Time history of the van der Pol oscillator for $\mu = 0.1$.

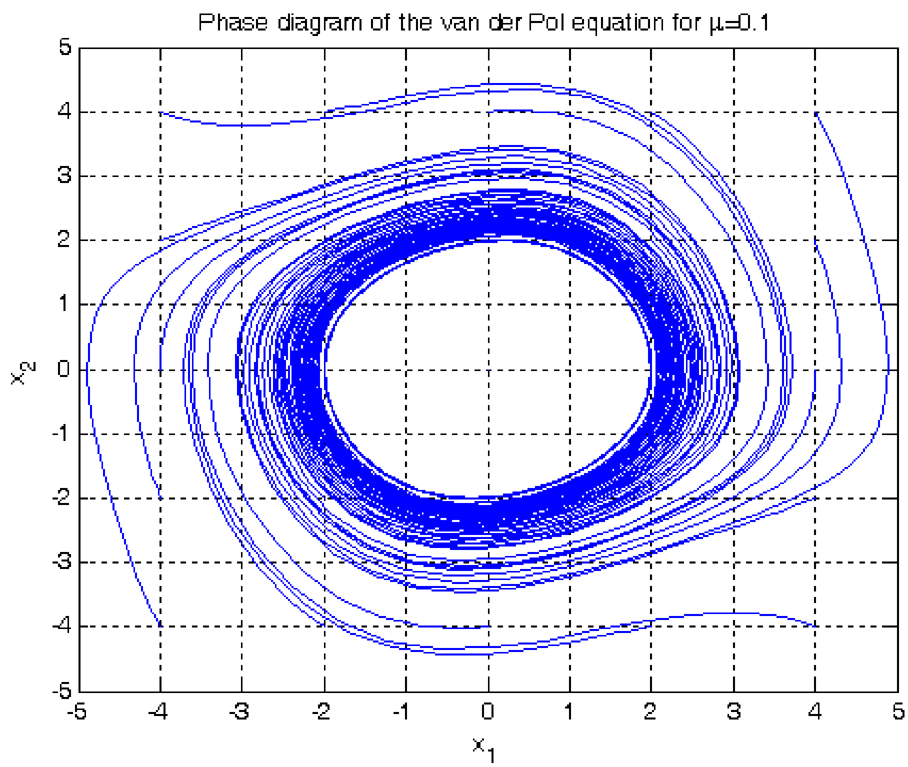

Figure C.4: Phase diagram of the van der Pol oscillator for $\mu = 0.1$.

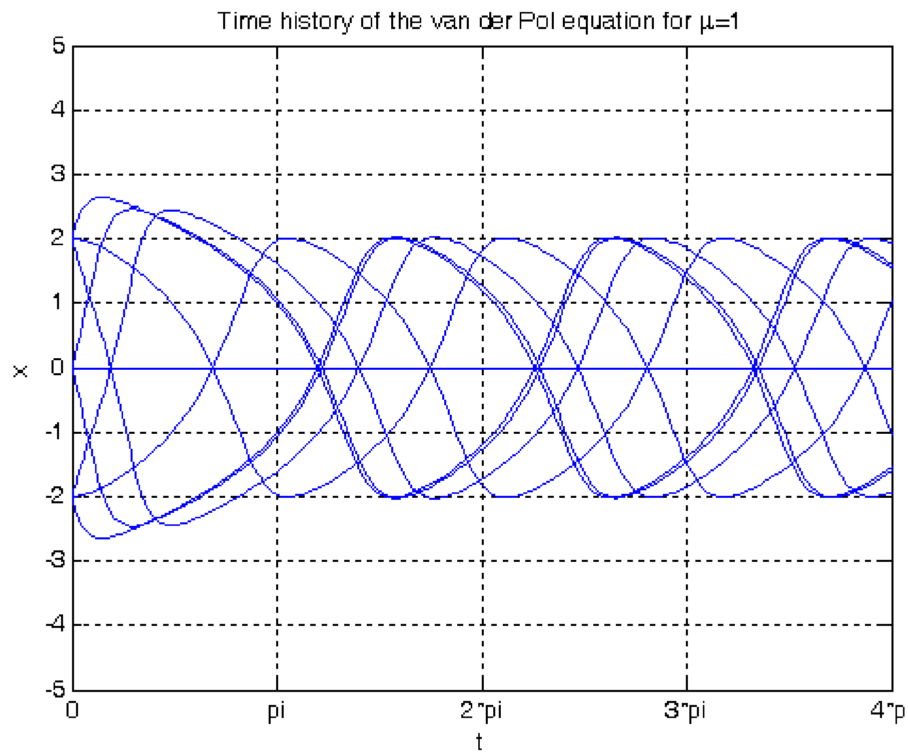

Figure C.5: Time history of the van der Pol oscillator for $\mu = 1$.

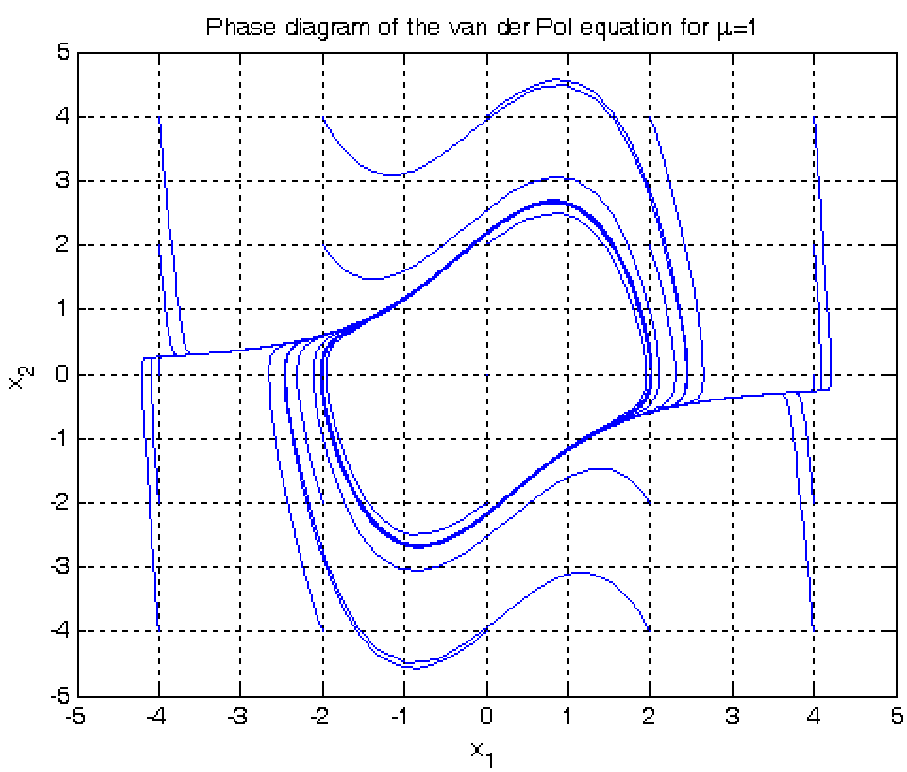

Figure C.6: Phase diagram of the van der Pol oscillator for $\mu = 1$.

Appendix D: Balance, Skyhook and Groundhook Algorithms

Semi–active suspension control algorithms are centered around balance, skyhook and groundhook algorithms [109].

Balance logic is applied in automotive engineering and aims at reducing chassis acceleration by modulating the damping force sequentially as

$$F_d = \begin{cases} k|x| \operatorname{sgn} \dot{x} & x\dot{x} \le 0 \\ 0 & x\dot{x} > 0 \end{cases} \quad \textbf{(D.1)}$$

where x is the relative displacement and $\dot{x}$ is the relative velocity across the damper.

Skyhook method is one of the most commonly used control methods for MR dampers as it is a straightforward and effective approach to improve ride comfort in vehicles with active suspensions [112,119,120,109]. The damper is regarded as being hooked to a fixed point in the sky. It uses a switching technique where the damper is either fully soft or fully stiff, depending on the velocity of the body and the relative velocity of the damper. Mathematically, the desired damping force is

$$F_d = \begin{cases} G\,\dot{x}_1 & \dot{x}\,\dot{x}_1 > 0 \\ 0 & \dot{x}\,\dot{x}_1 \le 0 \end{cases} \quad \textbf{(D.2)}$$

where G is the Skyhook gain, $\dot{x}_1$ is the velocity of the sprung mass and $\dot{x}$ is the damper velocity, in other words, the difference between the velocities of the sprung and unsprung masses. The idea is that when the velocity of the sprung mass and relative velocity of the damper are in the same direction, the damper will be at its maximum damping characteristics; when the velocities are in opposite directions, the damper will be at its minimum damping. In other words, when the velocity of the sprung mass is in the same direction as the relative velocity between the sprung mass and unsprung mass, an electric current is applied to the MR damper and no damping force is required otherwise. Since it is impossible for an MR damper to provide a zero force [119], semi–active damping force should be minimized without any electric current as

$$F_d = \begin{cases} f_{\max} & \dot{x}_2(\dot{x}_2 - \dot{x}_1) > 0 \\ f_{\min} & \dot{x}_2(\dot{x}_2 - \dot{x}_1) < 0 \end{cases} \quad \textbf{(D.3)}$$

where $\dot{x}_1$ is the velocity of the unsprung mass and $\dot{x}_2$ is the velocity of the sprung mass.

Groundhook logic aims at reducing the dynamic tire force and thereby improving handling and reducing road damage. Groundhook damper is assumed to be hooked to a fixed point on the ground. It is used in automotive applications and its formulation will not be included here.

Appendix E: Optimal Values of the Parameters Involved in the MR Damper

Parameters involved in the current–dependent Bouc–Wen model are optimized using genetic algorithms. These parameters are $[c_1, c_2, c_3, k_1, k_2, \alpha_1, \alpha_2, \alpha_3, \gamma_1, \gamma_2, F_{zo1}, F_{zo2}, F_{zo3}]$

Their optimal values are

k_1 =0.0952
k_2 =1.4941
c_1 =1.47
c_2 =–0.79
c_3 =–7
α_1 =0.7
α_2 =2.44
α_3 =0.08
γ_1 =2
γ_2 =1
F_{zo1} =997
F_{zo2} =1002
F_{zo3} =1005

CURRICULUM VITAE

Name Surname: Elmas ATABAY

Place and Date of Birth: Üsküdar, 1981

Address: Istanbul Technical University

Department of Aeronautical Engineering

34469, Maslak, Istanbul

E-Mail: anli@itu.edu.tr

B.Sc.: Istanbul Technical University,

Department of Astronautical Engineering

M.Sc.: Istanbul Technical University,

Aeronautical and Astronautical Engineering

Professional Experience and Rewards:

Research Assistant (Istanbul Technical University)

TÜBİTAK Ph.D. Scholarship

List of Publications:

Journal Articles

International

Baykuş, B., **Anlı, E.**, Özkol, İ., 2011: "Design and Kinematics Analysis of a Parallel Mechanism to be Utilized as a Luggage Door by an Analogy to a Four Bar Mechanism". Engineering, 3(4), 411–421.

Anlı, E., Özkol, İ., 2010 : "Classical and Fractional Order Analysis of the Free and Forced Double Pendulum". Engineering, 2(12), 935–949.

Yurt, S. N., **Anlı, E.**, Özkol, İ., 2007: "Forward Kinematics Analysis of the 6-3 SPM by Using Neural Networks". Meccanica, 42(2), 187–196.

Alp, H., **Anlı, E.**, Özkol, İ., 2007: "Neural Network Algorithm for Workspace Analysis of a Parallel Mechanism". Aircraft Engineering and Aerospace Technology, 79(1), 35–44.

Alp, H., **Anlı, E.**, Yurt S.N., Özkol, İ., 2004: "Workspace Analysis of the 6-4 Stewart Platform Mechanism". Transactions on Engineering, Computing and Technology 2, Enformatika v2 issn 1305-5313, 6–9.

Anlı, E., Alp, H., Yurt S.N., Özkol, İ., 2004: "The Stewart Platform Mechanism–A Review". Transactions on Engineering, Computing and Technology 2, Enformatika v2 issn 1305-5313, 106–109.

National

Anlı Ak, E., Akhisar, İ., 2010: "Forecasting of the Gross Domestic Product in Turkey Via Neural Networks Using Macroeconomic Factors". İstanbul Aydın Üniversitesi Fen Bilimleri Dergisi, 1 (1), 31–42.

Anlı, E., Alp, H., Yurt, S. N., Özkol, İ., 2005: "Paralel Mekanizmaların Kinematiği, Dinamiği ve Çalışma Uzayı". Hava Harp Okulu Havacılık ve Uzay Teknolojileri Dergisi, 2(1), 19–36.

Conference Proceedings

International

Dinç, M., **Anlı, E.**, Hajiyev, C., Özkol, İ., 2011: "Development of Integrated INS/GPS Navigation System for Unmanned Air Vehicle Based on Kalman Filtering Technique". Recent Advances in Space Technologies, İstanbul, 9–11 Haziran.

Anlı Ak, E., Özkol, İ., 2009: "Fractional Order Dynamics of the Horizontally and Vertically Forced Triple Pendulum". Eccomas Thematic Conference on Multibody Dynamics, Varşova, 29 Haziran–2 Temmuz.

Anlı, E., Yurt, S. N., Özkol, İ., 2005: "Forward Kinematics Analysis of a Purely Rotational Parallel Mechanism by Using Neural Networks". Eurogen Evolutionary and Deterministic Methods for Design, Optimization and Control with Applications to Industrial and Societal Problems, Münih, 12–14 Eylül.

Anlı, E., Yurt, S. N., Özkol, İ., 2005: "Error Analysis of the Purely Translational Motion of a Parallel Mechanism by Using Neural Networks". Ankara International Aerospace Conference, Ankara, 22–25 Ağustos.

Anlı, E., Alp, H., Yurt, S. N., Özkol, İ., 2004: "The Stewart Platform Mechanism–A Review". International Conference on Signal Processing, İstanbul, 106-109, 17–19 Aralık.

Alp, H., **Anlı, E.**, Yurt, S. N., Özkol, İ., 2004: "Workspace Analysis of the 6–4 Stewart Platform Mechanism". International Conference on Signal Processing, İstanbul, 6-9, 17–19 Aralık.

National

Baykuş, B., Uyar, Ö., **Anlı Ak, E.**, Özkol, İ., 2010: "Bagaj Kapağı Mekanizması Tasarımı ve Tasarımın 4-çubuk Mekanizma Sistemi ile Kinematik Analizi". 5. Otomotiv Teknolojileri Kongresi, Bursa, 7–8 Haziran.

Baykuş, B., **Anlı, E.**, Özkol, İ., 2006: "Euler ve Timoshenko tipi Kirişlerin Çeşitli Sınır Şartları Altındaki Davranışının Dalga İlerleme Yöntemi ile Analizi". Kayseri 6. Havacılık Sempozyumu, 12–14 Mayıs.

Anlı, E., Yurt, S. N., Özkol, İ., 2005: "Havacılıkta Uçuş Simülatörleri". Ulusal Havacılık Sempozyumu ve Çalıştayı, İstanbul, 9–10 Temmuz.

Anlı, E., Yurt, S. N., Özkol, İ., 2005: "Using Neural Networks In Solving The Forward Kinematics of a Purely Rotational and a Purely Translational Parallel Mechanism". Turkish Symposium on Artificial Intelligence and Neural Networks, İzmir, 16–17 Haziran.

Anlı, E., Yurt, S. N., Özkol, İ., 2005: "6–3 Stewart Platform Mekanizmasının Düz Kinematiğinin Yapay Sinir Ağlarıyla Çözülmesi". Otomatik Kontrol Ulusal Toplantısı, İstanbul, 2–3 Haziran.

Anlı, E., Alp, H., Yurt, S. N., Özkol, İ., 2004: "Uçuş Simülatörü Olarak Paralel Mekanizmalar". Havacılıkta İleri Teknolojiler ve Uygulamaları Sempozyumu, İstanbul, 343–350, 9–10 Aralık.

PUBLICATIONS/PRESENTATIONS ON THE THESIS

Atabay, E., Özkol, İ., 2012: Stability analysis of a landing gear mechanism with torsional degree of freedom. *Global Journal of Researches in Engineering, Aerospace Engineering,* 12(1), 17–27.

Atabay, E., Özkol, İ., 2012: On dynamics of a landing gear mechanism with torsional freeplay. *Global Journal of Researches in Engineering, Aerospace Engineering,* 12(1), 17–27.

Atabay, E., Özkol, İ., 2012: Application of an MR damper modeled using the current–dependent Bouc–Wen model for shimmy suppression in a nose landing gear having torsional degree of freedom with and without freeplay, *Joırnal of Vibration and Control*, (awaiting reviewer scores)

Atabay, E., Özkol, İ., 2012: Bir uçak burun iniş takımı mekanizmasının dinamik analizi üzerine, *İTÜ Dergisi.*